# Geology of the Kapit NE and Coastal Ore Zones, Lihir Gold Deposit, Papua New Guinea

**Erin Lawlis**
**B.Sc. (Hons.)**

Submitted in fulfilment of the requirements for the degree of
Doctor of Philosophy

February 2020

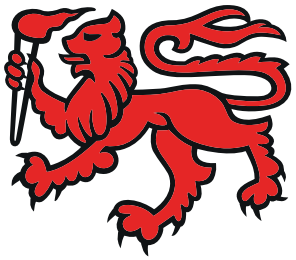

UNIVERSITY*of*
TASMANIA

CODES

# Declaration of Originality

This thesis contains no material that has been accepted for a degree or diploma by the University or any other institution, except by way of background information and duly acknowledged in the thesis. To the best of my knowledge and belief, no material has been previously published or written by another person except where due acknowledgment is made in the text of the thesis, nor does the thesis contain any material that infringes copyright

Signature: _____

Date: 08/06/2020

# Authority of Access

This thesis is not to be made available for loan or copying for eighteen months following the date this statement was signed. Following that time, this thesis may be made available for loan and limited copying and communication in accordance with the Copyright Act 1968.

Signature: _____

Date: 08/06/2020

# Abstract

The Lihir gold deposit is the world's largest alkalic low-sulfidation epithermal gold deposit in terms of contained gold (50 Moz). The deposit formed over the past ~500 kyr and records a progression from porphyry to epithermal-style hydrothermal activity. Lihir is located on the eastern shore of Lihir Island, in the TLTF island arc of New Ireland Province, Papua New Guinea. Its formation has been coincident with alkalic magmatism along arc-oblique extensional structures and sinistral rotation in the back-arc of the New Britain subduction zone. The deposit is centered on Luise Volcano, a well-preserved Plio-Pleistocene alkalic volcano with an elliptical, north-northeast-trending sector collapse amphitheater in its core. The major ore zones that make up the deposit (Lienetz, Minifie, Kapit, Coastal and Kapit NE) are situated in the footwall of the sector collapse detachment surface.

The Kapit NE and Coastal ore zones are located immediately northeast of the Lienetz open pit and have yet to be mined. The host rocks in these ore zones are dominated by a thick package of northeast-dipping, volcaniclastic debris flows that were deposited on the submarine flank of the locally emergent Luise volcanic edifice. On the same stratigraphic level at Minifie, the volcano-sedimentary sequence is dominated by south-dipping, intercalated volcanic debris flow deposits and minor pyroclastic facies that indicate subaerial deposition close to a vent. Both sequences were intruded by basaltic to andesitic sills and dikes that reflect emplacement into an unconsolidated and water-saturated sedimentary substrate in a submarine setting.

A voluminous, north-trending intrusive complex composed predominantly of porphyritic monzonite and latite stocks and dikes crosscuts the volcano-sedimentary sequence in Coastal and Kapit NE. Its emplacement spans the range of magmatic-hydrothermal activity at Lihir. New whole-rock geochemical results confirm that these intrusions have an alkalic and shoshonitic affinity and were emplaced in a supra-subduction zone tectonic setting. Biotite-feldspar-phyric, nepheline-bearing monzonites in Coastal contain abundant magmatic-hydrothermal features (e.g., miarolitic cavities) that provide evidence for volatile phase exsolution; however, there is no evidence that this intrusive phase is linked to gold mineralization. The intrusive complex hosts well-developed stockwork veins and breccia veins, whereas the predominantly clastic volcano-sedimentary sequence typically hosts mineralization of a more diffuse character, including discontinuous veins and alteration patches.

Evidence for porphyry-style hydrothermal activity is preserved at depth in the Kapit NE and Coastal ore zones. Porphyry stage features include pervasive alteration domains composed of phlogopite – K-feldspar ± magnetite (potassic) and chlorite – calcite (propylitic) assemblages, and widespread, low grade (<1 ppm Au and <0.3 wt% Cu) anhydrite-rich breccias and veins. In Kapit NE, there is an apparent zonation of pervasive alteration from proximal potassic to distal propylitic assemblages surrounding crystal-poor feldspar-phyric trachyte dikes. No single intrusive center has been identified that can account for the distribution of alteration across the Lihir deposit. New geochronological age constraints suggest that porphyry-style hydrothermal activity occurred in Kapit NE between ~481 ka and 345 ka. The transition from porphyry to epithermal conditions occurred as a result of volcanic sector collapse, which removed at least 1 km of volcano-sedimentary rocks from the top of Luise Volcano. This catastrophic mass wasting event depressurized rocks that had previously been at depth, resulting in extensional fracturing and increasing the hydraulic conductivity of the rock mass.

The epithermal stage in Kapit NE and Coastal was characterized by quiescent periods when banded vein infill and small-scale hydraulic breccias were formed, and brief, chaotic periods of tectonism and phreatic brecciation. The epithermal stage generated significant gold mineralization at shallow levels, which is hosted in veins and breccias containing gold-bearing pyrite and marcasite with variably abundant gangue minerals (quartz, chalcedony, adularia, carbonate, anhydrite and/or illite) and up to 10% open space. These veins and breccias are typically accompanied by intense, pervasive adularia – pyrite or quartz – illite – pyrite alteration. Brittle fault zones have locally concentrated or diluted porphyry and epithermal-stage mineralization. Gold is typically refractory, occurring within the crystal lattice of pyrite. Minor native gold and precious metal tellurides occur locally.

A period of maar-diatreme volcanism disrupted the Luise amphitheater during the latter stages of epithermal mineralization (between 151 and 55 ka). Phreatomagmatic and phreatic activity was triggered by the intrusion of feldspar-phyric andesite dikes into the ore-forming hydrothermal system and produced seven large volcanic-hydrothermal breccias focused along north- to northeast-trending structures. The diatreme breccia complex truncated several of the epithermal ore zones and was crosscut locally by Au-bearing calcite – quartz – pyrite epithermal veins in Kapit and Kapit NE. Modern geothermal activity has produced a layer of steam-heated smectite – kaolinite (argillic) and kaolinite – alunite (advanced argillic) alteration near surface. Downward percolating steam-heated fluids leached gold from large areas of mineralized rocks, which was reprecipitated within structures in the steam-heated alteration zone, producing thin gold-rich pyrite rims around earlier-formed sulfides.

Significant compositional variability exists in pyrite at Lihir, as recorded by LA-ICP-MS raster maps and lines. A principal component analysis of transformed pyrite data and subsequent K-means clustering of the principal components has identified six pyrite clusters that can be linked to different stages of the hydrothermal paragenesis. The porphyry stage is associated with Cluster 1 (high Cu, Co, Pb, Bi and Se; low Sb and Tl) and Cluster 3 (high Ni, Cr, V and Co; low As), which have relatively low concentrations of gold ($\bar{x}$ = 2.7 ppm Au; maximum 1,445 ppm Au) and total trace elements ($\bar{x}$ = 5,429 ppm). Texturally, these pyrites form aggregates of coarser-grained, euhedral, cubic and zoned crystals with corrosion vugs and rounded margins. The epithermal stage is associated with Cluster 4 (high Mo, Te, Pb, Ag and Au; low Mn and Zn), Cluster 2 (high Ag and Au; low Co and V), Cluster 6 (high Zn, As, Mn, Tl and Sb; low Au, Cu and Pb) and Cluster 5 (high Tl, Sb, Mn, As, Zn and Au; low Ag and Mo). These pyrites commonly form rims around earlier-formed pyrite, and also occur as fine-grained, anhedral to euhedral (equant, acicular, dendritic), porous and inclusion-rich aggregates with colloform, botryoidal or granular habit. Despite their textural variability, epithermal-stage pyrites are ubiquitously associated with high total trace element contents ($\bar{x}$ = 22,258 ppm). Clusters 2, 4, and 5 contain high concentrations of gold ($\bar{x}$ = 51.3 ppm Au; maximum 131,619 ppm Au), whereas Cluster 6 contains very low concentrations of gold (below detection limit). Epithermal stage veins and breccias display a characteristic progression from Cluster 4 to Cluster 2 to Cluster 5 pyrite, demonstrating that there was a repeated compositional evolution of the mineralizing fluids throughout the epithermal life cycle.

# Acknowledgments

This thesis was part of a larger research project entitled Exploring the Porphyry Environment, which was made possible through the financial support and vision of Newcrest Mining Limited. This research was also supported by the CODES Centre of Excellence in Ore Deposits at the University of Tasmania and a Society of Economic Geologists (SEG) Graduate Student Fellowship.

I would like to thank my primary supervisor, Prof. David Cooke, for sticking by me and getting me past the finish line. Your support, encouragement and scientific insight have been invaluable. Thanks to my secondary supervisors (Nic Jansen, Janina Micko and Angela Escolme) and numerous other researchers at CODES (especially Stephanie Sykora, Jocelyn McPhie, Bruce Gemmell, Gary Davidson, David Selley, and Noel White) for sharing their knowledge about geology and ore deposits. Thanks to Paul Olin, Sebastien Meffre, Sasha Stepanov, Ivan Belousov, Karsten Goemann and Sandrin Feig for your guidance and technical support with my SEM and LA-ICP-MS work. To Anya Reading, Izzy Von Lichtan, Al Cuison, Rose Pongratz, Chris Evans, Helen Scott, Jane Higgins, Deborah Macklin, Karen Huizing, Ian Little, Peter Cornish, Shaun Barker, and Troy Finearty, thank you for your help in navigating through life at the University. Very much appreciated!

This research would not have been possible without industry support. A big thank you to Anthony Harris, Karyn Gardner and Mary Harris at Newcrest Melbourne office. Thanks to everyone who facilitated my fieldwork at Lihir and the NTS in Brisbane, including Fiona Karaut, Jon Rutter, Geoff Smart, Warwick Fortune, Stephanie Grabovickic, Danilo Hermoso, Arnel Mejorada, Julius Pakule and the core shed samplers (Thomas Zikinbel, Patrick Kiaptabu, John Malom, Martin Aigal, Charles Ziklolot, Hugo Baibai, Joe Soles, Stanis Wirau, James Zanang).

I would like to thank my friends, family and two beautiful felines for their love, support and patience. Evan, thank you and thank you again for all the hours you've spent editing and revising my work, making me laugh and keeping me going when I felt like it was all too much. This thesis is dedicated to you.

# Table of Contents

# List of Figures

# List of Tables

# CHAPTER 1

# Introduction

## 1.1 Introduction

This PhD thesis is a study of the world-class Lihir (also known as the Ladolam) gold deposit, a young (<1 Ma) alkalic epithermal gold deposit located within the floor of a large sector collapse amphitheater at the summit of Luise Volcano on Lihir Island, Papua New Guinea (PNG; Fig. 1.1; Moyle et al., 1990; Sillitoe, 1994). It is the world's largest alkalic epithermal deposit in terms of contained gold, with a total resource of 690 Mt at 2.3 g/t Au (equivalent to 50 Moz Au; Newcrest Mining Limited, 2019).

Epithermal gold deposits consist of structurally controlled Au-bearing veins, hydrothermal breccias and altered rocks that have formed by replacement or precipitation into open space from fluids at low temperatures (<150°C to ~300°C) in the near-surface environment (<2 km; White and Hedenquist, 1995). Alkalic epithermal systems are similar to low sulfidation epithermal deposits, but are related to alkalic rather than calc-alkalic magmas. The most distinctive features of alkalic epithermal gold deposits include:

1. They are hosted within or adjacent to alkalic intrusive rocks and related volcanic structures. The alkalic intrusive rocks are defined as having high alkali contents ($Na_2O + K_2O$) over a range of $SiO_2$ contents

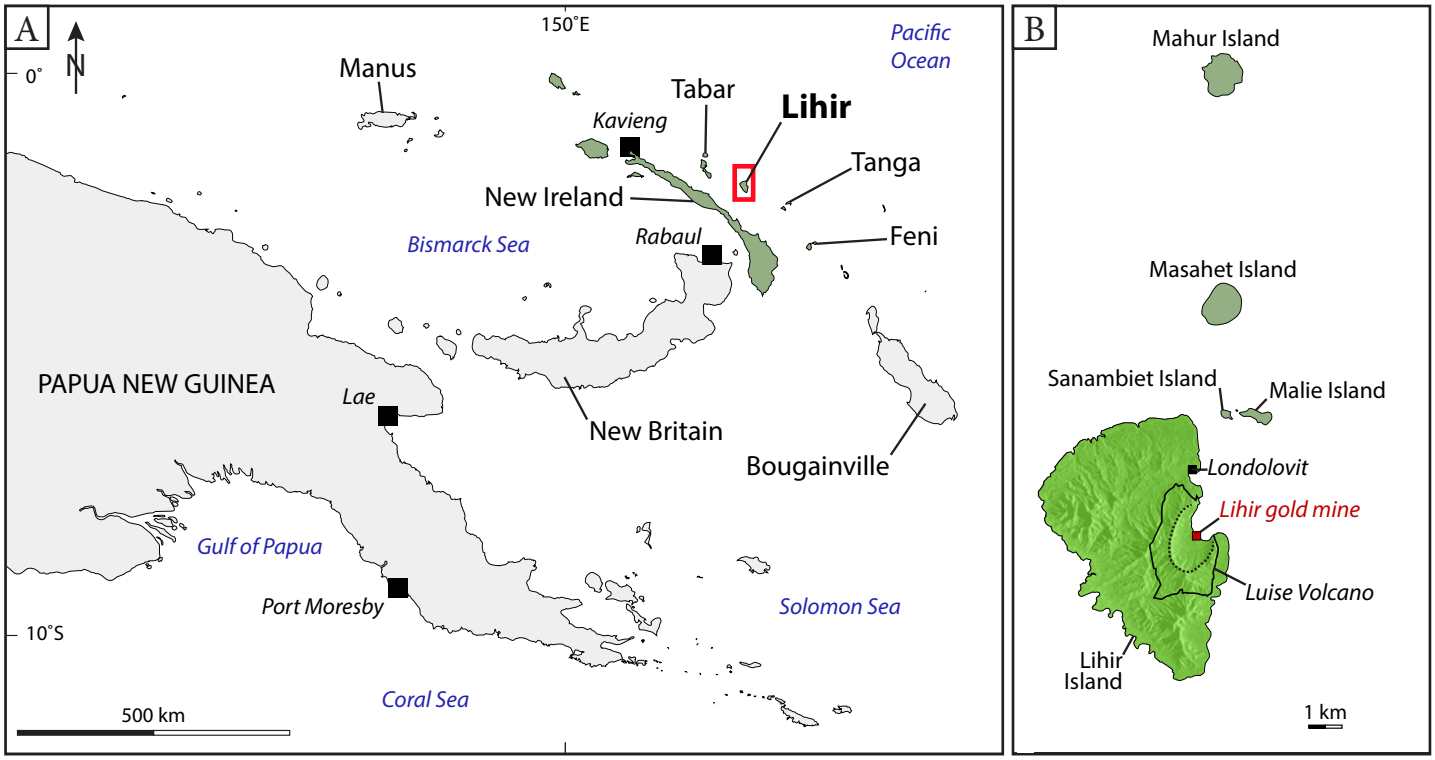


**Fig. 1.1.** Location of the Lihir gold deposit. **A.** Outline map of PNG, highlighting the location of the New Ireland Province (*green*) and the Lihir island group (*red box*). **B.** Map of the Lihir island group, showing the location of the Lihir gold mine within the Luise Volcano. The dashed line indicates the sector collapse amphitheater rim.

(41.5–74.8 wt%) and can be compositionally diverse (e.g., highly silica undersaturated to quartz-normative). The alkalic rocks typically contain hydrous phenocryst phases, indicating high water contents in the parent magmas (Richards, 1995), and are relatively oxidized (Jensen and Barton, 2000). Associated volcanic structures are variable in nature, ranging from calderas (Emperor, Fiji; Ahmad et al., 1987) to diatreme complexes (Cripple Creek, Colorado, USA; Jensen and Barton, 2000) and sector collapse amphitheaters (Lihir, PNG; Blackwell, 2010).

2. They are characterized by extensive and voluminous carbonate and K-rich alteration, with relatively minor or no hydrothermal quartz and/or acid alteration (Jensen and Barton, 2000). The ores typically contain precious metal tellurides, V-bearing minerals (especially roscoelite and vanadium muscovite; Spry and Scherbarth, 2006), and fluorite, and may also contain anhydrite and barite (Spry and Scherbarth, 2006; Richards, 1995, 2003).

3. They form in atypical tectonic settings that are indirectly associated with subduction zones, such as arc-collisional, post-subduction, and back-arc environments (Richards, 1995). The associated alkalic intrusive complexes are localized by regional-scale, deep-seated and commonly arc-oblique structures that may represent older lithospheric structures that have experienced tensional reactivation (Richards, 1995).

4. The epithermal mineralization is spatially associated with earlier-formed (typically sub-economic) porphyry-style magmatic-hydrothermal features.

Alkalic epithermal gold deposits make attractive exploration targets, because they rank among the largest epithermal gold deposits in the world (Fig. 1.2). Examples of well-known alkalic epithermal deposits include Porgera (PNG), Cripple Creek (USA) and Emperor (Fiji).

## 1.2 Location and access

The Lihir gold deposit is located on the east coast of Lihir Island (3˚08”S, 152˚38”E), approximately 900 km northeast of Port Moresby, in the Tabar-Lihir-Tanga-Feni (TLTF) island chain of New Ireland Province, PNG (Fig. 1.1). Lihir Island is the largest of five islands (Mali, Mahur, Masahet, Sanambiet and Lihir) that comprise the Lihir island group (Fig. 1.1B). Lihir Island is relatively small; it measures 30 km north-south by 15 km east-west. The island is thickly vegetated and has a rugged, volcanic landscape (Fig. 1.3A and C), which rises to 600 m rsl from local seafloor depths as low as –2,000 m rsl. The temperature ranges from 19 to 35°C and the annual rainfall averages about 5 m $yr^{-1}$. Access to Lihir Island is by air transport from Port Moresby, Cairns or Rabaul. The Niolam airport is located a few kilometers north of the town of Londolovit (Fig 1.1), where mine employees are accommodated. Travel to the mine from Londolovit is by road in company vehicles. Newcrest Mining Limited has scheduled bus services to and from the mine site every morning and evening.

## 1.3 Exploration and mining history

The Lihir gold deposit was discovered in 1982 as part of a regional gold reconnaissance program in the TLTF islands that was conducted by Kennecott Niugini Mining Joint Venture (KNMJV; Moyle et al., 1990). The exploration team had been alerted to the potential for epithermal gold mineralization on Lihir Island by an Australian Bureau of Mineral Resources report by Wallace et al. (1983), which mentioned massive, fractured and hydrothermally-altered felsic rocks at the center of Luise Volcano. In their first trip to Lihir Island, the KNMJV exploration team collected twenty outcrop and scree samples from a prominent, silicified and pyritized coastal bluff (Alaia rock; Fig. 1.3A; Hope, 2011). The samples averaged 1.79 g/t Au with values ranging from 0.53–4.36 g/t Au (Moyle et al., 1990). The favorable results led the KNMJV to apply for an exploration license in November 1982 (Hope, 2011). Geological mapping, soil and

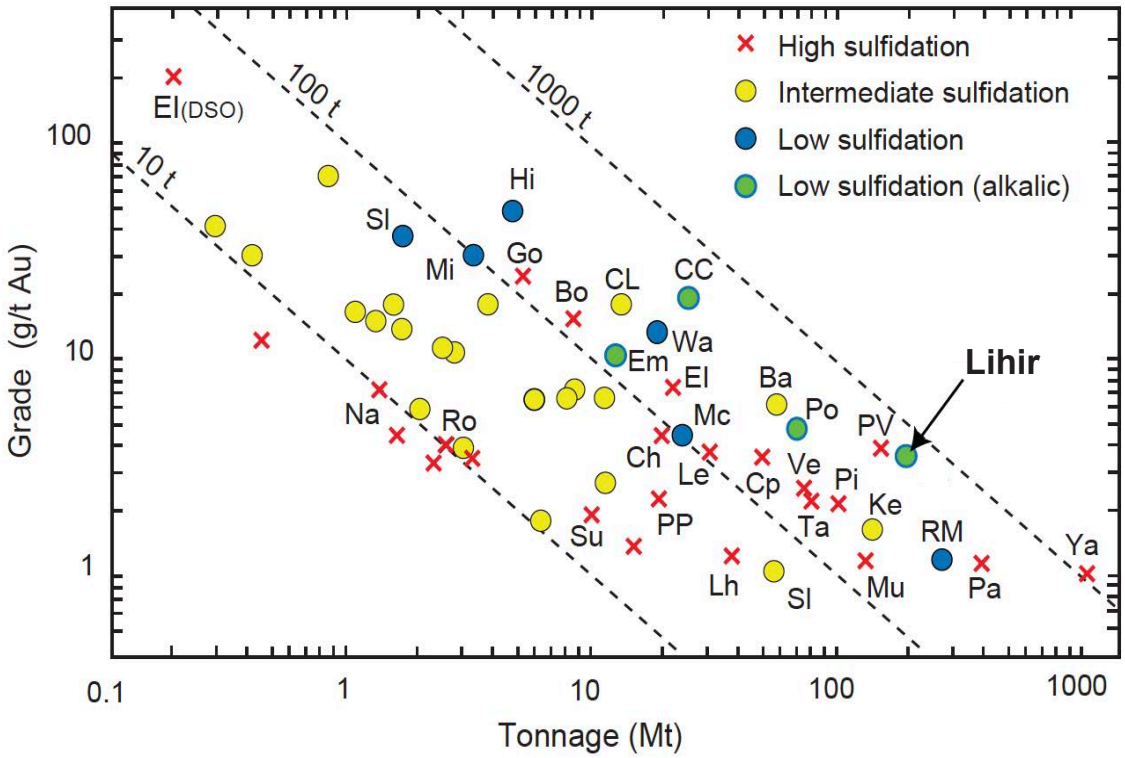


**Fig. 1.2.** Grades and tonnages of selected epithermal deposits. Figure modified after Ageneau (2012) and references therein. Abbreviations: Ba = Baguio, Philippines; Bo = Boliden, Sweden; CC = Cripple Creek, Colorado; Ch = Chinkuashih, Taiwan; CL = Comstock Lode, Nevada; Cp = Chelopech, Bulgaria; El = El Indio, Chile; El (DSO) = El Indio direct shipping ore; Em = Emperor, Fiji; Go = Goldfield, Nevada; Hi = Hishikari, Japan; Ke = Kelian, Indonesia; Lh = Lahóca, Hungary; Le = Lepanto, Philippines; Mc = McLaughlin, California; Mi = Midas, Nevada; Mu = Mulatos, Mexico; Na = Nansatsu district deposits, including Kasuga, Japan; Pa = Pascua, Chile; Pi = Pierina, Peru; Po = Porgera, Papua New Guinea; PP = Paradise Peak, Nevada; PV = Pueblo Viejo, Dominican Republic; Ro = Rodalquilar, Spain; RM = Round Mountain, Nevada; Sl = Sleeper, Nevada; Su = Summitville, Colorado; Ta = Tambo, Chile; Ve = Veladero, Argentina; Wa = Waihi, Martha Hill, New Zealand; Ya = Yanacocha, Peru.

rock chip sampling, and trenching of the coastal bluff were completed in mid-1983 (Moyle et al., 1990) and outlined large gold anomalies over three areas: Coastal, Kapit and Lienetz (Fig. 1.4; Moyle et al., 1990). In September 1983, the first hole (L1) was drilled to 180 m beneath the Coastal anomaly and intersected 29 m of oxide ore averaging 7.69 g/t Au and 21 m of sulfide ore averaging 7.09 g/t Au (Davies and Ballantyne, 1987). The second significant discovery was in June 1984, when diamond drill hole L13 in the Lienetz area intersected 54 m of oxide ore averaging 2.41 g/t Au and 70 m of sulfide ore averaging 5.10 g/t Au (Davies and Ballantyne, 1987). By October 1984, the Lihir resource was estimated to be 89.4 Mt at 3.19 g/t Au (Hope, 2011). In November 1986, drill hole L88 was collared in the Minifie area along the Upper Ladolam Creek, to follow up on a small soil geochemistry anomaly (>1 ppm Au; Moyle et al., 1990). The drill hole intersected 180 m of sulfide ore grading 5.81 g/t Au from 18 m to the bottom of the hole (Davies and Ballantyne, 1987; Moyle et al., 1990). In 1988, the RTZ Corporation (now Rio Tinto) acquired Kennecott from BP Minerals America and took over their part of the Lihir joint venture party with Niugini Mining Limited (Hope, 2011). By January 1990, the mining reserve in the Lienetz, Minifie and Coastal areas was approximately 19 Moz of contained gold, split between 4.7 Mt of oxide ore at 1.96 g/t Au and 168 Mt of sulfide ore at 3.48 g/t Au (Hope, 2011). Following completion of feasibility studies for the Minifie and Lienetz orebodies, the joint venture was granted a Special Mining Lease in March 1995 (Hope, 2011). Under the terms of the original project approvals, the Lihir operation was transferred to the ownership of a new PNG company called Lihir Gold Limited and Rio Tinto established the Lihir Joint Venture LMC (Lihir Management Company) to operate the mine on behalf of Lihir Gold Limited. Construction of the Lihir gold mine began in 1996 and open pit mining of the Minifie orebody com-

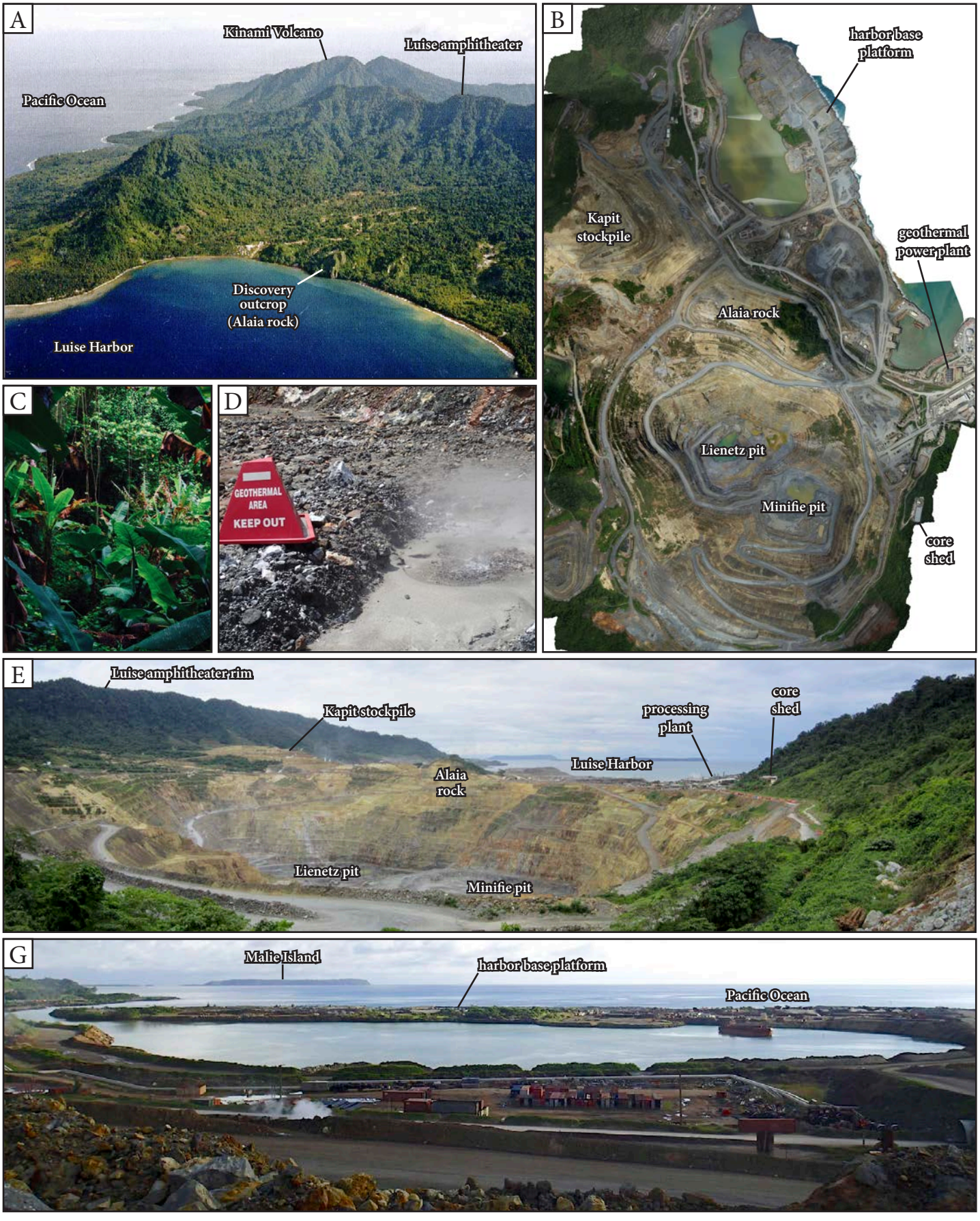
A
Kinami Volcano
Luise amphitheater
Pacific Ocean
Discovery outcrop (Alaia rock)
Luise Harbor
B
harbor base platform
Kapit stockpile
geothermal power plant
Alaia rock
Lienetz pit
Minifie pit
core shed
C
D
GEOTHERMAL AREA
KEEP OUT
E
Luise amphitheater rim
Kapit stockpile
processing plant
core shed
Luise Harbor
Alaia rock
Lienetz pit
Minifie pit
G
Malie Island
harbor base platform
Pacific Ocean

menced in mid-1997 (Hope, 2011). Two geothermal power plants have since been installed (Fig. 1.3B), which supply the mine with about one third of its power requirements. In 2002–2003, a feasibility report for the Kapit orebody was completed and Kapit's total probable reserves were reported to be 25.2 Mt at 5.28 g/t Au for a total of 4.3 Moz of contained gold (Kidd and Robinson, 2004). In August 2010, Newcrest Mining Limited acquired the Lihir operations as a result of a merger with Lihir Gold Limited. Recent exploration drilling from reclaimed land in the Luise Harbor (the harbor base platform; Fig. 1.3B and F) has defined another mineral deposit called Kapit NE (Fig. 1.4).

The principal mineralized zones that comprise the Lihir gold deposit as it is currently known are called Minifie, Lienetz, Kapit, Coastal, Kapit NE, Alaia, Link Zone and Borefields (Fig. 1.4). The present-day Lihir open pit is composed of two separate mining areas that target the Minifie and Lienetz orebodies (Fig. 1.3B and E). Geothermal activity poses challenges for mining. For instance, the water temperature at the bottom of the open pit can reach 80°C and there is potential for slope instability and geothermal outburst hazards (Fig. 1.4D).

Future mining will involve the expansion of the Lienetz pit to the north towards Kapit. Development of the Kapit pit will require relocation or use of the Kapit stockpile, geothermal depressurization and construction of a seepage barrier to mitigate seawater ingress (Fig. 1.3B and E). Kapit NE is mainly located outside of the proposed open pit. The limits of mineralization are still open at depth and to the north and east (limited by the Pacific Ocean). Exploratory work is ongoing. It is estimated that mining activities will continue until 2031 and that ore processing of lower grade stockpiles will be completed by 2044.

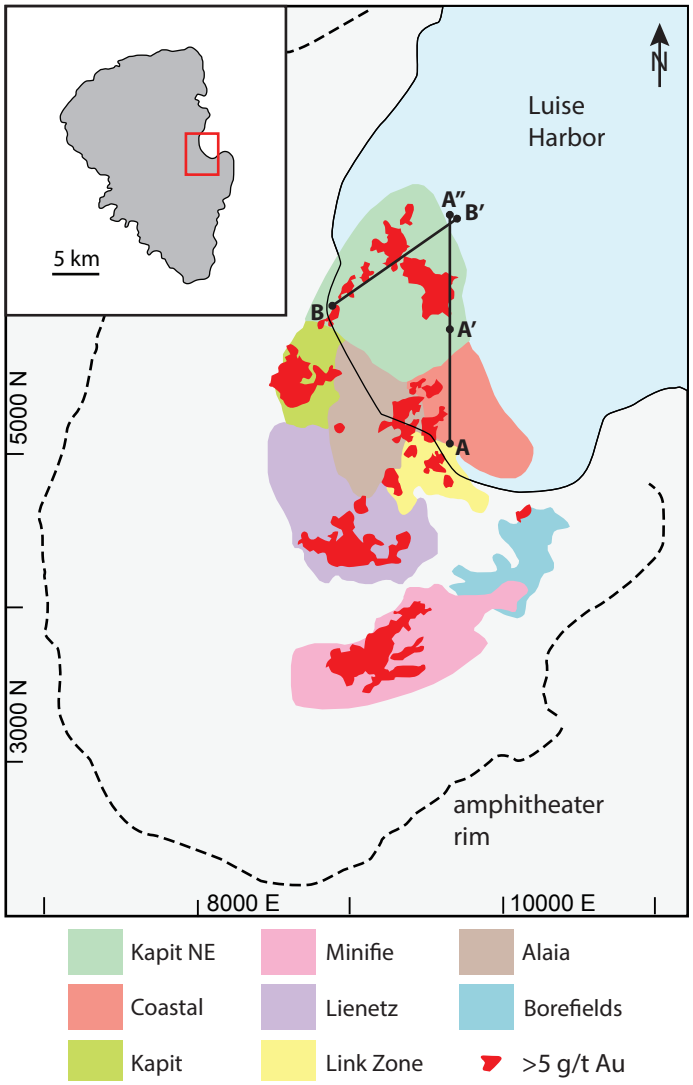


**Fig. 1.4.** Location of ore zones at Lihir and cross sections studied as part of this thesis. The >5 g/t Au polygon depicts the projection of Newcrest Mining Limited's 3-D grade shell model to 100 m rsl. The shoreline is shown as it was prior to the start of mining.

## 1.4 Previous work

The Lihir gold deposit has been the focus of many previous studies. These include the PhD studies of Carman (1994), Blackwell (2010), Ageneau (2012), and Sykora (2017), and the MSc study of Cater (2002). Several journal articles have been published from the results of the PhD

**Fig. 1.3.** (*Previous page*) Photographs of Lihir Island and Lihir gold deposit. **A.** Pre-mining aerial photograph of Luise amphitheater (facing south). The discovery outcrop, Alaia rock, is the coastal bluff in the foreground. The photo was taken by D. Royle in 1988 (Hope, 2011). **B.** Orthophoto of the Lihir gold mine. The image was captured using an UAV by Newcrest Mining Limited in December 2012. **C.** Dense tropical foliage on the amphitheater slope behind the core shed. **D.** Geothermal outburst hazard at the bottom of Lienetz open pit. **E.** Northeast-facing panorama Lihir open pit, Kapit stockpile and Alaia rock (June 2012). **F.** Northeast-facing panorama of the harbor base platform in Luise Harbor, which overlies parts of the Kapit NE prospect. The platform was built from piled waste rock and is the location from which many of the drill holes into the Kapit NE prospect were drilled. White geothermal pipelines can be seen in the foreground.

studies—geology, mineralization and hydrothermal evolution of the Lihir deposit (Carman, 2003), lithofacies associations in the Minifie ore zone (Blackwell et al., 2014), structure and significance of anhydrite-bearing veins from Lienetz (Sykora et al., 2018a) and trace element compositions of pyrite from Lienetz (Sykora et al., 2018b). A map showing the locations of all cross sections and mapping areas from these previous theses is provided in Appendix A1.

Other published research includes Davies and Ballantyne (1987), Lottermoser (1990), Moyle et al. (1990), Sillitoe (1994), Corbett et al. (2001), Müller et al. (2001, 2002a,b, 2003), Gemmell et al. (2004), Kidd and Robinson (2004), Brown and Bixley (2005), Kamenov et al. (2005), Simmons and Brown (2006), Rutter et al. (2008), Rae et al. (2010), White et al. (2010) and Jansen et al. (2017). A number of in-house studies by Lihir Gold Limited and Newcrest Mining Limited staff and their consultants, have also contributed to our understanding of the Lihir deposit.

As a result of previous work, the Kapit, Lienetz and Minifie orebodies have been described and their mineralization and associated alteration characteristics are well established. However, the Kapit NE and Coastal mineralized zones have not been previously studied and remain poorly understood.

### 1.5 Study objectives

The aim of this PhD study is to refine the genetic model for the giant (>52 Moz Au) Lihir alkalic epithermal gold deposit, through investigation of the Kapit NE and Coastal ore zones. The host succession is geologically young (Quaternary) and *in situ*, which provides an opportunity to document the characteristics and resolve relationships between lithofacies and gold mineralization. This study contributes to our understanding of alkalic epithermal gold deposits by characterizing the geological setting for this deposit type and providing an analogue for older, less well preserved and metamorphosed alkalic mineralized successions.

A unique challenge at Lihir is to deconvolute spatially juxtaposed porphyry, epithermal and geothermal systems that have been further complicated by multiple phases of magmatic- and volcanic-hydrothermal brecciation. A key aim of this study is to carefully document the paragenesis of hydrothermal veins, breccias and alteration in order to assess the relative importance of each of these factors on the distribution of gold ore. Another aim is to investigate the Fe-sulfide chemistry of ores, providing insight into the geochemical evolution of the ore-forming fluids. Characterization of gold deportment within the pyritic ore also provides insight into appropriate processing methods for refractory gold deposits.

### 1.6 Methods

Most of the geological data presented in this thesis were collected over three field seasons (May–June, 2012; November–December, 2012; August–September, 2013) at Lihir gold mine. Geological observations were based on graphic logging of 4,488 m of drill core from 17 drill holes along two cross sections in the Kapit NE and Coastal areas (Fig. 1.2; Appendix A1). Graphic logging of 70 m of drill core from the Ilkot prospect (near Londolovit) was conducted to provide regional context. Rapid drill core degradation in the tropical climate at Lihir (e.g., Jansen et al., 2017; Fig. 1.5) necessitated the preferential selection of recently drilled cores. Where the study of older drill core was required, substantial effort was spent cleaning and polishing samples with water and a diamond polishing plate prior to graphic logging and sampling. Photo core logging of an additional 474 drill holes was used to define the extent and geometry of the late stage volcanic hydrothermal breccia bodies across the Lihir deposit. The graphic logging method used was modified from Einaudi (1997), McPhie et al. (1993), Davies (2002), Gifkins et al. (2005) and Blackwell (2010). A floating scale was used.

Polished slabs were prepared from representative samples to facilitate description of igneous and volcanic textures

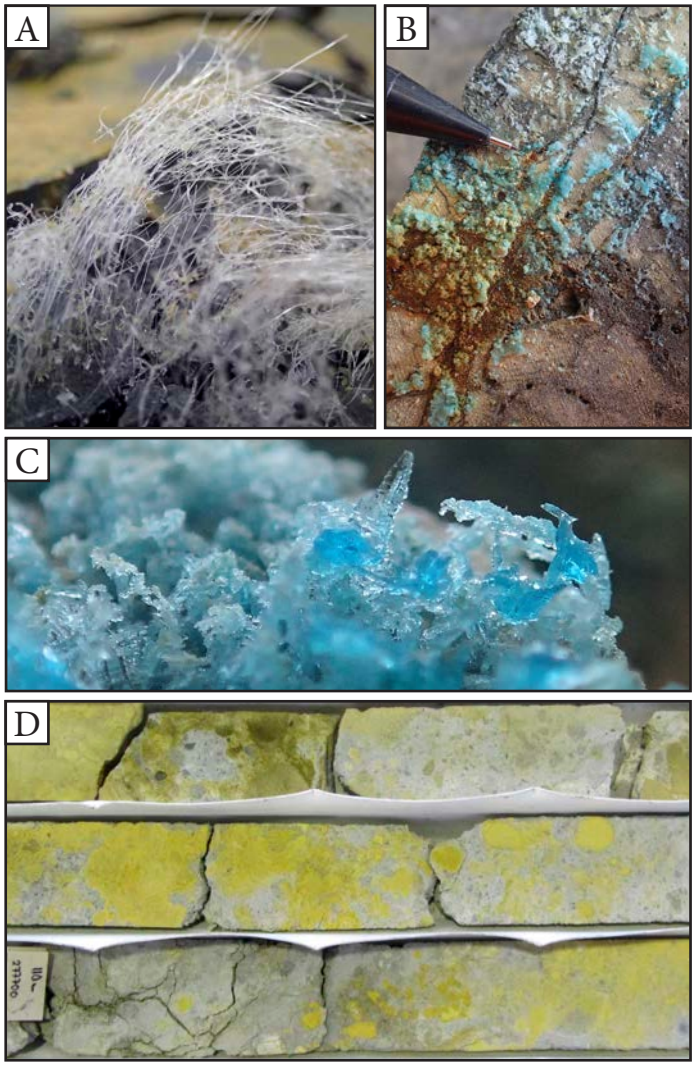


**Fig. 1.5.** Post-drilling degradation of drill core samples from Lihir. **A.** Macro photograph of white gypsum 'hair' (*foreground*) and yellow jarosite coating (*background*) that have grown from the surface of Fe-sulfide-rich samples. **B.** A colorful coating of cupriferous melanterite (*aqua*), jarosite (*yellow*), copiapite (*orange-brown*) and gypsum (*white*) on the surface of cut drill core. These secondary minerals are concentrated around chalcopyrite-, pyrite- and marcasite-bearing veins and alteration halos. **C.** Macro photograph of cupriferous melanterite. **D.** Jarosite and copiapite coating the cut surface of drill core. The samples have started to expand and crumble due to the swelling of clay alteration minerals (especially montmorillonite) on exposure to the humid conditions at Lihir.

and to help determine the relative timing and characteristics of hydrothermal features such as veins and breccias. In addition, approximately 80 polished thin sections were studied using a petrographic microscope.

Whole-rock geochemical analyses of major and trace elements for least-altered samples were conducted at Acme Analytical Laboratories Limited in Vancouver, Canada. Major elements were determined by inductively coupled plasma emission spectrometry (ICP-ES) and trace elements were analyzed by inductively coupled plasma mass spectrometry (ICP-MS). Details of the procedure, analytical conditions and instrumentation are provided in Chapter 3.

Laboratory-based methods were used to supplement mineral identification made during core logging and thin section petrography. Scanning electron microscopy (SEM) together with energy dispersive spectrometry (EDS) and back scattered electron (BSE) imaging were conducted at the Central Science Laboratory (CSL), University of Tasmania, Australia, for the purposes of identifying the composition and textural relationships of fine-grained alteration minerals. A TerraSpec mineral analyzer operating in the short wave infra-red (SWIR) range of the electromagnetic spectrum was used to identify key alteration minerals, including clays (e.g., illite), hydrated sulfates (e.g., gypsum) and micas (e.g., phlogopite). SWIR analyses were conducted both on-site at Lihir gold mine, and at the Centre for Ore Deposit and Earth Sciences (CODES), University of Tasmania, Australia. Systematic chemical feldspar staining of thin section offcuts and polished slabs was conducted at CODES, in order to estimate the modal abundances of K-feldspar and to aid in textural analysis. Selected samples were etched with sodium hypochlorite (NaClO) prior to petrographic observation in order to highlight chemical zonation in Fe-sulfide minerals (e.g., As-rich rims on pyrites).

Laser ablation inductively coupled mass spectrometry (LA-ICP-MS) raster maps and lines were constructed for paragenetically constrained pyrite grains at CODES Analytical Laboratories. Details of the instrumentation, procedures and analytical conditions are provided in Chapter 5. An unsupervised multivariate statistical analysis and machine learning algorithm of the LA-ICP-MS raster maps was then applied, in order to classify compositionally similar pyrite into relative groups that were then interrogated in X–Y space and with respect to their paragenesis, micro-textures and relationship with Au.

## 1.7 Thesis organization

This introduction is followed by five major chapters that describe and interpret aspects of the Lihir gold deposit:

- *Chapter 2* discusses the tectonic history, geology and metallogeny of Papua New Guinea with a particular focus on the Cenozoic events that led to the formation of the TLTF island arc and Lihir gold deposit.

- *Chapter 3* presents a detailed description of the volcano-sedimentary and intrusive rocks in the Kapit NE and Coastal areas. It also presents and discusses whole-rock geochemical data for volcanic and igneous rocks from Lihir Island. New Ar–Ar geochronology results constrain the timing of emplacement of early porphyritic intrusions and Cu-Au mineralization. These data are used to interpret the tectonic and magmatic evolution of the TLTF island arc. This is followed by an interpretation of the Plio-Pleistocene paleoenvironment of Lihir Island. This chapter is presented as a modified version of a manuscript that will be submitted to Ore Geology Reviews.

- *Chapter 4* documents veins and altered rocks from the Lihir gold deposit, with a particular focus on the Kapit NE and Coastal areas. A detailed paragenetic sequence for mineralization and alteration is provided, together with interpretation of alteration zonation patterns. New Re–Os and Ar–Ar age determinations delimit the absolute timing of porphyry and epithermal alteration and mineralization. A new, deposit scale 3-D model of late-stage, discordant, polymict breccias is presented and its minimum age is constrained by carbon isotope dating. The paragenetic sequence is compared and integrated with those previously defined for Minifie, Lienetz and Kapit. Parts of this chapter were published in the 13$^{th}$ Biennial SGA Meeting extended abstract volume (i.e., Lawlis et al., 2015) and minor aspects will be included in a Lihir gold deposit review paper for a special compilation volume to be published in 2020 (Cooke et al., in press).

- *Chapter 5* uses LA-ICP-MS raster maps to assess Au deportment in pyrite and to characterize the compositional variability of pyrite associated with different paragenetic stages.

- *Chapter 6* concludes this thesis by proposing a genetic model for the formation of the Lihir gold deposit and includes recommendations for future research and exploration. The outcomes of the study are applied to the alkalic epithermal gold deposit model and new insights are highlighted.

# CHAPTER 2

# Regional Geology

## 2.1 Introduction

Papua New Guinea is situated in one of the most tectonically complex and seismically active regions in the SW Pacific. Its Cenozoic geodynamic evolution has involved a wide range of tectonic processes operating on a complex mosaic of microplates between the obliquely converging Australian and Pacific plates. The main island of New Guinea has been constructed mainly via the accretion of island arc terranes onto a rifted fragment of the Australian continent. The evolution of the islands to the northeast has involved island arc formation, subduction inversion, asymmetric seafloor spreading and the collision of a large igneous plateau. The region hosts several giant gold-rich porphyry, skarn and epithermal deposits including Porgera, Frieda River, Ok Tedi, Wafi-Golpu, Lihir and Panguna, which account for a significant proportion of the world's gold and copper resources. In general, their formation is genetically related to intrusive activity during transitory periods of subduction perturbation in the late Oligocene to Recent (Cooke et al., 2005).

The Lihir gold deposit (3˚08”S, 152˚38”E) is located on the east coast of Lihir Island, one of a series of northwest-trending, Pliocene-Pleistocene (<3.5 Ma) alkalic volcanic islands that comprise the Tabar-Lihir-Tanga-Feni (TLTF) island chain in northwest Papua New Guinea (Fig. 2.1). The Lihir deposit formed in the last million years coincident with active volcanism and island arc formation that was associated with an extensional tectonic regime in the back-arc to the New Britain subduction zone. The purpose of this chapter is to review the tectonic history of Papua New Guinea, with a particular focus on the events that led to the formation of the Lihir gold deposit. This chapter provides the regional framework for the Lihir genetic model provided in Chapter 6.

## 2.2 Geotectonic provinces of Papua New Guinea

The three major geotectonic provinces in Papua New Guinea are the Australian Craton, New Guinea Orogen and Melanesian arc (Fig. 2.1; Williamson and Hancock, 2005). The geological elements that comprise the provinces are discussed below.

### *2.2.1 Australian Craton*

On the island of New Guinea, the Australian Craton consists of the Fly Platform, a broad, low-lying and flat region south of the Central Cordillera. The Fly Platform comprises a thick succession of sub-horizontal, shallow marine sediments that formed atop the passive northern margin of the Proterozoic-Permian Australian continent in the Triassic-Neogene (Williamson and Hancock, 2005). The largely undeformed sedimentary strata are locally covered by coarse Quaternary molasse derived from the Central Cordillera or by pyroclastic rocks, lahar deposits and reworked outwash derived from extinct Quaternary stratovolcanos of the New Guinea Orogen (Williamson and Hancock, 2005). The Australian Craton is separated from the rest of Papua New Guinea by the Papuan Thrust (Fig. 2.1), a basal thrust that is expressed as a co-linear series of shallow north-dipping thrust planes along the edge of the foothills of the Southern Highlands (Rogerson et al., 1987). Most of mainland Papua New Guinea is underlain by the Australian Craton (Verave and Kawagle, 2010).

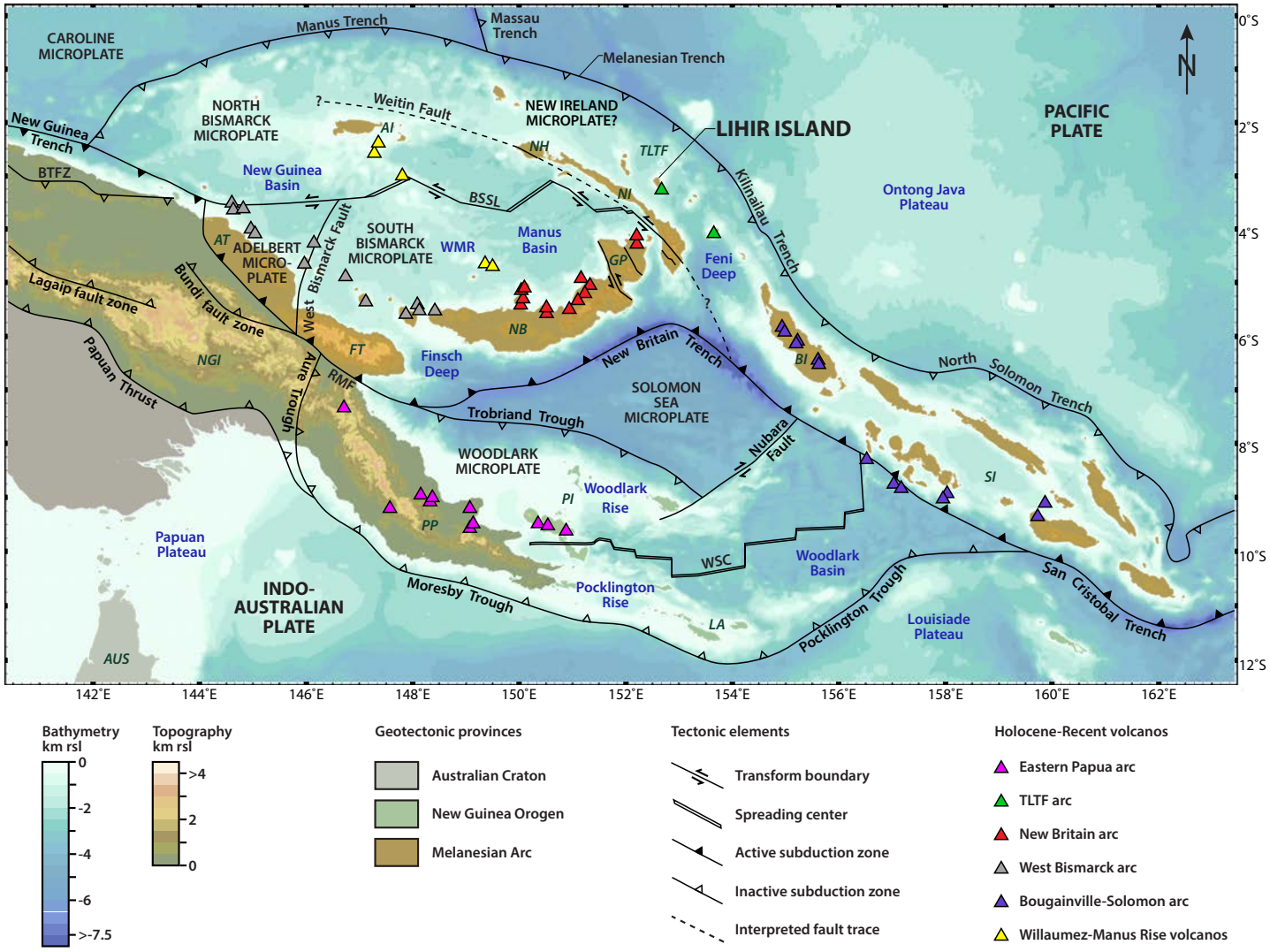


**Fig. 2.1.** Tectonic setting and Holocene volcanos of Papua New Guinea and the Solomon Islands. Parts of this figure were produced with GeoMapApp (http://www.GeoMapApp.org), using topography and bathymetry from Ryan et al. (2009). The the location of Holocene volcanos has been sourced from Global Volcanism Program (2013a). Tectonic plates are after Martinez and Taylor (1996), Holm et al. (2016) and Lindley (2016). Geotectonic provinces are after Williamson and Hancock (2005). Abbreviations: AI = Admiralty Islands, AT = Adelbert Terrane, AUS = Australia, BTFZ = Bewani-Torricelli fault zone, BI = Bougainville Island, BSSL = Bismarck Sea Seismic Lineation, FT = Finisterre Terrane, GP = Gazelle Peninsula, LA = Louisiade Archipelago, NB = New Britain, NH = New Hanover, NI = New Ireland, NGI = New Guinea Island, PI = Papuan Islands, PP = Papuan Peninsula, RMF = Ramu-Markham fault, SI = Solomon Islands, TLTF = Tanga-Lihir-Tabar-Feni Islands, WSC = Woodlark spreading center.

### *2.2.2 New Guinea Orogen*

The New Guinea Orogen makes up the mountainous spine that extends along the length of New Guinea Island and offshore to the Papuan Islands (Fig. 2.1). Pigram and Davies (1987) identified and described 32 tectonostratigraphic terranes in the New Guinea Orogen. The terranes are highly diverse, comprising accreted crustal and oceanic micro-continents and volcanic terranes, obducted Pacific oceanic crust and rifted fragments of the Australian Craton. There are also a number of Miocene and younger post-accretionary basins that have formed across terrane boundaries including the Lumi, Aitape, Wewak, and Aure Troughs (Pigram and Davies, 1987). The New Guinea Orogen can be divided into the Western and Eastern New Guinea Orogens (Williamson and Hancock, 2005). The Western New Guinea Orogen comprises two west-northwest-trending domains, the Papuan Fold Belt and the New Guinea Thrust Belt, that extend from the border with Indonesia to the Aure Deformation Zone. The Eastern New

Guinea Orogen extends eastward from about 146˚E along the Papuan Peninsula and is divided into the Eastern Fold Belt and Owen Stanley Thrust Belt (Williamson and Hancock, 2005). On the Papuan Peninsula, active volcanism historically occurred at Mt. Lamington, Mt. Victory, Waiowa and the Managalase Plateau in the Eastern Papua Volcanic Province (Fig. 2.1; Ruxton, 1966; Global Volcanism Program, 2013b). These volcanos are not associated with a Benioff zone. Volcanism may be related to partial melting of subduction-modified mantle triggered by regional uplift (Johnson et al., 1978).

### *2.2.3 Melanesian arc*

The Melanesian arc comprises a series of dismembered island arcs to the north of the New Guinea Orogen, within the segmented Pacific Plate margin (Williamson and Hancock., 2005). This geotectonic province occupies the mountain ranges that extend from the Huon Peninsula toward the northwest along the New Guinea coast (i.e., the Sarawaged-Finisterre-Adelbert Ranges and Bewani-Torricelli Mountains) and the islands of the Bismarck Archipelago (e.g., New Ireland, Britain, Manus, and Bougainville islands; Fig. 2.1). Basement rocks in the Melanesian arc consist of late Eocene intermediate and mafic pillow lavas, breccias and volcaniclastics that are interbedded with coralline limestone lenses. These rocks crop out in the Bewani mountains (Bliri Volcanics), Bougainville (Atamo Volcanics), Manus Island (Tinniwi Volcanics) and New Britain (Baining Volcanics; Fig. 2.2; Lindley, 2016). They are covered by late Oligocene volcaniclastic rocks (e.g., Merai Volcanics, Gazelle Peninsula; Jaulu Volcanics, New Ireland), intruded by late Oligocene-early Miocene diorites (e.g., Arabam Diorite, Gazelle Peninsula; Lemau Intrusive Complex, New Ireland) and unconformably overlain by extensive, thick sequences of early to middle Miocene platform carbonates (Fig. 2.2; Lindley, 2016). This distinctive Cenozoic stratigraphy is locally covered by Pliocene and younger clastic sediments, volcanics, and Quaternary reef limestones (Fig. 2.2; Davies, 2012). On the Gazelle Peninsula, Miocene-age andesite, flow-banded rhyolite and rhyolitic ashflow deposits (Nengmutka Volcanics) are also known (Lindley, 2006a).

There are four active (or recently active) volcanic belts in the Melanesian arc: (1) the tholeiitic to calc-alkalic West Bismarck arc, (2) the calc-alkalic Bougainville-Solomon arc, (3) the calc-alkalic New Britain arc, and (4) the alkalic TLTF arc (Fig. 2.1; McInnes, 1992; Woodhead et al., 2010; Holm and Richards, 2013). Volcanism in the West Bismarck, New Britain and Bougainville-Solomon arcs is related to subduction along the New Britain–San Cristobal trench. The TLTF arc does not overly the Benioff zone of the New Britain subduction system. The contiguous West Bismarck and New Britain arcs are considered as two separate entities due to their different geochemical signatures (Jakeš and Gill, 1970; Woodhead et al., 2010), which may reflect their positions overlying underthrust continental crust and typical subducted oceanic crust, respectively (Holm and Richards, 2013).

## 2.3 Geology and geochemistry of the TLTF arc

The TLTF island arc is a 250-km-long, northwest-trending chain of volcanic islands that is parallel to and 50 km northeast of the coastline of New Ireland (Fig. 2.2). Magmatism in the TLTF arc has inflated the northeastern portion of the ~100 km-wide New Ireland fore-arc basin that extends for 900 km from the Feni Islands to the Admiralty Islands (Exon and Tiffin, 1984; Marlow et al., 1988; Exon et al., 1986). The basin contains a >5 km-thick stratigraphic sequence consisting of Oligocene to early Miocene volcaniclastics, late Miocene shelf carbonates, late Miocene and Pliocene bathyal chalks and volcaniclastics, and Pleistocene to Recent sediments (hemipelagic ooze, chalk and foraminifera-bearing mud, sand and volcanic ash; Fig. 2.3; Exon et al., 1986; Horz et al., 2004). This sequence has been correlated with the stratigraphy on New Ireland and New Hanover (Fig. 2.3), and the rocks crop out in a substantial area on the Tabar islands (i.e., pre-middle Miocene volcanics and Lelet Limestone; Fig. 2.2; Exon et al., 1986; Hohnen, 1978).

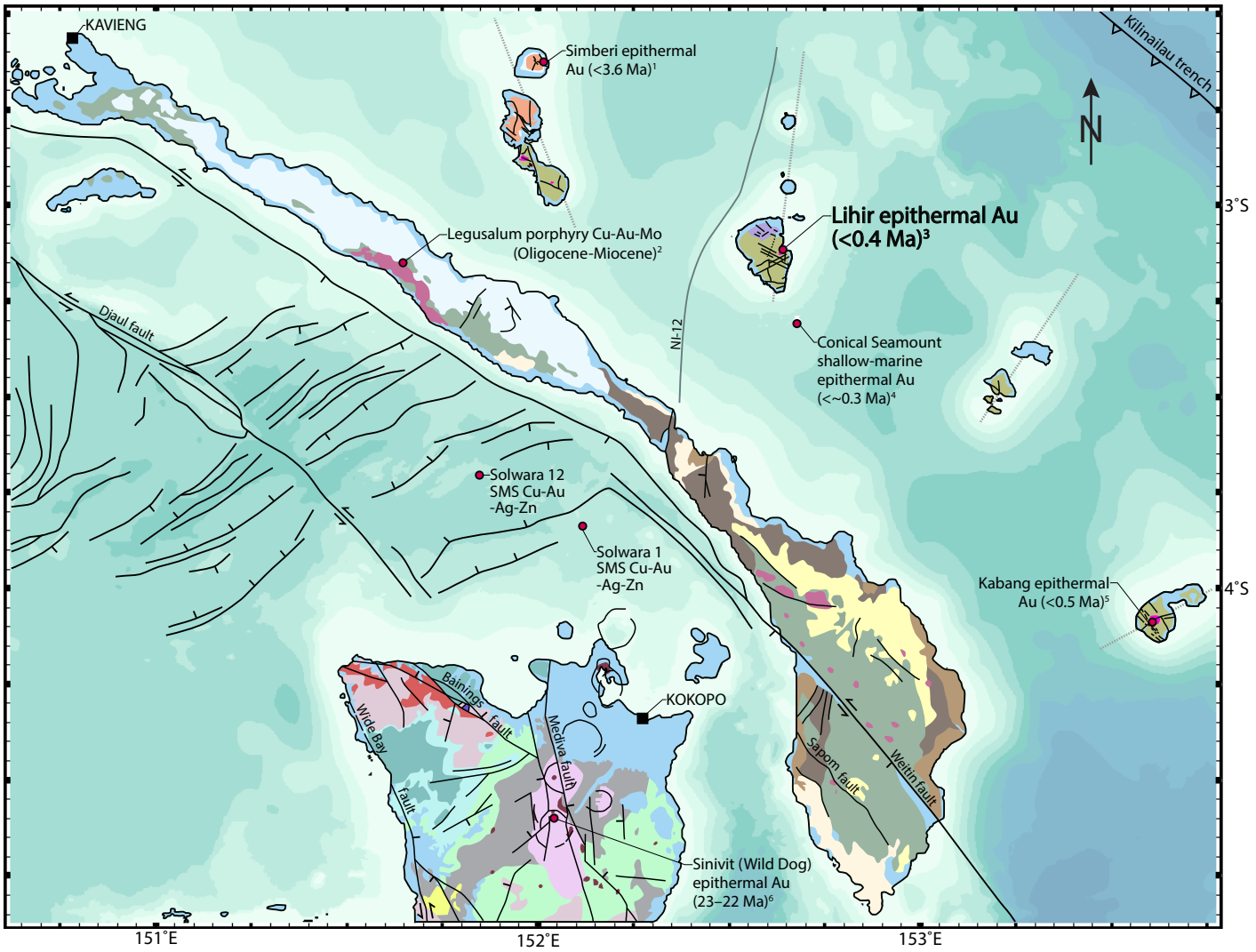


Pleistocene-Recent

- **Undifferentiated surficial deposits, volcanics and raised coral terraces**

Plio-Pleistocene

- **Quartz trachyte:** anorthoclase- and biotite-phyric quartz trachyte cumuludomes and rock pinnacles
- **Pliocene-Pleistocene volcanics:** alkaline mafic and intermediate lava flows, volcaniclastic deposits and dikes
- **Maton Conglomerate:** cobble and boulder conglomerate, pebbly sandstone
- **Punam Limestone:** chalky limestone, formainiferal calcarenite, coralline calcirudite

Pliocene

- **Lakit Limestone:** white bioclastic limestone

Mio-Pliocene

- **Miocene-Pliocene volcanics:** alkaline mafic lava flows, lithic tuff-breccia, volcanarenite, lahar and conglomerate
- **Sinewit Formation:** poorly to partly consolidated sandstone, minor limestone and breccia
- **Nengmutka Volcanics:** andesite, ashflow tuff, flow-banded rhyolite, siltstone
- **Lelet Limestone:** algal and coralline calcarenite and calcirudite; minor foraminiferal biomicrite

Upper Miocene

- **Rataman Formation:** andesitic and dacitic crystal-lithic tuff, volcanolithic arenite and lutite, formainiferal marl and limestone

Early to Middle Miocene

- **Yalam Limestone:** bioclastic limestone with interbeds of chalky limestone
- **Pre-middle Miocene volcanics:** mafic to intermediate lava flows and volcaniclastic deposits, including alkali basalt and andesite; locally contains pyroxenite nodules
- **Surker Limestone:** chalky limestone, clay-rich calcarenite and calcirudite; minor arenaceous limestone; rare calcareous and volcaniclastic sandstone
- **Bergberg Formation:** calcareous sandstone and mudstone; carbonaceous horizons
- **Arabam Diorite:** coarse-grained quartz diorite
- **Lemau Intrusive Complex:** granodiorite, tonalite, trondhjemote, gabbro, norite, diorite (mostly leucocratic), rhyodacite plugs

Oligocene

- **Diorite, leucogabbro and microdiorite**
- **Jaulu Volcanics:** porphyritic andesitic lapilli tuff and agglomerate; minor welded ash-flow tuff, amygdaloidal and pillow lava, tuffaceous limestone; limestone lenses
- **Merai Volcanics:** lithic tuff, andesite, breccia, basalt; minor limestone

Late Eocene

- **Baining Volcanics:** indurated breccia, tuff, andesite and basalt

Bathymetry (km rsl)

0
-2
-4

- Strike-slip fault with sense of displacement
- Fault with unknown sense of displacement
- Normal fault with barb on downthrown block
- Inactive subduction zone

Oligocene-Miocene basement rocks also crop out on Lihir Island (bedded volcaniclastic conglomerates; Gallasch, 1976) and Ambitle Island (bedded calcirudites; Wallace et al., 1983). The strata dip gently to the north and east away from New Ireland (Fig. 2.3; Exon et al., 1986).

The island groups of the TLTF chain are aligned along equally spaced (~75 km apart), north- to northeast-trending submarine ridges (Fig. 2.2; Lindley, 1988; Kamenov et al., 2005). The ridges are aligned with similarly north-trending normal faults on New Ireland and New Britain (Fig. 2.2; Lindley, 1988, 2006a). The trend of each volcanic ridge is rotated ~20˚ compared to the ridges adjacent to it, forming a splay that is broady radial about the convex bend in the New Britain trench (Lindley, 1988). Sykora (2017) has shown that there is a strong positive correlation ($R^2 = 0.996$) between the angle of the long axis of the Tanga, Lihir and Tabar ridges relative to that of the long axis of the Feni ridge and the distance of that island group to Feni. Seismic profiles show that horst and sediment-filled graben structures exist between the Tabar and Lihir Island groups and that the islands are bounded by normal faults (Fig. 2.3; Exon et al., 1986; Marlow et al., 1988). This suggests that extension and crustal thinning have been involved in the localization of the island groups (McKenzie, 1978). There is a step-like increase in depth to the ocean floor towards the southeast; the Tabar, Lihir, Tanga and Feni island groups rise to sea-level from ocean depths of 1,200 m, 1,600 m, 2,000 m and 2,400 m, respectively (Wallace et al., 1983).

The TLTF islands are composed of variably dissected volcanic complexes comprising Pliocene-Pleistocene alkalic lava flows, volcaniclastic deposits and mafic dikes that are fringed by tilted and multiply uplifted Miocene to Quaternary limestones (Wallace et al., 1983). Coherent volcanic facies are dense to vesicular, aphanitic to porphyritic (pyroxene-, feldspar- and/or olivine-phyric), and locally contain pyroxenite nodules (Wallace et al., 1983). The mineralogy of the mafic volcanic rocks is dominated by olivine, diopside, plagioclase and magnetite, with locally abundant hornblende and mica (biotite or phlogopite) and accessory apatite, feldspathoid (haüyne-sodalite, analcite, leucite, or nepheline), alkali feldspar and pyrrhotite-chalcopyrite (Wallace et al., 1983). Submarine volcanic cones south of Lihir Island (Edison, Conical and Tubaf seamounts) are composed of alkali-olivine basalts, clinopyroxene-rich basalts and phlogopite-phyric basalts with abundant mafic and ultramafic xenoliths (Herzig et al., 1994). Volcaniclastic rocks comprise pyroclastic facies and volcaniclastic breccias and are abundant on the Tabar and Lihir islands. Quartz trachytes, containing alkali feldspar, orthopyroxene, quartz, amphibole and magnetite, have intruded volcanos on several island groups (Fig. 2.2; Wallace et al., 1983). Limestones include fore-reef bioherms and back-reef facies with lenses of littoral calcareous and volcaniclastic sediment (Wallace et al., 1983; Blackwell, 2010). Several of the volcanic centers host hydrothermal alteration, thermal activity, shallow-level porphyry stocks and epithermal gold mineralization (Fig. 2.2). Submarine hydrothermal alteration and gold mineralization have also been discovered on Conical Seamount south of Lihir Island (Fig. 2.2; Herzig et al., 1994).

Volcanics of the TLTF islands are silica-undersaturated, nepheline-normative and range from subalkaline to shoshonitic ($K_2O$: up to 4.7 wt%; $Na_2O$: up to 7 wt%), which is unique amongst island arcs in the region (Wallace et al., 1983) and unusual for island arcs in general. Compositions of the volcanic rocks include phono-tephrite, ankaramite, basanite, alkali basalt, trachybasalt, trachyandesite and tra-

**Fig. 2.2.** (*Previous page*) Geology and ore deposits of New Ireland, the TLTF Islands and the Gazelle Peninsula (East New Britain). The trace of the seismic profile shown in Figure 2.3 (NI-12) is shown in gray. Parts of this figure were produced using GeoMapApp (http://www.GeoMapApp.org) and bathymetry from Ryan et al. (2009). Geology of New Ireland is after French (1966) and Hohnen (1978). Geology of Gazelle Peninsula is after Davies (1973), Lindley (1988), Lindley (2006a), Johnson et al. (2010) and Lindley (2016). Geology of the TLTF islands is after Hohnen (1978), Wallace et al. (1983) and Lindley (2016). Structures in the Manus Basin are after Martinez and Taylor (1996) and Lindley (2016). References for ages of mineralization for selected ore deposits are as follows: [1]Rytuba et al. (1993), [2]Singer et al. (2008), [3]this study, [4]Kamenov et al. (2008), [5]Sillitoe (1989), and [6]Lindley (1990).

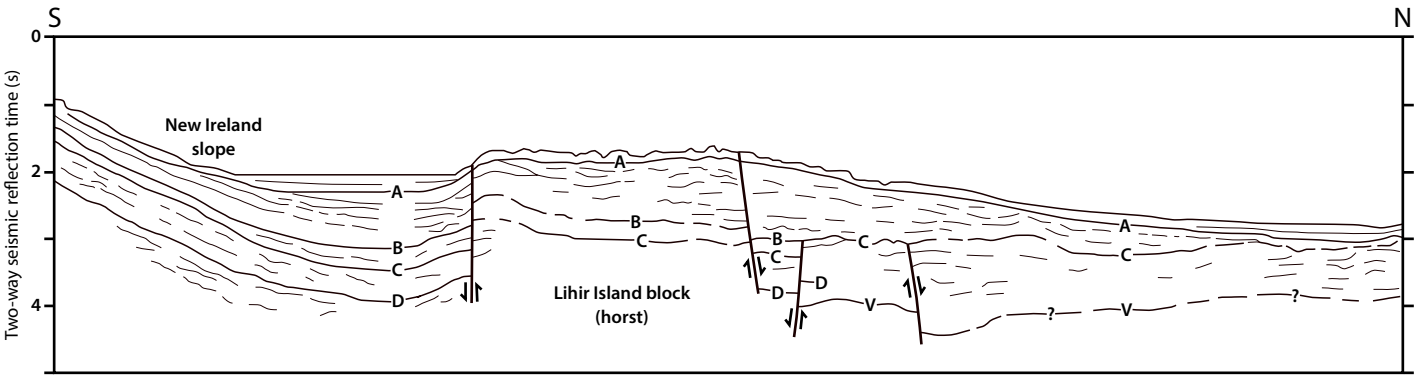


**Fig. 2.3.** Seismic profile NI-12 in the New Ireland fore-arc basin (modified from Exon et al., 1987). The trace of the seismic profile is shown in Figure 2.2. Seismic sequences are interpreted by Exon et al. (1987) as follows: *Seafloor–A*: Pleistocene to Recent hemipelagic oozes. *A–B*: Pliocene volcaniclastic turbidites interbedded with marls and chalks (equivalent to Rataman formation on New Ireland). *B–C*: Late Miocene to earliest Pliocene chalks and marls interbedded with volcaniclastic turbidites (equivalent to Punam limestone on New Ireland). *C–D*: Early to late Miocene platform and upper slope limestones (equivalent to Lelet Limestone on New Ireland). *D–V*: Eocene to early Miocene volcaniclastics? (equivalent to Jaulu volcanics on New Ireland). Overlies oceanic basement.

chyte (Johnson et al., 1976; Wallace et al., 1983; Kamenov et al., 2008). TLTF volcanics have trace element and Nd, Sr and Pb isotopic characteristics typical of subduction-related lavas—they are enriched in large ion lithophile elements (LILE), depleted in heavy rare earth elements (HREE) relative to light rare earth elements (LREE), have relatively low concentrations of high field strength elements (HSFE) and have negative Ce and positive Eu anomalies (Kennedy et al., 1990). In general, the trace element and isotopic signature of the TLTF volcanics suggest that they are the extrusive products of oxidized and volatile-rich magmas generated in a subduction-related environment (McInnes and Cameron, 1994; Müller et al., 2001).

The majority of radiometric ages for the TLTF arc were derived using the K–Ar isotopic dating technique, which is subject to thermal resetting and other complications (Tables 2.1 and 2.2). This is particularly important in the TLTF arc, where there are active high-temperature geothermal systems. For instance, rocks with temperatures >275°C have been recorded from Lihir geothermal wells (Simmons and Brown, 2006). These temperatures are comparable to the closure temperatures of the minerals dated, especially for K-feldspar (Table 2.1). For this reason, tectonic interpretations made using these data should be made with caution.

The oldest known volcanic rocks of the TLTF arc are pyroxene- and plagioclase-phyric mafic to intermediate lavas and dikes from the Tabar island group (Table 2.2; McInnes, 1992; Rytuba et al., 1993). Radiometric dating shows that overall, volcanic rocks progressively decrease in age from northwest to southeast along the TLTF arc (Table 2.2). However, there have been periods where volcanism has been active in all island groups simultaneously (Table 2.2). For instance, $\delta^{18}O$ values from foraminifera in submarine volcanic ash beds from the New Ireland Basin show that volcanic activity was particularly intense across the TLTF arc at ~75 to 35 ka (Herzig, 1996). Volcanism appears to have ceased within the TLTF arc, although

**Table 2.1.** Closure temperatures for minerals dated using the K–Ar and Ar–Ar dating techniques.

| Mineral | Closure temperature (°C) | Reference |
|---|---|---|
| ***K–Ar*** | | |
| Hornblende | 500 ± 50 | Harrison (1981) |
| Muscovite | 350 ± 50 | Hames and Bowring (1994) |
| Biotite | 300 ± 50 | Harrison et al. (1985) |
| K-feldspar | 150–350 | Lovera et al. (1989) |
| ***Ar–Ar*** | | |
| Hornblende | 400–600 | Harrison (1981); Dahl (1996) |
| Muscovite | 300–350 | Hames and Bowring (1994); Robbins (1972) |
| Biotite | 350–400 | Grove and Harrison (1996); Harrison et al. (1985) |
| K-feldspar | 150–350 | Lovera et al. (1991; 1997); Foland (1994) |

**Table 2.2.** Radiometric age data for igneous rocks from the TLTF island arc.

| Location | Age | Sample description | Material dated | Method | Reference |
|---|---|---|---|---|---|
| *Tabar Islands (~3.7–1.0 Ma)* | | | | | |
| Mt. Manambu | 3.5 ± 0.2 | Trachyte | Whole rock | K–Ar | Rytuba et al. (1993) |
| Mt. Manambu | 3.7 ± 0.2 | Trachyte | Whole rock | K–Ar | Rytuba et al. (1993) |
| Asllawa | 2.3 ± 0.4 | Basalt | Whole rock | K–Ar | Rytuba et al. (1993) |
| Asllawa | 3.1 ± 0.3 | Basalt | Whole rock | K–Ar | Rytuba et al. (1993) |
| Makopena | 2.8 ± 0.2 | Trachybasalt | Whole rock | K–Ar | Rytuba et al. (1993) |
| Mt. Tiro | 1.91 ± 0.10 | Trachybasalt | Whole rock | K–Ar | Rytuba et al. (1993) |
| Simberi | 2.9 ± 0.6 | Hawaiite | Amphibole | Ar–Ar | McInnes (1992) |
| Simberi | 2.94 ± 0.25 | Mugearite | Amphibole | Ar–Ar | McInnes (1992) |
| Simberi | 1.92 ± 0.27 | Alkali olivine basalt | Clinopyroxene | Ar–Ar | McInnes (1992) |
| Simberi | 3.13 ± 0.06 | Hawaiite | Amphibole | Ar–Ar | McInnes (1992) |
| Simberi | 3.6 ± 0.8 | Alkali olivine basalt | Amphibole | Ar–Ar | McInnes (1992) |
| Tabar | 0.986 ± 0.008 | Quartz trachyte | Plagioclase | K–Ar | Wallace et al. (1983) |
| *Lihir Islands (~1.1–0.2 Ma)* | | | | | |
| Luise amphitheater | 0.523 ± 0.009 | Hornblende-phyric andesite dike | Hornblende | Ar–Ar | This study (Ch.3) |
| Lienetz | 0.342 ± 0.036 | Pyroxene monzonite | Biotite | K–Ar | Davies and Ballantyne (1987); Moyle et al. (1990) |
| Lienetz | 1.09 ± 0.49 | Plagioclase-phyric andesite dike | Hornblende | Ar–Ar | Blackwell (2010) |
| Lienetz | 0.36 ± 0.03 | Monzonite porphyry | Biotite | K–Ar | Rytuba et al. (1993) |
| Tubaf Seamount | 0.222 ± 0.034 | Volcanics | Biotite | Ar–Ar | Kamenov (2008) |
| Conical Seamount | 0.287 ± 0.020 | ? | ? | ? | Kamenov (2008) |
| *Tanga Islands (~1.1–0.2 Ma)* | | | | | |
| Bitbok Island | 1.14 ± 0.08 | Quartz trachyte | Biotite | K–Ar | Wallace et al. (1983) |
| Bitbok Island | 1.08 ± 0.08 | Quartz trachyte | Biotite | K–Ar | Wallace et al. (1983) |
| Lif Island | 0.187 ± 0.02 | Trachybasalt | Whole rock | K–Ar | Wallace et al. (1983) |
| *Feni Islands (~1.5–0.002 Ma)* | | | | | |
| Babase Island | 1.53 ± 0.15 | Mafic lava | Hornblende | K–Ar | Wallace et al. (1983) |
| Ambitle volcano | 0.0023 ± 0.0001 | Phreatomagmatic tuff breccia | Volcanic ash | $^{14}C$ | Licence et al. (1987) |

very young phreatomagmatic deposits occur within the Feni group (2.3 ± 0.1 ka; Licence et al., 1987). The youngest volcanism within the Lihir group of islands occurs on Tubaf Seamount (222 ± 34 ka; Kamenov et al., 2008). North-northeast-trending swarms of low-magnitude, shallow earthquakes have been recorded south of Lihir Island (Johnson, 1979; McCue, 1988). This may indicate recently active normal faulting along the ridge-parallel structures bounding the Lihir group islands (Fig. 2.3; McInnes, 1992) and/or magmatism in the Lihir group submarine volcanos (Herzig, 1996; Herzig et al., 1998). Further radiometric dating is required to characterize the along-arc variations in age of the TLTF volcanics.

## 2.4 Present-day tectonic configuration

Papua New Guinea occupies a zone of oblique convergence between the Pacific and Indo-Australian plates that is occurring at a rate of ~10 cm per year on an azimuth of 070˚ (Tregoning et al., 2000). The relative direction of convergence has necessitated the development of oblique spreading centers, the Woodlark spreading center and the Bismarck Sea Seismic Lineation (BSSL), and the formation of numerous microplates (e.g., Adelbert, Solomon Sea, South Bismarck, North Bismarck, Caroline, New Ireland and Woodlark microplates; Fig. 2.1; Holm et al., 2016; Lindley, 2016). The TLTF island chain is situated within the North Bismarck microplate, which is bounded by the Mel-

anesian trench to the north and by the BSSL, Weitin fault and New Britain trench to the south (Fig. 2.1).

The Melanesian trench is a 3.0–4.5 km-deep, arcuate bathymetric feature composed of three segments—the North Solomon trench, the Kilinailau trench, and the Manus trench—that form a continuous line from the eastern Solomon Islands to the New Guinea trench (Fig. 2.1). The Kilinailau trench segment is immediately north and parallel to the TLTF island chain. The trench is considered to be a fossil feature related to the Oligocene-Miocene Outer Melanesian subduction system (Cooper and Taylor, 1987). Subduction along this trench is not considered to have been involved in the formation of the much younger (Pliocene-Pleistocene) TLTF islands. The North Bismarck microplate is currently moving northward relative to the Pacific plate at ~5–8 mm·yr$^{-1}$ (Tregoning et al., 1998). This relative movement has produced minor earthquake activity along the Outer Melanesian subduction suture and caused back-arc thrusting, sinistral strike-slip faulting and folding in the vicinity of Bougainville and western Solomon Islands (Bruns et al., 1989).

The major active convergent plate boundary in the TLTF region is the New Britain subduction zone, which accommodates dominantly north-directed subduction of the Solomon Sea microplate beneath the South Bismarck microplate. Its surface expression is the New Britain trench, a deep (~9 km), narrow (50–75 km), northeast-trending bathymetric feature flanking the south coast of the New Britain island arc (Fig. 2.1; Lindley 2006b). The eastern end of the trench lies to the south of Bougainville Island and is contiguous with the San Cristobal trench (Fig. 2.1). Its western end intersects mainland New Guinea near Lae, where it transitions into the Ramu-Markham fault (Fig. 2.1). In the region southeast of the Gazelle Peninsula and southern New Ireland (between 152˚30' and 153˚10'), the trough curves through a 70˚ angle and passes along the southwestern coast of Bougainville Island (Lindley, 2006b). The convergence rate along the New Britain trench is one of the highest on Earth; it varies along its length from 55 mm·yr$^{-1}$ at 147.5˚E to 130 mm·yr$^{-1}$ at 151.5˚E (Tregoning et al., 1998).

The subducting Solomon slab is continuous and moderately dipping around the bend in the New Britain trench to ~100 km depth (Fig. 2.4; Cooper and Taylor, 1989; Holm and Richards, 2013). Beyond this depth, the slab is steeply dipping, and there is evidence for large-scale contortion and segmentation (Fig. 2.4; Cooper and Taylor, 1989; O'Kane, 2008). Three-dimensional subducting slab models (O'Kane, 2008; Holm and Richards, 2013) depict a sub-vertical slab tear north of the bend in the New Britain trench and a segment of the slab that may be overturned (Fig. 2.4). The slab tear terminates beneath southern New Ireland and widens to the north, where it partly underlies the TLTF arc between Lihir and Tanga (Fig. 2.4; Holm and Richards, 2013). Deformation and segmentation of the Solomon slab may have developed in order to accommodate the subduction of the flat, rigid oceanic plate at the sharp curve in the New Britain trench and/or in response to sinistral transpression imposed on the subduction zone by the collision of the Ontong Java Plateau (Holm et al., 2015). Deep seismicity (>400 km) may originate within segments of the slab that have detached from the presently subducting slab (Cooper and Taylor, 1989).

The North Bismarck microplate is currently rotating counterclockwise (0.3–1.25˚ Ma$^{-1}$) and moving westward at 13–14 cm·yr$^{-1}$ relative to the South Bismarck microplate; concurrently, the South Bismarck microplate is rotating clockwise (~9˚ Ma$^{-1}$; Tregoning, 2002; Wallace et al., 2004, 2005). This oppositional relative motion has resulted in asymmetric seafloor spreading along the BSSL and opening of the Manus Basin (Fig. 2.1; Taylor, 1979; Martinez and Taylor, 1996). Magnetic anomalies along the spreading segments indicate that the average spreading vector along the BSSL is 13.2 cm·yr$^{-1}$ on an azimuth of 060˚ (Taylor, 1979). Volcanic rocks dredged from the spreading axes of the Manus Basin show a systematic variation from arc-like

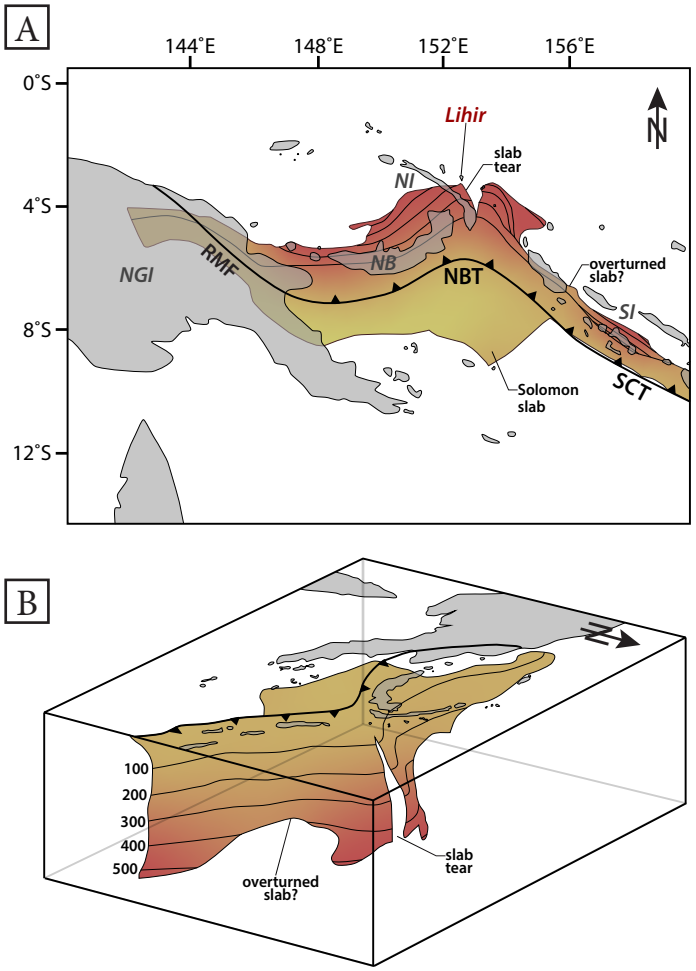


**Fig. 2.4.** 3-D model of the Solomon slab, which is actively subducting beneath the North Bismarck microplate at the New Britain and San Cristobal trenches. Slab depth is in kilometers and the top surface of the slab is contoured at 100 km intervals below the Earth's surface. **A.** Map view. The majority of tectonic elements have been omitted for simplicity. **B.** Moderately southwest-plunging view. Tectonic elements are the same as those in Figure 2.4A. Abbreviations: NB = New Britain Island, NBT = New Britain trench, NGI = New Guinea Island, NI = New Ireland, RMF = Ramu-Markham fault, SCT = San Cristobal trench, SI = Solomon Islands. Figure modified from O'Kane (2008) and Holm and Richards (2013).

to MORB-like compositions with increasing distance from the New Britain trench (Sinton et al., 2003; Taylor and Martinez, 2003).

The BSSL is composed of a series of linked wedge-like spreading centers and sinistral transform faults (Fig. 2.1; Taylor, 1979). Earthquakes along its trace are shallow (<50 km) and are focused along transform segments (Baldwin et al., 2012). The western extent of the BSSL forms a triple junction with the New Guinea trench (Fig. 2.1; Taylor, 1979). To the southeast, the BSSL extends between New Ireland and New Britain and is expressed subaerially in the surrounding area as a series of steeply dipping, west-northwest-trending transform faults (Figs. 2.1 and 2.2). The most significant of these faults are the Weitin and Sapom faults in New Ireland and the Baining, Mediva and Wide Bay faults on the Gazelle peninsula in New Britain (Fig. 2.2; Lindley, 2006a; Lindley, 2016). The Weitin fault can be traced southeast of New Ireland and terminates against the New Britain trench within the poorly defined region of the Feni Deep (Fig 2.1; Holm et al., 2016). Lindley (2016) connected the Weitin fault on New Ireland to a prominent west-northwest-trending fault on New Hanover (Fig. 2.1). It was proposed that the Weitin fault system divides the North Bismarck microplate into two segments: the narrow New Ireland microplate and the North Bismarck microplate (Fig. 2.1; Lindley, 2016).

From the Admiralty Islands north of the BSSL to the Witu Islands northeast of New Britain, there is a line of Holocene basalt and alkali-rich rhyolite volcanos that are not spatially associated with an actively subducting plate (Fig. 2.1). These volcanos are interpreted to have formed via intra-plate volcanism, and their location marks the present position of a hotspot that may be responsible for the northwest-trending Willaumez Rise that separates the New Guinea and Manus basins (Fig. 2.1; Johnson et al., 1978, Johnson et al., 1979).

## 2.5 Geodynamic evolution of Papua New Guinea

Following rifting and breakup of Gondwana from the late Jurassic to early Cretaceous, a passive continental margin developed along the northeast of the Australian continent (Hill and Hall, 2003). In the late Cretaceous, seafloor spreading initiated in the Tasman basin west of Australia (Weissel and Hayes, 1977). The axis of spreading propagated northwards until it reached the area of the Coral Sea, where rifting occurred between Australia and proto-New Guinea. In the Eocene, there was a change in Pacific Plate motion from dominantly northwards to westwards (Sharp

and Clague, 2006) and an increase in northwards motion of the Australian plate (Williamson and Hancock, 2005). This resulted in the termination of Coral Sea rifting and the initiation of subduction zones along the western margin of the Pacific Basin (Hilde et al., 1977; Kroenke, 1984). In the region northeast of proto-New Guinea, north-dipping subduction was initiated along the Papuan trench (composed of the Aure, Moresby and Pocklington segments), which produced the Sepik arc (Williamson and Hancock, 2005). Further east (~1,500 km), southwest-dipping subduction was initiated along the Manus-Kilinailau-North Solomon trench. This subduction system generated the northern segment of the Melanesian arc (aka. Outer Melanesian arc, Western Melanesian arc or Northern Melanesian arc; van Ufford and Cloos, 2005), which extended southward along the Solomon, Vanuatu, Fiji and Tonga island arcs to northern New Zealand (Chase, 1971; Kroenke, 1984).

At ~35–30 Ma, the northeastern edge of proto-New Guinea collided with the Sepik arc (van Ufford and Cloos, 2005), causing widespread uplift and regional metamorphism in the Papuan Peninsula (Sepik Event) and terminating volcanism within the Sepik arc. Continued convergence resulted in the accretion of the Sepik arc and the formation of the Papuan Ultramafic Belt (van Ufford and Cloos, 2005; Kroenke, 1984). Accommodation of continued convergence was taken up along the Outer Melanesian arc (Kroenke, 1984; van Ufford and Cloos, 2005).

The late Eocene (43–37 Ma) Baining Volcanics on the Gazelle Peninsula in New Britain represent the onset of Outer Melanesian arc volcanism (Fig. 2.2; Holm et al., 2013). Eocene to Miocene calc-alkalic volcanism associated with the southwest-dipping subduction zone built up a contiguous chain of islands east of New Guinea that formed the Adelbert, Finisterre, New Britain, Manus, New Ireland, and Bougainville-Solomon islands. Between proto-New Ireland and the Kilinailau trench, the sediments of the New Ireland basin were deposited. This fore-arc basin was a significant sedimentary depocenter and accumulated thick (>5 km-thick) deposits of intercalated volcaniclastics, tuffaceous limestones, mudstones, foraminiferal wackestones and organic-rich claystones (Fig. 2.3; McInnes and Amiribesheli, 2018). The mantle wedge beneath the New Ireland basin became strongly metasomatized by fluids sourced from the dehydrating Pacific slab (McInnes and Cameron, 1994; Grégoire et al., 2001; McInnes et al., 2001).

In the late Oligocene (~26 Ma), the large, plume-derived Ontong Java Plateau began to collide with the North Solomon trench and commenced a period of widespread tectonic reorganization in the SW Pacific (Holm et al., 2013). The collision resulted in the termination of Pacific plate subduction at the Melanesian trench. This was followed by intrusive activity in the Outer Melanesian arc that was associated with porphyry Cu(-Au-Mo) mineralization (Table 2.3; Fig. 2.5; Holm et al., 2013). These porphyry deposits are distributed widely throughout the arc, instead of being localized in the Solomon Islands near the site of plateau-trench collision (Fig. 2.5). Post-collision mineralizing intrusions from the Simuku porphyry complex in New Britain (Table 2.3; Fig. 2.5) have been shown to exhibit adakite-like geochemical signatures. This may indicate that partial melting of the stagnant Pacific slab was an important driver in this period of porphyry generation (Holm et al., 2013). Shortly after collision, localized extensional zones were established within the Melanesian arc (e.g., Central Solomon Basin) that may have been induced by the steepening of the Pacific slab (Holm et al., 2013). In eastern New Britain, north-northeast-trending extensional structures were formed that focused Miocene-Pliocene caldera-related volcanism (i.e., Nengmutka Volcanics) and associated epithermal gold mineralization (i.e., Sinivit gold deposit; Table 2.3; Figs. 2.2 and 2.5; Lindley, 1988; Lindley, 2006a).

By the early Miocene, magmatism had terminated across the majority of the western Outer Melanesian arc (Petterson et al., 1999; Lindley, 2006a). However, the occurrence of middle Miocene porphyry mineralization (Arie and Mt. Kren prospects; Table 2.3; Fig 2.5) on Manus Island

**Table 2.3.** Oligocene-Miocene mineral deposits of the Melanesian arc.

| # | Deposit | Location | Lat., Long. | Deposit type | Resource | Age | Reference |
|---|---|---|---|---|---|---|---|
| 1 | Simuku | New Britain | -5.72, 150.02 | P | Cu-Mo | 24–20 Ma | Holm et al. (2013) |
| 2 | Plesyumi | | -5.97, 150.38 | P | Cu-Au | 24 Ma | Titley (1978) |
| 3 | Mt. Nakru | | -5.97, 150.47 | P | Cu-Au-Mo | 24 Ma | Singer et al. (2008) |
| 4 | Esis | | -5.04, 151.74 | P | Cu-Au | 25 Ma | Hine et al. (1978) |
| 5 | Sinivit (Wild Dog) | | -5.04, 151.74 | LSE | Au | 23–22 Ma | Lindley (1998) |
| 6 | Arie | Manus Island | -2.02, 146.88 | P | Cu-Au | 15 Ma | Jaques and Webb (1975) |
| 7 | Mt. Kren | | -2.16, 146.94 | P | Cu | 15–12 Ma | Singer et al. (2008) |
| 8 | Legusalem | New Ireland | -3.18, 151.65 | P | Cu | Oligocene-Miocene | Singer et al. (2008) |
| 9 | Poha | Guadalcanal | -9.43, 159.83 | P | Cu | 24.4 Ma | Chivas and McDougall (1978) |
| 10 | Mbetilonga | | -9.61, 160.16 | P | Cu | Oligocene | Singer et al. (2008) |

Abbreviations: LSE = low sulfidation epithermal, P = porphyry.

suggests magmatism may have persisted within the arc, distal to the site of collision. During the Miocene hiatus in volcanic activity and related sedimentation, thick carbonate sequences accumulated on an extensive platform that spanned 5,600 km from southeast Asia through the New Guinea region to Fiji (Lindley, 2006a). Isolated remnants of Miocene shelf carbonates are preserved on Gazelle Peninsula (Yalam Limestone), New Ireland and the Tabar islands (Lelet Limestone; Fig. 2.2; Lindley, 2006a).

At ~20 Ma, south-dipping subduction of the Solomon Sea microplate along the Trobriand-Wewak trench was initiated in response to the termination of Outer Melanesian subduction (Fig. 2.1; Kroenke, 1984; Hall, 2002). Related continental arc magmatism generated the Maramuni arc intrusions and porphyry-epithermal deposits from ~17–12 Ma (Maramuni belt; Table 2.4; Fig. 2.5; Rinne, 2015). Between 15–12 Ma, the western end of the Outer Melanesian arc (Adelbert and Finisterre terranes; Fig. 2.1) began to collide with New Guinea, resulting in east to west closure of the Trobriand-Wewak trench and a period of uplift and compressional deformation on New Guinea (from 12–4 Ma; New Guinea Orogen; Hill and Raza, 1999; Cloos et al., 2005). The collision between the Adelbert and Finisterre terranes and New Guinea is ongoing (Pigram and Davies, 1987; van Ufford and Cloos, 2005), with rates of uplift in the Finisterre and Sarawaged ranges on the Huon Peninsula from 1–3 mm·yr$^{-1}$ (Chappell, 1974). No Oligocene-Miocene-age porphyry-epithermal deposits are known to occur within the Adelbert or Finisterre terranes (Fig. 2.5); the deposits may not have been preserved due to rapid uplift and erosion associated with the arc-continent collision.

By 12–6 Ma, there was a reversal in subduction polarity in the Papua New Guinea-Solomon Islands region, wherein northwest- to northeast-dipping subduction was established at the arcuate, New Britain–San Cristobal trench. The change in subduction direction caused the western margin of the Solomon slab to adopt an antiformal morphology, with north- and south-dipping limbs and a shallowly west-plunging hinge (Rinne, 2015). It has been proposed that westward migration of this shallow hinge zone beneath New Guinea has resulted in westward-younging magmatism and associated porphyry-epithermal deposits (post-Maramuni belt; Table 2.4; Fig. 2.5; Rinne, 2015).

North of New Guinea, south-dipping subduction was maintained along the New Guinea trench, where it continues to the present day (Tregoning and Gorbatov, 2004). Low-angle subduction associated with the collision of the Euripik Rise and New Guinea trench between 135˚E–140˚E (Gutscher et al., 2000) may have contributed to the formation of Au-rich porphyry deposits in central New Guinea, including Ok Tedi (Table 2.4; Fig. 2.5) and Grasberg (Irian

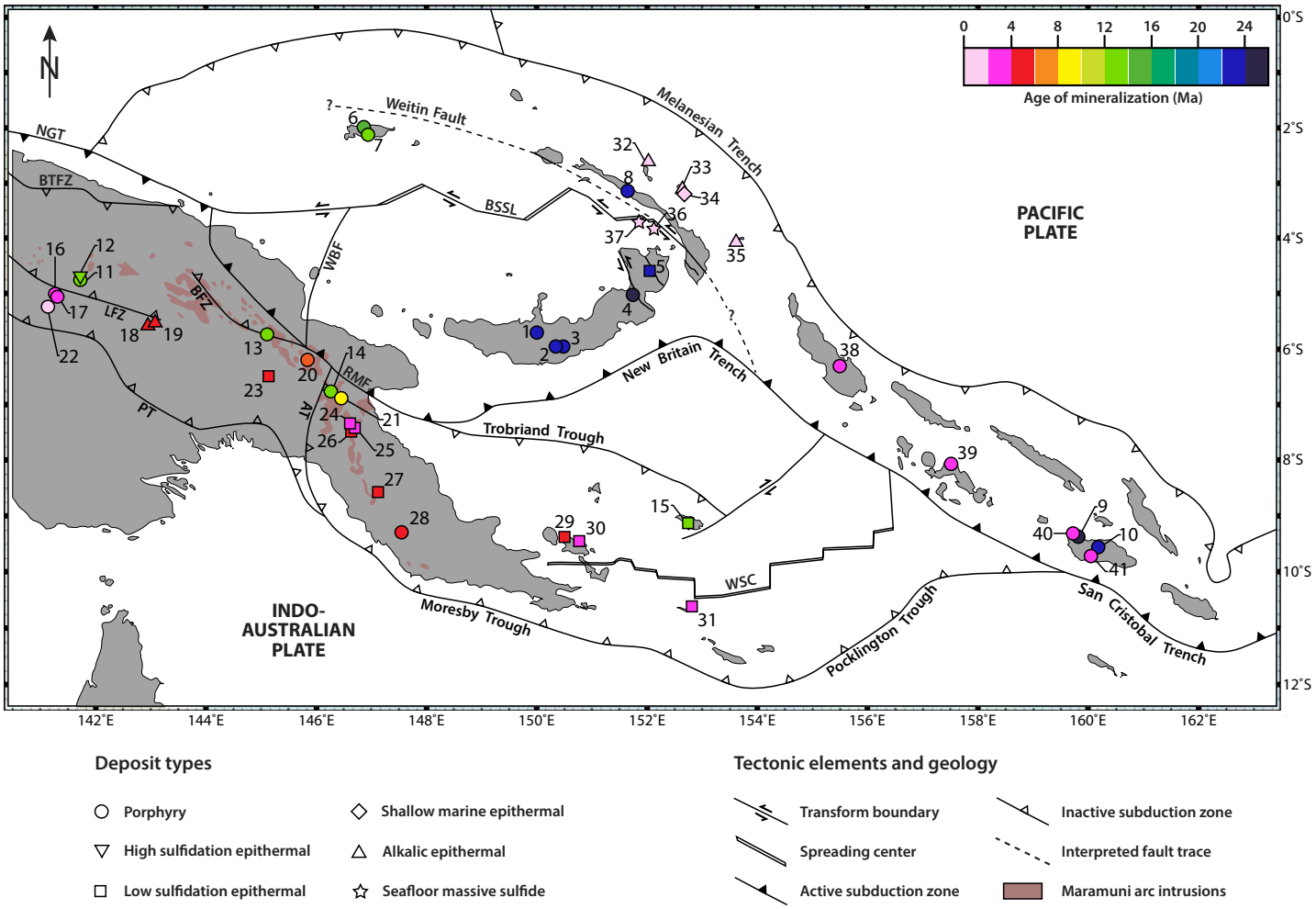


**Fig. 2.5.** Oligocene-Present mineral deposits of Papua New Guinea and the Solomon Islands. Parts of this figure were produced with GeoMapApp (http://www.GeoMapApp.org). Tectonic plates are after Martinez and Taylor (1996), Holm et al. (2016) and Lindley (2016). References for ages of mineralization are provided in Tables 2.3–2.5. Maramuni arc intrusions are from Cloos et al. (2005). Maramuni arc intrusions also occur on Woodlark Island (Webb et al., 2014), but are not visible at the scale of this map. Abbreviations: AT = Aure Trough, BFZ = Bundi fault zone, BSSL = Bismarck Sea Seismic Lineation, BTFZ = Bewani-Torricelli fault zone, LFZ = Lagaip fault zone, PT = Papuan Thrust, RMF = Ramu-Markham fault, WBF = West Bismarck fault, WSC = Woodlark spreading center. Mineral deposits: 1 = Simuku, 2 = Plesyumi, 3 = Mt. Nakru, 4 = Esis, 5 = Sinivit (Wild Dog), 6 = Arie, 7 = Mt. Kren, 8 = Legusalem, 9 = Poha, 10 = Mbetilonga, 11 = Frieda River, 12 = Nena, 13 = Yandera, 14 = Wamum, 15 = Woodlark, 16 = Star Mts. Nong River, 17 = Star Mts. Futik, 18 = Mt. Kare, 19 = Porgera, 20 = Kainantu, 21 = Wafi-Golpu, 22 = Ok Tedi, 23 = Crater Mountain, 24 = Edie Creek, 25 = Kerimenge, 26 = Hidden Valley, 27 = Tolukuma, 28 = Kodu, 29 = Wapolu, 30 = Gameta, 31 = Misima, 32 = Simberi, 33 = Lihir (Ladolam), 34 = Conical Seamount, 35 = Kabang, 36 = Solwara 1, 37 = Solwara 12, 38 = Panguna, 39 = Mase, 40 = Hidden Valley, 41 = Koloula.

Jaya; Cooke et al., 2005). The majority of other Pliocene to Recent mineral deposits in the New Guinea Orogen are low sulfidation epithermal Au(-Ag) deposits that are distributed within the Papuan Peninsula, Papuan Islands and Louisiade Archipelago (Table 2.4; Fig. 2.5). These deposits may be related to magmatic activity generated via lithospheric delamination and adiabatic decompression of the mantle following the collision of the Outer Melanesian arc (Cloos et al., 2005).

Renewed volcanism associated with the New Britain–San Cristobal subduction system (West Bismarck, New Britain and Solomon arcs; Fig. 2.1) overprinted the Eocene-Miocene Outer Melanesian basement rocks in the New Guinea and Solomon islands (Petterson et al., 1999) and was accompanied by widespread uplift and deposition of fluvial and marine volcaniclastics (Lindley, 2006a; Holm et al., 2013). Increased sediment input associated with the volcanic activity may have caused the death of the Miocene platform reef complex (Lindley, 2006a). South of the New Britain trench, counterclockwise rotation of the Solomon Sea microplate resulted in extension and the opening of the

**Table 2.4.** Mineral deposits of the New Guinea Orogen.

| # | Deposit | Location | Lat., Long. | Deposit type | Resource | Age | Reference |
|---|---|---|---|---|---|---|---|
| *Maramuni Belt* | | | | | | | |
| 11 | Frieda River | West Sepik | -4.66, 141.73 | P | Cu-Au | 13.6–11.5 Ma | Whalen et al. (1982) |
| 12 | Nena | | -4.65, 141.73 | HSE | Cu-Au | 13 Ma | Bainbridge et al. (1998) |
| 13 | Yandera (early-stage) | Madang | -5.74, 145.13 | P | Cu-Au | 14–12 Ma | Grant and Nielsen (1975) |
| 14 | Wamum | Morobe | -6.75, 146.28 | P | Cu-Au | 12.1–11.9 Ma | Holm et al. (2015) |
| 15 | Woodlark* | Woodlark Island | -9.19, 152.72 | LSE–ISE | Au | 12.5–12.2 Ma | Russell and Finlayson (1987); Burkett (2017) |
| *Post-Maramuni Belt* | | | | | | | |
| 16 | Star Mts. (Nong River) | Western Province | -5.02, 141.22 | P, S | Cu | 3.6 Ma | Singer et al. (2008) |
| 17 | Star Mts. (Futik) | | -5.07, 141.33 | P, S | Cu-Au | 3.7 Ma | Singer et al. (2008) |
| 18 | Mt. Kare | Enga | -5.57, 142.98 | AE | Au | 5.5 Ma | Richards and Ledlie (1993) |
| 19 | Porgera | | -5.46, 143.08 | AE | Au | 5.9 Ma | Ronacher et al. (2002) |
| 14 | Yandera (main-stage) | Madang | -5.74, 145.13 | P | Cu-Au | 6.5 Ma | Grant and Nielsen (1975) |
| 20 | Kainantu | Eastern Highlands | -6.20, 145.86 | P | Cu-Au | 9.4–6.2 Ma | Holm et al. (2015) |
| 21 | Wafi-Golpu | Morobe | -6.88, 146.45 | P, HSE ISE | | 8.8–8.6 Ma | Rinne et al. (2018) |
| *Other Pliocene to Recent deposits* | | | | | | | |
| 22 | Ok Tedi | Western Province | -5.21, 141.14 | P, S | Au-Cu | 1.2 Ma | Large et al. (2018) |
| 23 | Crater Mountain | Eastern Highlands | -6.49, 145.17 | P | Au | <Pliocene (?) | Noku et al. (2010) |
| 24 | Edie Creek | Morobe | -7.33, 146.67 | LSE | Au-Ag | <3.8 Ma | Page and McDougall (1972a) |
| 25 | Kerimenge | | -7.42, 146.72 | LSE | Au | <3.8 Ma | Page and McDougall (1972a) |
| 26 | Hidden Valley | | -7.46, 146.67 | LSE | Au-Ag | 4.2 Ma | Nelson et al. (1990) |
| 27 | Tolukuma | Central Province | -8.56, 147.13 | LSE | Au-Ag | Pliocene | Langmead and McLeod (1990) |
| 28 | Kodu | | -9.30, 147.58 | P, LSE | Cu-Au-Mo | 4.4 Ma | Dugmore and Leaman (1998) |
| 29 | Wapolu | Fergusson Island | -9.36, 150.50 | LSE | Au | Pliocene | McNeil (1990) |
| 30 | Gameta | | -9.42, 150.79 | LSE | Au | Pleistocene | Chapple and Ibil (1998) |
| 31 | Misima | Misima Island | -10.66, 152.81 | LSE | Au | 3.5 Ma | Appleby et al. (1996) |

*Woodlark consists of the Kulumadau, Busai and Bonaviat deposits. Abbreviations: AE = alkalic-type epithermal gold, HSE = high sulfidation epithermal, ISE = intermediate sulfidation epithermal, LSE = low sulfidation epithermal, P = porphyry, S = skarn.

Woodlark Basin at the Woodlark spreading center from ~6 Ma (Fig. 2.1; Taylor et al., 1995, 1999). Several porphyry deposits have formed on Bougainville and the Solomon Islands since the Pliocene (Table 2.5; Fig. 2.5). These may have been triggered by the subduction of the Woodlark spreading center at the San Cristobal trench (Mase porphyry prospect) or the subduction of lower plate structures marginal to the Woodlark Basin (Panguna, Hidden Valley, Koloula; Holm et al., 2015).

'Hard docking' of the Ontong Java Plateau at the North Solomon trench began at ~6 Ma, intensified at 4–2 Ma and continues today (Wessel and Kroenke, 2000). It has produced intense compressional deformation in the Solomon Islands near the site of collision (Malaita Anticlinorium; Pettersen et al., 1999) and widespread deformation along the northern margin of the Indo-Australian plate (Wessel and Kroenke, 2000). In the Bismarck Sea, rapid asymmetric back-arc spreading in the Manus Basin has been occurring since ~3.5 Ma, dividing the region into the North Bismarck and South Bismarck microplates (Taylor, 1979). Seafloor spreading has been coincident with large areas of hydrothermal activity and the development of seafloor massive sulfide deposits in the Manus Basin (e.g., Solwara 1 and Solwara 12; Table 2.5; Figs 2.2 and 2.5).

The alkalic TLTF arc and associated epithermal deposits (e.g., Lihir; Table 2.5; Figs. 2.2 and 2.5) have formed since

**Table 2.5.** Pliocene-Present mineral deposits of the Melanesian arc.

| # | Deposit | Location | Lat., Long. | Deposit type | Resource | Age | Reference |
|---|---|---|---|---|---|---|---|
| 32 | Simberi | TLTF islands | -2.75, 151.97 | AE | Au | <3.6 Ma | Rytuba et al. (1993) |
| 33 | Lihir | | -3.13, 152.63 | AE | Au | <0.4 Ma | This study (Ch. 4) |
| 34 | Conical Seamount | | -3.31, 152.66 | SME | Au | <~0.3 Ma | Kamenov et al. (2008); Herzig et al. (2003) |
| 35 | Kabang | | -5.72, 150.02 | AE | Au | <0.5 Ma | Sillitoe (1989) |
| 36 | Solwara 1 | Manus Basin | -3.80, 152.09 | SMS | Cu-Au-Ag-Zn | Active | Gena (2013) |
| 37 | Solwara 12 | | -3.70, 151.88 | SMS | Cu-Au-Ag-Zn | Active | Gena (2013) |
| 38 | Panguna | Bougainville | -6.33, 155.50 | P | Au-Cu | 3.4 Ma | Page and McDougall (1972b) |
| 39 | Mase | New Georgia | -8.08, 157.52 | P | Cu-Au | 3.6 Ma | Singer et al. (2008) |
| 40 | Hidden Valley | Guadalcanal | -9.37, 159.73 | P | Cu-Au | 2.6 Ma | Singer et al. (2008) |
| 41 | Koloula | | -9.78, 160.03 | P | Cu-Au | 2.4–1.6 Ma | Chivas and McDougall (1978) |

Abbreviations: AE = alkalic epithermal gold, P = porphyry, SME = shallow marine epithermal, SMS = seafloor massive sulfide, LSE = low sulfidation epithermal.

~3.7 Ma in a hybrid zone of oblique convergence (related to the collision of the Ontong Java Plateau) and transtension (related to its position in the back-arc to the New Britain–San Cristobal subduction system; Table 2.2; Wallace et al., 1983). Island formation has taken place episodically during northwest-directed translocation and counterclockwise rotation of the North Bismarck microplate relative to the South Bismarck microplate (Fig. 2.6; Sykora, 2017). Over this time period, parts of the TLTF arc have overlain a series of irregularities in the Solomon slab, including a V-shaped slab tear (Figs. 2.4 and 2.6; Holm et al., 2015; Sykora, 2017).

The parental magmas for the TLTF volcanics are thought to have formed by a multi-stage process (Fig. 2.7):

1. Normal subduction at the Melanesian trench in the Eocene-Oligocene caused dehydration melting of the mantle wedge above the Pacific slab and generation of the New Ireland island arc. In the shallower and colder fore-arc region, dewatering of the Pacific slab resulted in widespread hydrofracturing and hydration metasomatism of the overlying mantle wedge (Fig. 2.7A; McInnes et al., 2001; Kamenov et al., 2008).

2. The collision of the Ontong Java Plateau near the Solomon Islands resulted in the cessation of subduction along the Melanesian trench, and the Pacific slab became stalled beneath the New Ireland basin. The temperature rose within the mantle wedge and transferred heat to the stalled Pacific slab, which eventually reached its melting temperature. Partial melting of the seawater-altered basalts and sediments resulted in strongly oxidized, alkali-rich aluminosilicate melts enriched with Sr, Ba, Cl, F, sulfate, carbonate and water. The melts penetrated the previously subduction-modified mantle wedge. Reaction of mantle minerals with the alkali-rich aluminosilicate melt produced a hybridized and vertically zoned mantle wedge (Fig. 2.7B; McInnes and Cameron, 1994).

3. Partial melting of the hybridized mantle wedge was triggered at ~70 km depth beneath the New Ireland basin, producing the parental magmas of the TLTF volcanics (Fig. 2.7C and D; McInnes and Cameron, 1994).

Seismic profiles of the New Ireland basin provide evidence for high-angle extensional structures (horsts and grabens) between the TLTF island groups that were the result of Pliocene-Pleistocene extension (Fig. 2.3). It therefore follows that the final episode of partial melting may have been caused by adiabatic decompression related to extension in the New Ireland basin lithosphere (Fig. 2.7C and D). The extensional structures are approximately arc-normal to New Ireland and the Kilinailau trench and may have been

partly or wholly inherited from the pre-existing structural architecture of the New Ireland basin. Alternatively, the structures may have developed:

1. in response to and radially about a buckle in the Solomon slab (Carman, 2003),

2. as localized lithospheric perturbations associated with and perpendicular to the sinistral displacement of New Britain with respect to New Ireland (McInnes, 1992), or

3. in response to plate flexure and ridge development during periods of accumulating transpressional stress in the New Ireland basin lithosphere (Lindley, 2016).

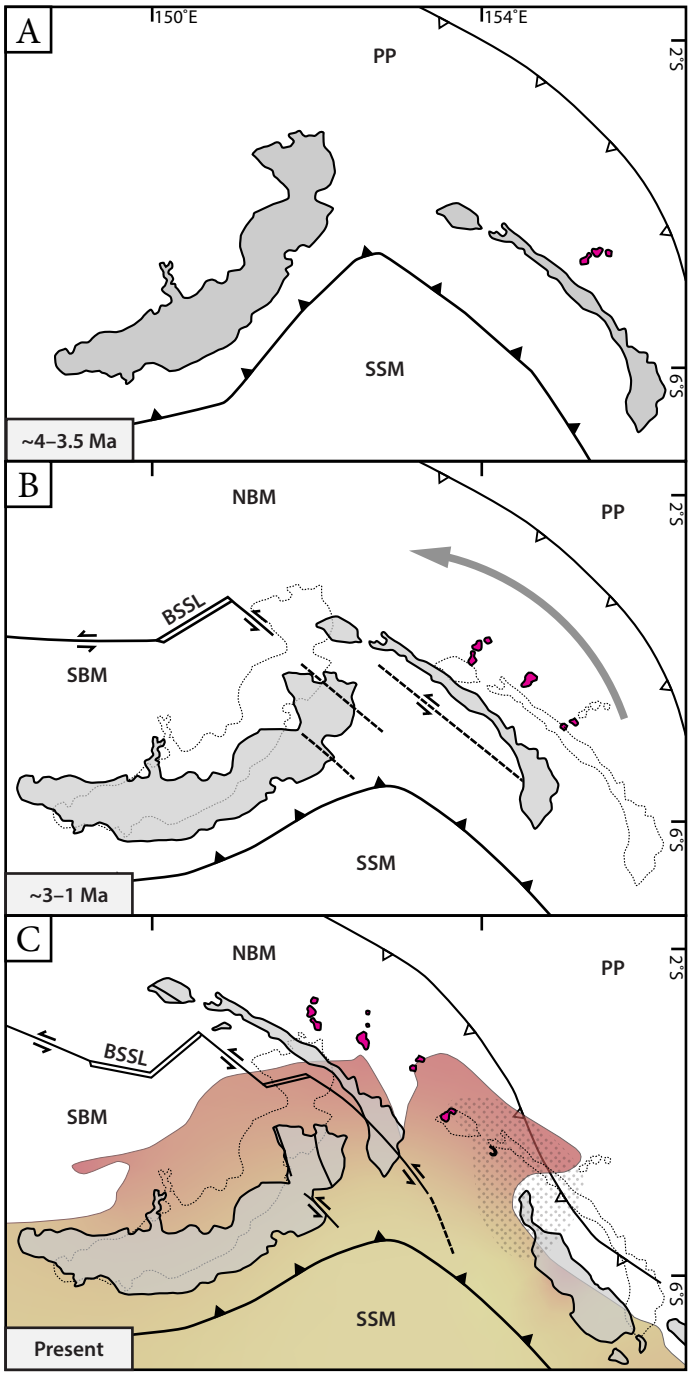


Sykora (2017) noted that the progressive counterclockwise rotation of originally east-northeast-trending extensional structures could have produced their present-day radial geometry (Fig. 2.6). Rotation may have brought the structures into the compressional field of strain and could have eventually lead to the progressive cessation of volcanism. Transient periods of localized compression related to torsion of the lithosphere may have promoted magmatic fractionation, intrusive activity and porphyry mineralization (e.g., at Lihir). Rotation of the Fiji Platform may also have been a factor in the formation of the Emperor alkalic epithermal gold deposit in Fiji.

An alternative theory is that asthenospheric upwelling through the Solomon slab tear (Holm and Richards, 2013; Holm et al., 2015) or related to other irregularities in the Solomon slab (Sykora, 2017), may have provided a local heat source that triggered partial melting. Sykora (2017) highlighted an east-trending splay of deep-seated exten-

**Fig. 2.6.** Tectonic reconstruction of the TLTF islands region from ~4 Ma to Present (modified from Sykora, 2017, and sources therein). **A.** *~4–3.5 Ma:* Formation of the Tabar island group along an east-northeast-trending ridge that is located to the east of the inflection in the New Britain trench. **B.** *~3–1 Ma:* The Bismarck Sea Seismic Lineation has been established in the Bismarck Sea, accommodating sinistral displacement of the North Bismarck microplate with respect to the South Bismarck microplate. The TLTF islands form progressively (from northwest to southeast) during northwest translocation and counterclockwise rotation. Extensional or transtensional structures controlling the emplacement of the island groups are rotated from their initial east-northeast orientation (cross-arc) into north-northwest to northeast orientations (oblique to the arc) over time. This puts the structures into compression and eventually leads to the progressive discontinuation of volcanism from northwest to southeast. **C.** *Present:* Current configuration of the TLTF islands and the Solomon slab (Fig. 2.4; Holm and Richards, 2013). The Feni island group, which has formed most recently, is aligned to the northeast. It currently overlies an area of deep-seated extensional earthquakes (*gray stippled area*). These earthquakes may represent an irregularity in the Solomon slab that has promoted magmatism (Sykora, 2017). The Solomon slab is colored yellow to red representing shallowest to deepest depths, respectively. Abbreviations: BSSL = Bismarck Sea Seismic Lineation, NBM = North Bismarck microplate PP = Pacific plate, SBM = South Bismarck microplate, SSM = Solomon Sea microplate.

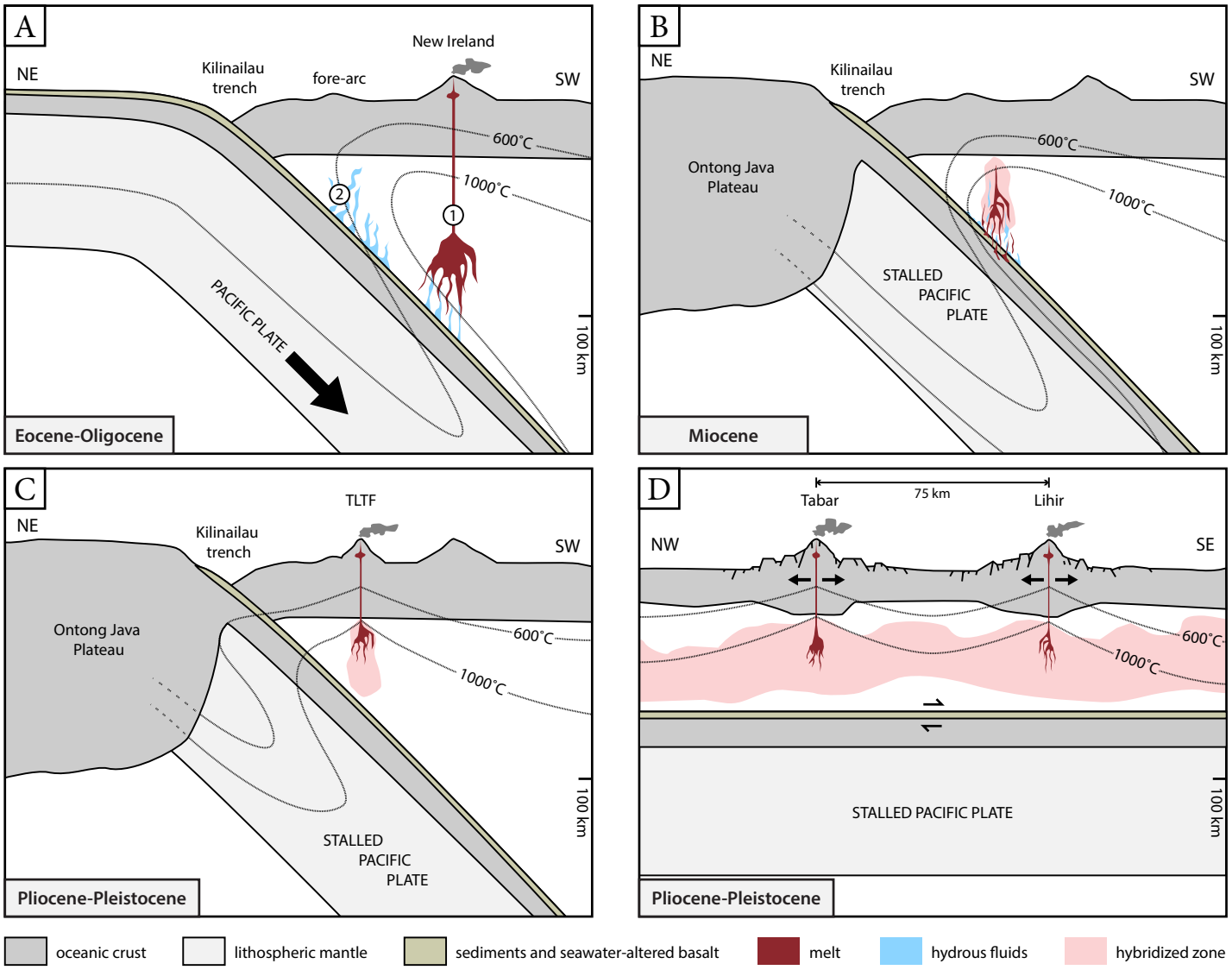


**Fig. 2.7.** Model for the origin of TLTF volcanism. Parts of this figure are modified from McInnes and Cameron (1994) and Kamenov et al. (2008). **A.** *Eocene-Oligocene:* Subduction of the Pacific plate at the Kilinailau trench produced dehydration melts (1), which ascended through the mantle wedge and generated volcanism in the New Ireland island arc. In the colder fore-arc region (2), dehydration of the sedimentary layer of the Pacific slab caused hydrous metasomatism and hydraulic fracturing of the mantle wedge. The geochemical signature associated with the sedimented portion of the slab was transfered into the mantle wedge with the fluids. **B.** *Miocene (<26 Ma):* Following the collision of the Ontong Java Plateau, subduction ceased along the Kilinailau trench and volcanism was discontinued in the New Ireland arc. Mantle isotherms gradually recovered in the stalled Pacific slab, resulting in slab melting subjacent to the New Ireland basin. The resultant oxidized, volatile- and alkali-rich aluminosilicate melts were highly reactive, and interacted with the previously metasomatized mantle wedge to form a hybridized mantle region. **C.** *Pliocene-Pleistocene (<3.7 Ma):* Partial melting of the hybridized mantle zone occurred by adiabatic decompression associated with upper plate extension in the New Ireland basin. As the extensional structures were progressively rotated into the compressional field of strain (Fig. 2.6), volcanism discontinued in the TLTF islands from northwest to southeast. **D.** Arc-parallel view of Figure 2.7C. This view provides a cross-section of the ridges, their equally spaced arc-perpendicular horst and graben structures and the dish-shaped mantle geotherms associated with adiabatic decompression melting of the hybridized zone. Sinistral strike-slip movement may have been transient along the boundary between the stalled Pacific plate and mantle wedge over this time period (Kilinailau fault; Lindley, 2016).

sional earthquakes along the Solomon slab to the southeast of the Feni Islands that may represent one of these irregularities (Fig. 2.6). In this model, the locus of volcanism would remain fixed over the heat source as the North Bismarck microplate migrated relative to it. This model would help to explain the apparent southeast younging of volcanism in the TLTF islands. However, it contradicts evidence for continuing volcanism in island groups that would have migrated away from any theoretical fixed point along the chain (Table 2.2).

## 2.6 Summary

The Papua New Guinea and Solomon Islands region has evolved within the obliquely and rapidly converging Indo-Australian and Pacific plate boundary zone. Its Cenozoic geodynamic evolution has involved a wide range of plate tectonic processes, including arc formation, subduction polarity reversal, arc accretion, back-arc spreading and the collision of a large oceanic plateau. Many of the region's porphyry and epithermal deposits formed during episodes of tectonic reorganization associated with major collision events. Others formed during transient periods of low-angle subduction caused by the subduction of buoyant oceanic crustal features (e.g., the Euripik Rise and Woodlark spreading center) or unusually shaped slab segments (e.g., the antiformal western Solomon slab) beneath oceanic island and continental arcs.

The TLTF island chain is an enigmatic feature of northeastern Papua New Guinea that has resulted from a complex and unique tectonic history. The most important tectonic events with respect to the formation of the TLTF island arc and the Lihir gold deposit were:

1. *Outer Melanesian subduction (Eocene to Oligocene).* This built up the New Ireland basement structure and adjacent fore-arc basin and metasomatized the underlying mantle wedge with volatiles derived from the subducting, seawater-altered Pacific slab.

2. *Collision of the Ontong Java Plateau with the Melanesian trench (~26 Ma).* This resulted in the cessation of Outer Melanesian subduction and the segmentation of the Indo-Australian Plate into a series of microplates (South Bismarck, North Bismarck and Solomon Sea microplates). The microplates developed different velocities and directions of rotation, due to the uneven stress imposed on different regions of the Indo-Australian plate by the collision.

3. *Subduction polarity reversal in the New Ireland region (12–6 Ma),* via initiation of north-directed subduction along the arcuate New Britain–San Cristobal trench.

4. *The opening of a series of linked spreading centers and sinistral transforms (BSSL) in the back-arc to the New Britain trench*, which accommodated counterclockwise rotation and westward motion of the North Bismarck microplate relative to the South Bismarck microplate. Ascent of magma along regularly spaced and deeply penetrating extensional structures allowed for the progressive and episodic formation of the TLTF islands from northwest to southeast. Tears or other irregularities in the down-going Solomon slab may have added heat from the mantle that promoted magmatism in the New Ireland region.

# CHAPTER 3

# Geology of the Kapit NE and Coastal Ore Zones

## 3.1 Introduction

This chapter documents the geology of the Kapit NE and Coastal ore zones and presents new whole-rock geochemical data and Ar–Ar geochronology results for a subset of the igneous rocks. These data are used to define the architecture of the host succession to the Lihir gold deposit and provides a framework from which to assess the relationship between the volcano-sedimentary host rocks, alkalic intrusions and both porphyry-style and epithermal gold mineralization in Chapter 4. A summary of the geology of Lihir Island and the host rocks in the Minifie, Lienetz and Kapit ore zones is also provided, based on a review of previous studies.

## 3.2 Geology of Lihir Island

Lihir Island is composed of five distinct volcanic blocks flanked by uplifted limestone terraces (Wallace et al., 1983; Komyshan, 1999; Fig. 3.1B). Each of the volcanic blocks comprises a thick (>100 m) package of interbedded mafic lavas, pyroclastic rocks, unconsolidated tephra and volcano-sedimentary rocks (Wallace et al., 1983). Rough age estimates were assigned for the volcanic blocks according to their geomorphological characteristics: Londolovit Block (late Miocene to Pliocene), Wurtol Wedge (Plio-Pleistocene), Huniho Volcano (Pleistocene), Kinami Volcano (Pleistocene), and Luise Volcano (Pleistocene to Holocene; Wallace et al., 1983). Argillic and phyllic alteration zones occur within most of the volcanic craters on Lihir Island and are partly localized on east-northeast-trending fracture zones (Komyshan, 1999; Fig. 3.1B and C). Generally, the best developed structures on Lihir Island are normal faults that strike 040˚ to 050˚ and dip 40 to 50˚ to the northwest (Wallace et al., 1983; Moyle et al., 1990; Pridmore, 1991; Komyshan, 1999; Fig. 3.1C). A tilt of 30˚ to the south has been identified in the volcano-sedimentary stratigraphy of the Luise Volcano in the Minifie ore zone and is inferred to be associated with regional uplift (Blackwell et al., 2014). A similar south to southwest tilt has been recognized in limestone platforms throughout the TLTF islands (Wallace et al., 1983). There is no evidence that regional metamorphism or ductile deformation have occurred since the formation of Lihir Island.

Luise Volcano features a north-northeast-trending elliptical (3.5 × 4 km) crater at its summit, referred to as the Luise amphitheater (Figs. 3.1 and 3.2). The amphitheater has steep (up to 70˚) sides that slope upwards to 640 m rsl and a raised floor that dips shallowly from 260 m rsl toward the Luise Harbor (Fig. 3.1; Blackwell et al., 2014). The amphitheater walls are breached on the northeastern side, having been disrupted by one or more volcanic sector collapse events (Davies and Ballantyne, 1987; Sillitoe, 1989; Moyle et al., 1990; Sillitoe, 1994; Blackwell, 2010; White et al., 2010). A debris avalanche (defined by hummocky topography with marginal levees) extending greater than 10 km offshore to the northeast has been identified from seafloor bathymetry images (Fig. 3.2; Herzig et al., 1998; Blackwell, 2010; White et al., 2010) and is likely related to sector collapse. The Lihir gold deposit is located beneath the floor of the amphitheater, spatially coincident with a large hydrothermal alteration zone and areas of modern geothermal activity (Fig. 3.1). Two overlapping circular demagnetized zones occur within the amphitheater: one is centered on the Lihir gold mine and the other is located beneath Luise Har-

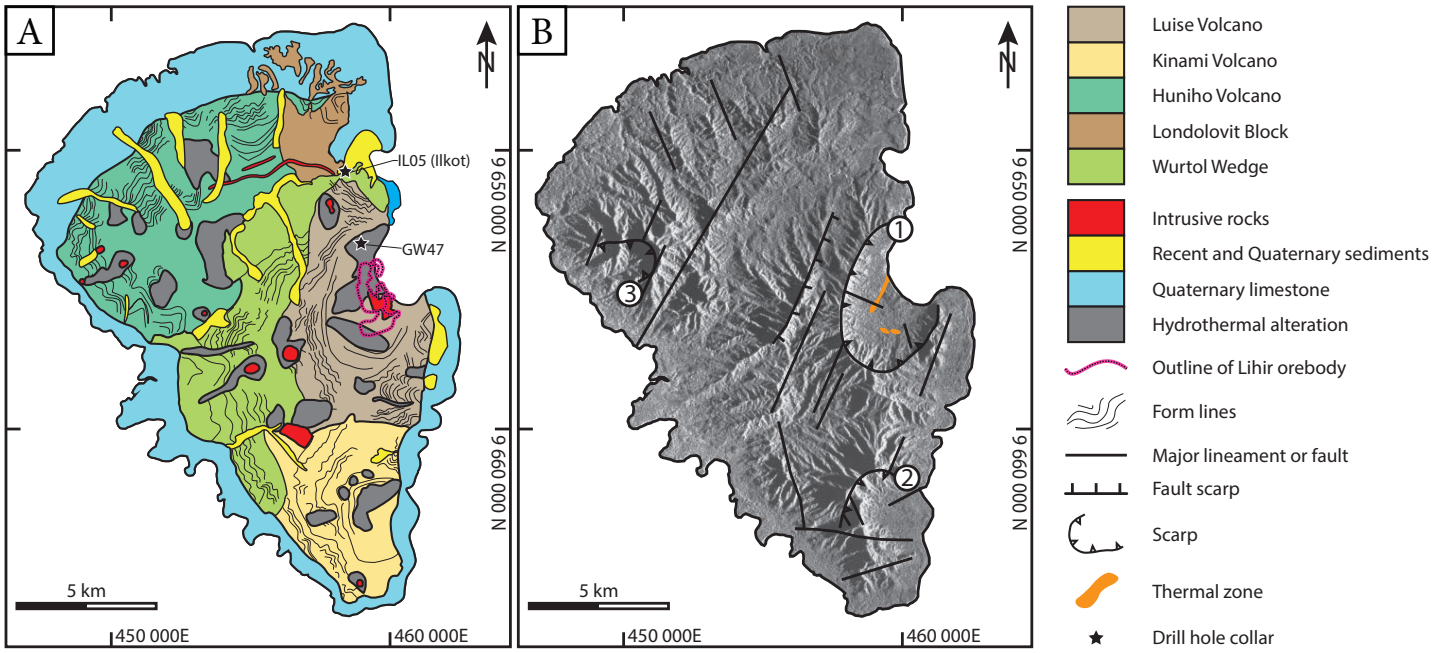


**Fig. 3.1.** Geology and geomorphology of Lihir Island. **A.** Simplified geology map of Lihir Island (after Komyshan, 1999), showing the five major geomorphological blocks, the location of outcropping intrusive rocks and the fringing limestone terrace. Hydrothermal alteration zones and the outline of the Lihir gold deposit are also shown. Digital elevation model of Lihir Island, highlighting the three volcanic amphitheaters (1 = Luise, 2 = Kinami, 3 = Huniho), major structural lineaments and the location of thermal activity (after Wallace et al., 1983).

bor (Komyshan, 1999), in the area now known as Kapit NE. The demagnetized zones have been interpreted as previously active volcanic centers (Komyshan, 1999).

The vent and cone region of the Luise Volcano is composed predominantly of volcaniclastic debris flow deposits interbedded with basaltic to andesitic lavas and shallow intrusions, and sedimentary conglomerates and sandstones (Appendices B1 and B2; Blackwell, 2010). Lavas and shallow intrusions include massive and columnar jointed coherent facies that are gradational to monomict breccias with jigsaw-fit to clast-rotated and chaotic internal organization. The volcano-sedimentary strata was crosscut by multiple generations of alkalic intrusions that dominate the sequence from approximately −200 to −620 m rsl (Appendix B2; Blackwell, 2010). The oldest intrusions are equigranular to weakly porphyritic (pyroxene ± feldspar-phyric) monzonite dike swarms (Appendix B3). The dikes are texturally heterogeneous with magnetite clots and mafic xenoliths (Blackwell, 2010). Younger intrusions consist of narrow (<20 m-wide), sub-vertical dikes that range from aphanitic to feldspar-phyric (Blackwell, 2010).

The Quaternary limestone unit that encircles Lihir Island consists of a 10–100 m-thick uplifted platform, with three distinct terraces separated by wave-cut notches (Komyshan, 1999; Blackwell, 2010). The stratigraphy of the limestone terraces suggests that there have been three stages of island subsidence associated with reef formation and three corresponding stages of uplift and limestone erosion (Blackwell, 2010). The terraces are best developed on the north of the island and are absent on the coastline of Luise Harbor, either as a result of locally inhospitable temperatures in the vicinity of the Lihir geothermal system (Wallace et al., 1983), or because the limestone terraces were destroyed during sector collapse of the Luise volcanic edifice (Blackwell, 2010). The limestone terraces are made up of forereef bioherm and back reef limestone facies with lenses of littoral calcareous and volcaniclastic sediments (Wallace et al., 1983). Foraminifera from a limestone clast-bearing volcanolithic arenite boulder sampled in a cave within Londolovit Block provide a minimum age for the limestone unit (and for Londolovit Block) of late Miocene to Pliocene (zone N18–N20; Gallasch, 1976; Wallace et al., 1983). In contrast, Th–U ages for three samples of limestone from

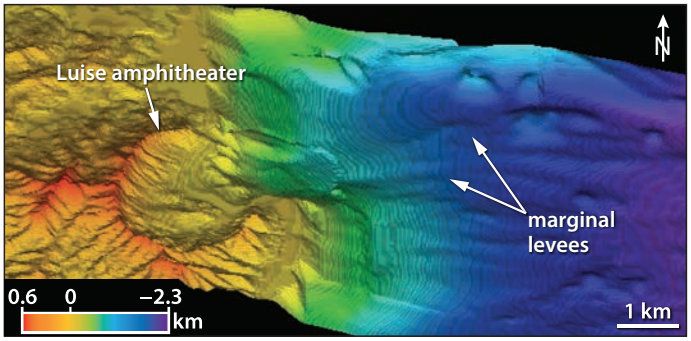


**Fig. 3.2.** Geomorphology of the Luise amphitheater and Luise Harbor (from Blackwell, 2010). The amphitheater consists of a 4.0 × 3.5 km wide, elliptical depression that is breached to the northeast. It is interpreted to have formed via northeast-directed sector collapse of a volcanic edifice that would originally have been >1 km in height. The model shows hummocky bathymetry and longitudinal ridges extending for ~10 km to the northeast offshore from the Luise Harbor, which have been interpreted as a debris avalanche deposit with marginal levees (Blackwell, 2010). The modeled surface is dipping 27˚ towards 180˚. View is plunging 63˚ towards 000˚.

near Putput village, east of Lihir gold deposit, suggest a very young history of limestone deposition (~0.2 Ma to Recent; Blackwell, 2010).

### 3.3 Host rocks in Minifie, Lienetz and Kapit ore zones

The rocks within and adjacent to the Minifie, Lienetz and Kapit orebodies are strongly altered and have locally been overprinted by hydrothermal breccias and veins, obscuring many primary features and contact relationships. Early workers (Davies and Ballantyne, 1987; Moyle et al., 1990; Corbett et al., 2001; Carman, 2003; Kidd and Robinson, 2004) recognized three main host rock types: undifferentiated volcanic basement, alkaline intrusives and pre-ore hydrothermal breccias (Ladolam breccia complex). Carman (1994, 2003) mapped the distribution of these major rock units on two cross sections (Appendix A1). Blackwell (2010) subdivided the volcanic basement into four volcanic and volcano-sedimentary facies within Minifie and Lienetz and mapped their distributions on five cross sections and two geological maps (Appendices B4–B5; Blackwell, 2010; Blackwell et al., 2014). More recently, Sykora (2017) combined the geological maps from Blackwell (2010) with new observations from pit mapping in Lienetz to create a geological map for the Lienetz and Minifie areas. Sykora (2017) also defined the geology along four cross sections in Lienetz (Appendix A1). Ageneau (2012) studied the geology of the Kapit ore zone and produced two geological cross sections through the orebody (Appendix A1).

The volcanic basement is best preserved at the periphery of the Lihir gold deposit and the flanks of the Luise Volcano (Carman, 2003; Blackwell, 2010). In the Minifie ore zone, the volcanic basement comprises a volcano-sedimentary succession that is ~200 m thick and dips shallowly (20–30˚) to the south (Blackwell, 2010). In the Lienetz ore zone, the volcanic basement has largely been obscured by magmatic-hydrothermal features, including a large biotite – anhydrite-cemented breccia body at depth (width: ~750 m; vertical extent: >300 m) and a texturally destructive clay alteration blanket near surface (<150 m above sea level; Blackwell, 2010; Sykora, 2017).

The oldest rocks in the succession are polymict breccias and sandstones that have been interpreted as volcaniclastic debris flow deposits and minor subaerial pyroclastic surge deposits (Appendix B4; Blackwell et al., 2014). These rocks are crosscut by pyroxene-phyric basalt dikes and associated breccias in Minifie that feed into a ~180 m-thick hyaloclastite sequence in Lienetz (Appendix B4; Blackwell, 2010). Overlying the volcaniclastic debris flow deposits in Minifie are laminated to massive mudstones that are interpreted to have been deposited in a subaqueous setting during a period of volcanic quiescence. The mudstone is intruded by a partly extrusive, plagioclase-phyric cryptodome (Blackwell et al., 2014). Overall, the volcano-sedimentary stratigraphy in Minifie and Lienetz has been interpreted to reflect the transition from a subaerial depositional environment proximal to an explosive volcanic vent to a subaqueous environment (Blackwell, 2010).

On the southern margin of the Lienetz ore zone, there is a large microdiorite stock (aerial extent: 200 × 100 m; vertical extent: >200 m) that is crosscut by feldspar-phyric syenite dikes (Blackwell, 2010). These dikes are spatially and temporally related to porphyry-style alteration assem-

blages, veins and magmatic-hydrothermal breccias (Blackwell, 2010; Sykora et al., 2018a). No intrusive igneous rock types have been observed in the Minifie ore zone.

The volcano-sedimentary host rocks in the Kapit ore zone consist of interfingered massive to vesicular pyroxene-phyric basalt and polymict, matrix-supported breccia that are similar to lithotypes in Minifie and Lienetz (Appendix B4; Ageneau, 2012). The stratigraphy has locally been crosscut by microdiorite to plagioclase-phyric diorite, a widespread shallow-level intrusion (Appendix B4; Ageneau, 2012). Late plagioclase-phyric dikes in Lienetz and Kapit are spatially associated with one or more phreatomagmatic breccias at the periphery of both ore zones (Appendix B4; Blackwell, 2010; Ageneau, 2012).

## 3.4 Geology of Kapit NE and Coastal ore zones

### *3.4.1 Introduction*

The host rocks of the Kapit NE and Coastal ore zones consist of a northeast-dipping (20–30˚), mafic volcano-sedimentary sequence that has been crosscut by a north-trending alkalic intrusive complex. Ten volcanic, volcano-sedimentary and intrusive lithotypes have been identified in this region, which are described below in their interpreted order of formation. Tables 3.1–3.4 summarize the lithotype descriptions provided in text and present further detailed information (e.g., petrographic characteristics).

### *3.4.2 Methods*

The data for this chapter were collected through graphic drill core logging and sampling of nine drill holes along north-oriented section A–A'–A" and seven drill holes on northeast-oriented section B–B' (Fig. 1.1; Appendix A1). An additional 17 drill holes on section A–A'–A" and 16 drill holes on section B–B' were logged from photographs from the Newcrest core photo library (Appendix A1). The graphic logging method used was based on the methods of McPhie et al. (1993), Einaudi (1997), Gifkins et al. (2005) and Blackwell (2010). A graphic logging technique was used to systematically record lithofacies descriptions, geometries, and contact relationships for the drill core samples. In total, 763 samples were collected on site and cut into slabs to provide a fresh viewing surface. Thirty slabs were polished with 3 μm diamond paste to highlight fine-scale textures in the rocks. A total of 81 polished thin sections and one polished grain mount were examined to establish modal mineral abundances, identify trace mineral phases and mineral inclusions and to observe microtextures.

### *3.4.3 Pre-mineralization volcanic stratigraphy*

#### *3.4.3.1 Polymict matrix-supported breccia (KNE1)*

Polymict weakly graded and diffusely bedded breccia (KNE1a) occurs throughout the stratigraphy and is the most abundant volcano-sedimentary lithotype in the northeast of Kapit NE (Figs. 3.3 and 3.4). The morphology of KNE1a is poorly constrained; however, its aerial extent in Kapit NE is at least 1.0 × 0.5 km and the sediment pile is at least 300 m thick (Figs. 3.3 and 3.4). The thickness of the sediment package may have been inflated because of later dike and sill emplacement (i.e., KNE2 and KNE3; Figs. 3.3 and 3.4). This lithofacies is typified by subangular to subrounded, moderately to poorly sorted, pebble- to cobble-sized clasts set in a lithic-rich, predominantly sand-sized matrix. KNE1a varies from non-graded and non-stratified to diffusely stratified with thick to very thick beds defined by weak normal grading and/or by alternating clast-poor (20–30% clasts) and clast-rich (30–70% clasts) domains (Figs. 3.5, 3.6A and B). This lithofacies also contains rare interbeds (<5 m thick) of thin- to medium-bedded polymict granule to pebble breccia and medium to coarse sandstone (Figs. 3.6A and B). Bedding in the sandstone-rich intervals

**Fig. 3.3.** (*Next page*) West-facing geology cross section A–A'–A" (9875 mE) through the Kapit NE and Coastal ore zones. Note that only map-scale volcanic-hydrothermal and hydrothermal breccias are shown.

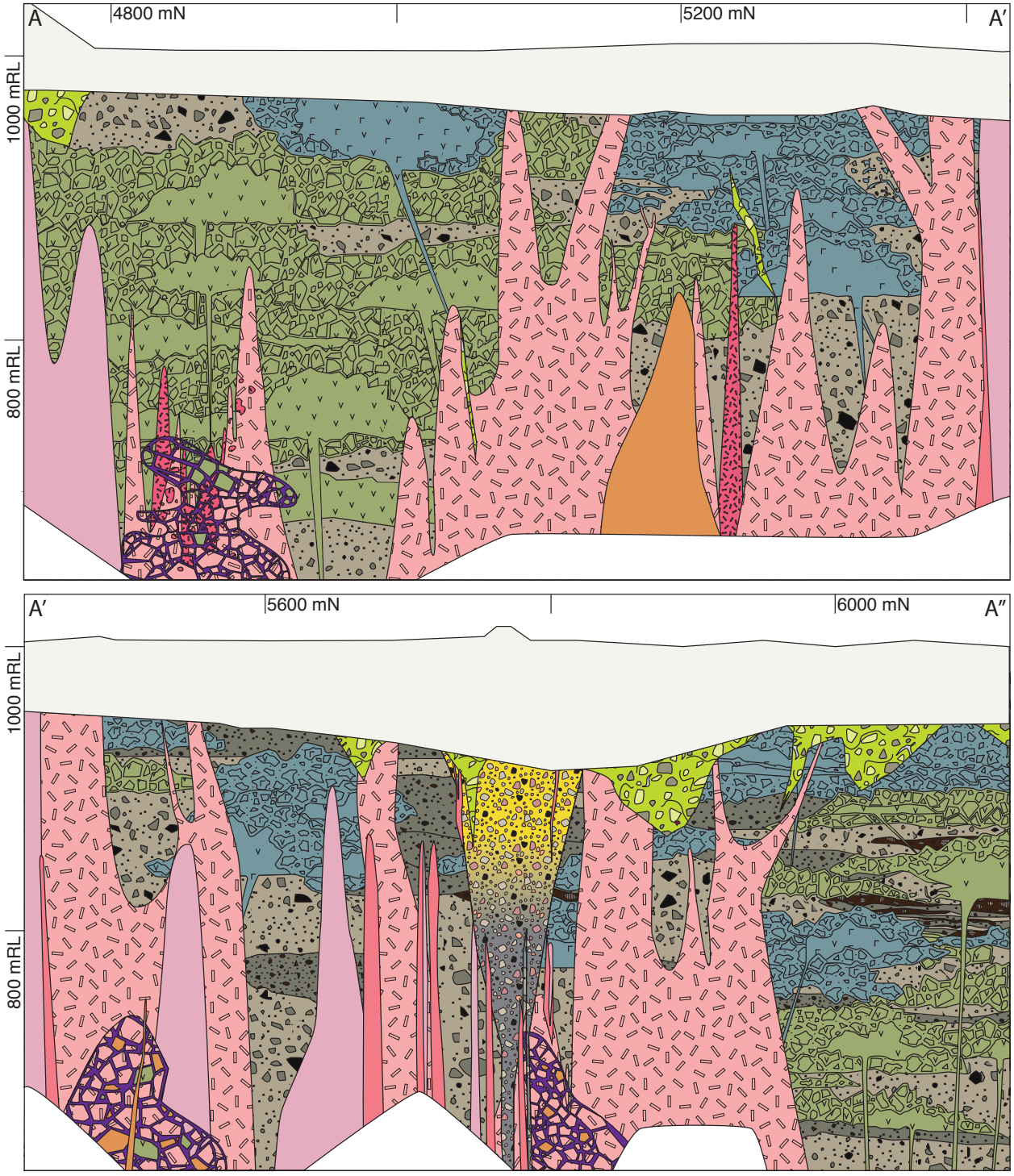
A
4800 mN
5200 mN
A′
1000 mRL
800 mRL
A′
5600 mN
6000 mN
A″
1000 mRL
800 mRL
(Volcanic-) hydrothermal breccias
Stage 4 Lihir diatreme breccia complex
Stage 2B quartz – pyrite-cemented breccia
Stage 1C polymict anhydrite – chlorite – calcite-cemented breccia
Coastal intrusive complex
Trachytic hornblende- feldspar-phyric latite (KNE9)
Coarse-grained hornblende-feldspar-phyric latite (KNE8)
Hornblende-bearing gabbro (KNE6)
Hornblende-biotite-bearing monzonite (KNE5)
Biotite-feldspar-phyric, nepheline-bearing monzonite (KNE4)
Volcano-sedimentary stratigraphy
Plagioclase-phyric basaltic andesite breccia (KNE3) / coherent andesite (inferred)
Pyroxene-phyric basalt breccia (KNE2b) / Pyroxene-phyric basalt (KNE2a)
Polymict breccia with sedimentary clasts (KNE1c)
Polymict normally graded conglomerate and pebbly sandstone (KNE1b)
Polymict weakly graded and diffusely bedded breccia (KNE1a)
Other
Harbor base fill (waste rock) / Pacific Ocean

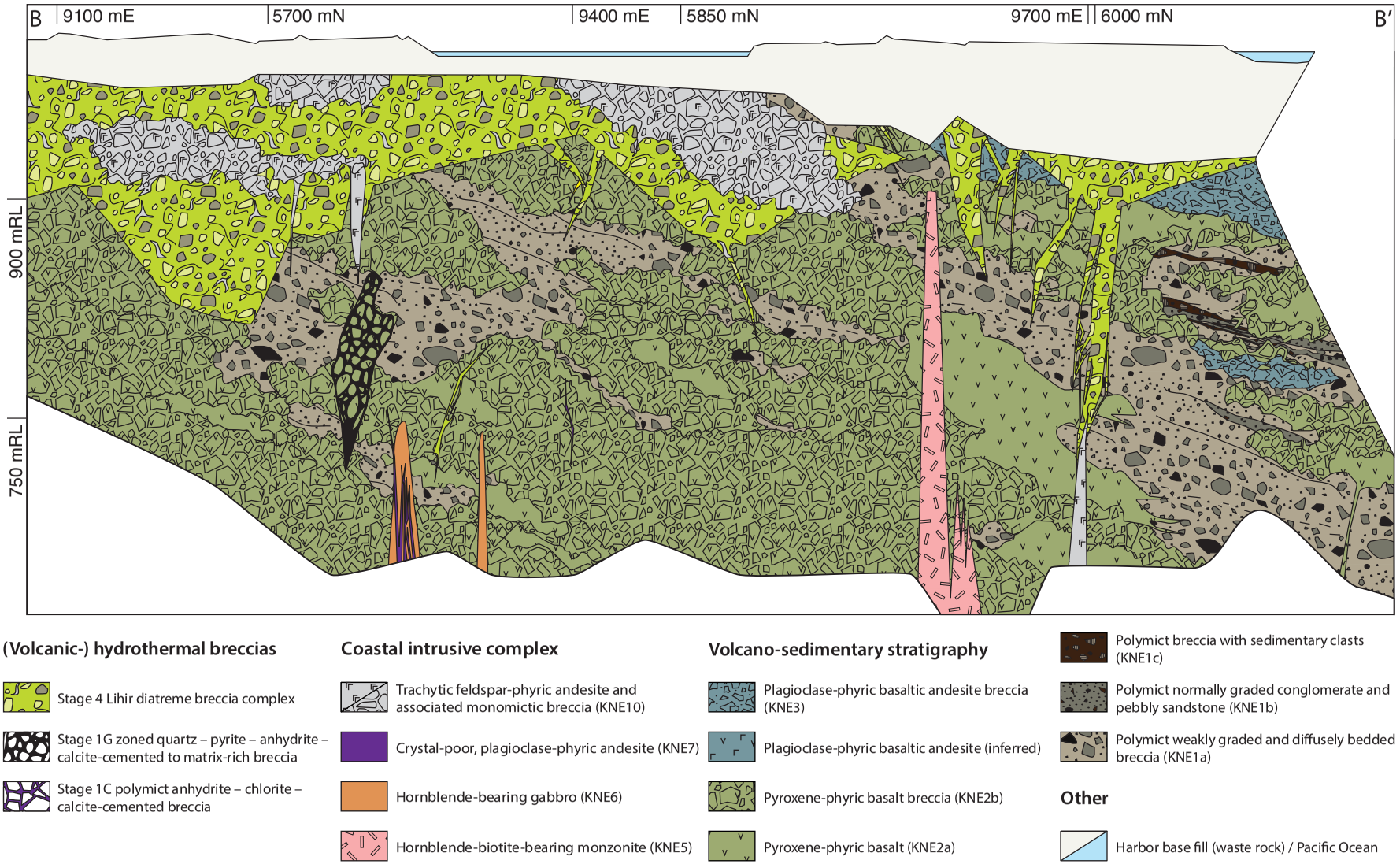


**Fig. 3.4.** Northwest-facing (oblique; 045˚) geology section B–B' through the Kapit NE ore zone. Note that only map-scale volcanic-hydrothermal and hydrothermal breccias are shown.

**Table 3.1.** Characteristics of the volcano-sedimentary host rocks from Kapit NE and Coastal.

| Lithotype | Textures/components | Lithofacies characteristics |
|---|---|---|
| *Polymict matrix-supported breccia (KNE1)* | | |
| Polymict weakly graded and diffusely bedded breccia (KNE1a) | **Clasts (20–70%):** mainly pebble- to cobble-sized, with outsized clasts up to 25 cm; subangular to subrounded; predominantly (>95 vol%) volcanic clasts (pyroxene-phyric basalt, (thermally oxidized) pyroxene-feldspar-phyric basaltic andesite (with illite alteration rinds), feldspar-phyric andesite, amphibole-feldspar-phyric andesite, fine-grained feldspar-phyric basalt and aphanitic volcanic clasts) and minor (<5 vol%) sedimentary clasts (massive and laminated mudstone and matrix-supported breccia)<br>**Matrix:** poorly sorted; fine to very coarse sand-sized (0.125–2.000 mm) lithic fragments (~70 vol%), feldspar crystal fragments (up to 20 vol%) and pyroxene crystal fragments (~5 vol%) set in a mud-sized matrix (5–10 vol%) | Polymict; moderately to poorly sorted; non-graded and non-stratified to diffusely stratified; thick to very thick beds defined by weak normal grading and/or by alternating clast-poor (20–30% clasts) and clast-rich (30–70% clasts) domains; lenses of abundant (locally >50 vol% of clasts) pyroxene-phyric basalt clasts; rare interbeds (<5 m thick) of thin- to medium-bedded polymict granule to pebble breccia and medium to coarse sandstone |
| Polymict normally graded conglomerate and pebbly sandstone (KNE1b) | ***Conglomerate***<br>**Clasts (<10–70%):** granule- to cobble-sized, with outsized boulders; subangular to rounded; predominantly composed of (amygdaloidal) pyroxene-phyric basalt, with lesser andesite and rare mudstone clasts<br>**Matrix:** silt- to granule-sized; lithic<br>***Pebbly sandstone***<br>Medium to coarse sand with outsized granules and pebbles; fragments are of the same composition as the associated conglomerate | Interbedded pebbly sandstone and conglomerate<br>***Conglomerate:*** massive to stratified (normally graded); poorly to very poorly sorted; polymict; matrix-supported; siltstone matrix-rich (>90% siltstone) intervals locally display convolute laminations<br>***Pebbly sandstone:*** massive |
| Polymict mud matrix-supported breccia (KNE1c) | **Clasts (70–80%):** pebble- to boulder-sized, subangular to subround; predominantly sedimentary clasts (distinctive graded and laminated mudstone, sandstone, massive mudstone and matrix-supported granule to pebble breccia)<br>**Matrix:** mud-sized (<0.0625 mm); massive | Clast-rotated to chaotic clast organization, poorly sorted |
| *Pyroxene-phyric basalt and basalt breccia (KNE2)* | | |
| Pyroxene-phyric basalt (KNE2a) | Crystal-poor to moderately crystal crowded and porphyritic with a hypocrystalline groundmass<br>**Phenocrysts (10–35%):** Clinopyroxene: 10–35%; 0.5–2.0 mm in length, outsized to 8 mm; euhedral; equant to stubby; locally glomerophyric; relict zoning \| Plagioclase: 0–10%; 0.5–1.5 mm; outsized to 3 mm; euhedral; tabular to blocky \| *Magnetite:* ~5%; 0.01–0.02 mm; outsized to 0.3 mm; euhedral; porous; locally displays ilmenite exsolution lamellae \| *Orthopyroxene:* trace; <1 mm; euhedral; tabular \| *Sanidine:* trace; 0.3–0.5 mm; euhedral; equant to blocky; relict simple twinning<br>**Amygdules (up to 40%):** <2 cm; irregular; low sphericity to elongate; contain fillings of calcite – illite – chlorite- or anhydrite – magnetite – apatite – K-feldspar<br>**Groundmass:** hypocrystalline; felty to weakly flow aligned plagioclase microlites (<0.15 mm) set in devitrified volcanic glass (altered to chlorite – rutile – hematite ± illite-smectite); relict perlitic fractures | Massive; amygdaloidal |
| Pyroxene-phyric basalt breccia (KNE2b) | **Clasts (50–90%):** granule- to boulder-sized; angular to subangular; diverse clast morphologies including blocky, splintery, irregular, amoeboid and pillow-like (rare, rounded boulders with radial and concentric fractures); angular and ragged or sharp and curviplanar margins; monomict clast population (pyroxene-phyric basalt; KNE2a)<br>**Matrix:** mud- to coarse sand-sized; angular; blocky to splintery; composed of lithic fragments (pyroxene-phyric basalt; KNE2a) and plagioclase and pyroxene crystals | Massive; monomict; jigsaw-fit to chaotic; matrix- to clast-supported; poorly to very poorly sorted; strongly altered intervals locally display false polymict texture |
| *Pyroxene-feldspar-phyric basaltic andesite breccia (KNE3)* | | |
| Pyroxene-feldspar-phyric basaltic andesite breccia (KNE3) | **Clasts (60–80%):** granule- to boulder-sized; angular to subangular; polyhedral, blocky or splintery clast morphologies; sharp, planar to curviplanar and cuspate clast margins; monomict clast population (pyroxene-feldspar-phyric basaltic andesite)<br>***Characteristics of the pyroxene-feldspar-phyric basaltic andesite clasts:***<br>Massive, crystal crowded and porphyritic with an aphanitic gray groundmass<br>Phenocrysts (30–50%): Feldspar:<35%; 0.2–2.0 mm in length, outsized to 5.5 mm; subhedral to euhedral; stubby to tabular; zoned \| Clinopyroxene: 7–10%; 0.5–3.5 mm, outsized to 5.0 mm; euhedral; equant to blocky \| Magnetite: ~5%; 0.1–1 mm; euhedral \| Relict amphibole: <3%; <1.0 mm; prismatic<br>Amygdules (<5%): contain fillings of anhydrite and chlorite<br>**Groundmass:** aphanitic; textures and composition obscured by alteration<br>**Matrix:** mud- to very coarse sand-sized; composed of lithic clasts (pyroxene-feldspar-phyric basaltic andesite) | Unstratified; monomict; clast- to matrix-supported; locally, smaller clasts (<5 mm) are altered to give the appearance of a more matrix-rich breccia; very poorly sorted; jigsaw-fit to clast-rotated (up to 15˚ clast rotation); locally contains xenoliths of pyroxene-phyric basalt (KNE2); relict perlitic fractures; amygdaloidal |

**Table 3.2.** Distribution, relationships, and interpretations for volcano-sedimentary host rocks from Kapit NE and Coastal.

| Lithotype | Contacts | Apparent thickness | Distribution | Interpretation | Associated facies |
|---|---|---|---|---|---|
| *Polymict matrix-supported breccia (KNE1)* | | | | | |
| KNE1a | Sharp contacts with interbeds of polymict mud matrix-supported breccia (KNE1c); sharp or gradational contacts with both the pyroxene-phyric basalt (KNE2) and pyroxene-feldspar-phyric basaltic andesite (KNE3) | >300 m thick | Occurs throughout the stratigraphy; most abundant lithofacies in Kapit NE; overall aerial extent is at least 1.0 × 0.5 km; individual units are laterally discontinuous (lensoid); bedding dips shallowly (20–30°) to the northeast | A successive accumulation of subaerially-derived volcaniclastic debris flow deposits deposited in a near-shore submarine setting; laterally equivalent to polymict matrix-supported breccia to sandstone (L1; Lienetz), polymict, weakly graded breccia to sandstone (M4a; Minifie) and polymict matrix-supported breccia (K3; Kapit) | Interbedded with packages of interbedded polymict normally graded conglomerate and pebbly sandstone (KNE1b) |
| KNE1b | Erosive lower contact with pyroxene-phyric basalt breccia (KNE2a); locally gradational to pyroxene-phyric basalt breccia (KNE2b) | <1–70 m thick | Occurs as clustered lobes within KNE1a at all levels of the stratigraphy, east of 9600 mE; pebbly sandstone is the most abundant component | | Spatially associated with KNE1a and KNE1c breccias |
| KNE1c | Sharp or faulted contacts with KNE1b; not observed to be in contact with other rock types | <4 m thick | Rare, lensoid beds; laterally continuous over tens of meters; occurs in northeast of Kapit NE | | Always bounded by KNE1b beds; occurs as large (> 5 m) boulders within diatreme breccias in eastern Kapit NE |
| *Pyroxene-phyric basalt and basalt breccia (KNE2)* | | | | | |
| KNE2a | Sharp and irregular contacts with polymict matrix-supported breccia (KNE1); gradational contacts with pyroxene-phyric basalt breccia (KNE2b) | KNE2a and KNE2b units coalesce to form packages up to ~250 m thick | Ubiquitous distribution; most abundant volcanic rock type in the Kapit NE and Coastal areas; KNE2b is more common than KNE2a (~5:1); intervals of KNE2 are laterally continuous between drill holes and are concordant to host rock layering | *KNE2a:* Coherent and disaggregated (peperitic) high-level dikes and sills; *KNE2b:* In-situ and resedimented hyaloclastite; pillow fragment breccia; *KNE2:* Polyphase, subaqueous basalt eruption onto/into unconsolidated, water-saturated sedimentary substrate; equivalent to pyroxene-phyric coherent and clastic facies association at Minifie and Lienetz (M2 and L2) and massive to vesicular pyroxene-phyric basalt in Kapit (K1) | Pyroxene-phyric basalt breccia (KNE2b) is typically gradational to and forms thick (>1 m and up to 100 m) envelopes around coherent basalt (KNE2a); correlates spatially with the pyroxene-phyric coherent and clastic facies (L2) that crops out in the eastern Lienetz pit wall |
| KNE2b | Gradational contacts with polymict matrix-supported breccia (KNE1), including polymict siltstone matrix-rich conglomerate (KNE1b) that contains amoeboid pyroxene-phyric basalt clasts with ragged clast margins | | | | |
| *Pyroxene-feldspar-phyric basaltic andesite breccia (KNE3)* | | | | | |
| KNE3 | Typically has strongly altered and obscured contacts; sharp irregular contacts with pyroxene-phyric basalt breccia (KNE2b); sharp contacts with polymict matrix-supported breccia (KNE1) | Individual units are <2–80 m thick; coalesce to form packages up to 200 m thick | Laterally continuous over up to 200 m; restricted to high levels of the stratigraphy (above ~750 mRL) and areas east of 9600 mE | In-situ hyaloclastite component of lavas or shallow intrusions; equivalent to feldspar-pyroxene-phyric basalt from the northern Luise amphitheater and monomict, polyhedral andesite boulder breccia (M1d) in Minifie | None observed |

dips approximately 20–30˚ to the northeast (045˚) based on measurements from drill core. Locally, lithofacies KNE1a is interbedded with packages of interbedded polymict normally graded conglomerate and pebbly sandstone (KNE1b) and has sharp contacts with interbeds of polymict mud matrix-supported breccia (KNE1c). Contacts are sharp or gradational with pyroxene-phyric basalt (KNE2; Fig. 3.6A) and pyroxene-feldspar-phyric basaltic andesite (KNE3).

Most of the clasts in KNE1a are volcanic (>95 vol%) and include pyroxene-phyric basalt, pyroxene-feldspar-phyric basaltic andesite, feldspar-phyric andesite, amphibole-feldspar-phyric andesite, fine-grained feldspar-phyric basalt, and green, gray and pink aphanitic volcanic clasts. The clasts typically range from pebble to cobble sized. Outsized cobbles and boulders up to 25 cm are also present, typically comprising angular to ragged, thermally oxidized py-

**Table 3.3.** Characteristics of intrusive phases of the Coastal intrusive complex.

| Lithotype | Textures/components | Lithofacies characteristics |
|---|---|---|
| Biotite-feldspar-phyric, nepheline-bearing monzonite (KNE4) | Crystal-crowded and porphyritic with a strongly-altered, aphanitic groundmass<br>**Phenocrysts (40–60%):** *Orthoclase:* 40%; 0.5–1.0 mm in length; subhedral; stubby to lath-shaped crystals with simple twinning \| *Plagioclase:* 25–35%; 0.05–2.00 mm in length; subhedral; tabular; albite twinning \| *Biotite:* 10–25%; 0.25–1.00 mm; euhedral; tabular or short prismatic crystals with inclusions of apatite and zircon; partly replaced at margins by shreddy biotite and rutile \| *Nepheline:* 10%; <0.5 mm; abundant melt and fluid inclusions; partly altered to cancrinite<br>**Groundmass:** aphanitic groundmass of feldspar, biotite, apatite and rutile; primary textures obscured by strong K-feldspar, anhydrite, muscovite, magnetite, pyrite and smectite alteration | Texturally heterogeneous; locally abundant (up to 5%), elongate and irregularly-shaped magnetite-rich clots (0.5–10.0 mm in length); very fine-grained mafic xenoliths (<2 cm diameter) |
| Hornblende-biotite-bearing monzonite (KNE5) | Crystal crowded and porphyritic with a strongly-altered, aphanitic groundmass<br>**Phenocrysts (60%):** *Plagioclase:* ~50%; bimodal grain size (<0.25 mm and 1–3 mm); euhedral; blocky to tabular \| *K-feldspar:* ~25%; 0.5–1.5 mm in length, outsized to 7 mm; stubby to blocky; gray or salmon \| *Biotite:* 15%; <0.5 mm; equant to stubby; locally partly replaced at margins by shreddy biotite \| *Relict hornblende:* 10%; 0.3–2.0 mm, outsized to 5 mm; stubby; well-preserved cleavage and moderately well-preserved crystal habit; locally leached forming crystal-shaped vugs<br>**Groundmass:** the texture and composition of the aphanitic groundmass has been obscured by strong to intense alteration of variable composition | Plagioclase phenocrysts are locally weakly flow aligned; locally xenolithic |
| Hornblende-bearing gabbro (KNE6) | Strongly crystal crowded and porphyritic with a fine-grained groundmass<br>**Phenocrysts (95%):** *Feldspar:* 55%; 1–5 mm; subhedral; blocky to stubby; embayed; completely replaced by K-feldspar or albite \| *Clinopyroxene:* 40%; 1–7 mm, outsized to 12 mm; euhedral; stubby to equant; locally glomerophyric and poikilitic \| *Relict amphibole:* <5%; 0.5–4.0 mm; euhedral; stubby to prismatic; replaced by K-feldspar or phlogopite; well-preserved cleavage traces \| *Magnetite:* 3–5%; 0.5–1.5 mm; octahedral<br>**Groundmass:** fine-grained (<0.2 mm); composed of feldspars and relict mafic minerals that have been strongly altered to patchy K-feldspar + smectite | Texturally heterogeneous; domains of coarse-grained clinopyroxene clusters; fine- to medium-grained mafic xenoliths (<2 cm in diameter) |
| Crystal-poor, feldspar-phyric trachyte (KNE7) | Crystal-poor and porphyritic with an aphanitic (pilotaxitic) groundmass<br>**Phenocrysts (5–12%):** *Orthoclase:* 60%; 0.5–3 mm in length; euhedral, stubby to blocky; simple twinning; cumulophyric crystal clusters \| *Plagioclase:* 25%; <0.5 mm; euhedral; blocky; albite twinning \| *Sanidine:* 15%; <0.5 mm; euhedral; bladed; simple twinning<br>**Groundmass:** pilotaxitic groundmass composed of randomly oriented, lath-like feldspar microlites (0.04–0.06 mm; outsized to 0.3 mm); altered to K-feldspar, magnetite, anhydrite and muscovite; locally overprinted by weak smectite alteration | Contains ovoid and amoeboid, anhydrite-, K-feldspar- and magnetite-filled amygdules (5–15%) |
| Trachytic hornblende-feldspar-phyric latite (KNE8) | Crystal-poor and porphyritic with a gray, aphanitic groundmass<br>**Phenocrysts (10–40%):** *Plagioclase:* 40%; 0.5–5.0 mm in length; subhedral to euhedral; tabular; relict albite twinning \| *Sanidine:* 35%; 0.1–0.5 mm in length; euhedral; tabular; relict simple twinning \| *Hornblende:* 20%; 0.1–1.0 mm in length, outsized to 3.0 mm; euhedral; stubby or prismatic; intensely altered to illite-smectite – rutile – pyrite – chlorite above ~800 mRL \| *Apatite:* 5%; <1 mm; euhedral; small, stubby to prismatic<br>**Groundmass:** very fine-grained to fine-grained (0.02–0.10 mm) trachytic groundmass consisting of feldspar microlites that locally wrap around phenocrysts | Strongly flow-aligned phenocrysts; contains ovoid and irregularly shaped, flow-aligned vesicles (0.5–25.0 mm) and amphibole-shaped vugs (0.1–1.0 mm) that together constitute up to 10 vol% open space |
| Coarse-grained feldspar-phyric latite (KNE9) | Moderately crystal crowded and porphyritic with an aphanitic beige to gray groundmass<br>**Phenocrysts (~45%):** *Relict K-feldspar and/or plagioclase:* 60%; 0.5–6.0 mm in length; euhedral, stubby to blocky and zoned; alternatively exhibit tabular, rounded and amoeboid morphologies; completely replaced by secondary feldspars and clays \| *Hornblende:* 40%; 0.1–3.0 mm in length; euhedral; prismatic; locally glomerophyric<br>**Groundmass:** texture and composition of the groundmass has been obscured by strong, patchy smectite – pyrite – rutile alteration | Massive |
| Feldspar-phyric andesite and associated monomict breccia (KNE10) | ***Feldspar-phyric andesite***<br>Crystal-poor to moderately crystal crowded and porphyritic with an aphanitic beige to gray groundmass<br>**Phenocrysts (10–45%):** *Relict feldspar:* 45%; 0.1–4.0 mm in length; euhedral; lath-like; randomly oriented to strongly flow aligned; completely replaced by montmorillonite \| *Relict pyroxene:* 35%; 0.1–2.0 mm; subhedral to euhedral; blocky; locally glomerophyric (crystal clusters up to 5 mm); typically replaced by pyrite and montmorillonite \| *Relict hornblende:* 20%; 0.05–1.50 mm; euhedral; stubby; typically replaced by pyrite and montmorillonite<br>**Groundmass:** predominantly plagioclase (?) microlites that are strongly and pervasively altered to montmorillonite; contains disseminated pyrite<br>***Feldspar-phyric andesite breccia***<br>**Clasts (30–90%):** sand to boulder sized fragments up to several meters in diameter; angular to rounded; monomict clast population of feldspar-phyric andesite; blocky, ragged, wispy and amoeboid clast shapes<br>**Matrix (10–70%):** <0.002 mm (clay), composed of pulverized host rock fragments and disseminated pyrite; locally altered to clay minerals (typically illite and smectite) | ***Coherent feldspar-phyric andesite:*** massive to strongly trachytic; locally banded<br>***Feldspar-phyric andesite breccia:*** massive; jigsaw-fit to chaotic clast organization; very poorly sorted; clast- to matrix-supported |

**Table 3.4.** Relationships, distribution and interpretations for intrusive phases of the Coastal intrusive complex.

| Lithotype | Contacts | Apparent thickness | Distribution | Interpretation | Associated facies |
|---|---|---|---|---|---|
| KNE4 | Sharp igneous contacts with pyroxene-phyric basalt (KNE2) and polymict matrix-supported breccia (KNE1); sharp and irregular internal contacts | <20 m thick | Occurs in the west of Coastal and Kapit NE prospects below 775 mRL | Polyphasic dikes; locally abundant miarolitic cavities; may have contributed hydrothermal fluids and metals to the early porphyry system | Occurs as rounded xenoliths in the hornblende-biotite-bearing monzonite (KNE5) and as a principal clast component within jigsaw-fit to chaotic, polymict anhydrite-pyrite-cemented breccia; may be related to the monzonite north of Kapit |
| KNE5 | Sharp, planar or irregular, igneous contacts with the volcano-sedimentary succession (KNE1–KNE3); crosscut by the KNE6 to KNE9 intrusions | Tens to hundreds of meters thick | North trending group of branched intrusions; observed east of 5600 mE; extents and orientations are poorly constrained due to the low drilling density surrounding the studied sections | Dike swarm | Contains xenoliths of nepheline-bearing monzonite (KNE4) and microdiorite; occurs as clasts within polymict quartz – pyrite-cemented breccia and within polymict anhydrite-pyrite-cemented breccia |
| KNE6 | Sharp contacts with anhydrite – pyrite – chlorite-cemented biotite-altered breccia; crosscut by porphyry-style alteration and veins; sharp, irregular contact with polymict matrix-supported breccia (KNE1) | <10 cm up to ~25 m thick | Observed in drill core below ~750 mRL as singular intrusions of unknown orientation | Polyphase dikes with syn-porphyry timing | |
| KNE7 | Sharp igneous contacts with hornblende-bearing gabbro (KNE6); chilled margins | <5 m thick | Narrow, steeply dipping intrusions; intersected in DDHL1928 below 700 mRL | Dikes | Interfingered with hornblende-bearing gabbro (KNE6) in DDHL1928 |
| KNE8 | Sharp, strongly altered contacts with polymict quartz – pyrite-cemented breccia and hornblende-biotite-bearing monzonite (KNE5); crosscut by Au-bearing pyrite veins, adularia – Fe-sulfide ± illite veinlets | A few meters to tens of meters thick | Vertical, northeast-trending intrusions intersected in drill core in Kapit NE between 5400–5800 mN | Dike swarm with inter-epithermal mineralization timing | Spatially associated with KNE9 latite dikes |
| KNE9 | Gradational contacts with trachytic hornblende-feldspar-phyric latite (KNE8) | <1–150 m thick | A series of northeast-trending dikes occurring between 5400–5800 mN on section A–A'–A" (9875 mE) | Coarser-grained core of KNE8 latite dikes (?) | Spatially associated with KNE8 latite dikes; locally, KNE9 latite is bounded by KNE8 latite; similar in texture and composition to feldspar-phyric syenite from Lienetz (L5) |
| KNE10 | Coherent feldspar-phyric andesite grades into monomict jigsaw-fit feldspar-phyric andesite breccia with a rock flour matrix and then into matrix-rich polymict breccia with blocky to wispy, juvenile feldspar-phyric andesite clasts; locally sharply crosscuts diatreme breccias; crosscuts main-stage Au-bearing pyrite veins; crosscut by late-stage Au-bearing calcite-quartz-pyrite breccia and pyrite veins | <20 m thick | Observed in drill core along section B–B' in Kapit NE; tabular to irregular morphologies, near-horizontal to steeply dipping orientations, and a consistent discordant nature | Dikes; triggered phreatomagmatic and phreatic brecciation; blocky peperite dikes formed via continued intrusion of KNE10 dikes into wet, unconsolidated diatreme fill; late-epithermal mineralization timing | Occurs within and subjacent to the root zones of the Lihir diatreme complex; occurs as locally abundant (up to 90%) juvenile clasts within diatreme breccia pipes; equivalent to plagioclase-phyric andesite dikes in Lienetz (L8) and Kapit (K7) |

**Fig. 3.5.** (*Next page*) Graphic drill core log of DDHL1995. See Appendix A1 for drill hole location and Table 3.1 for a summary of lithofacies descriptions.

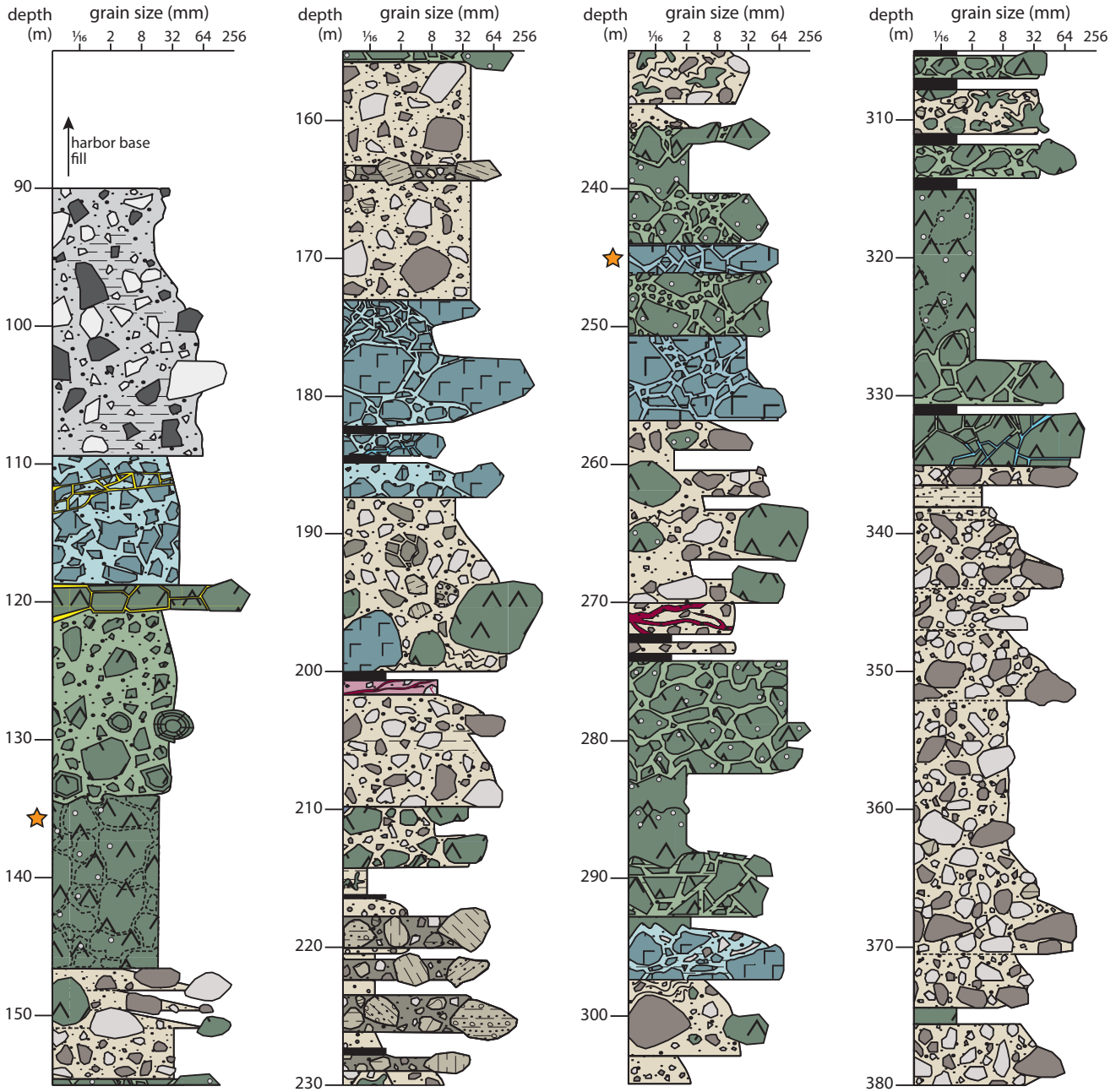


## Volcano-sedimentary stratigraphy

- Polymict, sand matrix-supported, weakly graded and diffusely bedded breccia (KNE1a)
- Polymict, mud matrix-supported breccia with laminated mudstone and sandstone clasts (KNE1b)
- Thinly interbedded volcanic lithic sandstone and siltstone (KNE1a)
- Massive, volcanic lithic sandstone (KNE1c)
- Polymict, normally graded conglomerate and sandstone (KNE1c)
- Pyroxene-phyric basalt (KNE2a)
- Monomict, jigsaw-fit to clast-rotated, sand matrix-supported, pyroxene-phyric basalt breccia (KNE2b)
- Monomict, chaotic, sand matrix-supported, pyroxene-phyric basalt breccia (KNE2b)
- Monomict, mud matrix-supported pyroxene-phyric basalt breccia (KNE2b)
- Polymict, mud matrix-supported pyroxene-phyric basalt breccia (KNE2b)
- Monomict, feldspar-phyric basaltic andesite breccia (KNE3)

## Hydrothermal facies

- Pyrite ± arsenopyrite ± anhydrite ± molybdenite ± tetrahedrite-tennantite-rich, milled matrix-supported breccia
- Discordant sandstone and mudstone
- Polymict, matrix-rich breccia
- Pyrite ± dickite ± illite ± marcasite-cemented breccia
- Calcite – quartz – pyrite-cemented breccia

## Other

- Apparent jigsaw-fit breccia texture
- Wispy texture
- Amygdules
- Fault zone
- Pillow clast with radial and concentric fractures
- Whole-rock geochemistry sample

roxene-feldspar-phyric basaltic andesite with illite-altered rinds (Fig. 3.6C and D). Pyroxene-phyric basalt clasts are locally abundant (>50 vol% of clasts). These concentrations of pyroxene-phyric clasts have a laterally discontinuous distribution, suggesting they occur in beds with lens-like morphologies. A similar 24 m-thick lens of polymict breccia with outsized pyroxene-phyric clasts was identified in the southeast of the Minifie ore zone (Blackwell et al., 2014). Other clasts in KNE1a are sedimentary (<5 vol%) and include massive mudstone, laminated mudstone and matrix-supported breccia clasts (Fig. 3.6E and F). No accretionary lapilli, juvenile clasts, glass shards or pumice fragments were identified. The matrix is composed of poorly sorted, fine to very coarse sand-sized lithic fragments (~70 vol%), feldspar crystal fragments (up to 20 vol%) and pyroxene crystal fragments (~5 vol%) set in a mud-sized matrix (5–10 vol%). The lithic fragments in the matrix have the same compositions as the larger clasts.

Polymict, normally graded conglomerate, pebbly sandstone and siltstone (KNE1b) consists of interbedded, poorly to very poorly sorted, polymict, sand matrix-supported conglomerate (Fig. 3.7C) and compositionally similar, massive pebbly sandstone (Fig. 3.7E). This unit occurs as thin to thick (<1–70 m) clustered lobes within KNE1a at all levels of the stratigraphy, and only occurs east of 9600 mE (Figs. 3.3 and 3.4). KNE1b contains subangular to rounded clasts of dominantly (amygdaloidal) pyroxene-phyric basalt (Fig. 3.7C and E), andesite and rare mudstone.

The conglomerate comprises granule- to cobble-sized clasts and outsized boulders supported by a matrix of silt- to granule-sized lithic fragments. It ranges from massive to very thickly bedded and normally graded. Massive intervals are very poorly sorted and typically contain rounded boulders in a sand-sized matrix. Massive and convolute laminated siltstone matrix-rich intervals (>90% siltstone) occur locally and some contain amoeboid clasts of pyroxene-phyric basalt (KNE2; e.g., Fig. 3.7A and B). These matrix-rich intervals are gradational to monomict, pyroxene-phyric basalt breccia (KNE2b).

Massive pebbly sandstone consists of medium to coarse sand and outsized granules and pebbles of the same composition as the conglomerate. Beds of massive pebbly sandstone are the most abundant and thickest (typically >5 m thick) among KNE1b subtypes, however, the beds are thinner (<1 m thick) where interbedded with KNE1c (Fig. 3.7A).

Polymict mud matrix-supported breccia with laminated mudstone and sandstone clasts (KNE1c) occurs as rare, thick (<4 m), massive, lensoid beds that are laterally continuous over tens of meters and are restricted to the northeast of Kapit NE (Figs. 3.3, 3.4 and 3.7A). However, volcanic-hydrothermal breccia bodies in the west of Kapit NE contain boulders of KNE1c breccia, suggesting that this facies may have a more widespread distribution. The KNE1c breccia has sharp or faulted contacts with KNE1b (Fig. 3.5), and is not observed to be in contact with other rock types. This lithofacies consists of subangular to subround, clast rotated to chaotic, poorly sorted, pebble- to boulder-sized sedimentary clasts (70–80%) supported by a massive mud-sized matrix. The most abundant clasts include distinctive graded and laminated mudstone and sandstone (Fig.3.7D). Other clast types include massive mudstone and matrix-supported granule to pebble breccia.

*Interpretation of KNE1*: The low primary dip of the predominantly very thick and diffuse bed forms, gravel-sized volcanic clasts, poor sorting, and the chaotic, clay- to sand-sized matrix-supported clast organization suggest that the KNE1a facies was deposited by a series of gravity-driven debris flows (e.g., Smith and Lowe, 1991). The thickness (>300 m) of the package of KNE1 breccias may be a product of the successive accumulation of several volcaniclastic debris flow deposits (which typically range from <1–100 m thick) and/or inflation through sill intrusions. The high rainfall, steep bathymetry, geothermal activity (clay-rich alteration), and high rates of seismicity in the vicinity of Lihir

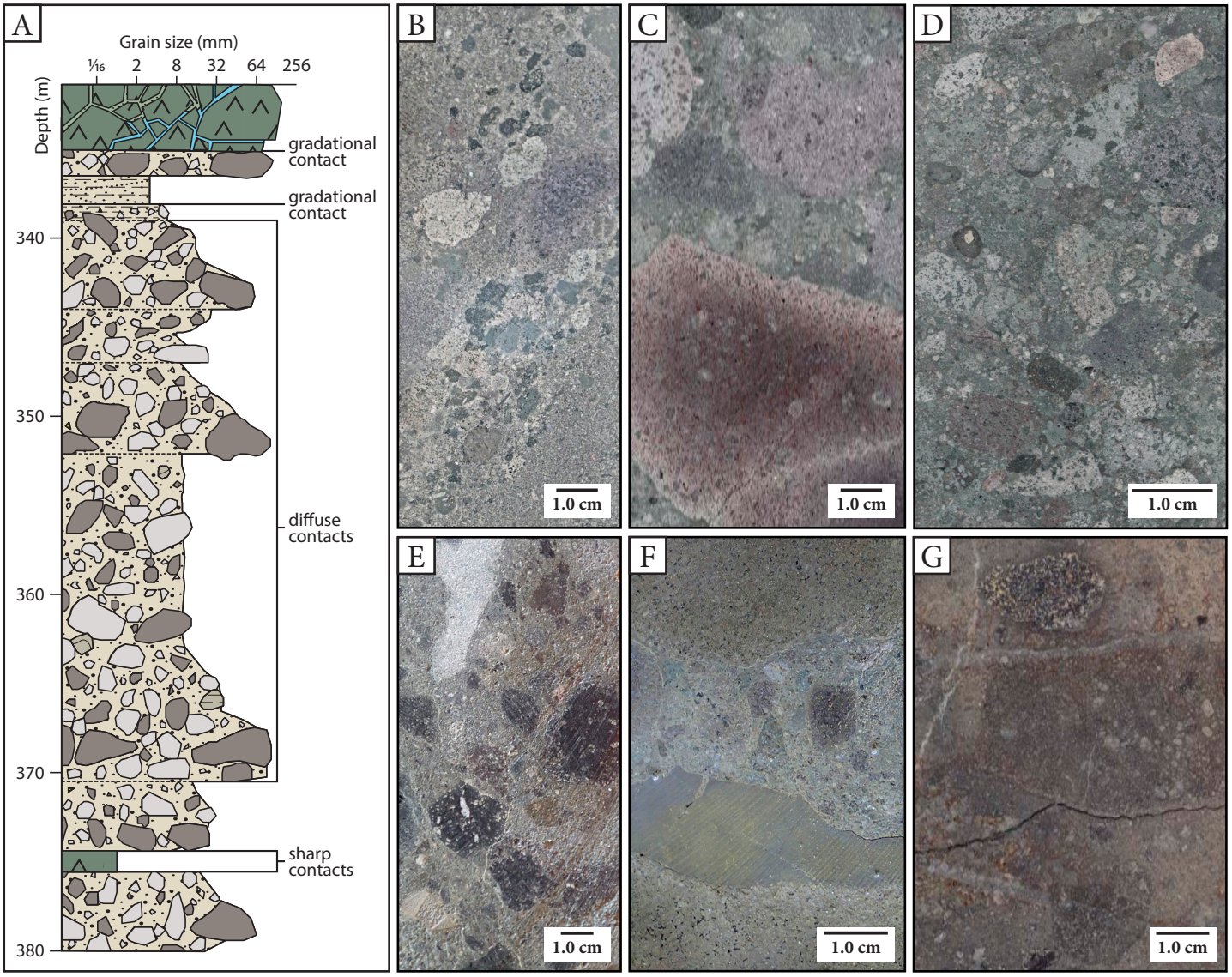


**Fig. 3.6.** Hand sample photographs of polymict, weakly graded and diffusely bedded breccia (KNE1a). **A.** Graphic log of DDHL1995, showing the distribution of polymict breccia (KNE1a), its sharp contacts with pyroxene-phyric basalt (KNE2a) and its gradational contact with pyroxene-phyric basalt breccia (KNE2b). **B.** Polymict breccia (KNE1a) with well-defined beds grading from pebble breccia to sandstone. Sample: DDHL1995 337.3 m. **C.** Polymict breccia (KNE1a) with outsized, thermally oxidized, pyroxene-feldspar-phyric clasts. Sample: DDHL1995 368.7 m. **D.** Polymict breccia (KNE1a) with abundant very coarse lithic wacke matrix, massive texture and poor sorting. Sample: DDHL1995 386.8 m. **E.** Polymict breccia (KNE1a) with abundant amygdaloidal pyroxene-phyric basalt (KNE4) clasts and lesser sedimentary clasts, including a mudstone clast (*bottom left, beige*) and an elongate, matrix-supported breccia clast (*top left, light gray green*). Sample: DDHL1995 195.8 m. **F.** Polymict breccia (KNE1a) with a tabular gray mudstone clast. Sample: DDHL1953 215.1 m. **G.** Polymict breccia (KNE1a) with strong intensity, pervasive biotite alteration. This sample contains feldspar-amphibole-phyric, feldspar-pyroxene-phyric and feldspar-phyric clasts. Sample: DDHL1968 247.7 m.

Island provide optimum conditions for debris flows. The lack of juvenile magmatic clasts and accretionary lapilli in KNE1 suggest that the debris flows were triggered by phreatic eruptions and/or seismic activity, rather than a volcanic eruption (e.g., McPhie et al., 1993).

The presence of texturally immature (angular to ragged), thermally oxidized clasts suggests that subaerially-derived volcanic sediments were incorporated into the debris flows (e.g., McPhie et al., 1993). The irregular and chaotic deposit morphology, predominantly gravel-sized clasts and sand-sized matrix, and the presence of subangular and ragged clasts indicate that the sediments were only transported a short distance from their source (e.g., Stow, 2005). Given that Lihir is an island, the sediments were most likely transported by seawater. The debris flows are therefore in-

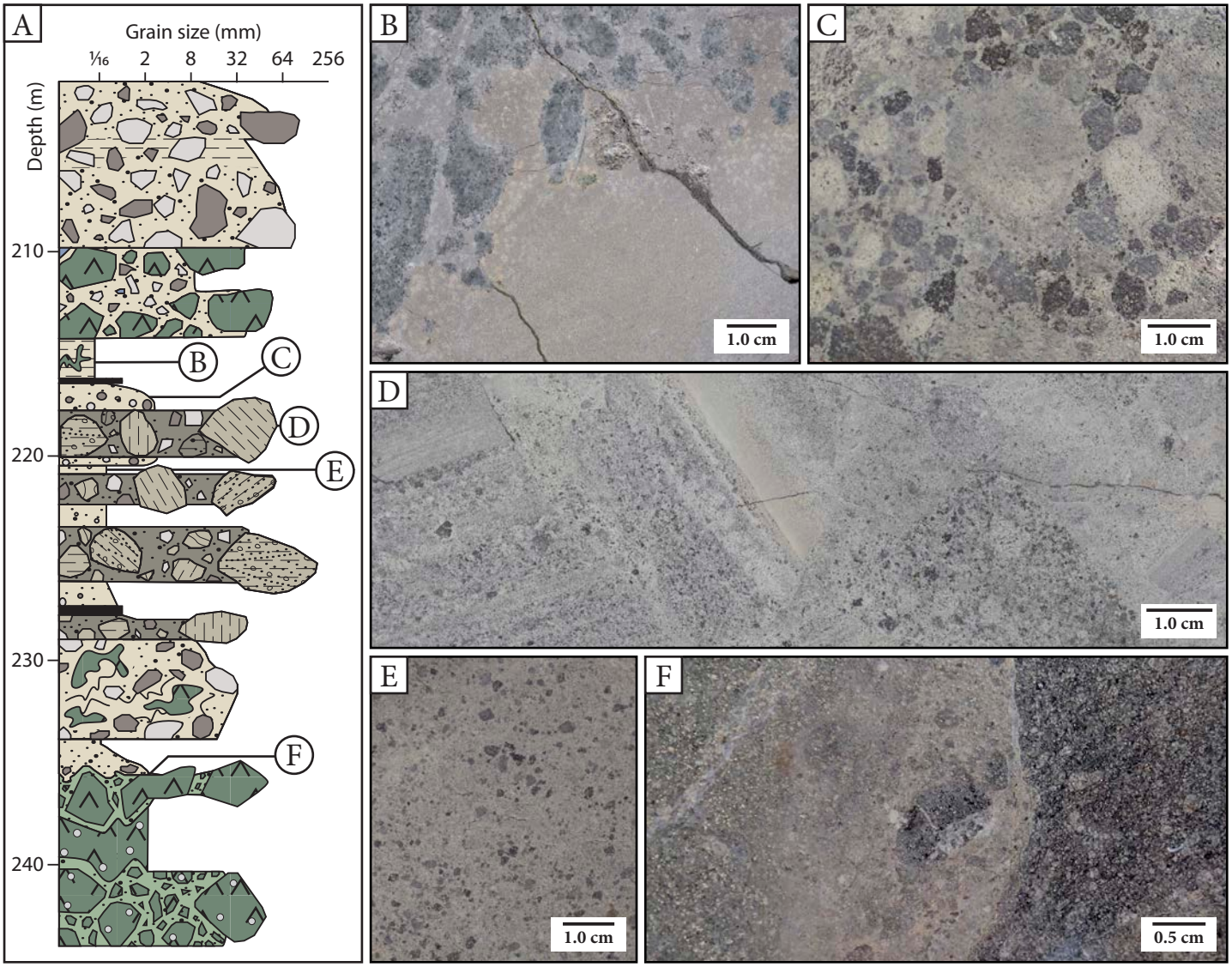


**Fig. 3.7.** Hand sample photographs of normally graded conglomerate (KNE1b), pebbly sandstone (KNE1b) and polymict, mud-matrix-supported breccia (KNE1c). **A.** Graphic log of DDHL1995, showing the distribution and contact relationships amongst KNE1 and KNE2 lithotypes. **B.** Siltstone (KNE1b) with amoeboid clasts of pyroxene-phyric basalt (KNE2), interpreted as peperite. Sample: DDHL1995 215.3 m. **C.** Clast-rich polymict conglomerate (KNE1b). Sample: DDHL1995 217.5 m. **D.** Polymict mud matrix-supported breccia with laminated mudstone and sandstone clasts (KNE1c). Truncated graded beds can be seen in larger clasts. Sample: DDHL1995 218.1 m. **E.** Massive pebbly sandstone (KNE1b) that has clasts of the same composition as the conglomerate depicted in Figure 3.7C. This sandstone is interbedded with and has sharp contacts with KNE1c. Sample: DDHL1995 220.9 m. **F.** Erosive lower contact of matrix-rich polymict conglomerate (KNE1b) with pyroxene-phyric basalt breccia (KNE2b), showing an erosive scour infilled with pyroxene-phyric rip-up clasts. Sample: DDHL1995 234.9 m.

terpreted to have been deposited in a near-shore submarine setting.

KNE1a is laterally extensive, occurring throughout Kapit NE and Coastal ore zones (Figs. 3.3 and 3.4) and has lateral equivalents in Lienetz, Minifie and Kapit (cf. Blackwell, 2010; Ageneau, 2012). A significant distinction is that the polymict matrix-supported breccias in Minifie are associated with accretionary lapilli-bearing pyroclastic facies.

*3.4.3.2 Pyroxene-phyric basalt and basalt breccia (KNE2)*

This lithofacies is the most abundant volcanic rock type in the Kapit NE and Coastal areas, with thicknesses of up to ~250 m. It is composed of two subtypes—pyroxene-phyric basalt (KNE2a) and pyroxene-phyric basalt breccia (KNE2b)—that occur in a ratio of ~1:5 (Figs. 3.3 and 3.4).

Pyroxene-phyric basalt (KNE2a) is texturally heterogeneous and varies significantly between individual units. It ranges from crystal poor (10% phenocrysts) to moderate (35% phenocrysts) and is locally amygdaloidal (Fig. 3.8B). The most abundant phenocrysts are fine- to coarse-grained, equant to stubby clinopyroxene crystals (10–35%) that locally form crystal clusters (Fig. 3.8A, E and H) and display relict zoning (Table 3.1; Fig. 3.8G). Other phenocryst phases include tabular to blocky euhedral plagioclase (up to 10%; Fig. 3.8A), euhedral porous magnetite with ilmenite exsolution lamellae (~5%; Fig. 3.8F). Trace quantities of tabular orthopyroxene (Fig. 3.8F) and equant to blocky sanidine (Table 3.1) are also present. The hypocrystalline groundmass (65–90%) is composed of felty to weakly flow aligned plagioclase microlites (up to 0.15 mm) set in devitrified volcanic glass that has commonly been altered to chlorite – rutile – hematite ± illite-smectite. Relict perlitic fractures are preserved locally. Irregular calcite – illite – chlorite- or anhydrite – magnetite – apatite – K-feldspar-filled amygdules can be abundant (up to 2 cm; up to 40 vol%; Fig. 3.8B and D). KNE2a typically has sharp contacts with polymict matrix-supported breccia (KNE1) and gradational contacts with pyroxene-phyric basalt breccia (KNE2b; Fig. 3.5). It is locally gradational to polymict, siltstone matrix-rich conglomerate (KNE1b) that contains amoeboid and irregular pyroxene-phyric basalt clasts with chilled, ragged and intricate clast margins (Figs. 3.5, 3.7B and 3.8C).

Pyroxene-phyric basalt breccia (KNE2b) is massive, monomict, jigsaw-fit to chaotic, and matrix- to clast-supported. It contains poorly to very poorly sorted, angular to subangular clasts that range from granule to boulder in size (Fig. 3.9). It is spatially associated with, and typically gradational to, coherent basalt (KNE2a), around which it forms thick envelopes (1–100 m thick). Coherent basalt has locally crosscut pyroxene-phyric basalt breccia, providing evidence for multiple episodes of volcanic activity. Contacts with polymict matrix-supported breccia (KNE1) are typically gradational (Fig. 3.5). However, there is at least one instance where the top of the pyroxene-phyric basalt breccia has been scoured by overlying polymict conglomerate (KNE1b; Fig. 3.7A and F). KNE2B typically contains 50–90% clasts of pyroxene-phyric basalt that have angular and ragged or sharp and curviplanar margins (Fig. 3.9A, B and D). The breccia displays a wide range of clast shapes including blocky, splintery and irregular (Fig. 3.9A and G). Locally, above ~900 mRL, the breccia contains rounded boulder-sized clasts with fragmented, pillow-like shapes and both radial and concentric fractures that occur at right angles to each other (Fig. 3.9C). The matrix is composed of mud- to coarse sand-sized angular, blocky and splintery fragments of basalt, plagioclase and pyroxene crystals. Where this breccia has been overprinted by strong biotite – K-feldspar – anhydrite alteration, it locally displays a false polymict texture caused by the preferential patchy to complete alteration of smaller clasts (Fig. 3.9F).

*Interpretation of KNE2*: The porphyritic nature and relatively uniform texture of KNE2a are typical of coherent igneous rocks. The generally high proportion of pyroxene and feldspar phenocrysts are consistent with a basaltic composition. The fine-grained groundmass implies rapid cooling, and a near-surface to extrusive level of emplacement. Where coherent KNE2a basalt is in contact with the host sedimentary material (KNE1 siltstones, sandstones and breccias), there is evidence for mingling between the two, including the presence of tongues and disconnected blobs of basalt within the sediment. This clastic texture is interpreted as peperite, a feature that is diagnostic of lavas emplaced into wet unconsolidated sediments (e.g., Skilling et al., 2002). In Kapit NE, there are several instances where peperitic textures are observed along the upper and lower margins of individual coherent units, which distinguishes them as sills rather than lavas (Macdonald, 1939; Branney and Suthren, 1988; Allen, 1992; Boulter, 1993; McPhie, 1993). Intervals of KNE2 are laterally continuous between drill holes and are concordant to host rock layering. Therefore, at least some of the shallow intrusions are interpreted to be sills.

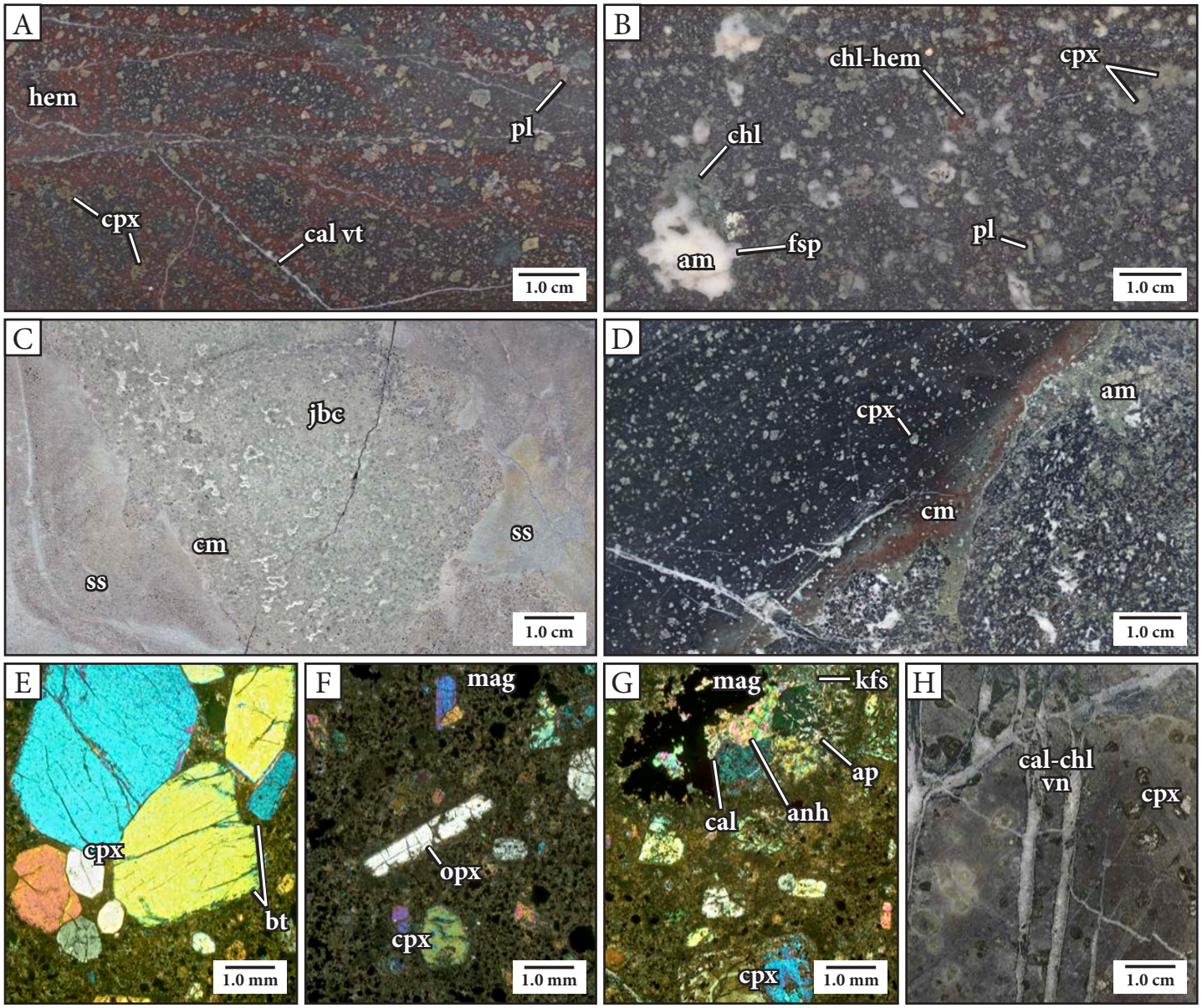


**Fig. 3.8.** Pyroxene-phyric basalt (KNE2a). **A.** KNE2a basalt with glomerophyric clinopyroxene and plagioclase phenocrysts. The sample is crosscut by calcite veinlets and overprinted by hematite – chlorite alteration. Sample: DDHL1995 292.2 m. **B.** Amygdaloidal pyroxene-phyric basalt (KNE2a). Amygdules are zoned, with chlorite – hematite rims and anhydrite – feldspar cores. Sample: DDHL1995 282.3 m. **C.** Fluidal clasts of pyroxene-phyric basalt in polymict, normally graded conglomerate (KNE1c) with a convolute laminated siltstone matrix. Sample: DDHL1995 229.9 m. **D.** Chilled lower margin of pyroxene-phyric basalt with frothy pyroxene-phyric basalt flow top. Sample: DDHL1995 284.7 m. **E.** Photomicrograph of clustered, equant, euhedral clinopyroxene phenocrysts. Sample: DDHL1856 369.1 m. **F.** Photomicrograph of stubby clinopyroxene and elongate orthopyroxene phenocrysts set in a biotite, rutile and anhydrite altered matrix. Opaques are magnetite (>98%) and subordinate pyrite (<2%). Sample: DDHL1856 369.1 m. **G.** Photomicrograph of zoned clinopyroxene phenocrysts and an anhydrite – K-feldspar – apatite – magnetite – calcite-filled amygdule. Sample: DDHL1856 369.1 m. **H.** Coarse, evenly distributed clinopyroxene phenocrysts in coherent pyroxene-phyric basalt. Phenocrysts have patchy calcite alteration. The sample has been crosscut by calcite – chlorite veins. Sample: DDHL1856 246.8 m. Abbreviations: am = amygdule, anh = anhydrite, ap = apatite, bt = biotite, cal = calcite, chl = chlorite, cm = chilled margin, cpx = clinopyroxene, fsp = feldspar, hem = hematite, jbc = juvenile basalt clast, kfs = K-feldspar, mag = magnetite, opx = orthopyroxene, pl = plagioclase, ss = siltstone, vn = vein, vt = veinlet.

In most cases, coherent pyroxene-phyric basalt is not in direct contact with the host sediments and instead grades into monomict basalt breccia (KNE2b). The basalt breccia has blocky, irregular and splintery clasts bounded by sharp, curviplanar margins and a dominantly jigsaw-fit to clast-rotated clast organization. These features are characteristic of hyaloclastites, volcaniclastic aggregates formed through quench fragmentation of lavas and intrusions (Cas and Wright, 1987). The presence of basaltic hyaloclastite enveloping coherent basalt is consistent with the intru-

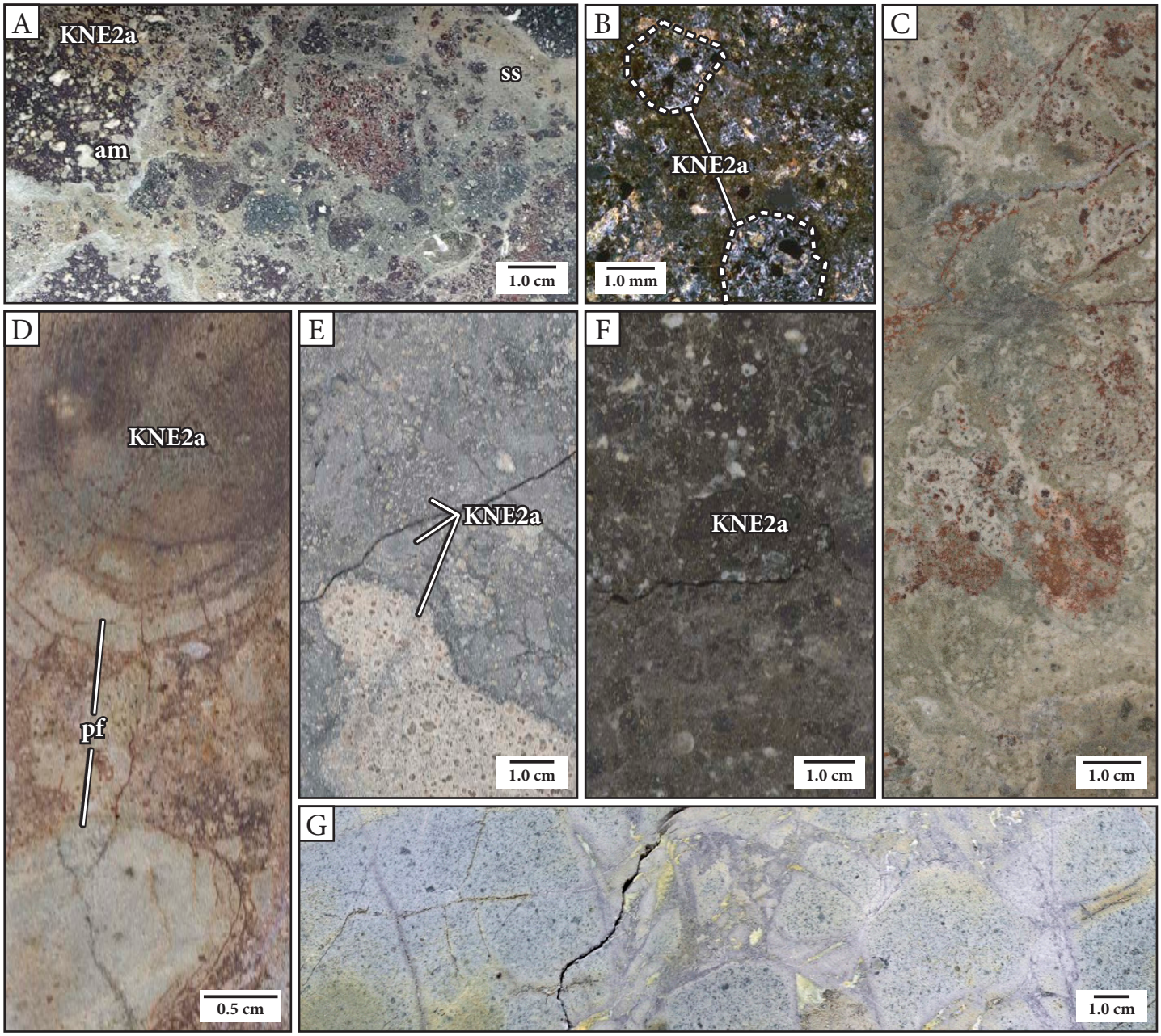


**Fig. 3.9.** Pyroxene-phyric basalt breccia (KNE2b). **A.** Amygdaloidal pyroxene-phyric basalt breccia with ragged and irregular clast shapes and a massive siltstone matrix. Sample: DDHL1995 277.5 m. **B.** Photomicrograph of amygdaloidal pyroxene-phyric basalt breccia matrix. Two, angular, curviplanar medium to coarse sand-sized grains have been outlined with a dashed line for clarity. Sample: DDHL1995 249.5 m. **C.** Strongly altered pyroxene-phyric basalt breccia. Clast margins have been obscured by feldspar – hematite – chlorite – illite alteration, which has also produced apparent wispy textures. Sample: DDHL1856 217.5 m. **D.** Chaotic monomict breccia with tabular to irregular pyroxene-phyric basalt clasts and pyroxene-phyric pillow lava fragments that have radial and concentric joints. DDHL1995 129.6 m. **E.** Apparent polymict texture in monomict, feldspar-pyroxene-phyric basalt breccia. Sample: DDHL1928 272.4 m. **F.** Apparent coherent texture in a jigsaw-fit, amygdaloidal pyroxene-phyric basalt breccia. Sample: DDHL1995 249.5 m. **G.** Pyroxene-phyric basalt breccia with angular, blocky clasts and clast-rotated internal organization. Sample: DDHL1995 120.5 m. Abbreviations: am = amygdule, pf = pillow fragment, ss = sand-sized matrix.

sion of lava into wet sediment and may also indicate the emplacement of lava in an aqueous setting (McPhie et al., 1993). The dominantly jigsaw-fit to clast-rotated organization of KNE2b suggest that most KNE2b hyaloclastites are in situ, while clast-rotated to chaotic domains give evidence for local resedimentation (McPhie et al., 1993).

Massive, monomict, matrix-supported, pyroxene-phyric basalt breccia containing pillow-like clasts with radial and concentric fractures is interpreted as pillow

fragment breccia (similar to Shimokita Peninsula, Japan; Yamagishi, 1987, 1991). The pillow fragment breccias are interpreted to have been produced through quenching and disintegration of tongues of low viscosity basaltic magma extending outward from feeder dikes in a submarine setting (Yamagishi, 1991). The presence of pillow fragment breccia may indicate that proximal coherent intervals of pyroxene-phyric basalt have a pillow lobe morphology that is not recognizable in drill core.

Pyroxene-phyric basalt (KNE2) clasts commonly occur in polymict matrix-supported breccia (KNE1). However, there are also sharp, igneous contacts between the pyroxene-phyric basalt (KNE2) and polymict weakly graded and diffusely bedded breccia (KNE1a), which suggest a later timing of emplacement for KNE2. This contradiction can be explained if the units have been deposited synchronously and/or cyclically. KNE2 is similar to pyroxene-phyric basalt that occurs in Minifie, Lienetz and Kapit, and correlates spatially with the pyroxene-phyric coherent and clastic facies that crops out in the eastern Lienetz pit wall (Blackwell, 2010).

#### *3.4.3.3 Pyroxene-feldspar-phyric basaltic andesite breccia (KNE3)*

KNE3 is unstratified, monomict, and clast- to matrix-supported. It is characterized by very poorly sorted (granule- to boulder-sized) clasts of crystal-crowded pyroxene-feldspar-phyric basaltic andesite in a compositionally identical, mud- to very coarse sand-sized matrix (Fig. 3.10). The breccia is jigsaw-fit to clast-rotated, with up to 15˚ clast rotation (Fig. 3.10). KNE3 breccia bodies are laterally continuous over distances of up to 200 m and are restricted to high levels of the stratigraphy (above ~750 mRL) and areas east of 9600 mE (Figs. 3.3 and 3.4). Individual KNE3 breccia bodies range from <2 to 80 m thick and locally coalesce to form packages up to 200 m thick (Figs. 3.3, 3.4 and 3.5). This lithotype is typically strongly altered and its contacts are obscured. In the least-altered exposures provided by drill hole DDHL1995 (Appendix A1), KNE3 has sharp, irregular contacts with pyroxene-phyric basalt breccia (KNE2b; Figs. 3.5 and 3.10E) and sharp contacts with polymict matrix-supported breccia (KNE1; Fig. 3.5). Pyroxene-feldspar-phyric basaltic andesite breccia locally contains pebble-sized clasts of pyroxene-phyric basalt (KNE2; Fig. 3.10E), indicating that KNE3 is younger.

The pyroxene-feldspar-phyric basaltic andesite breccia typically contains 60–80% clasts with polyhedral blocky or splintery morphologies and sharp, planar to curviplanar and cuspate margins (Fig. 3.10A and C–D). Locally, smaller clasts (<5 mm) and clast margins are altered such that they are barely distinguishable from the matrix, giving the appearance of a breccia that has a higher matrix content (e.g., Allen, 1988). The pyroxene-feldspar-phyric basaltic andesite clasts typically have a massive, crystal-crowded (30–50% phenocrysts) texture, sparse (<5%) amygdules and an aphanitic gray groundmass (Table 3.1; Fig. 3.10B). The dominant phenocryst phase is fine- to medium-grained, stubby to tabular feldspar (Fig. 3.10B). Less abundant phenocryst phases include fine- to coarse-grained, equant to blocky clinopyroxene, and fine-grained magnetite. Locally, fine-grained relict prismatic amphibole is present. The clasts locally have relict perlitic fractures (Fig. 3.10C).

*Interpretation of KNE3*: KNE3 breccia clasts display jigsaw-fit to clast-rotated organization, a wide range of clast sizes, polyhedral blocky or splintery morphologies, and sharp, planar to curviplanar and cuspate margins, consistent with formation via quench fragmentation (e.g., Cas and Wright, 1987). The lack of stratification, immature and monomict clast population, angular clast margins, and dominantly jigsaw-fit organization indicate minimal post-fragmentation transport (e.g., Maicher et al., 2000). The presence of relict perlitic fractures in the clasts indicates that those clasts were formerly glassy (McPhie et al., 1993). The pyroxene-feldspar-phyric basaltic andesite breccia (KNE3) is therefore interpreted as the in-situ hyaloclastite component of a series of lavas or shallow syn-volcanic intrusions (e.g.,

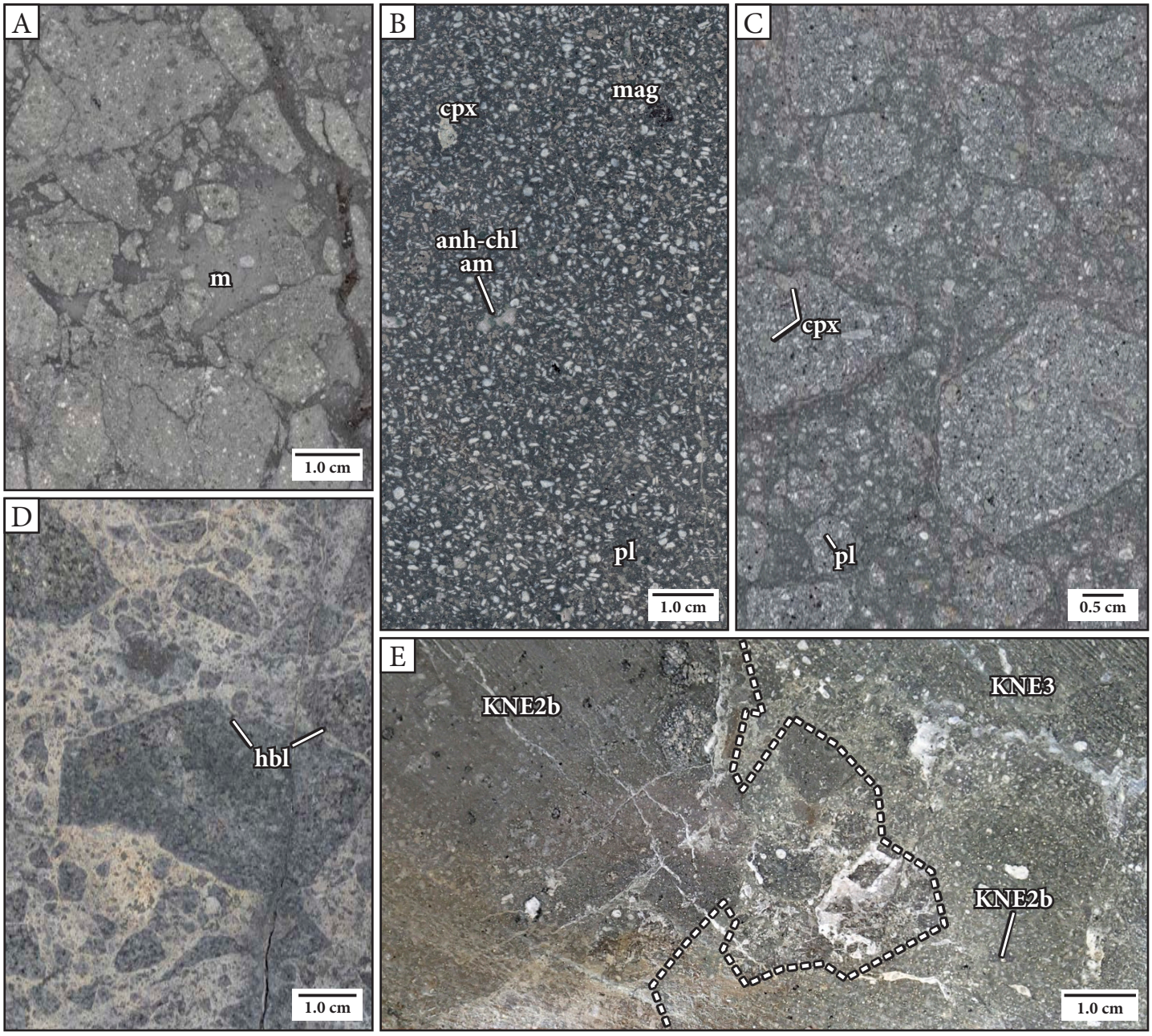


**Fig. 3.10.** Pyroxene-feldspar-phyric basaltic andesite breccia (KNE3). **A.** Pyroxene-feldspar-phyric basaltic andesite breccia with angular, blocky and splintery clasts, clast-rotated to chaotic clast organization and interstitial mud matrix. Sample: DDHL1995 295.7 m. **B.** Amygdaloidal pyroxene-feldspar-phyric basaltic andesite clast showing porphyritic texture of plagioclase, pyroxene and magnetite in an aphanitic gray groundmass. Amygdules are filled with anhydrite and chlorite. Sample: DDHL1995 245.0 m. **C.** Jigsaw-fit, amygdaloidal pyroxene-feldspar-phyric basaltic andesite clasts with curviplanar margins and local perlitic fractures. Sample: DDHL1995 175.0 m. **D.** Splintery, cuspate and curviplanar, jigsaw-fit to clast-rotated, pyroxene-feldspar-phyric basaltic andesite clasts. The sample contains several relict amphibole crystal shapes. Preferential illite-smectite and illite – pyrite alteration of the matrix has enhanced the clastic texture of the rock. Sample: DDHL1932 206.7 m. **E.** Irregular and brecciated contact between pyroxene-feldspar-phyric basaltic andesite breccia (KNE3; *right*) and pyroxene-phyric basalt breccia (KNE2b; *left*). There are clasts of KNE2b incorporated into KNE3, indicating that KNE3 is younger. Sample: DDHL1995 244.2 m. Abbreviations: am = amygdule, anh = anhydrite, chl = chlorite, cpx = clinopyroxene, hbl = hornblende, m = mud-sized matrix, mag = magnetite, pl = plagioclase.

Smith and Batiza, 1989; McPhie et al., 1993). KNE3 breccia crops out at the eastern periphery of the Minifie open pit (Fig. 3.11), where it has previously been referred to as monomict, polyhedral andesite boulder breccia and was also interpreted as a hyaloclastite (Blackwell et al., 2014).

Coherent pyroxene-feldspar-phyric basaltic andesite has not been intersected in drill core in the study area but

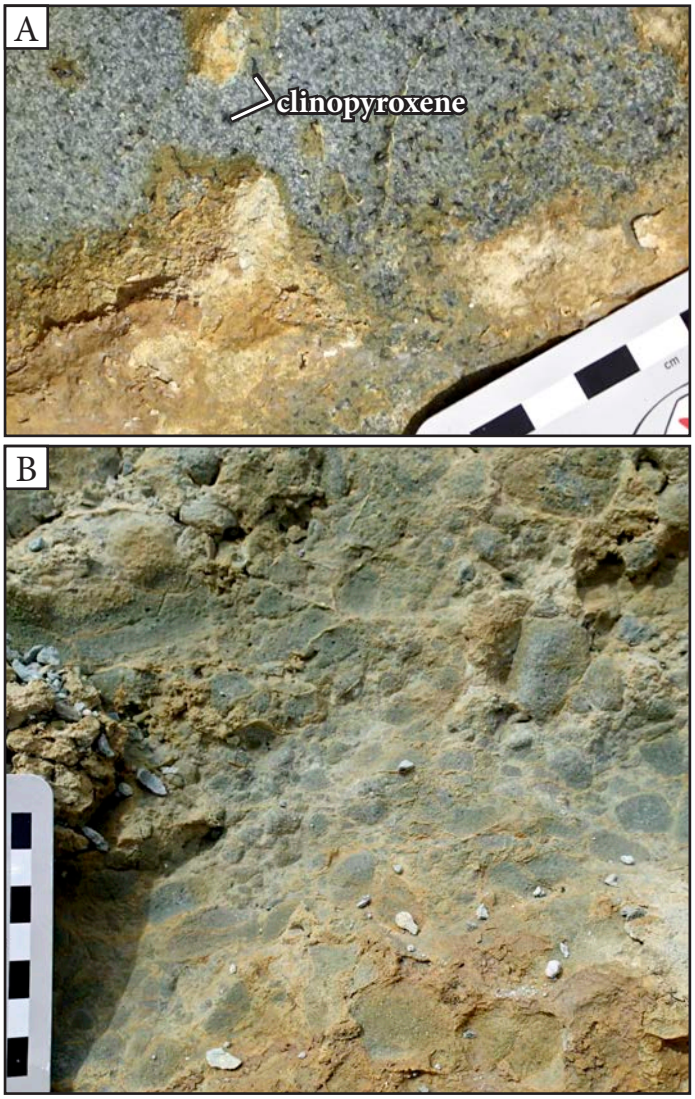


**Fig. 3.11.** Field photos of pyroxene-feldspar-phyric basaltic andesite breccia from Minifie open pit. This breccia is interpreted to be equivalent to the monomict, polyhedral andesite boulder breccia (M1d) of Blackwell et al. (2014). **A.** Close-up photograph of a pyroxene-feldspar-phyric basaltic andesite clast, highlighting the crystal-crowded texture. Phenocryst phases are clinopyroxene and feldspar. **B.** Photograph of basaltic andesite breccia illustrating the jigsaw-fit clast organization and poor sorting of clasts. Approximate coordinates of outcrop (AGD84; Zone 56S): 453955 mE, 9660156 mN.

may have a gradational contact with and form the core of individual units of pyroxene-feldspar-phyric basaltic andesite breccia bodies, as depicted in Figures 3.3 and 3.4. However, in-situ hyaloclastite can comprise the equivalent of entire lava masses with only feeder dikes remaining unfragmented (McPhie et al., 1993), which is an alternative explanation for the lack of coherent pyroxene-feldspar-phyric basaltic andesite occurrences.

### *3.4.4 Coastal intrusive complex*

#### *3.4.4.1 Biotite-feldspar-phyric, nepheline-bearing monzonite (KNE4)*

Volumetrically minor, biotite-feldspar-phyric, nepheline-bearing monzonite (KNE4) dikes occur in the west of the Coastal and Kapit NE ore zones (Fig. 3.3). The dikes are <20 m-thick and are intersected in drill core below 775 mRL (Fig. 3.3). Locally, KNE4 monzonite occurs as rounded xenoliths in the hornblende-biotite-bearing monzonite (KNE5; Fig. 3.12A), and as a principal clast component within jigsaw-fit to chaotic, polymict anhydrite-pyrite-cemented breccia (Fig. 3.12D). The KNE4 monzonite intrusions have sharp igneous contacts with pyroxene-phyric basalt (KNE2) and polymict matrix-supported breccia (KNE1) and are polyphase, displaying several, sharp and irregular internal contacts (Fig. 3.12B).

The KNE4 nepheline-bearing monzonite dikes are fine- to medium-grained, crystal crowded porphyritic rocks that contain predominantly orthoclase, with plagioclase, biotite (10–25%), and nepheline (<0.5 mm; 10%) phenocrysts in a brownish-gray, aphanitic groundmass of feldspar, biotite, apatite and rutile (Table 3.3; Fig. 3.12). The groundmass has been strongly altered to K-feldspar, anhydrite, muscovite, magnetite, pyrite and smectite (Fig. 3.12G). Orthoclase phenocrysts are white, subhedral, stubby to lath-shaped crystals that locally exhibit simple twinning (Fig. 3.12E). Plagioclase phenocrysts are white and tabular with albite twinning (Fig. 3.12F). Both feldspars have been partly replaced by anhydrite, orthoclase and illite, making differentiation between the two difficult, even in thin section. Black biotite phenocrysts are typically euhedral, tabular or short prismatic crystals that have been replaced at their margins by shreddy biotite and rutile (Fig. 3.12G). The biotite crystals commonly contain lamellae-parallel inclusions of acicular and hexagonal apatite (<25 microns) and less commonly include zircon (<50 microns; Fig. 3.12G and I). Small, acicular, randomly oriented apatites are locally

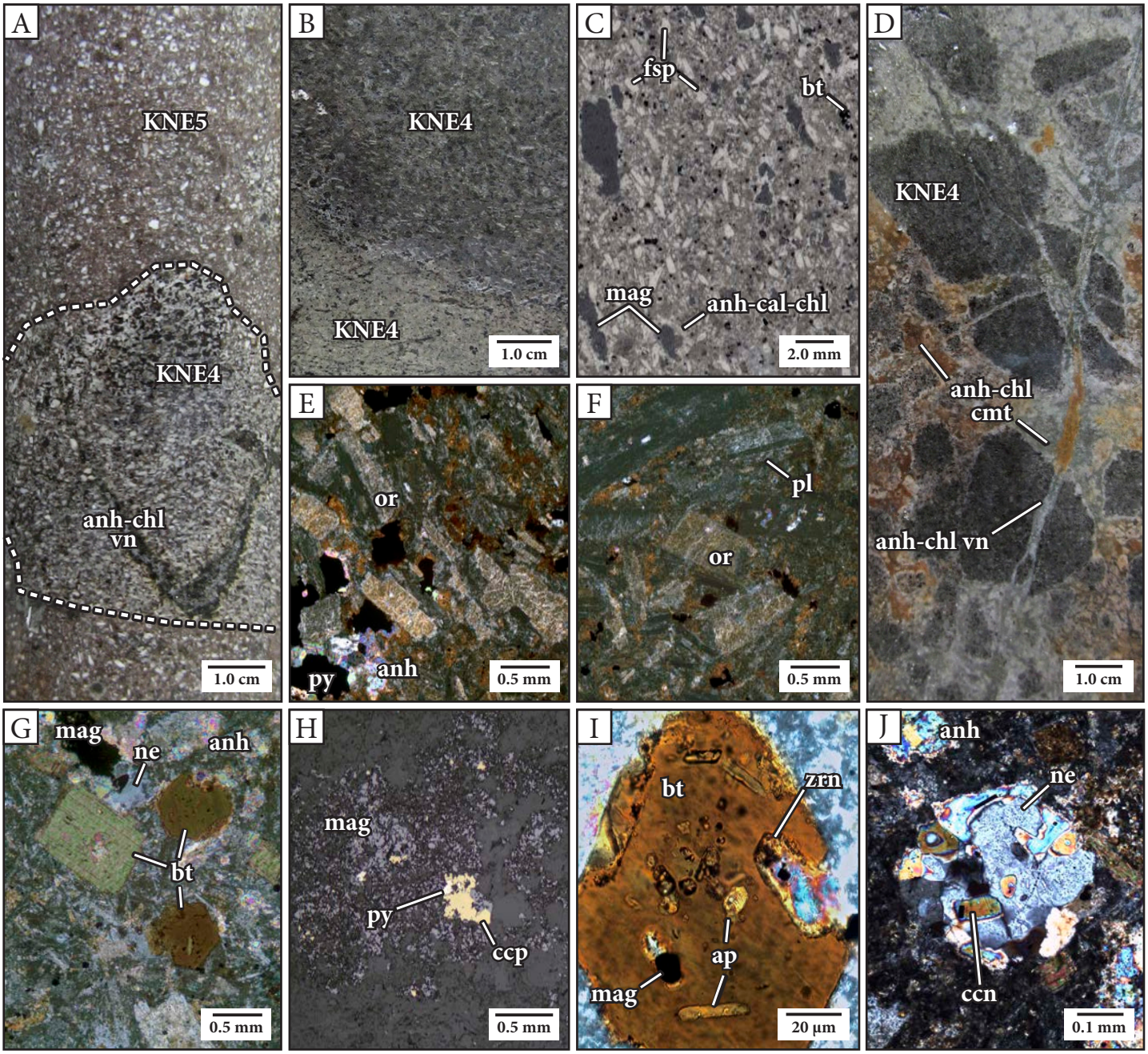


**Fig. 3.12.** Biotite-feldspar-phyric nepheline-bearing monzonite (KNE4). **A.** Xenolith of KNE4 monzonite in hornblende-biotite-bearing monzonite (KNE5). The KNE4 xenolith has a truncated anhydrite – chlorite vein. Sample: DDHL1856 389.7 m. **B.** Irregular, intrusive contact between two phases of KNE4 monzonite. The younger intrusion (top) has flow aligned feldspar phenocrysts and a smaller average phenocryst size at its margin. Sample: DDHL1856 355.8 m. **C.** Hand sample photograph of KNE4 monzonite highlighting the densely crystal-crowded texture of feldspar (K-feldspar and plagioclase) and biotite phenocrysts. The sample has irregular ovoid miarolitic cavities with cores of magnetite ± chalcopyrite ± pyrite and rims of anhydrite – calcite – chlorite. Sample: DDHL1856 311.4 m. **D.** Hand sample photograph of a concentration of KNE4 monzonite clasts within the polymict anhydrite – chlorite-cemented breccia. The cement and clasts have been crosscut by branching anhydrite – chlorite veins. Sample: DDHL1856 360.0 m. **E.** Photomicrograph of KNE4 monzonite showing abundant aligned feldspar phenocrysts, including blocky orthoclase phenocrysts with relict Carlsbad twinning. Sample: DDHL1856 308.8 m. **F.** Photomicrograph of KNE4 monzonite showing abundant feldspar phenocrysts, including plagioclase with relict albite twinning. Sample: DDHL1856 308.8 m. **G.** Photomicrograph of nepheline phenocrysts and near-pristine, euhedral biotite (viewed along and perpendicular to the c-axis of the crystals). Secondary shreddy biotite has weakly altered the rims of the biotite phenocrysts. There is a zoned anhydrite – magnetite-filled miarolitic cavity in the upper left corner of the photomicrograph. The groundmass of randomly oriented relict feldspars and biotite has been strongly altered to K-feldspar, anhydrite, muscovite, magnetite, pyrite and smectite. Sample: DDHL1856 311.4 m. **H.** Reflected light photomicrograph of a miarolitic cavity. The opaque minerals are octahedral and dodecahedral magnetite, chalcopyrite and pyrite. Sample: DDHL1856 311.4 m. **I.** Photomicrograph of a biotite phenocryst with abundant inclusions of euhedral apatite, magnetite and zircon. Sample: DDHL1856 311.4 m. **J.** Photomicrograph of a nepheline phenocryst that has been partly altered to cancrinite. The nepheline has abundant primary fluid and melt inclusions. Sample: DDHL1856 311.4 m. Abbreviations: anh = anhydrite, ap = apatite, bt = biotite, cal = calcite, ccn = cancrinite, ccp = chalcopyrite, chl = chlorite, cmt = cement, fsp = feldspar, mag = magnetite, ne = nepheline, or = orthoclase, pl = plagioclase, py = pyrite, vn = vein, zrn = zircon.

abundant in the groundmass and as inclusions in all other mineral phases. Nepheline phenocrysts contain abundant melt and fluid inclusions and are locally partly altered to cancrinite (Fig. 3.12J).

The KNE4 dikes are texturally heterogeneous with locally abundant (up to 5%), elongate, ovoid and irregularly-shaped magnetite – anhydrite – chalcopyrite ± chlorite ± calcite ± pyrite ± apatite ± hematite clots (up to 1 cm in length; Fig. 3.12C, G and H). They also contain very fine-grained mafic xenoliths (up to 2 cm in diameter). The magnetite-rich clots are zoned, with anhydrite ± calcite ± chlorite rims (Fig. 3.12C and G) and cores of octahedral or dodecahedral magnetite ± chalcopyrite ± pyrite cores (Fig. 3.12H) that are locally rimmed by hematite. The clots are interpreted to be miarolitic cavities, based on their irregular morphologies, discrete spatial distributions, zoned euhedral infill and lack of obvious alteration halos (e.g., Candela, 1997).

### *3.4.4.2 Hornblende-biotite-bearing monzonite (KNE5)*

A north-trending swarm of hornblende-biotite-bearing monzonite intrusions (KNE5) with irregular, branching morphologies occur east of 5600 mE in the Kapit NE and Coastal ore zones (Figs. 3.3 and 3.4). The KNE5 monzonite intrusions range from tens to hundreds of meters thick. KNE5 monzonite intruded discordantly into the consolidated volcano-sedimentary succession (e.g., Fig. 3.13). The KNE5 monzonite intrusions have a homogeneous, crystal-crowded porphyritic texture and an aphanitic, pink-gray to gray groundmass. The most common phenocryst phases in the KNE5 monzonite are medium- to coarse-grained plagioclase and K-feldspar, which occur at a ratio of roughly 2:1. Plagioclase phenocrysts have a bimodal distribution of grain sizes (<0.25 mm and 1–3 mm) and typically occur as euhedral, white, blocky to tabular crystals that are locally weakly flow-aligned (Fig. 3.14A, B and C). K-feldspar phenocrysts are stubby to blocky and are typically translucent gray (Fig. 3.14B) or salmon in color (Fig. 3.14A). Other

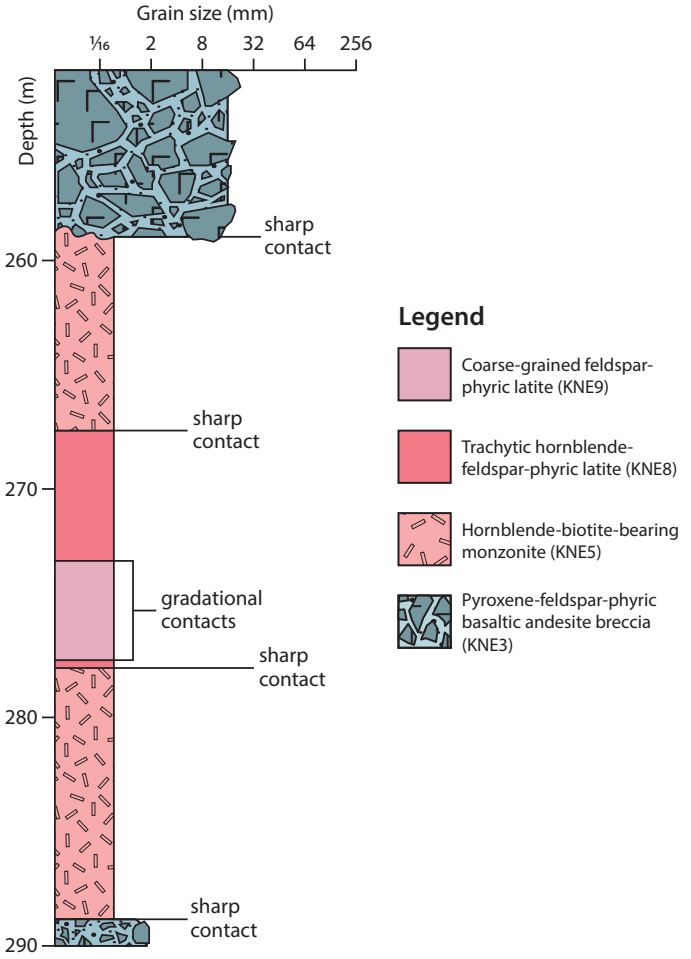


**Fig. 3.13.** Graphic log of DDHL1932 from 250–290 m down hole, showing the distribution and contact relationships between KNE5, KNE8 and KNE9.

phenocryst phases include black, equant to stubby biotite and relict stubby hornblende. Some biotite phenocrysts are partly rimmed by shreddy biotite. Hornblende phenocrysts are typically replaced by alteration minerals (e.g., chlorite, magnetite, anhydrite and pyrite, Fig. 3.14C; anhydrite and pyrite, Fig. 3.14E) but locally preserve amphibole cleavages (Fig. 3.14D). Locally, hornblende crystals have been leached, forming vugs (Fig. 3.14C). The texture and composition of the groundmass has been obscured by patchy illite – smectite – pyrite or biotite – K-feldspar – anhydrite alteration (Fig. 3.14D and E).

KNE5 monzonite contains rare xenoliths of KNE4 nepheline-bearing monzonite (Fig 3.12A) and microdiorite (Fig. 3.14F). One of the microdiorite xenoliths contains a truncated coarse-grained biotite – pyrite – magnetite –

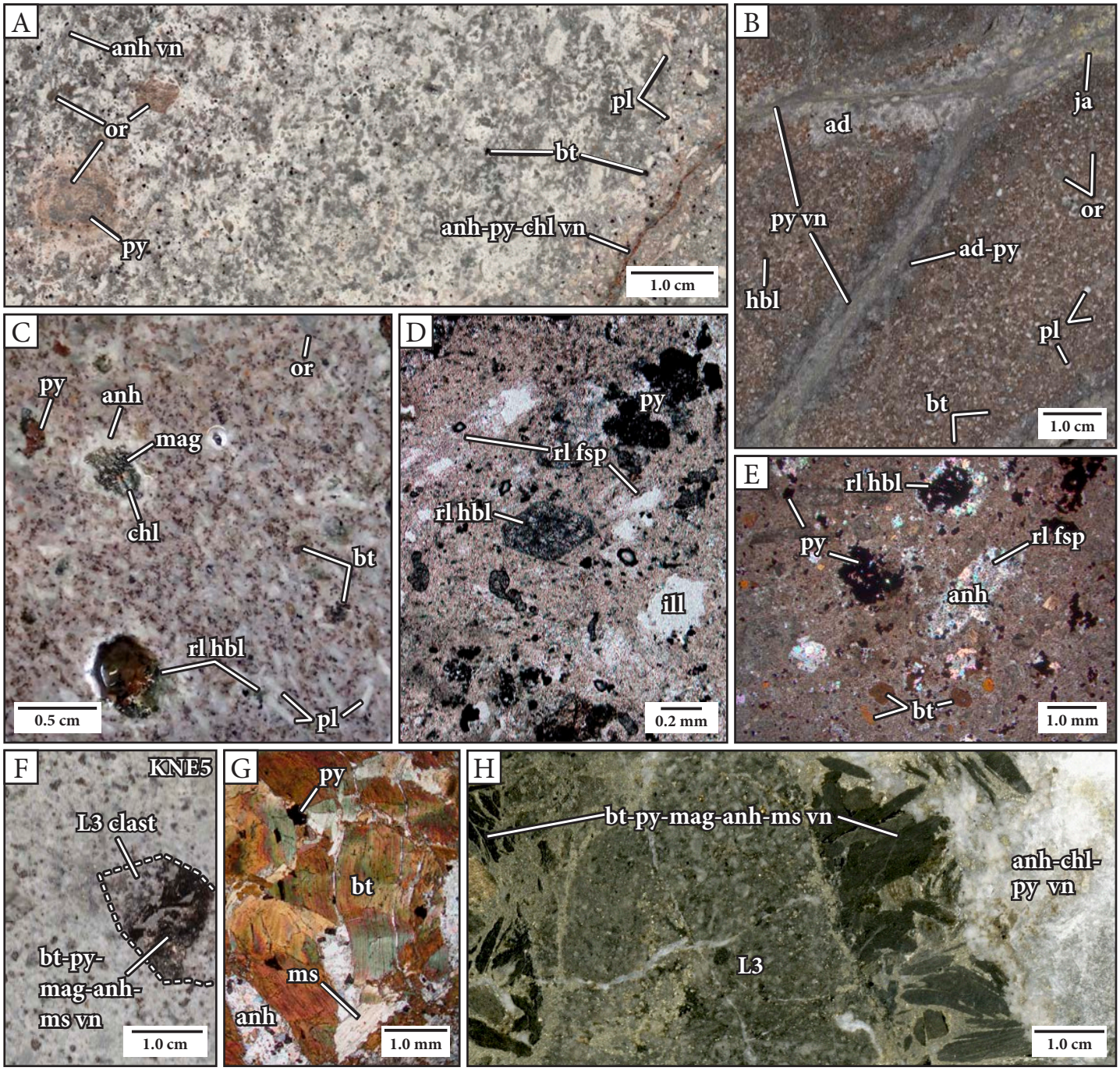


**Fig. 3.14.** Hornblende-biotite-bearing monzonite (KNE5). **A.** Hand sample photograph of KNE5 monzonite showing phenocrysts of plagioclase, biotite and outsized orthoclase. The sample was crosscut by anhydrite and anhydrite – pyrite – chlorite veins with pyrite – hematite – biotite – K-feldspar alteration halos that have locally imparted a pink coloration to orthoclase phenocrysts. Sample: DDHL1876 281.5 m. **B.** Hand sample photograph of KNE5 showing translucent gray orthoclase and white plagioclase phenocrysts in an aphanitic pinkish brown groundmass. The sample has been crosscut by a pyrite vein stockwork with conspicuous gray adularia – pyrite ± jarosite alteration halos. Sample: DDHL1924 356.5 m. **C.** Hand sample photograph of KNE5 monzonite with outsized relict hornblende phenocrysts that are completely replaced by patchy chlorite – magnetite ± pyrite and rimmed by anhydrite alteration. Locally, the relict hornblendes have been leached, resulting in a vuggy texture. Sample: DDHL1872 280.8 m. **D.** and **E.** Photomicrographs of KNE5 monzonite highlighting relict hornblende and feldspar phenocrysts. The samples have been strongly altered by illite – smectite – pyrite and biotite – K-feldspar – anhydrite, respectively. Samples: DDHL1873 174.2 m and DDHL1876 281.5 m. **F.** Hand sample photograph of KNE5 monzonite containing a xenolith of microdiorite (cf. L3, Blackwell, 2010; K2, Ageneau, 2012) that has been crosscut by a coarse-grained biotite – pyrite – magnetite – muscovite – anhydrite vein. Sample: DDHL1872 364.2 m. **G.** Photomicrograph of the truncated vein from Figure 3.13F showing deformed biotite and muscovite crystals with interstitial anhydrite and pyrite. Sample: DDHL1872 364.2 m. **H.** Hand sample photograph of L3 microdiorite from the Lienetz open pit (4075 mN, 9500 mE, ~800 mRL) that has been crosscut by coarse-grained biotite – pyrite – magnetite – muscovite – anhydrite veins that resemble the truncated vein from Figure 3.13F. The coarse-grained biotite veins in this sample are crosscut by anhydrite – chlorite – pyrite veins, which also crosscut the KNE5 monzonite in Kapit NE and Coastal (Fig. 3.13A). Abbreviations: ad = adularia, anh = anhydrite, bt = biotite, chl = chlorite, fsp = feldspar, hbl = hornblende, ill = illite, ja = jarosite, mag = magnetite, ms = muscovite, or = orthoclase, pl = plagioclase, py = pyrite, rl = relict, vn = vein.

muscovite – anhydrite vein (Fig. 3.14F and G), which resembles irregular anhydrite veins and breccia veins from the Lienetz open pit (Sykora et al., 2018a; Fig. 3.14H). This suggests that even though microdiorite and coarse-grained biotite-rich veins have not been observed within the Coastal or Kapit NE areas, they may occur at depth (below 600 mRL; Fig. 3.3). It also indicates that the intrusion of KNE5 monzonite post-dates the intrusion of microdiorite. KNE5 is crosscut by the KNE6 to KNE9 intrusions and occurs as clasts within porphyry and epithermal stage, polymict hydrothermal breccias (Fig. 3.3).

#### *3.4.4.3 Hornblende-bearing gabbro (KNE6)*

Hornblende-bearing gabbro (KNE6) occurs as two thin dikes (<10 cm wide) in the west of Kapit NE, as a larger (>22 m wide) dike in the west of Coastal and as a thin dike (10 cm wide) in the east of Kapit NE (Figs. 3.3 and 3.4). All intersections of KNE6 in drill core occur below ~750 mRL (Figs. 3.3 and 3.4). KNE6 is a strongly crystal crowded gabbro (95% phenocrysts) and is composed of medium- to coarse-grained clinopyroxene, feldspar, hornblende and magnetite (Fig. 3.15). Clinopyroxene phenocrysts are stubby to equant, and are locally glomerophyric and poikilitic (Fig. 3.15B and D). They are typically pseudomorphed by biotite, magnetite, smectite, and chlorite, whereas the feldspar inclusions are altered to K-feldspar, calcite, and anhydrite (Fig. 3.15D). Feldspar phenocrysts are blocky to stubby and have been partially resorbed, giving them a rounded appearance (Fig. 3.15B). They have typically been completely replaced by K-feldspar or albite. Relict amphibole phenocrysts are stubby to prismatic and have been partially to totally replaced by K-feldspar or phlogopite (Fig. 3.15B and D). Locally, amphibole cleavage traces have been altered to biotite, rutile, and smectite (Fig. 3.15D). Magnetite phenocrysts are octahedral and were partly replaced by hematite and pyrite proximal to anhydrite – pyrite and blocky anhydrite veins (Fig. 3.15A). The groundmass is composed of fine-grained (<0.2 mm) feldspars and relict mafic minerals that have been strongly altered to patchy K-feldspar + smectite (Fig. 3.15D). The primary texture of the groundmass has been obscured by alteration.

The hornblende-bearing gabbro has a heterogeneous texture, with domains rich in coarse-grained clinopyroxene clusters (Fig. 3.15A and B) and fine- to medium-grained mafic xenoliths up to 2 cm in diameter (Fig. 3.15C). One KNE6 gabbro dike crosscuts anhydrite – pyrite – chlorite-cemented biotite-altered breccia that contains clasts of gabbro with a similar composition and texture to KNE6 and clasts of hornblende-biotite-bearing monzonite (KNE5; Fig. 3.15B). KNE6 has also been crosscut by porphyry-style alteration and veins (e.g., magnetite – anhydrite veins, biotite – anhydrite veins, K-feldspar + biotite alteration). These relationships imply that KNE6 has a syn-porphyry mineralization timing, that it was emplaced in multiple stages and that at least one generation of gabbro dike emplacement post-dated the intrusion of the KNE5 monzonite.

#### *3.4.4.4 Crystal-poor, feldspar-phyric trachyte (KNE7)*

Several, narrow (<5 m wide), steeply dipping, crystal-poor (5–12% phenocrysts) feldspar-phyric trachyte dikes (KNE7) have been intersected in western Kapit NE below 700 mRL (Fig. 3.4). These intrusions have sharp, chilled margins where they crosscut hornblende-bearing gabbro (KNE6; Fig. 3.15C). KNE7 consists of fine- to medium-grained phenocrysts of orthoclase, plagioclase and sanidine in an aphanitic greenish-beige groundmass (Fig. 3.16). Orthoclase occurs as euhedral, stubby to blocky and simple twinned phenocrysts (Fig. 3.16C) and as cumulophyric crystal clusters (Fig. 3.16B) that are translucent to opaque white in hand specimen. Plagioclase and sanidine phenocrysts were only identified in thin section. The plagioclase phenocrysts are blocky and display albite twinning, whereas the sanidine phenocrysts are bladed and display simple twinning. The groundmass has a pilotaxitic texture consisting of randomly oriented, lath-like feldspar microlites that have been altered to K-feldspar, magnetite, anhydrite and muscovite and locally overprinted by weak

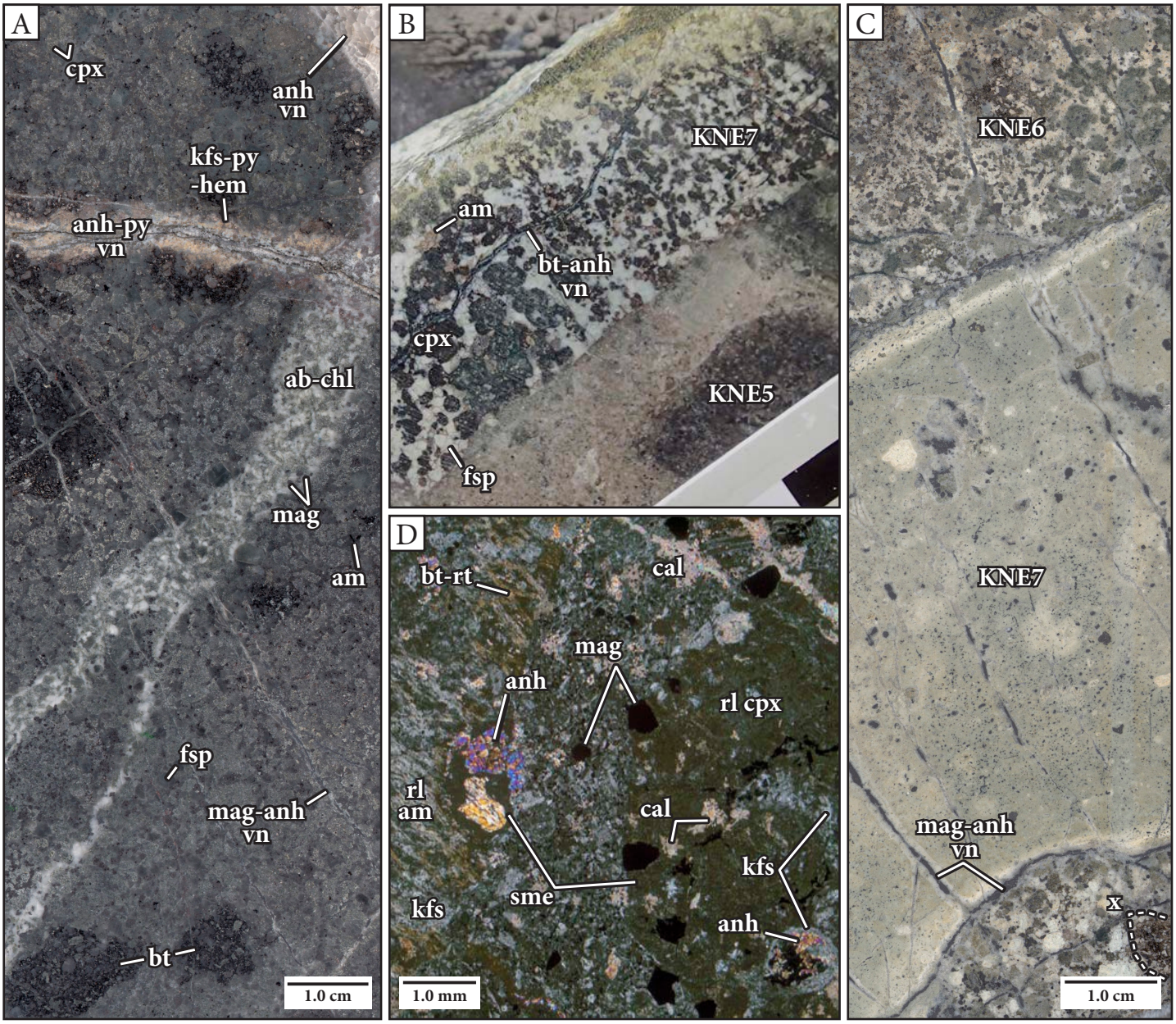


**Fig. 3.15.** Hornblende-bearing gabbro (KNE6). **A.** Hand sample photograph of KNE6 highlighting the phenocryst-rich texture of clinopyroxene, feldspar, magnetite and amphibole phenocrysts in an aphanitic groundmass. The sample has domains of patchy biotite alteration (false xenolithic texture) and structurally controlled domains of albite – chlorite alteration, which have been crosscut by anhydrite – pyrite, magnetite – anhydrite and blocky anhydrite veins. Sample: DDHL1928 329.6 m. **B.** Hand sample photograph of a KNE6 dike containing amphibole phenocrysts that have been completely replaced by pale brown phlogopite. The KNE6 dike has crosscut an anhydrite-cemented breccia associated that contains clasts of pyroxene-feldspar-phyric monzodiorite (KNE5) with orthoclase – anhydrite– biotite alteration rinds. The hornblende-bearing gabbro has been crosscut by biotite – anhydrite veins. Sample: DDHL1872 346.9 m. **C.** Hand sample photograph of hornblende-bearing gabbro that has been crosscut by crystal-poor, plagioclase-phyric andesite (KNE7) and magnetite – anhydrite veins. The sample features several small mafic xenoliths. Sample: DDHL1928 335.4 m. **D.** Photomicrograph of KNE6 showing relict phenocrysts of oikocrystic clinopyroxene and amphibole set in a fine-grained strongly K-feldspar + smectite-altered groundmass of feldspar, magnetite and relict mafic minerals. Cleavage within the relict amphibole has been altered to biotite – rutile and K-feldspar. Feldspar inclusions within the clinopyroxene have been altered to K-feldspar – anhydrite – calcite. Sample: DDHL1928 337.9 m. Abbreviations: ab = albite, am = amphibole, anh = anhydrite, bt = biotite, cal = calcite, chl = chlorite, cpx = clinopyroxene, fsp = feldspar, hem = hematite, kfs = K-feldspar, mag = magnetite, pl = plagioclase, py = pyrite, rl = relict, rt = rutile, sme = smectite, vn = vein, x = xenolith.

smectite alteration (Fig. 3.16B). KNE7 trachyte intrusions contain 5–15% ovoid and amoeboid anhydrite-, K-feldspar- and magnetite-filled amygdules.

#### *3.4.4.5 Trachytic hornblende-feldspar-phyric latite (KNE8)*

A swarm of vertical, northeast-trending, tabular, hornblende-feldspar-phyric latite dikes (KNE8) were intersect-

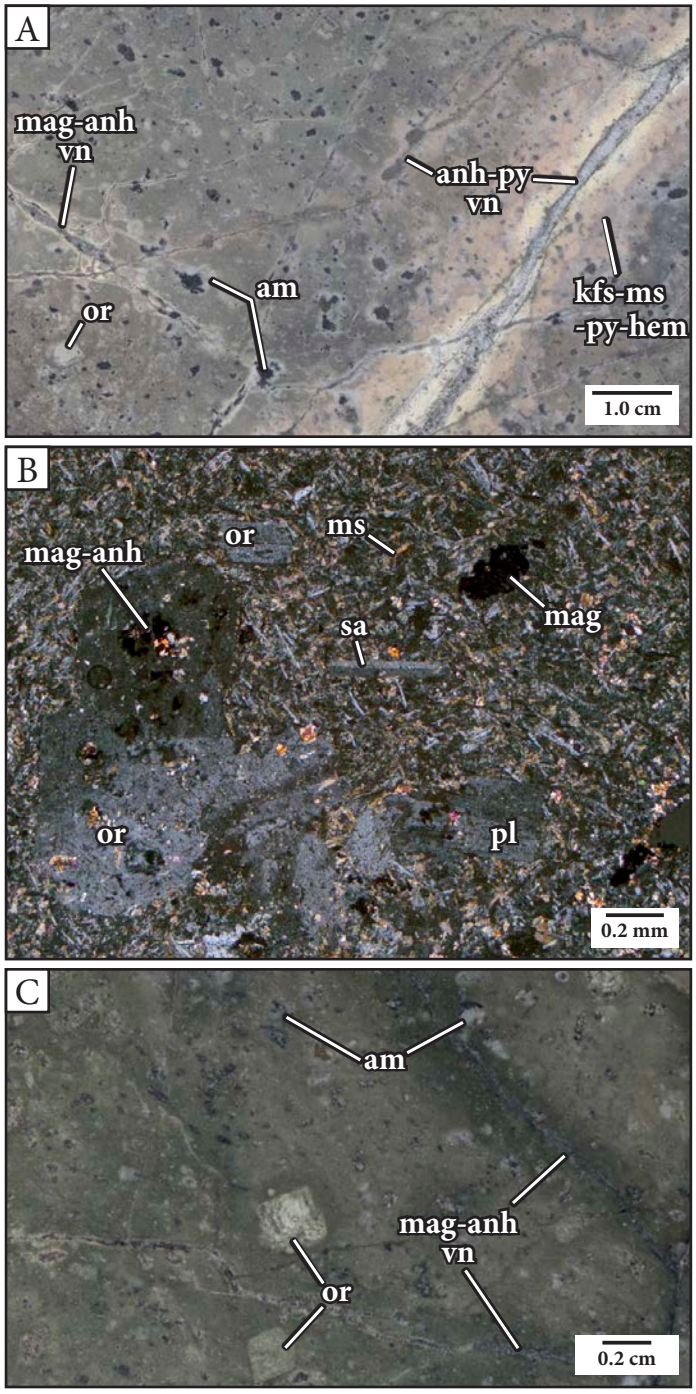


**Fig. 3.16.** Crystal-poor, feldspar-phyric trachyte (KNE7). **A.** Hand sample photograph of KNE7 illustrating sparse orthoclase phenocrysts and abundant anhydrite – magnetite-filled amygdules in an aphanitic greenish-beige groundmass. The sample has been crosscut by magnetite – anhydrite and anhydrite – pyrite veins with distinctive pink K-feldspar – muscovite – pyrite – hematite alteration halos. Sample: DDHL1928 344.3 m. **B.** Photomicrograph of the sample as in Figure 3.16A, showing sanidine, plagioclase and orthoclase phenocrysts, as well as an orthoclase crystal cluster, set in a pilotaxitic groundmass of sanidine and plagioclase microlites. The groundmass has been altered to muscovite, K-feldspar, anhydrite and smectite. Sample: DDHL1928 344.3 m. **C.** Hand sample photograph of KNE7 showing sparse orthoclase phenocrysts with oscillatory zoning. Sample: DDHL1928 347.1 m. Abbreviations: am = amygdule, anh = anhydrite, hem = hematite, kfs = K-feldspar, mag = magnetite, ms = muscovite, or = orthoclase, pl = plagioclase, py = pyrite, sa = sanidine, vn = vein.

ed in drill core on section A–A'–A" in Kapit NE and Coastal (Fig. 3.3). The intrusions range from a few meters to tens of meters thick. They have sharp, strongly altered contacts with polymict quartz – pyrite-cemented breccia (Fig. 3.13) and hornblende-biotite-bearing monzonite (KNE5).

The KNE8 latite dikes are crystal-poor (10–40% phenocrysts) with conspicuous, strongly flow-aligned phenocrysts of plagioclase, sanidine, hornblende and apatite set within a gray, aphanitic groundmass (Fig. 3.17A). Plagioclase phenocrysts are cream, white, peach or gray in hand specimen, with a tabular crystal habit (Fig. 3.17A) and display relict albite twinning (Fig. 3.17C). Sanidine crystals are tabular and euhedral with relict simple twinning (Fig. 3.17C). The feldspar phenocrysts have locally been altered to adularia – illite (Fig. 3.17C and F). Hornblende phenocrysts occur both as stubby and as prismatic euhedral crystals (Fig. 3.17A and E) and are intensely altered to illite-smectite – rutile – pyrite – chlorite above ~800 mRL (Fig. 3.17C and E). Apatite phenocrysts are small and stubby to prismatic (Fig. 3.17F). The groundmass is composed of very fine-grained to fine-grained feldspar microlites that are weakly flow-aligned and locally wrap around phenocrysts. Secondary pyrite has preferentially replaced hornblende phenocrysts and occurs as disseminations within the groundmass (Fig. 3.17E).

The KNE8 latite dikes locally contain vugs that constitute up to 10 vol% open space in the rock. The size of the vugs is bimodal, with a population of ovoid and irregularly-shaped vugs that range from 0.5–25.0 mm and a population of angular, equant or stubby vugs that range from 0.1–1.0 mm (Fig. 3.17F). The irregularly-shaped vugs are oriented parallel to the flow foliation defined by the alignment of tabular feldspar crystals. Feldspar crystals are wrapped around larger vugs. These irregularly shaped vugs are interpreted to be primary vesicles that formed as the latite dikes intruded the near-surface environment. Dikes with similar vesicular textures have been observed in a latite plug at Bingham Canyon, Utah, (Wilson, 1975; Wilson, 1978) and in a dac-

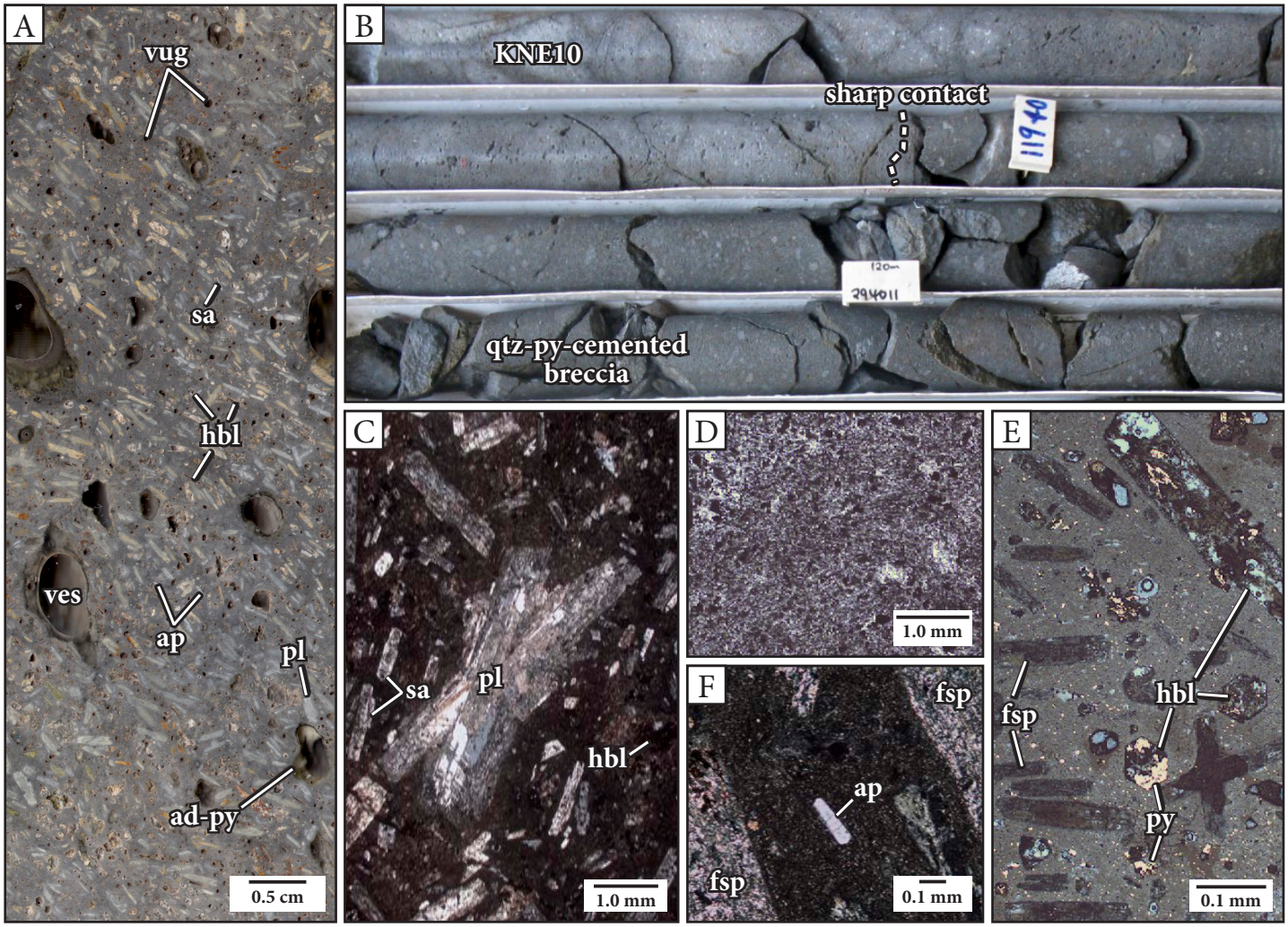


**Fig. 3.17.** Hornblende-feldspar-phyric latite (KNE8). **A.** Hand sample photograph of KNE8 illustrating its characteristic vuggy texture and trachytic alignment of feldspar (sanidine and plagioclase) phenocrysts. Sample: DDHL1931 115.0 m. **B.** Core tray photograph of KNE8 showing a sharp, igneous contact with quartz – pyrite-cemented breccia. The characteristic vuggy texture of KNE8 is visible at this scale. Interval: DDHL1931 118.0–122.0 m. **C.** Photomicrograph of KNE8 latite, showing flow-aligned crossed plagioclase phenocrysts with relict albite twinning and smaller sanidine phenocrysts with simple twinning. All of the feldspars have patchy adularia – illite alteration. Sample: DDHL1932 277.6 m. **D.** Photomicrograph of the very fine-grained to fine-grained, weakly flow-aligned microlitic groundmass of KNE8 latite. The groundmass has strong adularia – illite ± smectite alteration. Sample: DDHL1931 118.0 m. **E.** Reflected light photomicrograph of KNE8 latite showing the selective replacement of hornblende by pyrite (some of which is tarnished blue). Sample: DDHL1931 118.0 m. **F.** Photomicrograph of a small euhedral apatite phenocryst between two illite – adularia-altered feldspar phenocrysts. Sample: DDHL1932 267.6 m. Abbreviations: ad = adularia, ap = apatite, fsp = feldspar, hbl = hornblende, pl = plagioclase, py = pyrite, qtz = quartz, sa = sanidine, ves = vesicle.

itic dike at Yeoval, New South Wales (Ambler, 1979). The angular vugs have diamond-shaped cross-sections and are interpreted to have formed by dissolution of hornblende crystals. Locally, both the irregularly-shaped vugs and the angular vugs are partly to completely infilled by euhedral adularia, pyrite, marcasite, hematite, and apatite, which display open space-filling textures (Fig. 3.17A).

KNE8 latite dikes have been crosscut by gold-bearing botryoidal and colloform pyrite veins, adularia – Fe-sulfide ± illite veinlets and associated disseminated pyrite. The dikes crosscut gold-bearing polymict quartz – pyrite-cemented breccia. The dikes are therefore interpreted to have an inter-mineralization timing.

### *3.4.4.6 Coarse-grained feldspar-phyric latite (KNE9)*

Coarse-grained feldspar-phyric latite (KNE9) occurs as a series of northeast-trending dikes of variable thickness (<1–150 m thick) in Kapit NE (Fig. 3.3). The dikes are

spatially associated with KNE8 latite dikes (Figs. 3.3 and 3.13). The KNE9 latite is moderately crystal crowded with an aphanitic beige to gray groundmass (Fig. 3.18A). Phenocryst phases include randomly oriented feldspar and hornblende. Due to the complete replacement of feldspar phenocrysts by secondary feldspars and clays, the modal percentages of K-feldspar and plagioclase have not been determined in this study. Feldspar phenocrysts typically occur as euhedral, stubby to blocky, zoned crystals (Fig. 3.18). Feldspar phenocrysts exhibit tabular, rounded and amoeboid morphologies (e.g., top left in Fig. 3.18A). Hornblende phenocrysts are prismatic and locally form small clusters of phenocrysts (e.g., Fig. 3.18C). The texture and composition of the groundmass has been obscured by strong, patchy smectite – pyrite – rutile alteration (Fig. 3.18B and C).

KNE9 latite has a similar composition to KNE8 latite, with which it has gradational contacts (Fig. 3.13), and a spatial relationship. Locally, KNE9 latite is bounded by KNE8 (e.g., Figs. 3.3, 3.4 and 3.13). It is possible that KNE8 and KNE9 are the same lithotype, but have different textures due to their relative positions during emplacement. The increase in size and abundance of phenocrysts toward the center of the dike could have resulted from flow differentiation (e.g., Ross, 1986). Likewise, the trachytic alignment of phenocrysts near the margins of the dike could have resulted from shear stresses adjacent and parallel to the conduit walls (e.g., Ross, 1986; McPhie et al., 1993).

### *3.4.4.7 Feldspar-phyric andesite and associated monomict breccia (KNE10)*

Feldspar-phyric andesite (KNE10) occurs as coherent to brecciated intrusions less than 20 m-wide that have been intersected in drill core along section B–B' in Kapit NE (Fig. 3.4). The intrusions have tabular to irregular morphologies, near-horizontal to steeply dipping orientations, and a consistent discordant nature. They are interpreted to be dikes. The KNE10 dikes have a complex relationship and a strong spatial association with the root zones of the Li-

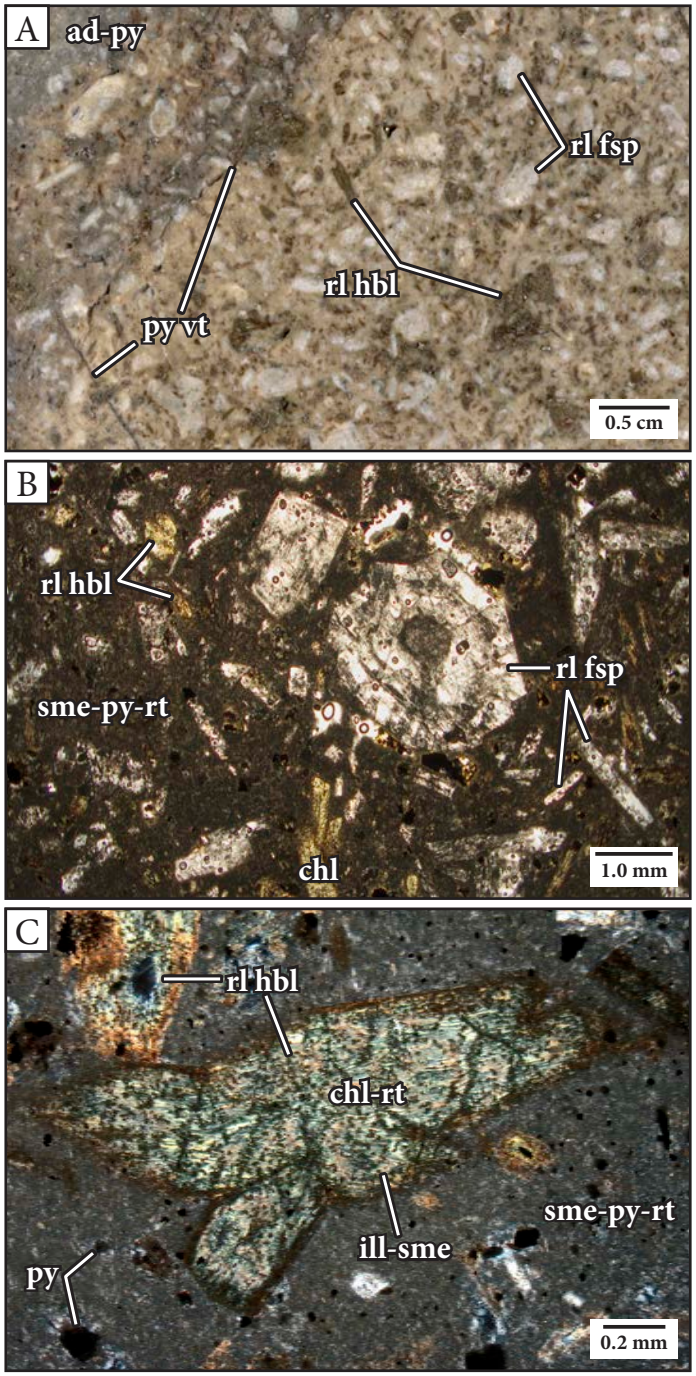


**Fig. 3.18.** Coarse-grained hornblende-feldspar-phyric latite (KNE9). **A.** Hand sample photograph of KNE9 latite illustrating the medium- to coarse-grained, stubby to blocky feldspar phenocrysts and prismatic hornblende phenocrysts in an aphanitic beige groundmass. The sample has locally been overprinted by adularia – pyrite alteration associated with pyrite veins outside of the field of view and crosscut by pyrite veinlets. Sample: DDHL1932 275.5 m. **B.** and **C.** Photomicrographs of KNE9 latite illustrating concentrically zoned feldspar phenocrysts and glomerophyric hornblende phenocrysts. Twinning is not discernible in the relict feldspars. Hornblende phenocrysts have been completely altered to chlorite with rims of illite-smectite. Abundant rutile inclusions can be distinguished within the hornblendes, especially along cleavage and fracture planes. The groundmass has been strongly altered to an assemblage of patchy smectite, pyrite and rutile. Sample: DDHL1932 275.5 m. Abbreviations: ad = adularia, chl = chlorite, fsp = feldspar, hbl = hornblende, ill-sme = illite-smectite, py = pyrite, rl = relict, rt = rutile, sme = smectite, vt = veinlet.

hir volcanic-hydrothermal breccia complex (Lawlis et al., 2015; Chapter 4), occurring both within and immediately subjacent to the breccia pipes (Fig. 3.4). In the root zone of the phreatomagmatic breccia bodies, coherent KNE10 andesite dikes grade into monomict jigsaw-fit feldspar-phyric andesite breccia with a rock flour matrix and then into matrix-rich polymict breccia with blocky to wispy, juvenile feldspar-phyric andesite clasts (Lawlis et al., 2015). Blocky, ragged and wispy feldspar-phyric andesite clasts also occur within polymict, clast-rich breccias in the main body of the diatreme complex (Lawlis et al., 2015). Some of the juvenile andesite clasts are armored by laminated mud matrix, which has preserved their delicate and intricate clast margins (Fig. 3.19D). This facies association is interpreted to have formed via subsurface explosive disaggregation of the KNE10 dikes as they intruded circulating hydrothermal fluids near surface (e.g., Davies et al., 2008b). Intrusion of the KNE10 andesite dikes is inferred to have triggered phreatomagmatic eruptions and provided heat for phreatic explosions that resulted in the formation of the Lihir diatreme breccias (Lawlis et al., 2015). This implies that a significant amount of uplift occurred to bring the porphyritic intrusions of Kapit NE and Coastal (e.g., KNE4–KNE9) from their depth of formation (typically 1–6 km; e.g., Seedorff et al., 2005) to a position near-surface, since they are presently on an equal relative level with the KNE10 andesite dikes.

The andesite dikes are heterogeneous, ranging from crystal poor to moderate and from massive to strongly trachytic. Locally, the dikes have concentric bands that are defined by differences in the proportions of aligned phenocrysts and fine-grained to aphanitic groundmass (Fig. 3.19C). The phenocryst phases in the KNE10 dikes are lath-like, randomly oriented to strongly flow aligned feldspar, blocky (locally glomerophyric) pyroxene and stubby euhedral hornblende. The dikes are strongly and pervasively altered to montmorillonite and contain disseminated pyrite (Fig. 3.19). The strong clay alteration has a distribution consistent with formation from the active geothermal system (Jansen and Cooke, 2013; Cooke et al., in press).

The andesite dikes locally have sharp contacts with the diatreme breccias (Fig. 3.19C), which is interpreted to reflect continuation of andesite intrusion after phreatomagmatic brecciation had discontinued. These late dikes range from coherent to brecciated, where brecciated intervals are very poorly sorted and clay matrix supported with a jigsaw-fit to clast-rotated organization (Fig. 3.19B and D). Flow alignment of tabular feldspar phenocrysts can be traced between the clasts (Fig. 3.19B and E). The clasts have splintery to blocky morphologies and sharp curviplanar margins (Fig. 3.19B and E). These monomict feldspar-phyric andesite breccias are interpreted as blocky peperites produced by quench fragmentation during andesite dike emplacement into wet, unconsolidated diatreme fill. The diatreme breccias contain clasts with truncated main-stage gold-bearing pyrite veins (Fig. 3.19H) and have been crosscut by gold-bearing calcite – quartz – pyrite veins and cemented breccias, and pyrite disseminations and veinlets (Fig. 3.19I). Therefore, the diatreme breccias and their causative intrusions (KNE10) are interpreted to have a late-mineralization timing.

## 3.5 Whole-rock geochemistry

### *3.5.1 Introduction*

This section presents and discusses the results of whole-rock geochemical analyses of intrusive and volcanic rocks from Lihir Island. Interpretations from the data are used to evaluate the tectonic setting of Lihir.

### *3.5.2 Samples*

Thirteen rock samples from Lihir Island were selected for whole-rock geochemical analysis (Table 3.5). An effort was made to analyze least-altered drill core for this study; however, all samples show at least a weak degree of hydrothermal alteration (Table 3.5; Appendix C). Two of the samples are basalts from Ilkot epithermal prospect, which is situated to the north of Lihir gold deposit within the Lon-

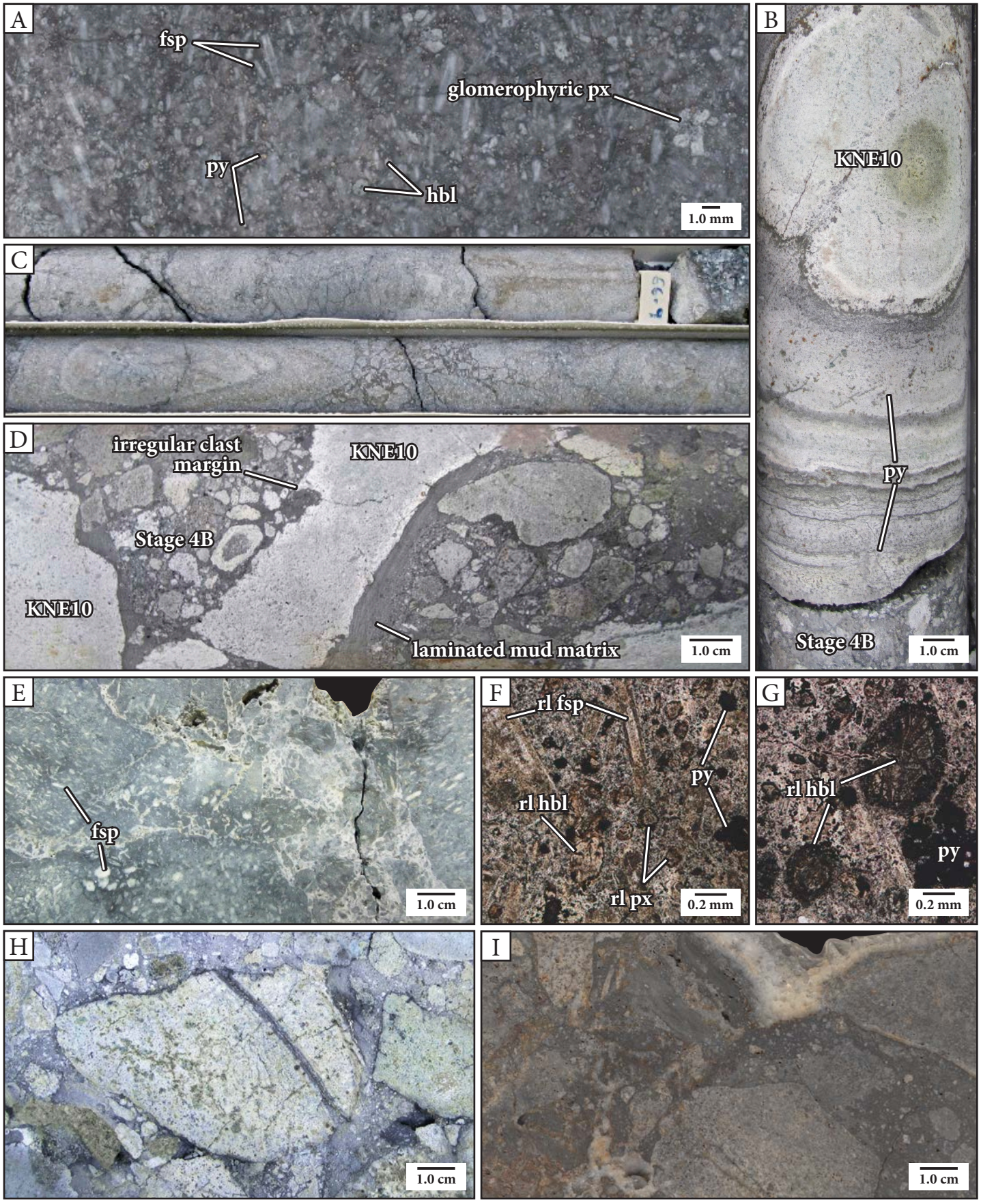
A
fsp
glomerophyric px
py
hbl
1.0 mm
B
KNE10
py
Stage 4B
1.0 cm
C
D
irregular clast margin
KNE10
Stage 4B
KNE10
laminated mud matrix
1.0 cm
E
fsp
1.0 cm
F
rl fsp
py
rl hbl
rl px
0.2 mm
G
rl hbl
py
0.2 mm
H
1.0 cm
I
1.0 cm

**Table 3.5.** Characteristics and location of whole-rock geochemistry samples.

| Sample ID | Location | Easting[1] | Northing[1] | Elevation[2] | Lithotype | Alteration minerals |
|---|---|---|---|---|---|---|
| **LH13SS001** | Lienetz open pit | 459290.3 | 9653971.4 | −259.5 | Monzodiorite (L3 microdiorite; Blackwell, 2010) | K-feldspar, biotite, anhydrite, pyrite |
| **LH13SS002** | | 459274.5 | 9654018.4 | −259.5 | | |
| **DDHL1872 364.2 m** | Kapit NE | 459883.4 | 9655553.2 | −305.1 | Hornblende-biotite-bearing monzonite (KNE5) | K-feldspar, phlogopite, anhydrite, calcite, pyrite, magnetite, muscovite, chlorite |
| **DDHL1876 281.5 m** | | 459899.4 | 9655084.2 | −236.8 | | K-feldspar, biotite, anhydrite, pyrite, chlorite |
| **DDHL1924 356.5 m** | | 459941.4 | 9655826.8 | −296.9 | | Adularia, pyrite, vermiculite |
| **DDHL1924 371.2 m** | | 459940.5 | 9655834.5 | −309.3 | Hornblende-feldspar-phyric latite (KNE8) | K-feldspar, biotite, muscovite, pyrite, vermiculite, montmorillonite, chlorite |
| **DDHL1995 136.7 m** | | 459794.6 | 9656065.5 | −116.9 | Pyroxene-phyric basalt (KNE2a) | Chlorite, calcite, montmorillonite, hematite |
| **DDHL1995 245.0 m** | | 459835.6 | 9656099.4 | −211.2 | Pyroxene-feldspar-phyric basaltic andesite breccia (KNE3) | Adularia, chlorite, pyrite, calcite, anhydrite |
| **IL05 41.5 m** | Ilkot prospect | 460202.1 | 9657555.4 | 86.4 | Amygdaloidal pyroxene-phyric basalt | Montmorillonite, kaolinite, chlorite, calcite |
| **IL05 58.7 m** | | 460195.6 | 9657550.2 | 71.4 | Amygdaloidal, sparsely pyroxene-phyric basalt | Gypsum, montmorillonite, kaolinite, chlorite, calcite |
| **GW47 886.0 m** | Northern extent of Luise amphitheater | 458372.7 | 9656593.5 | −651.7 | Crystal lithic sandstone | Chlorite, calcite, montmorillonite |
| **GW47 1130.0 m** | | 458277.0 | 9656556.3 | −873 | Feldspar-hornblende-phyric monzodiorite | |
| **GW47 1172.5 m** | | 458260.4 | 9656549.8 | −911.6 | Xenolithic, pyroxene-hornblende-phyric monzodiorite | |

[1]AGD84 (Zone 56S) coordinate projection; [2]Elevation units are meters relative to sea level.

dolovit Block (Table 3.5; Figs. 3.1A and 3.20). The remainder of the samples are from Luise Volcano. There are two monzodiorite samples from Lienetz open pit, six volcanic and intrusive samples from Kapit NE and Coastal, and two porphyritic intrusions and a sandstone from geothermal exploration drillhole GW47, located at the northern extent of Luise amphitheater (Table 3.5; Fig. 3.1A). Photographs for each sample are provided in Appendix C. The sample suite has been supplemented with geochemical data for igneous rocks from Lihir Island (Müller et al., 2001; Blackwell, 2010) and Conical Seamount (Müller et al., 2003), a Lihir island group seamount which is located ~10 km south of Lihir Island.

### *3.5.3 Methods*

The samples were inspected and the least-altered portions were selected for analysis. Veins and vein-halo alteration were removed from the samples where required. The samples were analyzed for major and trace element compositions at Acme Analytical Labs Ltd. in Vancouver, Canada. Samples were crushed to 85%, passing 200 mesh (74 μm) in an Essa standard stainless-steel mill. A small quantity (0.2 g) of each powdered sample was fused in a crucible with 1.5 g of $LiBO_2/LiB_4O_7$ flux and then dissolved in American Chemical Society Reagent Grade $HNO_3$. Major elements were determined using a Spectro ARCOS ICP-ES.

**Fig. 3.19.** (*Previous page*) Feldspar-phyric andesite and associated monomict breccia (KNE10). **A.** Hand sample photograph of a clast within the KNE10 andesite breccia. The photo shows aligned tabular feldspars, blocky glomerophyric pyroxene, and evenly distributed light green hornblende phenocrysts. The sample has strong pervasive montmorillonite alteration and disseminated pyrite. Sample: DDHL1968 90.0 m. **B.** Hand sample photograph of a trachytic feldspar-phyric andesite dike that has a sharp igneous contact with polymict, clast-rich volcanic-hydrothermal breccia (D2; Lawlis et al., 2015). Concentric bands within the dike are defined by differences in the proportions of aligned relict feldspar phenocrysts and fine-grained groundmass. Interfaces between some concentric bands are surfaces of weakness along which pyrite veinlets and disseminations were concentrated. Sample: DDHL1968 78.8 m. **C.** Core tray photograph of KNE10 andesite breccia showing granule- to boulder-sized, jigsaw-fit clasts of trachytic feldspar-phyric andesite in a mud matrix. Interval: DDHL1802 66.4 – 68.0 m. **D.** Hand sample photograph of polymict, clast-rich volcanic-hydrothermal breccia (D2; Lawlis et al., 2015) with distinctive KNE10 andesite clasts with delicate and ragged margins. The KNE10 andesite clasts are enveloped by a rind of concentrically laminated graded mud-sized matrix. These textures are interpreted to have formed during hot emplacement of the KNE10 andesite clasts at the time of breccia formation. Sample: DDHL1968 77.8 m. **E.** Hand sample photograph of KNE10 andesite breccia showing its clast-supported, jigsaw-fit texture and strongly montmorillonite-altered mud matrix. The alignment of feldspar phenocrysts can locally be traced between clasts. Sample: DDHL1803 68.0 m. **F.** and **G.** Photomicrographs of KNE10 andesite showing relict feldspar, pyroxene and hornblende phenocrysts that are completely replaced by montmorillonite and pyrite. Sample: DDHL1968 90.0 m. **H.** Hand sample photograph of a truncated botryoidal pyrite vein in a volcanic clast within polymict, clast-rich volcanic-hydrothermal breccia (D2; Lawlis et al., 2015). Sample: DDHL1928 97.9 m. **I.** Hand sample photograph of polymict, clast-rich volcanic-hydrothermal breccia that has been crosscut by late-stage drusy quartz – calcite – pyrite-cemented breccia. Hydrothermal minerals have preferentially precipitated along laminations within the laminated mud matrix. Sample: DDHL1928 128.8 m. Abbreviations: fsp = feldspar, hbl = hornblende, py = pyrite, px = pyroxene, rl = relict.

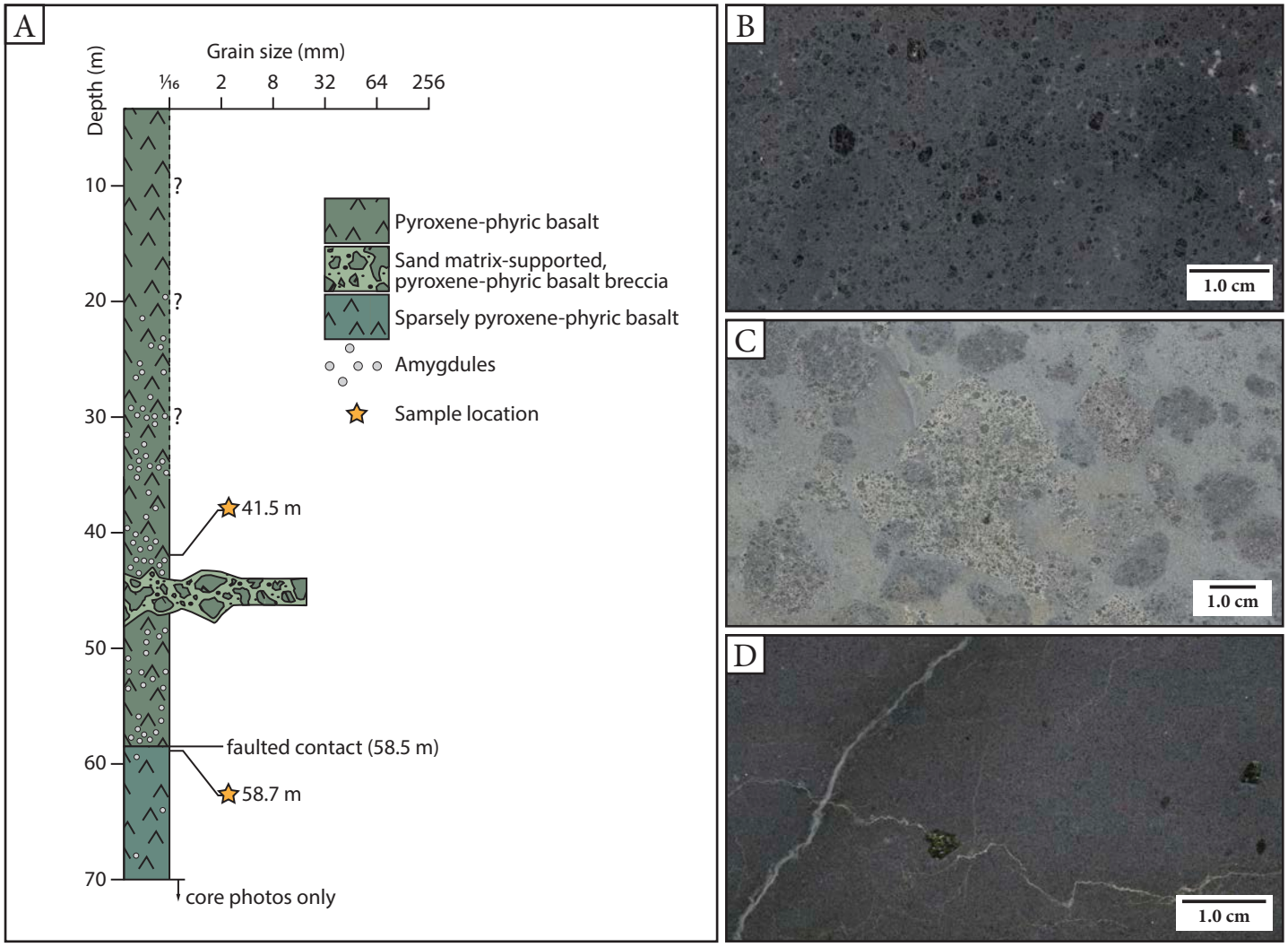


**Fig. 3.20.** Geological context for whole-rock geochemistry samples from the Ilkot prospect. **A.** Stratigraphic column for the upper 70 m of drill hole IL05. The top 35 m of drillcore were intensely weathered and the primary textures were obscured. **B.** Pyroxene-phyric basalt. Sample: IL05 41.5 m. **C.** Sand matrix-supported, pyroxene-phyric basalt breccia. Sample: IL05 44.5 m. **D.** Sparsely pyroxene-phyric basalt. Sample: IL05 58.7 m.

Trace elements were analyzed using a Perkin-Elmer ELAN 9000 ICP-MS. For both major and trace elements, calibration standards and reagent blanks were included in the sample sequence. Reported detection limits for the major elements are 0.01 wt% and <0.5 ppm for the majority of the trace elements, but <0.1 ppm for the rare earth elements.

### *3.5.4 Results*

The major and trace element whole-rock geochemistry for samples from Lihir Island are summarized in Tables 3.6–3.7, Figures 3.21–3.24 and Appendix C.

#### *3.5.4.1 Hydrothermal alteration effects*

Both porphyry and epithermal hydrothermal alteration are common and widespread in the Luise amphitheater and across Lihir Island (Fig. 3.1; Chapter 4) making it necessary to investigate element mobility in the selected samples. Loss on ignition (LOI) is the total volatile content of a rock sample, determined by ignition at 1000°C (Lechler and Desilets, 1987). The volatile materials commonly consist of water in the crystal structure of hydrous minerals (i.e., micas, amphiboles and clay minerals) and carbon dioxide in carbonates (e.g., calcite in amygdules), which are typical alteration minerals in porphyry and epithermal en-

**Table 3.6.** Major element whole-rock geochemistry results.

| Sample ID | LH13SS001 | LH13SS002 | DDHL1872 364.2 m | DDHL1876 281.5 m | DDHL1924 356.5 m | DDHL1924 371.2 m | DDHL1995 136.7 m | DDHL1995 245.0 m | IL05 41.5 m | IL05 58.7 m | GW47 886.0 m | GW47 1130.0 m | GW47 1172.5 m |
|---|---|---|---|---|---|---|---|---|---|---|---|---|---|
| $SiO_2$ | 45.93 | 47.30 | 53.65 | 48.85 | 53.90 | 54.79 | 42.50 | 46.67 | 42.64 | 44.08 | 43.20 | 55.92 | 48.97 |
| $TiO_2$ | 0.76 | 0.84 | 0.59 | 0.51 | 0.70 | 0.60 | 0.81 | 0.92 | 0.90 | 0.72 | 0.83 | 0.40 | 0.72 |
| $Al_2O_3$ | 15.04 | 16.80 | 17.95 | 17.47 | 17.64 | 18.18 | 12.08 | 16.09 | 14.63 | 11.96 | 17.23 | 20.10 | 14.90 |
| $Fe_2O_3$* | 10.49 | 9.24 | 2.74 | 5.73 | 4.72 | 4.48 | 10.99 | 10.30 | 12.14 | 10.59 | 9.50 | 4.36 | 9.85 |
| MnO | 0.24 | 0.22 | 0.07 | 0.05 | 0.05 | 0.07 | 0.27 | 0.20 | 0.22 | 0.16 | 0.25 | 0.09 | 0.18 |
| MgO | 5.52 | 3.93 | 1.52 | 2.46 | 4.21 | 3.00 | 6.98 | 5.83 | 7.28 | 9.45 | 4.61 | 1.49 | 6.06 |
| CaO | 9.96 | 7.79 | 4.83 | 5.14 | 1.16 | 1.09 | 7.66 | 3.60 | 12.41 | 13.96 | 8.00 | 2.52 | 10.35 |
| $Na_2O$ | 1.55 | 2.77 | 2.45 | 3.36 | 0.95 | 0.84 | 1.26 | 0.63 | 1.87 | 0.96 | 2.66 | 3.96 | 3.34 |
| $K_2O$ | 5.62 | 5.65 | 9.75 | 7.37 | 11.86 | 12.08 | 2.02 | 9.05 | 0.97 | 1.05 | 4.13 | 7.46 | 2.64 |
| $P_2O_5$ | 0.46 | 0.51 | 0.33 | 0.24 | 0.46 | 0.34 | 0.38 | 0.42 | 0.44 | 0.32 | 0.54 | 0.22 | 0.36 |
| LOI | 4.0 | 4.6 | 5.8 | 8.5 | 4.1 | 4.3 | 14.8 | 6.1 | 6.1 | 6.3 | 8.7 | 3.2 | 2.3 |
| Total C | 0.33 | 0.29 | 0.06 | 0.03 | 0.02 | <0.02 | 2.35 | 0.98 | 0.57 | 0.61 | 1.55 | 0.33 | 0.23 |
| Total S | 0.61 | 1.11 | 2.80 | 5.47 | 2.52 | 2.44 | 0.19 | 0.48 | 0.03 | 0.03 | 0.10 | 0.64 | 0.05 |
| Sum | 99.58 | 99.67 | 99.67 | 99.69 | 99.77 | 99.76 | 99.73 | 99.76 | 99.56 | 99.59 | 99.67 | 99.73 | 99.66 |

All values are reported in wt%. *$Fe_2O_3$ is total Fe.

vironments. High LOI can also be related to the presence of volcanic glass or organic matter; however, petrographic evaluation of the samples does not suggest that this is likely. Symbols in Figures 3.21–3.22 and 3.24 have been scaled to LOI to give a sense of the alteration intensity in each sample. Samples with the highest values for LOI are from this study and from Blackwell (2010) and were collected within and adjacent to the Lihir gold deposit. Basalt samples from Ilkot prospect (this study) are interpreted to have high LOI values due to the presence of carbonate amygdules (Fig. 3.20).

Alteration box plots (Fig. 3.21A and B) are graphical representations of alteration indices that can be used to display alteration effects and to group samples based on their altered composition. The alteration box plot defined by the Ishikawa alteration index (AI) plotted against the chlorite – carbonate – pyrite index (CCPI; Fig. 3.21A) was originally developed to differentiate between volcanic-hosted massive sulfide (VHMS)-related hydrothermal alteration and regional diagenetic alteration (Large et al., 2001). However, the box plot can be used to separate least-altered samples from those with hydrothermal alteration in general, and enables discrimination between alteration assemblages (Large et al., 2001). The Ishikawa AI is calculated according to the formula: AI = [100(MgO + $K_2O$)] / (MgO + $K_2O$ + $Na_2O$ + CaO) and quantifies Ca and Na depletion or enrichment relative to Mg and K (Ishikawa et al., 1976). The AI increases as a result of plagioclase destruction or chlorite, muscovite (sericite), and-K feldspar formation. Relative K depletion due to the alteration of K-feldspar to albite or Ca enrichment associated with carbonate alteration results in low AI values. The CCPI is calculated according to the formula: CCPI = [100(MgO + FeO)] / (MgO + FeO + $Na_2O$ + $K_2O$), where FeO is total Fe content of the rock (i.e., FeO + $Fe_2O_3$). The CCPI measures total alkali depletion relative to Mg and Fe enrichment associated with chlorite and pyrite formation and dolomite or ankerite-rich carbonate precipitation. The majority of samples from Lihir Island plot within the least-altered box in Figure 3.21A. There is a cluster of four data points that plot to the right of the least-altered box, indicating that they have been at least moderately altered to an assemblage containing muscovite ± chlorite – pyrite ± K-feldspar. Basalt samples from Ilkot prospect plot above the least-altered box, confirming that the carbonate amygdules have altered the composition of the rock.

Another alteration box plot, defined by the Ishikawa alteration index (AI) plotted against the advanced argillic alteration index (AAAI; Fig. 3.21B), was developed to il-

**Table 3.7.** Minor and trace element whole-rock geochemistry results.

| Sample ID | LH13SS001 | LH13SS002 | DDHL1872 364.2 m | DDHL1876 281.5 m | DDHL1924 356.5 m | DDHL1924 371.2 m | DDHL1995 136.7 m | DDHL1995 245.0 m | IL05 41.5 m | IL05 58.7 m | GW47 886.0 m | GW47 1130.0 m | GW47 1172.5 m |
|---|---|---|---|---|---|---|---|---|---|---|---|---|---|
| **Cr** | 7.6 | 4.8 | 2.6 | 1.7 | 5.3 | 2.4 | 90.0 | 2.9 | 7.2 | 7.7 | 1.2 | 2.5 | 30.1 |
| **Co** | 30.8 | 22.4 | 5.2 | 11.0 | 16.6 | 12.5 | 29.3 | 27.3 | 40.2 | 39.0 | 23.8 | 8.8 | 29.2 |
| **Ni** | 12.8 | 6.7 | 1.8 | 3.4 | 4.8 | 2.2 | 32.7 | 8.6 | 12.5 | 14.5 | 5.9 | 2.3 | 14.8 |
| **Rb** | 84.5 | 84.4 | 150.8 | 124.6 | 176.7 | 158.6 | 50.5 | 182.2 | 15.4 | 35.1 | 66.4 | 82.3 | 36.7 |
| **Sr** | 1548.1 | 1274.0 | 1418.8 | 1193.0 | 445.4 | 546.1 | 452.7 | 232.9 | 1511.7 | 1229.3 | 933.4 | 994.8 | 1254.5 |
| **Cs** | 1.7 | 0.8 | 1.3 | 1.3 | 2.2 | 1.5 | 4.3 | 1.6 | 10.5 | 3.6 | 0.6 | 0.7 | 0.2 |
| **Ba** | 365 | 283 | 764 | 660 | 404 | 514 | 147 | 257 | 182 | 187 | 272 | 479 | 216 |
| **Sc** | 24 | 16 | 4 | 8 | 11 | 5 | 36 | 20 | 31 | 45 | 15 | 3 | 31 |
| **V** | 316 | 286 | 107 | 185 | 169 | 157 | 307 | 278 | 359 | 280 | 340 | 146 | 281 |
| **Ta** | 0.1 | <0.1 | 0.2 | 0.2 | 0.1 | 0.1 | <0.1 | <0.1 | <0.1 | <0.1 | 0.1 | 0.2 | <0.1 |
| **Nb** | 1.5 | 1.2 | 2.6 | 2.3 | 1.8 | 2.4 | 1.1 | 1.5 | 1.5 | 0.9 | 1.9 | 2.4 | 1.0 |
| **Zr** | 61.6 | 62.6 | 97.3 | 75.8 | 94.1 | 101.3 | 55.3 | 79.4 | 62.3 | 45.9 | 72.7 | 71.9 | 55.4 |
| **Hf** | 1.8 | 1.7 | 2.4 | 2.1 | 2.4 | 2.6 | 1.6 | 2.3 | 1.8 | 1.4 | 1.9 | 1.7 | 1.7 |
| **Th** | 1.4 | 0.9 | 1.8 | 1.4 | 1.3 | 1.6 | 1.0 | 1.0 | 1.2 | 1.0 | 1.1 | 2.2 | 1.0 |
| **U** | 1.3 | 0.9 | 2.0 | 1.6 | 1.3 | 1.3 | 0.6 | 0.8 | 0.6 | 0.7 | 1.1 | 0.9 | 0.8 |
| **Y** | 16.7 | 19.9 | 18.6 | 12.6 | 19.4 | 18.6 | 15.0 | 23.1 | 18.0 | 13.4 | 21.2 | 6.1 | 15.4 |
| **La** | 15.7 | 14.6 | 17.4 | 12.1 | 14.2 | 13.4 | 11.8 | 13.1 | 14.1 | 10.8 | 16.1 | 9.9 | 10.5 |
| **Ce** | 32.7 | 28.0 | 33.1 | 20.2 | 26.7 | 25.6 | 23.7 | 25.7 | 28.9 | 21.6 | 31.9 | 15.6 | 21.1 |
| **Pr** | 4.37 | 3.84 | 4.29 | 2.61 | 3.60 | 3.43 | 3.41 | 3.81 | 4.30 | 3.23 | 4.65 | 1.81 | 2.97 |
| **Nd** | 18.8 | 17.6 | 18.5 | 11.1 | 15.7 | 15.2 | 16.1 | 17.7 | 20.3 | 14.6 | 20.7 | 7.5 | 13.6 |
| **Sm** | 4.57 | 4.29 | 4.22 | 2.42 | 3.47 | 3.80 | 3.83 | 4.25 | 4.88 | 3.58 | 4.99 | 1.43 | 3.34 |
| **Eu** | 1.43 | 1.42 | 1.52 | 0.86 | 1.14 | 1.21 | 1.20 | 1.49 | 1.57 | 1.17 | 1.60 | 0.77 | 1.10 |
| **Gd** | 4.17 | 4.35 | 4.13 | 2.35 | 3.93 | 3.76 | 3.69 | 4.89 | 4.80 | 3.56 | 4.64 | 1.32 | 3.45 |
| **Tb** | 0.64 | 0.63 | 0.61 | 0.38 | 0.65 | 0.58 | 0.57 | 0.76 | 0.63 | 0.52 | 0.72 | 0.20 | 0.52 |
| **Dy** | 3.34 | 3.62 | 3.45 | 2.08 | 3.71 | 3.16 | 2.92 | 4.44 | 3.57 | 2.82 | 4.13 | 1.10 | 2.91 |
| **Ho** | 0.61 | 0.75 | 0.70 | 0.45 | 0.74 | 0.71 | 0.55 | 0.89 | 0.67 | 0.57 | 0.78 | 0.23 | 0.55 |
| **Er** | 1.65 | 1.97 | 2.06 | 1.37 | 2.18 | 2.00 | 1.51 | 2.45 | 1.78 | 1.42 | 2.31 | 0.69 | 1.68 |
| **Tm** | 0.23 | 0.32 | 0.29 | 0.22 | 0.35 | 0.31 | 0.21 | 0.38 | 0.26 | 0.20 | 0.35 | 0.11 | 0.23 |
| **Yb** | 1.56 | 1.94 | 1.99 | 1.46 | 2.06 | 1.94 | 1.38 | 2.43 | 1.73 | 1.24 | 2.12 | 0.69 | 1.53 |
| **Lu** | 0.22 | 0.30 | 0.31 | 0.23 | 0.34 | 0.29 | 0.19 | 0.37 | 0.24 | 0.19 | 0.30 | 0.11 | 0.24 |
| **Cu** | 144.13 | 97.17 | 85.83 | 11.51 | 194.08 | 166.76 | 134.25 | 139.35 | 187.06 | 124.31 | 220.19 | 234.20 | 116.86 |
| **Zn** | 89.2 | 74.0 | 39.1 | 28.3 | 40.8 | 37.1 | 63.9 | 120.1 | 67.0 | 60.5 | 85.7 | 32.0 | 39.9 |
| **Pb** | 9.15 | 3.29 | 9.08 | 18.85 | 11.24 | 10.84 | 2.26 | 2.48 | 1.09 | 1.13 | 3.47 | 2.94 | 0.95 |
| **Mo** | 1.34 | 3.56 | 0.52 | 11.74 | 4.08 | 7.18 | 0.12 | 0.20 | 0.57 | 0.25 | 0.05 | 0.43 | 1.59 |
| **As** | 22.7 | 15.4 | 13.6 | 13.7 | 160.5 | 235.5 | 0.6 | 8.2 | 3.8 | 1.3 | 1.9 | 36.0 | 2.3 |
| **Sb** | 0.18 | 0.09 | 0.39 | 0.17 | 3.17 | 1.39 | 0.03 | 0.21 | 0.05 | 0.11 | 0.04 | 0.09 | 0.05 |
| **Au** | 0.0068 | 0.0095 | 0.0335 | 0.0086 | 0.2685 | 0.3373 | 0.0052 | 0.0018 | 0.0075 | 0.0019 | 0.0026 | 0.0527 | 0.0022 |
| **Ag** | 0.106 | 0.066 | 0.088 | 0.126 | 0.391 | 0.109 | 0.071 | 0.056 | 0.077 | 0.022 | 0.341 | 0.586 | 0.121 |
| **Re** | 0.015 | 0.012 | 0.002 | 0.001 | 0.016 | 0.020 | 0.001 | <0.001 | 0.002 | <0.001 | 0.003 | 0.002 | 0.003 |

All values are reported in ppm. See Appendix C for a complete range of elements.

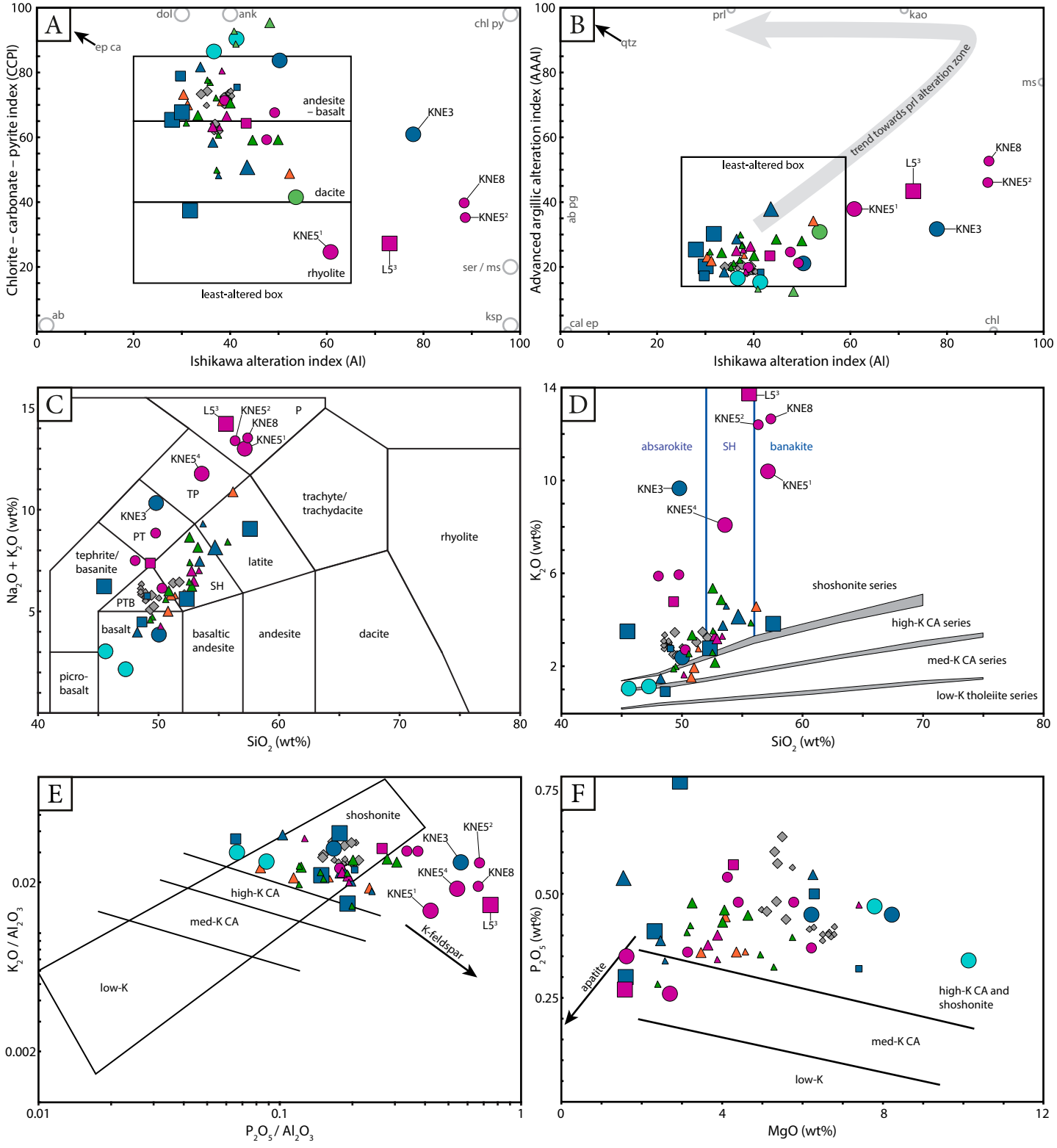


**Lithotype and Locality**

Lavas
- Luise Volcano
- Ilkot prospect
- Huniho Volcano, Londolovit Block and Wurtol Wedge
- Conical Seamount

Intrusions
- Luise Volcano
- Huniho Volcano, Londolovit Block and Wurtol Wedge

**Data Sources**
- This study
- Blackwell (2010)
- Muller et al. (2001)
- Muller et al. (2003)

**LOI (wt %)**
- <2
- 2–5
- >5

lustrate strong $SiO_2$ enrichment and destruction of chlorite, carbonate and feldspar—alteration trends typical of high-sulfidation epithermal systems (Williams and Davidson, 2004). The AAAI is calculated using the formula: AAAI = [100($SiO_2$)] / ($SiO_2$ + 10MgO + 10CaO + 10$Na_2O$). The Lihir Island samples do not plot along the trend towards rocks with advanced argillic alteration (Fig. 3.21B). However, a group of five samples plot to the right of the least-altered box indicating that they have undergone muscovite alteration. Four of these samples were previously shown to have some degree of muscovite alteration (Fig. 3.21A).

Crawford et al. (2007) proposed a plot that shows the effect of K-feldspar alteration on igneous rocks (Fig. 3.21E). In this diagram there is a cluster of six samples that plot well to the right of the least-altered field, indicating that they have been affected by K-feldspar alteration. These same samples account for the significant scatter in the total alkali silica (TAS) and $K_2O$–$SiO_2$ diagrams (Fig. 3.21C and D), and typically have high LOI (>5 wt%), $Na_2O$ + $K_2O$ (>10 wt%) and $K_2O$ (> 6 wt%). These samples also include a subset that was identified as having muscovite ± chlorite ± pyrite ± K-feldspar alteration on the alteration box plots (Fig. 3.21A and B). This is interpreted to reflect strong intensity hydrothermal alteration and $K_2O$ mobility, and these samples have been excluded from relevant interpretations below.

### *3.5.4.2 Major element geochemistry*

The least-altered samples from this study range from primitive to relatively evolved ($SiO_2$: 45.6–57.9 wt%; MgO: 1.5–10.1 wt%), have high $K_2O$ contents (<6 wt%) and are ubiquitously potassic ($K_2O$ > $Na_2O$ − 2), consistent with previous work on Lihir Island geochemistry by Müller et al. (2001).

On the TAS diagram (Fig. 3.21A), the least-altered volcanic samples from the Lihir island group plot in a wide range of fields from basalt to latite with most samples plotting as potassic trachybasalts or shoshonites. One sample plots in the basanite field, which is possibly due to weak K-feldspar alteration (see Fig. 3.21C). The intrusive samples follow a similar trend; however, a few more samples plot as basanite and phonotephrite (also possibly due to weak K-feldspar alteration; Fig. 3.21A and C). On a plot of $K_2O$ versus $SiO_2$, the samples plot in a wide range of fields from medium-K calc-alkalic to shoshonite series (Fig. 3.21B). To better assess the magmatic affinity of Lihir island group samples, they were also plotted on a $P_2O_5/Al_2O_3$ versus $K_2O/Al_2O_3$ diagram (Fig. 3.21C) where they unequivocally plot within the shoshonite field, removing the ambiguity observed in the $K_2O$ versus $SiO_2$ plot.

The depletion of MgO, CaO and $Fe_2O_3$ with increasing $SiO_2$ content (Fig. 3.22) indicates fractionation of clinopyroxene and Fe-oxides (magnetite), which is consistent with petrographic observations. An $Al_2O_3$ versus MgO variation diagram (Fig. 3.22C) highlights the considerable decrease in MgO contents that occur throughout the differentiation of mafic igneous rocks such as basalts, which are abundant in the sample suite. The relatively smooth antithetic relationship of $Al_2O_3$ versus MgO is typical of comagmatic rocks from a shared source region (Fig. 3.22C).

**Fig. 3.21.** (*Previous page*) Geochemical classification and alteration assessment diagrams for igneous rocks from the Lihir island group. **A.** Alteration box plot after Large et al. (2001), which is a graphical representation of the Ishikawa AI plotted against the CCPI. Formulae for calculating the alteration indices are presented in section 3.5.4. **B.** Alteration box plot after Williams and Davidson (2004), which plots the Ishikawa alteration index (AI) against the advanced argillic alteration index (AAAI). Formulae for calculating the alteration indices are presented in section 3.5.4. **C.** Total alkali silica (TAS; $Na_2O$ + $K_2O$–$SiO_2$) diagram with fields and nomenclature from Le Maitre (1989) and Le Bas et al. (1986, 1992). **D.** $K_2O$–$SiO_2$ diagram with fields for low-, medium- and high-K calc-alkaline rocks and shoshonites from Rickwood (1989) and sources therein. Subclassification fields for the shoshonite series, as delineated by the vertical blue lines, are from Peccerillo and Taylor (1976). **E.** $P_2O_5/Al_2O_3$–$K_2O/Al_2O_3$ diagram with fields from Crawford et al. (2007). The vector shows the effect of K-feldspar alteration. **F.** $P_2O_5$–MgO diagram with vector showing the effect of apatite fractionation. Classification fields are from Crawford et al. (2007). Abbreviations: ab = albite, ank = ankerite, CA = calc-alkaline, cal = calcite, chl = chlorite, dol = dolomite, ep = epidote, kao = kaolinite, ksp = K-feldspar, ms = muscovite, P = phonolite, pg = paragonite, prl = pyrophyllite, PT = phonotephrite, PTB = potassic trachybasalt, py = pyrite, qtz = quartz, ser = sericite, SH = shoshonite, TP = tephriphonolite. Samples: [1]DDHL1872 364.2 m. [2]DDHL1924 356.5 m. [3]08024 (L5 = feldspar-phyric syenite; Lienetz open pit; Blackwell, 2010). [4]DDHL1876 281.5 m.

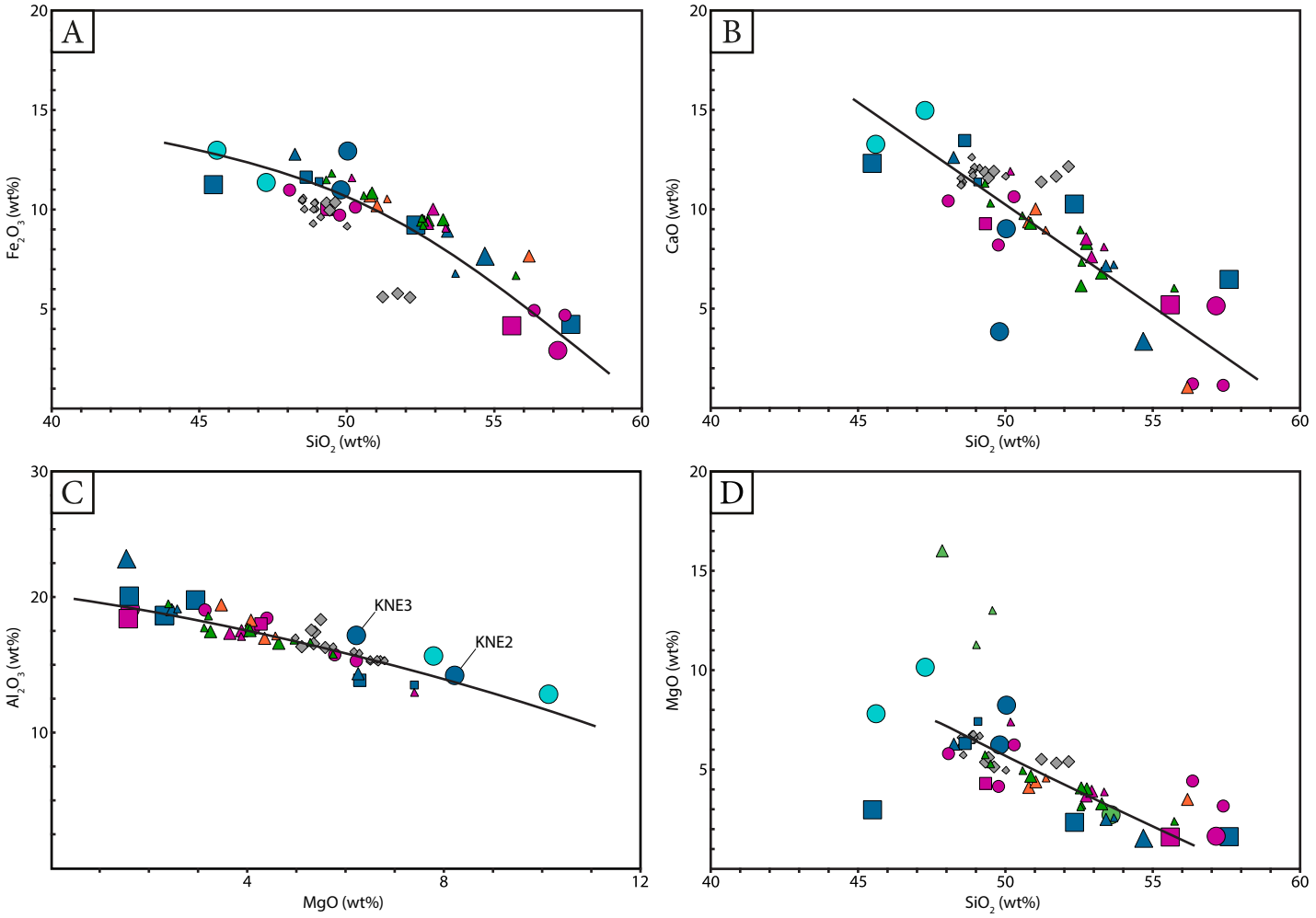


**Fig. 3.22.** Selected major element variation diagrams for igneous rocks from the Lihir island group. The sample legend and data sources are the same as in Figure 3.21. $Fe_2O_3$ is total Fe expressed as $Fe_2O_3$.

### *3.5.4.3 Trace element geochemistry*

Figure 3.23 shows primitive mantle-normalized spidergrams for Lihir island group volcanic and intrusive rocks. All suites are characterized by enrichment of LREE, flat or saggy HREE patterns and strong negative HFSE anomalies (Nb, Hf, Zr, Ti), especially Nb, which is characteristic of samples from a suprasubduction zone environment (Wilson, 1989; e.g., Baguio district, Hollings et al., 2011). A plot of Zr–Y (Fig. 3.24) corroborates that the alkalic rocks from the Lihir island group were emplaced in a subduction zone (arc-related) rather than a within-plate tectonic setting, consistent with previous interpretations made by Müller et al. (2001).

## 3.6 Ar–Ar geochronology

### *3.6.1 Introduction and sample description*

This section presents Ar–Ar age determinations for a pyroxene-hornblende-phyric monzodiorite intersected in a geothermal exploration drillhole from northern Luise amphitheater (Fig. 3.1; Fig. 3.25). The monzodiorite occurs as part of a dike swarm that crosscuts a weakly Cu-mineralized alkalic intrusive complex. Individual monzodiorite dikes are narrow and have sharp, chilled margins.

The monzodiorite is crystal crowded, with weakly aligned phenocrysts, and a light gray aphanitic groundmass

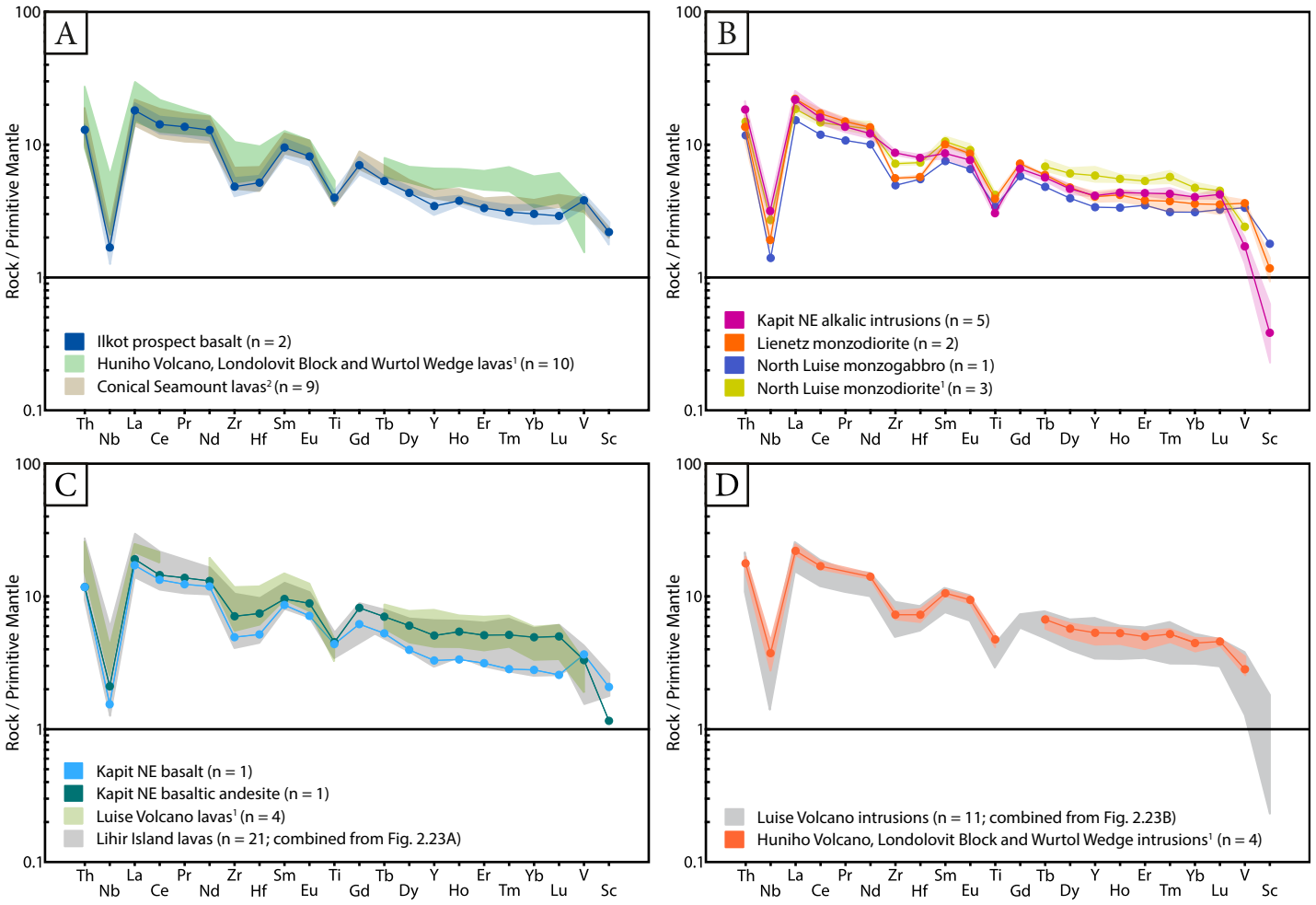


**Fig. 3.23.** Representative primitive mantle normalized diagrams for igneous rocks from the Lihir island group. Normalizing values are from Sun and McDonough (1989). Colored lines with circular nodes represent the mean rock/primitive mantle values for a group of samples (e.g., Kapit NE alkalic intrusions). The sample size (n) for each group is provided in the corresponding legend (e.g., n = 5). Shaded areas of the same (muted) color represent the range of rock/primitive mantle values for that group. To simplify Figures 2.23A and C, the mean rock/primitive mantle lines were omitted for some groups. The gray shaded areas in Figures 3.23C and D, represent the range of rock/primitive mantle values for Lihir Island lavas (as presented in Figure 2.23A) and Luise Volcano intrusions (as presented in Figure 2.23B), respectively. [1]Müller et al. (2001), [2]Müller et al. (2003).

(Fig. 3.25A). Phenocrysts include acicular hornblende (20–25%; <15 mm), subhedral, blocky clinopyroxene (15%; <3 mm), calcite-altered feldspar (10–15%; <3 mm) and trace magnetite and biotite (<0.5 mm; Fig. 3.25). The dikes include a large number and variety of subrounded xenoliths (up to ~20 cm in diameter), including coarse-grained pyroxenite with calcite veins, coarse-grained equigranular gabbro and monzodiorite, aphanitic basalt and both quartz and calcite vein-clasts (Fig. 3.25A). The sample has subtle to weak chlorite, calcite and montmorillonite alteration; however, the hornblende and clinopyroxene phenocrysts appear pristine in thin section (Fig. 3.25B).

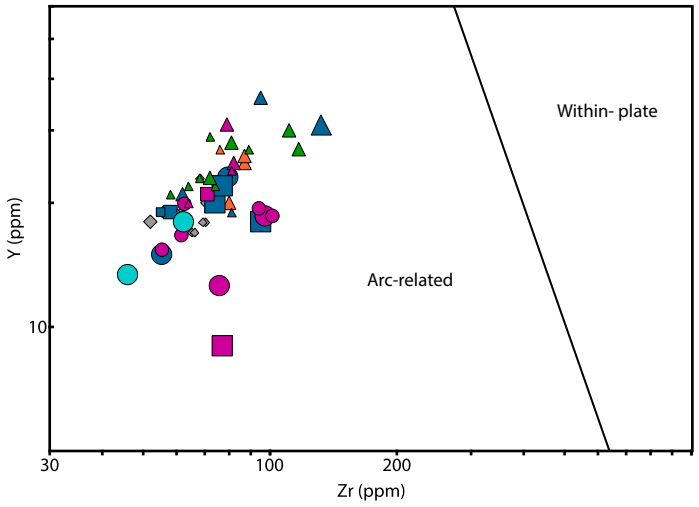


**Fig. 3.24.** Y–Zr diagram showing discriminant fields from Müller et al. (1992). The sample legend and data sources are the same as in Figure 3.21.

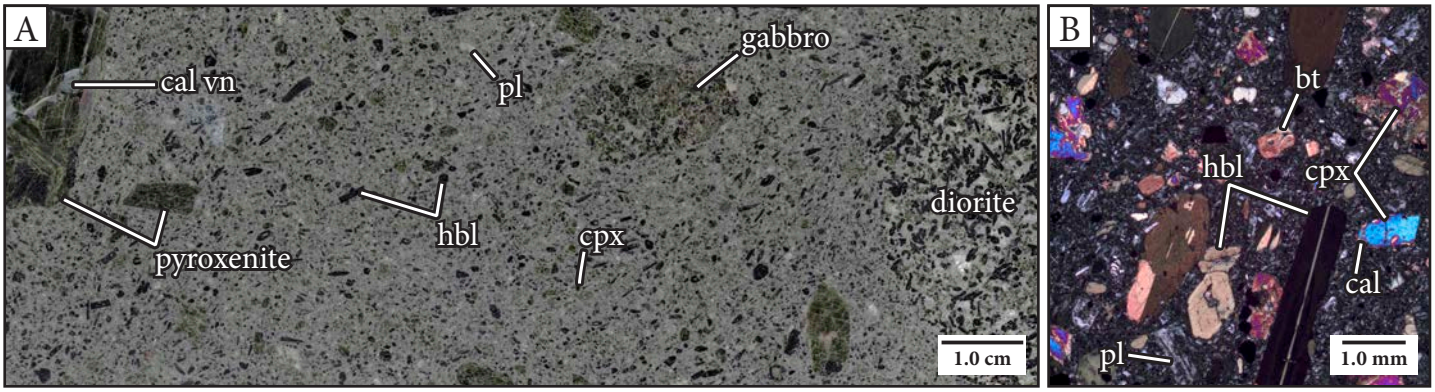


**Fig. 3.25.** Ar–Ar geochronology sample photographs. **A.** Hand sample photograph of xenolithic, pyroxene-hornblende-phyric monzodiorite. Prismatic dark green hornblende is the dominant phenocryst phase. Other phenocrysts include green clinopyroxene, black biotite, light gray plagioclase and black magnetite. Xenoliths include green pyroxenite with truncated calcite veins, gabbro and diorite. Sample: GW47 1172.5 m. **B.** Cross-polarized transmitted light photomicrograph showing unaltered hornblende phenocrysts and clinopyroxene crystals with calcite-altered margins. Plagioclase phenocrysts and the groundmass have weak feldspar and montmorillonite alteration. Rare, small crystals of apatite can be identified in the groundmass. Sample: GW47 1172.5 m.

### *3.6.2 Methods*

One drill core sample was submitted for mineral separation at the Argon Geochronology Lab at Oregon State University. Xenoliths were carefully cut out of the sample and discarded. Hornblende and clinopyroxene separates were irradiated at the OSU Radiation Center in the TRIGA experimental reactor. The samples were step-heated and Ar isotope contents were measured by D. Miggins using a Thermo-Fisher Scientific ARGUS-VI-D mass spectrometer. Plateau Ar–Ar ages were calculated relative to the FCT-NM (Fish Canyon Tuff sanidine) standard, with an assigned age of 28.201 Ma (Kuiper et al., 2008; Chiaradia et al., 2013). The ages were calculated using ArArCALC v2.7.0 – Beta version (Koppers, 2002). Further details of the instrumentation and analytic parameters are provided in Appendix D.

### *3.6.3 Results and interpretation*

One hornblende separate from pyroxene-hornblende-phyric monzodiorite yielded an Ar–Ar age of 497.4 ± 9.0 ka (Table 3.8; Appendix D; Fig. 3.26). Since the hornblende is phenocrystic, it may have been crystallized in a magma chamber some time before dike emplacement. Therefore, the result is interpreted as the maximum age of crystallization of the monzodiorite dike. Since field re-

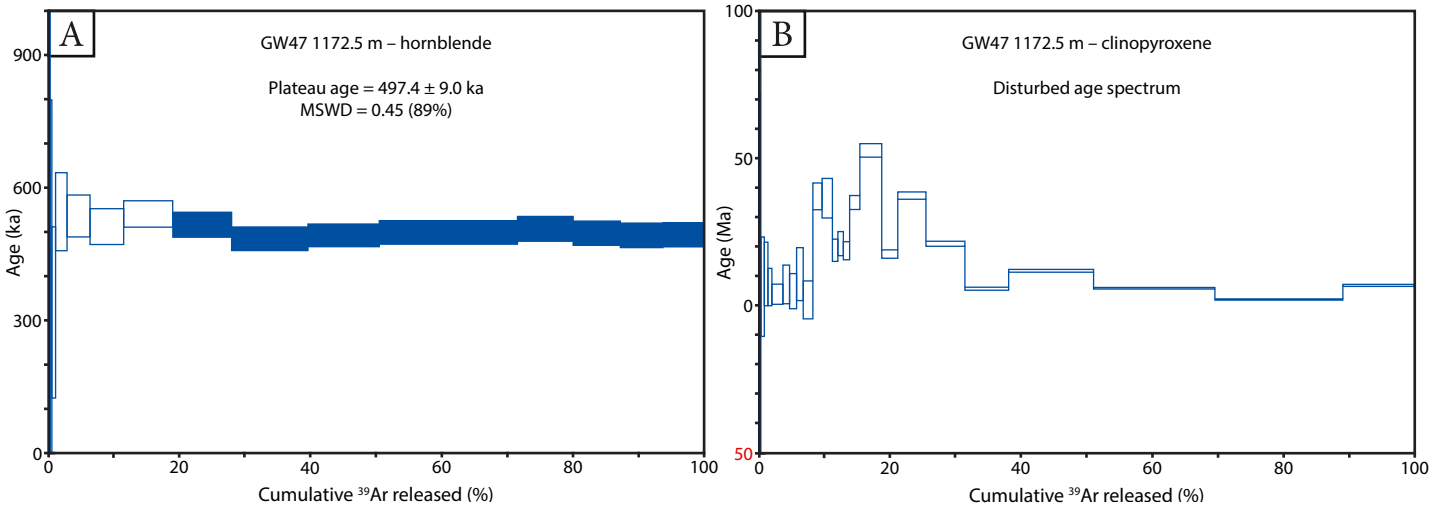


**Fig. 3.26.** Laser-heated $^{40}Ar$–$^{39}Ar$ age spectra for hornblende (**A.**) and clinopyroxene (**B.**) phenocrysts from pyroxene-hornblende-phyric monzodiorite in northern Luise amphitheater (GW47 1172.5 m). The ages were calculated using ArArCALC (Koppers, 2002). Plateau steps are filled blue, rejected steps are open. Box heights are 1σ.

**Table 3.8.** Ar–Ar geochronology results.

| Sample name | GW47 1172.5 m |
|---|---|
| Lithotype | Xenolithic, pyroxene-hornblende-phyric monzodiorite |
| Material dated | Hornblende phenocryst |
| $\%^{39}Ar$ | 81.00 |
| Plateau steps | 9 |
| MSWD | 0.45 |
| Age (ka ± 2σ) | 497.4 ± 9.0 |
| Interpretation | Minimum age of emplacement of the alkalic intrusive complex and associated porphyry Cu mineralization in the north of the Luise amphitheater |

lationships indicate that this dike is part of a swarm that crosscuts an alkalic intrusive complex and minor porphyry Cu mineralization, this age date also provides a minimum age for these features. The relative timing relationship between the dated monzodiorite and the alkalic intrusions within the Lihir gold mine area is unknown. Clinopyroxene Ar–Ar age dating of the same sample was also attempted; however, there was a disturbed age spectrum (excess argon) and no age was determined (Fig. 3.26; Appendix D).

## 3.7 Discussion – Geological evolution of Kapit NE and Coastal

The geology of the Kapit NE and Coastal ore zones records the history of volcanism and intrusive activity within the eastern side of the Luise amphitheater, which is currently in a submarine setting (Fig. 1.4). Previous studies at Minifie, Lienetz and Kapit have documented the geology of the southern and central parts of the amphitheater, which are currently exposed subaerially. The Lihir deposit spans a large area under the Luise amphitheater floor (~4 $km^2$ aerial extent). This area is large enough that there are substantial differences between the host rocks and their respective depositional environments between ore zones. This section highlights the key geological events in the evolution of the host rocks to the Lihir deposit and discusses them within the broader context of the Luise Volcano.

### *3.7.1 Volcano-sedimentary stratigraphy*

The oldest rocks of the volcano-sedimentary succession in the Kapit NE and Coastal areas consist of polymict matrix-supported breccia, conglomerate and sandstone (KNE1; Figs. 3.3, 3.4 and 3.5). These rocks are interpreted to have been deposited by a series of high-energy, gravity-driven debris flows that accumulated to form an alluvial fan that was a moderate distance (2.5–4.0 km) from the Luise volcanic vent (Fig. 3.27). Evidence for deposition of KNE1 in this environment includes the predominance of coarse-grained material (e.g., Figs. 3.3, 3.4 and 3.5), the presence of texturally immature clasts in weakly normally graded and massive breccia to sandstone beds (e.g., Fig. 3.6C and D), the discontinuous, lenticular geometry of bedding (Figs. 3.3, 3.4 and 3.7A), and the lack of primary pyroclastic material. The lack of deep-water facies such as turbidites or well-bedded mudstones as well as the lack of shallow-water sedimentary structures such as cross-bedding suggests deposition occurred at an intermediate depth below the storm wave-base (~40–200 m depth; e.g., Johnson and Baldwin, 1996; Fig. 3.27). The presence of amphibole-bearing volcanic clasts in KNE1 (e.g., Fig. 3.6C) implies that the Luise Volcano was the primary source of volcanic detritus, since it is the only volcano in the region known to have produced amphibole-bearing rocks (Wallace et al., 1983). Mudstone and sandstone clasts incorporated into the KNE1 breccia are similar to mudstones from Minifie and are interpreted to be intraformational. KNE1 contains thermally oxidized volcanic detritus, implying incorporation of subaerially-derived volcanic clasts in what was predominantly a submarine setting during sedimentation. However, there are no clasts in KNE1 that hint at a hydrothermal origin (e.g., veined or altered clasts), suggesting that hydrothermal activity was not yet established at surface at this time.

The volcano-sedimentary facies have complex relationships and are typically laterally discontinuous, suggesting that sedimentation occurred in a topographically complex

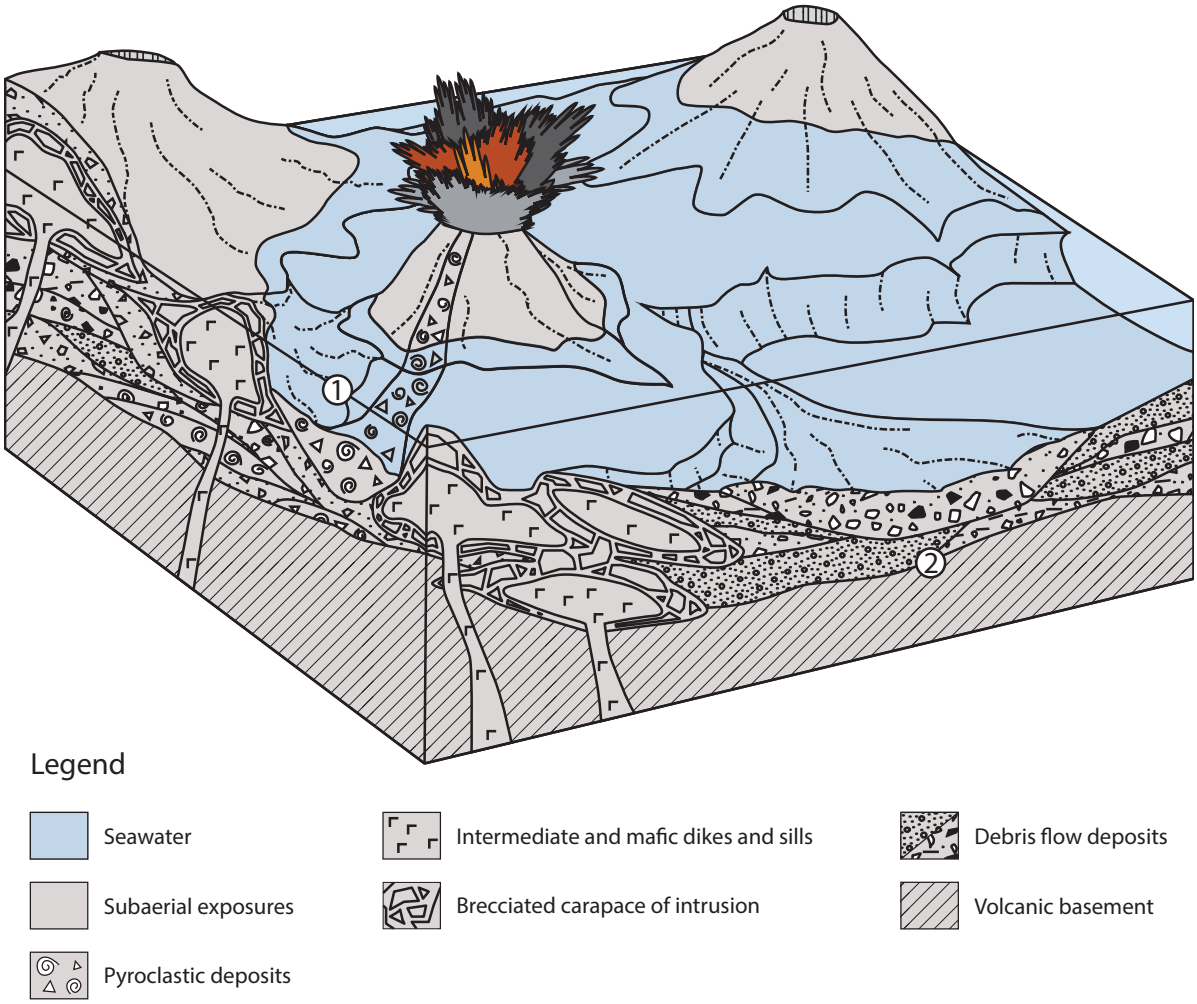


**Fig. 3.27.** Schematic paleogeographic reconstruction of the environment of deposition of the Minifie and Kapit NE host rocks. *1) Proximal volcanic environment:* Minifie sedimentary basin with interlayered, southward-dipping, subaerial pyroclastic surge deposits and volcaniclastic debris flow deposits. This was the source region for mudstones, sandstones and plagioclase-phyric andesite that were eroded, transported and redeposited as clasts within the polymict matrix-supported breccia (KNE1) in Kapit NE. *2) Distal volcanic environment*: Kapit NE sedimentary basin composed predominantly of NE-dipping submarine debris flows containing subaerially-derived volcanic and sedimentary clasts.

paleoenvironment (e.g., Fig. 3.3 and 3.4). There are no marker horizons or unconformities in the stratigraphy. It is concluded that drilling has not intersected the Wurtol Wedge basement rocks and that the Luise volcanic stratigraphy is at least 500 m thick in Kapit NE. In comparison, the volcano-sedimentary succession at Minifie was found to be ~200 m thick (Blackwell et al., 2014). The difference in thicknesses suggests that Kapit NE may have been at a local sedimentary depocenter. Blackwell et al. (2014) noted that the volcano-sedimentary sequence at Minifie had a dip of 20–30˚ to the south, which was interpreted to be a consequence of regional tilting. The sequence at Kapit NE dips 20–30˚ to the northeast, which is inconsistent with the hypothesis of regional tilting of the stratigraphy. Instead, the dipping strata are interpreted as primary dip slopes on the south and northeast flanks of the incipient Luise volcanic edifice, respectively (Fig. 3.27).

There are significant differences between the volcano-sedimentary sequences at Kapit NE and Coastal compared with Minifie, which is situated a minimum of ~1.5 km southwest of the study area (Fig. 1.4). At Minifie, the volcano-sedimentary sequence comprises a thick pile of interbedded polymict weakly graded breccia to sandstone and accretionary lapilli-bearing pebble breccia to sandstone (Blackwell et al., 2014). The lack of pyroclastic

debris and presence of conglomeratic horizons implies a more distal submarine setting for KNE1 compared to the proximal subaerial depositional environment interpreted for polymict breccias to sandstones in Minifie (Blackwell et al., 2014). The KNE1 and Minifie breccias are suspected to have been deposited synchronously, although radiometric age determinations and/or new exposures created during on-going mine development are required to confirm this hypothesis.

Across the Lihir deposit, polymict matrix-supported breccias were crosscut by plagioclase- and pyroxene-phyric basaltic to andesitic sills (Fig. 3.8C) and dikes (Figs. 3.3, 3.4, 3.8, 3.9 and 3.10) that locally have peperitic margins. Some of these intrusions were feeders to basaltic autoclastic breccias (e.g., Fig. 3.7F), and are interpreted to be time-equivalent to the volcano-sedimentary stratigraphy (Fig. 3.27). Based on the presence of quench fragmentation textures (e.g., Fig. 3.10D), local peperitic margins (Fig. 3.7B), in situ hyaloclastite textures (Fig. 3.10C) and local pillow fragment breccia (Fig. 3.9D), the pyroxene-phyric intrusions are interpreted to have been emplaced into water-saturated sediments (e.g., McPhie et al., 1993). Pyroxene-phyric basalts and basaltic breccias are an extensive component of the stratigraphy, especially in the Coastal ore zone (KNE2; Figs. 3.3 and 3.4). Equivalent facies are present in the Minifie, Kapit and Lienetz areas, but are less extensively developed. The basalts have highly variable textures and phenocryst populations (e.g., Figs. 3.8 and 3.9) implying that there have been multiple pulses of basaltic volcanism. The basaltic andesite-clast breccias at Kapit NE (KNE3; Figs. 3.3 and 3.4) have abundant quench fragmentation features (e.g., Fig. 3.10C) and are interpreted as *in situ* hyaloclastite. The KNE3 basaltic andesite breccias typically occur higher in the stratigraphy than, and locally occur as clasts within, KNE2 basalt and are therefore interpreted to be younger (Fig. 3.5). Geochemically, KNE3 basaltic andesite appears to be more evolved than KNE2 basalt (e.g., Fig. 3.22C). KNE3 extends to the northern end of the Luise amphitheater (feldspar-pyroxene-phyric coherent and clastic facies, Appendix B1; Blackwell, 2010) where it has an inverse timing relationship with pyroxene-phyric basalt. This implies that the two volcanic units were deposited cyclically.

### *3.7.2 Intrusive history*

Based on the mineralogical and textural compositions of intrusive rocks and their relative timing relationships, four discrete pulses of magmatism have been identified at Kapit NE and Coastal. None of these intrusions have quartz as a constituent mineral phase, but they typically contain orthoclase, and at least one phase contains nepheline (KNE4), consistent with their classification as alkalic intrusive rocks. Geochemical analysis suggests that the intrusions are ubiquitously shoshonitic (Fig. 3.21). They have geochemical signatures consistent with emplacement in a suprasubduction zone environment (Figs. 3.22 and 3.23). Based on their spatial an temporal relationships, the intrusions in Kapit NE and Coastal can be subdivided into four groups:

*Group 1 intrusions* are nepheline-bearing monzonite (KNE4) and hornblende-biotite-bearing monzonite (KNE5). These crystal-crowded porphyritic stocks contain abundant biotite phenocrysts (Figs. 3.12G and 3.13E). The presence of miarolitic cavities in these intrusions (Fig. 3.12C) provides evidence that they exsolved volatiles during the earliest stages of hydrothermal activity. Group 1 intrusions are included in clasts of polymict anhydrite – chlorite – calcite-cemented breccia (Figs. 3.3, 3.12D and 3.15B), one of the earliest stages of porphyry-style hydrothermal activity at Lihir.

*Group 2 intrusions* comprise the hornblende-bearing gabbro (KNE6) and crystal-poor feldspar-phyric trachyte (KNE7) dikes. The gabbro is distinguished by the presence of medium- to coarse-grained clinopyroxene, hornblende, feldspar and magnetite, and the absence of primary biotite or nepheline (Fig. 3.15). It is very crystal crowded (>95% phenocrysts) and locally has textures reminiscent of cumu-

late rocks. KNE7 trachyte is compositionally and texturally distinct from the gabbro, with which it has sharp igneous contacts. The trachyte contains sparse orthoclase, sanidine and plagioclase phenocrysts in a very fine-grained, feldspar-rich groundmass, and lacks mafic mineral phases and nepheline (Fig. 3.16). These two intrusions have been grouped together due to their close spatial distribution in western Kapit NE (Fig. 3.4) and because both intrusions have been crosscut by porphyry-style biotite – anhydrite, anhydrite – pyrite and magnetite – anhydrite veins (Figs. 3.15A and B, and 3.16A). In the Coastal ore zone, spatially separate from the trachyte (KNE7) dikes, gabbro has crosscut polymict anhydrite – chlorite – calcite-cemented breccia containing clasts of Group 1 intrusions (Figs. 3.3 and 3.15B). These crosscutting relationships imply that Group 2 intrusions were emplaced during later porphyry-style hydrothermal activity at Lihir. The tops of Group 2 intrusions have been intersected at depths greater than 750 mRL, which is below observed epithermal-style mineralization.

*Group 3 intrusions* include trachytic hornblende-feldspar-phyric latite (KNE8) and coarse-grained feldspar-phyric latite (KNE9). This group is defined by a series of dikes that have smaller average grain sizes than Groups 1 and 2 and are strongly porphyritic. The two intrusive units from Group 3 are interpreted as a single intrusive phase with a coarse-grained core and locally trachytic margins. Sparse, northeast-trending dikes of coarse-grained feldspar-phyric latite also occur in Lienetz (i.e., L5 feldspar-phyric syenite; Appendix B4; Blackwell, 2010), which was proposed as a potential source of porphyry-stage fluids and magmatic-hydrothermal breccias in that ore zone due to its spatial relationship with biotite alteration and biotite – anhydrite-cemented breccia (Blackwell, 2010; Sykora, 2017). No further evidence was found during this study to support these previous interpretations. Epithermal-stage pyritic veins and texturally destructive, gray adularia – pyrite alteration (e.g., Fig. 3.17B), have crosscut Group 3 intrusions at Kapit NE and Coastal.

*Group 4 intrusions* (feldspar-phyric andesite dikes and associated monomict breccia; KNE10; Fig. 3.19) comprise the most recent pulse of magmatism at Lihir. They triggered widespread volcanic-hydrothermal brecciation (Chapter 4), and their emplacement continued after diatreme formation. The volcanic-hydrothermal breccias contain clasts of both porphyry-stage and main-stage epithermal pyritic breccias (e.g., Fig. 3.19H). The KNE10 intrusions and associated volcanic-hydrothermal breccias have been crosscut by late-stage calcite – quartz – pyrite veins and breccias and associated epithermal gold mineralization and alteration (e.g., Fig. 3.19I; Chapter 4).

Groups 1 and 2 define an intrusive complex that is elongated approximately north-south, parallel to regional-scale features such as the alignment of islands and seamounts of the Lihir Island group. Group 3 intrusions strike northeast, similar to several surface geothermal features in the Luise amphitheater and offshore in the Luise Harbor. Group 4 intrusions are associated with volcanic-hydrothermal breccia complexes that are aligned along north-, northwest- and northeast-trending structures, and are concentrated on the western and northern sides of the Lihir deposit (Figs. 3.3 and 3.4; Chapter 4). The intrusive complex has been intersected in drill core as deep as 1,500 m below Kapit NE.

A second intrusive center occurs at the northern end of the Luise amphitheater. The intrusive rocks of this complex are intersected in drill core below 800 mRL and are associated with weak, alkalic porphyry-style mineralization (Rae et al., 2010). An age of 497.4 ± 9.0 ka has been obtained for a hornblende separate from pyroxene-hornblende-phyric monzodiorite that was emplaced late in the geological history of this intrusive complex, after porphyry-style mineralization had ceased. This age estimate provides a minimum age of emplacement of the intrusive complex and associated porphyry mineralization in the north of the Luise amphitheater. No direct crosscutting relationships have been observed been the northern intrusive complex and that in the Coastal and Kapit NE area. However, both intrusive

complexes are presumed to have been emplaced prior to sector collapse of the Luise Volcano. Therefore, this age also provides a maximum age for formation of the Luise sector collapse amphitheater and later epithermal mineralization.

### 3.8 Conclusions and implications for the genesis of the Lihir gold deposit

The volcano-sedimentary stratigraphy in the Kapit NE and Coastal ore zones predominantly comprises moderately dipping, mafic to intermediate lavas, shallow intrusions and volcanic breccias (including pillow-fragment breccia), interfingered with polymict breccia, conglomerate and sandstone. This facies assemblage is consistent with a setting on the submerged flank of a shoaling seamount. The base of the Minifie volcano-sedimentary sequence was deposited in a subaerial or near-shore setting and includes pyroclastic fall deposits intercalated with debris flow deposits. These time-equivalent sequences were deposited in proximal and medial settings compared to the volcanic vent, respectively, highlighting the complex and variable depositional setting of host rocks across Lihir. The recognition of the subaerial to submarine volcanic setting for the Lihir epithermal gold deposit has implications for the hydrologic model for this deposit type. However, similar ore types exist in Minifie, Kapit NE and Coastal areas suggesting that water depth during the time of deposition of the host rocks did not play a crucial role in determining the character of ores.

Igneous rocks in the Luise amphitheater are alkalic and shoshonitic and were emplaced in a subduction zone tectonic setting. In Kapit NE and Coastal areas, intrusive igneous rocks are mainly composed of porphyritic monzonite and latite stocks and dikes that form an approximately north-trending complex. These alkalic intrusions were not observed to be directly related to porphyry-style hydrothermal alteration or mineralization. A series of nepheline-bearing monzonite dikes in Coastal area were found to contain magnetite-, anhydrite- and chalcopyrite-bearing miarolitic cavities. This indicates that these intrusions were volatile-rich and may have contributed magmatic-hydrothermal fluids to the porphyry system.

The volcano-sedimentary sequence observed in Kapit NE and Coastal is interpreted to have been generated by the Luise Volcano, which has previously been assigned a Plio-Pleistocene age. Crosscutting relationships dictate that volcanism and sedimentation occurred prior to Cu–Au porphyry-style mineralization associated with the emplacement of alkalic intrusive rocks, and that all of this occurred prior to sector collapse and epithermal Au mineralization at the center of the Luise amphitheater. The hornblende Ar–Ar age of 497.4 ± 9.0 ka for pyroxene-hornblende-phyric monzodiorite from the northern part of the Luise amphitheater therefore provides an absolute constraint on the timing of magmatic activity in the Luise amphitheater, a minimum age for constructional volcanism and sedimentation of the Luise volcanic edifice and a maximum age for sector collapse.

# CHAPTER 4

# Alteration and Mineralization

## 4.1 Introduction

This chapter documents the hydrothermal alteration and vein paragenesis of the Kapit NE and Coastal ore zones. Two alteration cross sections have been constructed as the primary framework for this study, allowing the spatio-temporal relationships between gold distribution, primary lithotypes, alteration domains and hydrothermal vein and breccia stages to be discussed. A new model is proposed for the distribution, geometry, timing and genesis of volcanic-hydrothermal breccias that have been identified in the periphery of the Lihir deposit. The absolute age of porphyry-style mineralization is constrained using molybdenite Re–Os geochronology, and a minimum age of emplacement for the Lihir diatreme breccia complex is provided by the results of radiocarbon dating. Also discussed is the evolution of physicochemical conditions operating on the Lihir hydrothermal system over its geological history.

## 4.2 Methods

This section outlines methods used to describe the alteration and vein paragenesis in Kapit NE and Coastal. Descriptive data were collected through graphic drill core logging and sampling of 16 drill holes along cross sections A–A'–A" and B–B', according to the methods described in section 3.4.2 (Fig. 1.4; Appendix A1).

Definitions of terms used in this study to describe and interpret hydrothermal alteration, breccias and veins are provided in Tables 4.1 and 4.2. A descriptive, systematic and non-genetic approach has been used to describe and classify breccias, adapted from McPhie et al. (1993), Davies (2002) and Blackwell (2010). Each breccia description includes information about geometry, grain size, components, internal organization, fabric and alteration. A focus was placed on capturing compositional and textural variations at a variety of scales in order to identify discrete breccia facies and the relationships between them. Genetic classifications have been assigned based on breccia characteristics, breccia facies associations and comparison to diagnostic and characteristic criteria proposed in the literature (Table 4.3).

The textural characteristics and mineralogy of veins, breccias and alteration assemblages were determined using systematic observations of hand specimens (n = 763), polished thin sections and thin section offcuts (n = 77) and 25 mm-diameter polished mounts (n = 41; Appendix A2). Analytical methods used to aid in textural and mineralogical identification included: K-feldspar staining, short-wave infrared (SWIR) spectroscopy, scanning electron microscopy and Corescan hyperspectral core imaging. K-feldspar staining was performed by etching samples with hydrofluoric acid ($HF^-$) and then coating the etched surface with sodium cobaltinitrite ($Na_3Co(NO_2)_6$), which stains K-feldspar yellow.

SWIR analysis was used for identification of hydroxyl- and water-bearing minerals and mineral groups (e.g., clays, micas, zeolites, chlorites, opal, amphiboles, gypsum, etc.), sulfates and carbonates. Chip samples were collected at regular 10 m intervals (5 m intervals in DDHL1928 and DDHL1968) for logged drill holes. Selected hand samples and thin section offcuts were also analyzed. Sample locations are provided in Appendix A2 and interpreted SWIR

analyses are provided in Appendix E. Samples were analyzed with a TerraSpec Hi-Res Mineral Spectrometer at CODES, University of Tasmania. A spectrum collection time of 20 seconds was used regardless of the color of the rocks being analyzed. The Spectral Geologist (TSG™) spectral interpretation software was used to examine the collected SWIR data. The spectra were normalized (hull shape) and smoothed, then manually interpreted using spectral characteristics, including the position, intensity and width of absorption features.

A scanning electron microscope (SEM) was used to identify fine-grained minerals and to observe microtextural characteristics of hydrothermal features. Polished thin sections, 25 mm-diameter polished mounts and grain mounts were selected for SEM analysis. The grain mounts were produced by positioning vein or lithic fragments upon an SEM specimen stub covered with double-sided carbon tape. All samples were coated with ~20 nm of carbon. Backscattered electron (BSE) imaging and energy-dispersive X-ray spectrometry (EDS) were carried out on a Hitachi SU-70 Schottky field emission scanning electron microscope located at the Central Science Laboratory, University of Tasmania. The instrument is equipped with a Hitachi photo

**Table 4.1.** Definitions for hydrothermal alteration, fault and vein terminology used in this chapter. Definitions are based on Titley (1982), Cannell (2004), Gifkins et al. (2005) and Orovan (2016), and sources therein.

| Term | Definition |
|---|---|
| ***Alteration styles*** | |
| Pervasive | Alteration that affects all primary minerals. This type of alteration is typically strong or intense and is texturally destructive. |
| Selective | Alteration in which specific minerals or other elements (e.g., matrix, spherulites, etc.) in the host rock have been altered. Alteration of this type usually preserves or enhances primary rock textures. |
| Domainal | A type of selective alteration that refers to the alteration of patches, clots, or groups of clasts. |
| Vein halo | Alteration (pervasive or selective) that occurs in the wall rock immediately adjacent to a vein or veinlet. |
| Alteration rind | Alteration that occurs along the margins of clasts in a breccia. Alteration rinds commonly form during hydrothermal brecciation. Alteration rinds may also form post-brecciation through the processes of diagenesis, metamorphism and/or selective hydrothermal alteration, especially if there are readily altered elements at the clast margins (e.g., chilled margins consisting of volcanic glass with perlitic fractures). |
| ***Alteration intensities*** | |
| Weak | Alteration in which most crystal edges are visible and crystal cores are commonly replaced. This degree of alteration intensity does not modify primary rock textures. |
| Moderate | Alteration in which most crystal edges are visible and some crystal margins are ghosted (i.e., rimmed by alteration minerals causing them to blend in with the surrounding groundmass). Crystal cores are commonly replaced. This degree of alteration intensity partially obscures primary rock textures. |
| Strong | Alteration in which most crystal edges are ghosted and all primary minerals are almost completely replaced. This degree of alteration intensity partially obscures primary rock textures. |
| Intense | Alteration in which all primary minerals have been completely recrystallized or replaced by secondary minerals. This degree of alteration intensity obliterates primary rock textures. |
| ***Veins and faults*** | |
| Vein/veinlet | A fracture that is partially or totally infilled by minerals precipitated from aqueous fluids and contains <5% clasts. Veins are ≥2 mm wide; whereas, veinlets are <2 mm wide. |
| Centerline vein | A multi-stage vein in which fracturing and hydrothermal mineral infill occurs along a line of symmetry through the center of the vein. |
| Vein selvage | Mineral infill that occurs immediately adjacent to the vein wall. |
| Fault gouge | Very fine-grained (>70% of fragments <2 mm), incohesive material resulting from frictional wear and cataclastic deformation during slip along a fault. Fault gouge may be foliated. |

**Table 4.2.** Definitions for breccia terminology used in this chapter. Definitions are based on McPhie et al. (1993), Davies (2002), Davies et al. (2008a), Woodcock and Mort (2008), Mort and Woodcock (2008), Sykora (2017), Corbett (2018), and sources therein.

| Term | Definition |
|---|---|
| **Breccia** | A rock composed of >5% angular to sub-angular clasts that are consolidated by crystalline cement ± matrix, and which may contain void space. Breccia is used as a descriptive term and has no genetic connotation. Conglomerate is a variant of breccia with rounded or subrounded clasts. |
| **Sandstone** | A rock composed of sand-sized (63 μm to 2 mm) fragments that are consolidated by crystalline cement ± mud-sized matrix, and which may contain void space. Sandstone is used as a descriptive term and has no genetic connotation. |
| **Mudstone** | A rock composed of mud-sized (<63 μm) fragments that are consolidated by crystalline cement, and which may contain void space. Mudstone is used as a descriptive term and has no genetic connotation. |
| **Breccia vein** | A cement-rich breccia (>70% cement) with a tabular geometry. |
| **Breccia complex** | A discordant, hypogene clastic body composed of one or more breccia facies ± subordinate discordant clastic facies (e.g., discordant sandstone facies). |
| **Breccia facies** | A breccia with specific, defined characteristics (e.g., components, internal organization, alteration, etc.) that distinguish it from adjacent and potentially related breccias. |
| **Volcaniclastic breccia** | A breccia that is predominantly composed of volcanic clasts, irrespective of the process of its formation. For example, a sedimentary breccia formed at the base of a talus slope that predominantly contains basalt clasts can be termed a volcaniclastic breccia. |
| **Clast** | 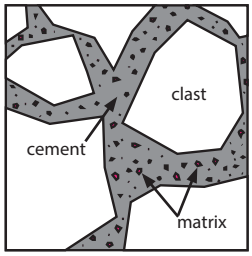 A coarse-grained (>2 mm) fragment of wall rock, vein infill, breccia cement or juvenile magmatic material. A wall rock clast may have been previously hydrothermally altered or crosscut by veins and/or breccias. |
| **Matrix** | Fine-grained (<2 mm) fragments of wall rock or juvenile magmatic material that occur between clasts. |
| **Cement** | The crystalline component of a clastic rock that binds together the fragmental constituents (clasts ± matrix). There are two main types of cement: (1) gangue and/or ore minerals precipitated from an aqueous fluid and (2) minerals crystallized from magma (i.e., igneous rock; e.g., monzonite-cemented breccia). Cement material is crystallized *in situ* via the infill of void space or by replacement of clasts ± matrix. |
| **Internal organization** | Describes the relationship between clasts and infill (matrix, cement and/or void space), based on the relative concentration of components and the degree of rotation of clasts away from their fully fitted position. |
| | 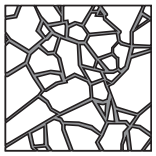 **Jigsaw-fit** A breccia with a high proportion of clasts (>75% clasts) and a low degree of clast rotation (<10˚). These breccias contain a low proportion of (or do not contain) a matrix component. Breccias with jigsaw-fit internal organization form via *in situ* fragmentation and may also be referred to as *in situ* or crackle breccias. |
| | 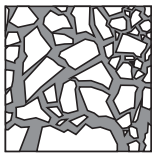 **Clast-rotated** A breccia with a moderate proportion of clasts (60–75%) and a moderate degree of clast rotation (10–20˚). A breccia with clast-rotated internal organization may also be referred to as a mosaic breccia. |
| | 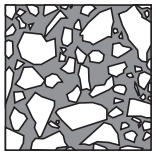 **Chaotic** A breccia with a low proportion of clasts (<60% clasts) and a high degree of clast rotation (>20˚). |
| **Cockade texture** | 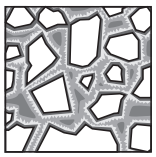 A texture in which individual clasts are surrounded by concentrically layered cement. The cement may contain cavities lined by euhedral and inward-projecting crystals. This texture occurs in breccias and veins with isolated wall-rock clasts, and is indicative of precipitation of cement into open space. |
| **Juvenile clast** | 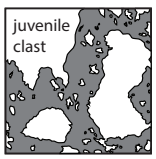 An igneous clast with a distinctive ragged, wispy or blocky and curviplanar morphology derived by fragmentation of a lava (above surface) or magma (sub-surface). |
| **Rock flour** | Mud-sized (<63 μm), angular to subangular lithic fragments formed via instantaneous pulverization of wall rocks during hydrothermal explosions ± subsequent comminution during transport, reworking and deposition of the explosion products. Rock flour can be strongly affected by syn-brecciation alteration as a result of its small particle size, especially when there is a high fluid to rock ratio during brecciation. |

**Table 4.3.** Characteristics of ore-related breccias in porphyry–epithermal environments. Note that overlap between fragmentation processes commonly occurs, producing breccias with hybrid characteristics. Aspects of this table have been compiled from Sillitoe (1985), McPhie et al. (1993), Davies (2002), Tămaș and Milési (2002, 2003), Gifkins et al. (2005), Auer et al. (2007), Davies et al. (2008a), Blackwell (2010), Johnson and Christiansen (2016), Valentine et al. (2017), Corbett (2018), and sources therein.

***1. Hydrothermal breccia***

**Definition and genesis:** A breccia formed through the interaction of hydrothermal fluids with wall rocks and/or magma. Hydrothermal breccia types include: (a) volcanic-hydrothermal (phreatomagmatic and phreatic), (b) magmatic-hydrothermal, (c) dissolution and (d) hydraulic breccias.

**Geometry, contacts and occurrence:**
- Discordant; highly variable morphology (e.g., pipe, dike-like, irregular, sill-like, etc.)
- Occurs as hypogene bodies ± associated surface deposits; best preserved in the subsurface environment

**Components, alteration and mineralization:**
- Contains hydrothermal cement (e.g., quartz, chalcopyrite, epidote, etc.)
- Commonly contains clasts that display evidence for pre-existing hydrothermal conditions (i.e., altered or mineralized clasts, clasts containing veins, vein fragments, etc.) and that may provide information about concealed mineralization; commonly contain clasts with syn-brecciation alteration (e.g., clasts with alteration rinds)

***A. Volcanic-hydrothermal breccia***

**Definition and genesis:** A breccia produced through the interaction of magma or magmatic heat with an external source of water (e.g., groundwater). The two end-member styles of volcanic-hydrothermal breccias are (i) phreatomagmatic and (ii) phreatic breccias. The term 'volcanic-hydrothermal' is used when a distinction between phreatomagmatic and phreatic brecciation processes cannot be interpreted, or when both processes are suspected to have been involved in brecciation. Where volcanic-hydrothermal breccias have breached the surface, the term 'eruption' is applied (e.g., phreatomagmatic eruption breccia).

**Geometry, contacts and occurrence:**
- Discordant; commonly steeply dipping and upward flaring
- Sharp contacts most common; irregular, interfingered and contorted contacts may occur where the breccias have intersected poorly consolidated or unconsolidated host rocks
- Occur as hypogene breccia bodies that may vent to surface
- Associated with volcanic environments and geothermal systems

**Facies characteristics**
- Chaotic to clast-rotated organization
- Typically massive, but may be stratified in the upper portion of the breccia body

**Components, alteration and mineralization:**
- *Clasts:* Highly polymict; primarily composed of locally derived lithic material; may contain accretionary lapilli, exfoliated spheroidal fragments and/or lithic fragments that display evidence of pre-existing hydrothermal conditions (altered, mineralized, veined or brecciated clasts, vein fragments, etc.)
- *Alteration:* Displays weak pervasive alteration as a result of fluid involvement during breccia emplacement

***i. Phreatomagmatic breccia***

**Definition and genesis:** A breccia generated through the direct interaction of magma with an external water at shallow depths (typically <2.5 km; e.g., when a dike is intruded into an active hydrothermal system). Fragmentation of both magma and wall rocks occurs through a wide range of explosive and non-explosive processes, including the instantaneous expansion and vaporization of external water, fluidization and upward transportation, gravitational collapse, and non-explosive quench fragmentation of magma. Over multiple generations of phreatomagmatic (± phreatic) explosions, a downward-tapering volcanic conduit called a diatreme may form, topped by a maar volcano at surface. Post-eruption collapse is common. Phreatomagmatic breccias are often colloquially referred to as milled matrix breccias.

Displays characteristics as described for volcanic-hydrothermal breccias in general, plus:

**Geometry, contacts and occurrence:**
- Typically forms large, vertically elongated, complex and polyphase breccia bodies (diameter: typically 1–3 km diameter; vertical dimensions: typically 1.5–3 km); may also form smaller (millimeter- to dekameter-scale), polyphase, massive or stratified breccia dikes exploiting structures such as faults

**Geometry, contacts and occurrence (*continued*):**
- The breccia body may vent to surface, forming a maar-diatreme volcanic complex:

  *Diatreme:* A downward-tapering, subsurface volcanic conduit that underlies a maar volcano; composed predominantly of phreatomagmatic breccias, but may locally contain phreatic, magmatic and collapse breccias; if emplaced within a hard substrate (e.g., coherent dacite with a fracture-controlled aquifer), the diatreme will be shaped like an inverted cone with an elliptical (commonly circular) base, steep sides and a cylindrical apex, and will flare outwards near surface (similar to a trumpet champagne flute); if intruded into a soft substrate (e.g., water-saturated unconsolidated sediments), the diatreme will form a broad bowl-shaped structure that flares outwards close to surface (similar to a margarita glass); less commonly may have an irregular or branching form; identification of carbonized wood and/or large blocks of maar deposits (as described below) indicates significant downward transport of components and confirms that the diatreme vented to surface (useful if associated maar has been eroded)

  *Maar:* A low-relief volcanic landform consisting of a central crater (<~200 m deep) surrounded by a tuff ring (tens of meters in height; deposits extend up to 10–15 km away from the vent); composed of interlayered base surge and airfall deposits; base surge deposits are fine grained and well-stratified with low-angle dune form crossbedding and beds of accretionary lapilli with reverse grading; airfall deposits are massive, unbedded and contain bomb sag structures; deposits contain juvenile volcanic material; tephra dip gently away from the vent; maar crater may be filled with lacustrine sediments rich in organic material and contain collapsed blocks of pyroclastic deposits from the tuff ring or tuff cone; generally unaltered or weakly altered
- Breccia body may be surrounded by ring faults, fractures and/or other types of breccias (e.g., 'contact breccias' consisting of monomict, jigsaw-fit to clast-rotated breccias), formed by the force of phreatomagmatic explosion on the surrounding host rocks
- Margins often feature large slump blocks that are tens or hundreds of meters across; slump blocks are composed of wall rock and/or phreatomagmatic eruption deposits from the associated maar volcano
- Spatial association with shallow-level intrusions that have the same or similar composition to the juvenile clasts; rarely, a gradational transition from an igneous intrusion (e.g., a dacite dike), to an *in situ* igneous clast breccia (e.g., monomict, jigsaw-fit dacite-clast breccia), and then to a polymict breccia containing juvenile clasts (e.g., polymict, matrix-rich breccia with juvenile dacite clasts) may be preserved
- Commonly crosscut by irregular ± peperitic igneous intrusions of the same composition as the intrusions that initially triggered phreatomagmatic brecciation; these intrusions may feed endogenous domes
- Close spatial relationship with phreatic breccias (where source of magma has been depleted) or magmatic breccias (where source of external water has been depleted)

**Facies characteristics**
- High degree of fragmentation (prevalence of matrix-supported and matrix-rich breccias common, i.e., 50–90% matrix); breccias may become finer grained and more matrix-rich inward from margins and clasts may become more rounded inward from margins (forming a central fluidization channel)
- Polyphase breccias with variable facies characteristics and complex relationships
- Typically contains massive breccias; may transition into stratified breccias near surface

**Components, alteration and mineralization:**
- *Clasts:* Subangular to rounded (milled and/or polished); polymict, especially near surface; contains juvenile clasts (typically poorly vesicular with ragged or cuspate margins and/or characteristic wispy shapes; note that juvenile clasts are not always preserved, and often, igneous clast components are inferred to be juvenile); contain a high proportion of wall rock clasts compared to juvenile clasts; may contain 'breccia-in-breccia' clasts (i.e., competent breccia clasts from previous episodes of phreatomagmatic brecciation); clasts are typically granule- to boulder-in size; the competency of wall rock types incorporated as clasts will partly determine their grainsize (e.g., weakly compacted sedimentary clasts will be more fragmented than granitic clasts, even if the granitic clasts have undergone much greater transport); commonly contains very large boulders (diameter: 10s–100s of meters)
- *Matrix:* Composed of rock flour ± tuffaceous material; may contain geopetal indicators such as graded bedding and slump structures; localized and chaotic bedding within otherwise massive breccias indicates small-scale collapse; commonly weakly and pervasively altered
- Typically lacks open space and contains little or no hydrothermal cement

**Components, alteration and mineralization (*continued*):**
- Late- or post-mineralization timing with respect to porphyry mineralization (venting of volatiles to surface negates their involvement in porphyry ore formation); variable timing with respect to epithermal mineralization (pre-, syn- and post-mineralization examples)
- Breccias associated with high-sulfidation epithermal systems may develop zoned advanced argillic alteration; whereas, those associated with low-sulfidation epithermal systems may develop zoned argillic phyllic and/or intermediate argillic alteration
- In some cases, the clay-rich alteration, fine average grain size and paucity of open space causes phreatomagmatic breccias to be incompetent, and therefore, impermeable to hydrothermal circulation; consequently, fluid flow and post-brecciation epithermal mineralization can be focused into adjacent wall rocks; elsewhere, phreatomagmatic breccias with competent quartz–sericite alteration or appreciable open space may provide the permeability pathways necessary for epithermal mineralization

***ii. Phreatic breccia***

**Definition and genesis:** A breccia produced by the explosive release of overpressurized steam from beneath an impermeable cap rock horizon at shallow levels. The steam is generated via phase separation (boiling) of groundwater that is heated by a proximal magmatic source. The explosion may initially be triggered by seismic activity, rapid unroofing (e.g., volcanic sector collapse), or sudden changes to the local hydrology (e.g., flash flooding). Multiple, repeated explosions may excavate a cavity into which wall rock fragments are deposited via implosion and/or gravitational collapse. The brecciation process involves no direct magmatic input and so, no juvenile material is incorporated into the resultant breccias. Phreatic brecciation may also initiate during the waning stages of phreatomagmatic brecciation, as the source of magma is depleted. Commonly, the phreatic explosions vent to surface, forming shallow craters and related ejecta aprons. The craters can then fill with hydrothermal fluids, forming hot springs.

Displays characteristics as described for volcanic-hydrothermal breccias in general, plus:

**Geometry, contacts and occurrence:**
- Generally produce small breccia bodies (i.e., diameter: cm- to m-scale structures or larger bodies up to 500 m; vertical dimensions: <300 m) with tabular, inverted cone, pipe-like or irregular, branching and anastomosing morphology; sharp contacts; may feature irregular, finger-like protrusions from the main body
- Emplaced at shallow depths (commonly at the depth of boiling, i.e., typically 200–300 m depth, not deeper than 1 km depth); commonly associated with discharge zones of geothermal systems

  *Surface deposits:* Hypogene phreatic activity may generate a low-relief ejecta apron extending not more than 10s or 100s of meters (and exceptionally rarely up to 1 km) away from the hydrothermal eruption vent; deposits are composed of poorly sorted, angular to sub-angular, and hydrothermally altered lithic clasts in a silty matrix of angular lithic fragments ± clay cement; clasts are typically centimeter- to decimeter-scale, and are not larger than 2–3 m across; surface deposits do not contain juvenile volcanic material; may contain mineralized clasts, hydrothermal breccia clasts and/or clasts with truncated veins; may contain accretionary lapilli; deposits are massive, or rarely, weakly stratified (poorly developed sub-parallel bedding and normal grading most common); may be associated with silica sinter or travertine deposits
- Structurally controlled emplacement; may transition laterally into fractured rocks with stockwork veins and/or jigsaw-fit breccias; may transition into vein-style epithermal mineralization at depth
- May overprint phreatomagmatic breccias

**Facies characteristics**
- Clast- to matrix-supported; jigsaw-fit to chaotic clast organization; matrix may be absent in the upper parts of the breccia; clast-supported breccias may contain significant void space
- Evidence for multiple stages of brecciation common, locally with crack-seal textures

**Components, alteration and mineralization**
- *Clasts:* Polymict; angular to rounded (typically more angular than phreatomagmatic breccias); granule to boulder in size (up to meter-scale clasts); pervasively altered; absence of juvenile clasts; breccias commonly contain a significant proportion of clasts with hydrothermal alteration, mineralization, truncated veins and breccias; clasts of silica sinter and carbonized wood indicate eruption at surface

**Components, alteration and mineralization (*continued*):**

- *Matrix + cement:* Variable abundance of matrix and cement (typically sums to <50%); matrix composed of sand-sized fragments of host rocks, clay minerals and previously formed vein material ± rock flour; matrix commonly replaced by quartz ± sulfides; hydrothermal cement is present; clay minerals and quartz are commonly widespread and abundant; cement may display open space-filling textures (e.g., cockade texture, drusy cavity fillings, etc.)
- High-grade epithermal mineralization may occur as cement or as replacement of clasts and matrix
- Hydrothermal cement and related alteration assemblages are composed of minerals that crystallize under moderate- to low-temperature, shallow-level to surficial conditions

### *B. Magmatic-hydrothermal breccia*

**Definition and genesis:** A breccia produced via the fragmentation of rock by fluids exsolved from a crystallizing magmatic intrusion, with or without the influence of external fluids. Magmatic-hydrothermal breccias are formed in five stages: (1) magmatic-hydrothermal fluids are exsolved during second boiling from a hydrous magma at hypabyssal depths (~1.0–3.6 km), (2) fluids accumulate beneath the carapace of the crystallizing intrusion until they attain a fluid pressure that exceeds the confining pressure and the tensile strength of the surrounding rock, (3) the fluids decompress and expand, lifting the overlying rock column and fragmenting the magmatic carapace and surrounding wall rocks, (4) lithic fragments collapse and/or implode into the newly formed open space, and (5) minerals are precipitated from the magmatic-hydrothermal fluids, cementing the breccia. Depending on the depth of formation and the nature and volume of the associated magmatic intrusion, magmatic-hydrothermal breccias may display different characteristic features. Two end-member types may be defined: (i) deep intrusion-related and (ii) porphyry-related. Pebble dikes are considered to be a type of porphyry-related magmatic-hydrothermal breccia. Deep intrusion-related magmatic-hydrothermal breccias are typically associated with more reduced intrusions; whereas, porphyry-related magmatic-hydrothermal breccias are typically associated with more oxidized intrusions.

**Geometry, contacts and occurrence:**

- Discordant; single or multiple pipes with lensoid, ovoid or circular cross section; axis of elongation is parallel to local structural trend; up to 2 km in diameter; pipes may have an upward tapering morphology; less commonly occurs as dike-like or irregular bodies
- Sharp contacts most common; may transition into fractured host rocks over several meters
- Breccia bodies are 'blind' (i.e., did not breach the paleosurface)
- Breccias commonly focused within the apex or along the margins of related igneous intrusions and extend upward into overlying host rocks
- Spatial association with igneous intrusions and/or breccias with an igneous cement

**Facies characteristics**

- Variable; depending on the conditions of emplacement
- Larger bodies may feature a central zone of matrix-rich breccia and a marginal zone of matrix-poor, cemented-breccia with jigsaw-fit organization

**Components, alteration and mineralization:**

- *Clasts:* Typically angular (limited transport); may contain juvenile clasts
- The hydrothermal cement and related alteration are composed of minerals that precipitated under high-temperature conditions from hydrothermal fluids that were (at least in part) derived from magmatic intrusions (e.g., biotite, tourmaline, chalcopyrite, orthoclase, etc.); may contain abundant and well-mineralized cement; cement has open space filling textures

#### *i. Deep intrusion-related magmatic-hydrothermal breccia*

**Definition and genesis:** A magmatic-hydrothermal breccia that has been emplaced at sub-porphyry crustal levels and is typically associated with unmineralized or weakly mineralized batholiths and stocks.

**Geometry, contacts and occurrence:**

- Breccias have a pipe morphology; pipes may occur in clusters (e.g., tens of pipes in an area spanning several square kilometers)
- Pipes may have bifid geometry at depth; pipes may have a domed roof
- The top and lateral margins of the breccia body are commonly enveloped by closely spaced vertical or curved (domed) sheeted fractures
- Occur within the upper parts, directly above or along the margins of stocks or plutons

**Facies characteristics**

- Commonly have jigsaw-fit organization
- May display decompressive shock textures (e.g., regions of breccia composed of exfoliated curvilinear clasts with rounded cores)
- The upper and outer margins of the breccia body may be characterized by 'shingle breccia', i.e., a breccia consisting of angular, shingle-like clasts whose long axes are oriented roughly parallel the walls and roof of the breccia body (forming a dome shape); the clasts may be jigsaw-fit or clast-rotated and imbricated; this breccia facies forms by the collapse of fragmented wall rocks superjacent and adjacent to the magmatic-hydrothermal explosion

**Components, alteration and mineralization:**

- *Clasts:* Angular to subrounded; typically monomict; clasts range from pebble- to boulder-sized, may contain outsized boulders that are tens of meters in diameter; clasts display evidence for minor downward displacement
- *Cement + matrix:* Variable abundance of matrix and cement (typically sums to 5–30%; proportion of cement is much greater than the proportion of matrix); cement may be very coarse-grained (individual crystals several centimeters in diameter); cement commonly composed of tourmaline; where present, matrix is composed of rock flour
- Alteration halos around breccia pipes extend for meters to tens of meters into the wall rocks; sericite alteration is most common and is typically associated with tourmaline cement; other common alteration styles include chloritization and silicification; potassic and propylitic alteration are minor and uncommon
- Copper is the most common associated commodity, followed by Mo, W, Au(-Ag), Bi and Ag-Pb-Zn; zoning of metals is common
- Mineralization occurs as a replacement of minerals within clasts and as cement that infills open space
- Mineralization is commonly best developed in the pipe 'lobes', the arcuate regions at the intersection of the breccia's margins and the long axis of the breccia's elliptical cross section
- In a cluster of breccia pipes, not all of the breccias will necessarily contain mineralization (e.g., <50% of pipes in cluster might be mineralized)
- Mineralization typically higher grade and lower tonnage than that associated with porphyry-related magmatic-hydrothermal breccias

#### *ii. Porphyry-related magmatic-hydrothermal breccia*

**Definition and genesis:** A magmatic-hydrothermal breccia that has been emplaced at porphyry crustal levels and is typically associated with pre- to syn-mineralization porphyry intrusions. Due to the more efficient release of larger volumes of fluid from porphyries as compared to deep-seated intrusions, porphyry-related magmatic-hydrothermal breccias feature a higher degree of fragmentation and clast displacement and display a greater variety of textures than deep intrusion-related magmatic-hydrothermal breccias.

**Geometry, contacts and occurrence:**

- Breccias have a less regular morphology than deep intrusion-related magmatic-hydrothermal breccias; breccias may form irregular bodies, dikes or composite pipes composed of multiple breccia facies; range in size from meter scale up to ~2 km; sharp contacts
- Commonly rooted in porphyry intrusions
- If there is a cluster of pipes, they commonly all related to a specific phase of porphyry intrusions (typically syn-mineralization)
- Breccias occupy a wide range of positions relative to porphyry ore bodies (e.g., centered, adjacent, enveloping, etc.)

**Facies characteristics**

- Typically clast-supported and cemented
- Range from jigsaw-fit to chaotic
- Decompressive shock textures are uncommon

**Components, alteration and mineralization:**

- *Clasts:* Angular to rounded (fragments more rounded than deep intrusion-related magmatic-hydrothermal breccias); polymict more common than monomict; commonly contains mineralized clasts (which upgrade ore); locally, there is evidence for appreciable ascent or descent of lithic fragments (i.e., hundreds of meters of transport); may contain exfoliated spheroidal clasts

**Components, alteration and mineralization (*continued*):**

- *Matrix + cement:* Variable abundance of matrix and cement that may vary substantially over short distances within the breccia body; cement commonly contains abundant quartz; other gangue minerals in the cement commonly include K-feldspar, biotite, chlorite, fluorite, apatite, siderite, tourmaline, magnetite and specularite; gangue in alkalic-type deposits contains little or no quartz and may contain garnet, clinopyroxene and anhydrite; ore minerals in the cement commonly include chalcopyrite, bornite, pyrite, molybdenite, and less commonly cassiterite and wolframite; rarely, cement may be wholly or partly composed of igneous rock; in general, contains a higher proportion of rock flour matrix compared to deep intrusion-related magmatic-hydrothermal breccias (locally up to 50% matrix); matrix may have an irregular, steeply dipping fabric; matrix may be strongly altered
- Contains minor open space (up to a few volume percent); open space is located in the triangular spaces between clasts
- Breccias are typically associated with widespread potassic alteration (biotite and/or K-feldspar) that may transition into or be overprinted by propylitic, sericitic or advanced argillic alteration; mineralization is correlated with areas of potassic alteration
- Mineralization tends to be distributed along the margin of the breccia body associated with cement-rich breccias; the interior of the breccia body typically contains unmineralized, cement- and altered matrix-rich breccias
- Mineralization has the same metal signature as associated porphyries (typically Cu, Au and/or Mo; more rarely Sn and/or W)
- Breccias tend to contain a higher abundance of ore minerals compared to vein stockworks in the surrounding host rocks; may have the highest grades ore at a deposit

#### *Pebble dike*

**Definition and genesis:** A dike-like magmatic-hydrothermal breccia produced by the rapid thermal expansion of magmatic fluids (derived via rapid degassing of ascending magmas to porphyry crustal levels) and/or meteoric fluids within the wall rocks adjacent to late-stage or post-mineralization porphyry dikes. The gas-charged clastic slurry is forcefully injected upwards along faults and/or fractures. Milling and hypogene exfoliation of clasts occurs as the wall rock fragments are transported upward and depressurized.

**Geometry, contacts and occurrence:**

- Discordant, with a dike-like and steeply dipping geometry; may be accompanied by sill-like bodies, pipes and irregular offshoots
- Dikes typically vary in thickness from ~1 cm to 10 m, reach vertical extents of >~0.5 km and may extend along strike for >1 km; may pinch and swell; occurs singly or in swarms
- Sharp contacts
- May transition into igneous-cemented breccias at depth
- Commonly localized along faults and fracture zones; may transition laterally into parallel sub-vertical fractures

**Facies characteristics**

- Moderately well- to well-sorted; typically clast-supported; chaotic clast organization
- Breccias may be finer grained along contacts

**Components, alteration and mineralization:**

- *Clasts:* Polymict or monomict; composed of non-juvenile lithic clasts derived from underlying or adjacent host rocks; clast population may suggest evidence for appreciable upward transport (e.g., >1.5 km); clasts are commonly pebble-sized, and correlate with breccia dike width; typically very well rounded morphology, may range from angular to very well rounded; clasts may become increasingly rounded closer to surface
- *Matrix + cement:* Matrix occurs in variable proportions (0–100%) and may vary in proportion considerably over short distances; matrix may be flow-banded; hydrothermal cement is locally present; breccias that do not contain cementing minerals may be friable and recessive in outcrop
- Weak hydrothermal alteration occurs within the breccia dike and extends into the surrounding host rocks
- Sulfides may occur as components of clasts or as detrital mineral fragments (typically not in sufficient quantity for the pebble dikes to be considered as ore)
- Pebble dikes may vector downwards towards a mineralized porphyry, especially if there is evidence of mineralization (e.g., mineralized clasts)

### *C. Hydraulic breccia*

**Definition and genesis:** A breccia produced by hydraulic fragmentation. Hydraulic breccias are formed in four stages: (1) compressed hydrothermal fluids within a fracture attain a fluid pressure that is greater than the sum of the confining pressure and the tensile strength of the surrounding rock, (2) the compressed hydrothermal fluids at the fracture tip expand, jacking the walls of the fracture apart, and creating a zone of low pressure, (3) adjacent wall rocks shatter and implode into the newly created low pressure zone, and (4) minerals precipitate from the depressurized hydrothermal fluids onto the margins of the clasts and adjacent wall rocks, cementing the breccia.

**Geometry, contacts and occurrence:**
- Discordant geometry
- Commonly tabular, with a strong structural control on emplacement
- Commonly spatially associated with and/or transitional to veins, tectonic breccias, faults and/or fractured rocks

**Facies characteristics**
- Massive and poorly sorted
- Jigsaw-fit to clast-rotated internal organization most common
- May have a central zone with chaotic clast organization, moderate sorting, rock flour matrix, polymict clast population and/or rounded clast morphology, indicative of multiple fragmentation and significant transport
- Polyphase breccias are common

**Components, alteration and mineralization:**
- *Clasts:* Monomict, consisting of locally derived, non-juvenile lithic material; angular, splintery and slabby morphologies; may be pervasively altered or have alteration rinds
- *Cement + matrix:* Contains abundant hydrothermal cement, commonly with open space filling textures (e.g., cockade texture, drusy texture, etc.); lacks or contains a minimal abundance of matrix material
- Variable quantity of void space
- Mineral species, crystal habit, fluid inclusions and isotopic data of the hydrothermal cement and/or related alteration assemblages can inform on the depth and temperature of breccia formation and the possible involvement of magmatic fluids

### *D. Dissolution breccia*

**Definition and genesis:** A breccia formed by the chemical corrosion of a fractured rock mass. This process leads to volume reduction and the potential for gravitational collapse into newly formed void spaces (i.e., solution collapse brecciation).

**Geometry, contacts and occurrence:**
- V-shaped breccia bodies, often with sharp, flat lower contacts
- Breccia may be (partly) concordant with bedding in sedimentary host rocks
- Contacts may be irregular and partly dissolved
- Commonly form in carbonate- or sulfate-rich rocks (e.g., limestones, sedimentary evaporites, anhydrite-cemented breccias and veins)
- May be associated with karst topography (e.g., sinkholes, caves, etc.)
- Host rocks may feature concentrically inward-dipping beds
- May contain or be associated with dissolution seams and/or stylolites (which represent fluid flow pathways)

**Facies characteristics**
- Clast organization ranges from jigsaw-fit to chaotic, depending on the degree of dissolution and transportation/mixing during collapse
- May be stratified, with sedimentary structures indicative of collapse and settling
- Stratified breccias may have inverse grading
- Polyphase breccias are common

**Components, alteration and mineralization:**
- *Clasts:* Monomict or polymict, consisting of non-juvenile lithic material; clasts are derived from the surrounding (especially overlying) host rocks; there may be vertical variations in clast types that mimic the sedimentary stratigraphic sequence; clast margins may be irregular, serrated and partly dissolved; angular to rounded (or pseudo-rounded due to corrosion of clast margins)
- *Matrix + cement:* Dominated by hydrothermal cement (commonly lacks or contains a minimal abundance of matrix); cement may have cockade texture or snow-on-roof texture (cement preferentially on one side of clasts); matrix may be draped between clasts
- Presence of vugs and larger cavities ± speleothem-like formations (e.g., stalactites composed of hydrothermal minerals)
- Strongly to intensely altered clasts and replacement textures
- May be strongly mineralized

### *2. Tectonic breccia*

**Definition and genesis:** A breccia formed by brittle or ductile shear deformation during movement along a fault. Tectonic breccias may undergo modification (decomposition, alteration, cementation) during contemporaneous or subsequent interaction with aqueous fluids. Hybrid tectonic-hydrothermal breccias are common, especially in the brittle region of the Earth's crust (<~10 km), where fluids exploit faults due to their high permeability.

**Geometry, contacts and occurrence:**
- Discordant
- May offset geology on either side of breccia body
- Spatial association with fault zones, compressional and dilational fault jogs and fault intersections
- Commonly associated with and/or transitional to other types of breccias
- Mylonite may transition into gneiss with increasing depth

**Facies characteristics**
- Tectonic breccias can be classified based on their facies characteristics as follows:

  *Fault breccias:* >30% clasts; cohesive or incohesive; foliated or unfoliated; subdivided into crackle, mosaic or chaotic fault breccias based on their internal organization

  *Cataclasites:* <30% clasts; cohesive; unfoliated

  *Mylonites:* <30% clasts; cohesive; strongly foliated

**Components, alteration and mineralization:**
- Contains angular to subangular and locally derived lithic clasts; does not contain juvenile clasts
- May display shear textures (e.g., foliation, S-C fabric, shear folds, etc.), fault gouge, slickensides and/or pseudotachylite (melanocratic, typically devitrified glass formed by frictional melting and quenching of components in a fault zone)
- Cataclasites and fault breccias may contain clusters of disaggregated (jigsaw-fit) and fractured clasts
- Mylonites may have ribbon texture (defined by highly elongated, lens-shaped aggregates of quartz) and/or rotated porphyroclasts with sigmoidal pressure shadows

### *3. Pseudobreccia*

**Definition and genesis:** A rock that appears to have a clastic texture as a result of diagenetic and/or hydrothermal alteration. For example, pseudobreccias may result when intense fracture-controlled alteration produces isolated domains (pseudoclasts) of one alteration phase or unaltered rock enclosed within a continuous interconnected domain (pseudomatrix) of another alteration phase, or when mixed glassy and spherulitically devitrified zones undergo domainal alteration.

**Geometry, contacts and occurrence:**
- Variable morphology, commonly irregular
- The apparent contacts are gradational and may crosscut primary geological features
- May transition into weakly altered or unaltered coherent rocks with quench fragmentation or perlitic fractures
- May transition into distinctly fracture-controlled alteration overprinting coherent rocks

**Facies characteristics**
- Variable; dependent on the primary characteristics of the host rock and nature of the fluid pathways

**Components, alteration and mineralization:**
- Mottled appearance; pseudoclasts and pseudomatrix may be distinguished by differences in color (alteration assemblages) rather than composition; pseudoclasts may have irregular and/or indistinct margins
- Preserved morphology of devitrification bands, lithophysae and nodules
- Presence of moderate to intense hydrothermal alteration
- Advanced argillic alteration may be associated with *gusano texture*—a pseudobreccia texture consisting of soft, rounded or amoeboid clusters of clay minerals, sulfates, and sulfides (especially pyrophyllite, diaspore, pyrite and/or alunite) surrounded by fine-grained granular quartz

diode BSE detector and an Oxford AZtec EDS system with XMax80 silicon drift detector. Conditions were 15 kV accelerating voltage, around 3 nA beam current, and 14.8 mm working distance. The 'Point & ID' mode was used. Spectra were acquired using the following settings: process time '3', live spectrum acquisition time of 10 seconds, 2,048 channels, and total energy range of 20 keV. Typical count rates were around 39,000 cps and total spectrum counts were >1,000,000. Compositional data was normalized to 100% for mineral identification.

## 4.3 Alteration

Three main stages of hydrothermal alteration are distinguished in Kapit NE and Coastal: early-stage phlogopite and chlorite alteration, main stage adularia – pyrite, vuggy adularia and quartz – illite – pyrite alteration and late-stage smectite – kaolinite and kaolinite – alunite alteration. These map-scale, pervasive alteration assemblages are summarized in Table 4.4 and their distributions are depicted on two cross-sections (Fig. 4.1). The cross-sections are partly schematic, limited by the drill hole spacing in these areas, and the resultant necessity for a large clip of 200 m on either side of the section line. The gold grade shells are clipped along the section line from a three-dimensional interpolant of gold grade based on Newcrest Mining Limited assay data. The pervasive alteration zones were created by projecting the collected alteration data (K-feldspar staining, TerraSpec, Corescan, HyLogger, physical and photo core logging) for drill holes on section to the clipping plane. The alteration zones have significant overlap of up to 100 m due to overprinting and gradational relationships that have not been depicted, but are discussed in the text where appropriate.

### *4.3.1 Early-stage alteration*

#### *4.3.1.1 Stage A1: Phlogopite alteration*

Stage A1 phlogopite alteration varies from weak to strong and is composed of patchy to pervasive zones of hydrothermal phlogopite, magnetite, orthoclase, albite, biotite and anhydrite (Table 4.4). The relative proportions of each mineral have been influenced by the original rock compositions. Within pyroxene-phyric basalt breccia (KNE2b), A1 is characterized by moderate to strong, clast-selective, dark gray magnetite – phlogopite alteration and matrix-selective, light gray to chestnut brown phlogopite – orthoclase – anhydrite + vermiculite alteration (Fig. 4.2A). Magnetite can comprise up to 15 vol% of altered KNE2 basalts, but is less abundant (<3 vol%) in the intrusive host rocks. Within hornblende-bearing gabbro (KNE6), phlogopite alteration consists of spots of disseminated biotite – phlogopite – magnetite alteration that preferentially affected xenoliths and clusters of clinopyroxene crystals (Fig. 4.10A). Typically, phlogopite is fine-grained and has partly to completely replaced mafic phenocrysts and groundmass minerals (Fig. 4.2C and E). It has locally been replaced by pale to peachy brown vermiculite (Fig. 4.2B). Vermiculite commonly forms by supergene alteration of Mg-bearing minerals (e.g., Moon et al., 1994). Therefore, identification of vermiculite using systematic SWIR analyses was used to help delineate the A1 phlogopite alteration zone. Fine-grained pyrite, minor chalcopyrite and rare molybdenite are disseminated throughout the A1 phlogopite alteration zone (Fig. 4.2B). Rutile and apatite are microscopic and ubiquitous, with rutile occurring abundantly within primary mafic minerals. Stage A1 alteration is preserved to the side of, and below, high-grade epithermal mineralization, but it has been obliterated within and proximal to the ore zones (Fig. 4.1). Stage A1 alteration is spatially related to Stage 1 and 3A anhydrite veins and cemented breccias (Fig. 4.9), and is associated with subeconomic (<0.2%) copper grades.

#### *4.3.1.2 Stage A2: Chlorite alteration*

Stage A2 chlorite alteration is composed of chlorite, calcite, Fe-oxides, illite, anhydrite, rutile and pyrite, with minor amounts of albite, titanite, epidote and tourmaline (Table 4.4). This alteration varies from weak to mod-

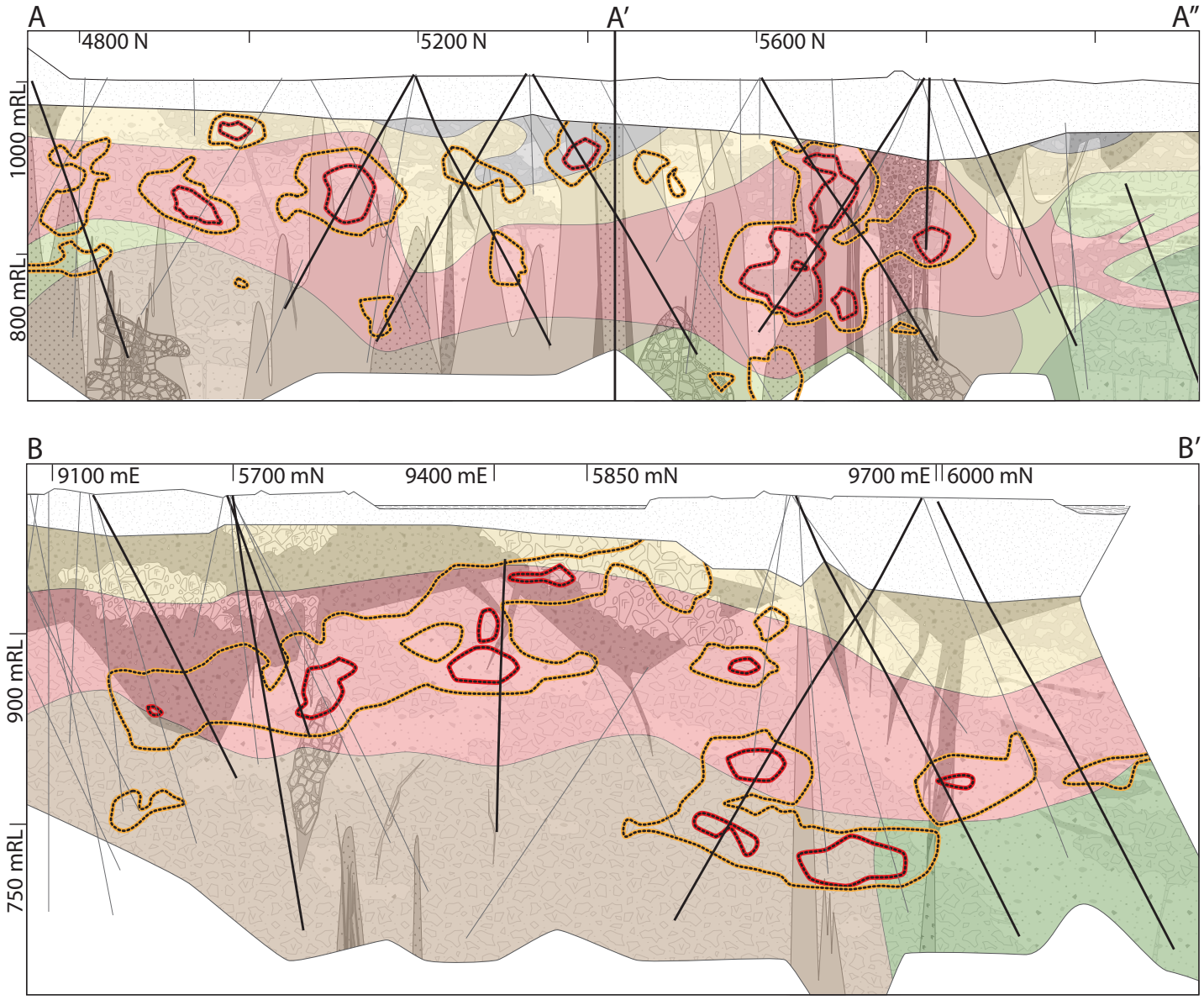


## Legend

### Lithotypes

- Feldspar-phyric andesite and breccia (KNE10)
- Trachytic hornblende- feldspar-phyric latite (KNE9)
- Hornblende-feldspar-phyric latite (KNE8)
- Crystal-poor, feldspar-phyric trachyte (KNE7)
- Hornblende-bearing gabbro (KNE6)
- Hornblende-biotite-bearing monzonite (KNE5)
- Nepheline-bearing monzonite (KNE4)
- Plagioclase-phyric andesite breccia (KNE3)
- Pyroxene-phyric basalt and basalt breccia (KNE2)
- Polymict matrix-supported breccia (KNE1)

### (Volcanic-)hydrothermal breccias

- Polymict volcanic-hydrothermal breccia
- Polymict quartz-pyrite-cemented breccia
- Polymict anhydrite-chlorite-calcite-cemented breccia

### Other

- Waste rock
- Drill trace – physically / photo logged

### Alteration

- Stage A7 – Quartz-alunite
- Stage A6 – Smectite-kaolinite
- Stage A3-A5 – Main-stage
- Stage A2 – Mg-chlorite
- Stage A2 – Fe-chlorite
- Stage A1 – Phlogopite

### Grade shells

- >5 g/t Au
- >3 g/t Au

**Fig. 4.1.** Map-scale distribution of pervasive alteration zones in Kapit NE and Coastal along north-trending cross section A–A'–A" (*top*) and northeast-trending cross section B–B' (*bottom*).

**Table 4.4.** Map-scale textures and pervasive alteration stages observed at Coastal and Kapit NE.

| Stage | Mineralization | Major minerals | Minor minerals | Intensity, textures and distribution | Interpretation |
|---|---|---|---|---|---|
| ***Early-stage*** | | | | | |
| Stage A1 phlogopite | Sub-economic Cu-Au | Phl, or, anh, mag, py, ms, cal, bt, rt + vrm | Ab, act, ttn, ap, ccp | Weak to strong; deep (>150 m), widespread, cuts across stratigraphic boundaries | Proximal porphyry-style alteration; unknown causative intrusion |
| StageA2 chlorite | - | Chl, cal, mag, hem, goe, anh, ill, py, rt | Ab, ttn, ep, tur | Weak to moderate; deep (>150 m), adjacent to and locally overprinting A1 biotite alteration; NE-trending zone of magnesian chlorite in Kapit NE; best developed in volcanic stratigraphy in DDHL1995 | Distal porphyry-style alteration |
| ***Main-stage*** | | | | | |
| Stage A3 vuggy adularia | Au | Ad, py | Qtz, cal | Weak to strong; occurs as crystal-shaped and irregular vugs, and open to partly-infilled fractures; replacement of remnant minerals to adularia, pyrite and minor quartz; locally overprints A1 and A2 zones adjacent to faults | Dissolution of mafic minerals, anhydrite veins and volcanic glass possibly related to the incursion of cold surface water |
| Stage A4 adularia – pyrite | Au | Ad, py, ill, rt, mrc, anh | Ap, apy, qtz, cal, vrm, zrn (?) | Weak to intense and texturally destructive; cuts across stratigraphic boundaries; best-developed overprinting A3 alteration; associated with ore-bearing pyritic faults, veins and breccias | Proximal low-sulfidation epithermal alteration |
| Stage A5 quartz – illite – pyrite | Au | Qtz, py, ill | Ad, cal, rt, vrm | Moderate to strong; spatially associated with quartz veins and breccias; where overprinting basalt breccia it has a pseudo-gusano texture | Proximal low-sulfidation epithermal alteration |
| ***Late-stage*** | | | | | |
| Stage A6 smectite – kaolinite | Localized Au | Sme, kln, py, mrc | Ill, ill-sme, cb | Moderate to intense and texturally destructive; near-surface (<70 m) subhorizontal blanket; roughly parallels topography; local, deep (~200 m), upward-flaring zones (likely relating to faults); spatially coincident with weathering and associated with strong post-drilling alteration (copiapite, jarosite, melanterite, chalcanthite, hematite, gypsum) | Steam-heated alteration |
| Stage A7 kaolinite – alunite | Au, sub-economic Cu | Kln, alu, qtz, sme, py, mrc, jar | Dck, ill, opl, cv, APS | Moderate to intense and texturally destructive; shallow (<100 m); forms core to deep, cone-shaped A6 alteration zones; associated with kaolinite-pyrite veins | Steam-heated acid-sulfate alteration |

Abbreviations: ab = albite, ad = adularia, act = actinolite, alu = alunite, anh = anhydrite, ap = apatite, APS = aluminum phosphate-sulfate minerals, apy = arsenopyrite, bt = biotite, cal = calcite, cb = carbonate, ccp = chalcopyrite, chl = chlorite, cv = covellite, dck = dickite, ep = epidote, goe = goethite, hem = hematite, ill = illite, ill-sme = illite-smectite, jar = jarosite, kln = kaolinite, mag = magnetite, mrc = marcasite, ms = muscovite, opl = opal, or = orthoclase, phl = phlogopite, py = pyrite, qtz = quartz, rt = rutile, sme = smectite, ttn = titanite, tur = tourmaline, vrm = vermiculite, zrn = zircon.

erate in intensity, has a patchy to pervasive distribution, and imparts a green, cream and/or red coloration to the host rocks (Fig. 4.3). Chlorite and abundant small, stubby rutile crystals have typically replaced mafic phenocrysts (Fig. 4.3D), and feldspars are replaced by calcite, albite and illite (Fig. 4.3B). The groundmass is altered to patches of chlorite, illite, albite and anhydrite. Within this alteration domain, Fe-oxides (primarily hematite with lesser goethite and magnetite), albite and calcite form an intricate network of irregular veinlets, patches and amygdule infill (Fig. 4.3A, C, E and G). Stage A2 alteration occurs at depths >150 m below sea level, adjacent to and locally overprinting phlogopite alteration (Fig. 4.1). Where overprinting relationships have been observed, there is a spatial association with chlorite-bearing veins and breccias (Stage 1C polymict anhydrite – chlorite – calcite-cemented breccia and Stage 1F anhydrite – calcite – chlorite veins). There is a distinct domain of Mg-rich chlorite that is roughly northeast-trending and intersects section A–A'–A" at its northern extent (Fig. 4.1).

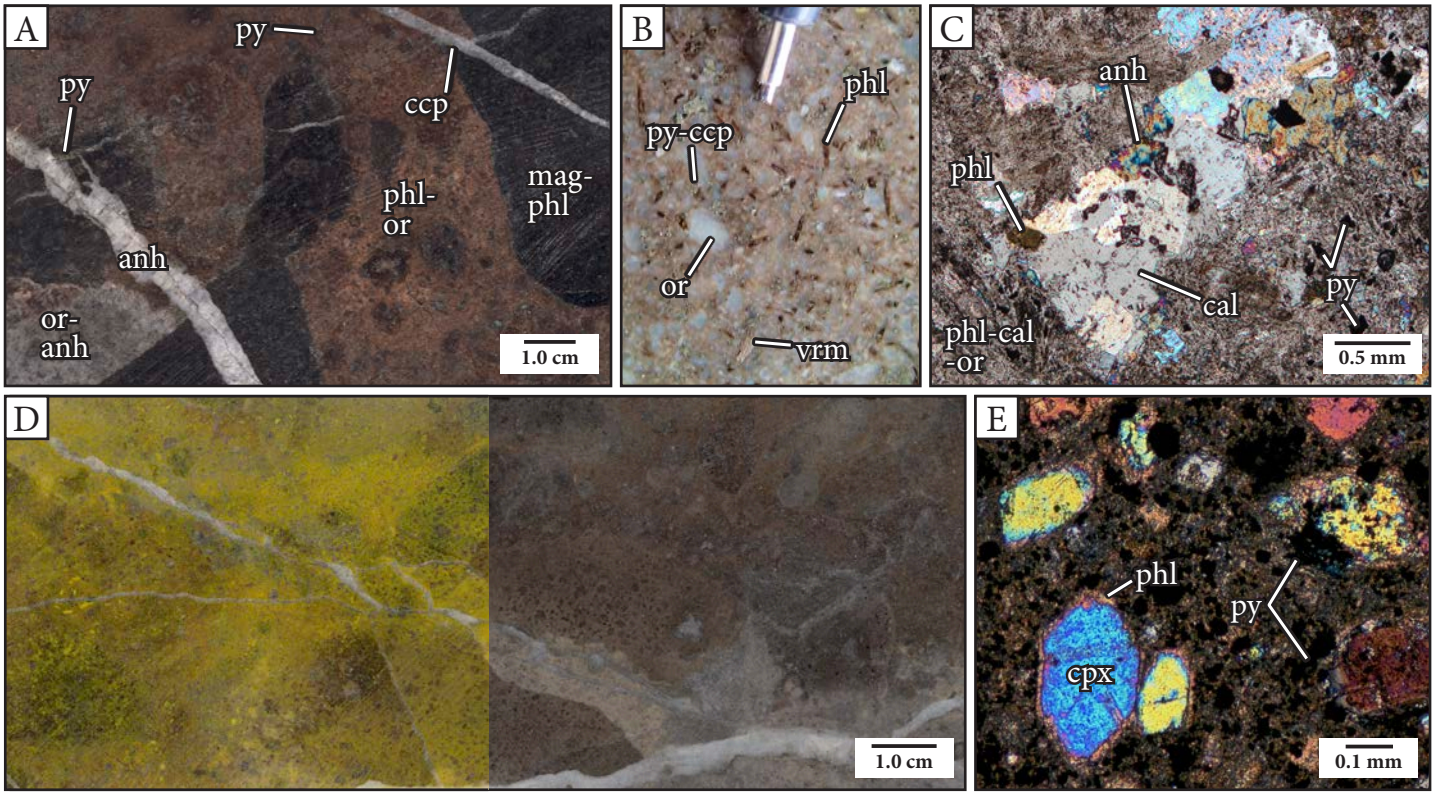


**Fig. 4.2.** Stage A1 phlogopite alteration. **A.** Moderate to strong A1 alteration of pyroxene-phyric basalt breccia (KNE2b). Large clasts have been selectively altered to magnetite and phlogopite, whereas smaller clasts and the matrix have been selectively altered to patchy light gray orthoclase – anhydrite – phlogopite and chestnut brown phlogopite – orthoclase – anhydrite + vermiculite. The margins of the larger clasts are altered similarly to the matrix. This alteration style gives the appearance of a matrix-rich breccia, however, the sample is clast-rich. The clasts and matrix are crosscut by branching anhydrite – pyrite – chalcopyrite veins. Sample: DDHL1968 310.2 m. **B.** Moderate A1 alteration in feldspar-phyric hornblende – biotite-bearing monzonite (KNE5). Most crystal edges of primary feldspar (plagioclase and orthoclase) phenocrysts are rimmed by hydrothermal orthoclase. Primary hornblende phenocrysts have been altered to phlogopite, which has broken down to pale peach vermiculite. The sample also contains disseminated pyrite and minor chalcopyrite. Pencil lead has a 0.5 mm diameter. Sample: DDHL1872 212.0 m. **C.** Photomicrograph of a relict hornblende phenocryst in hornblende – biotite-bearing monzonite (KNE5) that has been replaced mainly by calcite, with anhydrite, pyrite and phlogopite. The groundmass has been strongly altered to phlogopite – calcite with minor orthoclase. Sample: DDHL1872 364.2 m. **D.** Moderate to strong A1 alteration of pyroxene-phyric basalt breccia (KNE2b). The left half of the image shows the results of K-feldspar staining of the sample, which has dyed K-feldspar yellow. The K-feldspar alteration is patchy within the groundmass and matrix; it is inversely correlated with phlogopite alteration intensity (*chestnut brown*). The strongest K-feldspar alteration is within vein halos surrounding irregular Stage 1E anhydrite – orthoclase – pyrite veins. Pyroxene phenocrysts are altered to anhydrite – phlogopite – pyrite. Sample: DDHL1968 263.8 m. **E.** Photomicrograph of fine-grained hydrothermal phlogopite mantling clinopyroxene crystals in amygdaloidal pyroxene-phyric basalt (KNE2a). Patches of fine-grained phlogopite and orthoclase and abundant disseminated pyrite have replaced the groundmass. Sample: DDHL1856 369.1 m. Abbreviations: anh = anhydrite, cal = calcite, ccp = chalcopyrite, cpx = clinopyroxene, mag = magnetite, or = orthoclase, phl = phlogopite, py = pyrite, vrm = vermiculite.

### *4.3.2 Main-stage alteration*

#### *4.3.2.1 Stage A3: Vuggy adularia alteration*

Stage A3 vuggy adularia alteration is defined by competent, well-indurated, adularia-altered rocks with crystal-shaped and irregular vugs and/or open to partly infilled fractures (Table 4.4; Fig. 4.4). The alteration varies in intensity from weak to strong (5–40 vol% open space) and has obscured primary rock textures. This alteration stage resembles vuggy quartz as in silicic alteration in lithocaps, but is dissimilar in that the mineralogy of the remnant rock material is primarily altered to adularia rather than quartz (Fig. 4.4A and B). Typically, the vugs are small and evenly disseminated creating a fine, spongy, porous texture. The irregular-shaped vugs can have the superficial appearance of vesicles, and some of them may once have been vesicles or amygdules that have been leached. However, the irregular-shaped vugs also occur in a variety of rock types including sedimentary breccias and intrusive igneous rocks. The irregular-shaped vugs occur in the matrix of breccias and have locally crosscut clast margins. Rocks with vuggy adularia alteration are located at intermediate depths (most significantly at ~100–250 m depth below sea level) and are

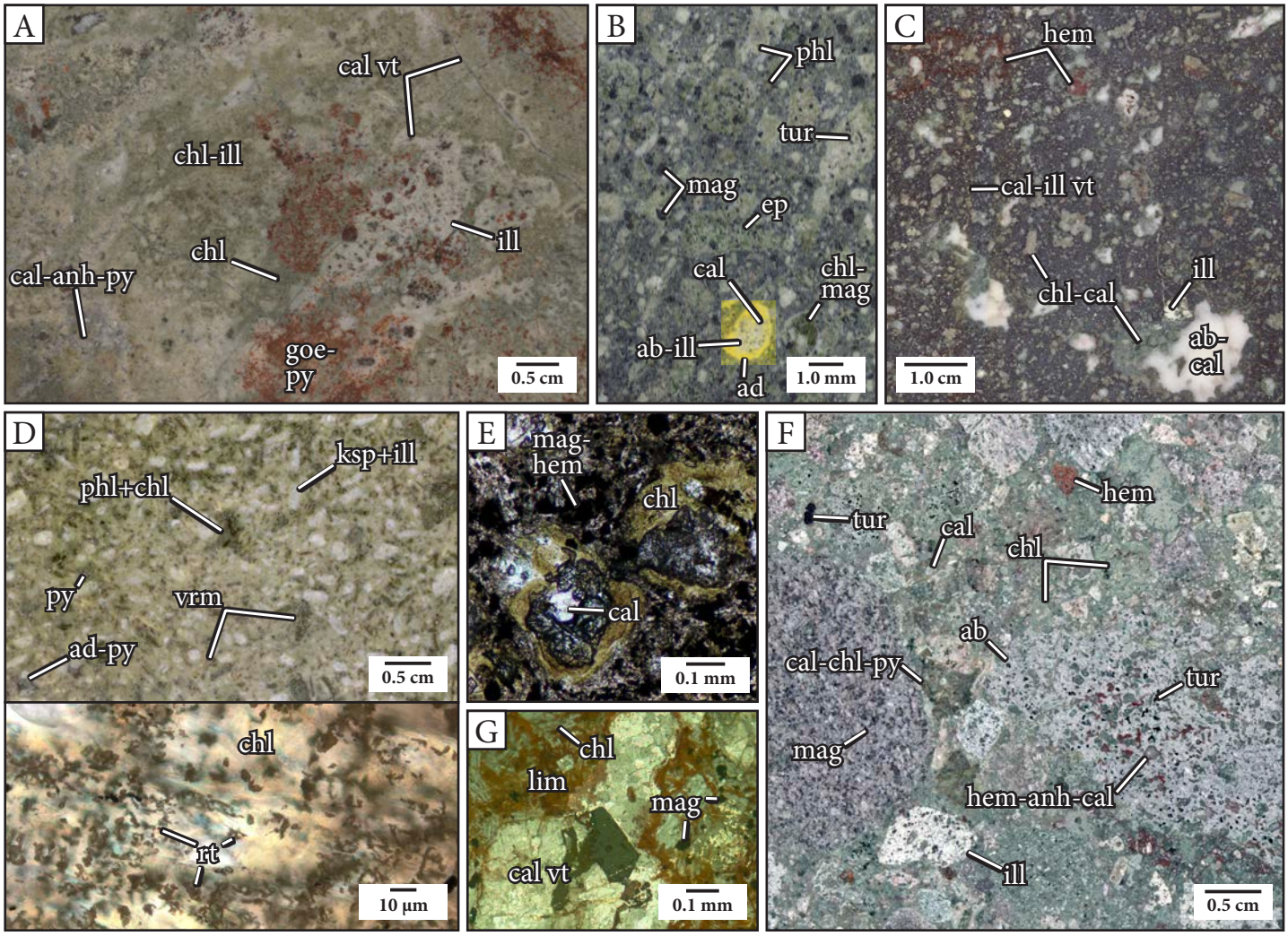


**Fig. 4.3.** **S**tage A2 chlorite alteration. **A.** Pyroxene-phyric basalt breccia (KNE2) that has been moderately altered to patchy illite – goethite, calcite – anhydrite – pyrite and chlorite – illite alteration domains, which obscure clast boundaries. Sample: DDHL1856 217.5 m. **B.** Moderate chlorite alteration of hornblende-bearing gabbro (KNE6). Chlorite – magnetite pseudomorphs after coarse clinopyroxene and patchy epidote – magnetite – chlorite alteration gives this sample the appearance of a crystal lithic sandstone. A section of the photograph (*lower middle*) has a superimposed photograph of the same sample that has been feldspar stained, illustrating late adularia alteration forming a rim around albite – illite – calcite-altered feldspar. Sample: DDHL1928 337.9 m. **C.** Pyroxene-phyric basalt (KNE2) with chlorite alteration. In this sample, amygdules are filled with irregular patches of albite – calcite, chlorite and/or hematite, pyroxene phenocrysts are altered to chlorite and calcite, and the groundmass is altered to magnetite, hematite, chlorite and illite. Small calcite – illite veinlets crosscut the sample and are related to zones of more intense hematite alteration and infill. Sample: DDHL1995 282.3 m. **D.** Weak chlorite alteration overprinting A1 phlogopite alteration in coarse-grained feldspar-phyric latite (KNE9). Hornblende phenocrysts, which were previously altered to phlogopite, are partly to completely replaced by chlorite and rutile. Feldspars have patchy K-feldspar alteration that has been later partly replaced by white illite. Vermiculite, adularia and pyrite are associated with an overprinting alteration stage. The photomicrograph (bottom) shows abundant stubby rutile inclusions in chlorite. Sample: DDHL1932 275.5 m. **E.** Photomicrograph of the same sample as in Figure 4.3C, showing zoned amygdules with cores of calcite and rims of chlorite. Opaques are aggregates of magnetite ± hematite. **F.** Both the clasts and matrix in this polymict matrix-supported breccia (KNE1) have been variably affected by chlorite alteration. Red clasts are altered to hematite, green signifies dominant chlorite alteration and cream clasts are mainly altered to illite. Calcite, hematite, tourmaline, pyrite and anhydrite infill small open spaces such as vesicles in basalt clasts. Sample: DDHL1995 386.8 m. **G.** Photomicrograph of a calcite veinlet within pyroxene-phyric basalt breccia (KNE2). The calcite veinlet has an alteration halo of limonite, consisting mainly of mixed goethite, hematite and iron-stained calcite. Disseminated fine-grained porous magnetite is ubiquitous. Sample: DDHL1995 292.2 m. Abbreviations: ab = albite, ad = adularia, anh = anhydrite, cal = calcite, chl = chlorite, ep = epidote, goe = goethite, hem = hematite, ill = illite, lim = limonite, ksp = K-feldspar, mag = magnetite, phl = phlogopite, py = pyrite, rt = rutile, tur = tourmaline, vrm = vermiculite, vt = veinlet.

strongly correlated with Au mineralization in Kapit NE and Coastal (Fig. 4.1). Stage A3 vuggy adularia alteration is associated with fault zones, and large areas of A3 alteration have formed by the amalgamation of smaller, structurally-controlled domains. Vuggy adularia alteration has sharply overprinted A1 and A2 alteration zones on the scale of centimeters adjacent to small faults (Fig. 4.4F).

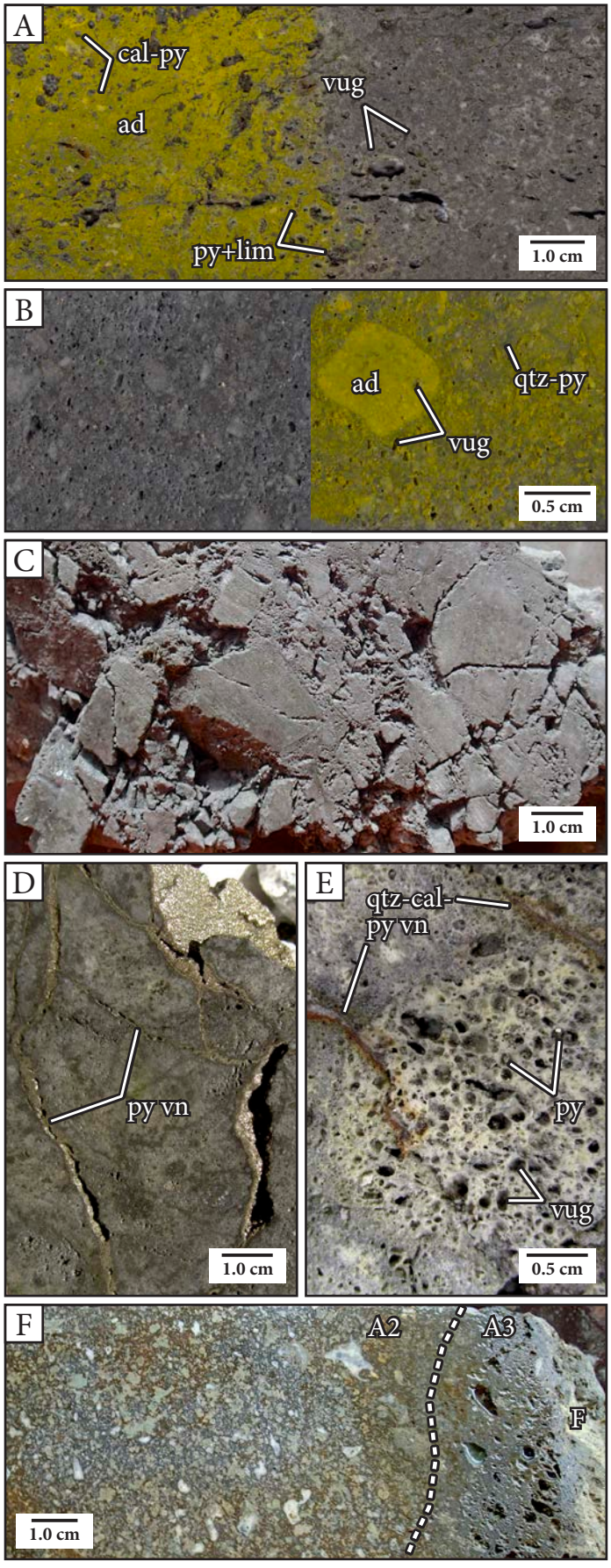


*4.3.2.2 Stage A4: Adularia – pyrite alteration*

Stage A4 alteration is typically strong to intense and texturally destructive. It consists of adularia, pyrite, rutile, illite, marcasite and anhydrite, with minor calcite and quartz, and accessory apatite (Table 4.4). Adularia, the most abundant alteration mineral, occurs as vuggy masses of fine-grained (typically <50 μm) rhombic crystals intergrown with rutile, illite and quartz (Fig. 4.5E). Pyrite is ubiquitous and abundant. It occurs as a replacement of earlier-formed ferromagnesian minerals, as veinlets and discontinuous chains, and in clusters of fine-grained aggregates (Fig. 4.5C and F). Subordinate marcasite, arsenopyrite and other sulfides (chalcopyrite, tetrahedrite, tennantite, molybdenite, sphalerite, galena) occur together locally with the pyrite. Calcite and anhydrite have infilled some vugs (e.g., Fig. 4.5B).

Adularia – pyrite alteration typically has a pervasive distribution and is the dominant alteration type at intermediate depths (~50–250 m below sea level; Fig. 4.1). At depths below ~250 m, strong adularia – pyrite alteration halos (<5 m-wide) surround epithermal veins, faults and breccias that overprint phlogopite and/or chlorite alteration (Fig. 4.5D). Outboard of these zones, weak adularia – pyrite alteration occurs along hairline fractures, as patch-

**Fig. 4.4.** Stage A3 vuggy adularia alteration. **A.** Intense vuggy adularia alteration of pyroxene-phyric basalt (KNE2a). The vugs are either amoeboid (like amygdules) or shaped like pyroxene crystals. Vugs of both types have been partly infilled by calcite, pyrite and limonite. Feldspar staining on the left side of the sample illustrates the pervasive distribution of the adularia alteration. Sample: DDHL1995 279.5 m. **B.** Strong vuggy adularia alteration of pebbly sandstone (KNE1b). Vugs occur in both the clasts and matrix of the sandstone. Feldspar staining on the right side of the image illustrates patchy adularia (*bright yellow*) and quartz – pyrite – adularia (*yellow-gray*) alteration. Sample: DDHL1931 121.0 m. **C.** Intense pervasive gray vuggy adularia alteration that has completely obliterated the primary rock texture. Small vugs (<0.5 mm) occur in clusters throughout the rock. This sample has the appearance of a brecciated rock from which hydrothermal infill has been leached. The sample is well indurated and competent. Sample: DDHL1876 190.9 m. **D.** Moderate pervasive vuggy adularia alteration. Fractures have been partly infilled with botryoidal pyrite. Sample: DDHL1947 133.3 m. **E.** Pyrite aggregates infilling pyroxene-shaped vugs in pyroxene-phyric basalt breccia (KNE2b). The vugs are most apparent within clasts. Sample: DDHL1928 149.5 m. **F.** This sample illustrates vuggy adularia alteration surrounding a fault that has crosscut chlorite-altered pyroxene-phyric basalt. The dashed line delineates the extent of A3 alteration. Sample: DDHL1995 239.0 m. Abbreviations: ad = adularia, cal = calcite, F = fault plane, lim = limonite, py = pyrite, qtz = quartz, vn = vein.

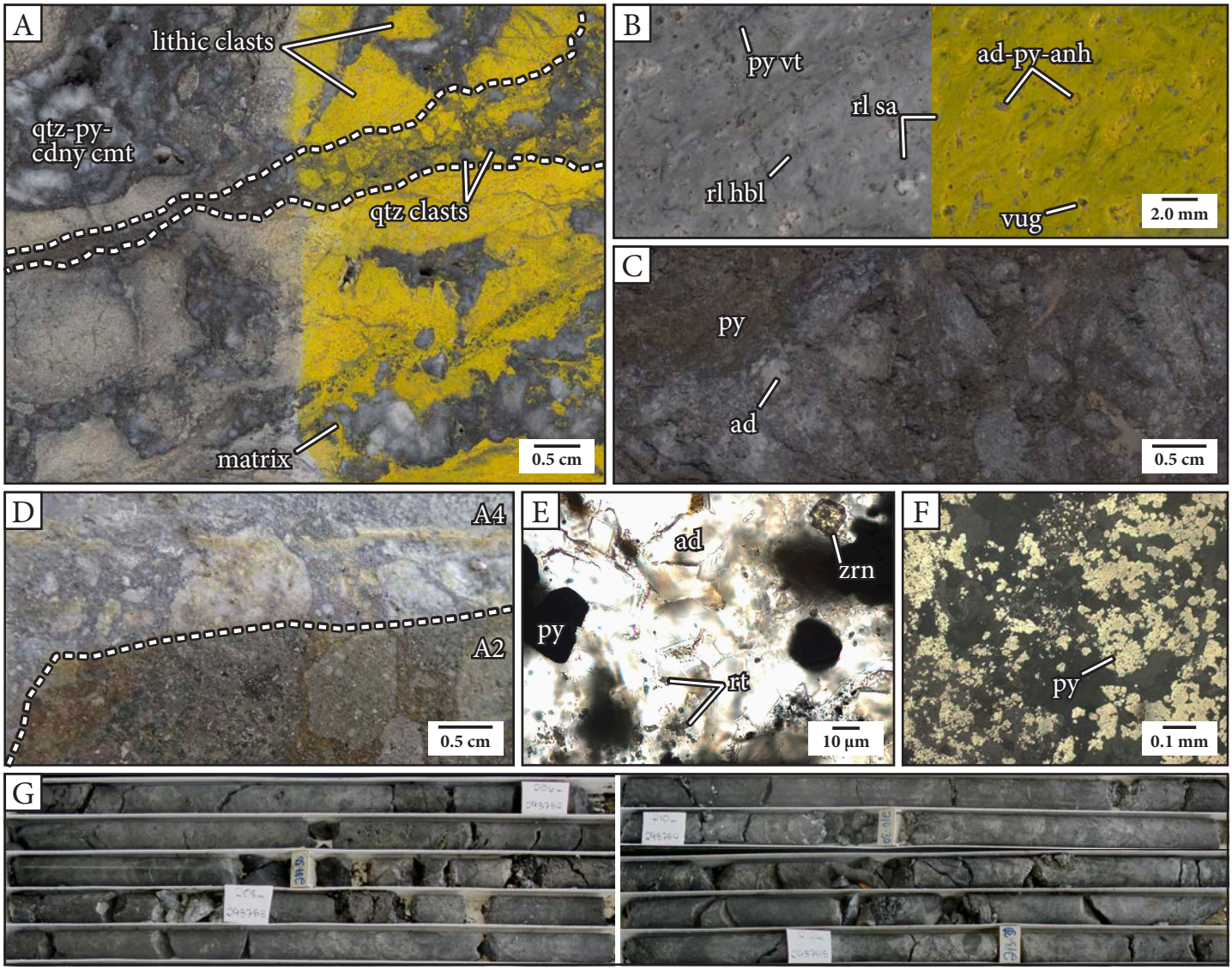


**Fig. 4.5.** Stage A4 adularia – pyrite alteration. **A.** Strong, pervasive adularia – pyrite – quartz alteration of clasts and matrix in a multi-stage, quartz – chalcedony – pyrite-cemented breccia that has crosscut pyroxene-phyric basalt breccia (KNE2b). The white dashed lines in the image outline the youngest stage of quartz clast-bearing, quartz – chalcedony – pyrite-cemented breccia, which has a flaring, wedge-shaped geometry. Feldspar staining of the right side of both sample highlights the distribution of adularia. Note that some patches have not stained yellow; they are altered to quartz and pyrite. Sample: DDHL1856 126.6 m. **B.** Strong, pervasive adularia – pyrite alteration of trachytic hornblende-feldspar-phyric latite (KNE8). Feldspar staining of the right side of the sample highlights the adularia alteration of all elements of the rock sample. Pyrite occurs as fine-grained disseminations and discontinuous veinlets, and has locally precipitated within vugs together with adularia, anhydrite, calcite and quartz. Relict hornblende phenocrysts are altered to pale green illite and pyrite. Sample: DDHL1931 118.0 m. **C.** Patches of dark gray pyrite-dominant alteration, dull brass-colored replacement-style massive pyrite, and light gray adularia alteration in feldspar-phyric andesite breccia (KNE3). In Kapit NE and Coastal areas, darker gray samples typically have a higher pyrite (and gold) content. Sample: DDHL1876 120.1 m. **D.** Hand sample photograph of adularia – pyrite alteration surrounding a fracture within chlorite-altered matrix-supported polymict breccia (KNE1). The alteration front, delineated by the dashed line, has a sharp boundary that crosscuts both clasts and matrix in the breccia. Sample: DDHL1953 229.6 m. **E.** Photomicrograph (plane polarized light) of fine-grained euhedral adularia rhombs with pyrite, zircon (relict?) and rutile. The image is slightly out of focus due to the presence of void spaces in the thin section. Sample: DDHL1924 273.2 m. **F.** Photomicrograph (reflected light) of clustered aggregates of fine-grained porous, zoned pyrite. Sample: DDHL1932 233.2 m. **G.** Dark gray, pyrite-rich A4 alteration and pyritic breccias overprinting vuggy adularia alteration, associated with high gold grades and sulfur contents. For the interval in this photograph (DDHL1930 206–212 m), gold grade averages 18 g/t and sulfur content averages 9% (n = 3; Newcrest Mining Limited two-meter composite assay data). Abbreviations: ad = adularia, anh = anhydrite, cdny = chalcedony, cmt = cement, hbl = hornblende, py = pyrite, qtz = quartz, sa = sanidine, rl = relict, rt = rutile, vt = veinlet, zrn = zircon.

es within the groundmass, and at the edges of previously altered phenocrysts. Stage A4 alteration is spatially associated with and has commonly overprinted vuggy adularia alteration. The highest gold grades in Kapit NE and Coastal areas occur in vuggy rocks that have been overprinted by dark gray pyrite-rich Stage A4 alteration (Fig. 4.5G), pyritic veins and cemented breccias. Typically, darker gray altered rocks contain higher gold content (Fig. 4.5G).

#### *4.3.2.3 Stage A5: Quartz – illite – pyrite alteration*

Stage A5 quartz – illite – pyrite alteration occurs at a moderate depth (150–250 m below sea level), near the intersection of the cross sections depicted in Figure 4.1 and slightly (<500 m) off section to the southwest of this point. Stage A5 occurs as a pocket within the Stage A4 alteration domain and has a similar alteration assemblage, consisting of mostly quartz, illite and pyrite with lesser adularia, calcite, rutile and vermiculite (Table 4.4). It could be considered a subset of adularia – pyrite alteration, but has been separated here due to its distinct appearance and its specific association with quartz – chalcedony and calcite – quartz veins and breccias. In general, Stage A5 alteration has a moderate to strong intensity. It consists of rounded and irregular patches of beige illite that surround clusters of quartz and pyrite that have replaced amygdules and phenocrysts (Fig. 4.6A–B). The quartz – pyrite spots are connected by a network of thin (<0.5 mm-wide) branching quartz veinlets (Fig. 4.6B). Darker patches consist of quartz-dominant alteration with illite – adularia – rutile ± vermiculite and disseminated pyrite. The illite alteration patches do not coincide with clast boundaries associated with the host rocks (Fig. 4.6B). Where quartz – illite – pyrite alteration has overprinted pyroxene-phyric basalt breccia (KNE2b) with amygdules and amoeboid clast morphology, it texturally resembles "ovoid" or "gusano" texture as described from the Tantahuatay high-sulfidation epithermal deposit, Peru (e.g., Noble et al., 2011), and Bantug lithocap, Philippines (Jimenez Torres, 2018). However, Stage A5 alteration is not associated with acid alteration minerals such as alunite or pyrophyllite, and there is no association with high-sulfidation copper or gold mineralization (e.g., enargite, covellite, etc.). Where overprinting vuggy adularia alteration, Stage 5 alteration has infilled the majority of the void spaces with gray fine-grained quartz, adularia and pyrite (Fig. 4.6C). In some cases, a pseudo-amoeboid or wispy clast morphology was produced where illite alteration patches extend from clasts into the matrix (Fig. 4.6C).

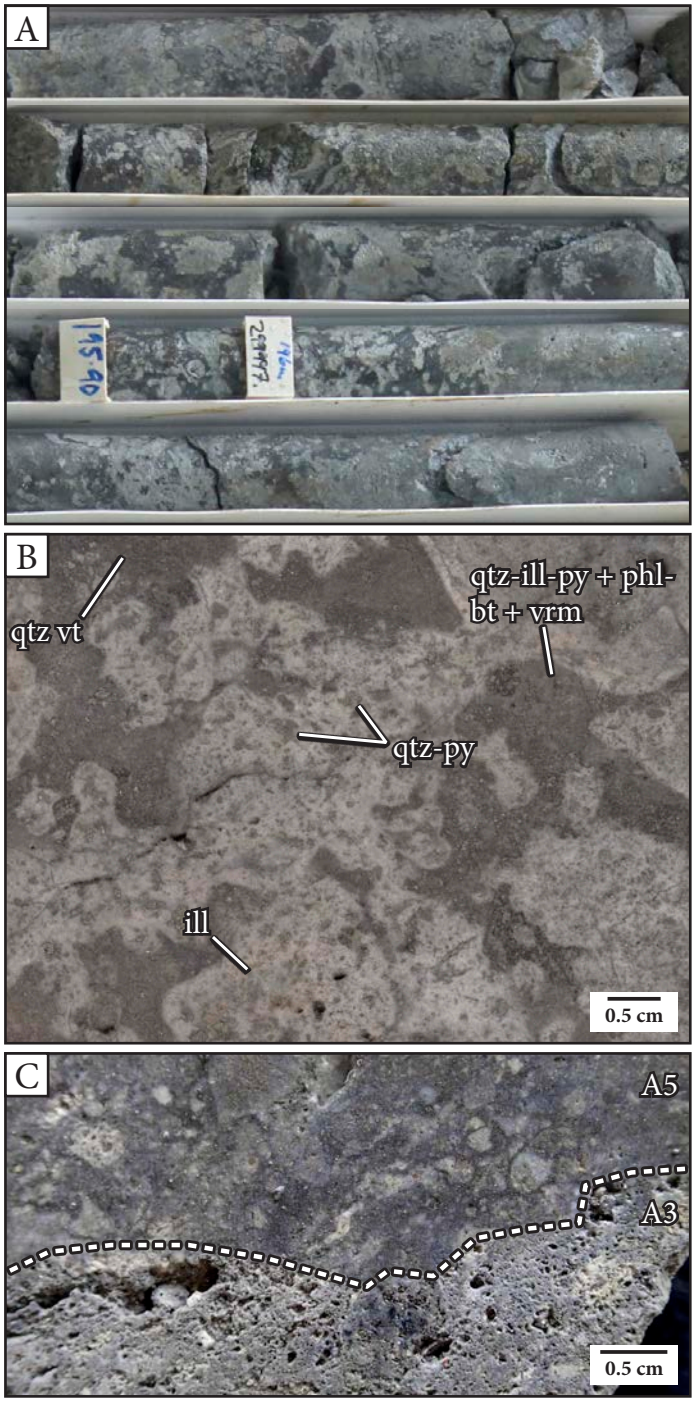


**Fig. 4.6.** Stage A5 quartz – illite – pyrite alteration. **A.** Core box photograph of patchy quartz – illite – pyrite alteration. The lighter colored alteration patches resemble juvenile magmatic clasts. Interval: DDHL1980 ~194.5–196.2 m. **B.** Pseudo-gusano texture (Stage A5 quartz – illite – pyrite alteration) within pyroxene-phyric basalt breccia (KNE2a), overprinting Stage A1 alteration. Conspicuous, globular, intense illite alteration patches surround clusters of quartz – pyrite that have replaced amygdules and phenocrysts and are interconnected by quartz veinlets. The boundaries of the alteration patches crosscut clast margins. Sample: DDHL1974 160.5 m. **C.** A gray-blue Stage A5 alteration front within polymict, matrix-supported breccia (KNE1). The quartz – pyrite dominant alteration infills and overprints Stage A3 vuggy adularia alteration and gives the appearance of some clasts with a wispy morphology. The dashed line delineates the alteration front. Sample: DDHL1953 269.8 m. Abbreviations: bt = biotite, ill = illite, phl = phlogopite, py = pyrite, qtz = quartz, vrm = vermiculite, vt = veinlet.

### *4.3.3 Late-stage alteration*

#### *4.3.3.1 Stage A6: Smectite – kaolinite alteration*

Stage A6 smectite – kaolinite alteration occurs near surface to 70 m below sea level, in a subhorizontal layer that roughly parallels topography. Deeper (down to ~200 m below sea level), upward-flaring zones occur less commonly (Fig. 4.1), and are associated with faults and fracture zones. The Stage A6 alteration domain is typically superjacent to high grade gold mineralization (Fig. 4.1). Smectite – kaolinite alteration is characterized by soft, white to gray-green rocks (Fig. 4.7), and consists of smectite clays (especially montmorillonite), kaolinite, Fe-sulfides (pyrite and/or marcasite) and carbonate (calcite and dolomite) with zones of illite-smectite, illite and muscovite (Table 4.4; Fig. 4.7). The Fe-sulfides occur as fine-grained disseminations, veinlets, discontinuous chains, or in kaolinite – pyrite – marcasite veinlets and veins with kaolinite alteration halos (Fig. 4.7A and D). This alteration ranges from moderate (Fig. 4.7B and D) to intense (Fig. 4.7A and C), commonly obliterates primary rock textures, and results in swelling and disintegration of drill core samples (Fig. 1.1D). It is spatially coincident with weathering and associated with strong post-drilling alteration to copiapite, jarosite, melanterite, chalcanthite, hematite and gypsum (Figs. 1.1

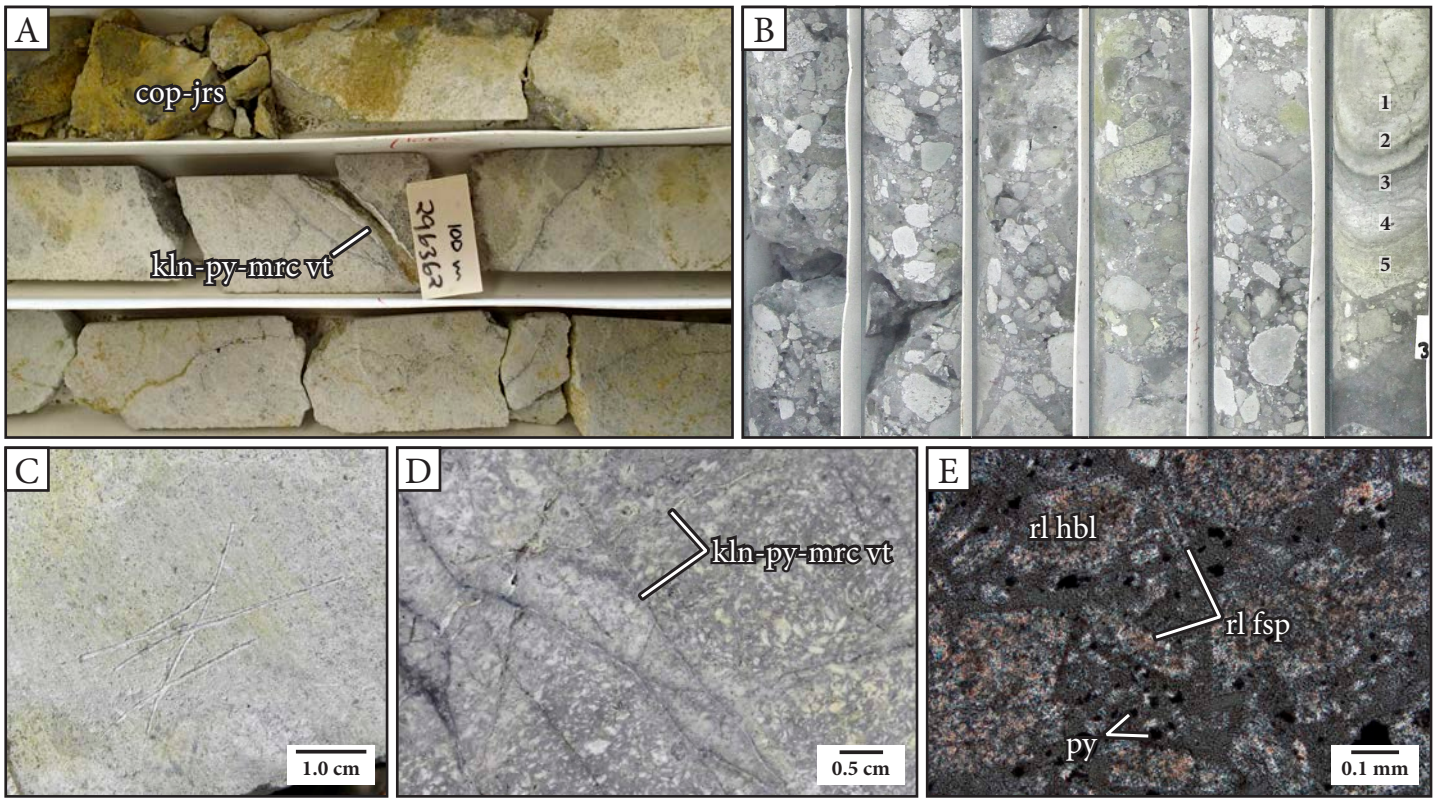


**Fig. 4.7.** Stage A6 smectite – kaolinite alteration. **A.** Core box photograph of strong to intense smectite – kaolinite alteration within pyroxene-phyric basalt breccia (KNE2b). Both clasts and matrix are altered to smectite ± kaolinite, blurring the visual distinction between the two rock components. Disseminated pyrite is ubiquitous. This interval also highlights the association of smectite – kaolinite alteration with kaolinite – pyrite – marcasite veinlets. This alteration zone is typically associated with weathering and intense post-drilling oxidation of drill core to copiapite and jarosite (pictured) and other sulfates. Interval: DDHL1953 ~99–101 m. **B.** Smectite – kaolinite alteration of a polymict, mud matrix-supported breccia with juvenile andesite clasts that has been crosscut by a feldspar-phyric andesite dike (KNE10). The dike has conspicuous dark gray concentric rings defined by pyrite – marcasite aggregates and chains and thicker, light gray rings defined by pervasive smectite alteration with disseminated pyrite. SWIR spectra were acquired at five locations (*labeled 1 to 5*) from the center of the dike to its margin. The primary clay alteration mineral at all five locations was identified as montmorillonite (Appendix E). Interval: DDHL1968 ~70.5–75.5 m. **C.** Intense smectite – kaolinite alteration that has completely obliterated the primary rock texture. The sample has been scored with a stainless steel scratching tool to highlight the earthy luster and softness of the altered rocks. Sample: DDHL1863 58.1 m. **D.** Moderate smectite – kaolinite alteration of hornblende-biotite-bearing monzonite (KNE5) with texturally constructive feldspar alteration to white kaolinite. The sample has been crosscut by a stockwork of kaolinite – pyrite – smectite veinlets with mm-scale, dark gray, pyritic alteration halos. Sample: DDHL1872 155.5 m. **E.** Photomicrograph (cross polarized light) of a light gray band in one of the feldspar-phyric andesite (KNE10) dikes shown in Figure 4.7B. The image shows strong alteration of both phenocrysts and groundmass to fine-grained intergrown smectite (brown), illite-smectite (pastels), kaolinite (white and gray) and pyrite (opaques). Sample: DDHL1968 78.8 m. Abbreviations: cop = copiapite, fsp = feldspar, hbl = hornblende, jrs = jarosite, kln = kaolinite, mrc = marcasite, py = pyrite, rl = relict, vt = veinlet.

and 4.7A). Outside of the Stage A6 alteration domain as depicted in Figure 4.1, subtle to weak smectite alteration has a widespread and ubiquitous distribution. The moderate to intense, pervasive clay alteration domains have sharp boundaries with older alteration zones (Stages A1–A5).

#### *4.3.3.2 Stage A7: Kaolinite – alunite alteration*

Stage A7 alteration produced soft to moderately hard, strongly fractured and veined rocks that have been altered to kaolinite, alunite, quartz, smectite, pyrite, marcasite, aluminum phosphate-sulfate (APS) minerals (primarily woodhouseite) and jarosite with rare dickite, illite and opal (Table 4.4). The rocks are typically mottled dark gray, peach, yellow or white (Fig. 4.8A). Native sulfur and halloysite were not observed in Kapit NE or Coastal, but have been identified together with kaolinite, alunite and opal at Alaia rock, near Coastal, and at Lienetz (Fig. 4.8C–D). Alunite crystals are predominantly pseudo-cubic, poorly to moderately crystalline and fine-grained (<5–200 µm; Fig. 4.8E). The alunite occurs both as a pervasive alteration and also within spatially associated alunite ± kaolinite ± pyrite ± opal veins and breccias (e.g., Fig. 4.8C–D). Fe-sulfides are fine-grained, have complex morphologies and occur as disseminations, patches, discontinuous and dendritic veinlets and as overgrowths on previously formed sulfide minerals. The APS minerals are interpreted to have formed through the dissolution and replacement of apatite under acid conditions (i.e., pH <3; e.g., Stoffregen and Alpers, 1987). Stage A7 alteration occurs subjacent to historical geothermal features in the near surface (<100 m). It transitions laterally into smectite – kaolinite alteration, and is situated above deep, fault-related Stage A6 alteration zones (Fig. 4.1). Stage A7 alteration zones are locally associated with high grade Au mineralization (Fig. 4.1) and elevated base metal contents, especially copper. The elevated copper contents are associated with Stage 3B quartz – marcasite – pyrite ± tennantite ± gold stockwork veins with rare replacement of chalcopyrite to covellite.

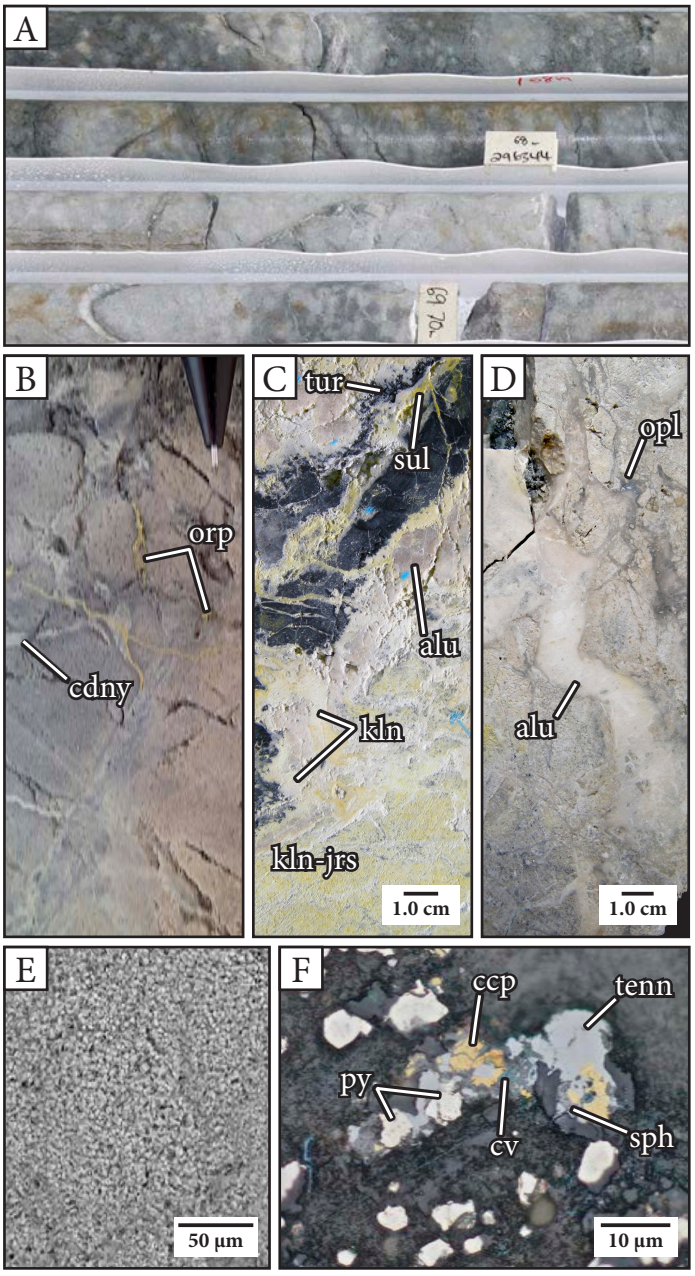


**Fig. 4.8.** Stage A7 kaolinite – alunite alteration. **A.** Core box photograph illustrating the typical mottled dark gray-light pink appearance of strong to intense kaolinite – alunite – quartz alteration in feldspar-phyric andesite breccia (KNE3). Darker gray patches are associated with increased quartz and pyrite content. Interval: DDHL1953 ~67–70 m. **B.** Quartz – alunite alteration that has overprinted Stage A3 vuggy adularia alteration. Milky white chalcedony and yellow-orange orpiment have partly infilled fractures and vugs. Pencil lead is 0.5 mm in diameter for scale. Sample: DDHL1872 57.2 m. **C.** and **D.** Alunite breccia veins within quartz – alunite-altered rocks from Alaia Rock (near Coastal) and Lienetz, respectively. Stage A7 alteration is typically distributed around similar alunite-bearing veins and fault zones. Samples: DDHL0773 108.1 m (C) and DDHL0754 76.2 m (D). **E.** SEM image of an aggregate of very fine-grained (<5 µm), moderately crystalline pseudocubic alunite grains from the cement of the breccia vein in Figure 4.8C. **F.** Local partial replacement of chalcopyrite by covellite within a quartz – chalcedony – pyrite – chalcopyrite – tennantite – marcasite stockwork vein. Sample: DDHL1872 99.5 m. Abbreviations: alu = alunite, ccp = chalcopyrite, cdny = chalcedony, cv = covellite, jrs = jarosite, kln = kaolinite, opl = opal, orp = orpiment, py = pyrite, sph = sphalerite, sul = native sulfur, tenn = tennantite, tur = tourmaline.

## 4.4 Hydrothermal breccias and veins

### *4.4.1 Stage 1: Anhydrite breccias and veins*

#### *4.4.1.1 Stage 1A: Albite ± actinolite veinlets*

Stage 1A albite ± actinolite veinlets are the oldest vein stage observed within the study area. The veinlets are rare, occurring over a restricted interval (DDHL1928 328.0–334.0 m) within hornblende-bearing gabbro (KNE6) and crystal-poor, plagioclase-phyric andesite (KNE7) at the western extent of Kapit NE (Fig. 4.9). Stage 1A consists of thin (<1 mm), irregular, branching, albite ± actinolite veinlets with conspicuous white albite alteration halos (up to 3 cm-wide; Fig. 4.10). The albite alteration is selective, affecting only the groundmass and feldspar phenocrysts. The selective style causes the alteration halos to have a crystalline, dike-like appearance (Fig. 4.10A). Stage 1A veins have been crosscut by Stage 1B anhydrite – magnetite veins, Stage 1E anhydrite – pyrite veins and Stage 1G anhydrite veins (Fig. 4.10) and have not been observed to crosscut any other vein stages. Stage 1A veins also occur within hornblende-bearing gabbro clasts in Stage 1C polymict, anhydrite – chlorite – calcite-cemented breccia in Coastal area (Fig. 4.12A), suggesting that Stage 1A veinlets may have a more widespread distribution than has been observed in this study.

#### *4.4.1.2 Stage 1B: Anhydrite – magnetite ± chalcopyrite ± chlorite veins and amygdules*

Stage 1B anhydrite – magnetite ± chalcopyrite ± chlorite veins and amygdules occur in the west of Kapit NE (e.g., DDHL1968 and DDHL1928) at depths >300 m (Fig. 4.9). This stage is characterized by the presence of euhedral, fine-grained anhydrite and anhedral magnetite as key mineral phases. Chalcopyrite and chlorite locally occur as dominant phases (Fig. 4.11E) or as fine-grained disseminations within veins (Fig. 4.11A). Minor phases include biotite, orthoclase and pyrite. Due to the presence of chalcopyrite, this stage is associated with a minor copper anomaly (e.g., 0.2 wt% Cu over 15 m; DDHL1968 305–320 m). However, it is not associated with significant gold mineralization.

Stage 1B locally formed stockworks, branching veins or amygdules. Stockworks are moderate to intense (e.g., with frequencies of up to hundreds of veins per meter; Fig. 4.11B) and consist of randomly oriented, branching and irregular hairline fractures or thin veins (<2 mm vein aperture) with sharp vein walls (e.g., Figs. 4.11A–B and 4.14B) and typically alternating mineralogy of anhydrite ± orthoclase and magnetite ± chalcopyrite ± pyrite ± chlorite (Fig. 4.11A). Individual veins in the stockworks commonly have a 'zigzag' form, with sharp, high-angle bends along their lengths. Branching veinlets are thin (0.5–1.0 mm) and anastomosing with diffuse, indistinct vein walls that blend in with the surrounding vein halo alteration (Fig. 4.11C). Infilled vesicles (amygdules) are zoned, with anhydrite lining the vesicle rim and magnetite in the core. The amygdules are only present within crystal-poor, plagioclase-phyric andesite (KNE7; e.g., Fig. 4.11A). Stage 1B veins and amygdules have thin (~1 mm), creamy white anhydrite ± albite alteration halos that locally contain disseminated magnetite (Fig. 4.11F). The alteration halos are best seen within crystal-poor, plagioclase-phyric andesite (KNE7; Figs. 4.11A and 4.14A–B).

Stage 1B veins crosscut Stage 1A albite – actinolite veinlets (Figs. 4.10A and C, and 4.11E). They are spatially associated with crystal-poor, plagioclase-phyric andesite (KNE7), occurring within KNE7 intrusions and adjacent to their contacts (Figs. 3.15C and 4.9). Stage 1B veins are crosscut by Stage 1E anhydrite – pyrite veins (Figs. 4.10A–B, 4.11C and 4.14A–B) and by Stage 1F anhydrite – calcite ± hematite veins (Fig. 4.11D). Near Stage 1E anhydrite – pyrite veins, the Stage 1B alteration halos are overprinted by orthoclase alteration and magnetite is partly replaced by platy, red hematite and pyrite (Figs. 4.11C–D and G, and 4.14A–C). This gives the Stage 1B veins and alteration halos a red to purple hue (Fig. 4.11C).

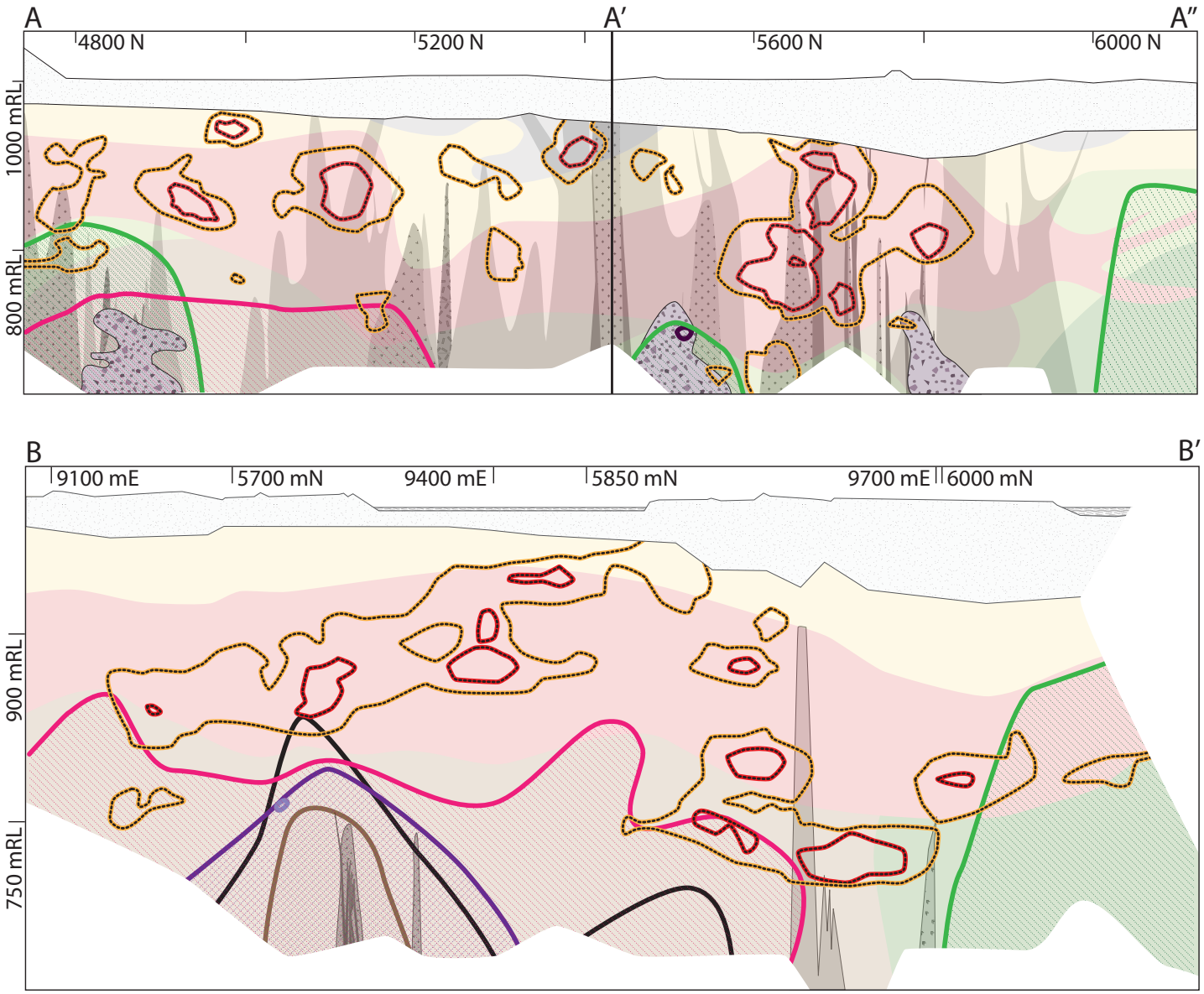


**Lithotypes**

- Waste rock
- Trachytic hornblende- feldspar-phyric latite (KNE9)
- Hornblende-feldspar-phyric latite (KNE8)
- Crystal-poor, feldspar-phyric trachyte (KNE7)
- Hornblende-bearing gabbro (KNE6)
- Hornblende-biotite-bearing monzonite (KNE5)
- Nepheline-bearing monzonite (KNE4)
- Volcano-sedimentary rocks (KNE1–3)

**Stage 1 veins and breccias**

- Stage 1I: Massive and banded anhydrite ± pyrite breccias and veins
- Stage 1H: Anhydrite vein-clast breccia
- Stage 1G: Tabular anhydrite and carbonate veins
- Stage 1F: Anhydrite – calcite – chlorite veins
- Stage 1E: Anhydrite – pyrite veins
- Stage 1D: Biotite – anhydrite veins
- Stage 1C: Polymict, anhydrite – chlorite – calcite-cemented breccia
- Stage 1A: Albite ± actinolite veinlets ***and*** Stage 1B: Anhydrite – magnetite ± chalcopyrite ± chlorite veins and amygdules

**Alteration**

- Stage A7 – Quartz-alunite
- Stage A6 – Smectite-kaolinite
- Stage A3-A5 – Main-stage
- Stage A2 – Mg-chlorite
- Stage A2 – Fe-chlorite
- Stage A1 – Phlogopite

**Grade shells**

- >5 g/t Au
- >3 g/t Au

**Fig. 4.9.** Distribution of Stage 1 hydrothermal breccias and veins on cross sections A–A'–A" and B–B' in Kapit NE and Coastal.

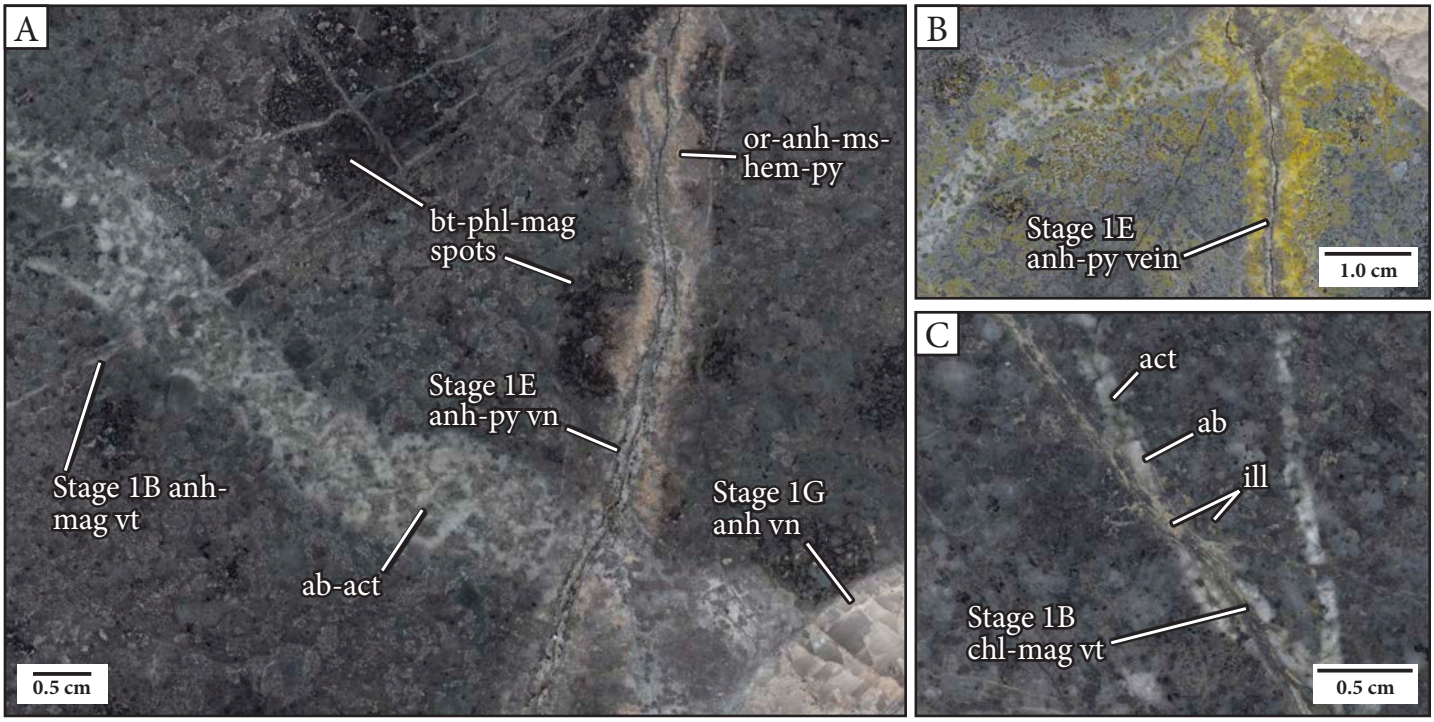


**Fig. 4.10.** Stage 1A albite ± actinolite veinlets with albite alteration halos. **A.** Hand sample photograph of a Stage 1A albite – actinolite veinlet and albite alteration halo within phlogopite-altered hornblende-bearing gabbro (KNE6). The albite – actinolite veinlet around which the conspicuous albite alteration halo is centered is almost indistinguishable, giving the vein/alteration halo the appearance of a diorite dike. This photograph shows several other stages of anhydrite veins (Stage 1B, Stage 1E and Stage 1G) crosscutting the Stage 1A vein. Sample: DDHL1928 329.6 m. **B.** Feldspar stained image of the same sample as in Figure 4.10A, showing that the white feldspars in the alteration halo to the Stage 1A vein are not K-feldspar. Strong pervasive orthoclase alteration is focused around Stage 1E anhydrite – pyrite and Stage 1B anhydrite – magnetite veins and overprints the Stage 1A albite alteration halo. Orthoclase alteration of mafic minerals (that had previously been altered to phlogopite) is strongest closest to the intersection of the Stage 1A, 1B and 1E veins, and becomes weaker with distance from the Stage 1E vein, with which it appears to be genetically associated. **C.** An example of well-defined, green actinolite – albite veinlets (~0.1 mm-wide) with albite alteration halos (up to 4 mm-wide). The Stage 1A veinlets have been crosscut by Stage 1B chlorite – magnetite – anhydrite – orthoclase veinlets, in which orthoclase has partly altered to beige illite. Sample: DDHL1928 344.7 m. Abbreviations: ab = albite, act = actinolite, anh = anhydrite, bt = biotite, chl = chlorite, hem = hematite, ill = illite, mag = magnetite, ms = muscovite, or = orthoclase, phl = phlogopite, py = pyrite, vn = vein, vt= veinlet.

#### *4.4.1.3 Stage 1C: Polymict, anhydrite – chlorite – calcite-cemented breccia*

Stage 1C breccias occur as two separate bodies that have been intersected along north-trending cross sections A–A' in Coastal and A'–A" in Kapit NE (Figs. 3.3 and 4.9). One of the two breccia bodies span from 5,500 to 5,800 mN in Kapit NE as a northeast-trending wedge that thickens and deepens to the northeast (plunge: ~25°/050°). The breccia is 250 m-wide, >370 m-long and has a variable thickness up to about 80 m. The second breccia body has a west-plunging (~24°/275°) ellipsoid morphology in the Coastal area (~4,900 mN) and is at least 300 m-long, 125 m-wide and up to 80 m-thick. Contacts observed in drill core were obscured by faults with late-stage montmorillonite – pyrite alteration. Stage 1C breccias have moderate average gold and copper contents (0.51 g/t Au and 0.04% Cu; Newcrest Mining Limited two-meter composite assay data; n = 121) associated with crosscutting veins and breccias.

In general, Stage 1C breccias have a subdued character and are difficult to identify without careful observation. They are typically massive, polymict, chaotic, and clast- to matrix-supported (60 to >90% clasts) with 1–10% cement composed of granular anhydrite, massive to euhedral, rhombic (locally Fe-stained) calcite, chlorite and pyrite (Fig. 4.12A and H). The clasts are pebble- to cobble-sized, moderately to poorly sorted, subangular to round and typically subspherical. Many of the clasts are faceted, with distinctive hexagonal and pentagonal shapes that probably reflect fracture patterns that formed in the host rocks prior to brecciation (Fig. 4.12E). There are a wide variety of lo-

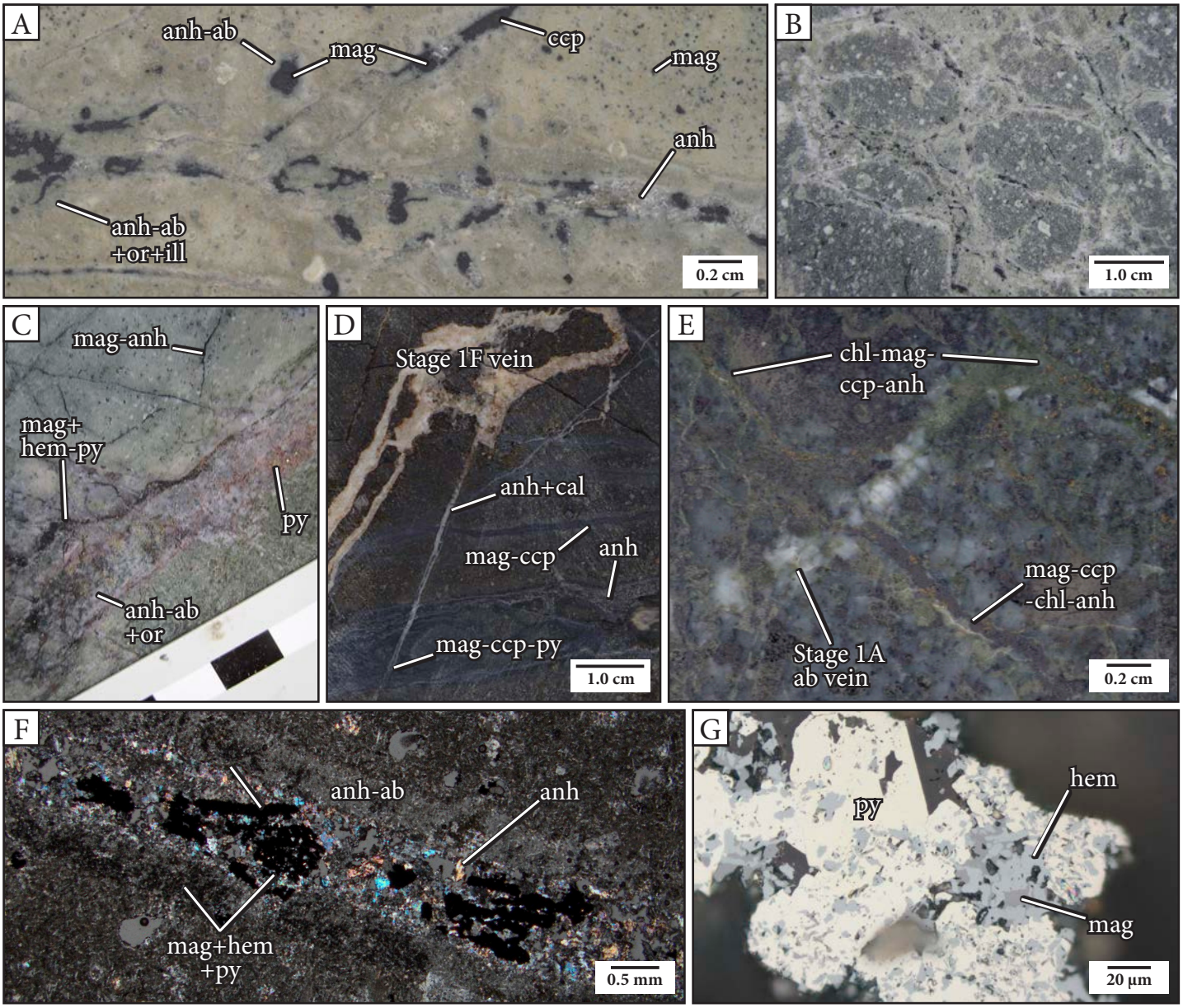


**Fig. 4.11.** Stage 1B anhydrite – magnetite ± chalcopyrite ± chlorite veins and amygdules with anhydrite ± albite ± magnetite alteration halos. **A.** Stage 1B anhydrite – magnetite veinlets and zoned amygdules within crystal-poor, plagioclase-phyric andesite (KNE7). The distribution of magnetite and anhydrite is uneven along the length of veinlets, with alternating magnetite ± chalcopyrite-dominant and anhydrite – orthoclase-dominant intervals. Light green to buff anhydrite – albite alteration halos (~1 mm-wide) have been altered to orthoclase + illite. Sample: DDHL1928 335.4 m. **B.** An intense stockwork of Stage 1B anhydrite – magnetite veinlets within hornblende-bearing gabbro (KNE6). Individual veinlets are irregular and bend along sharp angles or form branches. Sample: DDHL1928 337.9 m. **C.** Anastomosing, diffuse Stage 1B anhydrite – magnetite veinlets that appear to grade into the adjacent vein halo alteration. The reddish to purple hue around the vein is related to later alteration of magnetite to hematite + pyrite. Sample: DDHL1928 347.1 m. **D.** Dark blue Stage 1B magnetite – chalcopyrite – anhydrite veinlets within pyroxene-phyric basalt breccia (KNE2). The veins have been crosscut by Stage 1F anhydrite – calcite – hematite veins. Sample: DDHL1968 316.2 m. **E.** Chalcopyrite- and chlorite-rich Stage 1B veinlets within hornblende-bearing gabbro (KNE6) have crosscut Stage 1A albite – actinolite veinlets. Sample: DDHL1928 334.7 m. **F.** Photomicrograph of a vuggy Stage 1B veinlet with alternating anhydrite and magnetite domains. Very fine grained magnetite, anhydrite and albite alter the groundmass immediately adjacent to the vein. Sample: DDHL1928 344.3 m. **G.** Reflected light photomicrograph of magnetite from the centerline of a Stage 1B anhydrite – magnetite vein. The magnetite has been partly replaced by hematite and overprinted by pyrite. Sample: DDHL1928 347.1 m. Abbreviations: ab = albite, anh = anhydrite, cal = calcite, ccp = chalcopyrite, chl = chlorite, hem = hematite, ill = illite, mag = magnetite, or = orthoclase, py = pyrite.

cally sourced clast types, all of which were altered to Stage A1 phlogopite (Fig. 4.12A) or Stage A2 chlorite (Fig. 4.12F) prior to brecciation. The clast types include hornblende-biotite-bearing monzonite (KNE5), hornblende-bearing gabbro (KNE6; some of which contain truncated Stage 1A and 1B veins; Fig. 4.12A and F), magnetite (Stage 1B vein fragments; Fig. 4.12F), pyroxene-phyric basalt and basalt breccia (KNE2), coarse- and medium-grained diorite and

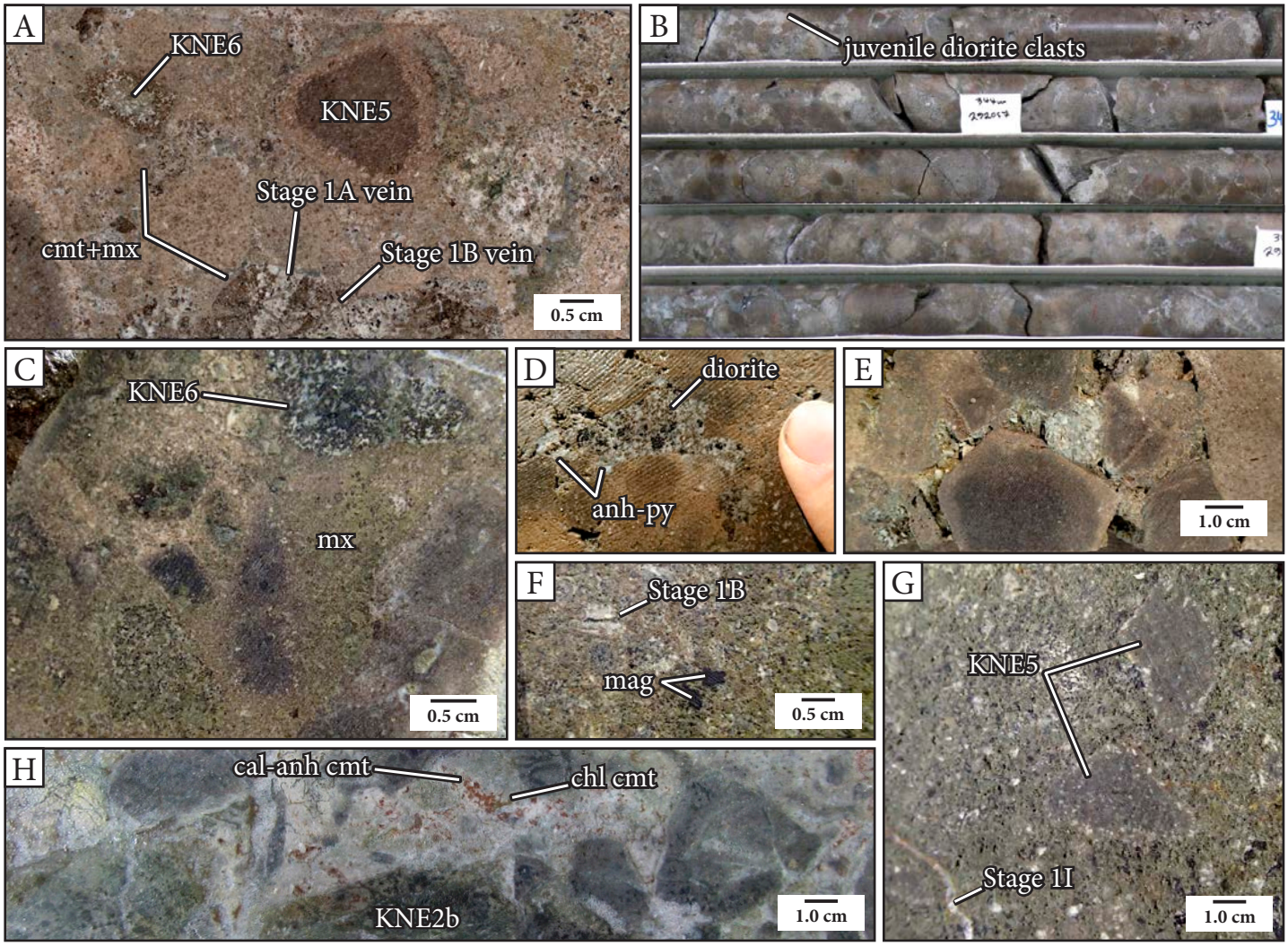


**Fig. 4.12.** Stage 1C polymict, anhydrite – chlorite – calcite-cemented breccia. **A.** Clast-supported, polymict breccia with inconspicuous anhydrite – chlorite – calcite – pyrite cement and sand-sized lithic matrix. Clasts and matrix in this sample are predominantly intrusive rock fragments (KNE5 and KNE6) with pervasive, pre-brecciation phlogopite – magnetite – orthoclase alteration. One of the gabbro clasts has truncated Stage 1A albite – actinolite and Stage 1B anhydrite – magnetite veins. The matrix, granule-sized clasts and the outer 0.5 cm outer rim of pebble- and cobble-sized clasts are altered to chlorite, calcite, anhydrite, vermiculite and pyrite. Sample: DDHL1872 369.4 m. **B.** Core box photograph of an interval of Stage 1C polymict breccia, highlighting the distribution of diorite cement (*gray*) between clasts and altered matrix (*pinkish brown*). Interval: DDHL1924 ~345.4–348.0 m. **C.** Matrix-rich, polymict, anhydrite – chlorite – calcite-cemented breccia. The sample has patchy, weak to intense chlorite and calcite alteration that blurs the distinction between clasts and matrix. Sample: DDHL1872 346.1 m. **D.** An irregular patch of diorite that is intergrown with euhedral anhydrite and pyrite infill within the cement of the polymict, anhydrite – chlorite – calcite-cemented breccia. Sample: DDHL1924 346.0 m. **E.** Subangular, subspherical clasts with anhydrite – orthoclase – calcite – vermiculite alteration rinds. The cement material has been leached, leaving void spaces between clasts. Sample: DDHL1924 333.7 m. **F.** A clast with a truncated Stage 1B vein and angular Stage 1B magnetite fragments in a calcite-chlorite-altered, matrix-rich Stage 1C breccia. Sample: DDHL1924 300.4 m. **G.** Matrix-rich Stage 1C breccia containing Stage 1B magnetite fragments and phlogopite-altered monzonite clasts (KNE5) with anhydrite – vermiculite – K-feldspar – calcite alteration rinds. The sample has been crosscut by a Stage 1I massive anhydrite vein. Sample: DDHL1924 300.6 m. **H.** Hand sample photograph of a clast-rotated and cement-supported breccia from Coastal (~4,900 mN). The cement is composed of Fe-stained rhombic calcite, fine-grained granular anhydrite and anhedral chlorite. The clasts are monomict, consisting of rounded pyroxene-phyric basalt breccia (KNE2b) with pervasive, pre-brecciation chlorite – magnetite – calcite alteration. The rims of the clasts have prominent white syn-brecciation alteration rinds of calcite, anhydrite, orthoclase, vermiculite, pyrite and chlorite. Sample: DDHL1856 330.1 m. Abbreviations: anh = anhydrite, cal = calcite, chl = chlorite, cmt = cement, mag = magnetite, mx = matrix, py = pyrite.

trachytic monzonite or latite (similar to KNE8). Pods of monomict (pyroxene-phyric basalt clast-bearing), anhydrite – chlorite – calcite-cemented breccia have formed at Coastal (Fig. 4.12H). Locally, the breccia contains juvenile diorite clasts and/or cement (Fig. 4.12B and D). The matrix is fine to coarse sand-sized and is composed of lithic fragments with the same compositions as the clasts. It typically has weak to intense, patchy chlorite alteration (e.g., Fig. 4.12C). Locally, the matrix and the outer margins of individual clasts have been altered to anhydrite, K-feldspar, calcite, vermiculite and actinolite (Fig. 4.12G). The alteration rinds have locally altered the appearance of the

breccia, producing 'blobby' clast shapes and blurring the distinction between clasts, matrix and cement components (Fig. 4.12C). Open space is absent to minor (0–9%) and is interpreted to have been produced post-brecciation via leaching of anhydrite from the cement as it is spatially associated with Stage A3 vuggy adularia alteration.

#### *4.4.1.4 Stage 1D: Biotite – anhydrite veinlets*

Stage 1D is very minor in the Coastal area (Fig. 4.9), consisting of a small cluster of thin (<1 mm), irregular, black biotite – anhydrite veinlets within a hornblende-bearing gabbro (KNE6) dike that has crosscut Stage 1C polymict, anhydrite – chlorite – calcite-cemented breccia (Fig. 4.13). The veinlets do not have any obvious associated alteration halos when viewed at the hand specimen scale.

#### *4.4.1.5 Stage 1E: Anhydrite – pyrite veins*

Stage 1E consists of narrow (<0.5 cm-wide), discrete, anhydrite – pyrite – orthoclase ± calcite ± chalcopyrite ± molybdenite ± phlogopite ± magnetite ± trace apatite veins that have distinctive, well-formed K-feldspar – anhydrite – phlogopite – muscovite – pyrite – rutile ± chalcopyrite ± molybdenite alteration halos (Figs. 4.10A–B and 4.14). Fine- to coarse-grained anhydrite is the dominant vein mineral. The anhydrite has either massive or cockscomb texture, defined by tabular, euhedral crystals that grow perpendicular to the vein walls (Fig. 4.14D). Orthoclase occurs as blocky crystals intergrown with anhydrite and granular calcite. Pyrite occurs as fine-grained, subhedral pyritohedra or as anhedral intergrowths with chalcopyrite, and often contains magnetite inclusions (Fig. 4.14E). Pyrite ± chalcopyrite ± molybdenite form preferentially at the margins of the veins and locally occupy the centerline of the vein (between anhydrite laths; Fig. 4.14D and G).

Stage 1E veins are sparse and are restricted to deeper levels of Kapit NE area, typically within Stage A1 phlogopite-altered rocks (Fig. 4.9). Stage 1E veins are observed to have crosscut Stage 1A–C; however, they have not been observed in contact with Stage 1D biotite – anhydrite veins.

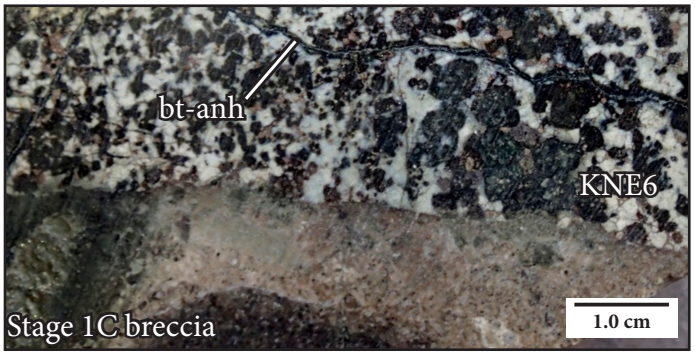


**Fig. 4.13.** Stage 1D biotite – anhydrite veinlets. **A.** Hand sample photograph of a wavy biotite – anhydrite veinlet that has crosscut a hornblende-bearing gabbro dike (KNE6). Sample: DDHL1872 346.9 m. Abbreviations: anh = anhydrite, bt = biotite.

#### *4.4.1.6 Stage 1F: Anhydrite – calcite – chlorite veins and breccias*

Stage 1F veins and breccia veins are sparsely distributed within the Stage A2 chlorite alteration domain (and to a lesser extent within the Stage A1 phlogopite alteration domain) and typically occur at >150 m below sea level (Fig. 4.9). Stage 1F veins are typically thin (<1 cm-wide) and branching, and they range from irregular with diffuse vein walls (Fig. 4.15A, B, D and F) or straight-sided with sharp vein walls (Fig. 4.15C). Many of the veins have layered mineral infill and have crosscut one another, providing evidence for multiple stages of emplacement (Fig. 4.15B). Tabular Stage 1F breccias occur rarely, and typically comprise <5 cm-wide intervals with monomict, cement-supported and clast-rotated organization (Fig. 4.15G). Stage 1F veins and breccias have crosscut Stage 1C polymict, anhydrite – chlorite – calcite-cemented breccia (Fig. 4.15A and D); however, they have not been observed in contact with Stage 1D biotite – anhydrite veinlets or Stage 1E anhydrite – pyrite veins.

Stage 1F veins and breccias are composed of anhydrite, calcite, chlorite, quartz, K-feldspar, actinolite, chalcopyrite, pyrite, sphalerite and galena in variable proportions and

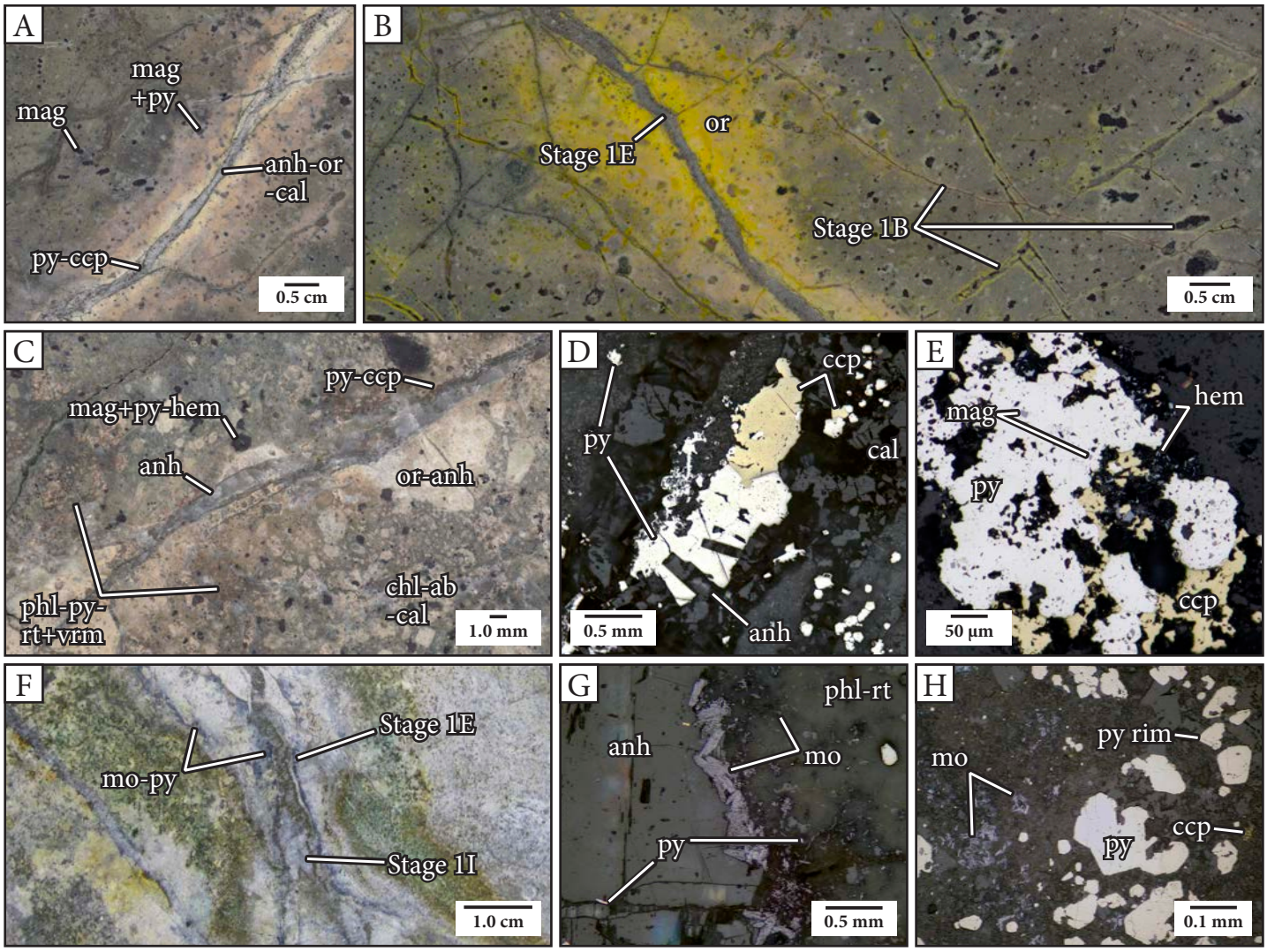


**Fig. 4.14.** Stage 1E anhydrite – pyrite veins. **A.** A Stage 1E anhydrite – orthoclase – calcite – pyrite – chalcopyrite vein within crystal-poor, plagioclase-phyric andesite (KNE7). The vein has a pronounced beige to peach alteration halo consisting of anhydrite – phlogopite – pyrite – chalcopyrite. Sample: DDHL1928 344.3 m. **B.** Feldspar-stained image of the reverse side of the same polished slab as in Figure 4.14A, highlighting the strong intensity of orthoclase alteration (*yellow stain*) around the Stage 1E vein. The orthoclase alteration in the halo around Stage 1B anhydrite – magnetite veins and interconnected amygdules decreases in intensity away from the Stage 1E vein, and is interpreted to be associated with Stage 1E. **C.** A typical Stage 1E anhydrite – pyrite vein within pervasively chlorite – albite – calcite – magnetite-altered hornblende-bearing gabbro (KNE6). The alteration halo in this sample is inconspicuous and selective, consisting of phlogopite – pyrite – rutile alteration of mafic phenocrysts and patches in the groundmass and orthoclase – anhydrite alteration of feldspars and patches within the groundmass. Magnetite phenocrysts and blebs in the alteration envelope have been altered to pyrite + hematite and much of the phlogopite has altered to vermiculite. Sample: DDHL1928 337.9 m. **D.** Reflected light photomicrograph showing intergrown pyrite and chalcopyrite occupying the centerline of the Stage 1E anhydrite – pyrite vein in Figure 4.14A and occurring as disseminations in the vein halo. Anhydrite vein fill has a cockscomb texture, defined by euhedral, tabular anhydrite crystals growing from the vein wall towards the center of the vein. **E.** Reflected light photomicrograph of disseminated intergrown pyrite (with magnetite inclusions) and chalcopyrite surrounded by very fine-grained hematite laths in the alteration halo of the Stage 1E vein in Figure 4.14A. **F.** Anastomosing Stage 1E anhydrite – orthoclase – molybdenite – pyrite veins with orthoclase – anhydrite – phlogopite – pyrite – molybdenite – chalcopyrite alteration halos. The Stage 1E veins have been overprinted by a branching, Stage 1I massive anhydrite – pyrite vein and pervasive illite-smectite ± montmorillonite alteration. Green copper and orange Fe-staining correspond with the presence of chalcopyrite and pyrite in the vein halo. Sample: DDHL1928 280.5 m. **G.** Reflected light photomicrograph of the Stage 1E vein from Figure 4.14F, showing a concentration of molybdenite along the selvage of the anhydrite-dominant vein. Minor pyrite has grown at crystal intersections and as inclusions within the anhydrite. The foggy brown appearance of the host rock is caused by internal reflections in fine-grained rutile within the phlogopite-rich alteration halo. **H.** Reflected light photomicrograph of the same sample as in Figure 4.14F, showing disseminated pyrite, chalcopyrite and molybdenite adjacent to the vein. Some of the molybdenite and pyrite grains have been rimmed by pyrite associated with the Stage 1I vein. Abbreviations: ab = albite, anh = anhydrite, cal = calcite, ccp = chalcopyrite, chl = chlorite, hem = hematite, mag = magnetite, mo = molybdenite, or = orthoclase, phl = phlogopite, py = pyrite, rt = rutile, vrm = vermiculite.

have well-developed vein halos of K-feldspar – actinolite ± chlorite ± hematite zoning outward to chlorite ± K-feldspar ± hematite (Fig. 4.15). The vein halos are magnetite-destructive and contain disseminated chalcopyrite, pyrite and hematite (Fig. 4.15E and F).

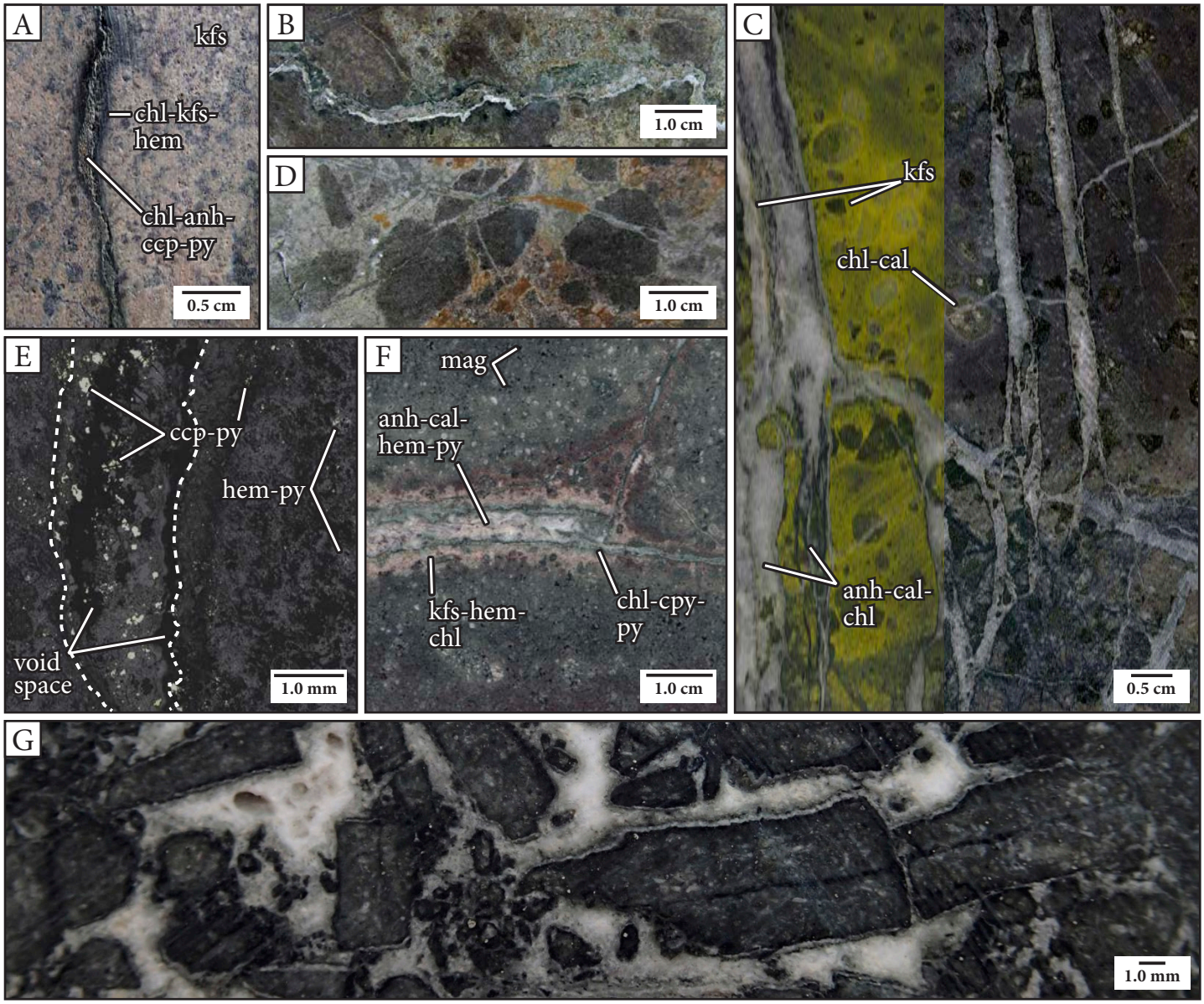


**Fig. 4.15.** Stage 1F anhydrite – calcite – chlorite veins. **A.** An irregular, chlorite – anhydrite – chalcopyrite – pyrite vein that has crosscut a clast within a Stage 1C polymict, anhydrite – chlorite – calcite-cemented breccia. The vein has a variable aperture and a dark green, chlorite – K-feldspar – hematite – chalcopyrite – pyrite alteration halo. Sample: DDHL1872 372.9 m. **B.** A banded, calcite – anhydrite – chlorite vein with an irregular morphology and diffuse vein walls. The vein has crosscut pyroxene-phyric basalt breccia (KNE2b) with Stage A1 phlogopite alteration. Sample: DDHL1856 223.5 m. **C.** A network of mutually crosscutting, branching, anhydrite – chlorite ± calcite ± K-feldspar veins with strong K-feldspar – chlorite alteration halos that have crosscut pyroxene-phyric basalt (KNE2a). The veins are locally banded, with layers of calcite, anhydrite, chlorite and minor K-feldspar. Pyroxene phenocrysts have been replaced by chlorite and calcite in the vein halo. Sample: DDHL1856 246.8 m. **D.** A branching Stage 1F vein that has crosscut Stage 1C polymict, anhydrite – chlorite – calcite-cemented breccia. The vein and breccia have similar mineralogies and alteration halos. Sample: DDHL1856 360.0 m. **E.** Reflected light photomicrograph of the sample shown in Figure 4.15A, highlighting blocky fine-grained chalcopyrite and pyrite within the vein (*the margins of which are outlined in white dashes*), adjacent void spaces, and patches of hematite – pyrite in the vein halo. **F.** A white anhydrite – calcite – hematite – pyrite vein with a dark green chlorite – chalcopyrite – pyrite selvage. The vein has a light pink to maroon to dark green K-feldspar, hematite and chlorite alteration halo, which is magnetite destructive. Sample: DDHL1995 376.7 m. **G.** A banded calcite – anhydrite – quartz – chlorite-cemented breccia with clast-rotated, cement-supported organization and ~5% open space. Clasts are monomict and are composed of pyroxene-phyric basalt (KNE2a). Sample: DDHL1995 187.3 m. Abbreviations: anh = anhydrite, cal = calcite, ccp = chalcopyrite, chl = chlorite, hem = hematite, kfs = K-feldspar, mag = magnetite, py = pyrite.

#### *4.4.1.7 Stage 1G: Tabular anhydrite and carbonate veins*

Stage 1G consists of thick veins (>5 cm-wide; Fig. 4.16) composed of coarse-grained anhydrite (>90%), interstitial calcite, clusters of fine-grained prismatic apatite (locally abundant) and minor pyrite, vermiculite, quartz and chalcopyrite. Anhydrite crystals form interlocking aggregates of white to gray, euhedral, tabular to prismat-

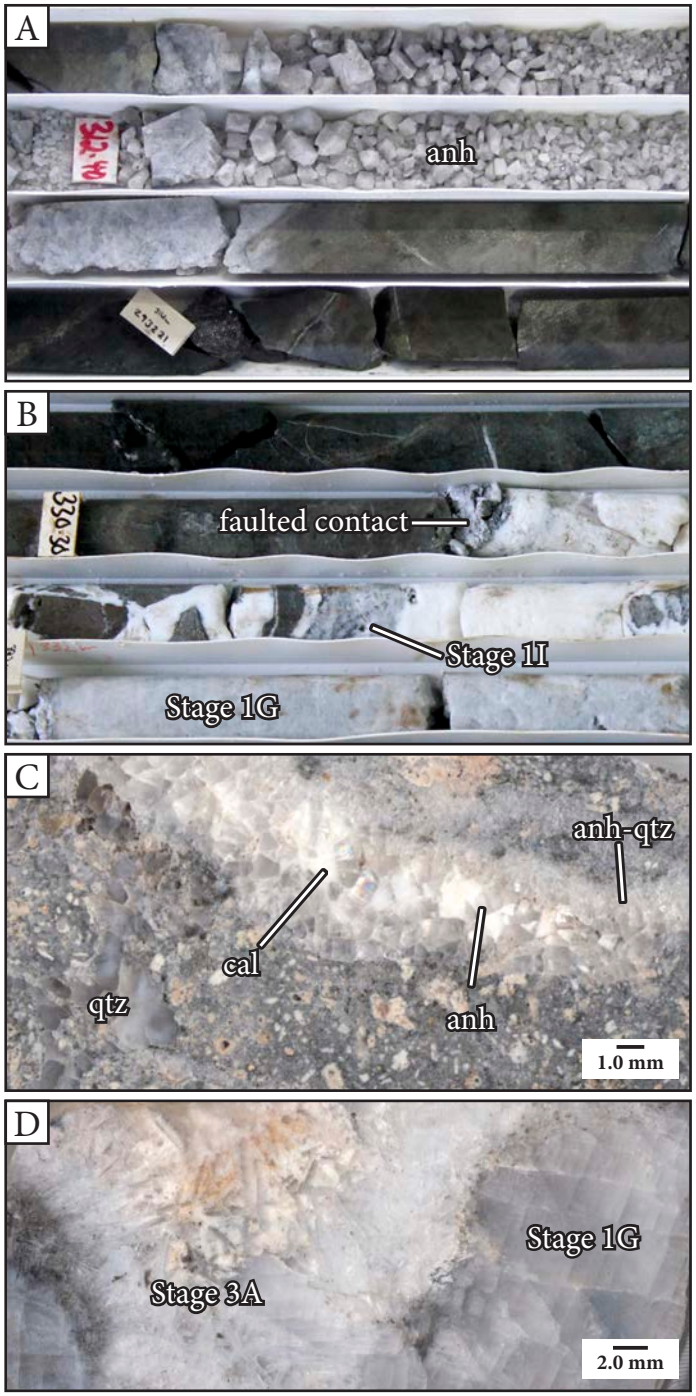


**Fig. 4.16.** Stage 1G anhydrite ± calcite veins. **A.** A 1.7 m-wide, euhedral anhydrite vein with sharp contacts and a weak anhydrite – K-feldspar alteration halo. The brittle anhydrite crystals have broken along pseudocubic cleavage planes, highlighting the coarse grain size of the crystals. Many of the crystal surfaces are encrusted with small amounts of fine-grained pyrite, vermiculite, quartz, calcite and chalcopyrite. Interval: DDHL1928 ~311.5–314.4 m. **B.** A Stage 1G tabular anhydrite vein containing several cobble-sized angular wall-rock fragments. The upper contact of the vein has been faulted and a Stage 1I banded anhydrite – pyrite vein has crosscut the center of the vein. Interval: DDHL1966 ~329.1–332.6 m. **C.** Close up view of a Stage 1G vein within pyroxene-phyric basalt breccia (KNE2b). The vein has a margin of fine- to medium-grained euhedral anhydrite – quartz transitioning to coarse-grained anhydrite laths (that have grown from the vein margins toward the center of the vein) and centerline massive white calcite. Sample: DDHL1928 272.4 m. **D.** Hand sample photograph highlighting the textural differences between a Stage 1G anhydrite vein and a crosscutting Stage 3 bladed anhydrite – pyrite – roscoelite – calcite vein. The Stage 1G vein contains translucent white, coarse-grained anhydrite and is sulfide-poor, whereas the Stage 3A vein contains thin-bladed translucent white anhydrite intergrown with abundant acicular pyrite (± roscoelite ± chalcopyrite) along the margins (*dark gray-brown*) and encrusted with calcite (*cream to orange*). Sample: DDHL1968 267.7 m. Abbreviations: anh = anhydrite, cal = calcite, qtz = quartz.

ic crystals that exhibit well-formed pseudo-cubic cleavages (Fig. 4.16A). Locally, Stage 1G veins are zoned, from intergrown granular anhydrite and quartz at the margin, transitioning to coarse-grained anhydrite, and then to massive white calcite along the centerline (Fig. 4.16C). This vein stage was not associated with significant gold or copper mineralization. Stage 1G veins have commonly been reopened during later hydrothermal activity, in particular by anhydrite veins and breccias associated with Stages 1I and 3A (Fig. 4.16B and D). Stage 1G veins are restricted to deeper levels (>150 m below sea level) in Kapit NE and are concentrated in a 200 $m^2$ area centered around ~9,280 mN/5,740 mE (Fig. 4.9). Their distribution is illustrated in Figure 4.9.

#### *4.4.1.8 Stage 1H: Anhydrite vein-clast breccia*

The anhydrite vein-clast breccia is volumetrically insignificant and was observed at only one location in Kapit NE (DDHL1968 240.1–241 m; Fig. 4.9). The breccia has sharp contacts; however, its orientation and extents are unknown. This breccia is non-bedded, matrix-rich (40% matrix), polymict, chaotic and moderately well-sorted (Fig. 4.17). The dominantly granule- to pebble-sized clasts (40%) were derived from the local wall-rocks and include distinctive Stage 1G tabular anhydrite vein fragments, pyroxene-phyric basalt (KNE2), hornblende-bearing gabbro (KNE6) and crystal-poor, plagioclase-phyric andesite (KNE7). The anhydrite vein clasts are subrounded, fractured and partly recrystallized. Very fine-grained anhydrite and muscovite cement has overgrown and infilled fractures and pits within the anhydrite vein clasts. Lithic clast shapes vary from subrounded to subangular. The matrix (40%) is mud- to medium sand-sized and composed of abraded lithics and crystals (anhydrite and biotite). Biotite – actinolite – an-

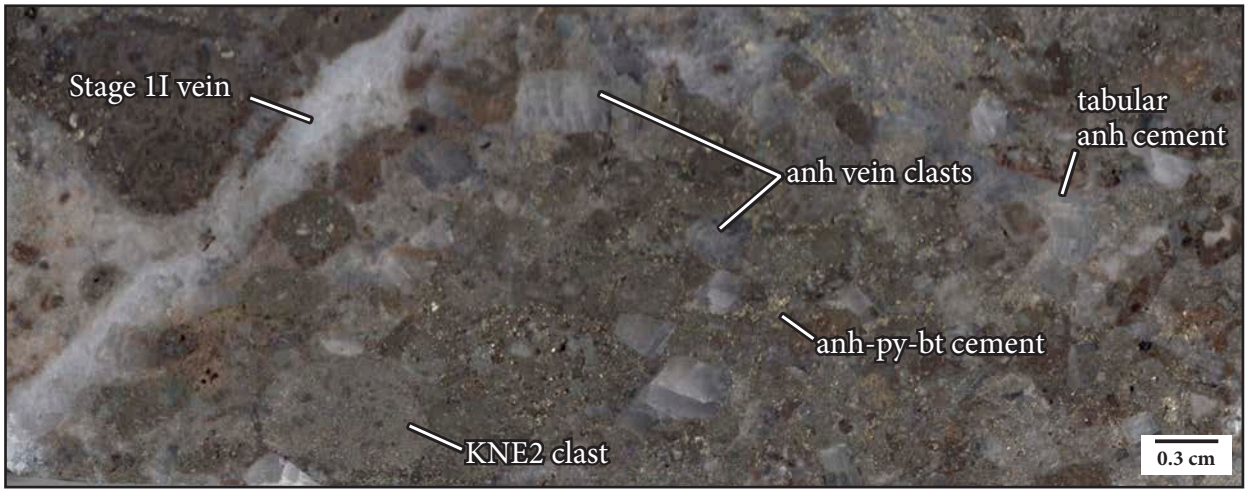


**Fig. 4.17.** Chaotic, matrix-rich Stage 1H breccia with subrounded and partly recrystallized Stage 1G tabular anhydrite vein clasts and biotite – anhydrite – pyrite-altered lithic fragments (i.e., KNE2, KNE6 and KNE7). The cement is composed of anhydrite, pyrite and biotite, with smaller amounts of actinolite, quartz, rutile, muscovite, K-feldspar, molybdenite and chalcopyrite. The sample has been crosscut by a Stage 1I massive anhydrite vein. Sample: DDHL1968 240.8 m. Abbreviations: anh = anhydrite, bt = biotite, py = pyrite.

hydrite – calcite alteration, disseminated fine-grained pyrite, molybdenite and chalcopyrite, and abundant micrometer-scale rutile occur throughout the clasts and matrix. The cement (20%) is composed of massive to tabular anhydrite, biotite, clusters of radiating needles of actinolite, muscovite, K-feldspar, granular quartz, sulfides and magnetite. The sulfides form crystal aggregates dominated by spongy pyrite (with abundant molybdenite and some magnetite inclusions) intergrown with chalcopyrite, magnetite, pyrrhotite and molybdenite.

#### *4.4.1.9 Stage 1I: Massive and banded anhydrite ± pyrite breccias and veins*

In Kapit NE, Stage 1I has a broader but overall similar distribution to Stage 1G (Fig. 4.9). The veins and breccias also occur within the Coastal area, nearest to Lienetz (Fig. 4.9). Stage 1I veins vary in thickness from ~0.5 cm to several meters across, have irregular and diffuse margins, and variable, pink-gray to brown, weak to moderate intensity, K-feldspar – biotite ± phlogopite alteration halos. Isolated fragments or bands of jigsaw-fit to clast-rotated wall-rock fragments occur within the veins (Fig. 4.18A, D and E). Stage 1I veins have commonly formed within or along the margins of Stage 1G anhydrite veins, where they occur as small breccias with blocky and partially dissolved Stage 1G anhydrite vein clasts (Fig. 4.18F).

Stage 1I veins are commonly banded, with white bands (0.1–5 cm thick) composed of fine-grained recrystallized anhydrite plus minor calcite and apatite, and dark gray bands (<0.01 to 5 mm thick) composed of pyrite, phlogopite, chlorite, rutile, chalcopyrite, sphalerite, galena, monazite, barite, celestine and wall-rock (Fig. 4.18A–C). The dark gray bands are typically irregular, wavy, lobate to discontinuous and give the veins a marbled appearance. Rarely, the dark gray bands are thin (<0.05 mm), serrated and resemble stylolites (Fig. 4.18A). The dark gray bands are interpreted to have formed by a combination of dissolution, shearing and recrystallization of previously formed anhydrite veins. Similar textures have been documented in the Lienetz ore zone and have been interpreted as dissolution seams or stylolites ($V1_{M1}$; Sykora et al., 2018a; Fig. 4.18H).

There are many narrow (typically <0.5 cm) and apparent randomly oriented veins at depths >250 m throughout Kapit NE and Coastal that are dominantly composed of anhydrite ± carbonate ± pyrite. These veins are grouped with Stage 1I as they contain mainly massive anhydrite.

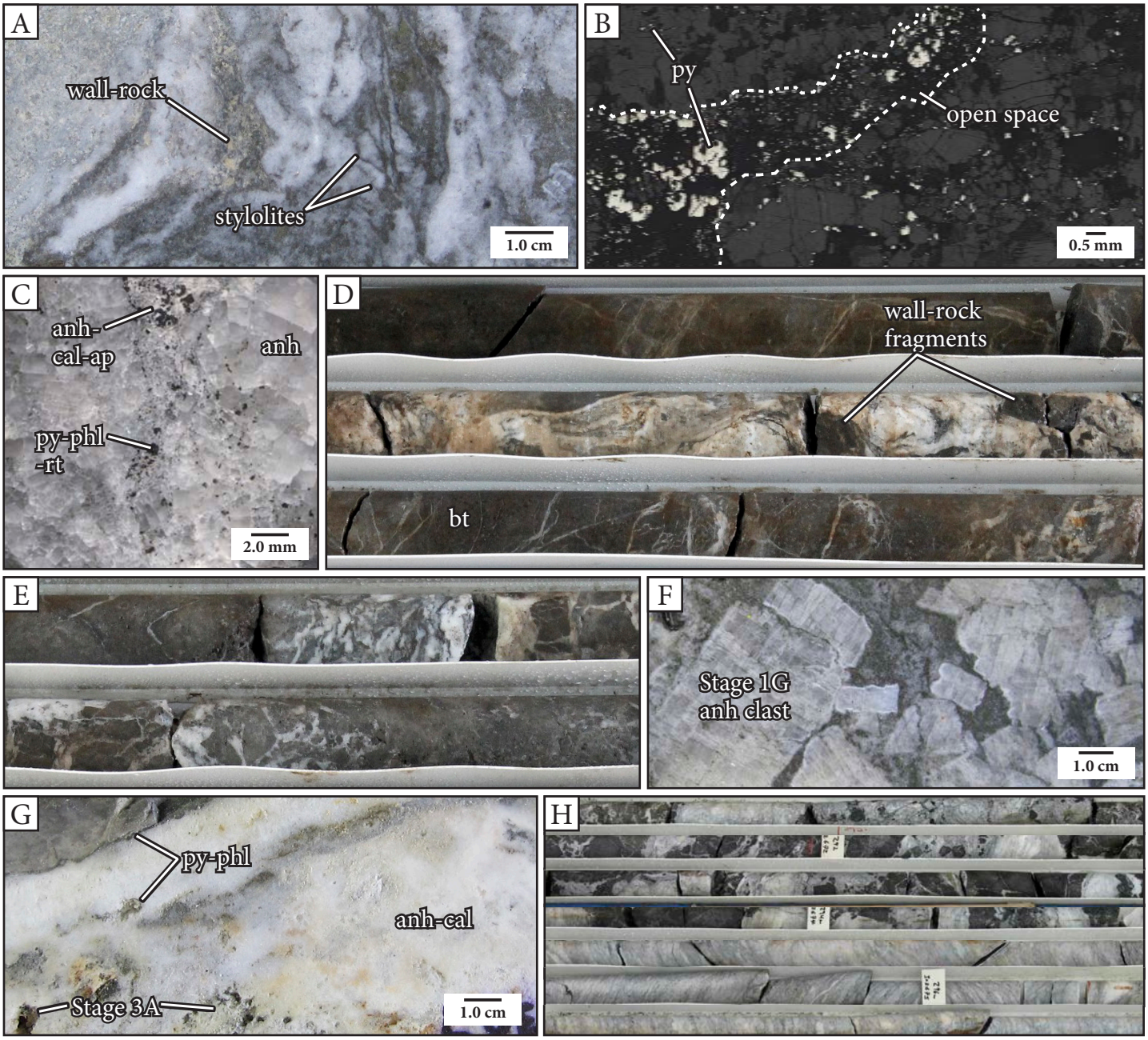


**Fig. 4.18.** Stage 1I banded anhydrite – pyrite veins. **A.** Irregular, lobate and discontinuous banding of white, recrystallized anhydrite – calcite and dark gray-brown pyrite – phlogopite – rutile + chlorite – montmorillonite in a Stage 1I vein that has crosscut the margin of a Stage 1G tabular anhydrite vein. The dark gray-brown bands are locally serrated and resemble stylolites. They are interpreted to have formed via a combination of dissolution, shearing and recrystallization of previously formed anhydrite veins. Sample: DDHL1928 274.1 m. **B.** Reflected light photomicrograph of one of the dark-gray bands from Figure 4.18A (*bounded by white dashed lines*) containing abundant rounded anhedral pyrite, and minor sphalerite, chalcopyrite and galena (not visible at this scale). All of the minerals are highly fractured, and the sample has ~10% open space. Anhedral pyrite also occurs within cracks and at the edges of anhydrite in the white bands (*areas outside of the white dashed lines*). Sample: DDHL1928 274.1 m. **C.** Close-up view highlighting the recrystallized, massive texture of anhydrite – calcite (intergrown with apatite – monazite) within one of the dark gray bands of variable thickness from Figure 4.18A (*center of the image*). Dark minerals within the band are pyrite, phlogopite, chlorite, rutile, with minor chalcopyrite, sphalerite and galena. **D.** Core box photograph showing a 0.7 m-wide Stage 1I vein with a marbled appearance defined by discontinuous dark gray bands and patches of pyrite, biotite, wall-rock and recrystallized anhydrite. The vein contains ~15% cobble- to boulder-sized biotite-altered wall-rock fragments with irregular wavy margins and has a dark gray-brown biotite – phlogopite alteration halo. The dark gray bands are locally parallel to and/or wrap around the wall-rock fragments. Interval: DDHL1967 ~306.5–308.8 m. **E.** A banded anhydrite – pyrite vein that contains intervals of abundant (~70%) jigsaw-fit to clast-rotated wall-rock fragments. Interval: DDHL1967 ~300.5–302.6 m. **F.** Blocky Stage 1G anhydrite clasts within a Stage 1I anhydrite – pyrite vein that have undergone partial dissolution and have corroded margins. Sample: DDHL1928 277.6 m. **G.** A Stage 1I vein containing predominantly recrystallized anhydrite intergrown with calcite, with wispy streaks of anhedral pyrite – phlogopite. The vein has a pyritic selvage and ~5% open space. Some of the vugs have been lined with euhedral quartz, calcite, anhydrite, adularia and pyrite associated with Stage 3A. Sample: DDHL1856 330.7 m. **H.** Core box photograph of irregular anhydrite veins and breccia veins ($V1_{M1}$) from northern Lienetz, which contain dark gray-green stylolites and dissolution seams. Interval: DDHL1991 ~290.9–297.3 m. Abbreviations: anh = anhydrite, ap = apatite, bt = biotite, cal = calcite, ksp = K-feldspar, phl = phlogopite, py = pyrite, rt = rutile.

### *4.4.2 Stage 2: Pyrite veins and breccias*

#### *4.4.2.1 Stage 2A: Pyrite – marcasite-cemented breccias and stockwork veins*

Stage 2A pyrite – marcasite-cemented breccias and stockwork veins are an abundant and voluminous vein stage in Coastal and Kapit NE. They are located predominantly between 100 and 200 m depth east of 9,500 mE (Fig. 4.19). These veins and breccias are associated with high gold assay values (~4–10 g/t Au). Stage 2A is defined by veins and breccias that are infilled with variable proportions of hydrothermal pyrite – marcasite ± adularia ± quartz ± rutile ± apatite ± arsenopyrite ± pyrrhotite (Fig. 4.20). Pyrite occurs as euhedral (cubic, pyritohedral or octahedral) or anhedral crystals, or as colloform and botryoidal mineral aggregates (Fig. 4.20H–J). Marcasite occurs as anhedral or acicular crystals, and as colloform and botryoidal mineral aggregates interlayered with pyrite (Fig. 4.20H–J). Marcasite has commonly overgrown euhedral pyrite cubes and pyritohedra (Fig. 4.20I). Anhedral arsenopyrite is intergrown with pyrite, marcasite and pyrrhotite, and occurs as bands of prismatic crystals, which are typically twinned and triangular (Fig. 4.20K Stage 2A mosaic). Adularia, quartz, rutile and apatite occur as minor, euhedral phases intergrown with sulfide minerals.

Stage 2A veins occur singly, with irregular branching forms, or as vein stockworks. They are characterized by their colloform banding and vuggy central seam (Fig. 4.20C and E). Locally, the colloform banding can be irregular, botryoidal or globular (Figs. 4.20B and I). Many of the veins have a narrow (<3 mm) and intense alteration halo of dark gray pyrite surrounded by a thicker (<10 cm), light gray alteration halo of pyrite – adularia – quartz – rutile (Fig. 4.20C). The alteration halos have locally coalesced, producing intense pervasive pyrite – adularia alteration.

Stage 2A breccia bodies are narrow (typically <0.5 m) and tabular and have either sharp or gradational contacts. Gradational contacts are defined by a transition from jigsaw-fit to clast-rotated or chaotic organization toward the center of individual breccia bodies (Fig.4.20A). Drill core measurements of sharp Stage 2A breccia contacts indicate that the breccias dip steeply (60–90°) to the north. The breccias are massive and monomict, with angular, blocky to splintery clasts that can appear rounded due to pyritic alteration rinds on clasts (Fig. 4.20A and F). Cement comprises between 5–70% of the breccias, and there can be up to 40% open space. Drill core containing Stage 2A breccias can often be unconsolidated or poorly consolidated due to the large amount of open space. The breccias locally have cockade texture, with fine-grained pyrite and marcasite defining bands around individual clasts (Fig. 4.20F).

Stage 2A pyrite – marcasite-cemented breccias and veins have been reactivated, brecciated and infilled by a variety of later vein stages, e.g., Stage 3C chalcedony – quartz – pyrite breccias and veins (Fig. 4.27K) and Stage 5B illite – pyrite – marcasite veins. Fragments of Stage 2A veins have been incorporated within Stage 2D pyritic fault zones (Fig.4.23B), Stage 3A bladed anhydrite and drusy quartz-cemented breccias (Fig. 4.24A) and Stage 4 volcanic-hydrothermal breccias (Fig. 4.34D). Stage 2A veins have not been observed in contact with Stage 1 anhydrite breccias and veins. Stage 2A breccias and veins are similar to the adularia – quartz – pyrite-cemented breccias (M5c, Blackwell, 2010) and the potassic(2) refractory sulfide ore stage (Carman, 1994) at Minifie and are also comparable to pyrite-cemented monomict breccia in Kapit (K5, aka. stage 3A pyrite-cemented breccia; Ageneau, 2012).

#### *4.4.2.2 Stage 2B: Quartz – pyrite-cemented breccia*

Stage 2B consists of a NE-trending (strike: 039°) body of quartz – pyrite-cemented breccia that is at least 130 m long and <120 m wide (Figs. 3.3 and 4.19). The Stage 2B breccia has sharp contacts with the host volcano-sedimentary stratigraphy (e.g., polymict, matrix-supported breccia, KNE1; Fig. 4.21B) and has been intruded by a series of nar-

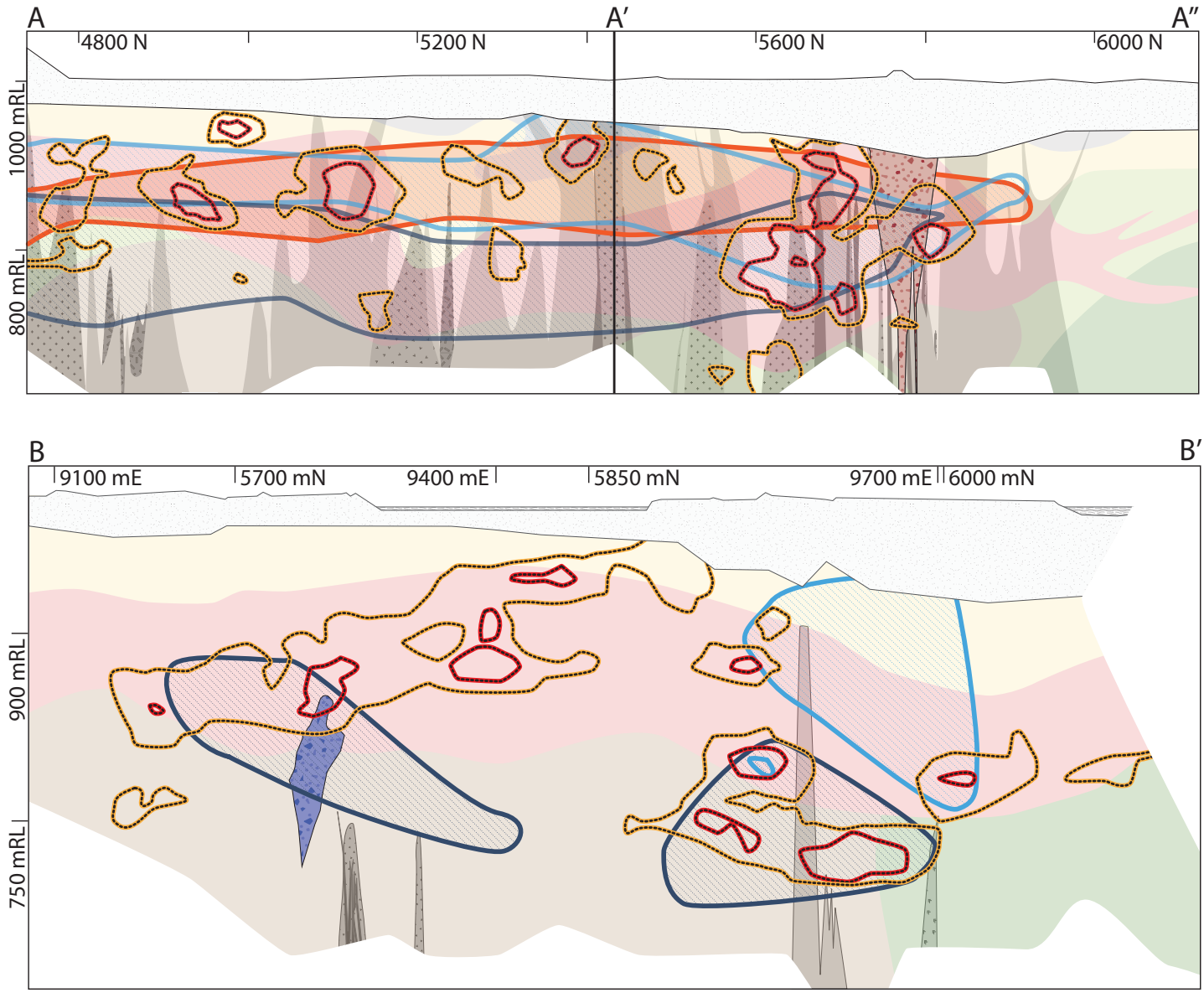


**Lithotypes**

- Waste rock
- Trachytic hornblende- feldspar-phyric latite (KNE9)
- Hornblende-feldspar-phyric latite (KNE8)
- Crystal-poor, feldspar-phyric trachyte (KNE7)
- Hornblende-bearing gabbro (KNE6)
- Hornblende-biotite-bearing monzonite (KNE5)
- Nepheline-bearing monzonite (KNE4)
- Volcano-sedimentary rocks (KNE1–3)

**Stage 2–3 veins and breccias**

- Stage 3B: Quartz – marcasite – pyrite ± tennantite ± gold veins ***and*** Stage 3C: Chalcedony – quartz – pyrite breccias and veins
- Stage 3A: Anhydrite – quartz – carbonate veins and breccias
- Stage 2C: Zoned, quartz – pyrite – anhydrite – calcite-cemented to matrix-rich breccia
- Stage 2B: Quartz – pyrite-cemented breccia
- Stage 2A: Pyrite – marcasite-cemented breccias and stockwork veins

**Alteration**

- Stage A7 – Quartz-alunite
- Stage A6 – Smectite-kaolinite
- Stage A3-A5 – Main-stage
- Stage A2 – Mg-chlorite
- Stage A2 – Fe-chlorite
- Stage A1 – Phlogopite

**Grade shells**

- >5 g/t Au
- >3 g/t Au

**Fig. 4.19.** Distribution of Stage 2 and 3 hydrothermal breccias and veins on cross sections A–A'–A" and B–B' in Kapit NE and Coastal.

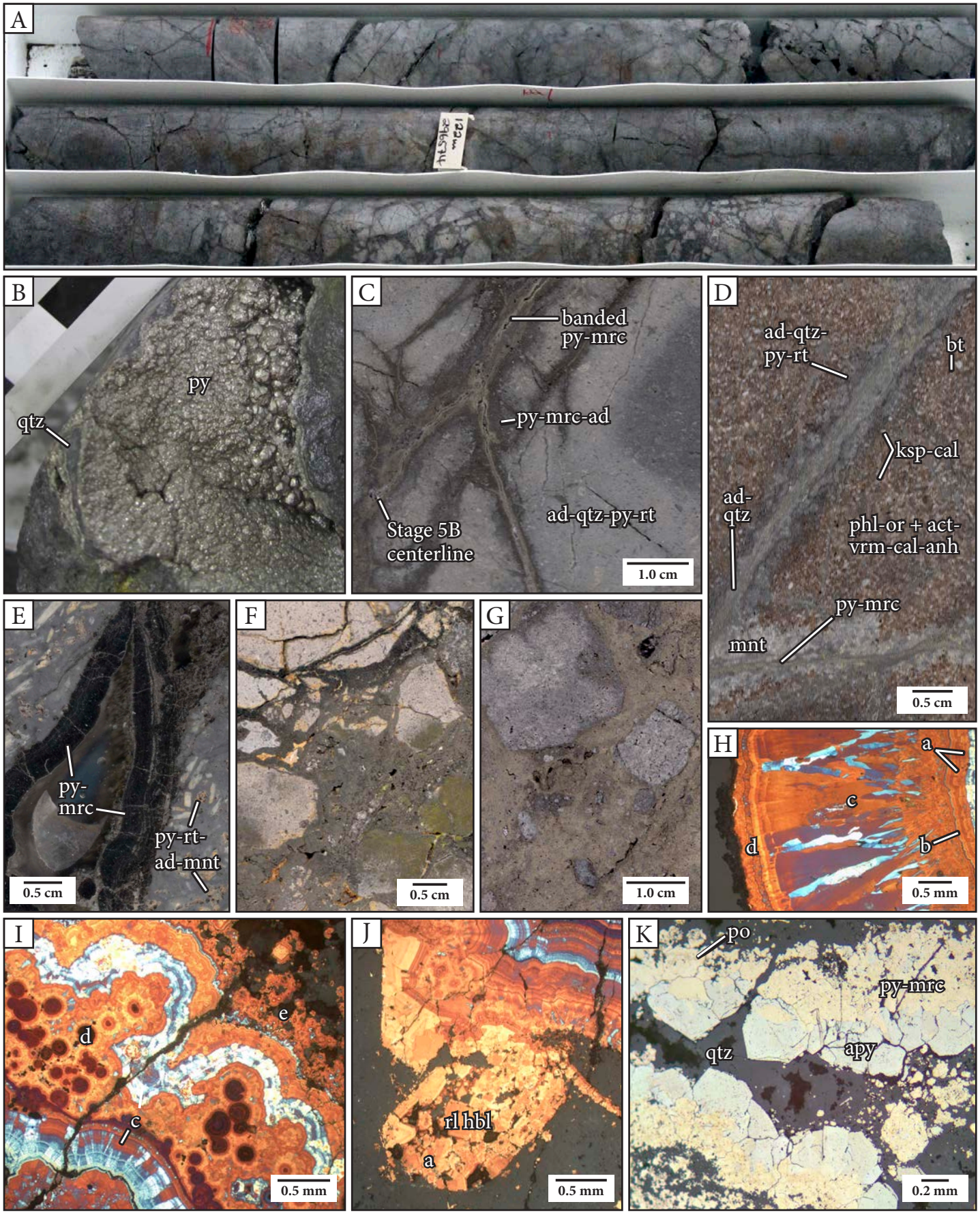
A
B
py
qtz
C
banded
py-mrc
py-mrc-ad
Stage 5B
centerline
ad-qtz-py-rt
1.0 cm
D
ad-qtz-
py-rt
bt
ksp-cal
ad-
qtz
phl-or + act-
vrm-cal-anh
py-mrc
mnt
0.5 cm
E
py-
mrc
py-rt-
ad-mnt
0.5 cm
F
0.5 cm
G
1.0 cm
H
a
c
d
b
0.5 mm
I
e
d
c
0.5 mm
J
rl hbl
a
0.5 mm
K
po
py-mrc
qtz
apy
0.2 mm

row, trachytic hornblende-feldspar-phyric latite dikes with sharp, igneous contacts (Fig. 4.21B). It has a downward-tapering form (Fig. 4.19).

The Stage 2B breccia is polymict, non-stratified, clast-rich (80–90% clasts) and cement-supported, with a chaotic clast organization (Fig. 4.21C). Sorting is moderate to poor. Clasts are dominantly subangular to subrounded and sand- to granule-sized, with rare outsized pebbles up to ~20 cm. A medium to coarse sand-sized matrix is locally present (0–15% matrix). The majority of clasts are derived from alkalic intrusions (KNE5 and KNE8), with volcano-sedimentary clasts (KNE1 and KNE2) less common. Stage 1 anhydrite vein fragments as well as latite (KNE8) clasts with truncated Stage 2A pyrite – marcasite veins have been observed (Fig. 4.21A). The clasts and matrix have been altered to quartz, adularia, rutile, illite and pyrite. The cement (5–10%) is composed of fine-grained quartz, pyrite and adularia and ranges in texture from massive to crustiform (layers of dominantly euhedral quartz growing into open space between clasts). Open space (>10%) occurs both between clasts and also in crystal-shaped vugs, where it is associated with a Stage A3 vuggy adularia alteration overprint.

Since the Stage 2B breccia contains clasts with truncated Stage 2A veins, and is also crosscut by Stage 2A veins, it is interpreted that Stage 2A most likely occurred over a protracted period, whereas Stage 2B formed at a discrete moment within the overall evolution of Stage 2A.

#### *4.4.2.3 Stage 2C: Zoned, quartz – pyrite – anhydrite – calcite-cemented to matrix-rich breccia*

Stage 2C produced a north-northeast-trending tabular breccia body in Kapit NE that is at least 175 m long and approximately 20 m wide (Fig. 4.19). The breccia body is truncated to the north by the Northern diatreme breccia pipe. Stage 2C has a very low average gold grade of 0.07 g/t Au (n = 34; Newcrest Mining Ltd. two-meter composite assay results).

The Stage 2C breccia is monomict, with a massive, chaotic, cement- to matrix-supported organization. The clasts and matrix consist predominantly of subrounded, poorly sorted, granule- to cobble-sized fragments of pyroxene-phyric basalt and basalt breccia (KNE2; Fig. 4.22B), reflecting the source region for the clasts (Fig. 3.3). The matrix is typically massive and sand-sized; however, the breccia is locally dominated by graded and/or

**Fig. 4.20.** (*Previous page*) Stage 2A pyrite – marcasite-cemented breccias and stockwork veins. **A.** Drill core photograph of a Stage 2A breccia with angular, blocky hornblende-biotite-bearing monzonite (KNE5) clasts. The breccia has clast-rotated, cement-supported domains with ~10% open space and jigsaw-fit, clast-supported domains that are gradational to stockwork veins. The fine-grained pyrite – marcasite – adularia cement has tarnished to a dark gray color. Interval: DDHL1947 ~120.6–123.2 m. **B.** Hand sample photograph of a fracture surface encrusted with Stage 2A botryoidal pyrite and quartz. Sample: DDHL1947 133.3 m. **C.** A banded Stage 2A pyrite – marcasite vein with a zoned alteration halo and Stage 5B clay – pyrite centerline infill. There is an inner halo (0.5–2.0 mm-wide) of strong intensity, dark gray pyrite – marcasite – adularia alteration and an outer halo (1–3 m-wide) consisting of moderate intensity, light gray adularia – quartz – pyrite – rutile alteration. Sample: DDHL1924 119.0 m. **D.** Close-up view of a Stage 2A stockwork that has crosscut biotite-feldspar-phyric, nepheline-bearing monzonite (KNE6). The monzonite has been overprinted by Stage A1 phlogopite – orthoclase alteration and later by calcite – actinolite – vermiculite – anhydrite alteration associated with a nearby, hectometer-scale, polymict, anhydrite – chlorite – calcite-cemented breccia (Stage 1C). The stockwork veins are composed of anhedral to banded pyrite and marcasite with white adularia and quartz that is locally significant. The stockwork veins have distinct, gray adularia – quartz – pyrite – rutile alteration halos that have patches of white montmorillonite. Sample: DDHL1924 356.5 m. **E.** Macroscopic banding in a vuggy colloform Stage 2A pyrite – marcasite vein that has crosscut trachytic hornblende-feldspar-phyric latite (KNE8). Pyrite – rutile – adularia + montmorillonite aggregates form pseudomorphs after hornblende phenocrysts adjacent to the vein. Sample: DDHL1931 118.0 m. **F.** A Stage 2A pyrite – marcasite-cemented breccia with a cockade texture defined by the amalgamation of individual clasts enveloped by colloform pyrite – marcasite. Sample: DDHL1803 79.6 m. **G.** Hand sample photograph of a chaotic, cement-rich Stage 2A breccia with equant, subrounded, adularia – pyrite-altered clasts. The sulfide-rich cement has a massive texture and there is <5% open space. Note the pyrite – marcasite – adularia alteration rinds, which have altered the appearance of the clast margins. Sample: DDHL1977 115.7 m. **H., I.** and **J.** Reflected-light photomicrographs of a Stage 2A banded pyrite vein that has been etched with NaOCl. The bands are made up of numerous layers of pyrite and marcasite with different growth forms (a: single and twinned, cubic and octahedral pyrite; b: fine-grained colloform pyrite; c: acicular radiating and globular marcasite; d: fine-grained botryoidal pyrite; e: colloform pyrite – acicular marcasite aggregates and overgrowths on singular pyrite crystals). Band widths range from ~0.01 mm to 2.5 cm. The cubic and octahedral crystals locally replace hornblende crystals adjacent to the veins. The etching shows that the cubic, colloform, and botryoidal pyrite bands display oscillatory ± sector zoning, which is related to variable trace element contents in the pyrite. Sample: DDHL1931 118.0 m. **K.** Reflected-light photomicrograph of a banded Stage 2A vein with distinct layers of pyrite – pyrrhotite, pyrite – marcasite – arsenopyrite and arsenopyrite. A Stage 3 quartz vein defines the centerline and contains Stage 2A pyrite – arsenopyrite vein-clasts. Sample: DDHL1924 119.0 m. Abbreviations: act = actinolite, ad = adularia, anh = anhydrite, apy = arsenopyrite, bt = biotite, cal = calcite, hbl = hornblende, ksp = K-feldspar, mnt = montmorillonite, mrc = marcasite, or = orthoclase, phl = phlogopite, po = pyrrhotite, py = pyrite, qtz = quartz, rl = relict, rt = rutile, vrm = vermiculite.

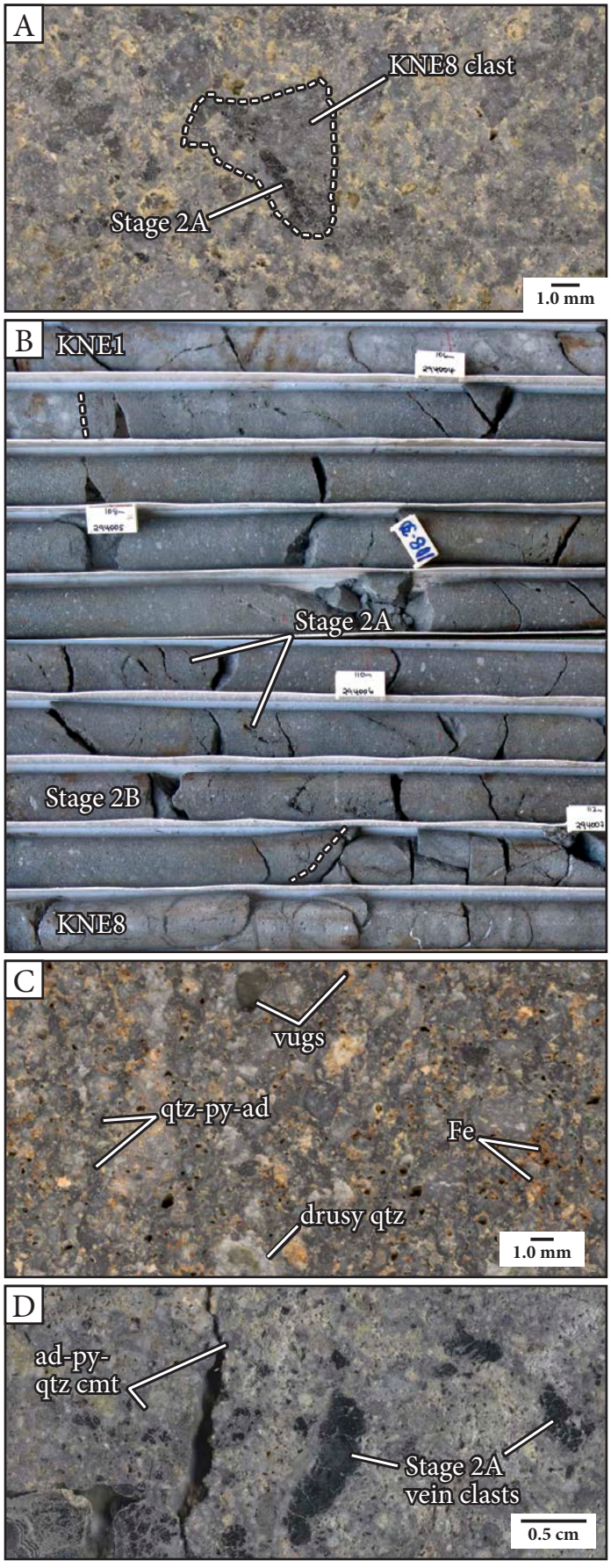


laminated mud matrix (Fig. 4.22D–E). Graded laminations are draped within the space between clasts, suggesting that the matrix may have settled into open space between clasts by collapse. Layers rich in hydrothermal pyrite are locally intercalated with the mud matrix (Fig. 4.22E). The clasts and matrix have cores with relict orthoclase – phlogopite alteration, rims that are altered to anhydrite, adularia, calcite, pyrite, and vermiculite and a late pervasive alteration overprint of illite-smectite and Mg-chlorite. The cement is characteristically zoned outward from the clast margins, from intergrown fine-grained granular pyrite – anhydrite, to colloform pyrite, to coarse euhedral prismatic quartz, tabular anhydrite, calcite and minor pyrite (Fig. 4.22B–C). Stage 2C breccias do not typically contain open space, except where it appears that the coarse-grained euhedral minerals in the cement have been partly leached. These rare, vuggy Stage 2C breccias are associated with moderate gold mineralization (e.g., DDHL1939 154–165 m depth averages 2.78 g/t Au).

#### *4.4.2.4 Stage 2D: Pyritic fault zones*

Stage 2D consists of an irregular array of fractures, faults, and tectonic breccias (fault breccias and cataclasites), which have a widespread distribution in the Kapit NE and Coastal areas. There is a protracted and poorly constrained movement history for Stage 2D faults, with multiple generations of fracture and faulting and an inconsistent relationship with gold mineralization. Displacement along the

**Fig. 4.21.** Stage 2B quartz – pyrite-cemented breccia. **A.** Hand sample photograph of a Stage 2B quartz – pyrite-cemented breccia containing a trachytic hornblende-feldspar-phyric latite (KNE8) clast with a truncated Stage 2A banded pyrite – marcasite vein. Sample: DDHL1931 144.2 m. **B.** Drill core photograph showing a Stage 2B quartz – pyrite-cemented breccia that has crosscut polymict, matrix supported breccia (KNE1) and has been crosscut by a trachytic hornblende-feldspar-phyric latite dike (KNE8). The breccia has also been cut by vuggy Stage 2A banded and botryoidal pyrite veins. Given that Stage 2B breccias contain Stage 2A clasts and have been crosscut by Stage 2A veins, it is interpreted that both stages were emplaced simultaneously. Interval: DDHL1931 ~109.6 – 113.9 m. **C.** Close-up view highlighting the quartz – pyrite – adularia (*gray*) to drusy fine-grained quartz (*white*) cement and vugs within a Stage 2B breccia. Some of the vugs have been partly infilled with jarosite, copiapite and Fe-oxides. Sample: DDHL1931 109.0 m. **D.** Close-up view highlighting a concentration of botryoidal and banded Stage 2A vein clasts and lithic clasts cemented by adularia – pyrite – quartz. Sample: DDHL1924 109.0 m. Abbreviations: ad = adularia, cmt = cement, Fe = jarosite, copiapite ± Fe-oxides, py = pyrite, qtz = quartz.

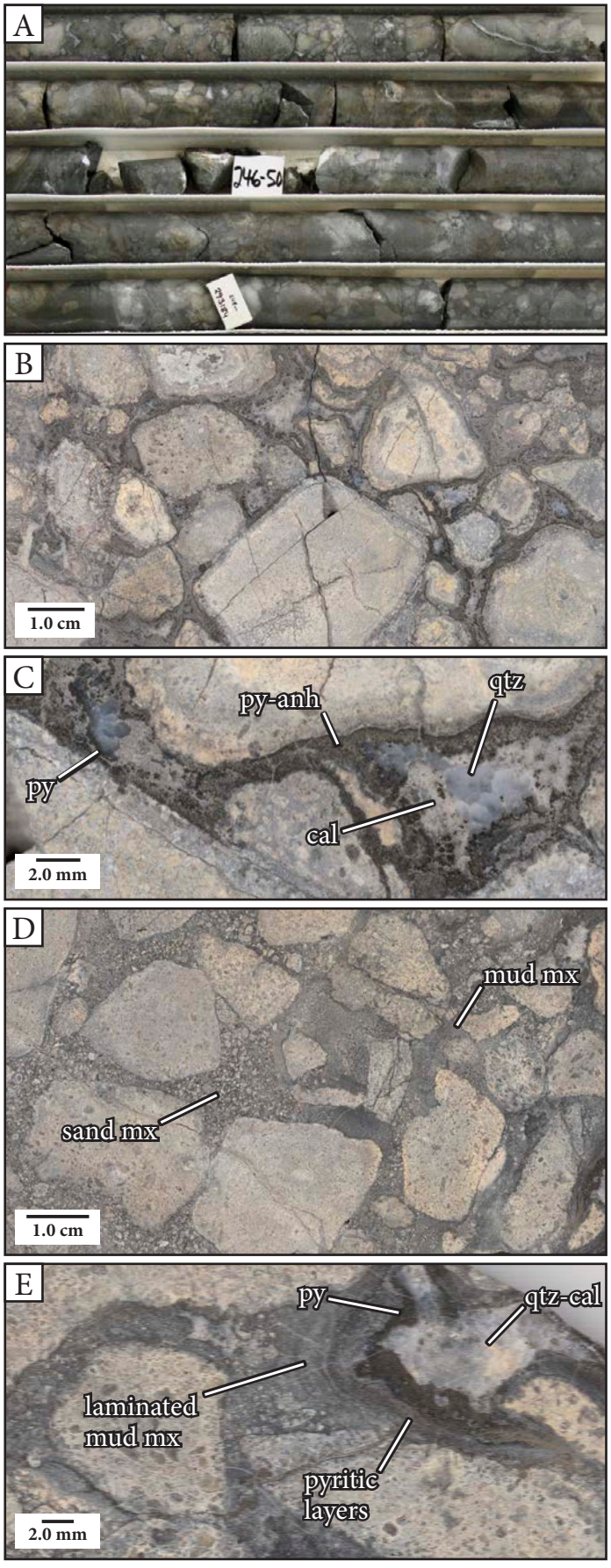


faults is interpreted to be small (cm to dm scale), with no significant post-mineralization movement (e.g., that would have offset major orebodies). The brittle faults and breccia zones range in width from 1 cm to 15 m and are characterized by dark gray, finely comminuted rock flour, pyrite – marcasite – adularia ± quartz ± chalcopyrite ± arsenopyrite ± anhydrite cement and moderate to strong intensity pyrite – adularia + illite + chlorite alteration (Fig. 4.23). Both fault breccias and cataclasites have been observed. The fault breccias vary widely from cohesive to incohesive and from foliated to unfoliated. They typically have clast-rotated to chaotic organization. Marcasite occurs as gold-rich acicular needles and pyrite occurs as pyritohedra (Fig. 4.23F–G) with variably low to high gold contents. Some of the fault zones incorporate crushed vein material (e.g., Stage 1 anhydrite, pyrite and molybdenite, Fig. 4.23C, E and G; Stage 2A pyrite and marcasite; Fig. 4.23B) and altered lithic fragments (Stage A1 and A4). The fault zones have crosscut Stage 2A pyritic stockwork veins and Stage 2B quartz – pyrite-cemented breccia (Fig. 4.23D) and are locally reactivated by late-stage montmorillonite-altered shear zones (Stage A6). Stage 2D cataclasite has been crosscut by Stage 3A anhydrite veins (Fig. 4.23F). Faults similar to Stage 2D occupy a comparable position in the paragenetic sequence of the Lienetz ore zone (Au2 structural trend, Domain IV; Sykora et al., 2018a). Although it is difficult to make accurate structural interpretations from the drill core data collected in

**Fig. 4.22.** Stage 2C zoned quartz – pyrite – anhydrite – calcite-cemented to matrix-rich breccia. **A.** Drill core photograph highlighting the meter-scale transition from cement-supported (*top*) to matrix-supported (*bottom*) organization within the breccia body. Interval: DDHL1928 ~244.6–248.7 m. **B.** Hand sample photograph of quartz – pyrite – anhydrite – calcite-cemented Stage 2C breccia with chaotic organization. Intergrown grayish brown pyrite – anhydrite and colloform pyrite has rimmed clasts, which accentuates their rounded, equant morphology. The monomict, pyroxene-phyric basalt breccia clasts have subtle cores of relict phlogopite – orthoclase alteration and rims that have been altered to anhydrite – K-feldspar – calcite – pyrite – vermiculite. The sample has been overprinted by pervasive illite-smectite and chlorite alteration. Sample: DDHL1928 237.2 m. **C.** Close-up view of zoned cement in a Stage 2C breccia. Immediately adjacent to the clasts are bands of granular anhydrite – pyrite and colloform banded pyrite, whereas triple junctions are infilled with euhedral, translucent white quartz, anhedral buff calcite and pyrite. Sample: DDHL1928 237.2 m. **D.** Hand sample photograph of Stage 2C matrix-rich breccia. The matrix grades from dominantly sand- to mud-sized. Sample: DDHL1928 248.9 m. **E.** Close-up view of the same sample as in Figure 4.22D focusing attention on the draped laminated mud matrix and centimeter-scale transition from matrix to cement. The transition is marked by layers dominated by pyrite cement. Abbreviations: anh = anhydrite, cal = calcite, mx = matrix, py = pyrite, qtz = quartz.

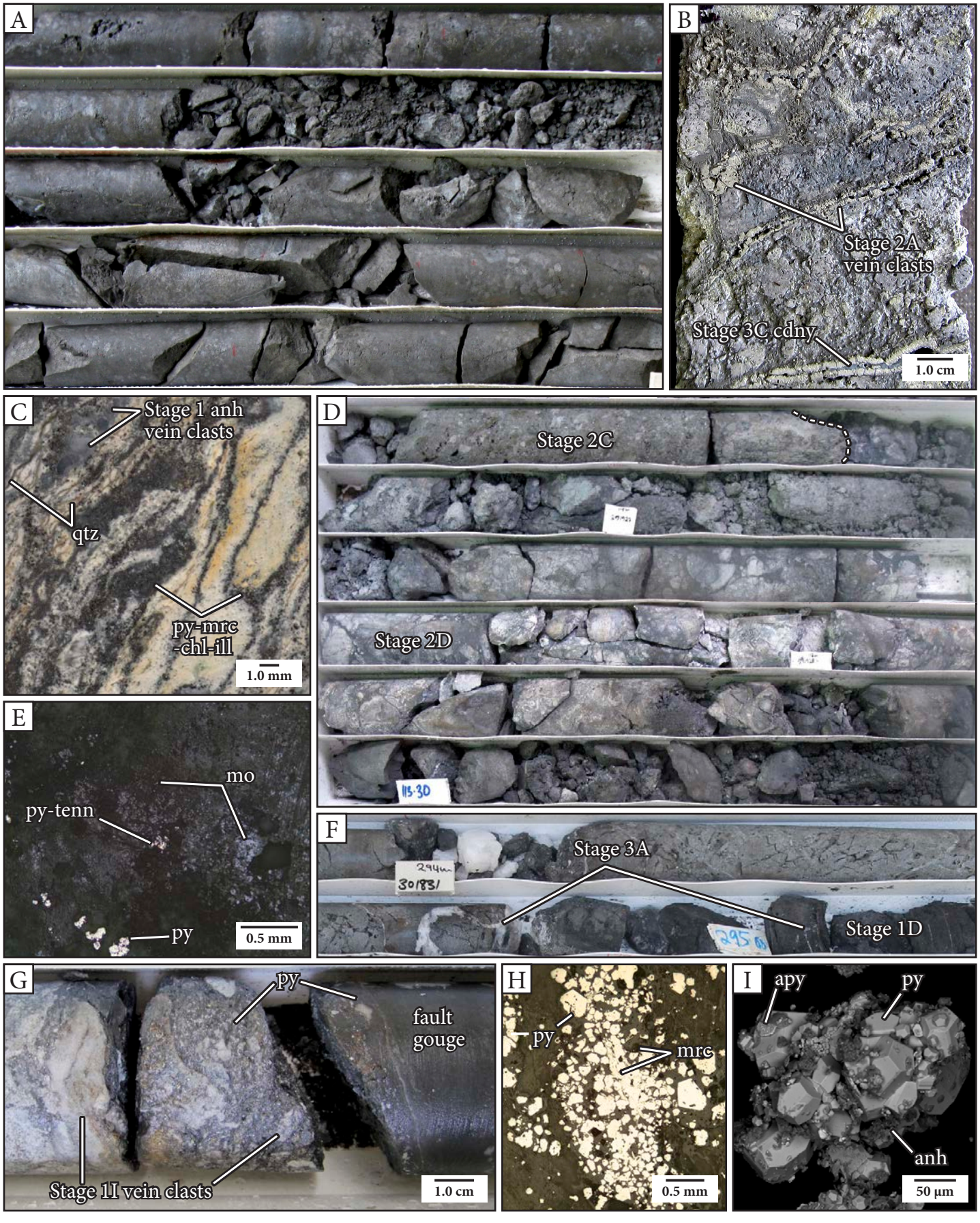
A
B
Stage 2A
vein clasts
Stage 3C cdny
1.0 cm
C
Stage 1 anh
vein clasts
qtz
py-mrc
-chl-ill
1.0 mm
D
Stage 2C
Stage 2D
E
mo
py-tenn
py
0.5 mm
F
Stage 3A
Stage 1D
G
py
fault
gouge
Stage 1I vein clasts
1.0 cm
H
py
mrc
0.5 mm
I
apy
py
anh
50 µm

this study, it can tentatively be interpreted that the Stage 2D faults in Kapit NE and Coastal have similar, moderately to steeply dipping and NE-trending orientations.

### *4.4.3 Stage 3: Quartz veins and breccias*

#### *4.4.3.1 Stage 3A: Anhydrite – quartz – carbonate veins and breccias*

Stage 3A veins and breccias have a widespread distribution in Kapit NE and Coastal (Fig. 4.19). They are typically located at medial depths (−120 to −300 m rsl; Fig. 4.19) and vary in thickness from about 0.5 cm to 5 m. The veins and breccias are most abundant in areas of vuggy adularia alteration. They appear to infill open spaces that may have remained after the dissolution of earlier-formed vein material (Fig. 4.24K). This stage is associated with moderate to high gold contents. For logged drill core intervals containing Stage 3A veins, 2-meter composite gold assay values average 3.6 g/t Au and range from ~0.5–41.1 g/t Au (n = 294).

Stage 3A veins and hydrothermal cement contain a wide range of minerals, and the mineralogy varies considerably between samples. The veins and breccias are dominantly composed of white to cream-colored gangue minerals: anhydrite, carbonate and quartz. Barite, celestine, roscoelite, illite, chalcedony, adularia and pyrite are also locally abundant (Figs. 4.24B–E and 4.25A and C). Anhydrite, which is the most common and abundant mineral overall, is typically medium- to coarse-grained (~0.2–2.0 cm) and displays euhedral, thin bladed to tabular crystal forms. Most commonly, the anhydrite has a lattice-bladed texture, defined by intersecting bladed crystals (Fig. 4.24A, G and M). Calcite and dolomite are the most common carbonate minerals. Kutnohorite was also observed and is associated with roscoelite and tellurides (Fig. 4.25A–B). The carbonates are massive or euhedral, with rhombohedral, nailhead spar and dogtooth spar forms. Platy calcite encrusted with fine-grained quartz (i.e., lattice-texture quartz) was observed in Kapit NE (Fig. 4.24L). Quartz occurs as white to translucent prismatic crystals and anhedral masses (Fig. 4.24E and G). Roscoelite ranges from Mg- to V-rich (Fig. 4.25E; Appendix F). Minor and trace minerals include apatite, rutile, anglesite, cerussite, monazite, xenotime, stilbite, marcasite, chalcopyrite, sphalerite, galena, tetrahedrite-tennantite, wulfenite, molybdite, molybdenite, argentite, acanthite, cerargyrite-bromyrite, altaite, tellurite, electrum, native silver and various gold and silver tellurides (including calaverite, hessite, stützite, petzite, and muthmannite; Figs. 4.24–4.25). Many of the minor and trace minerals are not visible at hand specimen scale. However, the presence of small quantities of native precious metals and precious metal telluride minerals is likely to produce a nugget effect on gold and silver grades and has implications for processing of ore containing these veins and breccias. Stage 3A veins and breccias are associated with moderate to intense

**Fig. 4.23.** (*Previous page*) Stage 2D pyritic fault zones. **A.** Drill core photograph showing Stage 2D pyritic fault breccia that ranges from well-consolidated to unconsolidated. Darker gray shades of rock correspond to higher abundances of rock flour matrix and very fine-grained sulfides (especially pyrite and marcasite). Interval: DDHL1856 ~162.4–164.0 m. **B.** Hand sample photograph of Stage 2A pyrite – marcasite veins that have been disaggregated to varying degrees within a Stage 2D fault breccia. Stage 3E chalcedony has locally infilled open space within Stage 2A vein fragments. Sample: DDHL1856 162.8 m. **C.** Close up image of shear bands and patches within a Stage 2D pyritic fault zone. Dark bands consist of pyrite – marcasite – chlorite – illite ± molybdenite and light bands consist of K-feldspar – illite-altered host rock and clasts of Stage 1G anhydrite veins. The fault zone also contains abundant anastomosing quartz veins. Sample: DDHL1995 273.2 m. **D.** Core box photograph of a moderately consolidated, Stage 2D molybdenite and gold-bismuth alloy-bearing fault zone with several discrete intervals of weakly foliated clay gouge surrounded by fault breccia. The angular clasts have jigsaw-fit to clast-rotated organization and strong intensity, white, anhydrite – quartz – pyrite alteration that has been overprinted by montmorillonite alteration. The blue-gray matrix consists of very fine-grained rock flour and contains pyrite, molybdenite, tennantite and chalcopyrite. The breccias and gouge are cemented by quartz. The Stage 2D breccia has a sharp contact with Stage 2B quartz – pyrite-cemented breccia at ~109.0–109.9 m depth down hole. Interval: DDHL1924 ~109.0–113.5 m. **E.** Reflected light photomicrograph of the same sample as in Figure 4.23D, highlighting the very fine grain size of pulverized molybdenite crystals in the fault breccia matrix, and the presence of both pyrite and tennantite. **F.** Core box photograph of a Stage 2D cataclasite that has been crosscut by Stage 3A anhydrite veins. Interval: DDHL1983 ~294.0–295.2 m. **G.** Laminated Stage 2D fault gouge that is gradational to foliated Stage 2D cataclasite containing elongate (foliation-parallel), rounded and irregular Stage 1I banded anhydrite – pyrite vein clasts, angular lithic clasts and disseminated pyrite. Sample: DDHL1968 232.6 m. **H.** Reflected light photomicrograph highlighting the presence of layer-parallel marcasite needles within a band of pyrite from the same sample as in Figure 4.23C. The sample also contains very fine-grained (<0.05 mm) flecks of molybdenite. **I.** High-resolution FE-SEM image of a cluster of very fine-grained (5–60 μm) pyritohedral pyrite with crusts of arsenopyrite and anhydrite from a sample of unconsolidated Stage 2D pyritic fault gouge. Sample: DDHL1856 209.8 m. Abbreviations: ad = adularia, anh = anhydrite, apy = arsenopyrite, cdny = chalcedony, chl = chlorite, ill = illite, mo = molybdenite, mrc = marcasite, py = pyrite, qtz = quartz, tenn = tennantite.

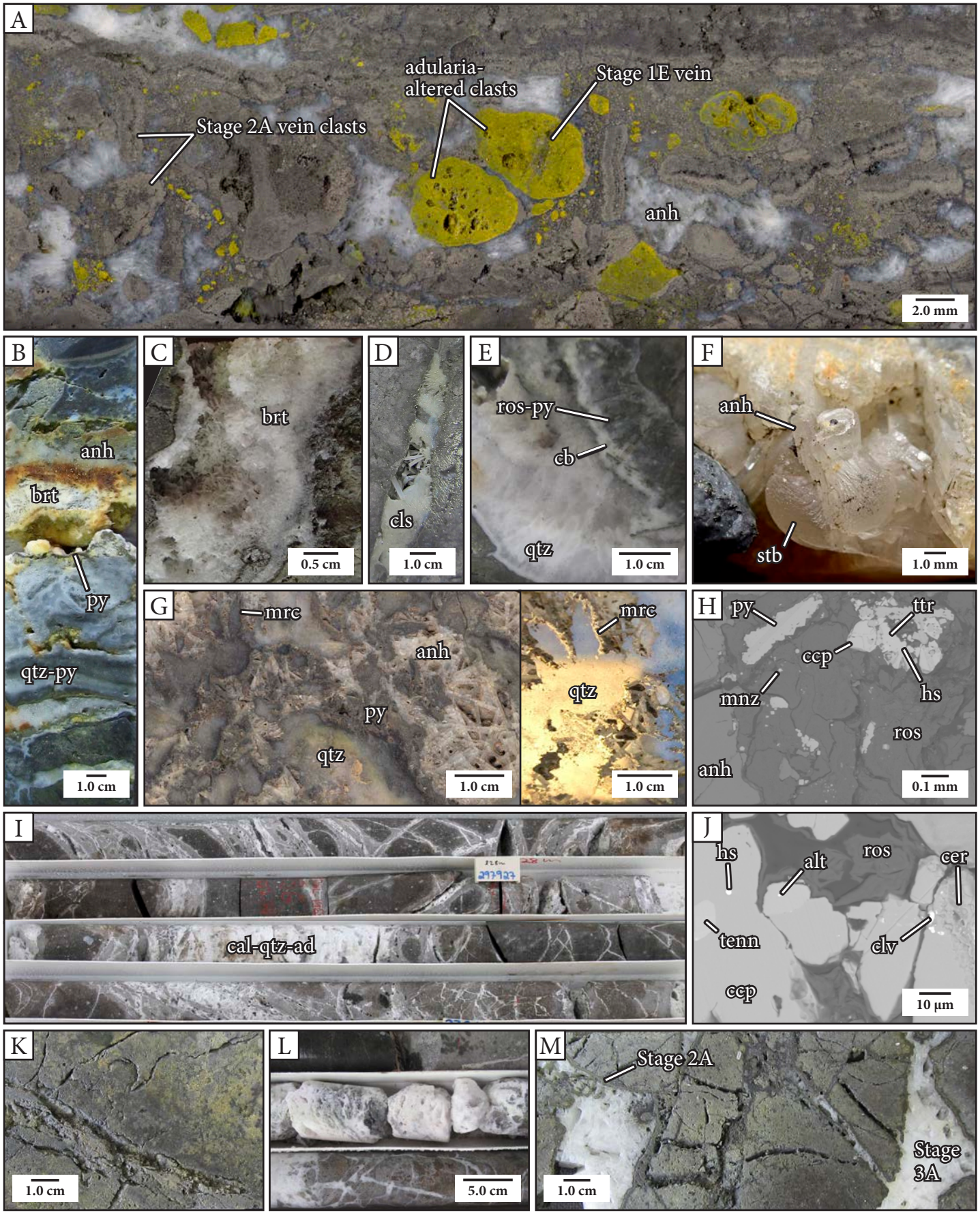
A
adularia-
altered clasts
Stage 1E vein
Stage 2A vein clasts
anh
2.0 mm
B
anh
brt
py
qtz-py
1.0 cm
C
brt
0.5 cm
D
cls
1.0 cm
E
ros-py
cb
qtz
1.0 cm
F
anh
stb
1.0 mm
G
mrc
anh
py
qtz
1.0 cm
mrc
qtz
1.0 cm
H
py
ttr
ccp
mnz
hs
ros
anh
0.1 mm
I
cal-qtz-ad
J
hs
alt
ros
cer
tenn
clv
ccp
10 µm
K
1.0 cm
L
5.0 cm
M
Stage 2A
Stage
3A
1.0 cm

gray adularia ± quartz ± illite alteration (Fig. 4.24A and I).

Stage 3A veins and breccias are typically porous (up to 20% open space) and display some open space filling textures typical of low-sulfidation epithermal veins, for example, massive, drusy and either symmetrical or asymmetrical crustiform banded textures. Breccias range from chaotic to jigsaw fit. They are massive, cement-supported (20–80% cement), moderately to very poorly sorted, and contain <5% matrix material. Some examples display cockade texture. Clasts are very angular to subrounded and are composed of locally derived lithic clasts and vein fragments. Stage 2A colloform pyrite – marcasite vein clasts are especially prevalent (Fig. 4.24A). There are many examples of Stage 3A veins that have precipitated along the centerline of Stage 2A veins (e.g., Fig. 4.24M). Other Stage 3A breccias and veins fill open space within Stage 1I and 1H anhydrite veins. The open space may have originated due to the partial dissolution of Stage 1 anhydrite.

Stage 3A is approximately equivalent to calcite – anhydrite – quartz veins and breccia veins in Lienetz ($V1_{M2}$; Sykora et al., 2018a). However, $V1_{M2}$ structures differ in that they are most commonly expressed as breccia veins rather than veins, they are much thicker (ranging from 1 cm to 35 m) and more extensively developed, and they are associated with outer biotite vein halo alteration. It is possible that Stage 3A veins and breccias are a time equivalent distal correlative of $V1_{M2}$.

#### *4.4.3.2 Stage 3B: Quartz – marcasite – pyrite ± tetrahedrite-tennantite ± gold veins*

Stage 3B consists of dark gray-blue quartz veins that are variable in width (1 mm to 10 cm) and continuous and irregular in form. The veins occur as single, isolated veins (Fig. 4.26A), as mutually crosscutting, branching veins (Fig. 4.26B–C) and in vein stockworks (Fig. 4.26D). They have well-developed, narrow (<1 cm-wide), patchy and irregular, dark gray-blue quartz – pyrite – adularia alteration halos (Fig. 4.26D). Quartz within Stage 3B veins is granular and very fine-grained (typically ~20 μm). Medium-grained (0.1–5.0 mm), white, granular quartz (Fig. 4.26B) and drusy quartz-lined cavities occur locally (Fig. 4.26C). The dark appearance of the quartz veins is caused by the presence of abundant, very fine-grained, acicular marcasite, pyrite (pyritohedral and octahedral forms), chalcopyrite, tetrahedrite-tennantite, and rarely, sphalerite, galena and arsenopyrite (Fig. 4.26E–J). The veins also contain disseminated euhedral stubby rutile (Fig. 4.26I), blocky apatite (Fig. 4.26J) and locally, amoeboid grains of native gold (Fig. 4.26B–C and F). EDS analysis of the native gold shows that it contains <3% Ag (n = 7; Appendix F). Marcasite is the most abundant sulfide mineral in the quartz veins. It

**Fig. 4.24.** (*Previous page*) Stage 3A anhydrite – quartz – carbonate veins and breccias. **A.** Example of a massive, chaotic, cement-supported and poorly sorted Stage 3A breccia with a polymict clast population, consisting of locally derived, vuggy adularia-altered wall-rock clasts, clasts with truncated Stage 1 veins, and abundant Stage 2A colloform pyrite – marcasite vein clasts. The sample has been feldspar stained to highlight the adularia alteration (*yellow*) in the clasts. The cement is composed of bladed to tabular anhydrite, with minor quartz and pyrite. Sample: DDHL1856 207.6 m. **B.** A composite Stage 3A vein that contains zones of rhythmically banded quartz, anhydrite and pyrite, massive white anhydrite, colloform pyrite and massive to fibrous, brownish white barite. Sample: DDHL1924 196.3 m. **C.** A Stage 3A vein composed of drusy barite. Sample: DDHL1931 248.9 m. **D.** A divergent spray of white bladed celestine crystals intergrown with bladed anhydrite, infilling a leached vein. Sample: DDHL1856 197.0 m. **E.** An asymmetrical Stage 3A quartz – carbonate – roscoelite – pyrite vein. On one side, the quartz is coarse-grained, euhedral and inward-terminating. On the other side, the quartz is intergrown with lamellar roscoelite and acicular pyrite aggregates and infilled with white carbonate. Sample: DDHL1974 173.8 m. **F.** A bladed anhydrite and globular stilbite vein. The stilbite has bow-tie (wheat sheaf) crystal habit and appears to fill the interstices between anhydrite blades. Stilbite may have been precipitated sometime after Stage 3A. Sample: DDHL1876 196.0 m. **G.** A Stage 3A vein composed of globular quartz surrounded by marcasite needles, pyrite and bladed anhydrite. The macro photograph at right was taken on an oblique angle to allow an enhanced view of the marcasite needles, which have preferentially nucleated on one side of the quartz globules. Sample: DDHL1856 194.3 m. **H.** BSE image of a Stage 3A anhydrite – roscoelite vein. The roscoelite hosts fine-grained, acicular and equant pyrite, monazite, and clusters of chalcopyrite – tennantite – hessite. Sample: DDHL1968 267.7 m. **I.** Core box photograph of a banded Stage 3A calcite – quartz – adularia vein stockwork with intense adularia alteration halos. Interval: DDHL1963 ~326.5–329.9 m. **J.** BSE image of the same sample as in Figure 4.24H, highlighting a chalcopyrite – tetrahedrite cluster with inclusions of cerargyrite and diverse telluride minerals. **K.** Open space within an intensely adularia-altered pyroxene-phyric basalt breccia (KNE2b) that has the geometry of a leached vein stockwork. The open space has been cemented by fine-grained thin bladed anhydrite, adularia and pyrite. Sample: DDHL1856 195.3 m. **L.** Platy calcite encrusted with quartz. Sample: DDHL1968 246.3 m. **M.** Stage 3A lattice-bladed anhydrite infilling open space within Stage 2A colloform pyrite veins. Sample: DDHL1856 357.0 m. Abbreviations: ad = adularia, alt= altaite, anh = anhydrite, brt = barite, cal = calcite, cb = carbonate, ccp = chalcopyrite, cer = cerargyrite, cls = celestine, clv = calaverite, hs = hessite, mnz = monazite, mrc = marcasite, py = pyrite, qtz = quartz, ros = roscoelite, stb = stilbite, tenn = tennantite, ttr = tetrahedrite.

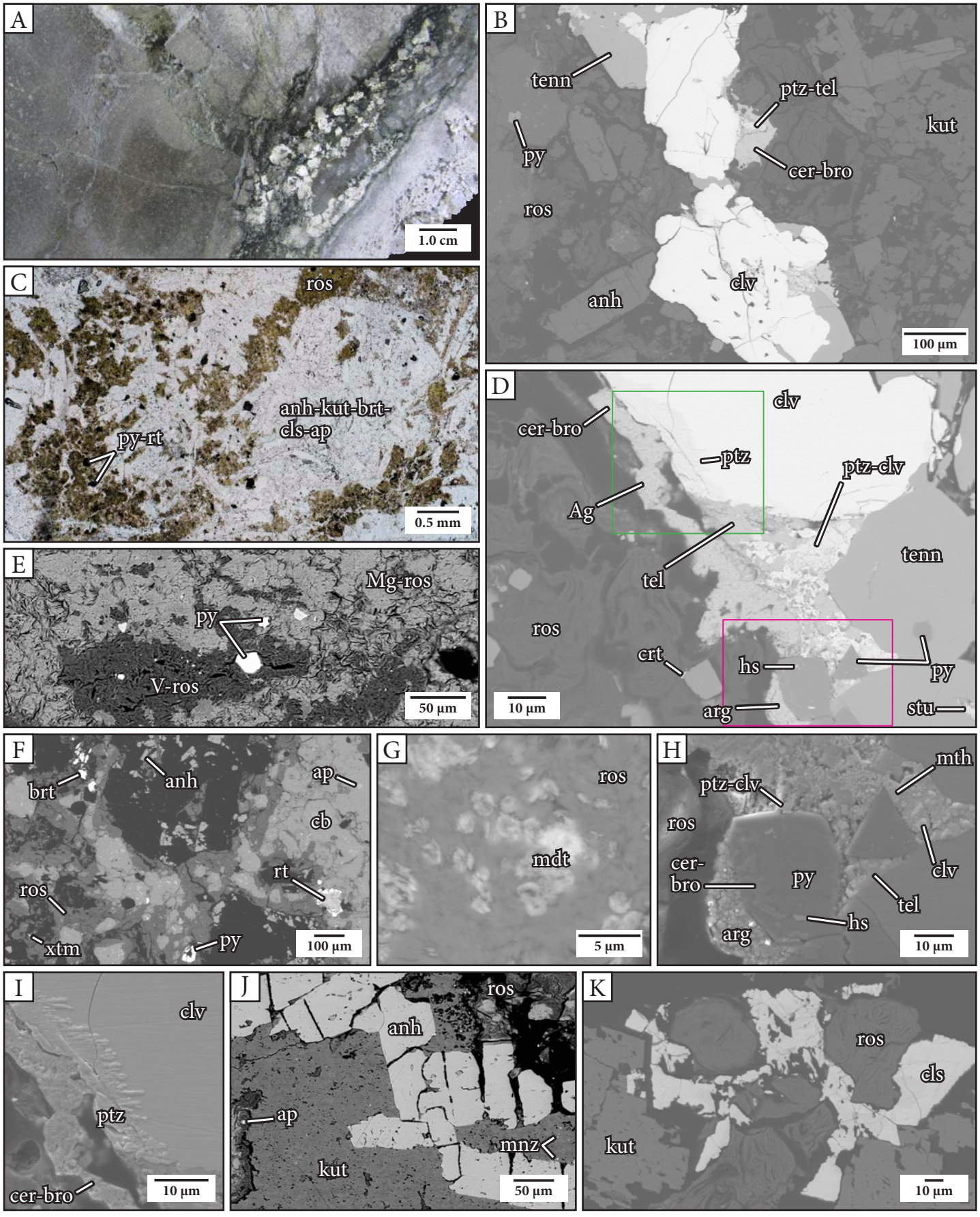
A
1.0 cm
B
tenn
ptz-tel
kut
py
cer-bro
ros
clv
anh
100 µm
C
ros
anh-kut-brt-
cls-ap
py-rt
0.5 mm
D
clv
cer-bro
ptz
ptz-clv
Ag
tenn
tel
ros
crt
hs
py
arg
stu
10 µm
E
Mg-ros
py
V-ros
50 µm
F
brt
anh
ap
cb
rt
ros
xtm
py
100 µm
G
ros
mdt
5 µm
H
mth
ptz-clv
ros
clv
cer-
bro
py
tel
hs
arg
10 µm
I
clv
ptz
cer-bro
10 µm
J
ros
anh
ap
mnz
kut
50 µm
K
ros
cls
kut
10 µm

is acicular and typically occurs as randomly oriented disseminations in quartz (Fig. 4.26E), as wispy patches, and as chain-like aggregates (Fig. 4.26A). Marcasite also occurs as acicular crystal aggregates radiating from the vein wall, surrounding native gold, or surrounding clusters of pyrite – chalcopyrite ± tennantite (Fig. 4.26F–G). Stage 3B veins have crosscut Stage 2A pyrite – marcasite veins and related adularia – pyrite vein halo alteration (Fig. 4.26A) and drusy Stage 3A quartz – calcite – anhydrite veins (Fig. 4.46G). There are several examples of Stage 3B veins with Stage 2A colloform pyrite – marcasite vein clasts (e.g., Fig. 4.26A).

Stage 3B veins occur between –60 and –240 m rsl to the east of 9,500 mE (Fig. 4.19). They are much less abundant and voluminous than Stage 3A and Stage 3C veins and breccias. The average 2-meter composite gold assay value for intervals containing Stage 3B is 4.09 g/t Au and the range is 0.14–23.3 g/t Au (n = 105). Locally, Stage 3B veins are associated with small copper anomalies, because they contain chalcopyrite and tetrahedrite-tennantite. For example, the average 2-meter composite copper assay value for the interval DDHL1872 74–120 m is 0.16% Cu (n = 23). This is significant compared to the average 2-meter composite copper assay value for all samples in Newcrest Mining Limited's assay database for Lihir of 0.03% Cu (n = 192,967).

#### *4.4.3.3 Stage 3C: Chalcedony – quartz – pyrite breccias and veins*

Stage 3C is characterized by complex multi-stage breccias and veins with diverse forms and features. They are typically located at shallow to medial depths (–50 to –230 m rsl) and are spatially associated with Stage 3B veins (Fig. 4.19). The breccias and veins have intense adularia – pyrite – quartz alteration halos (Fig. 4.27G). There is likely a strong structural control on the distribution of Stage 3C features, since the veins and breccias typically have straight, sharp and parallel margins (Fig. 4.27A). The orientation of the structures was not possible to discern from the drill core samples studied, due to the discontinuity of structures between drill holes and the lack of oriented drill core. Stage 3C veins and breccias are typically associated with ore grades (87% of intervals containing Stage 3C breccias and veins have 2-meter composite gold assay values >1 g/t Au). The average 2-meter composite gold assay value for intervals containing Stage 3C is 3.49 g/t Au and the range is 0.32 to 12.98 g/t Au (n = 173).

Stage 3C breccias are cement- to matrix-supported and have highly variable proportions of components (30–70% clasts; 20–40% matrix; 10–30% cement). Massive, chaotic, matrix-rich breccias are most common (Fig. 4.27A–E); however, cement-supported breccias with clast-rotated organization also occur (Fig. 4.27H). Locally, Stage 3C breccias are moderately foliated adjacent to contacts (Fig. 4.27B and E). Stage 3C cement is composed of chalcedony, quartz, and pyrite with minor marcasite and adularia (Fig. 4.27F) and locally, red, pink or white jasper (Fig. 4.27C). The cement has a massive or granular texture and a moderate degree of intergranular porosity (Fig. 4.27F). Blue, gray and/or white,

**Fig. 4.25.** (*Previous page*) Precious metal-bearing minerals in a Stage 3A anhydrite – carbonate – roscoelite vein from sample DDHL1974 220.8 m. Figures 4.25B, D–G and J–K are BSE images. Figures 4.25H–I are secondary electron images. Quantitative EDS X-ray microanalysis data and spot locations are provided in Appendix F. Where possible, mineral labels point to the location of spot analyses. **A.** Hand sample photograph showing the Stage 3A vein that was investigated using the SEM. The vein consists mainly of dark green roscoelite – anhydrite – kutnohorite and contains carbonate – smectite and quartz – pyrite vein clasts. **B.** Fractured crystals of calaverite rimmed by tennantite and associated with petzite, tellurite and cerargyrite – bromyrite. These minerals are surrounded by anhydrite, kutnohorite, roscoelite and pyrite. The pink and green rectangles show the extents of Figures 4.25H and I, respectively. **C.** Transmitted light photomicrograph of the Stage 3A vein material showing intergrown domains of roscoelite – pyrite – rutile and anhydrite – kutnohorite – barite – celestine – apatite. **D.** Close-up view of calaverite – tennantite – pyrite with inclusions of pyrite, stützite, hessite and petzite. This mineral aggregate is encrusted by tellurite – petzite – calaverite, cerargyrite – bromyrite – native silver and argentite. **E.** Mg- and V-rich domains in roscoelite. **F.** Roscoelite – carbonate domains containing barite, apatite, pyrite, rutile and xenotime. The black areas are composed of epoxy and represent where smectite-rich carbonate – anhydrite vein clasts were washed away during preparation of the thin section. **G.** Very fine-grained, blade-like aggregates of molybdite in roscoelite. **H.** Close-up view of the area within the pink rectangle in Figure 4.25B, highlighting the texture of fine-grained telluride – tellurite intergrowths and inclusions of cerargyrite – bromyrite and hessite in pyrite. **I.** Close-up view of the area within the green rectangle in Figure 4.25B, showing lamellar-like petzite at the margin of a calaverite crystal. **J.** A blocky anhydrite and kutnohorite domain. The kutnohorite contains monazite inclusions. **K.** Close-up view of an intergrowth of celestine, roscoelite and kutnohorite. Abbreviations: Ag = native silver, anh = anhydrite, ap = fluorapatite, arg = argentite, brt = barite, bro = bromyrite, cb = carbonate, cer = cerargyrite, cls = celestine, clv = calaverite, crt = cerussite, hs = hessite, kut = kutnohorite, Mg-ros = magnesium-rich roscoelite, mdt = molybdite, mnz = monazite, mth = muthmannite, ptz = petzite, py = pyrite, ros = roscoelite, rt = rutile, stu = stützite, tenn = tennantite, tel = tellurite, V-ros = vanadium-rich roscoelite, xtm = xenotime.

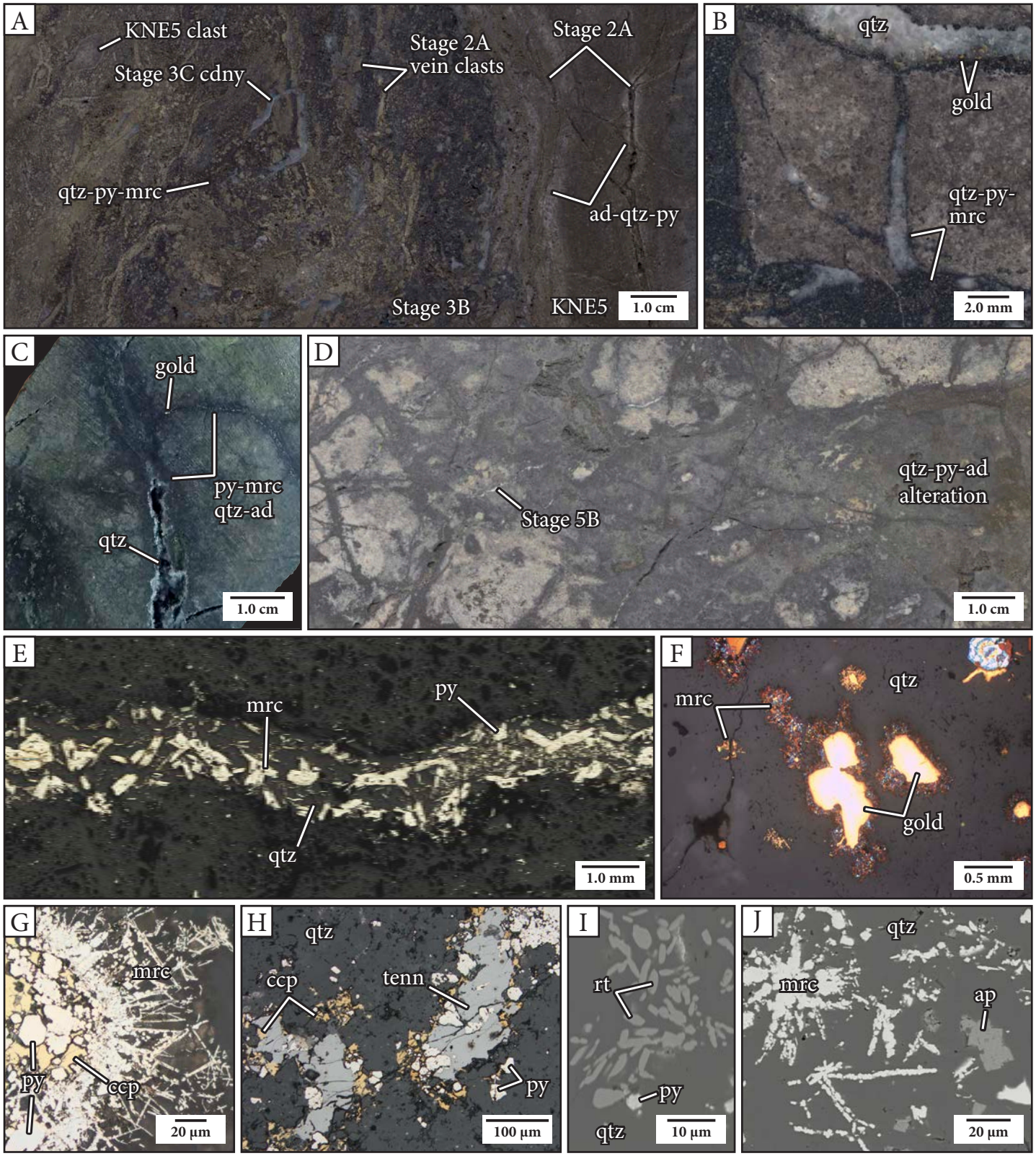


**Fig. 4.26.** Stage 3B quartz – pyrite ± chalcopyrite ± tetrahedrite-tennantite ± gold veins. **A.** Hand sample photograph of a multiphase, dark blue-gray Stage 3B breccia vein that has crosscut Stage 2A pyrite – marcasite veins and associated adularia – quartz – pyrite alteration halos within hornblende-biotite-bearing monzonite (KNE5). The intricate breccia vein is composed of wispy patches and chain-like aggregates of pyrite, marcasite and quartz, KNE5 wall-rock clasts with pyrite – marcasite rinds, abundant Stage 2A banded pyrite – marcasite vein clasts. The sample has been crosscut by several curved and irregular Stage 3C chalcedony veins. Sample: DDHL1924 122.8 m. **B.** Close-up view of vuggy, adularia – pyrite-altered, polymict matrix-supported breccia (KNE1) hosting a Stage 3B vein stockwork. The veins contain zones of very fine-grained, blue-gray quartz intergrown with pyrite and marcasite and zones of sulfide-poor, white to translucent gray quartz that contain rounded grains of

concentrically banded chalcedony locally infills open spaces surrounded by matrix-rich domains (Fig. 4.27A). The mixture of gray quartz, chalcedony and adularia, abundant fine-grained pyrite ± marcasite and mud-sized rock flour matrix causes many of the breccias to have a uniform, brownish-gray coloration (Fig. 4.27A–E). Clasts are moderately to poorly sorted and are subrounded to highly angular. The grain size of the clasts is gradational with the mud- to very coarse sand-sized matrix and ranges from granule to cobble. Clast populations are polymict and consist of locally sourced lithic clasts, breccia clasts and vein clasts. Clasts of earlier-formed Stage 3B and 3C breccias are particularly abundant (Fig. 4.27C–D). Some Stage 3C clasts are rimmed by banded pyrite (Fig. 4.27D).

Stage 3C veins are irregular to straight-sided and have sharp margins. In general, these veins have a later timing of emplacement than Stage 3C breccias (Fig. 4.27B). Both forms are included in Stage 3C due to their comparable mineralogy and strong spatial association. Stage 3C veins are principally composed of opaque, multicolored chalcedony (white, brown, tan, gray, peach and black), with less abundant, clear to white quartz, cream to peach adularia and very fine-grained pyrite. The veins are typically colloform banded and botryoidal (Fig. 4.27B, G and J–K), massive, moss-textured (Fig. 4.27I) or may display subtle and gradational color and compositional variations (Fig. 4.27G). Locally, fine-grained euhedral quartz forms drusy cavity linings. Brown and tan coloration in chalcedony has elsewhere been attributed to finely disseminated hydrocarbon residue and dendritic electrum (e.g., McLaughlin hot springs Au deposit, USA; Sherlock, 2000). However, no hydrocarbon spheres or native gold were found when observing brown chalcedony samples from Coastal under the SEM (e.g., Fig. 4.27G).

### *4.4.4 Stage 4: Lihir diatreme breccia complex*

Stage 4 (the Lihir diatreme breccia complex) consists of a cluster of discordant, multi-stage breccia bodies that crop out at the western, northern and southwestern margins of the Lihir gold deposit. The breccia bodies are primarily composed of polymict breccias that contain abundant fine-grained rock flour matrix. This section documents the characteristics and geometry of these breccias and details the relationships between structure, breccia formation and mineralization. In addition to graphic logging of drill core on cross sections A–A'–A" and B–B' as outlined in section 4.2, information regarding the extents and characteristics of the Lihir diatreme breccia complex was collected from photo core logging of a further 474 drill holes from across the Lihir deposit.

#### *4.4.4.1 Previous work*

Lihir gold deposit is primarily hosted within multiply brecciated rocks of various types and origins. Extensive and recurrent episodes of brecciation would have provided the necessary conditions for the efficient circulation of ore fluids and may have been a factor in the formation of such a large deposit. However, not all processes of brecciation result in an increase in the hydraulic conductivity of a rock.

(*continued from previous page*) visible gold. Sample: DDHL1931 237.1 m. **C.** Branching, dark gray-blue quartz – pyrite – marcasite veins that contain visible gold. The veins have irregular and diffuse margins and pyrite – marcasite – quartz – adularia alteration halos. The quartz infill has a drusy texture where the vein has a wider aperture. Sample: DDHL1924 237.4 m. **D.** A dense Stage 3B quartz – pyrite vein stockwork with strong intensity quartz – pyrite – adularia alteration halos that coalesce forming dark gray domains. The Stage 3B stockwork has been crosscut by white, wispy Stage 5B alunite – augelite – pyrite veinlets. Sample: DDHL1872 99.0 m. **E.** Reflected light photomicrograph of an irregular Stage 3B quartz – marcasite – pyrite veinlets, highlighting the random orientation, even distribution and wide range of grain sizes (<0.1–1.0 mm) of pyrite and marcasite. Sample: DDHL1931 237.1 m. **F.** Reflected light photomicrograph of rounded, amorphous grains of highly reflective native gold that have been enveloped by radiating sprays of acicular marcasite. The marcasite needles also occur as isolated patches within the quartz infill. The sample was NaOCl etched, revealing that the marcasite surrounding native gold (*blue, white, brown, orange*) has a higher arsenic content compared to the marcasite in quartz or adjacent to pyrite (*orange, yellow*). Sample: DDHL1931 237.1 m. **G.** Reflected light photomicrograph of a quartz vein containing an aggregate of chalcopyrite and pyrite surrounded by marcasite needles. Sample: DDHL1872 99.0 m. **H.** Reflected light photomicrograph of tennantite – chalcopyrite – pyrite in a granular quartz vein. Sample: DDHL1872 99.0 m. **I.** BSE image of hydrothermal rutile and pyrite in a quartz vein. Sample: DDHL1931 237.1 m. **J.** BSE image of hydrothermal apatite adjacent to rosette-like aggregates of marcasite in a quartz vein. Sample: DDHL1872 99.0 m. Abbreviations: ad = adularia, ap = apatite, ccp = chalcopyrite, cdny = chalcedony, mrc = marcasite, py = pyrite, qtz = quartz, rt = rutile, tenn = tennantite.

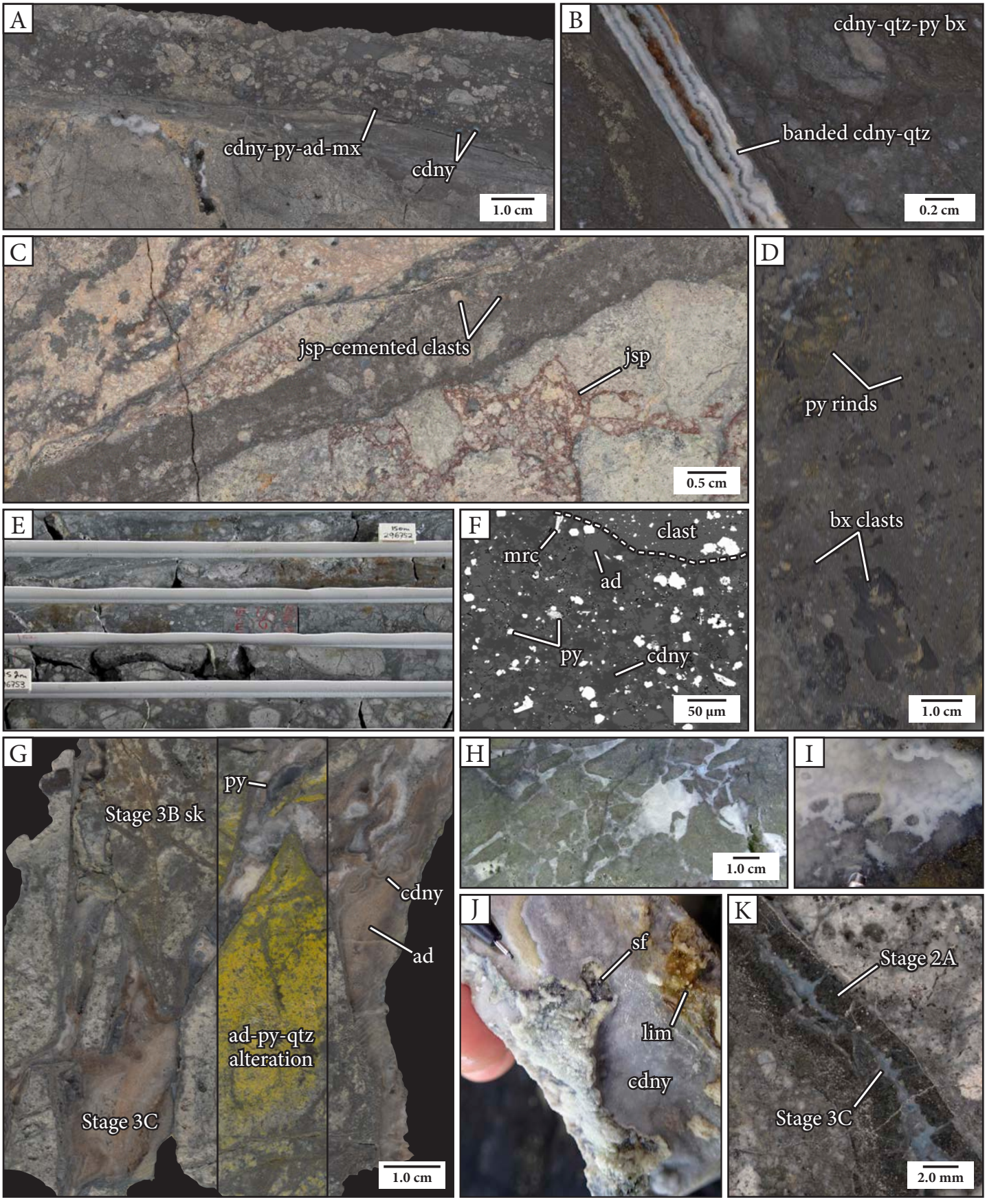
A
cdny-py-ad-mx
cdny
1.0 cm
B
cdny-qtz-py bx
banded cdny-qtz
0.2 cm
C
jsp-cemented clasts
jsp
0.5 cm
D
py rinds
bx clasts
1.0 cm
E
F
clast
mrc
ad
py
cdny
50 µm
G
Stage 3B sk
py
cdny
ad
ad-py-qtz
alteration
Stage 3C
1.0 cm
H
1.0 cm
I
J
sf
lim
cdny
K
Stage 2A
Stage 3C
2.0 mm

Breccias produced by explosive volcanic-hydrothermal processes, such as those that form the subsurface portions of diatreme breccia bodies, are typically fine-grained and matrix-supported (50–90% matrix material; Sillitoe, 1985). These characteristics may limit porosity and permeability necessary for the flow of hydrothermal fluids (Sillitoe, 1985). In some cases, volcanic-hydrothermal breccias have been known to act as aquicludes, diverting and focusing the flow of ore-forming hydrothermal fluids into adjacent wall rocks (e.g., Kelian gold deposit, Indonesia; Davies et al., 2008a).

Breccias produced by explosive processes were recognized in the earliest studies of the Lihir gold deposit. Moyle et al. (1990) identified breccias containing fragments of charcoal within and around circular features up to 200 m across in the Kapit area. The morphological features were interpreted as either phreatic explosion craters or maars (Moyle et al., 1990). Initially, volcaniclastic brecciated host rocks and gold mineralized breccias were grouped together as part of the Ladolam breccia complex, described as an elliptical (~3 km long axis) composite breccia body centered on alkaline intrusive rocks within the Luise Volcano (Davies and Ballantyne, 1987; Moyle et al.,1990; Carman, 1994, 2003). The breccia complex was interpreted to have formed within the upper part of a diatreme breccia pipe (Carman, 1994, 2003). Volcanic-hydrothermal brecciation was thought to have occurred immediately following sector collapse of the Luise volcano due to the rapid decompression of an active porphyry-style magmatic-hydrothermal system (Carman, 2003). Phreatomagmatic and hydraulic breccias at shallow levels of the breccia complex were interpreted to be the major hosts to gold mineralization at Lienetz and Minifie, suggesting that epithermal gold mineralization occurred in the later stages of diatreme formation and continued as steady-state hydrothermal activity prevailed.

Subsequent studies by Blackwell (2010) and Ageneau (2012) reported on the presence of magmatic-hydrothermal and phreatomagmatic breccias at the Lienetz and Kapit ore zones. A key difference was that the phreatomagmatic breccias were mapped adjacent to (rather than coincident with) mineralized centers. The breccias were interpreted as having a post-mineralization timing, based on the evidence that they contained clasts of porphyry-stage anhydrite and epithermal-stage pyrite veins and cemented breccias (Blackwell, 2010; Ageneau, 2012). In Minifie ore zone, Corbett et al. (2001) mapped two distinct volcanic-hydrothermal breccia pipes in the upper benches of the Minifie open pit (Ramp and Mamboo diatremes; Table 4.5). In contrast, Blackwell et al. (2014) did not identify phreatomagmatic breccias in the Minifie ore zone. They interpreted that the brecciated host rocks occupying the Minifie ore zone and surrounding area were formed by volcanic and/or sedimentary processes. Gold ore-related epithermal breccias were

**Fig. 4.27.** (*Previous page*) Stage 3C chalcedony – quartz – pyrite breccias and veins. **A.** A quartz – chalcedony – pyrite-cemented, matrix-supported breccia dike (Stage 3C) with subangular to subround polymict clasts. Open spaces have been infilled with banded blue to white chalcedony. Sample: DDHL1856 111.0 m. **B.** A straight-sided and symmetrically banded Stage 3C chalcedony – quartz vein with a drusy centerline. The vein has crosscut a Stage 3C chalcedony – quartz – pyrite breccia. Sample: DDHL1856 114.2 m. **C.** A Stage 3C chalcedony – pyrite-cemented breccia dike that has obliquely crosscut the clasts and cement of a Stage 3C red jasper – pyrite-cemented breccia. The chalcedony – pyrite vein dike contains clasts of red jasper – pyrite-cemented breccia. Sample: DDHL1953 275.6 m. **D.** Hand sample photograph of a matrix- and clast-rich Stage 3C pyrite – chalcedony-cemented breccia dike. The angular clasts are predominantly composed of matrix-rich pyrite – chalcedony-cemented breccia and have been rimmed by banded pyrite. Sample: DDHL1953 278.5 m. **E.** Core box photograph of a multi-stage and chaotic Stage 3C breccia with polymict, very poorly sorted granule- to boulder-sized clasts. Adjacent to internal contacts the breccia is laminated and the clasts are relatively fine-grained (e.g., granule- to pebble-sized). Interval: DDHL1962 ~149.4–153.6 m. The average 2-meter composite gold assay value for the interval from 148–154 m is 5.20 g/t Au. **F.** BSE image showing granular chalcedony – adularia – pyrite – marcasite cement and an adularia – pyrite-altered clast. There is micron-scale porosity in the cement at the interstices between adularia rhombs. Sample: DDHL1856 111.0 m. **G.** A network of coalescing Stage 3C veins composed of banded peach adularia, white and gray chalcedony and dark gray pyrite that have crosscut a Stage 3B quartz vein stockwork. The sample has been feldspar stained (*yellow = adularia*), which shows that the Stage 3C veins are associated with adularia – pyrite vein halo alteration that decreases in intensity over ~5 cm from the vein wall. Sample: DDHL1872 97.9 m. **H.** A clast-rotated chalcedony-cemented breccia (Stage 3C) with subangular to subround pyroxene-phyric basalt breccia clasts (KNE2b). Sample: DDHL1974 174.3 m. **I.** Moss texture in a white and translucent gray Stage 3C chalcedony vein. The pencil lead (*bottom, centered*) is 0.5 mm across. Sample: DDHL1953 276.2 m. **J.** Botryoidal surface of a white Stage 3C chalcedony vein with very thin layers of fine-grained gray sulfides (pyrite) that have partially oxidized to limonite. Sample: DDHL1970 95.6 m. **K.** A pale blue Stage 3C chalcedony vein that has precipitated along the vuggy centerline of a Stage 2A banded pyrite vein. Sample: DDHL1856 162.8 m. Abbreviations: ad = adularia, bx = breccia, cdny = chalcedony, jsp = jasper, lim = limonite, mrc = marcasite, mx = matrix, py = pyrite, qtz = quartz, sf = fine-grained sulfide minerals, sk = stockwork.

interpreted to have been produced by hydraulic fracturing ± hydraulic jacking.

Overall, there appear to be disagreements and contradictions between previous studies regarding the characteristics, extents and timing of volcanic-hydrothermal breccias at Lihir. The current study seeks to reexamine these aspects of volcanic-hydrothermal brecciation across the Luise volcano and to comment on the genetic and exploration implications of these new findings.

*4.4.4.2 Breccia geometry*

In this study, seven, discordant and composite volcanic-hydrothermal breccia bodies were identified (Far North, Kapit, Karot, Diwai, Saddle, Ramp and Mamboo breccias; Table 4.5; Figs. 4.28–4.29). Other less voluminous volcanic-hydrothermal breccia bodies also occur within and adjacent to the deposit. The map-scale geometries of the breccias have been modeled using Leapfrog Geo™ (Figs. 4.28–4.29) and summarized in Table 4.5. Overall, the Lihir diatreme breccia complex is oriented parallel to the N- to NE-trending elongation of the Luise amphitheater, and the submarine bathymetric ridges (Fig. 4.28B). This NE structural trend has also localized surface geothermal activity at Lihir (Wallace et al., 1983). Individual breccia bodies are spatially associated with amphitheater-scale structural lineaments (Fig. 4.29). The breccias do not typically contain large-scale shear fabrics, suggesting that movement along the faults ceased prior to breccia emplacement.

The Far North, Kapit, and Saddle breccias define downward tapering ellipsoidal bodies that flare markedly outward near surface (similar to a margarita glass; Fig. 4.28A). They have been emplaced within predominantly clastic rocks—brecciated mafic and intermediate lavas and near-surface intrusions (dikes and sills) and volcaniclastic breccias. The Far North breccia is generally NE-trending and moderately NW-dipping (Fig. 4.28); however, it is poorly defined at its northern and western extents due to the limits of drilling away from the ore zones. The Kapit breccia is elongated to the north and dips moderately to the northwest (Fig. 4.28). Saddle breccia is defined by three coalesced, upright, N- to north-northwest-trending breccias with distinct root zones that are aligned approximately north-south (Fig. 4.29B). The polymict, accretionary lapilli-bearing, matrix-supported breccia with sharp discordant contacts mapped at the western margin of the Lienetz open pit by Blackwell (2010) is interpreted here as part of the Saddle breccia (Fig. 4.30).

The Ramp, Mamboo and Karot breccias are narrow, steep-sided pipes that are localized along structural intersections (Fig. 4.28–4.29). Ramp breccia is located on the southern side of the Minifie open pit at the intersection between east- and northeast-trending structures. Mamboo breccia is located on the southwestern side of the Minifie open pit at the intersection between N- and NE-trending structures. Karot breccia is located at the intersection of NW- and NE-trending structures in the Coastal area (Fig. 4.29). Karot breccia is an isolated, equant, carrot-shaped pipe that is surrounded by many (>10), small (<20 m) breccia pods and dikes with sharp contacts. Similar, dekameter-scale breccia pipes were identified at surface in the Coastal area during geological mapping prior to mining (Moyle et al., 1990). The Karot breccia pipe and surrounding breccias were emplaced within monzonitic intrusive rocks. The contacts with the monzonite are gradational over the scale of meters. Hydrothermal mud-matrix dikes and jigsaw-fit breccias with hydrothermal mud matrix are typical adjacent to the contact (Fig. 4.39A). The Mamboo and Ramp breccias were mapped from exposures within the Minifie open pit by Corbett et al. (2001). Mamboo breccia was described as having steep contacts with volcanic and collapse breccias in the lower pit and strongly flared, dipping contacts with volcanic breccias near surface. Ramp breccia was described as a deeply eroded breccia pipe associated with a trachytic intrusion (Corbett et al., 2001).

Diwai breccia is composed of a series of coalesced and irregularly-shaped, branching breccia bodies that have

**Table 4.5.** Geometry of volcanic-hydrothermal breccia bodies at Lihir.

| Breccia | Geometry | Host rocks | Location description | Structural trend | Root coordinates** | Dimensions |
|---|---|---|---|---|---|---|
| Far North breccia* | A downward tapering, elliptical breccia pipe; moderately steep (60°) southern and eastern margins that flare sharply southeastwards above 200 m depth; margins to the north and west are undefined | Lavas, subvolcanic intrusions and volcaniclastic breccias | Northwest of Kapit NE ore zone | NE-trending and moderately NW-dipping | 9,210 mE<br>6,300 mN<br>≥375 m | 800 × 500 × ≥375 m |
| Kapit breccia* | A downward tapering, elliptical breccia pipe; the western, northwestern and southern margins are sharp and steep (80°); the northeastern and eastern margins are strongly flared | Lavas, subvolcanic intrusions and volcaniclastic breccias | North of Kapit ore zone | N-trending and moderately NW-dipping | 8,880 mE<br>5,650 mN<br>≥385 m | 600 × 400 × ≥385 m |
| Karot breccia* | An isolated, subvertical breccia pipe; several (>10), small (<20 m) pods and dikes with sharp contacts surround the main body | Monzonite | Within Coastal ore zone | Steeply SSW-plunging; centered on the intersection of NW- and NE-trending structures; small pods localized along an ENE trend | 9,700 mE<br>5,030 mN<br>≥260 m | 150 × 150 × ≥260 m |
| Diwai breccia* | A series of coalesced and irregularly-shaped, branching breccia bodies | Subvolcanic intrusions and volcaniclastic rocks crosscut by alkaline intrusions | Between Kapit and Kapit NE ore zones | Branches of the breccias follow N- and NE-trending structures; a N-trending branch connects Diwai breccia to Far North breccia | 9,375 mE<br>5,850 mN<br>150–200 m | 700 × 500 × ~175 m |
| Saddle breccia* | Three, shallow, coalescing, downward tapering breccia pipes; the northern margin is steep and links with the Kapit breccia at ~50 m depth; the western and eastern margins are sharp and steep (80°); the southern margin is moderately steep (60°) and flares strongly near surface, forming a 50 m-thick blanket-like body of bedded breccias extending south from 4,000 mN to 3,700 mN; bedded breccias at 8,870 mE, 3,653 mN dip 30–60° to the southeast[a] | Microdiorite, polymict, matrix supported breccia, and anhydrite – biotite – orthoclase-cemented breccias | Bounds the Lienetz and Kapit ore zones to the west | NNW-trending breccia bodies that lie along a N-trending structure | 8,760 mE<br>4,980 mN<br>165 m<br>8,800 mE<br>4,680 mN<br>175 m<br>8,850 mE<br>4,200 mN<br>≥200 m | 1.9 × 700 × >200 m |
| Ramp breccia[b] | A vertical and steep-sided breccia pipe | Volcanic and intrusive rocks[b] | East Minifie[b] | E-trending; centered on the intersection of E-trending and NE-trending structures | ~9,600 mE<br>~3,400 mN[b] | Undefined |
| Mamboo breccia[b] | A steep-sided breccia pipe that flares strongly outward near surface; surrounded by thick-bedded accretionary lapilli-bearing tuff ring deposits[b] | Volcanic breccia and collapse breccia[b] | Bounds Minifie ore zone to the southwest[b] | N-trending; centered on the intersection of N-trending and NE-trending structures | ~9,100 mE<br>~3,100 mN[b] | Undefined |

*Named during this study.
**Depth coordinate of root is presented in meters below sea level.
[a]Blackwell (2010), [b]Corbett et al. (2001)

crosscut a combination of volcano-sedimentary rocks and alkaline intrusions. The breccia has a NE-elongated wedge-like shape that narrows to a point in the southwest. Several dekameter-scale breccias surround the main breccia body near surface. Branches of Diwai breccia are alternatively N- and NE-trending and one of the N-trending branches connects the Diwai breccia and Far North breccias (Fig. 4.29B).

#### *4.4.4.3 Breccia facies*

Saddle, Kapit, Diwai and Far North breccias each consist of a complex of volcanic-hydrothermal breccia pipes and dikes, which are composed of six breccia facies (Table 4.6; Stage 4A–F). The breccias vary in appearance due to local variations in clast type, size, abundance and degree of rounding, as well as the intensity of post-brecciation alteration. In general, the breccias are light to dark gray, polymict and matrix-supported with similar matrix components (pulverized polymict lithic clasts with abundant feldspar fragments).

Consistent crosscutting relationships between breccia

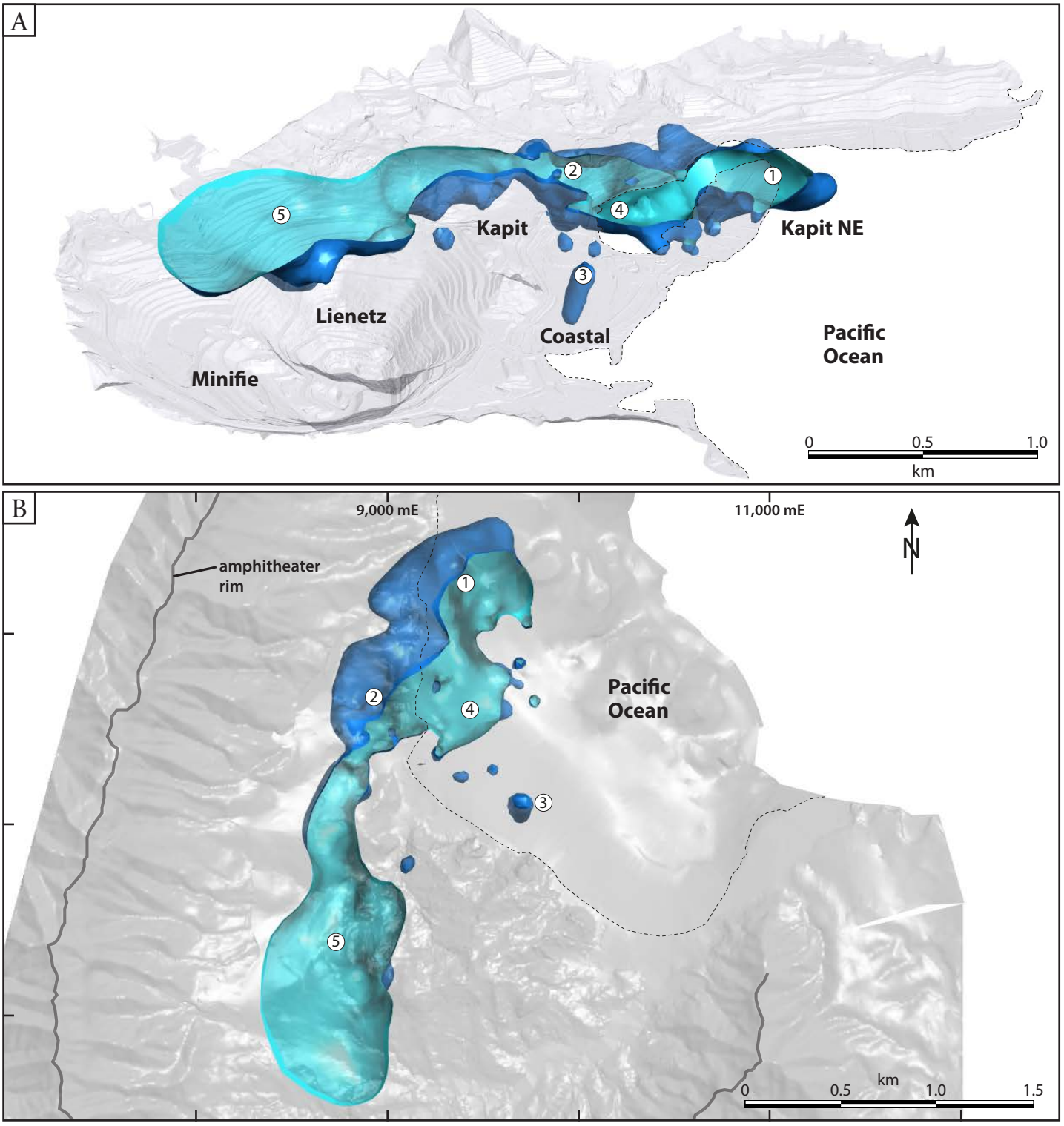


**Fig. 4.28.** Three dimensional geometry of the Lihir diatreme breccia complex, as modeled using Leapfrog Geo™. The outside surface of the breccias has been colored dark blue and the inside surface has been colored cyan. **A.** Oblique view (plunging 35˚NW). The translucent gray surface is the digital elevation model for the Lihir gold mine (2013) and the dashed black line follows the shoreline. **B.** Plan view. The translucent gray surface is the pre-mining topography of the Luise amphitheater and near-shore bathymetry of the Luise Harbor. The dashed black line follows the pre-mining shoreline. 1 = Far North breccia, 2 = Kapit breccia, 3 = Karot breccia, 4 = Diwai breccia, 5 = Saddle breccia. Mamboo and Ramp breccias were not modeled.

facies were observed within each of the breccia bodies, as exemplified on geological section BB' for the Diwai breccia in Kapit NE (Fig. 4.31). Note that the geological section bisects Diwai breccia longitudinally. Stage 4A polymict ma-

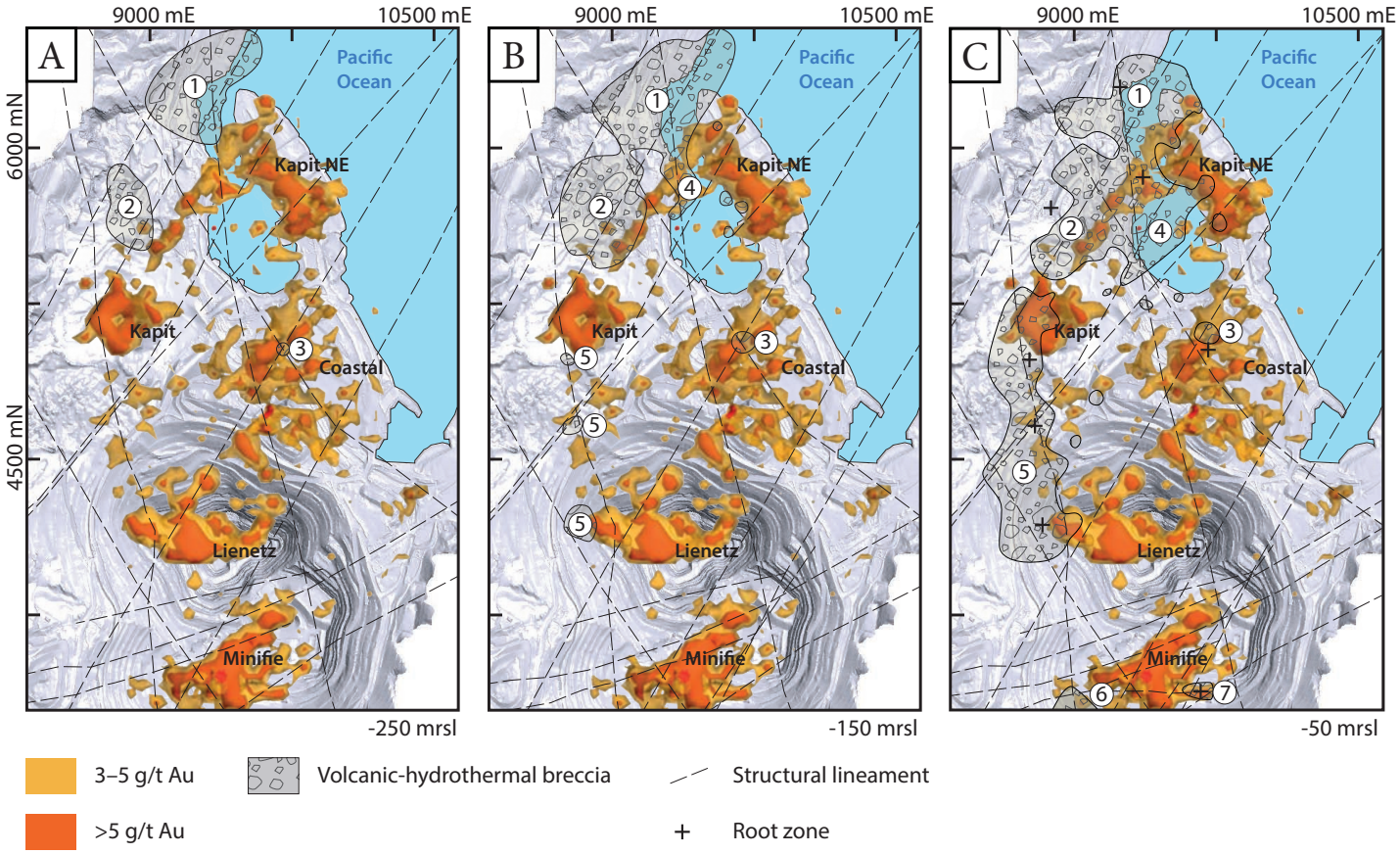


**Fig. 4.29.** Volcanic-hydrothermal breccias and their relationship with gold orebodies at Lihir. The figure shows three plan view horizontal slices through the Lihir gold deposit, showing the location of volcanic-hydrothermal breccias and their associated root zones (as modeled in Leapfrog Geo™), amphitheater-scale structural lineaments (as defined by previous workers and consultants) and gold grade shells (unsliced). Plan view horizontal slices are at **A.** –250 m, **B.** –150 m, and **C.** –50 m relative to sea level. 1 = Far North breccia, 2 = Kapit breccia, 3 = Karot breccia, 4 = Diwai breccia, 5 = Saddle breccia, 6 = Mamboo breccia, 7 = Ramp breccia.

trix-rich breccia and Stage 4B polymict clast-rich breccia, sandstone and mudstone are the most volumetrically significant facies. Diwai breccia in particular is predominantly composed of Stage 4B polymict clast-rich breccia (Figs. 4.31–4.32). Stage 4A and 4B breccias typically have sharp contacts with one another, forming nested pipes or discrete adjacent breccia bodies (Fig. 4.34E); however, gradational contact relationships have also been observed between the two. In the deepest parts of the breccia bodies, Stage 4A or Stage 4B breccias transition into Stage 4C matrix-rich polymict breccia with wispy juvenile andesite clasts and then into Stage 4D jigsaw-fit to clast-rotated feldspar-phyric andesite-clast breccias centered on coherent feldspar-phyric andesite dikes (KNE10; Fig. 4.31). The upper portions of the breccia bodies contain megablocks (meter- to dekameter-scale fragments) of Stage 4E stratified, accretionary lapilli-bearing breccias and sandstones that are locally cross-bedded (Fig. 4.31). Narrow pipes and dikes of Stage 4F breccia, sandstone and mudstone cross-cut Stage 4A–E and the surrounding host rocks. Karot breccia is a monophase breccia pipe composed entirely of Stage 4G matrix-rich monzonite-clast breccia that is spatially associated with small pods and dikes of Stage 4H siliceous mud matrix-supported breccia. The Mamboo and Ramp breccias contain milled matrix-rich breccias (similar to Stage 4A polymict, matrix-rich breccia) and abundant juvenile magmatic clasts (similar to Stage 4C polymict, matrix-rich breccia with wispy andesite clasts; Corbett et al., 2001). The upper portions of Mamboo breccia contain charcoal fragments and accretionary lapilli-bearing bedded breccias (similar to Stage 4E; Corbett et al., 2001).

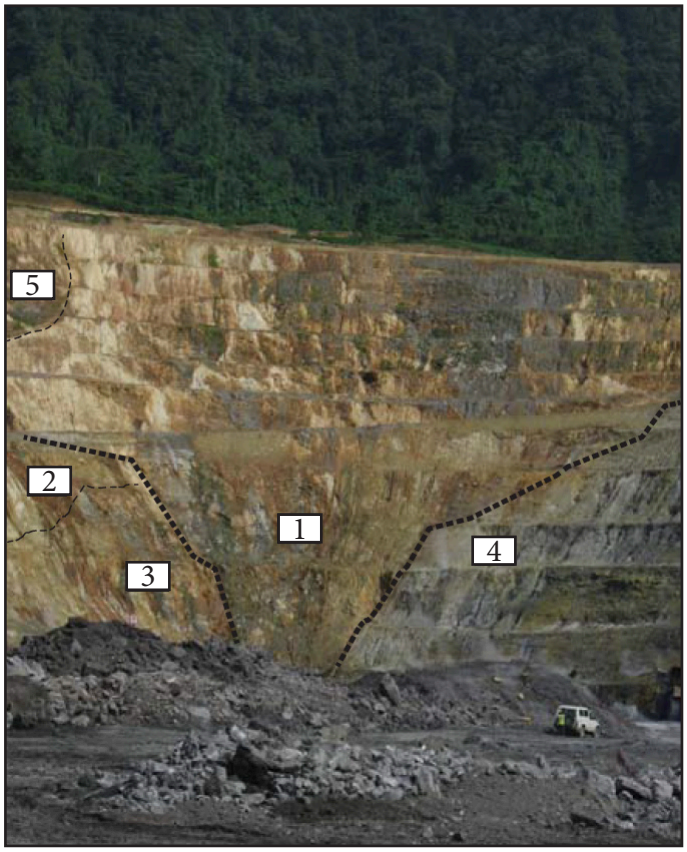


**Fig. 4.30.** Saddle breccia (1) in the western wall of Lienetz open pit. The breccia has sharp contacts with polymict, matrix-supported breccia to sandstone (2), microdiorite (3), and anhydrite – biotite – orthoclase-cemented breccias (4). Plagioclase-phyric andesite (5) crosscuts Saddle breccia as a near-vertical dike. Bench heights are 12 m. Modified from Blackwell (2010).

Stage 4 volcanic-hydrothermal breccias contain a large range of clasts types. The most abundant clasts are volcanic—in particular, feldspar-phyric andesite (KNE10; Figs. 3.19, 4.33E and 4.35), pyroxene-feldspar-phyric andesite (KNE3; Figs. 4.33A–B and 4.35C) and pyroxene-phyric basalt (KNE2; Fig. 4.33A–B). Various altered and unidentifiable volcanic clasts also occur, some of which are apparently aphanitic. Volcanic clasts are typically subangular to very angular with moderate sphericity and range from sand to boulder size (up to ~ 5 m diameter). Sedimentary and igneous clasts are less common and include polymict matrix-supported breccias, sandstone and laminated to massive mudstone (similar to KNE1; Fig. 4.33B), biotite-feldspar-phyric, nepheline-bearing monzonite (KNE4; Fig. 4.32), hornblende-biotite-bearing monzonite (KNE5; Figs. 4.32 and 4.33A), trachytic hornblende-feldspar-phyric latite (KNE9; Fig. 4.32).

Feldspar-phyric andesite clasts (KNE10) are typically angular and blocky to equant (Fig. 4.35E and F). However, many of the feldspar-phyric andesite clasts have amoeboid shapes and delicate and ragged margins that are enveloped in laminated fine sand to mud (Fig. 3.19D). This is particularly noticeable in pebble and boulder clasts. Some feldspar-phyric andesite clasts have wispy and irregular shapes with wavy, indistinct margins and an association with chaotic, wavy and lenticular matrix textures (Figs. 4.32 and 4.35A–D). These wispy clasts may wrap around other clasts or have been compressed between clasts (Fig. 4.35B–C). Some andesite clasts have partially wispy and partially blocky margins.

Rare, intact and fragmented accretionary lapilli (<~1 cm diameter) are randomly distributed throughout Stage 4A and 4C breccias. They are more common within Stage 4E well-stratified, matrix-rich sandstone and mudstone and occur primarily along bedding planes (Fig. 4.33F) although they also occur disseminated throughout the breccia (Fig. 4.33B). The upper portions of the breccia bodies contain charcoal fragments (typically <10 cm across; Figs. 4.32 and 4.33G) as well as megablocks (meter- to dekameter-scale fragments) of Stage 4E stratified, accretionary lapilli-bearing breccias and sandstones that are locally cross-bedded (Figs. 4.31 and 4.33F). At Saddle breccia in western Lienetz, Blackwell (2010) observed plagioclase-phyric andesite, vesicular and dense pyroxene-phyric basalt, mudstone, microdiorite, and polymict matrix-supported breccia clasts, as well as charcoal fragments, rare accretionary lapilli and armored lapilli with andesite cores. Within Kapit breccia in Kapit, Ageneau (2012) documented a similar range of clasts, specifically: pyroxene-phyric basalt, microdiorite to plagioclase-phyric diorite, polymict matrix-supported breccia, mudstone, accretionary lapilli, and charcoal.

Breccia clasts, vein fragments and clasts with truncated veins have been observed in drill core samples from Diwai breccia in Kapit NE, including Stage 1 anhydrite-cemented

**Table 4.6.** Summary of Stage 4 volcanic-hydrothermal breccia facies at Lihir.

| Facies | Clast organization, geometry and internal contact relationships | Clasts | Matrix | Interpretation |
|---|---|---|---|---|
| **Stage 4A**: Polymict, matrix-rich breccia | Polymict, massive, chaotic, matrix-supported, poorly to very poorly sorted; crosscuts Stage 4B and 4E breccias sharply, forming large pipes and tabular bodies; transitions gradually into Stage 4C breccia | **15–50%**; **Grain size:** 2 mm to 5 m; **Shape:** angular to round; equant, ragged, tabular, or splintery; **Components:** *Common:* feldspar-phyric andesite, (vesicular) pyroxene-phyric basalt, fine- to coarse-grained diorite, polymict matrix-supported breccia; *Rare*: Stage 4E breccia with accretionary lapilli, laminated mudstone and sandstone, biotite-phyric monzonite, accretionary lapilli, charcoal, anhydrite, pyrite – kaolinite – dickite and pyrite vein clasts | Dark gray, moderately sorted, fine sandstone to mudstone matrix composed of milled fragments of the same composition as clasts; disseminated pyrite | Stage 4A and 4B breccias are interpreted to have formed primarily via subsurface explosive phreatomagmatic brecciation; ragged feldspar-phyric andesite clasts are interpreted to be juvenile magmatic clasts; the high degree of rounding in some Stage 4B breccias suggests significant clast abrasion and transport from the site of fragmentation |
| **Stage 4B:** Polymict, clast-rich breccia | Polymict, massive to graded (fining upward from dominantly cobble-sized to granule-sized clasts over tens of meters), chaotic, matrix-supported to clast-supported, moderately to well sorted; crosscut by all other breccia facies | **50–90%**; **Grain size:** 2 mm to 50 cm; **Shape:** angular to well rounded; equant, ragged, tabular; **Components:** as Stage 4A; some feldspar-phyric andesite clasts with armored (mud-matrix coated) clast margins; clasts with pyrite rinds and banded pyrite veins | Massive; dark gray mud- to light gray coarse sand-sized matrix composed of pulverized rock; domains of very poorly sorted and well sorted matrix; disseminated pyrite | |
| **Stage 4C:** Polymict, matrix-rich breccia with wispy andesite clasts | Polymict, massive, chaotic, matrix-supported; spatially associated with and transitional to Stage 4D breccia over several meters | **15–50%**; **Grain size:** 2 mm to 3 m; **Shape:** angular, ragged, wispy, blocky, blobby; **Components:** as Stage 4A, with up to 90% clay-altered feldspar-phyric andesite clasts | Dark gray, mud- to fine sand-sized matrix composed of pulverized rock; disseminated pyrite | Phreatomagmatic breccias in the root zones of diatremes; wispy andesite clasts are interpreted as juvenile magmatic clasts |
| **Stage 4D:** Jigsaw-fit to clast-rotated andesite-clast breccia | Monomict, matrix-supported; transitions from coherent andesite into jigsaw-fit then clast-rotated andesite-clast breccia over 0.2–10 m, less commonly chaotic; highly irregular contacts at the cm-scale; gradational contacts with Stage 4A–4C | **60–95%**; **Grain size:** 2 mm to 2 m; **Shape:** predominantly fractured, angular, blocky and disaggregated clasts, rarely occurs as rounded, blobby and irregular clasts; **Components:** variably altered feldspar-phyric andesite clasts | Dark gray mud-sized matrix composed of pulverized rock; massive or laminated; laminations may form U-shaped sags between clasts | Dikes that triggered maar-diatreme formation; post-eruptive dikes with peperitic margins |
| **Stage 4E:** Well-stratified, matrix-rich breccia | Polymict, matrix-supported, moderately to very poorly sorted; massive, parallel planar, wavy, lenticular and/or cross-stratified; contains soft-sediment deformation features such as flame structures; sharp contacts with Stage 4A and 4B; occurs in the upper portions of the diatreme breccia bodies | **0–60%**; **Grain size:** 2 mm to 10 cm; **Shape:** subangular to rounded; **Components:** predominantly volcanic clasts (pyroxene-phyric basalt and andesite), Stage 4E breccia (rip up clasts), possible accretionary lapilli (intact, broken and deformed), armored lapilli with andesite cores | Variegated light and dark gray, moderately sorted, mud-sized matrix containing feldspar crystal fragments | Post-diatreme lacustrine sediments; remnants and large, slumped blocks of phreatomagmatic base surge and fallout deposits |
| **Stage 4F:** Discordant breccia, sandstone and mudstone | Polymict, poorly sorted, massive or stratified with planar parallel, wavy or lenticular laminations and thin beds that are subparallel to contacts; displays shear textures; occurs as narrow bodies crosscutting all other breccia facies or forming small breccia dikes extending into the host sequence; contacts are sharp and planar, irregular or contorted | **0–30%**; **Grain size:** Sand- and/or mud-sized fragments with outsized granules and pebbles; **Shape:** angular to subangular; **Components:** Light to dark gray altered fragments of dominantly andesite and basalt, rare accretionary lapilli and feldspar crystal fragments; clay gouge | Dark gray mud-sized rock flour matrix | Phreatomagmatic or phreatic breccias, sandstones and mudstones; some may have acted as slip planes during collapse of the maar volcano |
| **Stage 4G:** Matrix-rich monzonite-clast breccia | Monomict, massive, chaotic, matrix-supported, poorly to very poorly sorted; steep and thin monophase pipes that have sharp, penetrative contacts with surrounding country rocks | **30–70%**; **Grain size:** 2 mm to 30 cm; **Shape:** angular to subangular; blocky, faceted, tabular and splintery; **Components:** strongly clay-altered, equigranular to porphyritic monzonite | Medium gray matrix of fine sand- and mud-sized fragments of milled monzonite | Phreatic breccia pipes |
| **Stage 4H:** Siliceous mud matrix-supported breccia | Monomict or polymict, poorly sorted, matrix- to cement-supported; massive or stratified, draped laminations common; meter-scale pipes and dikes occurring near-surface in Coastal area, subjacent to documented geothermal features; crosscutting relationships with other Stage 4 facies have not been observed | **0–60%; Grain size:** 2 mm to 20 cm; **Shape:** angular to subangular; rarely slabby or wispy; **Components:** clay-altered fragments of typically andesite and basalt; locally contains disrupted laminated siliceous mudstone clasts | Light gray, fine sand- to mud-sized rock flour matrix cemented by and/or gradational to opal and/or chalcedony | Small-scale phreatic eruption breccias, subsurface phreatic breccias and collapse breccias |

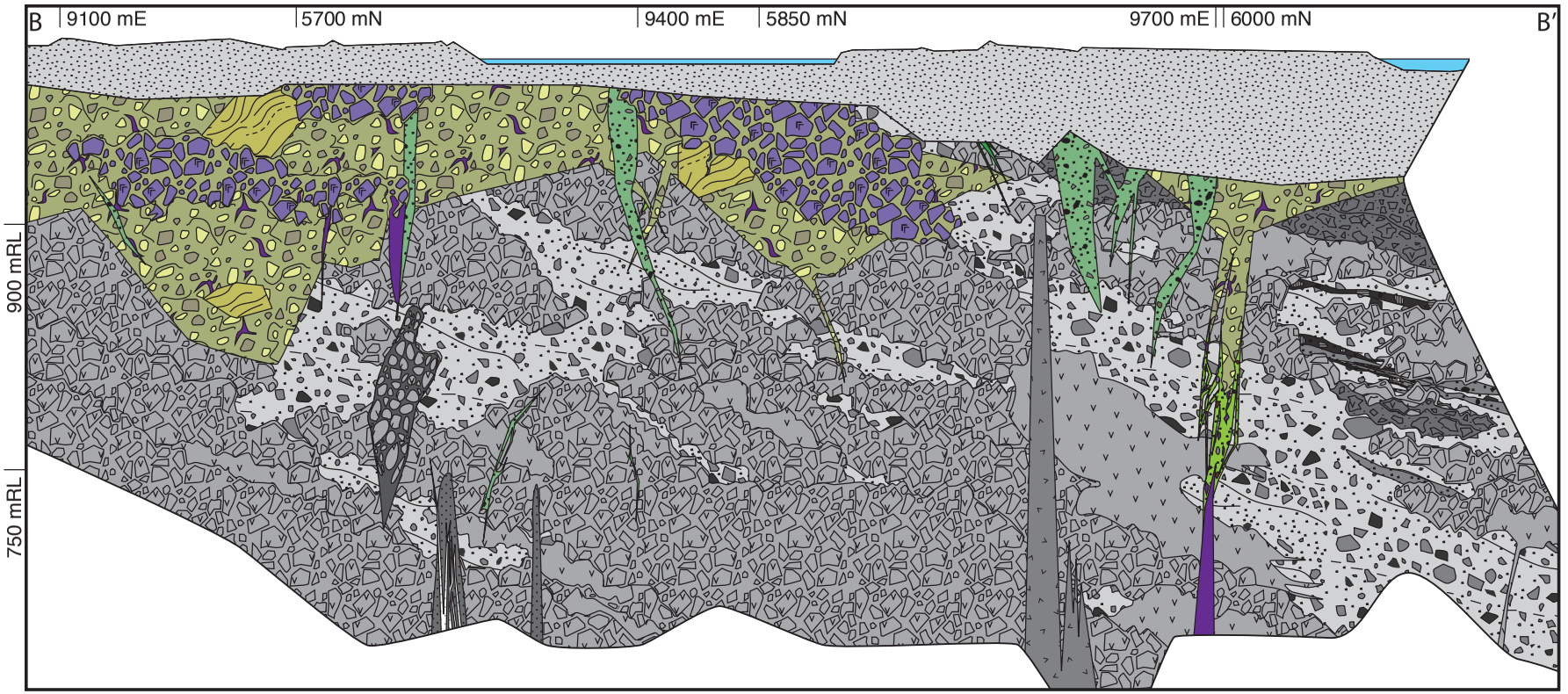


**Volcanic-hydrothermal breccias**

- Stage 4F discordant breccia, sandstone and mudstone
- Stage 4E well-stratified, matrix-rich breccia and sandstone
- Stage 4D jigsaw-fit to clast-rotated andesite-clast breccia (KNE10)
- Feldspar-phyric andesite (KNE10)
- Stage 4C polymict matrix-rich breccia with wispy andesite clasts
- Stage 4B polymict clast-rich breccia

**Hydrothermal breccias**

- Stage 2C quartz – pyrite cemented breccia

**Kapit NE intrusive complex**

- Crystal-poor, plagioclase-phyric andesite (KNE7)
- Hornblende-bearing gabbro (KNE6)
- Hornblende-biotite-bearing monzonite (KNE5)

**Volcano-sedimentary stratigraphy**

- Plagioclase-phyric andesite breccia (KNE3)
- Plagioclase-phyric andesite (inferred)
- Pyroxene-phyric basalt breccia (KNE2b)
- Pyroxene-phyric basalt (KNE2a)
- Polymict breccia with sedimentary clasts (KNE1c)
- Polymict normally graded conglomerate and pebbly sandstone (KNE1b)
- Polymict weakly graded and diffusely bedded breccia (KNE1a)

**Other**

- Harbor base fill (waste rock and Kapit landslide deposits)
- Pacific Ocean (seawater)

**Fig. 4.31.** Northwest-facing (oblique; 045˚) geology section B-B' through Kapit NE. Stage 4 volcanic-hydrothermal facies have been highlighted using colored patterns, whereas the host volcano-sedimentary and intrusive rocks as well as the overlying waste rock and landslide deposits have been illustrated in gray scale.

breccia and vein clasts (Figs. 4.32 and 4.33H), Stage 2A pyrite – marcasite-cemented breccia and vein clasts (Figs. 4.32 and 4.33D), Stage 3 quartz – chalcedony – pyrite vein clasts (Fig. 4.35C), Stage 3C jasper – pyrite fragments (Fig. 4.35C), truncated Stage 5A pyrite veins (Fig. 4.33A) and truncated Stage 5B clay – pyrite veins (Figs. 4.32 and 4.45A). Additionally, anhydrite – biotite – orthoclase-cemented breccia clasts, pyrite-cemented breccia and vein clasts, and pyrite – kaolinite – dickite vein clasts were observed within Saddle breccia (Blackwell, 2010) and pyrite-cemented breccia clasts were observed in Kapit breccia (Ageneau, 2012). The breccia facies of the Lihir diatreme breccia complex have been separated into eight stages (Stage 4A–4H).

*Stage 4A: Polymict, matrix-rich breccia*

Stage 4A chaotic, massive and matrix-supported polymict breccias are distinguished by their high relative proportion of dark gray matrix component (50–85%; Table 4.6; Figs. 4.34A, D and G, and 4.36B). The breccias have angular to subrounded (rarely rounded), poorly to very poorly sorted clasts. Conspicuous, ragged and wispy andesite clasts (up to 10% of the clast component) have a widespread distribution throughout. Sparse, randomly distributed accretionary lapilli occur locally. The matrix is composed of moderately sorted, fine sand- to mud-sized milled lithic fragments and in some areas contains disseminated pyrite. The texture of the matrix ranges from massive to stratified, with planar, irregular or convolute laminations (Fig. 4.34G). Locally, the matrix is poorly consolidated and friable (Fig. 4.34A). Stage 4A breccias occur as large pipes and tabular bodies that have sharp contacts with Stage 4B and 4E breccias. They are volumetrically significant within the center of the Saddle, Kapit and Far North breccia bodies, and occur rarely in the Diwai breccia.

*Stage 4B: Polymict, clast-rich breccia, conglomerate and sandstone*

Stage 4B breccias are similar to those typical of Stage 4A, except that they are clast-rich and matrix- to clast-supported (Table 4.6; Figs. 4.32, 4.34B–C and E–F, and 4.35D). Stage 4B breccias are typically chaotic and massive, with moderately to well sorted, angular to subrounded clasts. Locally, these breccias can be poorly to very poorly sorted and contain well-rounded clasts ranging from granule to boulder in size. Intervals are typically graded, fining upward from dominantly cobble- to boulder-sized clasts to dominantly granule- to pebble-sized clasts over tens of meters (Fig. 4.32). The coarsest clasts occur near the breccia contacts with the host rocks and are accompanied by an increased and variable proportion of mud-sized fragments in the matrix (Figs. 4.32 and 4.33E). Fissures between some of the larger clasts contain draped laminated mudstone and pyrite (Figs. 4.32 and 4.33C). The composition of the clasts and matrix within Stage 4B breccias is the same as or similar to that of Stage 4A breccias. One difference is that clasts of Stage 4A breccia have been observed within Stage 4B in Diwai breccia (Figs. 4.32 and 4.33E).

In Diwai breccia, Stage 4B breccias form branching, irregular bodies and pipes. On longitudinal section B–B', Stage 4B breccias appear as two, broad, downward-tapering bodies that coalesce near surface and one discrete, narrow, bifurcating, near-vertical breccia body that flares outward near-surface (Fig. 4.31). In three dimensions and at a larger scale (e.g., Fig. 4.28), the breccias depicted on section B–B' have a NE-trending long axis. The pipe-like morphologies appear as 'bumps' along trend. In the Saddle, Kapit and Far North breccias, Stage 4B breccias more commonly occur as large pipes with moderate to steep sides and discrete steeply-dipping dikes.

*Stage 4C: Polymict, matrix-rich breccia with wispy andesite clasts*

Stage 4C consists of massive, dark gray, polymict, matrix-rich (up to 50%) breccias that contain abundant and distinctive feldspar-phyric andesite clasts (10–90% of clast components). The feldspar-phyric andesite clasts are either

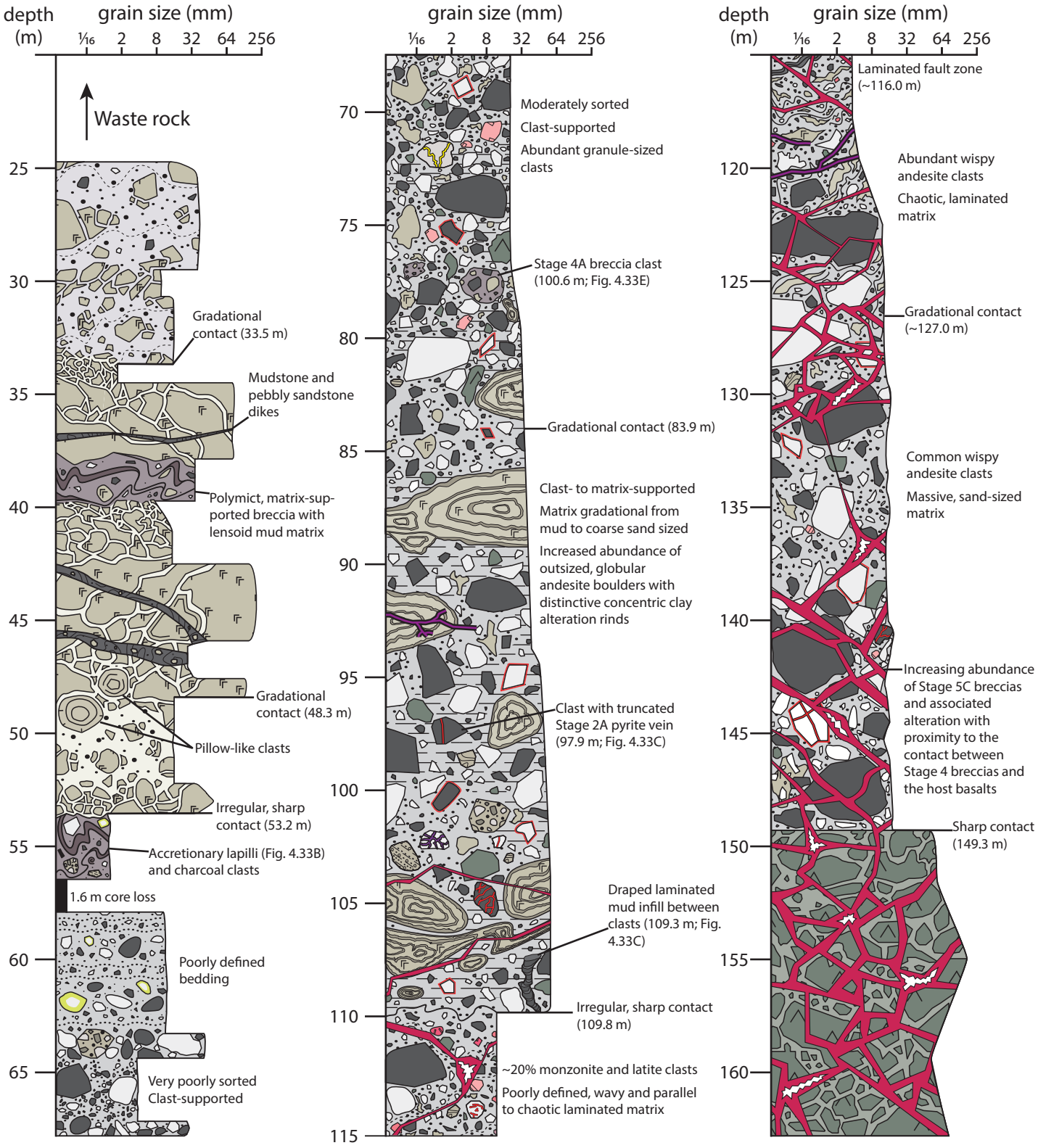


**Fig. 4.32.** Graphic log highlighting Stage 4 breccias within drill hole DDHL1928 in Kapit NE. Refer to Appendix A1 for the location of drill hole DDHL1928. The legend is on the following page.

### Volcano-sedimentary stratigraphy


Jigsaw-fit to clast-rotated, sand matrix-supported, pyroxene-phyric basalt breccia (KNE2b)

### Volcanic-hydrothermal facies


Stage 4B polymict, moderately sorted, clast-rich breccia with a variable sand- to mud-sized matrix


Stage 4B polymict, very poorly sorted sorted, clast-rich breccia


Stage 4B weakly stratified, polymict, poorly sorted, clast-rich breccia


Stage 4C polymict, chaotic, sand matrix-rich breccia with abundant feldspar-phyric andesite clasts


Stage 4D (KNE10) monomict, clast-rotated to chaotic, sand matrix-rich feldspar-phyric andesite-clast breccia


Stage 4D (KNE10) monomict, jigsaw-fit to clast-rotated, feldspar-phyric andesite-clast breccia


Stage 4E polymict, matrix-rich breccia with chaotically laminated and lensoid matrix


Stage 4F mudstone and pebble breccia dikes

### Clast types


Volcano-sedimentary clasts (KNE1, unidentifiable)


Volcanic clasts (KNE2, KNE3, unidentifiable)


Biotite-feldspar-phyric, nepheline-bearing monzonite (KNE4)


Hornblende-biotite-bearing monzonite (KNE5)


Trachytic hornblende-feldspar-phyric latite (KNE9)


Wispy feldspar-phyric andesite (KNE10) clasts with delicate margins ± mud matrix rinds


Globular feldspar-phyric andesite (KNE10) clasts with concentric clay–pyrite alteration rinds


Amoeboid feldspar-phyric andesite (KNE10) clasts with delicate margins ± mud matrix rinds


Clast with truncated Stage 1 anhydrite-cemented breccia


Clast with truncated Stage 2A pyrite vein(s)


Clast with truncated Stage 5B clay–pyrite veins


Accretionary lapilli


Charcoal clast


Volcanic clast with intense clay alteration rind


Clast with pyritic rim

### Late-stage breccias and veins


Stage 5A pyrite veins


Stage 5C calcite-quartz-pyrite breccias and veins


Vuggy cement/centerline

### Other


Chaotic laminations


Wispy texture


Fault zone

amoeboid (equant to moderate sphericity) with ragged margins, wispy (highly elongate or elongate) with irregular and delicate margins, or angular and blocky with cuspate margins (Table 4.6; Fig. 4.35). Locally, the long axes of the wispy andesite clasts are aligned (Fig. 4.35C). Many of the andesite clasts are enveloped by a rind of concentrically laminated mud matrix (Fig. 3.19D). The remainder of the clast population is composed of polymict lithic clasts of similar compositions to those observed in Stage 4A and Stage 4B breccias. Charcoal clasts have not been observed. Accretionary lapilli are present locally.

Stage 4C is a transitional facies between Stage 4A and Stage 4D and has gradational contacts with Stage 4A and Stage 4D (Fig. 4.35G). Contacts with Stage 4B have not been observed. On longitudinal section B–B' through Diwai breccia, several meter-scale Stage 4C breccias that are associated with a feldspar-phyric andesite dike occur at the base of a pipe dominated by Stage 4B breccias (Fig. 4.31). In the Saddle and Kapit breccias, Stage 4C breccias occur deep within the breccia complexes as 5–20 m-wide envelopes around, and especially overlying, Stage 4D monomict andesite-clast breccias.

*Stage 4D: Jigsaw-fit to clast-rotated andesite-clast breccia*

Stage 4D consists of massive, clast- to matrix-supported, feldspar-phyric andesite-clast breccias (Table 4.6; Figs. 4.32 and 4.35E–G). These breccias are documented in Section 3.4.4.7 (KNE10); however, since they form part of

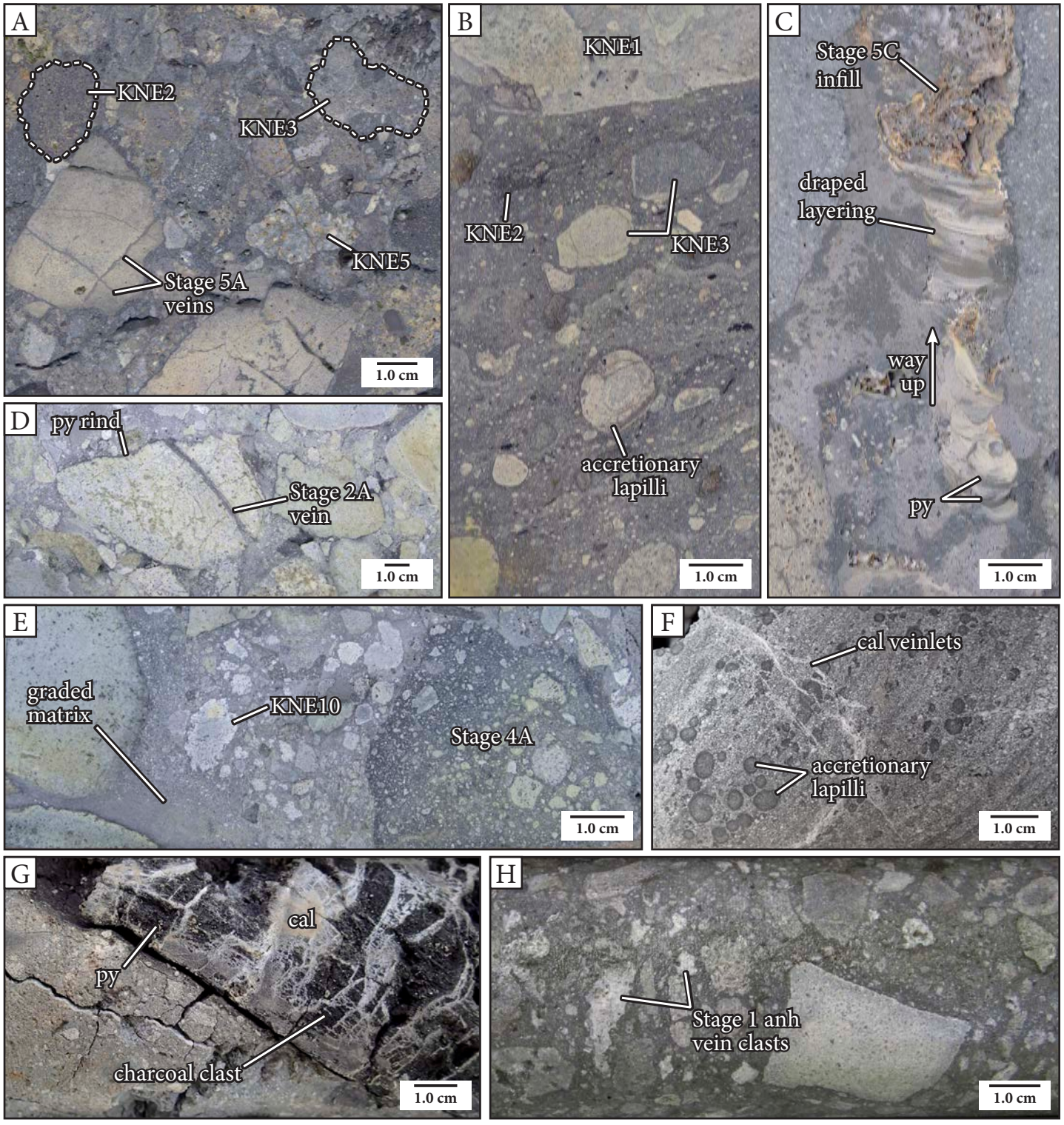


**Fig. 4.33.** Examples of clast types and textures observed within Stage 4 volcanic-hydrothermal breccias. **A.** Hand sample photograph of a Stage 4B clast-rich breccia with a diverse range of clast types, including pyroxene-phyric basalt (KNE2) with chlorite alteration (Stage A2), a pyroxene-feldspar-phyric andesite breccia clast (KNE3) with weak adularia – pyrite alteration (Stage A4), a hornblende-biotite-bearing monzonite clast (KNE5) with a truncated Stage 2A pyrite vein and strong adularia – pyrite alteration (Stage A4), and several pyroxene-feldspar-phyric andesite clasts (KNE3) with intense smectite – kaolinite alteration (Stage A6) and truncated Stage 5A dendritic pyrite veins. Sample: DDHL1803 129.4 m. **B.** A Stage 4E polymict, matrix-rich breccia with a lenticular mudstone matrix and variably altered clasts. The majority of the clasts have moderate intensity chlorite – illite ± tourmaline ± magnetite ± hematite alteration (Stage A2), including an outsized boulder of polymict, matrix-supported breccia (KNE1) and several irregularly shaped, dark gray pyroxene-phyric basalt clasts (KNE2). Other clasts, including an accretionary lapilli fragment, have weak to strong intensity smectite ± pyrite alteration (Stage A6). There is a truncated domain of strong smectite alteration within the rightmost

the diatreme breccia complex, additional aspects of these breccias are described here.

Stage 4D breccias contain abundant (60–95%), angular, poorly sorted clasts that have cuspate or irregular margins and jigsaw-fit to clast-rotated organization (Figs. 4.32 and 4.35E). Some of the clasts are fractured and disaggregated. The clasts have undergone moderate to strong intensity clay alteration that is pervasive or focused along internal fractures and the clast margins (Fig. 4.35E–G). The mineralogy of the clay alteration varies from kaolinite – montmorillonite – pyrite to illite – pyrite ± quartz. The dark gray, mud- to sand-sized matrix is composed of finely comminuted lithic material and contains broken feldspar crystals. The matrix is typically massive, but is locally laminated, and may drape between clasts (Fig. 4.35G).

Stage 4D breccias have been observed in gradational contact with coherent feldspar-phyric andesite dikes (KNE10; Figs. 4.31–4.32) and are locally transitional to Stage 4C breccias over a 1–5 m interval (Fig. 4.35E). This facies association occurs as pods and irregular fingers within larger volumes of Stage 4A and Stage 4B breccias (Fig. 4.32). A number of near-vertical to steeply east-tilted plagioclase-phyric andesite dikes (<10 m-wide) were identified by Blackwell (2010) in the western Lienetz pit wall, which have sharp, clay-altered contacts with a polymict, accretionary lapilli-bearing breccia (interpreted here as Saddle breccia; Fig. 4.30). These dikes were also observed to be spatially associated with zones of monomict, plagioclase-phyric andesite-clast breccia (interpreted here as Stage 4D).

*Stage 4E: Well-stratified, matrix-rich breccia to mudstone*

Stage 4E consists of stratified breccias, sandstones and mudstones (Table 4.6; Fig. 4.36) that can be subdivided into three facies: interbedded, normally graded breccia to mudstone (Facies A), accretionary lapilli-bearing breccia (Facies B), and wavy to lenticular bedded breccia (Facies C). In general, Stage 4E deposits are located at shallow depths (<150 m below sea level), within and overlying the Kapit, Far North and Diwai breccias (Fig. 4.37).

Stage 4E occurs in two ways: (1) as isolated and randomly oriented meter- to dekameter-scale blocks that are surrounded by massive, polymict breccia (Stage 4A–B; Figs. 4.31 and 4.37); and (2) as flat-lying to shallowly-dipping bedded deposits within a sedimentary basin that has a sharp, unconformable lower contact (Fig. 4.37). All three facies of Stage 4E occur both as blocks and as layered infill within the basin. The margins of the basin are difficult to define precisely due to textural similarities between Stage 4E and adjacent breccias (e.g., Stage 4B) and the variable degrees of lithification and alteration. The tops of the breccias were locally truncated by a landslide in the Kapit area that occurred in 2005. The landslide deposited chaotic, weakly stratified, polymict, matrix-rich and poorly consolidated

(*Continued from previous page*) of the two labeled pyroxene-feldspar-phyric andesite clasts (KNE3). Sample: DDHL1928 53.5 m. **C.** A narrow domain between clasts within a sample of Stage 4B polymict clast-rich breccia that has been infilled with laminated, mud-sized material composed of alternating rock flour and hydrothermal pyrite. These laminations are draped along the edges, which indicates that the infill formed via settling after the initial explosive formation of the surrounding breccia. The draped laminations also indicate a way-up direction, which is towards the present-day surface. This implies that the Stage 4B breccia body has not been overturned. Stage 5C calcite – quartz – pyrite veins have locally exploited the bedding planes between laminations. Sample: DDHL1928 109.1 m. **D.** Hand sample photograph highlighting a pyroxene-phyric basalt clast (KNE2) with a prominent, truncated Stage 2A pyrite vein and smectite – pyrite alteration (Stage A6). This clast, and several others in the photograph, have thin (< 1mm), discontinuous pyrite alteration rinds. Sample: DDHL1928 97.9 m. **E.** A massive, chaotic, polymict, clast-rich breccia (Stage 4B) with several Stage 4A breccia clasts and ragged, feldspar-phyric andesite clasts (KNE10). The gray, milled matrix is gradational from coarse sand- to mud-sized. Coarse sand-sized domains within the matrix are associated with granule-sized clasts and are moderately sorted; whereas, mud-sized domains are associated with pebble-sized and larger clasts and are poorly to very poorly sorted. Sample: DDHL1928 100.6 m. **F.** Hand sample photograph of a Stage 4E polymict, matrix-rich breccia clast with thin to thick laminations of alternating fine to coarse sandstone composed of variably smectite-altered lithic fragments. The sample also contains several, poorly defined layers of broken and intact accretionary lapilli (0.1–6.0 mm diameter) that are parallel to the laminations and has been crosscut by anastomosing calcite veinlets. Sample: SRW1661 ~250.0 m. **G.** A Stage 4A polymict, matrix-rich breccia containing a fragment of pyritized and charcoalized wood that has been crosscut by a calcite-cemented breccia. The charcoal clast indicates that there was a link to a subaerial paleosurface during the eruption of the diatreme breccia complex. The charcoal was dated using the radiocarbon dating method (Section 4.6). Sample: DDHL2153 36.0 m. **H.** Hand sample photograph of a Stage 4A polymict, matrix-rich breccia highlighting the presence of several anhydrite vein fragments (Stage 1). The anhydrite vein fragments have irregular and corroded margins. Sample: DDHL1968 120.9 m. Abbreviations: anh = anhydrite, cal = calcite, py = pyrite.

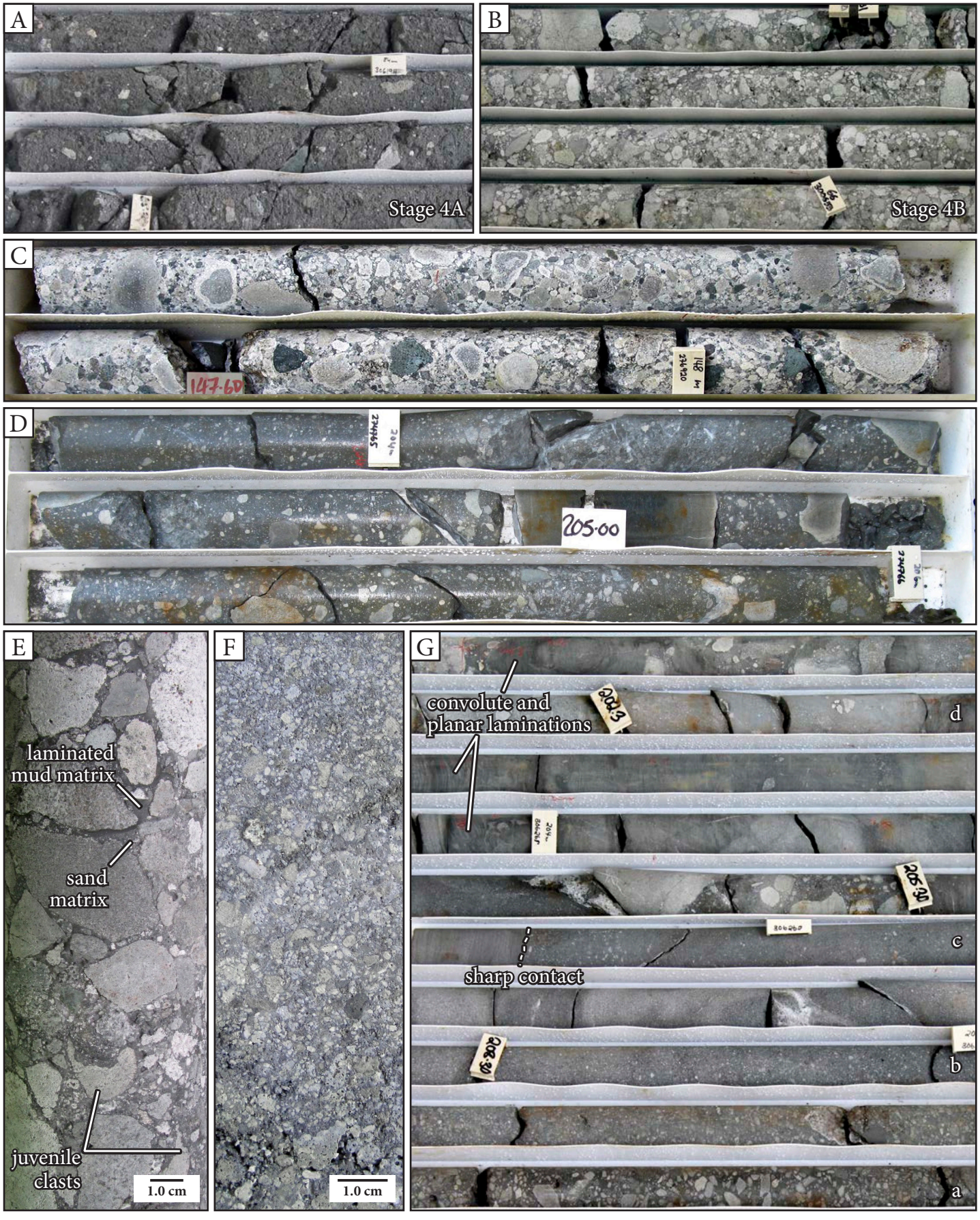
A
Stage 4A
B
Stage 4B
C
147.60
D
205.00
E
laminated mud matrix
sand matrix
juvenile clasts
1.0 cm
F
1.0 cm
G
convolute and planar laminations
sharp contact
d
c
b
a

breccias and sandstones at the present-day surface. Many of the landslide deposits contain rounded pebbles and boulders of unaltered or weakly calcite – chlorite-altered amygdaloidal basalts, which are interpreted to have been derived from the amphitheater walls.

*Interbedded, normally graded breccia to mudstone (Facies A)* typically consists of light to medium gray sandstone and mudstone with planar or wavy bed forms and lesser, matrix- to clast-rich breccia interbeds. Clasts are composed of polymict lithic material and range from angular to subangular. Sandstone and mudstone beds are laminated to very thinly bedded, whereas sandstone and breccia interbeds are very thickly bedded. Some very thick beds are normally graded from pebble breccia to sandstone. Soft sediment deformation features are common within interbedded mudstone and sandstone, and include rip up clasts, flames, dish and pillow structures, syneresis cracks, syn-sedimentary faults and convolute laminations (Fig. 4.36C and E). Interbedded, normally graded breccia to mudstone is the most abundant of the three facies and has a flat-lying, widespread distribution. It has a variable vertical extent (~0.1 to 65 m-thick) and is thickest at the center of the basinal depocenter (Fig. 4.37).

*Accretionary lapilli-bearing breccia (Facies B)* consists of dark gray, planar, wavy and low-angle cross-stratified mudstones that locally contain large (1–3 cm-across), strongly altered ovular features with concentric layering (Fig. 4.36D). Locally, cross-stratified mudstones are intercalated with pebble breccia beds (Fig. 4.36A). The ovular features range from sparse, randomly oriented and matrix-supported to densely packed (Fig. 4.36D). They can be elongate or irregularly shaped, as if they have been compressed and/or deformed post-deposition. They typically have a chaotic distribution, but may also be concentrated along bedding planes (Fig. 4.36D). The ovoid features are tentatively interpreted as accretionary lapilli. An alternative interpretation is that they are rounded lithic fragments with concentric alteration rinds and halos. However, the ovoid features have a consistent appearance in all instances that they have been observed. Therefore, the layering is considered to be a primary feature rather than an alteration feature and the accretionary lapilli interpretation is preferred. This facies occurs as an elongate (700 × 100 m), northeast-trending lozenge that is approximately centered on the northeast-trending structural lineament that bisects the basinal sedimentary depocenter (Fig. 4.37). It ranges in vertical thicknesses from ~0.1 to 20 m. The upper contacts are gradational to other Stage 4E facies. The lower contacts are typically sharp with Stage 4A or 4B breccias or gradational with interbedded, normally graded breccia to mudstone.

*Wavy to lenticular bedded breccia (Facies C)* consists of mudstone and sandstone intercalated with very thick beds of massive, unsorted, dark gray (carbonaceous?) mud matrix-rich polymict breccia (Fig. 4.36F). The mudstone and sandstone beds have wavy to lenticular stratification. The breccia beds contain angular to rounded polymict lithic clasts, with less common ragged and amoeboid andesite clasts, rare charcoal clasts, armored lapilli with andesite cores and both broken and intact accretionary lapilli (Figs. 4.32, 4.33B and F, and 4.36F). Soft-sediment deformation features such as slump folds have been observed at the

**Fig. 4.34.** *(Previous page)* Stage 4A polymict, matrix-rich breccia and Stage 4B polymict, clast-rich breccia. **A.** Core box photograph of poorly consolidated Stage 4A polymict, matrix-rich breccia from the Kapit breccia complex in Kapit. Interval: DDHL1899 82.6–85.9 m. **B.** Core box photograph of Stage 4B polymict, clast-rich breccia that is typical of the Diwai breccia complex in Kapit NE. Interval: DDHL1968 ~63.8–66.3 m. **C.** Core box photograph of Stage 4B polymict, clast-rich breccia from Kapit breccia in Kapit. The interval contains clasts with quartz – illite – pyrite alteration rinds. Interval: DDHL1612 ~146.5–148.2 m. **D.** Core box photograph of a characteristic interval of Stage 4A polymict, matrix-rich breccia from the Kapit breccia. Interval: DDHL1579 ~203.7–206.0 m. **E.** Close-up view of the same Stage 4B breccia as in Figure 4.32B. The subrounded to angular clasts are composed of porphyritic andesite and basalt. The sample has a clast-supported, chaotic organization, a variable sand- to mud-sized rock flour matrix, and contains several ragged to wispy feldspar-phyric andesite clasts (KNE10) interpreted as juvenile magmatic clasts. Sample: DDHL1968 68.4 m. **F.** Stage 4B polymict, clast-rich breccia predominantly composed of angular, granule-sized clasts. The rock flour matrix is clay-sized and has locally been washed away, leaving voids between clasts. Sample: DDHL1928 65.8 m. **G.** Core box photograph illustrating a fining upwards sequence within an interval of Stage 4B, which grades from polymict, clast-rich pebble to cobble breccia with a dark gray mudstone matrix (a) to polymict, clast-rich granule breccia (b) to pebbly sandstone (c). At 205.5 m depth, there is a sharp contact between Stage 4B pebbly sandstone and Stage 4A polymict, poorly sorted, matrix-rich breccia (d). The Stage 4A breccia locally displays planar and convolute laminations. Interval: DDHL1899 ~201.2–209.7 m.

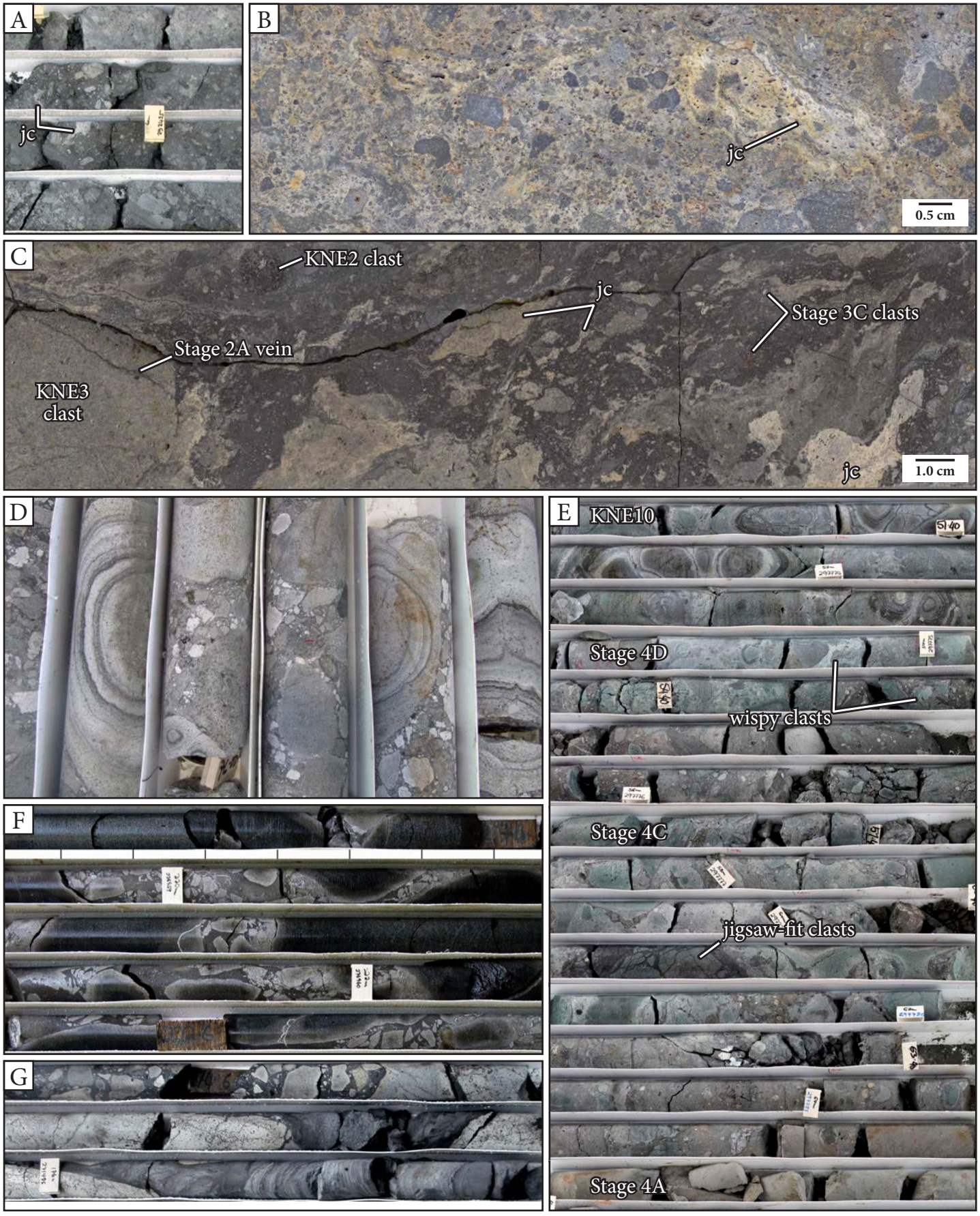
A
jc
B
jc
0.5 cm
C
KNE2 clast
jc
Stage 3C clasts
Stage 2A vein
KNE3
clast
jc
1.0 cm
D
E
KNE10
Stage 4D
wispy clasts
Stage 4C
jigsaw-fit clasts
Stage 4A
F
G

base of the matrix-rich polymict breccia beds and within the laminated mudstone intervals (Figs. 4.33F and 4.36F). This facies ranges in vertical thicknesses from ~0.5 to 30 m. It has commonly been crosscut by Stage 4D andesite-clast breccia in Kapit NE area (Fig. 4.32). Locally, it overlies accretionary lapilli-bearing breccia with a gradational contact.

Blackwell (2010) documented a bedded outcrop to the west of Lienetz open pit (4,436 mN, 8,515 mE, 977 mRL), which is close to the western margin of Saddle breccia. The outcrop is composed of boulder conglomerate draped by stratified pebble breccia and sandstone containing abundant charcoal fragments and faintly cross-bedded intervals (Blackwell, 2010). Corbett et al. (2001) similarly documented thick-bedded, accretionary lapilli-bearing breccias similar to Stage 4E occurring in a broad flat rim at the top of Mamboo breccia, overlying brecciated volcanic rocks. Blocks of bedded accretionary lapilli were also observed within the deeper portions of the Mamboo breccia from lower Minifie pit wall exposures (Corbett et al., 2001).

*Stage 4F: Discordant breccia, sandstone and mudstone*

Stage 4F is composed of polymict, poorly sorted breccias, sandstones and mudstones that are typically stratified, with planar parallel, wavy, wispy or lenticular laminations and thin beds that are subparallel to its contacts (Table 4.6; Fig. 4.38). Many of the breccias display shear textures, and clay gouge is a common component. The angular to subangular clasts are predominantly composed of variably clay-altered andesite and basalt, with rare accretionary lapilli and feldspar crystal fragments. Juvenile magmatic clasts were not observed. The matrix of Stage 4F breccias is composed of dark gray, finely comminuted lithic material. Stage 4F occurs as narrow pipes and dikes that have crosscut Stage 4A–C breccias and the surrounding host rocks (Fig. 4.31). The breccias have sharp and planar, irregular or contorted contacts (Fig. 4.38B).

*Stage 4G: Matrix-rich, monzonite-clast breccia pipe*

Stage 4G consists of monomict, monzonite-clast breccias. They are chaotic, massive and matrix-supported (Table 4.6; Fig. 4.39). The angular to subangular, hornblende – biotite-bearing monzonite clasts (KNE5) range from equigranular to porphyritic. They are typically strongly clay-altered and very poorly sorted, with blocky, faceted, tabular and splintery morphologies. The clasts generally range from about 0.2 to 5 cm. Larger (up to 30 cm) clasts are present locally. Juvenile clasts were not observed. The medium gray, fine sand to mud-sized matrix is composed of finely milled monzonite and contains disseminated pyrite. At the margins of the breccias, there is a gradation to decimeter-scale, monomict, jigsaw-fit monzonite-clast breccias with hydrothermal mud matrix, and to intervals of coherent monzonite that have been crosscut by discrete, 0.1 to 2 m-wide hydrothermal mud dikes (Fig. 4.39B–C). Some of the hydrothermal mud dikes have wavy and irregular laminations (Fig. 4.39C).

Stage 4G breccias form steep, narrow monogenetic

**Fig. 4.35.** (*Previous page*) Stage 4C polymict, matrix-rich breccia with wispy andesite clasts and Stage 4D jigsaw-fit to clast-rotated andesite-clast breccia. **A–C.** Examples of wispy and irregular juvenile feldspar-phyric andesite clasts (KNE10; *lightest gray*) within Stage 4C polymict matrix-rich breccias from Diwai breccia in Kapit NE. Note the clasts with truncated Stage 3C jasper – pyrite and high abundance of quartz, chalcedony, pyrite and jasper fragments in Figure 4.35C. This breccia has crosscut a source region with abundant Stage 3 quartz and chalcedony veins and breccias. Samples: **A:** DDHL1927 ~58.0–61.0 m; **B:** DDHL1928 116.5 m; **C:** DDHL1953 275.2 m. **D.** Core box photograph of a concentration of concentrically banded feldspar-phyric andesite dikes and globular boulders (Stage 4C) within Stage 4B breccia. The boulders are also juvenile magmatic clasts. However, they are not interpreted to have triggered diatreme breccia formation. Instead, they are interpreted to have formed via disaggregation of andesite dikes that intruded into wet and unconsolidated diatreme breccia fill just after its formation. Interval: DDHL1968 ~75.1–78.9 m. **E.** Core box photograph showing a gradual transition from coherent feldspar-phyric andesite (KNE10; *top*) to monomict feldspar-phyric andesite-clast breccia (Stage 4D) to polymict matrix-rich breccia with wispy andesite clasts (Stage 4C) to polymict matrix-rich breccia (Stage 4A; *bottom*). The andesitic clasts in the transition zone are either wispy and irregular or blocky and disaggregated with jigsaw-fit organization. Interval: DDHL1963 50.6–66.0 m. **F.** Jigsaw-fit to clast-rotated Stage 4D andesite-clast breccia with interstitial massive mud matrix from Kapit breccia. The feldspar-phyric andesite clasts have distinctive smectite alteration rinds. Interval: DDHL1612 ~219.0–223.1 m. **G.** U-shaped sags and chaotic laminations within the mud matrix of a clast-rotated to chaotic Stage 4D andesite-clast breccia from Kapit breccia. Interval: DDHL1561 ~174.4–176.7 m. Abbreviations: jc = juvenile andesite clast.

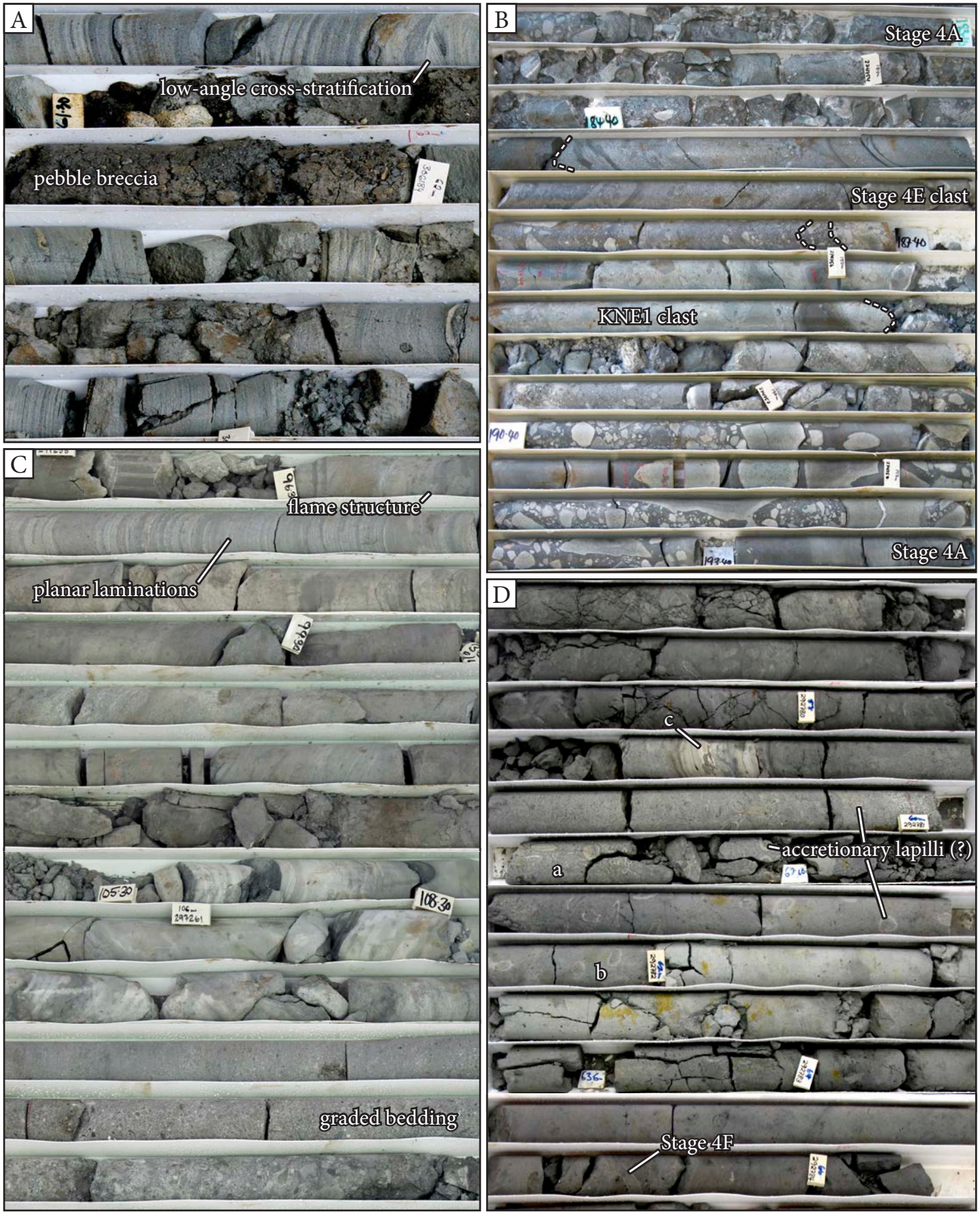
A
low-angle cross-stratification
pebble breccia
B
Stage 4A
Stage 4E clast
KNE1 clast
Stage 4A
C
flame structure
planar laminations
graded bedding
D
c
accretionary lapilli (?)
a
b
Stage 4F

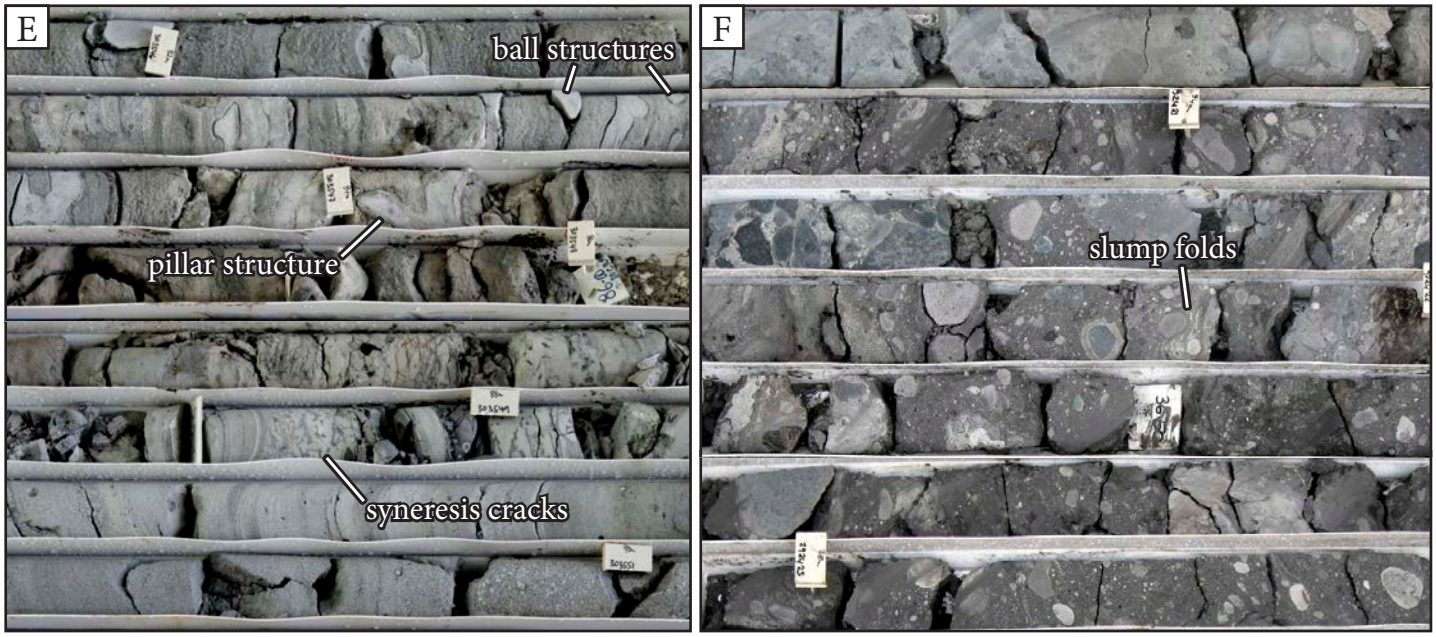


**Fig. 4.36.** Stage 4E well-stratified, matrix-rich breccia. **A.** Low-angle cross-laminated mud interbedded with moderately sorted, massive to planar-bedded lithic pebble breccia. The deposits occur within a megablock that has been incorporated into Kapit breccia. Interval: DDHL1899 ~60.7–63.4 m. **B.** A boulder (~2.0 m across) of interbedded, planar-stratified sandstone and breccia in an interval of Stage 4A polymict, matrix-rich breccia from Diwai breccia. The boulder has sharp, uneven edges that truncate bedding in the sandstone. A subset of the light gray clasts in the Stage 4E breccia clast have amoeboid shapes and ragged margins (e.g., ~187.0 m). The interval also features a boulder (~1.7 m across) of chlorite – illite-altered polymict, matrix-supported breccia (KNE1). Interval: DDHL1579 ~182.5–193.8 m. **C.** Well-stratified sandstone, mudstone and matrix-rich pebble breccia grading into massive, polymict clast-rich breccia over approximately 10 m. The mainly planar-stratified interval includes examples of soft-sediment deformation structures such as flames, syn-sedimentary faults and contorted layering. Interval: DDHL1961 ~95.9–111.5 m (Far North breccia). **D.** Massive to laminated mudstone containing abundant, large (up to 3 cm across) accretionary lapilli with onion skin-like cross-sections and clay-altered rims. Some of the accretionary lapilli are elongate or irregularly shaped. Densely-packed accretionary lapilli (*a*) are apparently randomly oriented and are associated with chaotic laminations. Sparse accretionary lapilli (*b*) are associated with massive mudstone. An approximately 10 cm-thick interval of planar-bedded mudstone contains accretionary lapilli that are elongated parallel to the bedding plane (*c*). The interval has been crosscut by a narrow (~2 cm wide) Stage 4F hydrothermal mud dike. Interval: DDHL1926 ~56.2–66.1 m. **E.** Interbedded sandstone and mudstone with distorted sand layers (ball, pillar and dish structures) that are interpreted here to have formed via a combination of dewatering and slumping on an unstable slope in a maar crater setting. Mudstone layers locally contain sinuous syneresis cracks that are interpreted to have formed by dewatering during syn-sedimentary seismic activity and subsequent distortion as the sediments settled on a slope. Interval: DDHL1989 ~81.9–90.1 m (Far North breccia). **F.** Poorly consolidated, chaotic, dark gray matrix-rich breccia with wispy stratified sandstone layers and soft-sediment deformation structures, including slump folds and convolute bedding. Interval: DDHL1927 ~32.5–38.5 m (Diwai breccia).

pipes (Table 4.6). The Karot breccia in Coastal area is composed entirely of Stage 4G breccia. It has a cone shape with aerial dimensions of 150 $m^2$ and a vertical extent of >250 m (Table 4.5; Fig. 4.28). The main breccia body is surrounded by >20 m-wide, Stage 4G breccia bodies.

Stage 4G was not observed to be in contact with any other Stage 4 breccias. Stage 4G breccias have locally crosscut Stage 2A pyrite – marcasite breccias and veins and some of the monzonite clasts within Stage 4G breccias contain truncated Stage 2A veins. Stage 4G hydrothermal mud has also infilled the vuggy centerline of some Stage 2A pyrite – marcasite veins (Fig. 4.39A–B). Disseminated pyrite in the matrix is locally composed of milled Stage 2A veins.

*Stage 4H: Siliceous mud matrix-supported breccia*

Stage 4H consists of chaotic, massive or stratified, siliceous mud matrix-supported breccias with monomict or polymict clay-altered clasts (Table 4.6; Fig. 4.40). The angular to subangular clasts (up to 60% of total components) are poorly sorted and range from granule to boulder in size (0.2–20 cm; Fig. 4.40A). The clasts are composed of locally derived host rocks, typically pyroxene-phyric basalt (KNE2), pyroxene-feldspar-phyric andesite (KNE3) and/or hornblende-biotite-bearing monzonite (KNE5). The majority of the clasts are blocky; however, concentrations of clasts with tabular and slabby morphologies occur in some breccias. Rare, irregular and wispy fragments of the laminated siliceous mudstone clasts also occur (Fig. 4.40E).

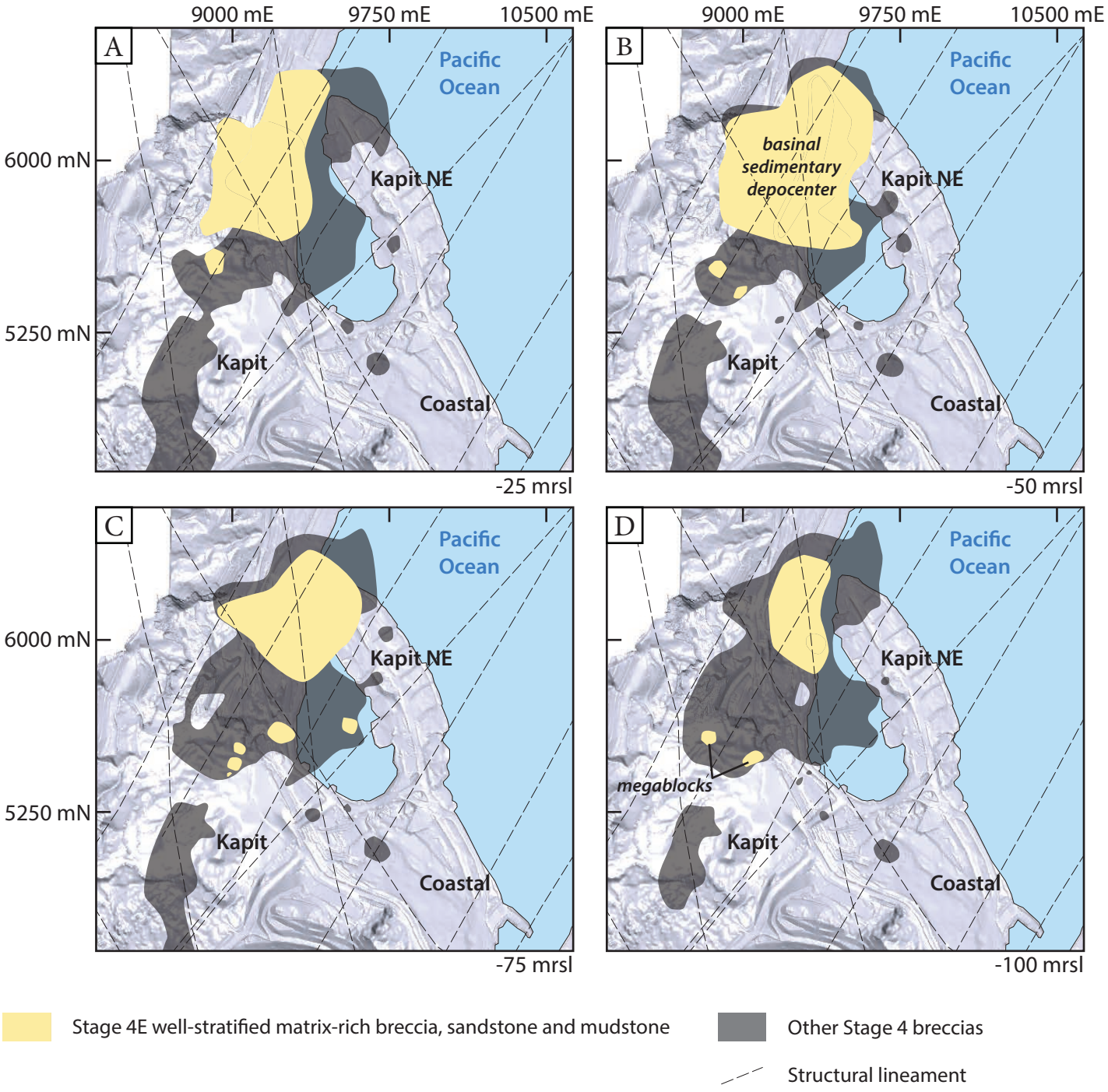


**Fig. 4.37.** Near-surface plan view horizontal slices through the geological model for Stage 4 volcanic-hydrothermal breccias, showing the distribution of Stage 4E breccias and amphitheater-scale structural lineaments. Plan view horizontal slices are at **A.** −25 m, **B.** −50 m, **C.** −50 m, and **D.** −100 m relative to sea level.

The massive or laminated, light gray to beige, fine sand- to mud-sized matrix is cemented by and/or gradational to infill dominated by translucent, locally color-banded, blue-gray and/or white chalcedony or gray opal with minor pyrite and marcasite (Fig. 4.40B and D). Draped laminations and soft-sediment deformation features such as microfaults and chaotic laminations are common (Fig. 4.40C). Curved, tube-like irregularities that resemble burrow traces occur locally within the siliceous mud matrix (Fig. 4.40C).

Stage 4H breccias occur near-surface as meter-scale pipes and dikes that are subjacent to surface geothermal features near Coastal. Due to the limited distribution of Stage 4H, crosscutting relationships with other Stage 4 facies have not been observed. Stage 4H has been crosscut by Stage 5C calcite – quartz – pyrite veins and associated alteration. Where this occurs, Stage 4H breccias contain clasts with 'pinhole' texture and vuggy rinds, and the cement is locally leached, leaving open spaces filled with crusts and drusy euhedral linings of calcite, quartz and pyrite (Fig. 4.40C).

#### *4.4.4.4 Relationship to alteration and mineralization*

Hydrothermal fluids associated with Stage 4 volcanic-hydrothermal breccia formation produced fine-grained disseminations of pyrite in the matrix and pyritic coatings on clast margins (Fig. 4.33D). Quartz – illite – pyrite alteration rinds are common (Figs. 4.34C and 4.35E–F). Many of the clasts have relict Stage A1–Stage A5 alteration (e.g., Fig. 4.33A). The presence of hydrothermally cemented breccia and vein clasts from Stages 1, 2 and 3 within the volcanic-hydrothermal breccias provides evidence that a mineralizing hydrothermal system was well established prior to fragmentation. However, mineralized vein fragments are not common and the average grade within the breccias is 0.84 g/t Au, which is less than half the average gold grade in the mineral resource (2.2 g/t Au; Newcrest Mining Ltd., 2013).

The Diwai and Kapit breccias are spatially associated with NE-trending mineralized zones consisting of Stage 5C drusy calcite – quartz – pyrite-cemented breccias and veins and associated strong, pervasive adularia – pyrite – quartz – calcite alteration at 100–150 m below sea level (Figs. 4.29, 4.32, 4.41 and 4.47). This mineralization overprints the Kapit and Diwai breccias, demonstrating a late-mineralization timing for these breccias. There is also an ENE-trending, high-grade (up to 70.5 g/t Au) mineralized zone spatially associated with Stage 4 breccias in the Coastal area at 140–175 m below sea level (Figs. 4.29). This relationship requires further investigation; however, it appears that the mineralization is associated with Stage 2A pyrite – marcasite-cemented breccias that have used the same structures as later Stage 4 breccias. Stage 4G hydrothermal mudstone dikes have exploited the vuggy center-

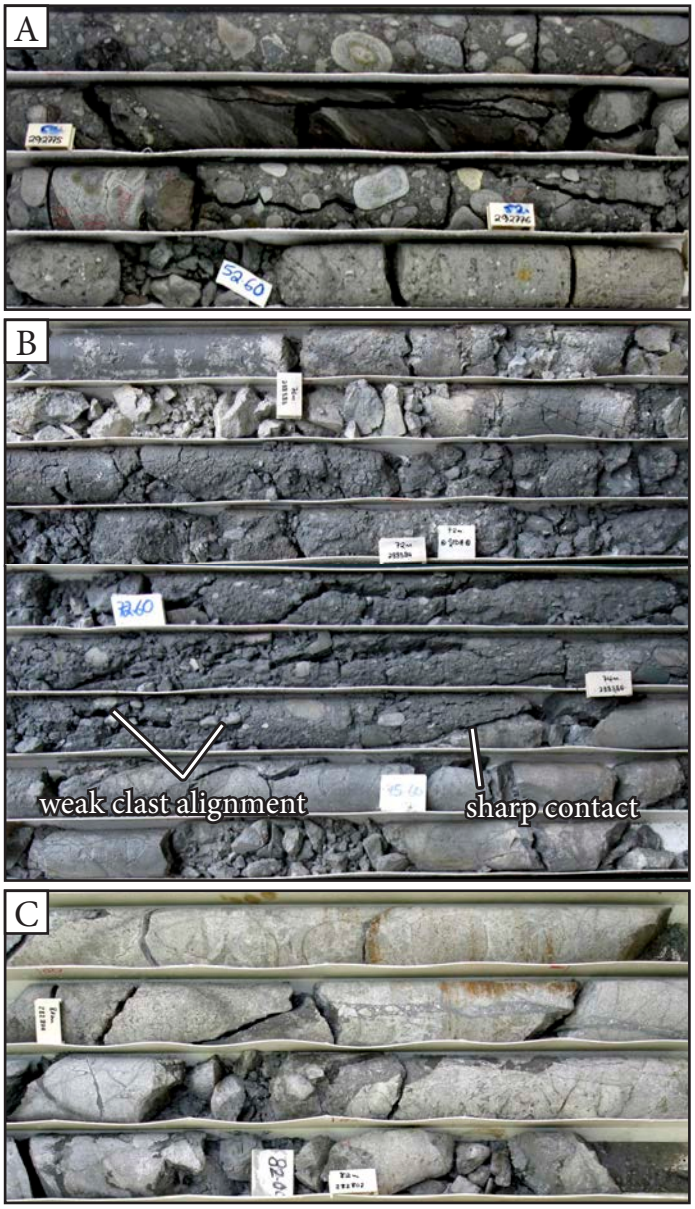


**Fig. 4.38.** Stage 4F discordant breccia, sandstone and mudstone. **A.** Stage 4F mudstone that has crosscut stratified Stage 4E polymict, matrix-supported breccia. The mudstone has wispy, wavy and lenticular laminations that are oriented sub-parallel to its contacts with the host rocks. Interval: DDHL1926 ~46.5–54.0 m (Kapit breccia). **B.** Chaotic, mud matrix-rich Stage 4F breccia that has crosscut pyroxene-phyric basalt breccia (KNE2b) in the Coastal area. The breccia has sharp contacts and a weak foliation defined by aligned clasts and fractures within the poorly consolidated muddy matrix. Interval: DDHL1856 ~68.9–76.7 m. **C.** Narrow (<10 cm-across), irregular, mud matrix-supported Stage 4F breccias that have crosscut pyroxene-phyric basalt breccia (KNE2b). The clasts are angular and composed of locally derived pyroxene-phyric basalt. Interval: DDHL1812 79.1–82.3 m.

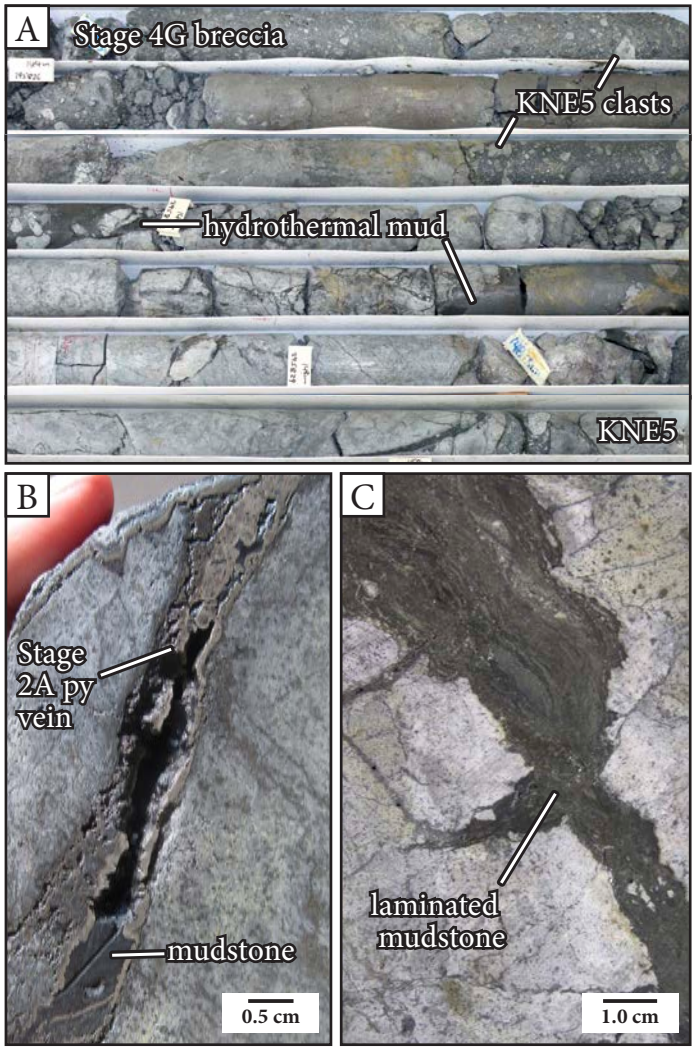


**Fig. 4.39.** Stage 4G matrix-rich, monzonite-clast breccia pipe (Karot breccia, Coastal ore zone) **A.** Core box photograph of Stage 4G matrix-rich, monzonite-clast breccia, showing its contact with hornblende-biotite-bearing monzonite (KNE5). The contact is marked by a series of hydrothermal mud dikes that are gradational to jigsaw-fit breccias with hydrothermal mud matrix. The hydrothermal mud dikes contain sparse, subrounded hornblende-biotite-bearing monzonite clasts (KNE5). Interval: DDHL1889 ~237.1–238.5 m. **B.** Close up view of a massive Stage 4G hydrothermal mudstone dike that has exploited the vuggy centerline of a Stage 2A botryoidal pyrite vein. The mudstone dike is very soft and friable. The deep groove cutting across the bottom of the sample was made with a tungsten carbide-tipped scratching tool. Sample: DDHL1947 140.6 m. **C.** Close up view of a laminated Stage 4G hydrothermal mudstone dike that has crosscut smectite-altered host rocks adjacent to the Karot breccia pipe. The laminations are wavy and irregular, and are oriented approximately parallel to the walls of the dike. Sample: DDHL1947 140.3 m. Abbreviations: py = pyrite.

line of Stage 2A pyrite veins (Fig. 4.39B). The Mamboo, Saddle and Far North breccias have a post-mineralization timing, bounding the ore zones to the north, west and south (Fig. 4.29).

Clasts with weak to intense, late-stage smectite – kaolinite and kaolinite – alunite alteration (Stage A6–A7; e.g., Fig. 4.40B), clasts with truncated clay – pyrite veinlets (Stage 5B; Figs. 4.32 and 4.45) and pyrite – dickite – kaolinite vein clasts (Blackwell, 2010) have been documented within Stage 4 breccias across Lihir. In Kapit and Kapit NE areas, Stage 4 breccias are crosscut by clay – pyrite veinlets and overprinted by a blanket of Stage A6 smectite – kaolinite and Stage A7 kaolinite – alunite alteration near surface (Figs. 4.1 and 4.45; Ageneau, 2012). Saddle breccia has crosscut the late-stage clay ± alunite alteration blanket, suggesting a different, later time of emplacement for that breccia body (Ageneau, 2012).

### *4.4.5 Stage 5: Late-stage veins and breccias*

#### *4.4.5.1 Stage 5A: Dendritic pyrite veins and disseminated pyrite*

Stage 5A dendritic pyrite veins and associated disseminated pyrite occur at shallow levels in the Kapit NE and Coastal ore zones (< 150 m depth below sea level), and are spatially associated with the Stage A6 smectite – kaolinite and Stage A7 kaolinite – alunite alteration zones (Fig. 4.41). Stage 5A is associated with domains of moderate grade gold mineralization (1–5 g/t Au). It is one of three gold-bearing stages that crosscut the Stage 4 volcanic-hydrothermal breccias (Figs. 3.19B, 4.41and 4.42F).

Stage 5A consists of hairline veins and stockworks (with <0.5 mm vein aperture), irregular and discontinuous chains, patches and disseminations composed of pyrite ± marcasite ± chalcopyrite ± pyrrhotite ± sphalerite ± galena ± tennantite ± rutile. Commonly, these minerals have infilled vugs within Stage A3 vuggy adularia alteration zones that have been overprinted by Stage A6 or A7 alteration (Fig. 4.42D). Pyrite is the most abundant mineral, occurring primarily as anhedral masses, but also as subhedral cubes and pyritohedra, colloform bands in open spaces and overgrowths on earlier-formed sulfides. Stage 5A Fe-sulfides are very reactive in air, and they are quickly altered

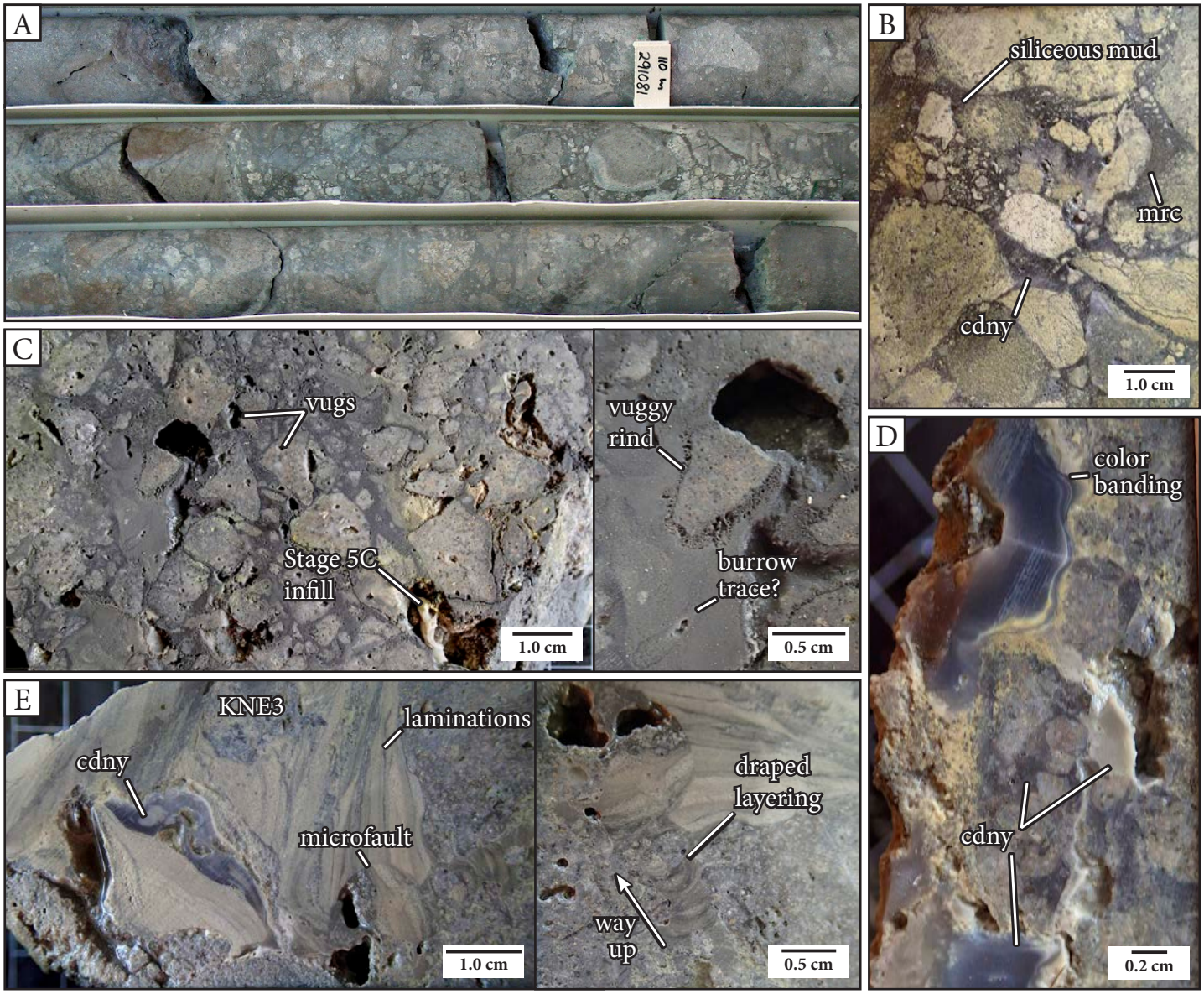


**Fig. 4.40.** Stage 4H siliceous mud matrix-supported breccia. **A.** Core box photograph of a Stage 4H siliceous mud matrix-supported breccia with poorly sorted angular clasts, local chalcedony – pyrite – marcasite cement and chaotic clast organization. The majority of clasts within the interval are illite-smectite – pyrite and kaolinite – alunite-altered pyroxene-feldspar-phyric andesite (KNE3). Interval: DDHL1876 ~109.6–111.8 m. **B.** Photograph of a polymict, Stage 4H breccia with angular, clast-rotated to chaotic, strongly kaolinite – alunite – pyrite-altered clasts. The material between clasts grades between zones of siliceous mud-matrix to zones of chalcedony and/or marcasite cement. Sample: DDHL1876 107.1 m. **C.** Chaotic Stage 4H breccia with subrounded pyroxene-feldspar-phyric andesite (KNE3) clasts and a mottled siliceous mud matrix. The clasts have vuggy alteration rinds (see close-up view in image at right). There are curved, tube-like irregularities within the siliceous mud matrix that resemble burrow traces, and it is possible that there has been some minor bioturbation. Vugs have been partly infilled with crusts and drusy euhedral linings of Stage 5C calcite – quartz – pyrite. Sample: DDHL1876 106.5 m. **D.** Close-up view of a vuggy Stage 4H breccia with a translucent bluish-gray to beige chalcedony cement and late-stage banded veins. Clasts within the breccia are composed of hornblende-biotite-bearing monzonite (KNE5) that have been strongly altered to quartz, illite-smectite, vermiculite and pyrite. Sample: DDHL1876 106.9 m. **E.** Stage 4H breccia composed of deformed laminated siliceous mudstone and pyroxene-feldspar-phyric andesite (KNE3) clasts within disrupted layers of siliceous mud. The breccia is interpreted to have formed via collapse within a hydrothermal vent crater (shallow marine or lacustrine setting). The largest of the clasts has a distinct, thicker layer of chalcedony and a wispy, tapered shape that is interpreted to have formed as a result of soft-sediment deformation during transport. The sample contains a listric microfault that has disrupted the layered sediments and a small fissure infilled with draped laminations of siliceous sand and silt. The image on the right presents a close-up view of the draped fissure infill. The way up towards the paleosurface is indicated with an arrow. Sample: DDHL1876 111.5 m. Abbreviations: cdny = chalcedony, mrc = marcasite.

to jarosite and copiapite in drill core samples (Fig. 4.42A). Stage 5A veins have a similar form and mineralogy to Stage 2A veins; however, the two differ in that Stage 5A veins are not vuggy, have a consistently thin vein aperture (<1 mm) and the Fe-sulfides are not visibly colloform banded.

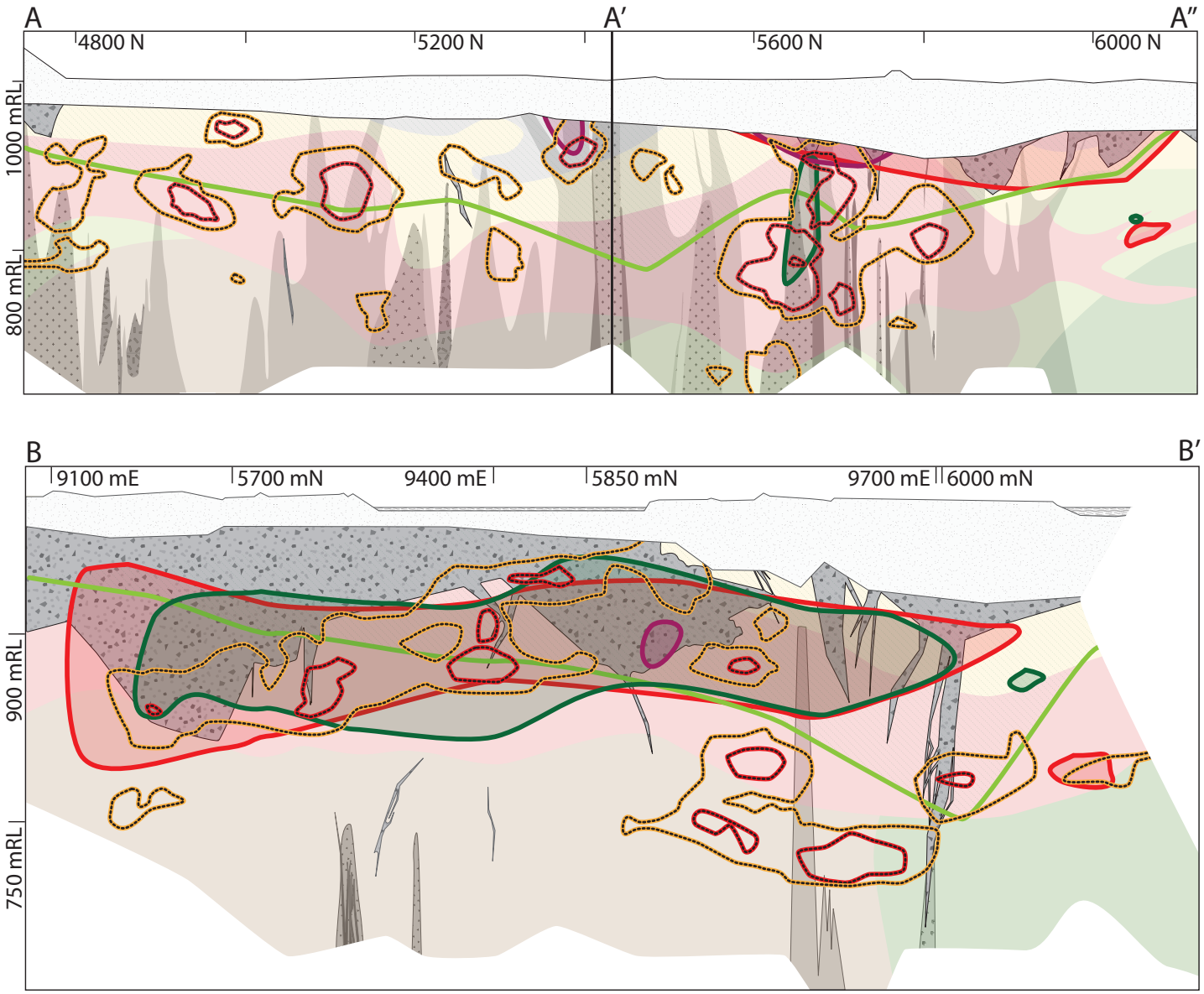


**Lithotypes**

- Waste rock
- Trachytic hornblende- feldspar-phyric latite (KNE9)
- Hornblende-feldspar-phyric latite (KNE8)
- Crystal-poor, feldspar-phyric trachyte (KNE7)
- Hornblende-bearing gabbro (KNE6)
- Hornblende-biotite-bearing monzonite (KNE5)
- Nepheline-bearing monzonite (KNE4)
- Volcano-sedimentary rocks (KNE1–3)

**Stage 4–5 veins and breccias**

- Stage 5D: Orpiment – realgar veinlets and breccias
- Stage 5C: Calcite – quartz – adularia – pyrite – limonite-cemented veins and breccias
- Stage 5B: Clay – pyrite-cemented breccias and veins
- Stage 5A: Dendritic pyrite veins and disseminated pyrite
- Stage 4: Lihir volcanic-hydrothermal breccia complex

**Alteration**

- Stage A7 – Quartz-alunite
- Stage A6 – Smectite-kaolinite
- Stage A3-A5 – Main-stage
- Stage A2 – Mg-chlorite
- Stage A2 – Fe-chlorite
- Stage A1 – Phlogopite

**Grade shells**

- >5 g/t Au
- >3 g/t Au

**Fig. 4.41.** Distribution of Stage 4 and 5 hydrothermal breccias and veins on cross sections A–A'–A'' and B–B' in Kapit NE and Coastal.

Stage 5A veins are surrounded by conspicuous, thin (<1 mm-wide) gray 'dendrites'—centimeter-scale halos of chaotic hairline fractures with intense pyrite alteration (Fig. 4.42A–C and F). Pyrite and marcasite within the dendrites occur as pseudomorphs and partial replacements of phenocrysts and irregular, discontinuous patches of groundmass (Fig. 4.42G). Chaotic to regular fracture arrays such as these commonly form because brittle deformation effects are not only restricted to main fractures, but also extend outward to regions of high and low strain (the "damage zone"; e.g., Faulkner et al., 2010). These faults and fractures provide high-permeability pathways that can be exploited by contemporaneous or later fluid movement. At Kapit NE and Coastal, sulfur ± iron-rich fluids are inferred to have been channeled along hairline fractures during formation of the Stage 5A stockwork. Pyrite then grew outward from the hairline fractures into the surrounding wall rock, rather than filling in open space as is more typically seen for epithermal veins.

#### *4.4.5.2 Stage 5B: Clay – pyrite-cemented breccias and veins*

Stage 5B is composed of multiple overlapping phases of clay – pyrite ± sulfate-cemented breccias and veins. The dominant clay or sulfate mineralogy varies between veins and is loosely correlated with near-surface, map scale alteration zones. Within the Stage A7 kaolinite – alunite alteration zone, Stage 5B veins and breccias typically consist of alunite ± kaolinite ± augelite ± pyrite ± marcasite ± quartz ± pyrophyllite ± dickite ± vermiculite and have pyritic selvages (Fig. 4.43A–C and H). Minor minerals identified by SEM in Stage 5B samples from the Stage A7 alteration zone include natrojarosite, goyazite, limonite, Fe ± Cu ± As sulfates (e.g., pitticite, chalcanthite, etc.), atacamite and APS minerals, especially woodhouseite (Fig. 4.44; Appendix F). Stage 5B veins and breccias found within the Stage A6 smectite – kaolinite alteration zone consist of montmorillonite ± illite ± pyrite ± marcasite ± pyrrhotite (Fig. 4.43D–F and I–J). Overall, the veins and breccias have a highly variable appearance. Many of the veins have white clay infill that is in stark contrast with a dark gray to blue, sulfide mineral-rich selvage (Fig. 4.43C). The veins can be irregular and diffuse (Fig. 4.43H) or can have sharp wall-rock contacts and form a stockwork (Fig. 4.43C). Vein infill is locally zoned or banded (Fig. 4.44B). Within the Stage A7 kaolinite – alunite alteration domain in Coastal area (cross-section A–A'–A''; Fig. 4.41), Stage 5B veins crosscut and/or infill open space in Stage 3B quartz stockwork veins (Fig. 4.44A). Some Stage 5B veins have reopened Stage 2A or 5A pyrite vein stockworks (Fig. 4.43C and G). In the vicinity of Stage 3B veins and breccias, Stage 5B pyrite ± marcasite form banded overgrowths around earlier-formed disseminated pyrite (Fig. 4.44F).

Stage 5B breccias are typically 5–50 cm in width and have sharp contacts with the surrounding host rocks. They

**Fig. 4.42.** (*Next page*) Stage 5A pyrite veinlets and disseminations. **A.** Core box photographs of Stage 5A pyrite veinlets and disseminations that have preferentially exploited radial and concentric fractures in clasts within montmorillonite – kaolinite-altered pyroxene-phyric basalt breccia (KNE2b). The photographs were taken immediately after drilling by Newcrest Mining Limited geologists (*top image*; 2011-12-13) and two years later by the author (*bottom image*; 2013-09-02). Yellow-orange Fe-oxides and Fe-sulfates (especially copiapite and jarosite) precipitated on the split core surface post-drilling and their abundance correlates with that of Stage 5A pyrite veinlets and disseminations. Interval: DDHL1953 ~90.0–93.2 m. **B.** Close-up photograph of pyritic 'dendrites'—branching hairline fractures with intense halos of Fe-sulfide alteration. Sample: DDHL1876 130.3 m. **C.** Hand sample photographs of a typical network of thin (<1 mm wide), irregular and branching Stage 5A veinlets. The close-up view (*bottom image*) shows that pyrite and marcasite have replaced the host rock adjacent to fractures and have infilled the fractures discontinuously. Sample: DDHL1970 170.4 m. **D.** Patches and veinlets of Stage 5A pyrite – marcasite partially infilling vugs associated with Stage A3 vuggy adularia – quartz alteration. One of the veinlets occurs along a clast margin. Sample: DDHL1970 215.6 m. **E.** Stage 5A pyrite disseminations and patches associated with strong intensity Stage A6 montmorillonite alteration overprinting Stage A2 calcite – chlorite – anhydrite alteration in polymict, matrix-supported breccia (KNE1). Sample: DDHL1873 165.5 m. **F.** Hand sample photograph of a smectite – kaolinite-altered, feldspar-phyric andesite (KNE10) dike with bands of Stage 5A disseminated to patchy pyrite – marcasite that are parallel to compositional layering in the andesite. Stage 5A dendritic pyrite – marcasite veinlets with Fe-sulfide replacement halos have cut obliquely across this same compositional layering. Sample: DDHL1928 93.7 m. **G.** Reflected light photomicrograph of a Stage 5A pyrite band that formed along a concentric flow band within a feldspar-phyric andesite dike (KNE10). The photomicrograph highlights that the pyrite band has been formed by replacement of irregular and discontinuous patches of groundmass and tabular feldspar phenocrysts, rather than by infill of an open fracture. The pyrite is mainly anhedral; however, small aggregates and disseminations of singular pyrite pyritohedra also occur. Due to the highly reactive character of the pyrite in this thin section, it is deep yellow-orange in color and has an iridescent tarnish. Refer to Figure 3.19C for a hand specimen photograph of this sample. Sample: DDHL1968 78.8 m. Abbreviations: anh = anhydrite, cal = calcite, chl = chlorite, cop = copiapite, Fe = Fe-oxides and hydroxides, frc = concentric and radial fractures, fsp = feldspar, jrs = jarosite, mnt = montmorillonite, mrc = marcasite, py = pyrite, rl = relict.

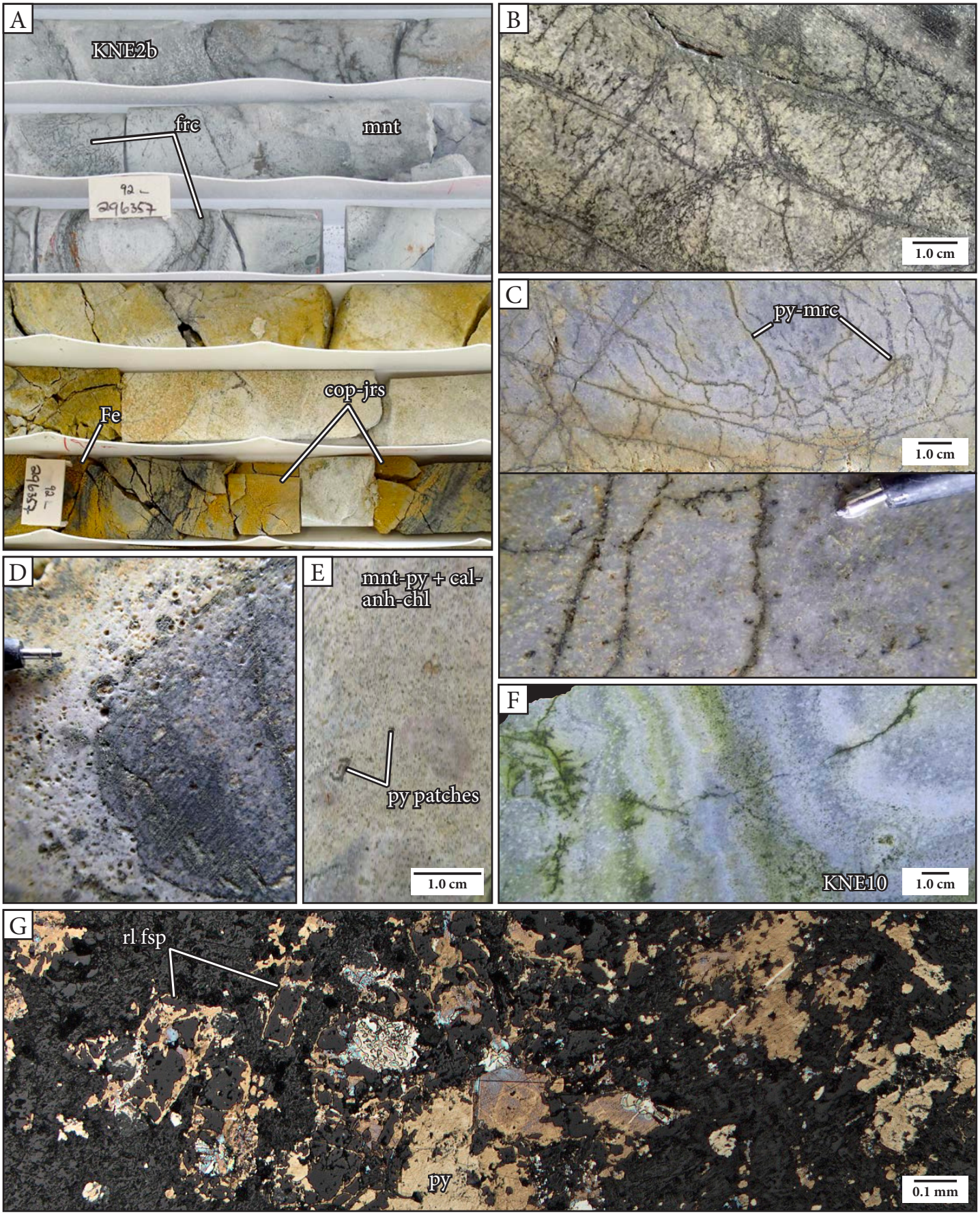
A
KNE2b
frc
mnt
Fe
cop-jrs
B
1.0 cm
C
py-mrc
1.0 cm
D
E
mnt-py + cal-anh-chl
py patches
1.0 cm
F
KNE10
1.0 cm
G
rl fsp
py
0.1 mm

are monomict to polymict, containing clasts derived from the host rocks and older veins and breccias (e.g., Stage 2A vein clasts: Fig. 4.43F). They have a chaotic to clast-rotated, cement-supported organization and are moderately to poorly sorted. The breccias are multi-phase. Locally, they contain clay – pyrite vein fragments and multiple layers of clay – pyrite infill (Fig. 4.43E). They may also contain discontinuous, irregular and/or banded clay ± pyrite veinlets that wrap around clasts rather than cutting across them, suggesting that they formed when the Stage 5B breccia was still unconsolidated (Fig. 4.43D and F).

Clasts with truncated Stage 5B veins have been observed within Stage 4 volcanic-hydrothermal breccias (Fig. 4.45A). Stage 5B veins are observed to have crosscut Stage 4 breccias (Fig. 4.45B) and Stage 5A veins (Fig. 4.43G). This suggests that Stage 5B took place over a protracted period that began before Stage 4 and continued after Stage 5A.

#### *4.4.5.3 Stage 5C: Calcite – quartz – adularia – pyrite – limonite-cemented veins and breccias*

Stage 5C consists of calcite-dominant breccias and interconnected, irregular veins with non-uniform aperture (<0.5–30 mm thickness; Fig. 4.46). The breccias contain angular to subrounded wall-rock clasts with cement-supported, jigsaw-fit to clast-rotated organization and 1–30% open space (Fig. 4.46A–B). Stage 5C displays textures typical of low sulfidation epithermal veins, including colloform and crustiform banding, and breccias with cockade texture (Fig. 4.46A and C). The veins and breccias have conspicuous orange-brown stained selvages and/or alteration halos consisting of pyrite and ankerite that has decomposed to limonite (e.g., Fig. 4.46A, E and I). Calcite crystals characteristically form masses of coarse (0.2–1.0 cm) prismatic rhombohedral and scalenohedral crystals (dogtooth and nailhead spar and combinations thereof; Fig. 4.46C–D), but may also exhibit colloform, massive, sugary-textured, or encrusting habits (Fig. 4.46A–B and E). Rarely, calcite forms lattice-textured bladed masses (Fig. 4.46F). Massive to sugary-textured calcite can be porous (up to 20% open space). The calcite is locally intergrown with elongate prisms of clear quartz, thin bladed anhydrite, carbonate (dolomite to ankerite), abundant stubby rutile (microscopic) and thin crusts of illite (Fig. 4.46A). The mineral infill is relatively sulfide-poor (<5%) and contains dominantly euhedral pyrite (<0.5 mm; Fig. 4.46A), with marcasite, arsenopyrite and minor base-metal sulfides (sphalerite, chalcopyrite) that fill the interstices between calcite crystals.

Stage 5C is spatially associated with irregular vugs, disseminated porosity, hard, gray to pale yellow, pervasive quartz – adularia – illite alteration (Fig. 4.46B) and vein halos with abundant (10–30%) fine-grained disseminated

**Fig. 4.43.** (*Next page*) Stage 5B clay ± pyrite-cemented breccias and veins. **A.** Core box photograph showing several, wavy Stage 5B alunite – kaolinite veinlets with dark gray pyrite selvages. The veinlets have crosscut feldspar-phyric andesite breccia (KNE3) with mottled Stage A7 kaolinite – alunite – quartz alteration. Interval: DDHL1953 ~62.3–66.5 m. **B.** A massive, powdery Stage 5B breccia vein composed predominantly of vermiculite clay, with pyrite, quartz, copiapite, jarosite, and Fe-oxides and hydroxides. The vein has a halo of vermiculite, calcite and quartz alteration. The vermiculite in the breccia vein has expanded, fractured and become friable post-drilling due to the absorption of water. Sample: DDHL1872 230.1 m. **C.** Hand sample photograph of a kaolinite – pyrite – quartz stockwork that has crosscut hornblende – biotite-bearing monzonite (KNE5). The stockwork veins have dark gray pyritic selvages and alteration halos. Feldspar phenocrysts adjacent to the stockwork have been replaced by white kaolinite. Sample: DDHL1872 187.0 m. **D.** Multi-phase Stage 5B breccia with montmorillonite – pyrite – quartz + gypsum cement and montmorillonite-altered clasts. The breccia contains discontinuous and irregular montmorillonite veins and banded pyrite veins that wrap around clasts rather than cutting across them, suggesting that these veins formed when the Stage 5B breccia was still unconsolidated. Sample: DDHL1924 99.2 m. **E.** Multi-phase Stage 5B breccia vein with angular montmorillonite – pyrite vein fragments, montmorillonite-altered lithic clasts and montmorillonite – pyrite cement. The breccia vein has crosscut Stage 5A pyrite veinlets and disseminated pyrite. Sample: DDHL1984 71.5 m. **F.** Massive, fine-grained pyrite, marcasite, montmorillonite and pyrrhotite (Stage 5B) infilling open space in a Stage 3C chalcedony – quartz – pyrite cemented breccia. The sample also contains discontinuous Stage 5B montmorillonite veinlets as in Figure 4.43D. Sample: DDHL1872 192.3 m. **G.** Stage 5B kaolinite – pyrite – quartz veins with pervasive, dark gray pyrite alteration halos that have reopened a subset of the structures associated with a stockwork of Stage 5A pyritic dendrites. Sample: DDHL1876 142.1 m. **H.** Anastomosing pyrophyllite – quartz – pyrite veins and associated montmorillonite alteration halos crosscutting Stage 2B quartz – pyrite-cemented breccia. Sample: DDHL1924 126.0 m. **I.** Hand sample photograph of a Stage 1E vein that has been infilled by centerline Stage 5A illite – pyrite – marcasite. The Stage 5A vein has produced a patchy orange pyrite – goethite – illite alteration halo. Sample: DDHL1873 65.6 m. **J.** A kaolinite – pyrite – quartz-cemented Stage 5B breccia. The angular, locally-sourced feldspar-phyric andesite breccia (KNE3) clasts are cement-supported, have strong montmorillonite alteration and pyrite alteration rinds. The cut surface of the sample has locally altered to yellow copiapite and jarosite. Sample: DDHL1995 113.0 m. Abbreviations: alu = alunite, cmt = cement, cop = copiapite, Fe = pyrite, iron oxides, hydroxides and sulfates, goe = goethite, gyp = gypsum, ill = illite, jrs = jarosite, kao = kaolinite, mnt = montmorillonite, mrc = marcasite, po = pyrrhotite, prl = pyrophyllite, py = pyrite, qtz = quartz, rt = rutile, vrm = vermiculite.

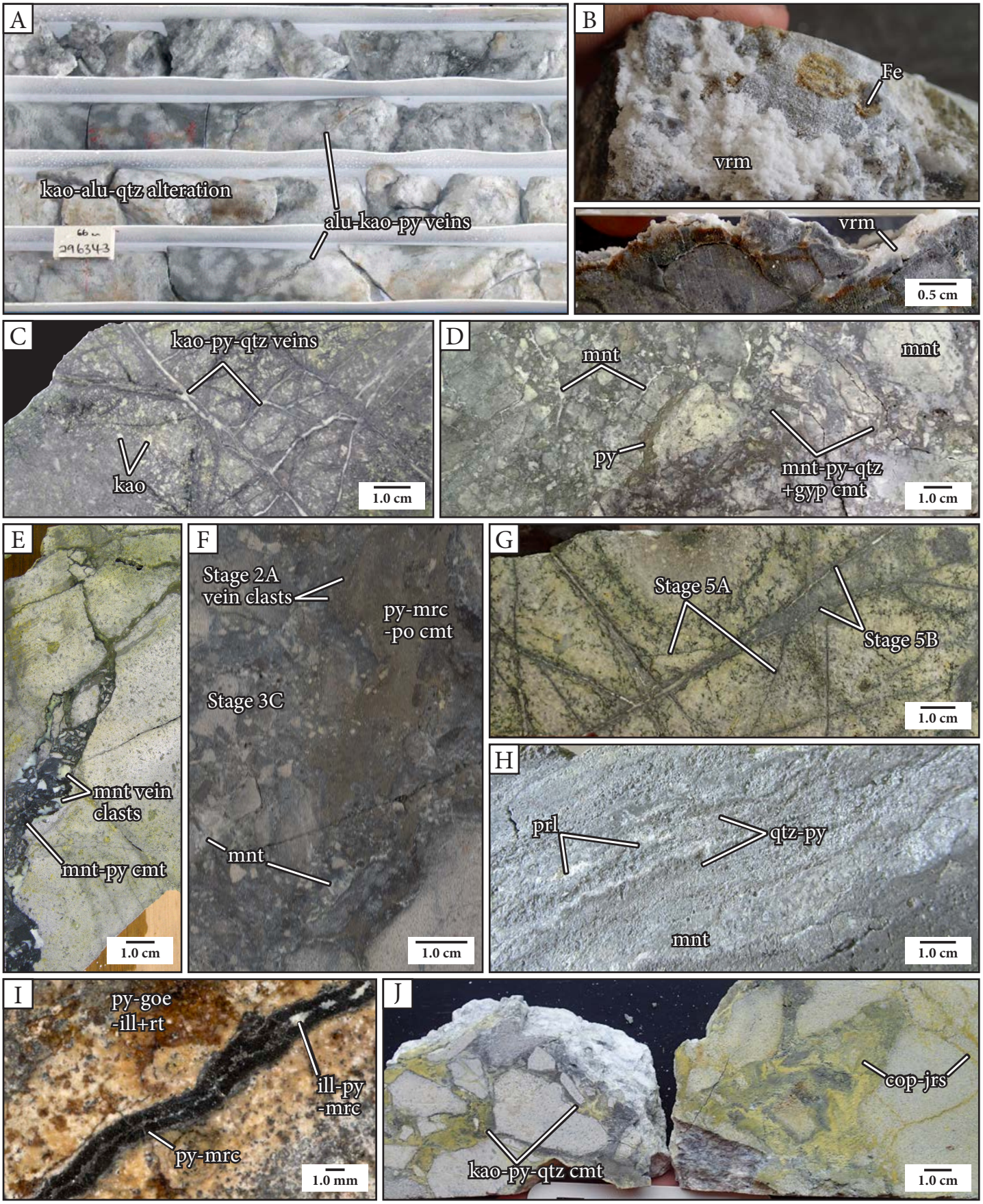
A
kao-alu-qtz alteration
alu-kao-py veins
B
Fe
vrm
vrm
0.5 cm
C
kao-py-qtz veins
kao
1.0 cm
D
mnt
mnt
py
mnt-py-qtz
+gyp cmt
1.0 cm
E
mnt vein
clasts
mnt-py cmt
1.0 cm
F
Stage 2A
vein clasts
py-mrc
-po cmt
Stage 3C
mnt
1.0 cm
G
Stage 5A
Stage 5B
1.0 cm
H
prl
qtz-py
mnt
1.0 cm
I
py-goe
-ill+rt
ill-py
-mrc
py-mrc
1.0 mm
J
cop-jrs
kao-py-qtz cmt
1.0 cm

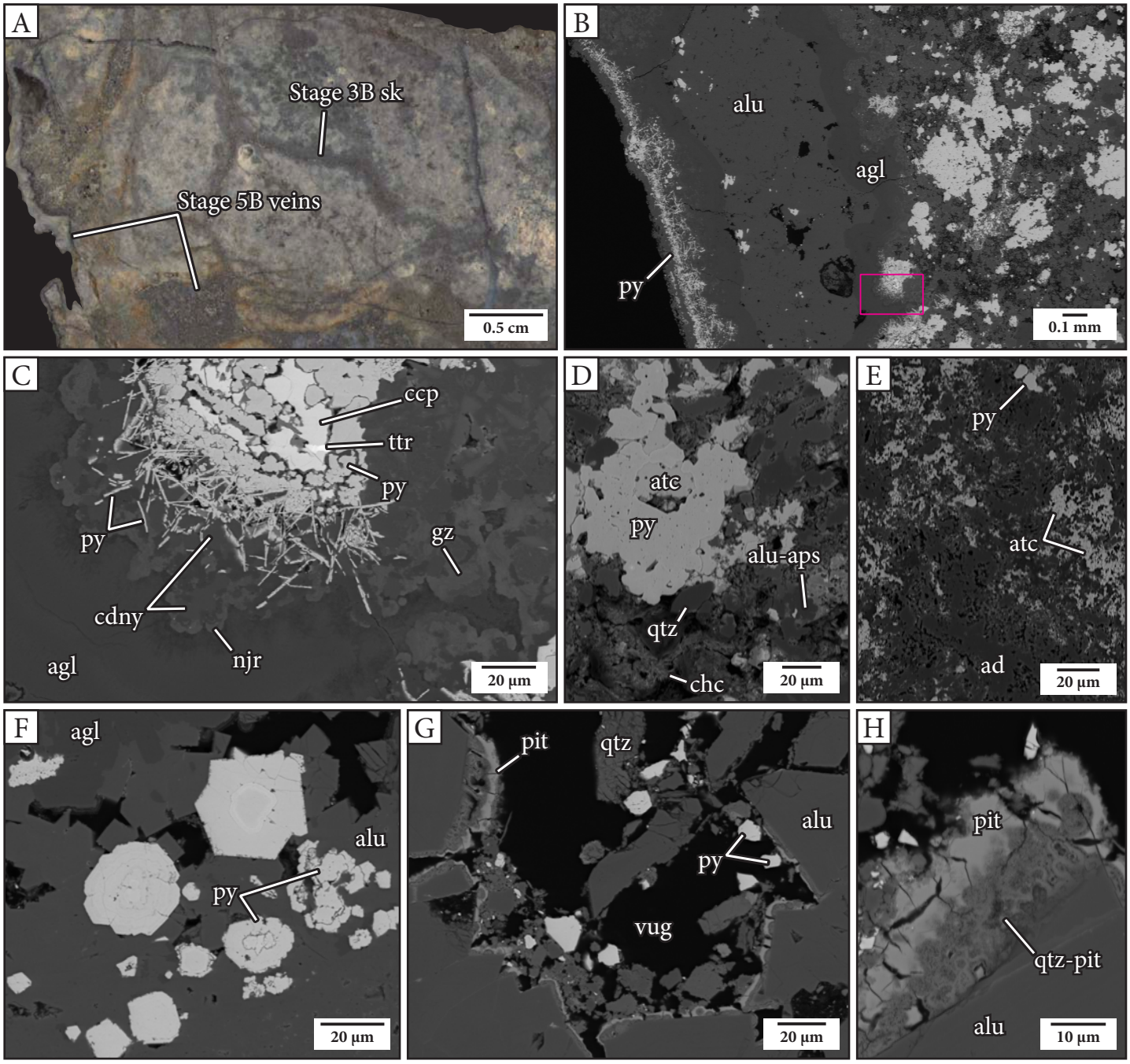


**Fig. 4.44.** Relationship between Stage 5B and Stage 3B veins and alteration in sample DDHL1872 99.0 m. Figures 4.44B–H are BSE images. Quantitative EDS X-ray microanalysis data and spot locations are provided in Appendix F. Where possible, mineral labels point to the location of spot analyses. **A.** Hand sample photograph showing white Stage 5B alunite – augelite – pyrite veins with orange to blue-green alteration halos infilling and/or crosscutting Stage 3B quartz stockwork veins with gray quartz – adularia – pyrite alteration halos. The Stage 5B alteration halos are composed of alunite, APS minerals, pyrite, limonite, Fe ± Cu ± As sulfates and chlorides. **B.** Cross sectional view through a composite vein. The vein walls are discontinuously lined with Stage 3B chalcedony vein material and infilled by a Stage 5B vein that is zoned inward from colloform augelite to very fine-grained alunite – pyrite with a vuggy centerline. The pink box shows the location of Figure 4.44C. **C.** Close-up view of the transition from Stage 3B to Stage 5B in the composite vein from Figure 4.44B. The Stage 3B vein consists of a pyrite – chalcopyrite – tetrahedrite aggregate surrounded by acicular pyrite and chalcedony. Stage 5B natrojarosite ± goyazite forms a layer over the chalcedony and transitions into colloform augelite. **D.** Intensely altered wall-rock in the vein halo around a Stage 5B vein. The primary mineralogy of the host rock was first replaced by vuggy quartz and pyrite associated with Stage 3B vein emplacement. During Stage 5B, vugs were partly infilled with alunite ± APS minerals (especially woodhousite). Copper, which may have been remobilized from Stage 3B chalcopyrite – tetrahedrite-tennantite – pyrite aggregates, was redeposited as chalcanthite and atacamite in open spaces. **E.** Amorphous, vuggy atacamite infilling open space within previously vuggy adularia – pyrite-altered wall-rock in the vein halo of a Stage 5B alunite vein. **F.** Composite grains of pyrite, with Stage 3B pyrite cores and Stage 5B pyrite overgrowths. **G.** Rhombohedral alunite terminating into a vug at the center of a Stage 5B vein. The alunite is encrusted with quartz, pitticite and As ± Cu-rich pyrite. **H.** Close-up view of a botryoidal pitticite ± quartz overgrowth on alunite. Abbreviations: ad = adularia, agl = augelite, alu = alunite, aps = aluminum-phosphate-sulfate mineral (woodhousite), atc = atacamite, ccp = chalcopyrite, cdny = chalcedony, chc = chalcanthite, gz = goyazite, njr = natrojarosite, pit = pitticite, py = pyrite, qtz = quartz, ttr = tetrahedrite.

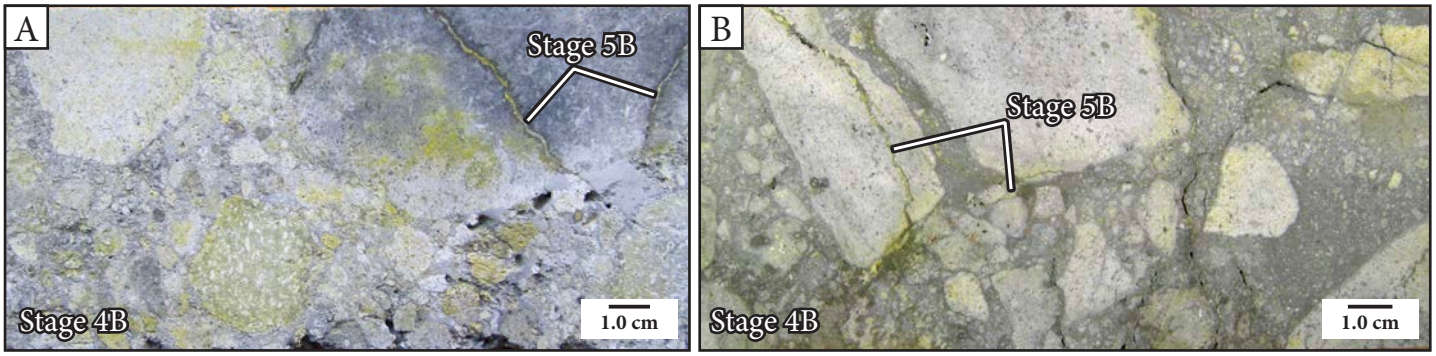


**Fig. 4.45.** Crosscutting relationships between Stage 5B clay – pyrite-cemented breccias and veins and Stage 4 volcanic-hydrothermal breccias. **A.** Feldspar-phyric andesite breccia (KNE3) clasts containing truncated Stage 5B clay – pyrite veins within Stage 4B polymict, clast-rich breccia. Sample: DDHL1928 72.9 m. **B.** Stage 5B clay – pyrite vein that has crosscut clasts and matrix of Stage 4B polymict, clast-rich breccia. Sample: DDHL1984 60.4 m.

pyrite, marcasite and minor sphalerite (<2%; Fig. 4.46E and I–M). Pyrite, marcasite and arsenopyrite have formed anhedral or colloform-banded rims around previously formed pyritohedral, octahedral, cubic-octahedral or acicular pyrite ± marcasite (Fig. 4.46J–L). Many crystal-shaped vugs are partly filled with euhedral pyrite, calcite and quartz crystals and are coated with illite.

There is a positive correlation between the intensity of Stage 5C veins and gold grades at the dekameter scale (Fig. 4.47A), making Stage 5C an important contributor to the total gold resource in Kapit NE. The sulfides in the alteration halos are gold- and trace element-rich and are the likely repository of gold in this stage. Native gold and gold tellurides were not observed. Stage 5C breccias and veins occur at shallow depths (~100–150 m below sea level) and are localized along the NE-trending margin of the Diwai diatreme breccia, crosscutting both the diatreme and the surrounding host rocks (Figs. 4.29 and 4.41). Stage 5C has not been observed in the Coastal ore zone. Stage 5C has overprinted Stage 3 (Fig. 4.46B and G), Stage 4 (Fig. 4.46C and 4.47A) and Stage 5A and B veins and breccias

**Fig. 4.46.** (*Next page*) Stage 5C calcite – quartz – adularia – pyrite – limonite-cemented veins and breccias. **A.** Hand sample photograph of a clast-rotated, cement-supported Stage 5C breccia with cockade texture. The breccia cement consists of banded sugary-textured white calcite, fine-grained prismatic quartz, and cream-colored massive ankerite with minor interstitial and discontinuous bands of pyrite and limonite. Pyrite and limonite also occur in fractures and along the margins of clasts. Sample: DDHL1928 152.5 m. **B.** A chaotic Stage 5C breccia with a vuggy cement composed of massive calcite, prismatic drusy quartz and minor pyrite. The wall-rock clasts have limonite – pyrite alteration rinds, strong, pervasive adularia – quartz – calcite alteration and disseminated pyrite. The sample has been etched and then treated with sodium cobaltinitrite, which stains adularia yellow, to better show its distribution. The sample has a polymict clast population, including pyroxene-phyric basalt (KNE2) clasts, feldspar-phyric andesite breccia (KNE3) clasts, abundant rounded, sand-sized (<0.5 mm) pyrite vein clasts (of unknown derivation) and a Stage 1I banded anhydrite – pyrite vein fragment. Sample: DDHL1928 128.8 m. **C.** Hand sample photograph of Stage 5C quartz – calcite – ankerite – pyrite – limonite veins that have crosscut a Stage 4B polymict, clast-rich breccia. The veins have preferentially precipitated along draped bedding planes that probably formed due to the settling of fine-grained rock flour into void spaces following the explosive phases of Stage 4 volcanic-hydrothermal brecciation. Pyrite – limonite occurs within the selvage of the Stage 5C vein and has infiltrated along small fractures and other void spaces within the Stage 4B breccia matrix. Sample: DDHL1928 128.8 m. **D.** Close-up view of coarse-grained (~0.2–0.7 cm) euhedral calcite in a drusy Stage 5C vein. The sample contains dogtooth spar, nailhead spar and combined forms of calcite and some of the crystal faces exhibit crosswise striations. Sample: DDHL1968 237.5 m. **E.** A vuggy, banded Stage 5C vein featuring inward-terminating rhombic calcite and acicular quartz crystals. The Stage 5C vein, with its narrow (<0.5 mm wide), brown, well-defined pyrite – adularia – limonite alteration halo has crosscut pyroxene-phyric basalt breccia (KNE2b) with Stage A2 chlorite alteration. Sample: DDHL1995 144.7 m. **F.** Lattice-textured bladed calcite that has locally been encrusted with fine-grained sugary white quartz and pyrite. Sample: DDHL1968 267.1 m. **G.** Hand sample photograph of a thin Stage 5C calcite – pyrite – limonite vein that has obliquely crosscut a Stage 3B blue quartz – marcasite – pyrite vein, which has in turn crosscut several Stage 3A anhydrite – quartz veins. Sample: DDHL1931 221.8 m. **H.** Hand sample photograph of drusy Stage 5C quartz – calcite veins with pyrite – ankerite – limonite selvages and vein halos that have reopened and precipitated along Stage 5B illite – marcasite – pyrite veins. The Stage 5C veins have also partly infilled open fractures associated with Stage A3 vuggy adularia alteration. Sample: DDHL1924 129.5 m. **I.** Reflected light photomicrograph of a Stage 5C quartz – calcite vein. The photo highlights the decrease in abundance of disseminated pyrite and very fine-grained Fe-sulfides away from the vein margin. The host rocks have been leached in the area around the vein, leaving abundant sub-millimeter-sized vugs. Sample: DDHL1928 152.5 m. **J.** Reflected light photomicrograph highlighting colloform arsenopyrite that has mantled round (corroded) marcasite crystals and pyrite pyritohedra. The outer layers of arsenopyrite are embayed and irregular, also due to corrosion. Sample: DDHL1928 152.5 m. **K.** Reflected light photomicrograph of a chain-like aggregate of marcasite crystals intergrown with minor sphalerite and chalcopyrite, as well as a small pyritohedral pyrite crystal. Both have been partly mantled by ragged, porous marcasite. There is space between the first layer of marcasite and the crystals that they are enveloping, which may have been dissolved away. Sample: DDHL1928 152.5 m. **L.** Reflected light photomicrograph showing marcasite needles and colloform overgrowths on porous, octahedral and pyritohedral pyrite with fractured margins. The sample also contains very fine-grained (<10 μm), disseminated tennantite, sphalerite and pyrite. Sample: DDHL1928 152.5 m. **M.** Reflected light photomicrograph of an aggregate of fine-grained and porous, pyrite, marcasite and sphalerite, with overgrowths of colloform pyrite. Sample: DDHL1928 128.8 m. Abbreviations: ad = adularia, anh = anhydrite, apy = arsenopyrite, cal = calcite, ccp = chalcopyrite, lim = limonite, mrc = marcasite, py = pyrite, qtz = quartz, sf = Fe-sulfides, sph = sphalerite, tenn = tennantite.

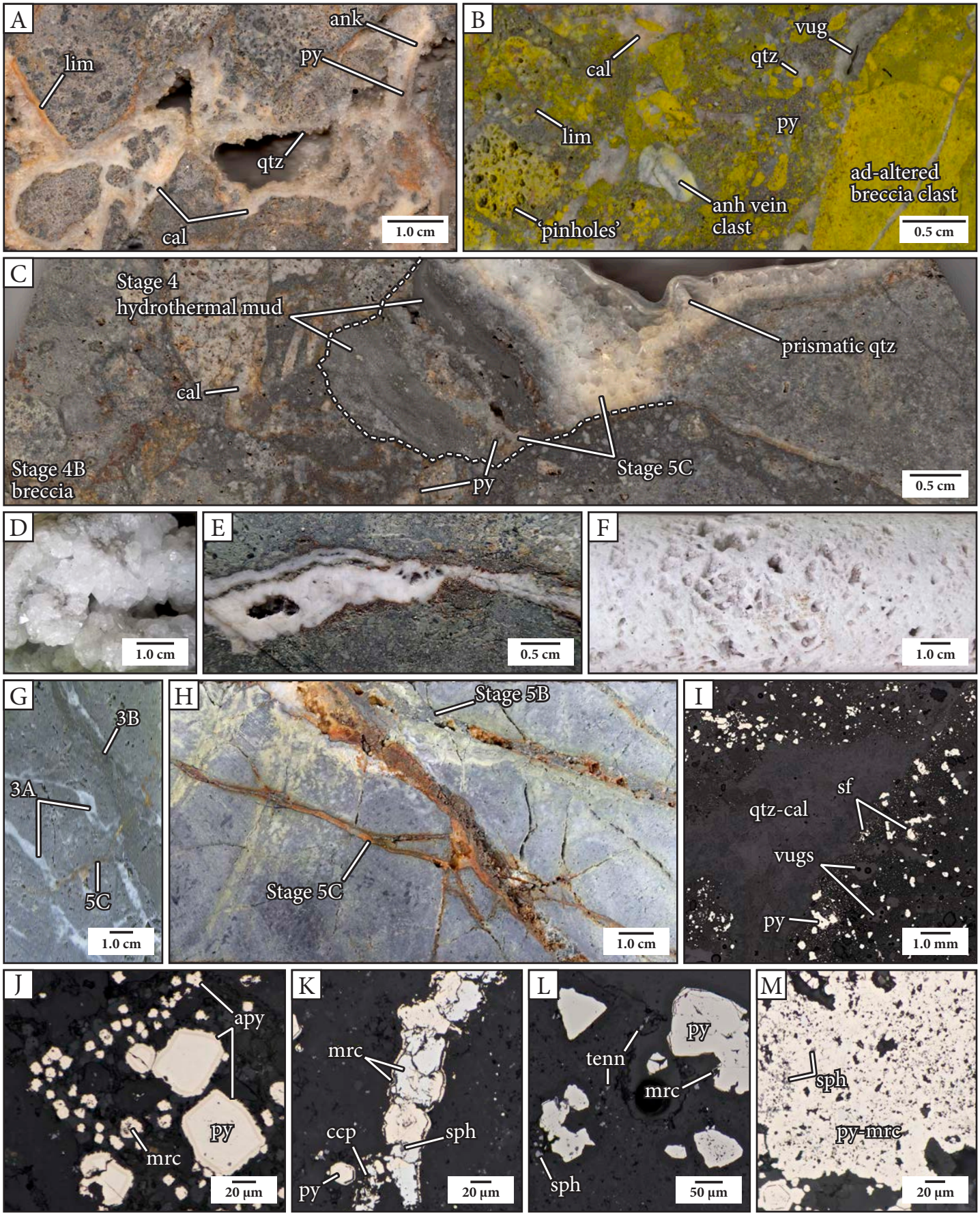
A
ank
lim
py
qtz
cal
1.0 cm
B
vug
cal
qtz
lim
py
ad-altered breccia clast
anh vein clast
'pinholes'
0.5 cm
C
Stage 4 hydrothermal mud
prismatic qtz
cal
Stage 4B breccia
py
Stage 5C
0.5 cm
D
1.0 cm
E
0.5 cm
F
1.0 cm
G
3B
3A
5C
1.0 cm
H
Stage 5B
Stage 5C
1.0 cm
I
sf
qtz-cal
vugs
py
1.0 mm
J
apy
py
mrc
20 µm
K
mrc
ccp
sph
py
20 µm
L
py
tenn
mrc
sph
50 µm
M
sph
py-mrc
20 µm

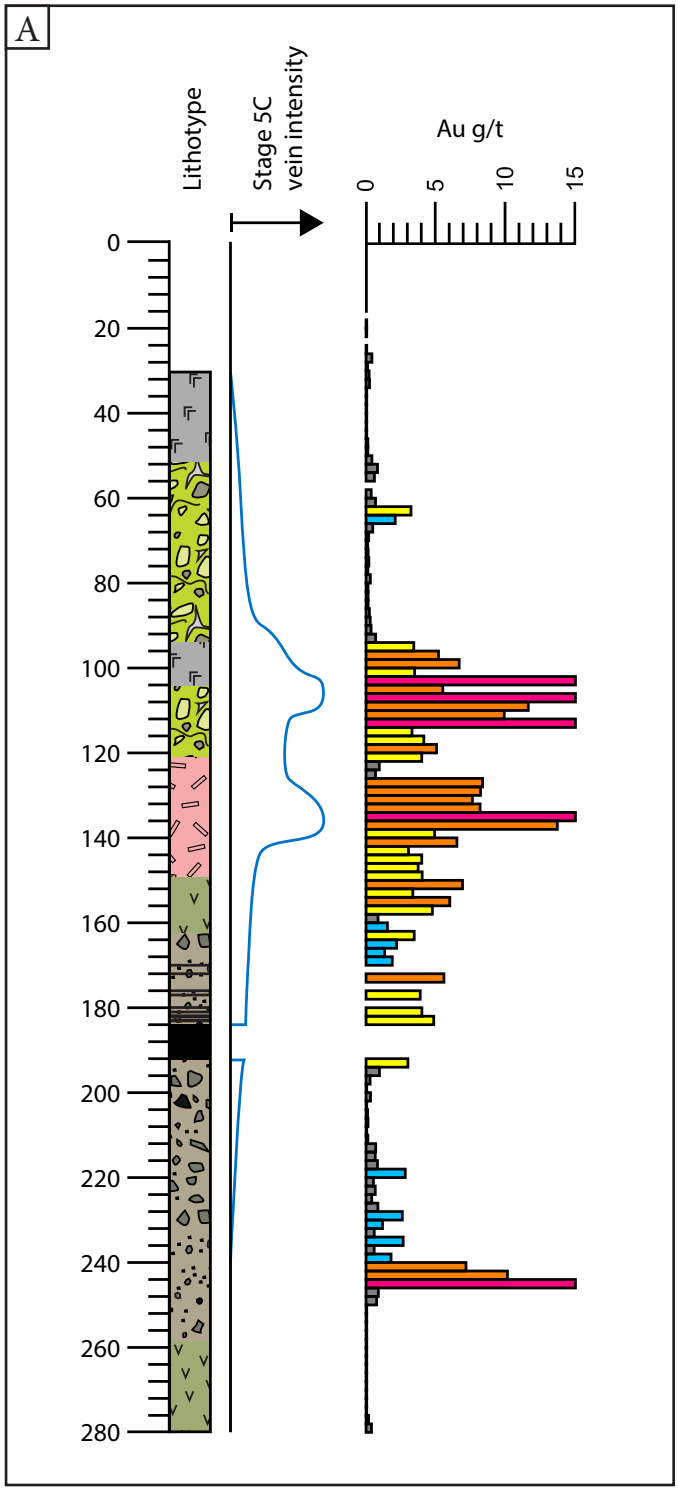




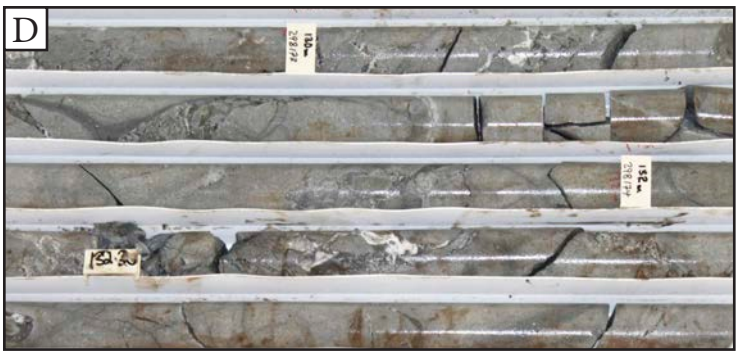


**Lithotype**

- Feldspar-phyric andesite-clast breccia (KNE10)
- Polymict volcanic-hydrothermal breccia (Stage 4)
- Hornblende-biotite-bearing monzonite (KNE5)
- Pyroxene-phyric basalt and basalt breccia (KNE2)
- Polymict matrix-supported breccia (KNE1)
- Cavity

**Au g/t**

- > 15
- 5–15
- 3–5
- 1–3
- < 1

(Fig. 4.46H) and is interpreted as the last major phase of gold mineralization.

#### *4.4.5.4 Stage 5D: Orpiment – realgar veinlets and breccias*

Stage 5D consists of irregular veinlets and narrow (<5 cm), monomict, jigsaw-fit to clast-rotated breccias containing orpiment and realgar (Fig. 4.48). The veins and breccias are restricted to shallow levels (<120 m depth; Fig. 4.41). They have commonly crosscut Au-bearing epithermal veins and breccias (i.e., Stages 2 and 3; Figs. 4.48A–B and D) and are not crosscut by any other vein stages. Stage 5D does not contain free Au or Au-bearing minerals. Intervals containing Stage 5D have an average of 0.1% As and 7.8% S (values are averaged over intervals intersected on sections A–A'–A" and B–B' using Newcrest Mining Limited assay data; n = 25).

Stage 5D veinlets and breccias are sparse (typically <1 per meter) and contain >50% open space. They are not associated with an obvious alteration assemblage. Orpiment occurs as singular prismatic orange crystals (Fig. 4.48D), yellow powder (Fig. 4.48C) or as drusy, botryoidal reddish-orange aggregates with realgar (Figs. 4.48A and C). Realgar commonly occurs in small aggregates of striated, euhedral red crystals that have partly broken down to orange, powdery, pararealgar as a result of post-drilling exposure to light (e.g., Douglass et al., 1992; Fig. 4.48B). Locally, the veins are associated with thin crusts of gray amorphous silica. Stage 5D breccia cement is typically zoned, with orange crystalline to powdery yellow orpiment lining clasts and filling small veinlets and with reddish-orange realgar occupying the central space (Fig. 4.48C).

## 4.5 Re–Os geochronology

### *4.5.1 Introduction*

The absolute ages of veins from Lihir were obtained by Re–Os dating of molybdenite from paragenetically constrained samples. These results are used to assess the timing and duration of hydrothermal activity at Lihir.

### *4.5.2 Samples*

Five samples were selected for Re–Os dating. Sample photographs and brief descriptions are provided in Figure 4.49 and sample coordinates are provided in Appendix A2. The sample set consisted of one porphyry-stage anhydrite vein from Kapit NE (Stage 1E; DDHL1928 280.5 m), one porphyry-stage anhydrite – magnetite vein from Minifie (DDHL1415 169.0 m), one epithermal-stage cataclasite from Kapit NE containing finely comminuted porphyry-stage molybdenite (Stage 2D; DDHL1924 110.8 m) and two epithermal-stage quartz veins from Lienetz (DDHL0791 226.8 m and LH14SS074). The molybdenite in the sample from Minifie ore zone occurs within the biotite alteration halo of an anhydrite – magnetite vein classified as Stage I according to the scheme of Carman (1994). The quartz veins from Lienetz can be categorized as Stage III blue-gray quartz veins according to the vein paragenesis of Carman (1994) or alternatively as quartz – anhydrite veins, breccia veins, and vug fill ($V4_{qtz}$) according to the scheme of Sykora et al. (2018a). One additional epithermal-stage roscoelite – carbonate – quartz – anhydrite – precious metal telluride vein from Kapit NE (Stage 3A; DDHL1974 220.8 m; Fig. 4.25) was also submitted for

**Fig. 4.47.** (*Previous page*) Relationship between Stage 5C, lithotype and gold grade. **A.** Graphic log of drillhole DDHL1966 in Kapit NE, comparing lithotype, Stage 5C vein intensity and gold grade with depth down hole. The drillhole had an average surveyed dip of -63.5°, meaning that depth down hole is shallower than depth below sea level. At <200 m depth down hole, there is a positive correlation between gold grade and Stage 5C vein intensity that is centered on the contact between the Diwai breccia (Stage 4B polymict, clast-rich breccia) and hornblende-biotite-bearing monzonite (KNE5). **B.** Core box photograph of typical, barren Stage 4B polymict, clast-rich breccia that has not been crosscut by Stage 5C veins. Interval: DDHL1966 ~78.5–81.6 m. **C.** Core box photograph showing abundant, irregular and interconnected, drusy calcite – quartz – adularia – pyrite – limonite-cemented veins and breccia veins with vuggy, intense, dark gray and rust-colored, quartz – adularia – illite – pyrite – marcasite – sphalerite alteration halos. These gold-bearing Stage 5C veins and breccia veins have crosscut Stage 4B polymict, clast-rich breccia near its contact with hornblende-biotite-bearing monzonite (KNE5). Interval: DDHL1966 ~106.5–114.5 m. **D.** Core box photograph of abundant, gold-bearing Stage 5C drusy calcite – quartz – adularia – pyrite – limonite-cemented veins and breccia veins that have crosscut hornblende-biotite-bearing monzonite (KNE5). The veins and breccia veins are more tabular and discrete, and the alteration halos are more narrow than the irregular veins and breccias shown in Figure 4.47B. Interval: DDHL1966 ~129.6–133.0 m.

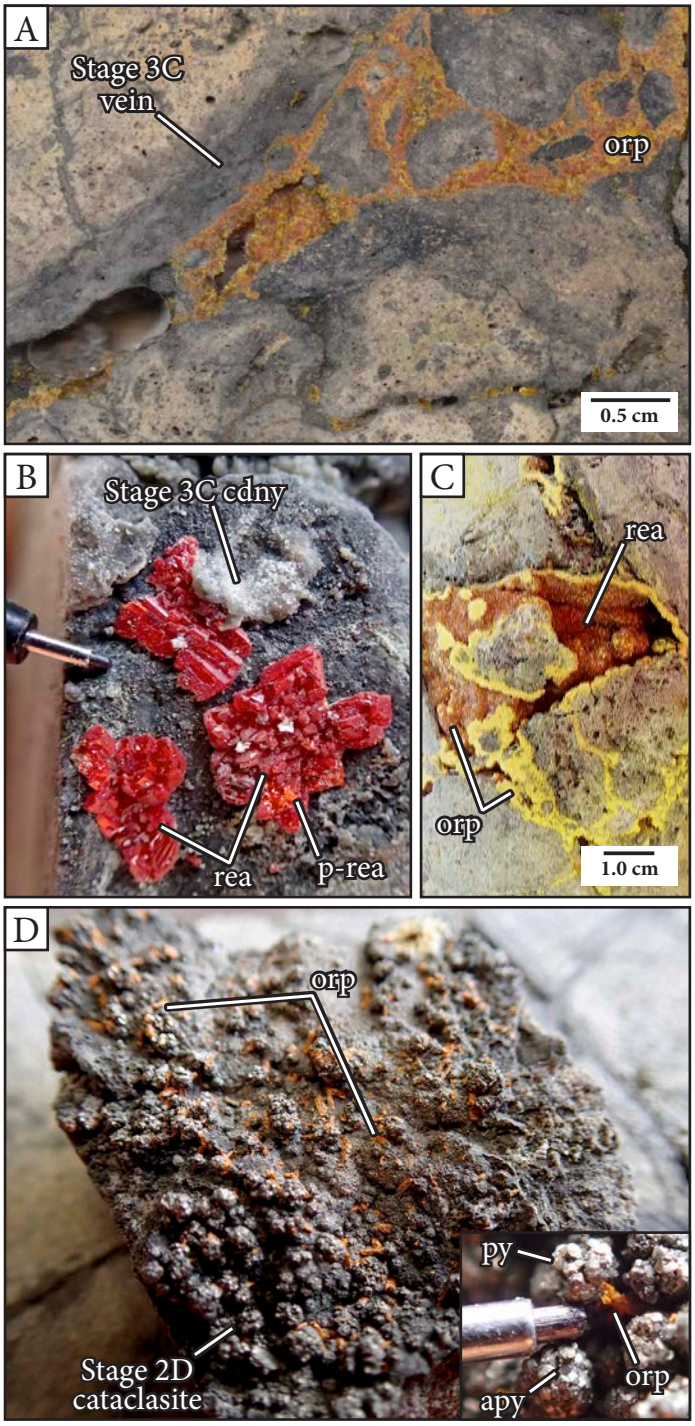


**Fig. 4.48.** Stage 5D orpiment – realgar veinlets and breccia veins. **A.** A clast-rotated to chaotic orpiment-cemented breccia vein (Stage 5D) that has crosscut and includes angular clasts of pyroxene-phyric basalt breccia (KNE2b) and Stage 3C chalcedony – quartz – pyrite cemented breccia. The orpiment occurs as drusy prismatic crystal aggregates and powdery yellow masses. Sample: DDHL1924 103.5 m. **B.** Clusters of red, prismatic and striated realgar crystals that have partially degraded to orange pararealgar under exposure to light (post-drilling). The realgar crystals precipitated within a fractured Stage 3C chalcedony vein. Pencil lead is 0.5 mm in diameter for scale. Sample: DDHL1872 95.2 m. **C.** A Stage 5D breccia vein with zoned cement. Powdery yellow orpiment surrounds clasts and is encrusted with ball-like, radiating aggregates of small, orange, prismatic orpiment crystals. Euhedral, reddish-orange realgar crystals have grown from the orpiment into void spaces. Sample: DDHL1924 103.5 m. **D.** Singular, prismatic and bright orange Stage 5D orpiment crystals with chisel-shaped and triangular pyramidal terminations. The orpiment has nucleated on the uneven surface of an unconsolidated Stage 2D pyritic cataclasite. Pencil lead within inset is 0.5 mm in diameter for scale. Sample: DDHL1872 87.5 m. Abbreviations: apy = arsenopyrite, cdny = chalcedony, orp = orpiment, py = pyrite, p-rea = pararealgar, rea = realgar.

Re–Os age dating, but the results were not returned prior to submission of this PhD thesis.

### *4.5.3 Methods*

#### *4.5.3.1 Molybdenite separation*

The five selected rock samples (Fig. 4.49) were sent to Dr. Robert Creaser at the University of Alberta Radiogenic Isotope Facility for mineral separation and Re–Os dating. Molybdenite in quartz vein sample LH14SS074 was found to have completely oxidized to blue, low-temperature molybdenum oxy-hydroxide minerals; therefore, molybdenite separation was not attempted. Samples DDHL0791 226.8 m and DDHL1415 169.0 m were processed by a room-temperature hydrofluoric acid chemical separation technique according to the method of Lawley and Selby (2012), but yielded no recoverable molybdenite. A molybdenite mineral separate was made for sample DDHL1928 280.5 m by metal-free crushing followed by gravity and magnetic concentration methods as described in Selby and Creaser (2004). This molybdenite separate was impure, containing about 25% molybdenite by visual estimate. Other sulfides such as pyrite remained and could not be physically separated. Despite this, the molybdenite separate had a moderately high Re content of 672.7 ppm (Table 4.7). For sample DDHL1924-110.8, molybdenite "crust" was scraped from a surface with a carbide tool.

#### *4.5.3.2 LA-ICP-MS analysis of molybdenite*

In order to investigate the deportment of Re and other trace elements in the molybdenite samples to be dated, LA-ICP-MS raster images and spot analyses were obtained. Two polished 2.5-cm-wide laser mounts were

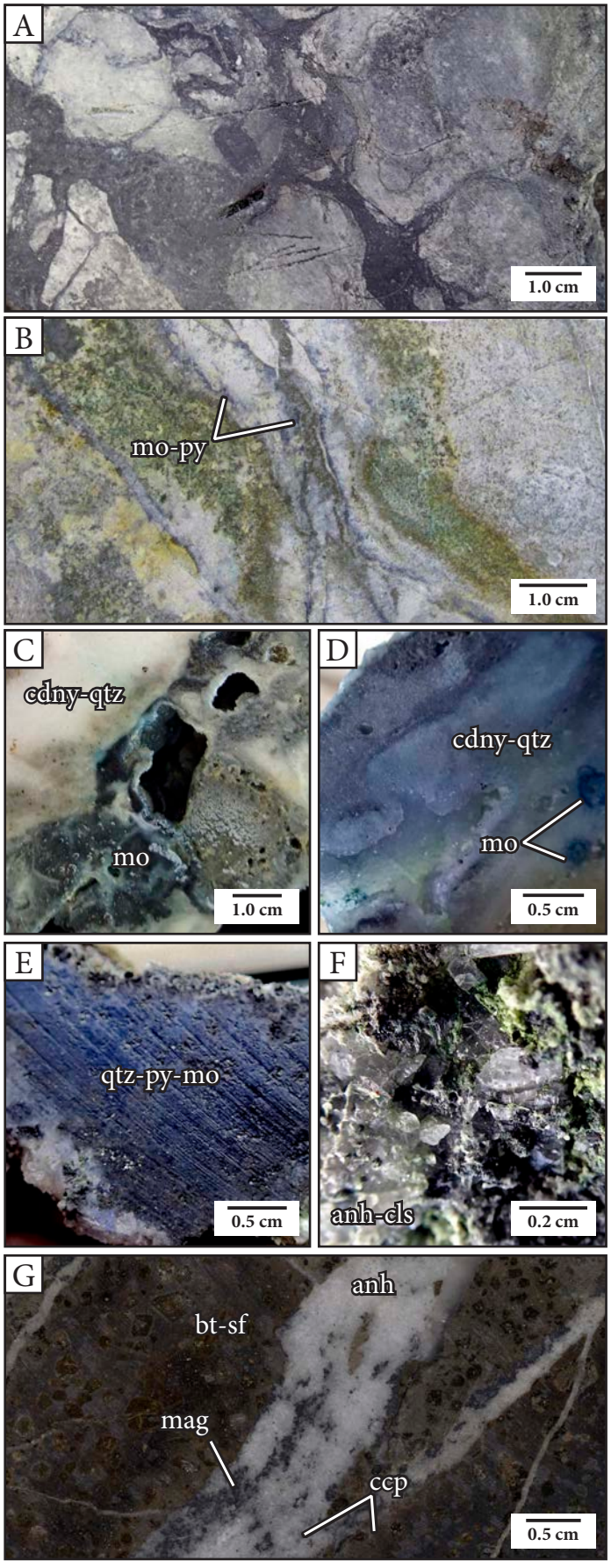


made from samples DDHL1928 280.5 m and DDHL1924 110.8 m. One aggregate of molybdenite from laser mount DDHL1928 280.5 m was chosen for LA-ICP-MS element mapping (Fig. 4.50A–B) and an area of very fine-grained disseminated molybdenite spanning a clast and matrix of the cataclasite in laser mount DDHL1924 110.8 m was selected for ten LA-ICP-MS spot analyses (Fig. 4.50C and D).

*In situ* analysis of molybdenite by LA-ICP-MS was conducted at the CODES Analytical Laboratories, University of Tasmania, Australia. The details of the equipment and settings for the LA-ICP-MS analyses are as follows: Resolution (Australian Scientific Instruments) S155 193-nm Excimer laser ablation system using 2.3–2.7 J/cm$^2$ fluence, coupled with an Agilent 7700 ICP-MS with 0.95 Ar and 0.70 He l/min carrier gas flow rates and tuned to <0.25% (ThO/Th) oxide production. Forty-two elements were analyzed (Na, Mg, Al, Si, S, K, Ca, Ti, V, Cr, Mn, Fe, Co, Ni, Cu, Zn, As, Se, Zr, Mo, Ag, Cd, In, Sn, Sb, Te, Ba, Nd, Gd, Tm, Hf, Ta, W, Re, Pt, Au, Hg, Tl, Pb, Bi, Th and U). Memory effects and instrumental drift sensitivities were controlled by regular measurements of the background (every 2 hours) and calibration standards (before and after analysis of each image and set of spots). The error on average, estimated from the standards, is <5%, with the notable exception of sulfur, which is strongly affected by the instrumental drift and fractionation. The detection capability was estimated

**Fig. 4.49.** Re–Os (molybdenite) geochronology sample photographs. **A.** Stage 2D cataclasite from Kapit NE. The blue-gray matrix consists of very fine-grained rock flour and contains disseminated sulfides including molybdenite. Sample: DDHL1924 110.8 m. **B.** Stage 1E anhydrite – orthoclase – molybdenite – pyrite veins with orthoclase-rich alteration halos from Kapit NE. Sample: DDHL1928 280.5 m. **C.** and **D.** Chalcedony – quartz vein from Lienetz containing minor quantities of very fine-grained disseminated sulfides including molybdenite. The molybdenite has partly altered to molybdenum oxy-hydroxide minerals, giving the vein a blue-gray coloration. Sample: DDHL0791 226.8 m. **E.** and **F.** Dark blue-gray, quartz-rich vein from Lienetz open pit containing molybdenite (altered to molybdenum oxy-hydroxide minerals), marcasite, arsenopyrite, chalcanthite, bladed anhydrite and celestine. Sample: LH14SS074. Sample coordinates (AGD84): 459,611.2 mE 9,654,165.2 mN, –270.1 m **G.** Anhydrite – magnetite – chalcopyrite vein from Minifie with strong intensity biotite – anhydrite – chalcopyrite – pyrite – molybdenite alteration halo. Molybdenite is very fine-grained and is not visible at the scale of this photograph. It was primarily observed partly replacing pyroxene phenocrysts in the alteration halo of the vein. Sample: DDHL1415 169.0 m. Abbreviations: anh = anhydrite, bt = biotite, ccp = chalcopyrite, cdny = chalcedony, cls = celestine, mag = magnetite, mo = molybdenite, py = pyrite, sf = sulfides, qtz = quartz.

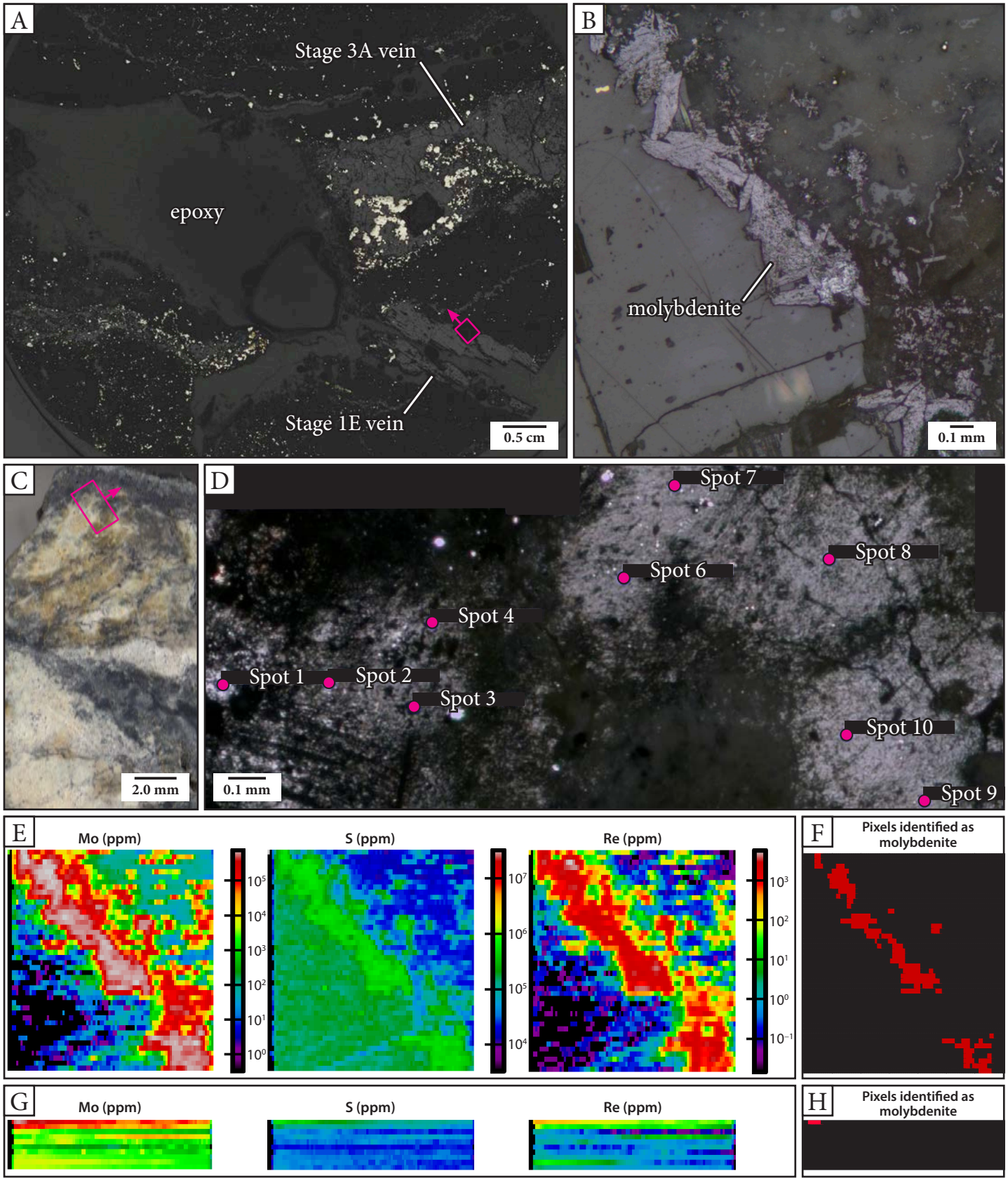


**Fig. 4.50.** Rhenium distribution in molybdenite. **A.** Reflected-light photomicrograph of laser mount DDHL1928 280.5 m, showing the distribution of Stage 1E and 3A anhydrite veins. The Stage 1I vein does not contain molybdenite. The pink box and arrow show the location and orientation of images in Figure 4.50B, E and F. Note

from noise-on-gas background, and the measurements below the detection limit threshold values were replaced by half of the detection limit.

LA-ICP-MS imaging proceeded by ablating the surface of each molybdenite grain following the methods outlined in Large et al. (2009), Danyushevsky et al. (2011), and Gregory et al. (2013). Imaging was conducted using a set of parallel lines with spacing equal to the laser beam size to cover the area of interest. Each line was pre-ablated to remove surface deposition from previous ablations and other surface contaminants. A square beam with a width of 17 μm was used. Lines were ablated at 10 Hz repetition rate and a constant speed, covering the size of the beam in 1s. For spot analysis, a circular beam with a diameter of 43 μm and 10 Hz repetition rate were used. Each spot was pre-ablated prior to analysis.

Images and spots were processed using unpublished software that was developed at the University of Tasmania. The software uses known compositions for reference standards to convert signals collected for each measured element (in units of counts per second) into concentrations (in units of parts per million) and displays this data in X–Y space. Concentrations of lithophile elements were calculated using an in-house glass standard (GSD; Guillong et al., 2005) and chalcophile elements were calculated using a lithium-borate glass standard (STDGL-2b2; Danyushevsky et al., 2011). Spots were processed as lines, where pixels from left to right represent analyses that are increasingly deeper into the mineral being ablated.

LA-ICP-MS trace element data were investigated using ioGAS™. Only minerals identified as molybdenite (i.e., pixels with characteristic elemental ratios and compositions of molybdenite; Fig. 4.50F and H) were queried.

#### *4.5.3.3 Re–Os analytical methods*

The $^{187}$Re and $^{187}$Os concentrations in molybdenite were determined by isotope dilution mass spectrometry using Carius-tube, solvent extraction, anion chromatography and negative thermal ionization mass spectrometry techniques. A mixed double spike containing known amounts of isotopically enriched $^{185}$Re, $^{190}$Os, and $^{188}$Os analysis was used. Isotopic analysis was made using a ThermoScientific Triton mass spectrometer by Faraday collector. Total procedural blanks for Re and Os are less than <3 picograms and 2 picograms, respectively, which are insignificant for the Re and Os concentrations in most molybdenite samples. Molybdenite powder HLP-5 (Markey et al., 1998) was analyzed as a standard. Over a two-year period, this control sample yielded an average Re–Os age date of 221.56 ± 0.40 Ma (1SD uncertainty, n = 10), which is identical to the age date reported by Markey et al. (1998; 221.0 ± 1.0 Ma).

### *4.5.4 Results and interpretation*

#### *4.5.4.1 Trace element deportment in molybdenite*

*Sample DDHL1928 280.5 m:* The molybdenite has a relatively high Re content ranging from 552–5,739 ppm (mean 2,291 ppm; n = 308 pixels; Fig. 4.50E–F). LA-ICP-MS maps show that the molybdenite crystals do not display Re zoning (Fig. 4.50E), which can complicate molybdenite dating using the Re–Os method. The molybdenite contains elevat-

(*Continued from previous page*) that the laser mount has a large epoxy-filled hole at its center that originated during laser mount preparation. **B.** Reflected-light photomicrograph of the area mapped by LA-ICP-MS. Molybdenite occurs as platy crystals that form radial aggregates at the selvage of the Stage 1E anhydrite vein and as very fine-grained single crystals disseminated in the vein halo. Individual molybdenite laths range from ~0.005–0.5 mm in length. Sample: DDHL1928 280.5 m. **C.** Photograph of laser mount DDHL1924 100.8. The pink box and arrow show the location and orientation of the image in Figure 4.50D. **D.** Reflected-light photomicrograph showing the location of spots (*pink circles*; to scale) analyzed by LA-ICP-MS. Note that Spot 5 is outside of the frame of the image. The molybdenite crystals are very fine-grained (<10 μm) and have tabular to platy crystal forms. Sample: DDHL1924 110.8 m. **E.** LA-ICP-MS images for Mo, S and Re. Sample: DDHL1928 280.5 m. **F.** Distribution of pixels (n = 308) representing molybdenite. Sample: DDHL1928 280.5 m. **G.** LA-ICP-MS spots imaged as lines for Mo, S and Re. Each line from top to bottom corresponds to a laser spot with an equivalent count (e.g., row one in the image corresponds to Spot 1 from Figure 4.50C). Columns from left to right represent the analyses that occurred at the same spot over time, as the laser beam ablated deeper into the sample. Sample: DDHL1924 110.8 m. **H.** Distribution of pixels (n = 6) representing molybdenite. All of the uncontaminated molybdenite pixels are from Spot 1. Sample: DDHL1924 110.8 m.

ed V, Fe, Se, Ag, Cd, Te, W, Re, Pb and Bi compared to the surrounding minerals (Appendix G).

*Sample DDHL1924 110.8 m:* The results reflect impure molybdenite analyses. Only Spot 1 intersected pure molybdenite (Fig. 4.50H). The molybdenite contains elevated V, Co, Ni, Se, Ag, Cd, Te, Re, Tl, Pb, and Bi compared to the surrounding minerals (Appendix G).

#### *4.5.4.2 Re–Os age determinations*

The results of the Re–Os age determinations are presented in Table 4.7. Molybdenite from the Stage 2D cataclasite sample from Kapit NE returned a Re–Os age of 481 ± 19 ka, with a Re content of 63 ppm (Table 4.7). The molybdenite in this sample is interpreted to have crystallized during the porphyry stage, and was then incorporated into the Stage 2D fault zone. This age is within analytical uncertainty of the minimum age of emplacement determined for xenolithic pyroxene-hornblende-phyric monzonite from northern Luise amphitheater (497 ± 9 ka; Chapter 3).

A Stage 1E anhydrite vein yielded an age of 345 ± 3 ka, with a Re content of 673 ppm (Table 4.7). Assuming molybdenite accounted for 25% of the material analyzed and that all Re was hosted in molybdenite, then the Re content of molybdenite would have been 4× higher (i.e., 2,691 ppm). This value is closer to the mean Re content in the molybdenite analyzed by LA-ICP-MS (2,291 ppm). The age for Stage 1E anhydrite veins is similar to the K–Ar ages previously attained for biotite phenocrysts from monzonite (342 ± 36 ka) and for biotite from a coarse-grained biotite – magnetite + anhydrite vein (336 ± 30 ka), both from Lienetz (Davies and Ballantyne, 1987; Rytuba et al., 1993).

The two Re–Os ages provide the absolute timing of porphyry-style mineralization in the Kapit NE area. They also provide a maximum age for sector collapse and epithermal mineralization at Lihir. The ages suggest that the giant and high-grade epithermal ore at the Lihir deposit has formed within the last 345,000 years.

## 4.6 Radiocarbon dating

### *4.6.1 Sample information*

A fragment of charcoal (carbonized wood) from a Stage 4A polymict matrix-rich breccia was selected for radiocarbon dating (DDHL2153 36.0 m; Fig. 4.33G). The charcoal was found within the near-surface portion of the Saddle breccia, west of Lienetz ore zone (AGD84 coordinates: 459399 mE, 9652994 mN; elevation: 31 m rsl) and contained late-stage carbonate veins (Fig. 4.33G).

### *4.6.2 Radiocarbon dating methods*

The charcoal sample was submitted to A. Hogg at the Waikato Radiocarbon Dating Laboratory (WRDL) at the University of Waikato, New Zealand. Prior to analysis, the sample was inspected under >10× magnification to isolate the most reliable fraction for dating. Contaminants such as carbonate vein material were removed where possible. The sample was milled (<2 mm fragments) and transferred to a beaker that was pre-baked at 500°C. A dilute acid/dilute alkali/dilute acid (AAA) treatment was undertaken to remove remaining traces of contaminants. The sample was washed in 1M hydrochloric acid (HCl) at 80°C, thoroughly rinsed, and then washed multiple times in 1M sodium hydroxide (NaOH) at 80°C. The NaOH insoluble fraction

**Table 4.7.** Re–Os data for molybdenite from Kapit NE ore zone

| Sample | Vein stage | Re ± 2σ (ppm) | $^{187}$Re ± 2σ (ppb) | $^{187}$Os ± 2σ (ppb) | Age ± 2σ (ka)* |
|---|---|---|---|---|---|
| DDHL1928 280.5m | Stage 1E | 672.7 ± 1.7 | 422.8 ± 1.1 | 2.428 ± 0.019 | 345 ± 3 |
| DDHL1924 110.8m | Stage 2D | 63.43 ± 0.16 | 39.87 ± 0.10 | 0.320 ± 0.012 | 481 ± 19 |

*The age uncertainty includes all known analytical uncertainty, including uncertainty in the decay constant of $^{187}$Re.

was again treated with 1M HCl at 80°C, filtered, rinsed with Milli-Q® water (pH>5), sonicated, and dried at 80°C. The supernatant was removed after each step by pipette.

The sample was converted to $CO_2$ by oxidation at 800°C overnight in the presence of pre-baked CuO wire and silver wire. The conversion took place within a glass vacuum line dedicated to the combustion of organic samples. Reduction of the $CO_2$ to graphite proceeded according to the method outlined in Santos et al. (2004). The reduction occurred within a reactor with a 550°C furnace and a three-way vacuum fitting attached to a 0–30 psi transducer, a 6 mm quartz tube containing pre-baked iron powder and a 6 mm quartz tube containing magnesium perchlorate ($Mg(ClO_4)_2$). This setup was designed to remove water from the reaction. The reaction was monitored in real-time using a customized LabView program to ensure quick determination of reaction completion and to reduce the possibility of fractionation due to methane production.

On completion, the cooled graphite was pressed to 350 psi using a NEC cathode press. The pressed graphite was stored in a wet cabinet with NaOH reservoir to reduce $CO_2$ concentration for no more than four weeks before being analyzed. Both primary and secondary standards were pretreated and graphitized at the same time as unknowns to prevent any storage offset (Beverly et al., 2010).

The sample was sent to the Keck-Carbon Cycle Accelerator Mass Spectrometer (AMS) facility at the University of California, USA. The pressed graphite was analyzed on a NEC 0.5MV 1.5SDH-1 AMS system coupled with an in-house modified ion source (Beverly et al., 2010). Six primary OxII standards were used to setup and tune the AMS system and normalize the $^{14}C/^{12}C$ ratios (Santos et al., 2007). For every 10–17 unknowns loaded into the AMS wheel (60 capacity), one blank and one in-house secondary standard were used for background correction and quality control, respectively. Data analysis was undertaken as per the method of Santos et al. (2007).

### *4.6.3 Results and interpretation*

Radiocarbon dating results are provided in Table 4.8. Errors are quoted at one standard deviation. The sample was too old for the age to be resolved using the radiocarbon dating technique. Therefore, the result provides a minimum age for the charcoal clast of 55 ka.

**Table 4.8.** Radiocarbon dating results for charcoal from Saddle Breccia, Lienetz.

| Sample ID | Vein stage | $D^{14}C$ (%) | $F^{14}C$ (%)[1] | Result[2] |
|---|---|---|---|---|
| DDHL2153 36 | Stage 4A | -999.7 ± 0.4% | 0.0 ± 0.0% | >55,000 yrs |

[1] $F^{14}C$ (%) is also known as percent modern carbon (pMC).
[2] Result is based on the Libby half-life of 5568 years with correction for isotopic fractionation applied, following Stuiver and Polach (1977).

The charcoal clast is interpreted to have been derived from a tree that was growing at surface at the time of the volcanic-hydrothermal eruption that formed the Saddle diatreme. The eruption is interpreted to have carbonized wood from the tree and drawn this and other surface materials downwards during subsequent collapse. The age of the charcoal fragment would therefore be a maximum age for the diatreme into which it was incorporated. However, the radiocarbon dating results only constrain the minimum age for the charcoal. This implies that the Saddle breccia at the western margin of Lienetz ore zone is constrained to >55 ka.

## 4.7 Evolution of the Lihir hydrothermal system

### *4.7.1 Porphyry stage*

Pervasive phlogopite – orthoclase – anhydrite ± magnetite (Stage A1) and chlorite ± calcite ± hematite (Stage A2) alteration zones are present at >150 m depth in Kapit NE and Coastal (Fig. 4.1). These alteration assemblages contain high- to moderate-temperature minerals that commonly occur in the potassic and peripheral propylitic alteration zones of porphyry ore deposits (Sillitoe, 2010; Table 4.9). There is an apparent concentric zonation of alteration assemblages surrounding crystal-poor trachyte dikes (KNE7)

in western Kapit NE. Within and surrounding the dikes, Stage A1 phlogopite alteration is dominant; this transitions to Mg-rich chlorite at medial distances and then to Fe-rich chlorite further away (Fig. 4.1; Appendix E). At Batu Hijau, Mg in chlorite has been shown to decrease exponentially in concentration with increasing distance from a porphyry center (Wilkinson et al., 2015). This suggests that the trachyte dikes may have been or are close to the source for the heat and fluids that produced the pervasive porphyry-style alteration in Kapit NE.

A variety of Stage 1 veins are concentrated around the crystal-poor trachyte dikes (KNE7) in western Kapit NE, including: albite ± actinolite veinlets (Stage 1A), anhydrite – magnetite ± chalcopyrite ± chlorite veins and amygdules (Stage 1B), anhydrite – pyrite veins (Stage 1E), tabular anhydrite and carbonate veins (Stage 1G) and the anhydrite vein-clast breccia (Stage 1H). These are interpreted to have formed under porphyry-style conditions. Evidence supporting this interpretation includes: (1) their occurrence within rocks that have been pervasively altered to a potassic mineral assemblage (Stage A1 phlogopite; Fig. 4.9); (2) vein infill, breccia cement and associated alteration (i.e., vein halo alteration and selective alteration of lithic matrix and clast material) composed of minerals stable under high-temperature conditions (e.g., anhydrite, biotite, phlogopite, orthoclase, actinolite, chalcopyrite, magnetite and molybdenite; Figs. 4.10–11, 4.14 and 4.16–17), and (4) local association with porphyritic dikes (KNE7). Anhydrite – calcite – chlorite veins and breccias (Stage 1F) mainly occur within the chlorite alteration domain (Stage A2) and are interpreted as a distal expression of the anhydrite – pyrite veins (Stage 1E).

The Stage 1H anhydrite vein-clast breccia is interpreted to be a pebble dike, which is a type of porphyry-related magmatic-hydrothermal breccia (Table 4.3; Sillitoe, 1985). The pebble dike most likely formed by the rapid thermal expansion and upwards injection of magmatic ± meteoric fluids within the wall rocks adjacent to a late porphyry-stage dike (Table 4.3; Sillitoe, 1985). This interpretation is supported by the sharp contacts and small size of the breccia body (<1 m across), subrounded and moderately well-sorted clasts, presence of clastic matrix, and the high-temperature mineralogy of the cement and associated alteration of clastic components (e.g., biotite, actinolite, muscovite, chalcopyrite, etc.). Unfortunately, it is not clear whether the breccia has a dike-like geometry, because it was only observed in one drill core interval. The interpretation that the Stage 1H breccia is a pebble dike implies proximity to a hydrous intrusive complex in western Kapit NE. It is possible that the nearby crystal-poor trachyte dikes (KNE7) with their abundant, ovoid to amoeboid anhydrite – K-feldspar – magnetite amygdules (miarolitic cavities?), were the source of fluids for the formation of the Stage 1H anhydrite vein-clast breccia. Similar breccias crop out as rare, narrow (3–5 m-wide), northeast-striking pebble dikes in Minifie (biotite – K-feldspar – anhydrite – calcite-cemented breccia; M5a; Blackwell et al., 2014) and as narrow (~2–6 m-wide), east-northeast-striking, steeply dipping pebble breccia dikes in Lienetz ($Bx2_{pebble}$; Sykora, 2017; Sykora et al., 2018a).

Stage 1C breccias are interpreted to have formed as part of one or more porphyry-related magmatic-hydrothermal breccia complex(es). Fragmentation probably occurred at moderate depths (~1–3 km) by fluids exsolved from a crystallizing magmatic intrusion (Table 4.3; Sillitoe, 1985). It is uncertain whether the Stage 1C breccias are separate bodies that have formed at different times, or whether they are part of a large complex that connects at depth. The morphology of Stage 1C breccias may have been modified by faulting and its contacts have been obscured by faults. Evidence for a porphyry-related magmatic-hydrothermal origin for Stage 1C breccias includes: (1) occurrence as large (>100 m-diameter), discordant, irregular or upward tapering breccia bodies; (2) spatial association with the Coastal intrusive complex (Fig. 4.9); (3) subangular to rounded, polymict clast population with abundant igneous clasts; (4) variations from cement- to matrix-supported organi-

**Table 4.9.** Temperature stability of hydrothermal minerals and mineral assemblages that occur in Kapit NE and Coastal.

| Mineral | Range of thermal stability (°C) | Reference |
|---|---|---|
| Actinolite | >280 | Reyes (1990)[1] |
| Adularia | 190 to 300 | Reyes (1990)[1] |
| Adularia – quartz | >230 | Browne (1978)[2] |
| Albite | Stable* | Schardt et al. (2001)[3] |
| Alunite | 40 to 320 | Masterman (2003)[4] |
| Amorphous silica | <100 | Corbett and Leach (1998)[4] |
| Anhydrite | >180 | Reyes (1990)[1] |
| Biotite | >280 | Reyes (1990)[1] |
| Chalcedony | <100 | Heaney (1993)[4] |
| Chalcopyrite | <300 to 500 | Simon et al. (2000)[5] |
| Chlorite* | >140 | White and Hedenquist (1995)[4] |
| Dickite | 120 to 280 | Reyes (1990)[1] |
| Dolomite | <180 | Reyes (1990)[1] |
| Epidote^ | >200 | Reyes (1990)[1] |
| Hematite | <300 to >750 | Simon et al. (2000)[5] |
| Hematite – magnetite – pyrite | 475 | Simon et al. (2000)[5] |
| Illite | 220 to 310 | Reyes (1990)[1] |
| Illite-smectite | 140 to 220 | Henley and Ellis (1983)[6] |
| Jarosite | <120 | White and Hedenquist (1995)[4] |
| Kaolinite | <200 | Reyes (1990)[1] |
| K-feldspar | >160 | Henley and Ellis (1983)[6] |
| Magnetite | >440 | Simon et al. (2000)[5] |
| Marcasite | <240 | Murrowchick and Barnes (1986)[4] |
| Muscovite | 200 to 360 | Masterman (2003)[4] |
| Native sulfur | <300 | White and Hedenquist (1995)[4] |
| Opal | <110 | Reyes (1990)[1] |
| Phlogopite | 200 to 410 | Jensen (2003); Carman (2003)[7] |
| Pyrite | Stable* | White and Hedenquist (1995)[4] |
| Pyrite – quartz | >230 | Browne (1978)[2] |
| Pyrophyllite | 160 to 360 | Reyes (1990)[1] |
| Pyrrhotite | <300 to >750 | Simon et al. (2000)[5] |
| Quartz | Stable* | Griffen (1992)[8] |
| Realgar – orpiment | 50 to 75 | Migdisov and Bychkov (1998)[9] |
| Rutile | >180 | Reyes (1990)[1] |
| Smectite | 20 to 200 | Reyes (1990)[1] |
| Sphalerite – galena | 150 to 350 | Bortnikov (1995)[10] |
| Stilbite | 100 to 110 | Henley and Ellis (1983)[6] |
| Titanite | >200 | Reyes (1990)[1] |
| Tourmaline | Stable* | van Hinsberg et al. (2011)[4] |

[1]Based on empirical evidence from Philippine geothermal systems.
[2]Based on empirical evidence from Otake geothermal area, Japan.
[3]Based on the results of numerical modeling.
[4]Based on review of previous studies.
[5]Based on temperature-$fO_2$(g) diagram for the Fe-Cu-S-O system under feldspar-stable conditions. P = 1.5 kbar (<~6 km depth), pH = 7, log Cl = 2, log $a_{\Sigma S_{(aq)}} = -1$.
[6]Based on empirical evidence from various geothermal systems (e.g., Salton Sea, Cerro Prieto, etc.).
[7]Based on sulfur isotope thermometry from base metal and sulfate assemblages in phlogopite-bearing polymetallic veins from Cripple Creek (Cresson Pit: 223°C, 277°C; Ajax Mine: 317°C–407°C) and fluid inclusion homogenization temperatures (200°C–300°C) for phlogopite-bearing Stage II anhydrite – adularia veins at depth (>200 m below sea level) from Lihir. Phlogopite stability at lower temperatures may be related to higher fluorine content (Carman, 2003). Hydrothermal phlogopite at Cripple Creek contains up to 4.5 wt% fluorine (Jensen, 2003) and hydrothermal phlogopite at Lihir contains up to ~1.7 wt% fluorine (Carman, 1994).
[8]Based on stability fields of α- and β-quartz in P-T space.
[9]Based on empirical evidence from an active geothermal system at Uzon caldera, Russia, which is currently precipitating Hg-Sb-As mineralization.
[10]Based on a compilation of fluid inclusion homogenization temperatures for veins containing coexisting sphalerite and galena from 30 ore deposits (skarn Pb-Zn deposits, vein Sn and Sn-Pb-Zn deposits, epithermal Au and Pb-Zn-Ag deposits, Mississippi Valley-type deposits, strata-bound carbonate-hosted deposits, vein Pb-Zn deposits and carbonate-hosted replacement Pb-Zn deposits).
*Chlorite may occur as interlayered chlorite-smectite at ~140°C–220°C (White and Hedenquist, 1995).
^Crystalline epidote, as it typically exists in hydrothermal veins and alteration, occurs at temperatures >280°C (Reyes, 1990).
*Stable over the entire range of temperatures relevant to the precipitation of minerals in porphyry-epithermal systems (e.g., <100°C to >500°C).

zation; (5) cement containing abundant hydrothermal anhydrite (typical in place of quartz in alkalic-type porphyry systems) as well as K-feldspar and chlorite; (6) cement that locally displays open space filling textures (e.g., void spaces, zoning); (7) alteration of clast margins and matrix to anhydrite, K-feldspar, calcite, vermiculite (after biotite or phlogopite) and actinolite, and (8) the presence of juvenile diorite clasts and/or cement (Fig. 4.12B and D; Table 4.3). There is a biotite – anhydrite vein (Stage 1D) within a hornblende-bearing gabbro dike (KNE6) that has sharply crosscut the Stage 1C breccia in Coastal. This suggests that there were multiple pulses of magmatism and associated hydrothermal activity in the Coastal area.

The final stage of hydrothermal activity associated with porphyry-style conditions was Stage 1I, which produced massive and banded anhydrite ± pyrite breccias and veins (Stage 1I). The veins are most abundant within the Coast-

al area, nearest to Lienetz, and in a broad area in western Kapit NE (Fig. 4.9). Key features associated with Stage 1I veins and breccias include recrystallization textures, dissolution seams and stylolites, partly dissolved wall-rock and anhydrite vein-clasts, and both vein halo alteration assemblages (K-feldspar, biotite and phlogopite) and vein infill/breccia cement assemblages (e.g., anhydrite, phlogopite, chalcopyrite, etc.) indicative of formation under high-temperature conditions (Fig. 4.18). These features suggest that the veins formed in two stages: (1) by precipitation of mineral infill from hydrothermal fluids under porphyry-style conditions, and (2) by partial dissolution and recrystallization of those minerals under applied differential and shear stress (e.g., Sykora et al., 2018a). Stage 1I veins are similar to, though much less voluminous than, Stage $V1_{M1}$ veins and breccia veins in Lienetz (Fig. 4.18), which were interpreted to have formed by the modification of earlier-formed anhydrite – biotite veins ($V1_{biotite}$) and anhydrite – K-feldspar veins ($V1_{K\text{-}feldspar}$; Sykora et al., 2018a). Stage $V1_{M1}$ veins and breccia veins were shown to have localized shear strain and may have facilitated the sector collapse that resulted in the transition to epithermal-style conditions (Sykora, 2017; Sykora et al., 2018a).

Early porphyry-style veins and breccias locally contain mineralization, characterized by minor vein and disseminated chalcopyrite, pyrite and molybdenite (e.g., Figs. 4.11E and 4.14G). However, the low gold grades (<1 ppm) and variable, but typically low, copper grades (<0.3 wt% Cu) suggest that: (1) the porphyry system was incipient and did not produce significant mineralization prior to the change to epithermal-style conditions; (2) the porphyry system was not very productive, or (3) there is a high-grade porphyry center at Lihir that has yet to be identified.

### *4.7.2 Early epithermal stage*

Stage A3–A5 alteration and Stage 2–3 breccias and veins are interpreted to have formed under low-sulfidation epithermal conditions (i.e., by precipitation from near-neutral pH hydrothermal fluids at depths <1.5 km and temperatures <300°C; Buchanan, 1981; White and Hedenquist, 1995; Simmons et al., 2005; Table 4.9). Evidence for this includes: (1) the presence of adularia and/or illite as components of pervasive and vein halo alteration assemblages (Table 4.9); (2) low-temperature vein infill and breccia cement assemblages typical of low-sulfidation deposits (e.g., major minerals: adularia, pyrite, marcasite, quartz, chalcedony, anhydrite, illite and calcite; minor minerals: tetrahedrite-tennantite, barite, arsenopyrite, base metal sulfides, tellurides and native gold; Table 4.9); (3) the presence of void spaces such as vugs and open fractures; (4) open space-filling textures such as crustiform-colloform banding, druse-lined cavities and cockade texture; (5) bladed mineral habit of anhydrite and calcite (Stage 3A; e.g., Simmons and Christenson, 1994; Simmons and Browne, 2000); (6) evidence for multiple episodes of vein formation and/or brecciation; and (7) associated Au ± Ag ± Te mineralization. These epithermal features have overprinted porphyry-style veins and altered rocks at intermediate depths in Kapit NE and Coastal (i.e., ~100–250 m depth; Figs. 4.4F, 4.5D and 4.19). This relationship has been documented in all other mineralized zones at Lihir and is interpreted to reflect the catastrophic mass wasting of at least 1 km of volcano-sedimentary rocks overlying the locus of hydrothermal activity (e.g., via sector collapse of the Luise volcano; Sillitoe, 1994; Carman, 1994; Blackwell, 2010; Ageneau, 2012; Sykora, 2017; Sykora et al., 2018a). There is substantial evidence that one or more sector collapse events occurred, including the geomorphology of Luise volcanic edifice (Blackwell, 2010) and the presence of a submarine debris avalanche deposit that extends up to 10 km away from the Luise Harbor (Herzig et al., 1998; Fig. 3.2). Dissolution and shear deformation of low angle to subhorizontal $V1_{M1}$ veins in Lienetz (and equivalent Stage 1I veins in Kapit NE and Coastal) may have weakened the volcanic edifice, making it susceptible to collapse (Sykora et al., 2018a).

Stage A3 vuggy adularia alteration was the first epithermal-stage event. It is characterized by the presence

of open to partly infilled fractures and by abundant, amoeboid and crystal-shaped vugs, which give the altered rocks their porous, spongy texture (Fig. 4.4). It is interpreted that these features have formed by the dissolution and/or corrosion of unstable primary mafic minerals and volcanic glass (e.g., Pettijohn, 1975; Gifkins et al., 2005), and anhydrite veins and previously anhydrite-altered minerals (e.g., Sykora et al., 2018a). Stage A3 is interpreted to have occurred during or shortly after the sector collapse event(s), due to an incursion of cold groundwater and/or seawater into the recently depressurized and fractured rocks. These fluids typically have low salinities and temperatures (e.g., modern seawater contains an average ~3.5 wt% total dissolved salts and sea surface temperatures are <35°C) and near-neutral to slightly alkaline pH (seawater pH ranged 7.5 to 9 in the Phanerozoic; Halevy and Bachan, 2017) and may have been able to dissolve anhydrite due to its retrograde solubility at <350°C (Blount and Dickson, 1969). The base of the vuggy adularia alteration zone is interpreted to represent the level below which conditions did not favor dissolution of anhydrite. High water-rock ratios (continually diluting calcium sulfate from solution despite its addition via dissolution of anhydrite), high fluid flow velocities, and/or the presence of sulfur-reducing bacteria would have substantially increased the dissolution rate for anhydrite (James and Lupton, 1978; Klimchouk, 1996). Based on the presence of pervasive adularia alteration of the remaining components, the fluids associated with Stage A3 alteration were in the temperature range of ~180°C–300°C (Reyes, 1990), which is higher than the temperature at which gypsum is stable in the near-surface environment (<40°C; Yamamoto and Kennedy, 1969). This would require heating of the downgoing groundwater or seawater from surface temperatures through water-rock interaction or mixing with rising, higher-temperature hydrothermal fluids. It is interpreted that dissolution of anhydrite would have been most intense prior to the establishment of the epithermal ore-forming hydrothermal system. Stage A3 vuggy adularia alteration also occurs in Minifie ore zone (Fig. 4.51), where it has previously been described as 'pinhole texture' (Corbett et al., 2001). In Minifie, this style of alteration is best developed within and around hydrothermal breccia zones (Carman, 2003).

Stage A3 alteration may have provided much of the porosity and permeability required for later hydrothermal fluid flow and ore deposition. Domains of vuggy adularia alteration have locally been overprinted by Stage A4 (adularia – pyrite) and A5 (quartz – illite – pyrite) alteration, and void spaces such as open fractures have been infilled by Stage 2–3 veins and breccias. Similar relationships have been documented in Lienetz, where epithermal-stage veins and breccias ($V3_{adu}$, $V4_{qtz}$ and $Bx3_{py\text{-}adu}$) infill cavities in the upper parts of partially dissolved porphyry-stage breccias (e.g., $Bx1_{biotite\text{-}anhydrite}$; Sykora, 2017; Sykora et al., 2018a). The highest gold grades in Kapit NE and Coastal areas occur in vuggy rocks that have been overprinted by dark gray pyrite-rich Stage A4 alteration, typically in association with Stage 3 veins. In general, Stage 2–3 veins and breccias and deposit-scale gold grade shells are distributed within areas of Stage A3–A5 alteration in Kapit NE and Coastal (Fig. 4.19). This spatial relationship suggests that the majority of gold mineralization was associated with the early epithermal stage.

Stage A5 alteration has a patchy distribution that is partly controlled by the location of Stage 3 veins and breccias. Stage A5 alteration domains may represent coalesced regions of intense vein-halo and structurally controlled alteration associated with Stage 3. Within the Stage A5 alteration domain, pyroxene-phyric basalts (KNE2b) display pseudogusano texture, defined by white, ovoid or amoeboid illite – quartz – pyrite alteration patches connected by quartz veins (Fig. 4.6B). The alteration patches do not coincide with the distribution of clasts and commonly crosscut clast margins. Stage A5 alteration is not considered to be true gusano texture, which forms via the interaction of high temperature, acid, halogen-bearing fluids with volcanic rocks, and produces minerals stable under acidic conditions (e.g., pyrophyllite, diaspore, alunite, APS, muscovite,

pyrite, and bornite; Jimenez Torres, 2017). It is interpreted that pseudogusano texture at Lihir formed during intermittent pulses of low temperature, slightly acidic fluids (i.e., pH 5–6) during a period otherwise dominated by low-temperature near-neutral hydrothermal activity (i.e., Stage A4, adularia-stable conditions; pH > 6; e.g., Corbett and Leach, 1998). Pyroxene-phenocrysts within the clasts and matrix of the basalt appear to have been precursor features to the alteration patches. The fluids responsible for alteration are inferred to have migrated through the rock along a network of very thin and hairline fractures, which are now represented by quartz veins.

Stage 2 resulted in the generation of a variety of pyrite-rich epithermal veins and breccias that contain metallic minerals diagnostic of low to intermediate sulfidation state (e.g., tennantite-tetrahedrite, pyrite, chalcopyrite; Giggenbach, 1997; Einaudi et al., 2003) and vein-halo alteration assemblages stable at neutral to alkaline pH conditions (e.g., adularia, quartz, illite, pyrite and calcite; Simmons et al., 2005). The veins and breccias are widespread in Kapit NE and Coastal and are particularly abundant at intermediate depths (100–200 m bsl) within domains of Stage A3–A4 alteration. Stage 2A was the first epithermal stage to produce gold-bearing veins and breccias. The vein infill and cement are composed predominantly of interlayered, colloform-banded pyrite, arsenian-pyrite and marcasite (Fig. 4.20C, E, H and I). This signifies periodic changes in fluid composition and/or fluctuating ambient conditions that would favor transient precipitation of marcasite (i.e., pH <5 and temperature <240°C; Hannington and Scott, 1985; Murrowchick and Barnes, 1986; Schoonen and Barnes, 1991a, 1991b; Benning et al., 2000). Gold is typically refractory, occurring within the crystal structure of arsenian pyrite and marcasite, as is the case for correlated vein stages in other ore zones at Lihir (e.g., Stage 3A pyrite-cemented breccia, Kapit, Ageneau et al., 2011; $V3_{adu}$, Lienetz, Sykora et al., 2018b). The colloform habit of the Fe-sulfide minerals reflects rapid crystallization at low-temperatures (i.e., disequilibrium conditions; Xu and Scott, 2005), conditions which promote the development of surface defects and adsorption of Au onto growing crystal surfaces (Zhu et al., 2011).

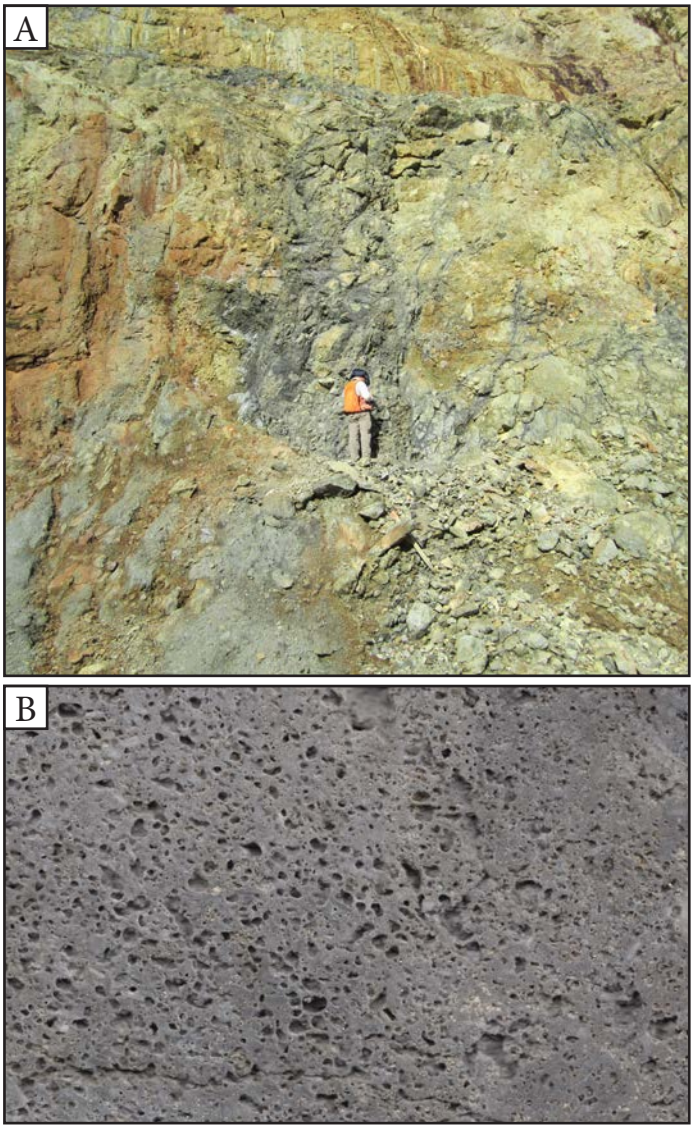


**Fig. 4.51.** Stage A3 vuggy adularia alteration in Minifie open pit (2012). **A.** Photograph of the northwest pit wall in Minifie, showing a large domain of gray, vuggy adularia alteration. **B.** Photograph of a polished hand sample collected from the outcrop shown in Fig. 4.51A, highlighting the presence of abundant vugs and residual adularia – pyrite altered groundmass and feldspar phenocrysts. Sample: LI12EL005 (Mine grid coordinates: 9914 mE, 3835 mE, 133 m bsl).

Both the quartz – pyrite-cemented breccia (Stage 2B) and zoned, quartz – pyrite – anhydrite – calcite-cemented to matrix-rich breccia (Stage 2C) are interpreted as phreatic breccias that formed under epithermal conditions. Evidence for this includes: (1) the small size of the breccia bodies (e.g., <500 m diameter); (2) the downward-taper-

ing (Stage 2B) or tabular (Stage 2C) morphologies of the breccia bodies; (3) the location of the breccias within a discharge zone of the present-day hydrothermal system; (3) the presence of variably abundant matrix and hydrothermal cement components; (4) subangular to subrounded clasts and matrix that are reflective of the underlying source region (Stage 2B: polymict lithic clasts dominated by igneous rock clasts from the Coastal intrusive complex; Stage 2C: monomict, consisting of pyroxene-phyric basalt breccia clasts); (5) the absence of juvenile clasts; (6) clasts and matrix that have been altered to low-temperature alteration assemblages (e.g., Stage 2B: quartz, adularia, rutile, illite and pyrite; Stage 2C: anhydrite, adularia, calcite, and pyrite; Fig. 4.9); (7) cement that is composed of minerals that have precipitated from hydrothermal fluids at low temperatures (Stage 2B: quartz, pyrite and adularia; Stage 2C: pyrite, anhydrite, quartz, calcite; Table 4.9); and (8) open space filling textures in Stage 2C cement (zoned cement with colloform-textured pyrite and crustiform-textured quartz). There is no evidence that either breccia erupted at surface (e.g., associated tephra apron, inclusion of silica sinter or travertine fragments, etc.; Table 4.3). The observation that the quartz – pyrite-cemented breccia pipe (Stage 2B) contains mineralized colloform pyrite vein clasts (Stage 2A) and has also been crosscut by colloform pyrite veins (Stage 2A) implies that Stage 2B occurred synchronously with mineralization and that the breccia exploited the same structures that were active during gold mineralization. It is possible that brecciation occurred due to the explosive release of overpressurized steam from within a vein sealed by Stage 2A pyrite – marcasite infill. Phreatic breccias commonly occur in other active geothermal districts (e.g., Taupo Volcanic Zone, New Zealand; Hedenquist and Henley, 1985) and in association with low-sulfidation epithermal deposits (e.g., Favona epithermal gold deposit, New Zealand; Torckler et al., 2006).

Stage 2D pyritic fault zones are interpreted to have been formed by hybrid tectonic-hydrothermal processes due to: (1) their discordant, tabular geometry; (2) the presence of shear textures (e.g., foliated matrix and cement), disaggregated and rotated clasts, and clay gouge; (3) hydrothermal alteration of clasts and surrounding host rocks to an assemblage of pyrite – adularia + illite – chlorite; (4) presence of hydrothermal cement composed of pyrite – marcasite – adularia ± quartz ± chalcopyrite ± arsenopyrite ± anhydrite; and (5) the lack of juvenile clasts. These steeply-dipping, high-permeability structures would have provided optimal pathways along which hydrothermal fluids could rise. It is likely that there were several phases of faulting over a protracted period, only some of which were synchronous with gold mineralization (i.e., contain refractory gold in pyrite as a component of the cement and alteration assemblage). Some of the Stage 2D faults have exploited the same structures as Stage 1–2C veins and/or breccias and have incorporated these materials as clast and matrix components, resulting in gold-rich domains within otherwise barren fault zones.

Stage 3 generated a variety of gold-bearing, quartz-rich epithermal veins and breccias in Kapit NE and Coastal, many of which have also re-opened structures occupied by Stage 1–2 infill (e.g., Figs. 4.16D, 4.18G, 4.24A and 4.27K). As in Stage 2, the majority of gold occurs within Fe-sulfides; however, small quantities of native metals (gold, silver and tellurium), electrum and precious metal tellurides were produced during Stages 3A and 3B (e.g., Figs. 4.24H and 4.26B). These native metals locally occur together with other ore and gangue minerals typically associated with alkalic-type epithermal gold deposits such as roscoelite, barite, adularia, carbonates, celestine, lead tellurides, base metal sulfides, sulfosalts, and rutile (e.g., Richards, 1995; Figs. 4.24–4.25). They occur in association with features that indicate boiling conditions during deposition, such as bladed anhydrite and calcite, adularia vein-halo alteration, and crustiform-colloform banding (Fig. 4.24A, G and L; e.g., Simmons and Christenson, 1994; Simmons et al., 2000). Correlated veins in Lienetz ore zone ($V1_{M2}$) were interpreted to have formed by modification of porphyry-stage anhydrite veins under epithermal conditions (Sykora, 2017,

2018a). At Kapit NE and Coastal, the majority of vein infill is interpreted to have formed by precipitation from hydrothermal fluids rather than by dissolution and re-precipitation, since many Stage 3 veins occur in areas that lack Stage 1 anhydrite veins (cf. Figs. 4.9 and 4.19), and because many Stage 3 veins do not contain anhydrite.

Stage 2A and Stage 3 breccias are interpreted to have formed by sub-surface hydraulic fragmentation. Evidence for this includes their: (1) discordant, tabular geometry, (2) abundant hydrothermal cement, locally with open-space filling textures (e.g., cockade texture, open cavities; Fig. 4.20A and F), (3) typically massive, poorly sorted and jigsaw-fit to clast-rotated organization (e.g., Fig. 4.27H), and (4) association with veins (Table 4.3; e.g., Jébrak, 1997). Polymict, Stage 2A and Stage 3 breccias with chaotic organization and breccia-in-breccia clasts (e.g., Fig. 4.27D) may have been generated over multiple episodes of higher energy fragmentation. Formation of these breccias likely involved some degree of clast transport. In contrast, Stage 2A and Stage 3 breccias dominated by cockade, crustiform and colloform banded cement, indicate formation via sustained hydrothermal fluid flow and pulsing of hydrothermal fluids within open structures.

### *4.7.3 Volcanic-hydrothermal stage*

Stage 4 breccias are interpreted to have formed in a near-surface, subaerial environment under epithermal conditions. Evidence for this interpretation includes: (1) a syn-brecciation alteration assemblage composed of quartz, illite and pyrite (stable at ~220°C–310°C; Figs. 4.34C and 4.35E–F; Reyes, 1990); and (2) clasts of charcoalized terrestrial plant material (Fig. 4.33G). The following section discusses the genesis of the Lihir diatreme breccia complex and the various facies of which it is composed.

#### *4.7.3.1 Volcanic-hydrothermal breccia interpretations*

Stage 4 breccias are interpreted to have formed as a direct result or in association with phreatomagmatic eruptions. The recognition of juvenile components (juvenile clasts ± tuffaceous matrix) within Stage 4 breccias has been important in making this interpretation. The following characteristics were used to identify juvenile clasts in Stage 4 breccias at Lihir:

- Distinctive, amoeboid, fluidal (also referred to as wispy) or blocky clast morphologies;
- Ragged, delicate or cuspate, chilled margins (with aligned phenocrysts and fining of groundmass grain size towards the clast margins);
- Syn-depositional coatings of secondary minerals (e.g., pyrite rinds) and/or matrix material (armored clasts; Cioni et al., 1992);
- Low vesicularity, feldspar-phyric texture and andesitic composition (KNE10);
- A lack of pre-brecciation hydrothermal features; and
- A spatial association with andesite dikes (KNE10).

The following section outlines the key components, textures and spatial associations used to interpret the origins of the individual facies of Stage 4. A summary of these interpretations is provided in Table 4.6.

*Phreatomagmatic eruption breccias (Stage 4A–4C)*

Stage 4A, 4B and 4C breccia facies make up the bulk of the infill within the Lihir diatreme breccia complex. Stage 4B breccias are particularly abundant in Diwai breccia (Figs. 4.31 and 4.32). These breccias contain similar components (Table 4.6) and are differentiated primarily based on the relative proportions of these components. All of these facies contain abundant rock flour matrix (up to 85% matrix) and a high abundance and diversity of wall rock

fragments, indicating that they formed as a result of highly explosive volcanic activity. This evidence, in combination with their typically steeply dipping discordant geometries and the recognition of juvenile feldspar-phyric andesite clasts, suggests that the breccias have formed primarily by subsurface phreatomagmatic brecciation (Fig. 4.52). Clasts of Stage 4A breccia within Stage 4B breccia and crosscutting relationships between these breccias (Figs. 4.32 and Fig. 4.52) indicate that formation of the breccia bodies occurred over numerous episodes.

Stage 4A–4C breccias contain both intact and broken, matrix-supported accretionary lapilli that are not associated with stratified pyroclastic deposits. Accretionary lapilli form when volcanic ash particles are bound together by electrostatic attraction and the capillary forces of liquid bridges from condensed moisture, forming increasingly larger and concentrically laminated ash balls (Schumacher and Schmincke, 1995). Their presence provides evidence for wet, gas-rich transport (Crowe and Fisher, 1973; Lorenz, 1974, Lorenz, 1985; Wohletz, 1998; Németh et al., 2001). These conditions may be met in a diverse range of volcanic environments (e.g., Moore and Peck, 1962; Self and Sparks, 1978), but they are especially common in phreatomagmatic tephra deposits (Schumacher and Schmincke, 1991). There are several possible origins for the accretionary lapilli in Stage 4A–4C:

1. They may have formed during fallout from an eruption column or within turbulent pyroclastic flows or surge deposits associated with phreatomagmatic eruption (e.g., Lorenz, 1974; Schumacher and Schmincke, 1995; Brown et al., 2010). In this case, the accretionary lapilli would have been drawn down and incorporated into the breccia. This would provide evidence for Stage 4A–4C breccias having vented to the paleosurface. The presence of charcoal and blocks of base surge deposits also suggests that there was a connection to a subaerial surface during brecciation (e.g., Sillitoe, 1985). Therefore, this is the preferred interpretation for the origin of the accretionary lapilli.

2. They may have formed within fluidized, vapor-rich channels in the subvolcanic environment during phreatomagmatic eruption (e.g., Oreskes and Einaudi, 1990; Carman, 1994).

3. They may have been derived from unconsolidated pyroclastic host rocks associated with a previous volcanic eruption.

Domains within Stage 4B breccias contain dominantly subrounded to rounded clasts and rare clasts of Stage 4A breccia ('breccia-in-breccia' clasts; Figs. 4.32 and 4.33E). These breccias likely underwent significant clast transport and abrasion (Roache et al., 2000) due to clast recycling over multiple episodes of phreatomagmatic and/or phreatic brecciation and collapse (Houghton and Smith, 1993). Breccia-in-breccia clasts are rare because lithification does not typically occur between cycles of phreatomagmatic brecciation. Near surface, Stage 4B breccias display weak normal grading over tens of meters. The coarser-grained base of the breccia contains minor open space and draped laminated matrix (Fig. 4.32). These features are interpreted to have formed via gravitational collapse and later settling of fine-grained matrix material between clasts. The slightly greater permeability of these breccias locally allowed for post-brecciation fluid flow and deposition of Stage 5C veins and breccias.

Stage 4C breccias contain a higher proportion of juvenile clasts than Stage 4A and 4B (e.g., up to 90%) and contain a high proportion of fine-grained rock flour matrix (50–85%; Table 4.6). They are commonly contiguous with andesite dikes and andesite-clast breccias (KNE10 and Stage 4D; Fig. 4.51). Since the preservation potential for juvenile clasts is low (irregular morphologies and delicate clast margins are easily modified during transport and abrasion), this suggests that Stage 4C breccias experienced little or no reworking during later phreatomagmatic or phreatic

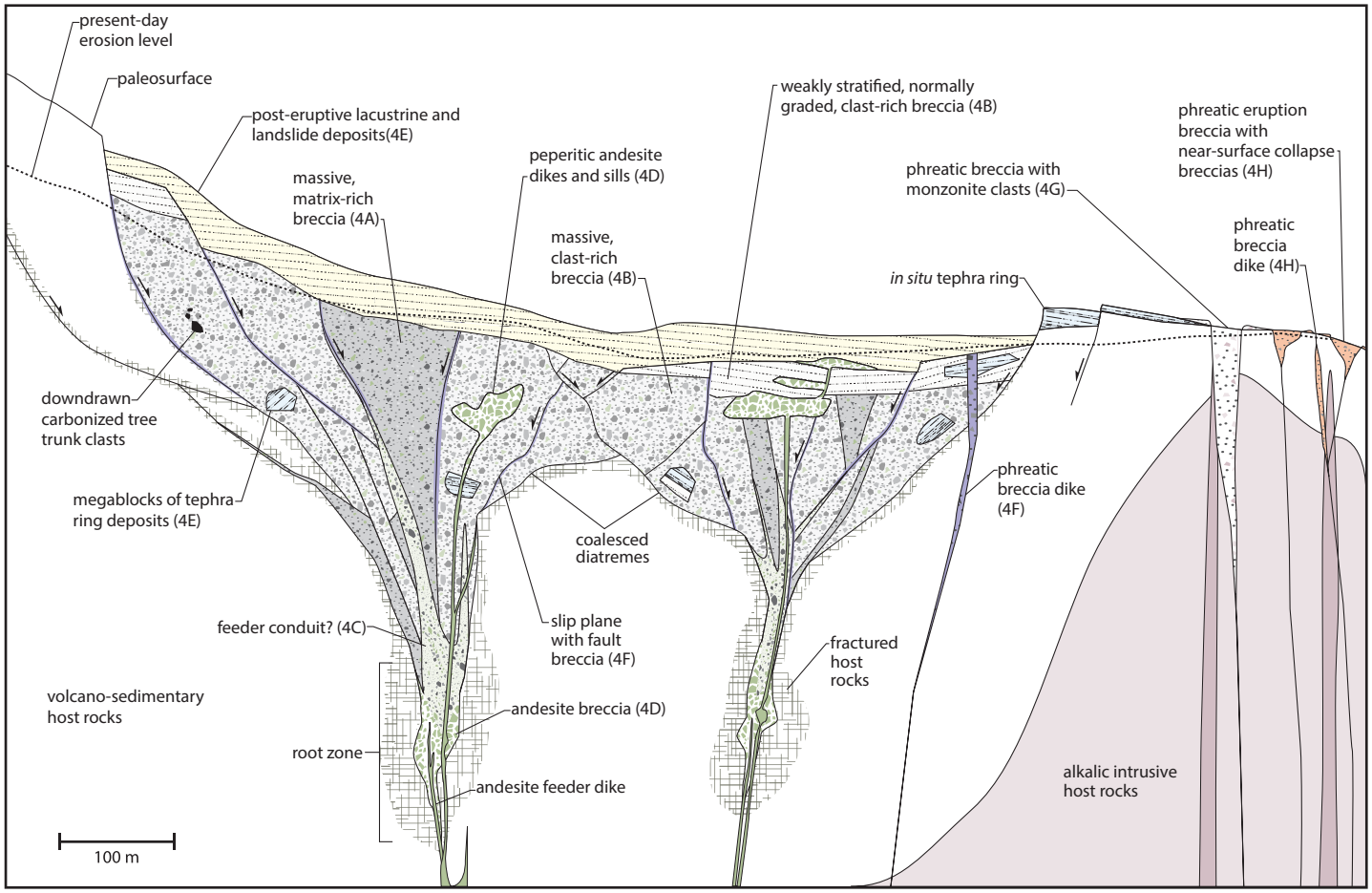


**Fig. 4.52.** Schematic diagram of an idealized north-northwest-facing cross section through the Lihir diatreme breccia complex.

episodes. It also indicates close proximity to the source of a juvenile material and a relatively late timing of emplacement relative to the timeline of diatreme formation. Steeply dipping Stage 4C breccias that originate in the root zone may represent feeder conduits—channels that would have transported clouds of vapor-rich tephra to the upper portions of the diatreme (Fig 4.52; e.g., Lorenz, 2003).

*Feeder dikes and contact breccias (KNE10/ Stage 4D)*

Intervals of coherent feldspar-phyric andesite (KNE10), interpreted as dikes, have been identified in the deepest parts of the modeled diatremes. Here, the andesite intrusions have gradational contacts to jigsaw-fit and clast-rotated andesite-clast breccias (Stage 4D), which in turn have a gradational contacts with juvenile clast-rich phreatomagmatic breccias (Stage 4C; Fig. 4.35E). This facies association is interpreted to represent the preserved root zones of the diatreme breccias. The andesite dikes are interpreted as feeder dikes (Fig. 4.52; e.g., Lorenz and Kurszlavkis, 2007), which would initially have instigated phreatomagmatic brecciation and later provided magmatic input during the phreatomagmatic episodes. This facies association has been identified only rarely, and this may relate to destruction of the root zone during later explosive activity (e.g., Davies et al., 2008b).

The andesite-clast breccias in the root zone (Stage 4D) contain abundant jigsaw-fit, blocky juvenile andesite clasts. These are interpreted as 'contact breccias', i.e., breccias produced by explosive disaggregation at the site of contact between the intruding andesitic magma and circulating hydrothermal fluids (Fig. 4.52). Swirly and draped laminated matrix textures between large andesite clasts are inter-

preted to have been formed during late-stage settling of the maar-diatreme complex.

*Post-eruptive intrusions with peperitic margins (KNE10/ Stage 4D)*

Feldspar-phyric andesite (KNE10) also occurs as dike and sill-like intrusions that crosscut the diatremes (e.g., Fig. 4.30). It is common for late dikes that intrude diatreme pipes to have the same composition and texture as those associated with diatreme emplacement (Lorenz and Kurszlavkis, 2007). Many of the andesite intrusions probably grew by expansion of a chilled, ductile crust, as occurs in small pillow buds (e.g., Moore and Lockwood, 1978; Walker 1992). This might explain the presence of globular andesite dikes and boulders with 'growth rings' (e.g., Figs. 4.32 and 4.35D). The andesite intrusions have commonly risen to shallow levels where they 'blew out' into laterally extensive, feldspar-phyric andesite-clast breccias (Figs. 4.31 and 4.52). The andesite clasts display a wide range of morphologies. Some are blocky and have jigsaw-fit texture, resembling hyaloclastites produced by quench fragmentation (e.g., Hanson, 1991; McPhie et al., 1993). Another subset of breccias contain abundant wispy juvenile andesite clasts. These breccias are interpreted as fluidal peperite that has formed where magma has interacted with wet unconsolidated diatreme infill (Stage 4A–4E; Busby-Spera and White, 1987; Hanson and Hargrove, 1999; Martin and Németh, 2007). Fluidal peperite is favored where the host sediment is fine grained and fluidization of the sediment can occur (Kokelaar, 1982; Busby-Spera and White, 1987; Branney and Suthren, 1988; Boulter, 1993; Brooks, 1995).

*Tuff ring and maar crater deposits (Stage 4E)*

Stage 4E deposits mainly occur within a shallow and irregularly shaped basin that partly overlies Diwai, Kapit and Far North diatremes (Fig. 4.37). The basin is predominantly infilled with flat-lying to shallowly-dipping, interbedded mudstones and sandstones (Facies A) with planar stratification, soft-sediment deformation features (e.g., convolutions, dish and pillow structures, slump structures, flame structures, etc.) and sporadic, normally graded breccia beds. Soft-sediment deformation features are interpreted to have formed by earthquake-induced liquefaction and/ or fluidization of water-saturated, unconsolidated, and non-cohesive sediments prior to their lithification, which commonly occurs in lacustrine environments in seismically active regions (Üner, 2014). Wavy to lenticular bedded breccias (Facies C), which have rounded clasts of diverse origins (lithic clasts, charcoal fragments, accretionary lapilli and possible juvenile clasts), are interpreted as resedimented pyroclastic deposits of unknown origin. Based on the position of the basin relative to the subsurface diatreme structures, the basin is interpreted to be a maar crater. The lacustrine deposits of Facies A and resedimented pyroclastic rocks of Facies C are interpreted as maar crater infill. The sharp lower contact of the basin represents the paleosurface at the bottom of the maar crater. The irregular shape of the maar crater may reflect the complexity of the coalesced diatreme bodies with which it is associated (e.g., Jordan et al., 2013).

The maar crater deposits are not surrounded by a preserved tuff ring (e.g., with tephra dipping shallowly away from the center of the basin), suggesting it may have eroded away. However, the northeast-trending lozenge of accretionary lapilli-bearing breccia (Facies B), which has well-developed bedding, unidirectional bedforms (low-angle cross laminations) and both layered and matrix-supported accretionary lapilli, may represent phreatomagmatic base surge and co-surge fallout deposits (i.e., remnants of an *in situ* tuff ring) that were initially deposited within a topographic low and remained below the level of erosion. The cross-laminations could alternatively indicate that Facies B breccias were deposited in a sedimentary environment with localized water currents (such as a tide-dominated coastal environment). In this case, the accretionary lapilli-bearing breccias would be interpreted as resedimented pyroclastic deposits that locally infilled the maar crater.

Stage 4E deposits also occur as large isolated intervals with random bedding orientations that are surrounded by Stage 4A–C breccias (Figs. 4.37 and 4.52). These are interpreted as blocks of tuff ring deposits that were drawn down during syn- and post-eruptive collapse of the eruptive breccia facies (Fig. 4.52).

*Phreatic breccias (Stage 4F–4H)*

Stage 4F–4H breccias have discordant geometries and define smaller pipes and dikes within and peripheral to the main volcanic-hydrothermal breccia bodies as defined in Figures 4.28–4.29 and Table 4.6. These breccias are poorly sorted and poorly consolidated. They contain finely comminuted clasts and clay-rich rock flour matrix that are interpreted to have been derived via explosive fragmentation of the surrounding host rocks. The rock flour matrix locally exhibits an irregular ('swirly') alignment of its constituent particles, a fabric that has elsewhere been attributed to fluid streaming (e.g., Central Breccia at Los Bronces, Warnaars et al., 1985; rock flour matrix-supported polymict breccia from Oruro tin deposit, Sillitoe, 1985). Stage 4F and 4H breccias are polymict, whereas Stage 4G breccias are monomict (hornblende – biotite-bearing monzonite), reflecting the range of lithotypes within their source regions. Juvenile clasts were not identified. Therefore, Stage 4F–4H are interpreted to be phreatic breccias (Fig. 4.52). These phreatic breccias form during phase separation (boiling) of hydrothermal fluids in the upper kilometer of the Earth's crust, when large volumes of steam are produced that ascend rapidly to near surface. Locally, steam can become trapped in sealed fractures. It will accumulate until the vapor pressure exceeds the lithostatic pressure, potentially triggering a phreatic explosion and excavating a small crater. In an instant, the bottom of the crater becomes the new ground surface and the underlying column is rapidly depressurized, promoting a massive release of volatiles and further steam explosions. As this process continues, the crater becomes incrementally wider and deeper. The process stops when enough cool groundwater infiltrates the crater to quell the heat of the rising steam.

Stage 4H breccias are clustered near the pre-mining coastline, in areas of historic surface geothermal features and outcropping breccia pipes. They locally contain possible burrow traces and clasts composed of deformed, laminated siliceous mudstone within disrupted layers of siliceous mud (Fig. 4.40). These features are interpreted to have formed within partially collapsed hydrothermal steam explosion craters in a shallow marine or subaerial (lacustrine) setting. Therefore, it is interpreted that some Stage 4H breccia pipes erupted at surface (Fig. 4.52; e.g., Sillitoe, 1985). However, no hydrothermal eruption aprons were identified, and it is hypothesized that these have been eroded (Fig. 4.52). Hydrothermal steam explosion craters will typically begin to fill back in with small, hydrothermally altered clasts, clay-rich mud-sized particles and hydrothermal fluids. Over time, the clays settle out of suspension in the water, forming laminated lacustrine deposits. When the crater is blown apart during subsequent hydrothermal steam explosions, the semi-consolidated lacustrine deposits are blown apart into clasts that collapse back into the crater. These clasts behave plastically when they are compressed between more consolidated lithic clasts, deforming their internal laminations and causing them to adopt irregular shapes (e.g., Fig. 4.40E).

Stage 4F consists of narrow clastic dikes with sharp, planar contacts. Locally, they contain shear textures and clay gouge (Table 4.6). It is interpreted that some of the Stage 4F breccia bodies acted as slip planes during the settling and collapse of the maar-diatremes (Fig. 4.52).

### *4.7.3.2 Volcanic-hydrothermal breccia bodies*

*Diatreme breccias*

The Kapit, Diwai, Saddle, Mamboo, Ramp and Far North breccias are interpreted to be diatreme breccia pipes, the feeder structures of maar volcanic edifices that have

since been eroded. Evidence for this interpretation includes:

1. The breccias are discordant with respect to the host volcano-sedimentary and intrusive rocks (e.g., Figs. 4.30–4.32).

2. The breccias have large vertical extents (Fig. 4.28).

3. Juvenile feldspar-phyric andesite clasts ± tuffaceous matrix material have been identified in each of the breccia bodies (Fig. 4.35; Corbett et al., 2001; Blackwell, 2010; Ageneau, 2012).

4. The root zones of the breccias are spatially associated with coherent feldspar-phyric andesite intrusions (KNE10). The intrusions have gradational contacts with jigsaw-fit andesite-clast breccias (Stage 4D), which are transitional to matrix-rich polymict breccias with juvenile andesite clasts (Stage 4C; Figs. 4.31 and 4.35).

5. The breccias contain abundant rock flour matrix (e.g., Stage 4A–C breccias range from 10–85% matrix).

6. The breccias contain clasts with porphyry- and epithermal-stage alteration, veins and breccias (Figs. 4.32–4.33).

7. Kapit, Diwai and Far North breccias contain very large blocks (>10 m diameter) and smaller clasts of tephra ring deposits (Stage 4E; Figs. 4.31 and 4.36B) and Saddle and Kapit breccias contain charcoal clasts (Figs. 4.32–4.33; Blackwell, 2010; Ageneau, 2012). This indicates that the phreatomagmatic explosions erupted at surface and produced a maar volcano. Bedded breccia facies interpreted here as *in situ* tuff ring deposits have been identified immediately west of Saddle breccia (Blackwell, 2010) and/or in the upper parts of Mamboo breccia (Corbett et al., 2001).

Individual diatremes are elliptical in plan view and downward tapering (Table 4.5; Fig. 4.28). At shallow depths, they are broad and bowl-shaped and have an association with marginal collapse structures. They have coalesced into a single, large north-northeast-trending body (Fig. 4.28). The underlying root zones are narrow and shaped like inverted cones, with steeply dipping contacts (Figs. 4.28–4.29 and 4.52). This morphology is typical of diatremes that have intruded into soft substrates with porous-media aquifers (Auer et al., 2007). Weaker and water-saturated substrates are more susceptible to liquefaction by shock waves related to phreatomagmatic eruption (White, 1996). They may undergo large-scale collapse via block sliding and emplacement of gravity flows toward the center of the diatreme conduit (Sohn and Park, 2004; Auer et al., 2007). The large and immediate sediment input impedes the replenishment of water to the root zone and causes the phreatomagmatic explosion locus to remain shallow, resulting in diatremes with a shallow angle of repose (Auer et al., 2007). In Kapit NE, the Diwai and Kapit diatremes feature various offshoots and isolated steep-sided pipes, and it is interpreted that this is a result of their emplacement into a mixture of both soft and hard substrates.

It is interpreted that two or more phreatomagmatic events were involved in the formation of the diatremes at Lihir. Evidence for this interpretation includes:

1. The diatremes have separate root zones (Table 4.5; Fig. 4.29).

2. There are examples of phreatomagmatic base surge and fallout deposits (Stage 4E) superjacent to the diatremes (Fig. 4.37). This suggests that the surficial deposits were derived from an adjacent phreatomagmatic eruption that occurred at a later time.

3. Kapit, Diwai and Far North breccias have been overprinted by strong steam-heated alteration (Stage A6–A7 alteration) and have localized late-stage epithermal mineralization (Stage 5C) along their margins

(Fig. 4.29). In contrast, Saddle breccia has crosscut steam-heated alteration (Blackwell, 2010) and is not spatially associated with late-stage epithermal mineralization (Fig. 4.29). This suggests that Saddle breccia was emplaced later in the paragenesis than Kapit, Diwai and Far North breccias. The relationship between alteration and mineralization at the Ramp and Mamboo breccias has not been assessed.

Further work, such as high-resolution U–Pb geochronology of juvenile magmatic clasts, is required to resolve the absolute timing of phreatomagmatic activity associated with each diatreme.

A table comparing the features of 28 diatreme breccias associated with porphyry and epithermal deposits has been modified from Harrison (2018; Table 4.10). The majority of the documented diatremes occur in circum-Pacific magmatic arcs within convergent geodynamic settings, and greater than half of the diatremes occur in the tropical southwest Pacific island arcs of Indonesia, Papua New Guinea and the Philippines. All of the diatremes are Eocene or younger in age (Table 4.10). The Lihir diatreme breccias are constrained between 55–345 ka, making them the youngest diatreme breccias within the dataset. The paucity of Paleozoic diatremes related to porphyry and epithermal deposits is likely a result of their shallow depth of emplacement (<1.5 km) in rapidly evolving terranes and their consequent low preservation potential.

The surface dimensions of the Lihir diatreme breccia complex (3.1 × 1.2 km) are within the typical range of previously documented diatreme breccias (length: 0.3–4.0 km, width: 0.2–3.1 km; Table 4.10). The aspect ratio of these surface dimensions is higher at Lihir (2.6:1) than on average (1.6:1; Table 4.10). This suggests that there may have been a more pronounced structural control on diatreme emplacement. The north-northeast-trending elongation of the Lihir diatremes is parallel to the long-axis of the Luise amphitheater and the alignment of the islands and submarine ridges of the Lihir island group (Figs. 2.2 and 4.28B). Regional, arc-perpendicular extensional forces are therefore interpreted to have contributed the most to the elongation and orientation of the diatremes. The number of discrete diatreme breccia bodies at Lihir (6) is the highest in the dataset (range: 1–6). Most deposits (~75%) are associated with one or two diatreme breccia pipes (Table 4.10).

Previously documented diatremes are associated with porphyry, skarn and epithermal deposits. Gold is the most common associated commodity (Table 4.10). The timing of ore formation with respect to diatreme brecciation is highly variable. The majority of porphyry deposits (75%) form prior to diatreme brecciation (Table 4.10). Epithermal mineralization commonly occurs after diatreme emplacement, and in many of these cases, mineralization is localized within and around the diatreme margins (e.g., Acupan, Philippines: Cooke et al., 1996; Kelian, Indonesia: Davies et al., 2008b; Colquijirca, Peru: Bendezú and Fontboté, 2009; Table 4.10). At Lihir, diatreme brecciation was not genetically related to or synchronous with ore formation. The diatremes were emplaced after porphyry and main-stage epithermal mineralization. Late-stage epithermal mineralization occurred after diatreme brecciation and was focused along its contacts.

*Phreatic breccias*

Karot breccia is a narrow breccia pipe composed entirely of matrix-rich monzonite clast breccia (Stage 4G). It is interpreted to be a phreatic breccia pipe. Evidence for this interpretation includes:

1. The breccia is discordant with respect to the host monzonites (e.g., Figs. 4.30 and 4.32) and has a subvertical, pipe-like geometry (Table 4.5; Fig. 4.28). There was a strong structural control on breccia emplacement (Fig. 4.29).

2. The breccia is located within the discharge zone of the

**Table 4.10.** Comparison of the features of 31 diatreme breccia complexes associated with porphyry and epithermal deposits. The table has been modified from Harrison (2018), with additional/amended information from JICA (1983), Rinne (2015), Rinne et al. (2018) and this study. Where an absolute age for diatreme emplacement was provided in the literature (e.g., U–Pb age of juvenile clasts = 23.4 ± 0.6 Ma), then that age was taken as the average age and the error values were added or subtracted to determine the maximum and minimum ages, respectively. Where an age range was provided in the literature (e.g., Pliocene, 20–30 Ma, etc.), then the extents of the range were taken as maximum and minimum ages, and the average age was calculated from those values. Where only a maximum age was provided in the literature (e.g., <3 Ma), then the minimum age was assigned a value of zero, and the average age was calculated as half of the maximum age.

| Deposit | Region | Country | Length (km) | Width (km) | Aspect ratio | # of breccia bodies | Min. age (Ma) | Max. age (Ma) | Ave. age (Ma) | Primary ore type | Primary commodity | Secondary ore type | Secondary commodity | Relationship of porphyry ore to diatreme | Relationship of epithermal ore to diatreme | Position of post-diatreme ore with respect to diatreme | Reference |
|---|---|---|---|---|---|---|---|---|---|---|---|---|---|---|---|---|---|
| **Cripple Creek** | Colorado | USA | 4.0 | 3.1 | 1.3 | 1 | 27.9 | 29.3 | 28.6 | A-LSE | Au | | | | Post | Marginal | Sillitoe and Bonham (1984); Thompson et al. (1985); Thompson (1992); Jensen (2003) |
| **Martabe** | Sumatra | Indonesia | 4.0 | 2.0 | 2.0 | >3 | 0.0 | 2.0 | 1.0 | HSE | Au-Ag-Cu | | | | Post | | Sutopo (2013) |
| **Tumpangpitu** | Java | Indonesia | 3.1 | 2.2 | 1.4 | >4 | 2.2 | 3.2 | 2.7 | HSE | Au-Ag-Cu | P | Au-Cu-Mo | Pre | Pre, Syn, Post | | Harrison (2018) |
| **Lihir** | TLTF Islands | PNG | 3.1 | 1.2 | 2.6 | 6 | 0.1 | 0.3 | 0.2 | A-LSE | Au | A-P | Au-(Cu) | Pre | Pre, Post | Marginal | Moyle et al. (1990); Blackwell (2010); this study |
| **Colquijirca** | | Peru | 2.7 | 2.5 | 1.1 | 1 | 12.1 | 12.2 | 12.1 | HSE | Cu-Zn-Pb-Au-Ag | | | | Post | Marginal | Vidal and Ligarda (2004); Bendezú and Fontboté (2009) |
| **Sari Gunay** | | Iran | 2.7 | 2.5 | 1.1 | 2 | 11.0 | 11.7 | 11.4 | LSE | Au | | | | Syn, Post | | Richards et al. (2006) |
| **Cerro de Pasco** | | Peru | 2.6 | 2.5 | 1.0 | 1 | 15.3 | 15.4 | 15.4 | E | Pb-Zn-Ag-Cu | | | | Post | Marginal | Baumgartner et al. (2009) |
| **Ortiz** | New Mexico | USA | 2.1 | 1.2 | 1.8 | 1 | 30.0 | 33.9 | 32.0 | A-LSE | Au | | | | Post | Marginal | Wright (1983); Maynard (1995) |
| **Montana Tunnels** | Montana | USA | 2.1 | 0.6 | 3.5 | 3 | 45.0 | 47.8 | 46.4 | E | Au-Ag | | | | Post | Central | Sillitoe et al. (1985) |
| **Rio Blanco** | | Chile | 1.8 | 1.8 | 1.0 | 1 | 3.9 | 4.9 | 4.4 | P | Cu-Mo | HSE | | Pre | | | Sillitoe and Bonham (1984); Warnaars et al. (1985); Piquer et al. (2015) |
| **Grasberg** | Papua | Indonesia | 1.6 | 1.6 | 1.0 | 1 | 3.2 | 3.3 | 3.3 | P | Au-Cu | S | Cu-Au | Post | | | MacDonald and Arnold (1994); Pollard et al. (2005); Leys et al. (2012) |
| **Acupan** | | Philippines | 1.6 | 0.6 | 2.7 | >1 | 1.0 | 5.2 | 3.1 | LSE | Au | | | | Syn, Post | Marginal | JICA (1983); Cooke et al. (1996) |
| **Wau** | Papua | PNG | 1.4 | 1.4 | 1.0 | >1 | 2.4 | 4.0 | 3.2 | LSE | Au | | | | Post | Marginal | Sillitoe et al. (1984) |
| **Selodong** | Lombok | Indonesia | 1.3 | 1.0 | 1.3 | >1 | 5.3 | 11.6 | 8.5 | E | Au-Ag-Cu | P | Au-Cu | Pre | Post | | Rompo et al. (2012) |
| **El Teniente** | | Chile | 1.2 | 1.2 | 1.0 | 1 | 4.6 | 4.7 | 4.7 | P | Cu-Mo | | | Syn, Post | | | Howell and Molloy (1960); Cannell et al. (2005); Klemm et al. (2007) |
| **Batu Hijau** | Sumbawa | Indonesia | 1.2 | 0.9 | 1.3 | >1 | 2.6 | 5.3 | 4.0 | E | Au-Ag-Cu | P | Au-Cu | Pre | Pre, Syn, Post | | Clode et al. (1999); Maryono and Priowasono (2000) |
| **Caspiche** | | Chile | 1.1 (?) | 1.1 (?) | 1.0 | 2 | 24.0 | 25.4 | 24.7 | P | Au-Cu | HSE | | Pre, Syn | Pre, Syn, Post | | Sillitoe et al. (2013) |
| **Tanjung** | Java | Indonesia | 1.15 | 0.5 | 2.3 | 1 | 8.3 | 8.7 | 8.5 | HSE | Au-Ag-Cu | P | Au-Cu-Mo | Post | Post | | Harrison (2018) |
| **Rinti** | Sumbawa | Indonesia | 1.0 | 1.0 | 1.0 | >1 | 0.0 | 2.5 | 1.3 | E | Au-Ag-Cu | P | Au-Cu | Pre | Pre, Syn, Post | | Garwin (2000); Maryono and Setyandhaka (2011) |
| **Agua Rica** | | Argentina | 1.0 | 0.7 | 1.4 | 1 | 5.3 | 11.6 | 8.5 | P | Cu-Mo-Au | HSE | Cu-Au-Ag-As-Pb-Zn | Pre | Pre | | Landtwing et al. (2002) |
| **Yanacocha** | | Peru | 1.0 | 0.7 | 1.4 | >5 | 8.4 | 12.4 | 10.4 | HSE | Au-Ag-Cu | P | Au-Cu | Pre | Pre, Syn, Post | | Turner (1997); Teal and Benevides (2010); Longo et al. (2010) |
| **Boyongan** | | Philippines | 0.9 | 0.9 | 1.0 | 1 | 0.0 | 2.0 | 1.0 | P | Cu-Au | | | Post | | | Braxton (2007); Braxton et al. (2009) |
| **Roșia Montană** | | Romania | 0.9 | 0.4 | 2.3 | 1 | 12.8 | 13.6 | 13.2 | ISE | Au-Ag | | | | Post | Open fractures; breccia infill | Wallier et al. (2006) |
| **Kelian** | Kalimantan | Indonesia | 1.6 | 1.0 | 1.6 | >3 | 15.9 | 23.1 | 19.5 | LSE | Au-Ag | | | | Post | Marginal | Davies et al. (2008a, 2008b) |
| **Wafi-Golpu** | Papua | PNG | 1.1 | 0.5 | 2.2 | 1 | 8.5 | 8.7 | 8.6 | P | Cu-Au | HSE/ISE | Au | Pre | Post | | Rinne (2015); Rinne et al. (2018) |
| **Elang** | Sumbawa | Indonesia | 0.7 | 0.5 | 1.4 | 3 | 2.6 | 3.6 | 3.1 | HSE/LSE | Au-Ag-Cu | P | Au-Cu | Pre | Pre, Syn, Post | | Maryono et al. (2005) |
| **Brambang** | Lombok | Indonesia | 0.3 | 0.2 | 1.5 | >1 | 5.3 (?) | 11.6 (?) | 8.5 (?) | HSE/LSE | Au-Ag-Cu | P | Au-Cu | Pre | Pre, Syn, Post | | Maryono et al. (2013) |
| **Lepanto-Far South East** | | Philippines | ? | ? | ? | 2 | 1.2 | 1.6 | 1.4 | HSE | Cu-Au | P | Cu-Au | Pre, Syn | Pre, Syn | | Garcia (1991); Hedenquist et al. (1998); Chang et al. (2011) |
| *Minimum* | | | 0.3 | 0.2 | 1.0 | | | | 0.2 | | | | | | | | |
| *Maximum* | | | 4.0 | 3.1 | 3.5 | | | | 46.4 | | | | | | | | |
| *Average* | | | 1.7 | 1.3 | 1.6 | | | | 10.3 | | | | | | | | |

Abbreviations: A-LSE: alkalic low sulfidation epithermal, A-P = alkalic porphyry, ave. = average, E = epithermal (unspecified), ISE = intermediate sulfidation epithermal, LSE = low sulfidation epithermal, max. = maximum, min. = minimum, P = porphyry, S = skarn.

present-day geothermal system.

3. The dimensions of the main breccia body are comparatively small (150 $m^2$ at surface; Table 4.5; Fig. 4.28). There are irregular, small (<20 m) offshoots surrounding the main breccia body.

4. No juvenile magmatic components were identified within the breccia.

5. The breccia contains abundant rock flour matrix (e.g., Stage 4G breccias range from 30–70% matrix).

6. The clasts are more angular than those in the phreatomagmatic breccias. Clasts range in size up to large boulders (<30 cm), but no large blocks (>10 m across) were identified. The clasts have strong hydrothermal clay alteration (Table 4.6).

Karot breccia pipe is circular in plan view and has a large vertical extent, with near-vertical to steeply dipping contacts (Table 4.5; Fig. 4.28). It is interpreted that this vent morphology has been influenced by its emplacement along the intersection of steeply dipping structures within a hard substrate with fracture-filling aquifers.

#### *4.7.3.3 Timeline of diatreme formation*

The Lihir diatreme breccia complex (Stage 4) is interpreted to be the product of maar-diatreme volcanism, related tectonism and hydrothermal activity. The following section documents the sequence of events interpreted to have produced and modified these breccias.

*1) Pre-diatreme configuration*

- A north to east-northeast-trending fault and fracture system developed beneath the floor of the Luise sector collapse amphitheater.
- An ore-forming hydrothermal system was established, forming Stage 2 and 3 veins and breccias and Stage A3–A5 main-stage alteration in Kapit NE and Coastal. Epithermal-stage gold-bearing veins ($V3_{adu}$, $V4_{qtz}$ and $V1_{M1}$) were localized along steeply-dipping northeast- to east-northeast-trending structures with extensional to hybrid characteristics in Lienetz (Sykora et al., 2018a).

*2) Andesite intrusion and commencement of maar-diatreme volcanism*

- Andesitic magma ascended to shallow depths along the same faults that were active during main-stage epithermal mineralization.
- Where andesite intrusions intercepted the active hydrothermal system, phreatomagmatic explosions were initiated. Each root zone (Fig. 4.29) is interpreted as the point at which andesitic magma came into contact with hydrothermal fluid.
- The initial subsurface products of phreatomagmatic explosions were formed (Stage 4A–4C).

*3) Diatreme excavation and maar crater formation*

- Phreatomagmatic explosions continued as new magma and hydrothermal fluid were introduced into the volcanic conduit. New episodes of phreatomagmatic activity initiated at progressively deeper levels, resulting in downward excavation of wall rock. The downward-tapering forms of the diatreme breccia bodies began to take shape.
- The phreatomagmatic explosions erupted to surface, forming maar craters and associated tephra ring deposits (Stage 4E).
- New hypogene phreatomagmatic breccias continued to form, crosscutting and in some cases incorporating ear-

lier-formed breccias (Stage 4A–4C).

- The products of earlier phreatomagmatic activity that been deposited within the diatremes underwent increasingly greater degrees of fragmentation and reworking in subsequent eruptions, locally resulting in more milled and abraded clasts (e.g., as seen in Stage 4B). Locally, juvenile clasts became indistinguishable from wall-rock clasts due to the loss of delicate clast margins (except where armored by muddy matrix rinds).

- Contact breccias (Stage 4D) formed by quenching and disaggregation of feeder dikes where they came into contact with abundant hydrothermal fluids, and explosion and implosion/collapse of wall rocks in the root zone.

*4) Subsidence and phreatic explosions*

- As magmatic input decreased, phreatic explosions became dominant over phreatomagmatic activity within and around the diatreme breccia bodies, forming phreatic breccia bodies (Stage 4B and 4G) that crosscut older phreatomagmatic breccias (Stage 4A–4D) and/or the surrounding host rocks.

- Phreatic eruptions in Kapit NE and Coastal area formed irregular bodies and small pipes (Stage 4G and 4H).

- Fallout and settling of eruptive material produced stratified breccia facies in the upper parts of the diatreme (Stage 4B).

- Collapse breccias formed by gravitational collapse in the upper parts of smaller phreatic eruption breccia pipes in Kapit NE and Coastal (Stage 4H).

- Megablocks of surficial material (e.g., tephra ring material, tree trunks, etc.) were slumped into the diatremes due to gravitational collapse and/or implosion (Stage 4E). Some of the slumping occurred via normal faulting along tabular phreatic breccias that became preferred sites for continued phreatic brecciation (Stage 4F).

- Fine-grained clastic material settled into open spaces, forming draped matrix (e.g., as in Stage 4B; Figs. 4.32 and 4.33C).

*5) Post-diatreme events*

- Intrusion of andesitic magma into the newly formed, unconsolidated and water saturated diatreme breccia infill (Stage 4A–4C and Stage 4E) produced peperitic andesite sills and dikes near surface (KNE10 and Stage 4D; Figs. 4.31 and 4.52).

- A new, steady-state hydrological regime was established, associated with renewed epithermal gold mineralization (Stage 5A–C) that was focused along the margins of the NE-trending Diwai breccia in Kapit and Kapit NE and around Stage 4G and H phreatic breccias in Coastal. A blanket of steam-heated alteration overprinted large areas of the diatreme complex.

- Uplift and erosion removed the majority of *in situ* surficial deposits (e.g., tephra rings and phreatic tephra aprons) and brought the sector collapse amphitheater floor to the present-day erosion level (Fig. 4.52).

- Mining activities locally excavated diatremes (e.g., Minifie and Lienetz open pits) and elsewhere resulted in the deposition of waste rock cover (e.g., Kapit stockpile).

- A landslide resulted in the deposition of unconsolidated sedimentary cover over the Kapit area.

#### *4.7.3.4 Implications for mineralization*

The previously established genetic model for Lihir postulated that sector collapse of the Luise Volcano unloaded

an active magmatic-hydrothermal system (i.e., an incipient alkalic porphyry), triggering phreatomagmatic explosions and rapid deposition of epithermal gold mineralization in shallow breccia pipes (Carman, 2003). However, this study highlights a lack of evidence for early-formed volcanic-hydrothermal breccias or a genetic relationship with epithermal gold mineralization. The new model presented in this chapter shows that the main period of epithermal gold mineralization (Stages 2–3) occurred prior to volcanic-hydrothermal brecciation and only a minor amount of epithermal gold was deposited afterwards (Stage 5). There is no evidence that epithermal gold mineralization occurred synchronous with the emplacement of the breccias. It is instead proposed that the sector collapse(s) must have occurred during a period of magmatic-hydrothermal quiescence and that epithermal mineralization occurred sometime after, associated with a new magmatic heat source. In the case of late phreatomagmatic activity, as at Lihir, it is important to note that the main body of ore may be truncated and/or redistributed. This is pertinent to exploration as it implies that mineralization may be on the far side of a barren and potentially large body of matrix-rich breccias.

Some post-diatreme mineralization is focused along the margins of the Diwai, Far North and Kapit breccias; however, only minor mineralization is hosted within the diatreme breccias themselves. This suggests that the diatremes acted as aquitards to hydrothermal fluid flow. Instead, fluids were focused along marginal fractures that were generated during breccia emplacement (Fig. 4.52).

### *4.7.4 Late epithermal stage*

Pervasive smectite – kaolinite – Fe-sulfide ± carbonate (Stage A6; argillic) and kaolinite – alunite ± quartz ± Fe-sulfide (Stage A7; advanced argillic) alteration zones form a continuous layer near surface in Kapit NE and Coastal (<150 m bsl; Fig. 4.1) and have a widespread distribution across the Luise amphitheater (from present-day surface to ~250 m depth; Jansen and Cooke, 2013). These alteration domains have sharply crosscut veins, breccias and altered rocks generated in all previous stages of porphyry and epithermal activity, including the Lihir diatreme breccia complex (Fig. 4.41). The argillic alteration zone is interpreted to have developed at low temperatures (<180°C) in the shallow epithermal environment through interaction with steam-heated bicarbonate waters; whereas, the advanced argillic alteration zone is interpreted to have formed at slightly lower temperatures (<120°C) and shallower levels through interaction with steam-heated acid-sulfate waters (e.g., Simmons et al., 2005). Steam-heated fluids are produced as a by-product of boiling epithermal fluids. When $CO_2$ and $H_2S$ partition into the vapor phase during boiling, they rise upwards and condense into groundwater in the vadose zone, where they form acid via oxidation reactions (e.g., Hedenquist et al., 2000). Evidence supporting a steam-heated origin for these stages of alteration includes: (1) the flat-lying distribution of alteration; (2) the distribution of advanced argillic alteration subjacent to geothermal features and superjacent to argillic alteration zones; (3) the pseudo-cubic, poorly to moderately crystalline and fine-grained habit of alunite, (4) the low-temperature, acid-stable (pH 2–3) alteration assemblages including smectite, kaolinite and marcasite (Stage A6) and opal, kaolinite, and marcasite (Stage A7; Fig. 4.10; Corbett and Leach, 1998), and (5) the absence of high-temperature alteration minerals (e.g., pyrophyllite, diaspore, zunyite, etc.; e.g., White and Hedenquist, 1995; Simmons et al., 2005; Table 4.9). A steam-heated origin has previously been proposed for advanced argillic alteration at Lihir (Davies and Ballantyne, 1987; Carman, 2003). Silica sinter was not observed in this study; however, hot springs and gas vents surrounded by sulfurous sinter and alunite – sulfur – cristobalite-rich (advanced argillic) altered rocks have previously been identified in the 'Kapit thermal area' (spatially equivalent to Coastal area as defined in this study; Williamson, 1983). Coastal also features large resistant outcrops composed predominantly of opal (e.g., Alaia rock; Jansen and Cooke, 2013). This suggests very shallow and/or surficial development of advanced argillic alteration and a genetic relation-

ship with the modern geothermal system. The Kapit NE mineralized zone does not contain advanced argillic alteration (Fig. 4.1). This is likely due to its position offshore, which may have inhibited steam-heated alteration (Jansen and Cooke, 2013). The common occurrence of co-existing clay mineral species that form at different temperatures and depths (e.g., smectite overprinting illite) within the argillic alteration zone may indicate fluctuating levels of the water table, for example, due to multiple sector collapse or other mass wasting events (e.g., White et al., 2010). The advanced argillic alteration has a restricted distribution, occurring in small, structurally rooted, upward flaring zones that transition with depth into narrow argillic alteration domains containing higher temperature alteration minerals such as illite, muscovite and dickite (e.g., up to 360°C; Fig. 4.1; Table 4.9). It is interpreted that these structures were high temperature upflow zones for the steam-heated fluids that generated the Stage A6–A7 alteration domains.

The steam-heated alteration zone locally contains dendritic pyrite veinlets and fine-grained disseminated pyrite (Stage 5A; Fig. 4.42) and variable, multi-stage clay – pyrite ± sulfate-cemented breccias and veins (Stage 5B; Fig. 4.43) with disseminated vein-halo pyrite ± marcasite (which forms banded overgrowths around earlier-formed disseminated sulfides; Fig. 4.44F). These structures locally host moderate grade gold mineralization (1–5 g/t Au). It is possible that due to a drop in the paleowater table (e.g., caused by a catastrophic mass wasting event), acidic steam-heated fluids were able to percolate downward through large volumes of previously formed epithermal mineralization. The gold in solution could then be mobilized and reprecipitated as fine-grained disseminations and overgrowths of Fe-sulfides in a process similar to supergene enrichment (e.g., Ebert and Rye, 1997).

Stage 5C was the last epithermal stage that produced significant gold mineralization. The Stage 5C calcite – quartz – pyrite-cemented breccias and veins were focused along the contacts of the Diwai breccia complex in Kapit NE and Kapit and therefore have a NE-trending distribution (cf. Figs. 4.29, 4.32, 4.41 and 4.47). This stage contains vein infill, cement and vein-halo alteration assemblages (carbonate minerals, quartz, adularia, anhydrite, illite, rutile, Fe-sulfides, base metal sulfides), as well as open-space filling textures (lattice-textured bladed calcite and anhydrite) that are indicative of formation from boiling fluids in the epithermal environment (e.g., Simmons and Christenson, 1994; Simmons et al., 2000). Stage 5B–5D breccias are interpreted to have formed by sub-surface hydraulic fragmentation, similarly to those formed during Stages 2A and 3. This genetic classification is based on their (1) discordant geometry, (2) small size (e.g., <1 m-across), (2) abundant hydrothermal cement (Figs. 4.43J, 4.46A and 4.48A), (3) monomict, locally derived and non-juvenile clast population, (4) low percentage of matrix material (<5%), (5) typically massive, poorly sorted and jigsaw-fit to clast-rotated organization (e.g., Figs. 4.27H and 4.46A), (6) associated clast-selective alteration and/or alteration rinds on clasts (e.g., Figs. 4.43J and 4.46B), and (7) association with veins (Table 4.3; e.g. Jébrak, 1997).

Stage 5D veins and breccias contain orpiment and realgar, which are commonly formed in low-temperature hydrothermal veins together with other arsenic minerals such as stibnite and native arsenic (Ferrini et al., 2003). They also occur as a volcanic sublimation product and as deposits associated with hot springs. The proposed temperature of formation for Stage 5D is 50–75°C (Table 4.9). Precipitation of realgar and orpiment on fractures that crosscut arsenian pyrite- and arsenopyrite-bearing veins (Stages 2–3 and 5A–C) indicate that sulfur activity and/or temperature of the fluids changed during the waning stage of hydrothermal activity. For example, there may have been a decrease in temperature and sulfur activity through dilution, boiling and sulfidation reactions. Veins of orpiment and realgar have not previously been documented at Lihir. However, fracture linings and open space fillings consisting of realgar, orpiment, alacranite, stibnite, colloform pyrite, amorphous silica, galena and sphalerite were identified at

nearby Conical Seamount (Petersen et al., 2002). The As-Sb mineralization at Conical Seamount was also shown to have formed late in the paragenesis, post-dating the precipitation of gold (Herzig et al., 1999).

### 4.8 Relationship between host rocks and epithermal mineralization

Epithermal mineralization and alteration at Kapit NE and Coastal is interpreted to be epigenetic and is hosted in both volcano-sedimentary rocks and subvolcanic intrusions (Figs. 4.1, 4.19 and 4.41). There is no obvious localization of high-grade gold mineralization within or around any particular igneous intrusion or stratigraphic horizon in the volcano-sedimentary stratigraphy. However, the rheology of the host rocks has influenced the styles of mineralization. The coherent intrusive rocks are preferential hosts for well-developed vein stockworks and narrow breccia veins with well-defined alteration halos (e.g., Fig. 4.53B). In contrast, the volcaniclastic breccias have behaved in a less coherent fashion, so that veins and breccias are more poorly developed, discontinuous and diffuse, with more broad pyrite-rich alteration patches developed around the mineralized structures (e.g., Fig. 4.53C).

### 4.9 Constraints on the relative and absolute timing of alteration and mineralization

The volcanic host rocks to the Lihir gold deposit are interpreted to have been deposited between the latest Miocene (<5.57 Ma) and 497 ka, since they are younger than the Londolovit Block volcanics (5.57–3.59 Ma; Table 4.11) and older than the pyroxene-hornblende-phyric monzodiorite intrusions intersected in geothermal exploration well GW47 (NW Luise amphitheater; 497.4 ka ± 9.0 ka; Chapter 3). Constructional volcanism of the Luise Volcano is interpreted to have ceased when porphyry dike and stock formation initiated (Fig. 4.54). The absolute timing of this transition is unknown.

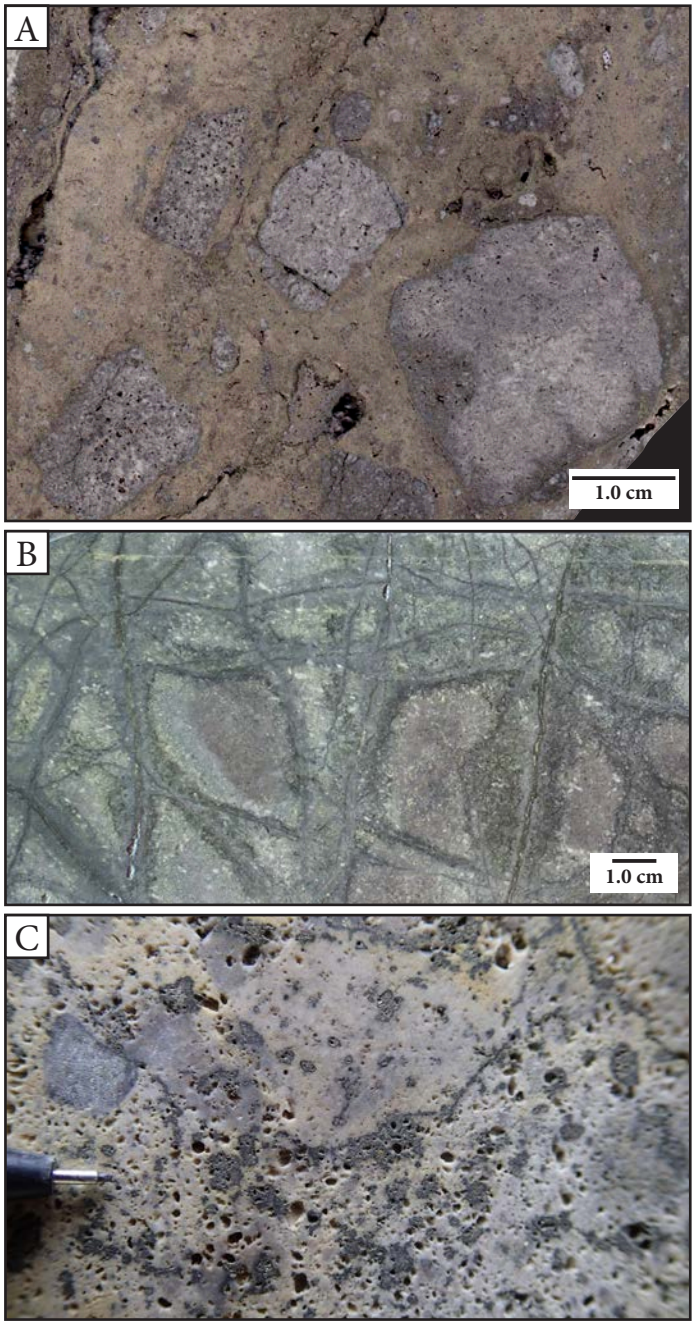


**Fig. 4.53.** Relationship between host rock type and styles of epithermal gold mineralization. **A.** An example of a tabular, monomict, pyrite-cemented breccia. The hornblende-biotite-bearing monzonite clasts (KNE5) have a porous texture defined by dissolved mafic sites. Sample: DDHL1977 115.7 m. **B.** This specimen of hornblende-biotite-bearing monzonite (KNE5) is crosscut by a dense stockwork of colloform pyrite – marcasite veins with distinctive gray adularia – pyrite alteration halos. Many of the veins are incompletely filled, leaving a central vuggy seam that has later been lined with illite – pyrite. Mineralization in coherent rocks such as KNE5 is typically expressed as stockworks, breccia veins and cataclasites. Sample: DDHL1872 79.9 m. **C.** This sample of pyroxene-phyric basalt breccia (KNE2b) has a porous texture due to the dissolution of primary phenocrysts and crystal fragments. Patches of anhedral pyrite nucleated around clinopyroxene sites. Discontinuous pyrite veinlets and disseminations are concentrated along the previously glassy margins of clasts. Mineralization in fragmented rocks such as this basalt breccia is typically diffuse, consisting of wavy, singular or discontinuous veins, breccias, disseminations and patchy replacement-style mineralization. Pencil lead is 0.5 mm thick. Sample: DDHL1970 215.6 m.

The age of pyroxene-hornblende-phyric monzodiorite (497.4 ka ± 9.0 ka) also provides a maximum age for the porphyry-stage mineralization intersected in GW47. The maximum age for porphyry mineralization does not overlap within uncertainty with the Re–Os dates acquired for Stage 1E and 2D porphyry-related events in Kapit NE (Stage 2D: 481 ± 19 ka; Stage 1E: 345 ± 3 ka; Table 4.7; Fig. 4.54). This suggests that there has been episodic porphyry-style magmatic-hydrothermal activity in the NW Luise amphitheater and Kapit NE areas and that porphyry conditions predominated at Lihir for >164 ky.

The difference between the youngest Re–Os (molybdenite) and the limestone age determinations suggests that the transition from porphyry to epithermal conditions lasted approximately 150 ky. During this time, it is interpreted that there was a period of magmatic-hydrothermal quiescence and an influx of cool groundwater (Sykora et al., 2018a). This would have allowed for the dissolution and recrystallization of anhydrite, which has retrograde solubility at <350°C (Blount and Dickson, 1969; Hanor, 2000). Evidence for a period of magmatic-hydrothermal quiescence includes the absence of volcanic-hydrothermal breccia bodies that pre-date epithermal mineralization and the widespread presence of void spaces produced via the dissolution of anhydrite.

It is interpreted that main-stage epithermal mineralization (Stage 2–3), volcanic-hydrothermal brecciation (Stage 4) and late-stage epithermal mineralization (Stage 5) have occurred since sector collapse unroofed the Luise Volcano (Fig. 4.54). U–Th disequilibrium dating of a fringing limestone terrace in Luise Harbor provides a tentative maximum age for the sector collapse of <190 ka (Blackwell, 2010). However, the limestone age displays open-system U–Th behavior and is highly uncertain. Also, this maximum age assumes that the limestone terrace was partly destroyed during the sector collapse event. It is possible that coral reefs did not grow in the area of the Luise Harbor due to elevated seawater temperatures and/or acidity arising from local hydrothermal activity. The Re–Os (molybdenite) age for Stage 1E anhydrite – pyrite veins provides an alternate and more definitive maximum age for the sector collapse and subsequent epithermal mineralization of <345 ka.

Previous ages for porphyry- and epithermal-stage veins and alteration are based on K–Ar and Ar–Ar dating and are difficult to interpret (Table 4.11; Fig. 4.54). It is not certain whether the minerals dated are of porphyry or epithermal affinity. Thermal resetting of these minerals dated is likely considering their low closure temperatures (i.e., adularia: 150 ± 30°C, Harrison and McDougall, 1980; alunite: 280 ± 20°C, Love et al., 1998; Table 2.1) and the high ambient temperatures of the modern Lihir geothermal system (>275°C; Simmons and Brown, 2006). Ar–Ar (adularia) age data reported in Carman (2003) is not accessible in the cited reference (Carman, 1994) and its quality cannot be assessed. Overall, data from previous work indicates that mineralization at Lihir has occurred since ~0.9 Ma.

In this study, the minimum age for the Lihir diatreme breccia complex was determined via radiocarbon dating of a charcoal clast to be >55 ka. Blackwell (2010) attempted to date a plagioclase-phyric andesite (equivalent to KNE10) that crosscuts the Saddle Breccia west of Lienetz orebody; however, an imprecise Ar–Ar (hornblende) age of 1.09 ± 0.49 Ma was obtained. This age is interpreted to be erroneous due to the low K content in the hornblende dated. The radiocarbon age brackets the timing of sector collapse, main-stage epithermal mineralization (Stage 2–3) and volcanic-hydrothermal brecciation (Stage 4) to between 190 and 55 ka (Fig. 4.54). Late-stage epithermal mineralization (Stage 5) occurred synchronous with volcanic-hydrothermal brecciation and persisted for some time afterwards. Therefore, the only constraint on the timing of Stage 5 is that it is younger than sector collapse (i.e., <190 ka). Taking the more conservative Re–Os (molybdenite) age for Stage 1E as the maximum age for sector collapse, this suggests epithermal gold at Lihir was deposited in a very short time span of <345 ky. Similar short time frames have been es-

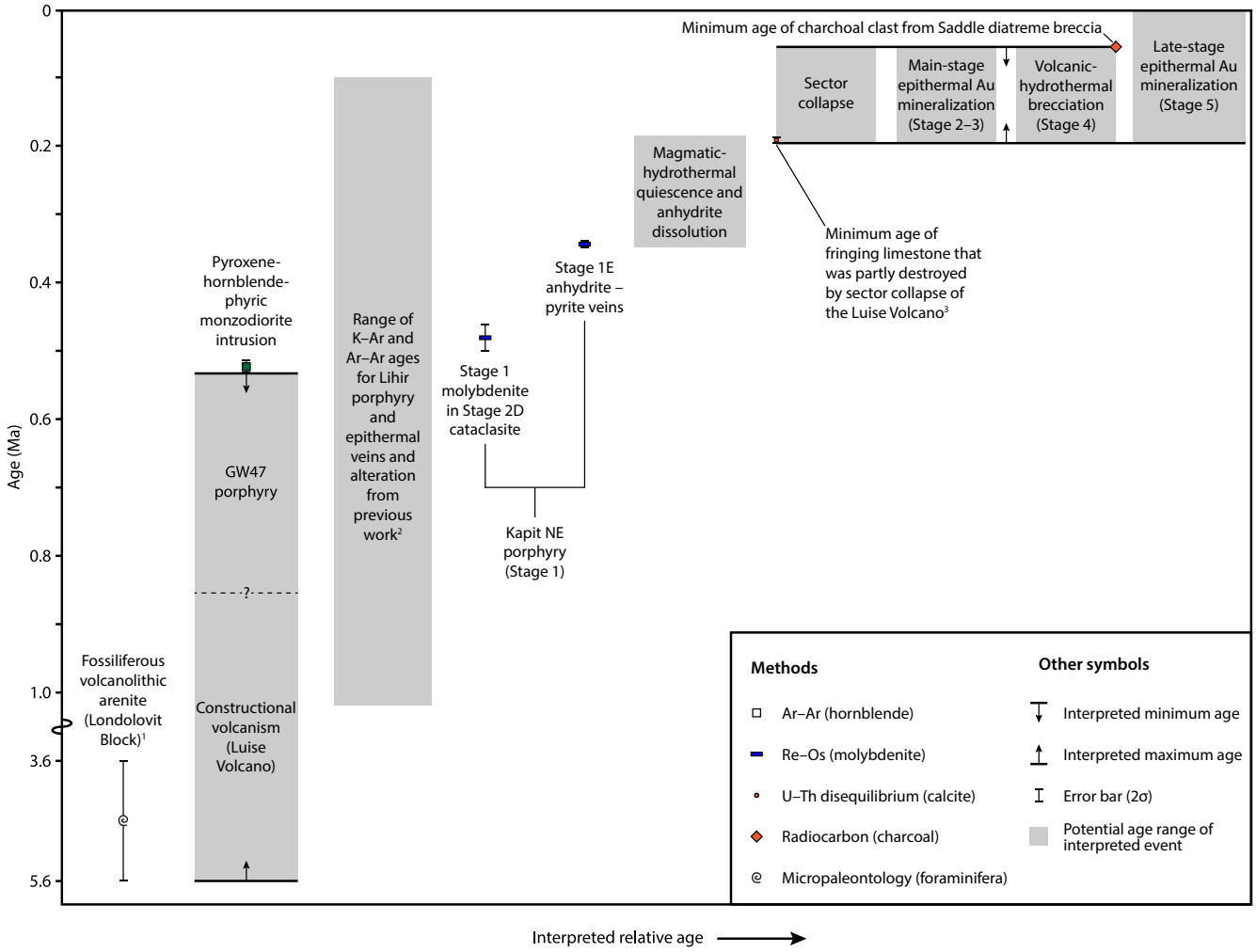


**Fig. 4.54.** Summary of the geochronology of events in the geological history of the Lihir gold deposit. K–Ar ages for Lihir porphyry and epithermal veins and alteration from previous work are provided in Table 4.10 and discussed in text. [1]Gallasch (1976); [2]Davies and Ballantyne (1987), Moyle et al. (1990), Rytuba et al. (1993), Carman (1994); [3]Blackwell (2010).

tablished in other porphyry-epithermal deposits including Wafi-Golpu (~347–195 ky, Rinne et al., 2018) and Far Southeast-Lepanto (~300 ky, Arribas et al., 1995).

## 4.10 Summary and conclusions

The veins and altered rocks of the Lihir gold deposit record a transition from porphyry to low sulfidation epithermal styles of mineralization. At deeper levels of Kapit NE and Coastal, evidence for early porphyry-style activity is preserved in hydrothermal breccias and veins infilled by high-temperature minerals such as anhydrite, actinolite, magnetite, biotite, K-feldspar, chalcopyrite and molybdenite and enveloped by vein-halo alteration consisting of biotite, phlogopite, magnetite, K-feldspar and/or muscovite. They have low gold grades (<1 ppm) and variable copper concentrations (typically low, but rarely up to 0.3 wt% Cu). Pervasive phlogopite – K-feldspar ± magnetite (potassic) and chlorite – calcite (propylitic) alteration zones are also present at deeper levels. No single intrusive center has been identified that can account for the distribution of porphyry-style hydrothermal alteration across the Lihir deposit. However, in Kapit NE, there is an apparent zonation of pervasive alteration surrounding a cluster of crystal-poor feldspar-phyric trachyte dikes (KNE7), from proximal potassic to distal propylitic assemblages (Fig. 4.1). Albite – actinolite veins and anhydrite-rich veins and cemented breccias, including a pebble dike, are also

**Table 4.11.** Isotopic constraints on the ages of volcanic rocks and hydrothermal alteration at the Lihir gold deposit from previous work. UTM coordinates are reported in AGD84 (Zone 56S).Sample descriptions are taken from their respective references. References: 1 = Blackwell (2010), 2 = Moyle et al. (1990), 3 = Davies and Ballantyne (1987), 4 = Rytuba et al. (1993), 5 = Carman (2003), 6 = Gallasch (1976).

| Location | Easting | Northing | Elevation (m rsl) | Age (Ma) | Sample description | Method | Significance | Reference |
|---|---|---|---|---|---|---|---|---|
| SW Luise amphitheater | 461943 | 9655303 | 0 | 0.000177 ± 0.000028 | Reef front biolithite | U-series disequilibrium (limestone) | The youngest of the ages for limestone that was likely partly destroyed during sector collapse is ~190 ka; this provides a maximum age for sector collapse of <190 ka; the limestone ages have a high degree of uncertainty and display open-system U–Th behavior | 1 |
| | 461933 | 9655293 | 15 | 0.234679 ± 0.003331 | Biomicrite | | | |
| | 461933 | 9655293 | 15 | 0.273963 ± 0.005770 | Biomicrite | | | |
| | 461838 | 9655153 | 40 | 0.190628 ± 0.002296 | Reef flat biomicrite | | | |
| Lienetz | 459084 | 9654294 | – 29 | 0.151 ± 0.015 | Alunite-rich rock | K–Ar (whole rock) | The varying ages recorded by K–Ar dating reflect different stages of alteration related to the intrusion of monzonite stocks, porphyry-related mineralization and overprinting by the ore-forming epithermal and modern-day geothermal systems; the ages obtained from K-feldspar and illite are difficult to interpret. Both of these minerals may have been formed during porphyry or the later epithermal alteration; imprecise ages are likely due to thermal resetting of K–Ar system in biotite and K-feldspar (Table 2.1) at the ambient temperatures of the Lihir geothermal system (>275°C; Simmons and Brown, 2006) | 2, 3 |
| Kapit | 458981 | 9655140 | – 137 | 0.2 ± 0.1 | Siliceous breccia zone | K–Ar (K-feldspar) | | 2 |
| Minifie | 458953 | 9653129 | 13 | 0.3 ± 0.1 | Potassic-altered volcanic | K–Ar (K-feldspar) | | 2 |
| Lienetz | 459403 | 9654316 | – 353 | 0.336 ± 0.027 | Au-bearing, anhydrite – biotite – magnetite vein | K–Ar (biotite) | | 2, 3, 4 |
| Lienetz | 459250 | 9653965 | – 345 | 0.342 ± 0.036 | Pyroxene monzonite | K–Ar (biotite) | | 2, 3 |
| Lienetz | 459250 | 9653965 | – 345 | 0.36 ± 0.03 | Monzonite porphyry | K–Ar (biotite) | | 4 |
| Minifie | 459304 | 9653469 | – 93 | 0.5 ± 0.1 | Siliceous breccia zone | K–Ar (K-feldspar) | | 2 |
| Minifie | 458953 | 9653129 | – 71 | 0.7 ± 0.2 | Clay – silica zone | K–Ar (illite) | | 2 |
| Minifie | 458783 | 9652982 | – 74 | 0.7 ± 0.2 | Weakly propylitized volcanic | K–Ar (whole rock) | | 2 |
| Coastal | 459701 | 9654599 | – 84 | 0.917 ± 0.1 | Strongly biotite-altered volcanic | K–Ar (biotite) | | 2, 3 |
| Minifie | ? | | | 0.52 ± 0.11 | Sulfide-rich ore | Ar–Ar (adularia) | Provides an age for epithermal mineralization in Minifie ore zone; the quality of the data cannot be assessed, because it was not included in the reference | 5 |
| | | | | 0.61 ± 0.25 | | | | |
| Lienetz | 458834 | 9654129 | ? | 1.09 ± 0.49 | Plagioclase-phyric andesite (L8) | Ar–Ar (hornblende) | Indicates that the age of andesite dikes that crosscut the Lihir diatreme breccia complex are <1.58 Ma; the age is imprecise due to low K in hornblende | 1 |
| Near Londolovit town (Fig. 1.1), Londolovit Block | ? | | | 3.59–5.57 (Zone N18–N20) | Fossiliferous volcanolithic arenite | Micropaleontology (foraminifera) | Latest Miocene to Pliocene foraminifera were identified from volcano-sedimentary rocks in Londolovit Block; the Luise Volcano was constructed on top of the Londolovit Block (Wallace et al., 1983); therefore, Luise volcanics must be younger than latest Miocene (i.e., they have a maximum age of 5.57 Ma) | 6 |

spatially associated with the trachyte dikes. The alteration zonation suggests a cooling trend with increasing distance from these intrusions and a probable genetic relationship to the hydrothermal alteration. The presence of the pebble dike implies proximity to a hydrous intrusion exsolving fluids at porphyry crustal depths. Biotite-feldspar-phyric, nepheline-bearing monzonite intrusions in Coastal area (KNE4) contain abundant magmatic-hydrothermal features (e.g., miarolitic cavities) that provide evidence for volatile phase exsolution; however, no evidence has been found for a genetic link between this intrusive phase and porphyry-style hydrothermal activity. New geochronological age constraints suggest that the porphyry stage was active between ~481 ka and 345 ka (Table 4.7).

The transition from porphyry- to epithermal-style hydrothermal activity occurred as a result of volcanic sector collapse (~180 ka; Table 4.11), which removed at least 1 km of volcano-sedimentary rocks from the top of the Luise volcano (Moyle et al., 1990; Sillitoe, 1994; Carman, 2003; Blackwell, 2010). Dissolution of anhydrite and shear deformation localized along porphyry-stage anhydrite veins that are prevalent in the deeper levels at Lienetz (and occur locally in Kapit NE and Coastal) may have weakened the Luise volcanic edifice, facilitating its collapse (Sykora et al., 2018a). This catastrophic mass wasting event depressurized rocks that had previously been at depth, resulting in extensional fracturing and increasing the hydraulic conductivity of the rock mass. Cold groundwater and/or seawater

was then able to percolate downward, dissolving anhydrite veins and alteration, unstable primary mafic minerals and volcanic glass, and leaving behind abundant amoeboid, sheet-like and crystal-shaped cavities. As the cold fluids equilibrated with the higher ambient temperatures at depth according to the local geothermal gradient or through mixing with hydrothermal fluids, the remnant material was altered to an assemblage of adularia ± pyrite.

The epithermal stage in Kapit NE and Coastal was characterized by long, quiescent periods when banded vein infill and small-scale hydraulic breccias were formed (Stage 2A, Stage 3, Stage 5) and brief, chaotic periods of tectonism (Stage 2D), phreatic brecciation (Stage 2B and 2C) and diatreme volcanism (Stage 4). The epithermal stage generated significant gold mineralization at shallow levels, which is hosted in veins and breccias containing gold-bearing Fe-sulfides (pyrite > marcasite) with variably abundant gangue minerals (quartz, chalcedony, adularia, carbonate, anhydrite and/or illite) and up to 10% open space. These veins and breccias have crosscut all rock types that occur at shallow levels and are typically accompanied by intense adularia – pyrite or quartz – illite – pyrite alteration. Brittle fault zones have locally concentrated or diluted porphyry and epithermal-stage mineralization. Gold is typically refractory, occurring within pyrite, as is the case for other ore zones at Lihir (e.g., Kapit, Ageneau, 2012; Lienetz, Sykora et al., 2018b). However, minor native gold and precious metal tellurides occur locally. In general, gold grade can be correlated with the abundance of pyrite, which can be qualitatively estimated by the hue and shade of the sample (darker gray samples have more disseminated pyrite).

Seven volcanic-hydrothermal breccia bodies were identified at the periphery of the Lihir gold deposit, which define the Lihir diatreme breccia complex. These breccias provide evidence for phreatomagmatic and phreatic activity late in the history of mineralization. Volcanic-hydrothermal activity was focused along N- to NE-trending structures that later controlled the spatial distribution of late-stage gold mineralization in Kapit NE and Kapit. Diatreme volcanism occurred prior to 55 ka, based on radiocarbon dating of charcoal fragments (Table 4.8). The modern, high-temperature geothermal system was most likely established in the Luise amphitheater by the time of diatreme formation, and definitely by 151 ka, based on a K–Ar whole-rock age for an alunite-rich rock (Table 4.11). Modern geothermal activity has produced a layer of steam-heated (argillic and advanced argillic) alteration near surface. Downward percolating steam-heated fluids leached gold from large areas of mineralized rocks, which was reprecipitated within structures in the steam-heated alteration zone.

# CHAPTER 5

# Pyrite Chemistry

## 5.1 Introduction

The purpose of this chapter is to characterize the compositional variability and deportment of gold in pyrite from different paragenetic stages at Kapit NE and Coastal. This is achieved through an unsupervised multivariate statistical analysis of pyrite LA-ICP-MS raster element map and line data, which classifies compositionally similar pyrite into relative groups that can be interrogated in X–Y space.

## 5.2 Methods

### *5.2.1 Sample selection and preparation*

Nine samples from Coastal, 31 samples from Kapit NE and one sample from Minifie were selected for LA-ICP-MS analysis (Appendices A2 and H1; Figure 5.1–5.2; Table 5.1). The samples are representative of each of the five major paragenetic stages of mineralization in Kapit NE and Coastal (Chapter 4; Table 5.1). Two additional samples from Lienetz, which were previously reported in Sykora (2017) and Sykora et al. (2018a), were included for comparative purposes. The samples were cut into 2.54 cm-diameter rounds, mounted in epoxy, polished with 0.25 µm diamond paste, cleaned with methanol and rinsed in warm water at the University of Tasmania lapidary.

### *5.2.2 Pyrite etching*

A subset of the polished mounts was etched using sodium hypochlorite (NaClO; 6–14% w/v of active chlorine) to reveal internal textures. The samples were immersed in NaClO for three minutes, then rinsed in distilled water and air dried. The NaClO functions as an oxidizing agent and tarnishes the surface of pyrite grains. The intensity of the tarnish varies according to the mineral composition, crystal lattice orientation and duration of the etch (Fleet et al., 1993; Peterson and Mavrogenes, 2014). The etched samples were examined under reflected light. Photomicrographs of the etched samples were taken on a Leica DFC420 camera affixed to a Leica DM 6000 M microscope. Some of the images were stitched together to make image mosaics using LEICA QWin Pro V.3 software.

### *5.2.3 LA-ICP-MS raster imaging*

*In situ* analysis of pyrite by LA-ICP-MS was conducted at CODES Analytical Laboratories, University of Tasmania. The analysis was conducted using a RESOlution (Australian Scientific Instruments) 193-nm Excimer laser ablation system with an S155 large format sample cell coupled to an Agilent 7700 ICP-MS. The laser was operated using 10 Hz repetition rate and 2.3 to 2.7 J/cm$^2$ fluence for pyrite measured at the sample surface. A helium flow rate of 0.40 L/min was maintained through the sample cell and mixed with Ar carrier gas at a flow rate of ~1.0 L/min. Thirty-nine elements were analyzed ($^{23}$Na, $^{24}$Mg, $^{27}$Al, $^{29}$Si, $^{34}$S, $^{39}$K, $^{43}$Ca, $^{49}$Ti, $^{51}$V, $^{53}$Cr, $^{55}$Mn, $^{57}$Fe, $^{59}$Co, $^{60}$Ni, $^{65}$Cu, $^{66}$Zn, $^{75}$As, $^{77}$Se, $^{90}$Zr, $^{95}$Mo, $^{107}$Ag, $^{111}$Cd, $^{115}$In, $^{118}$Sn, $^{121}$Sb, $^{125}$Te, $^{137}$Ba, $^{157}$Gd, $^{178}$Hf, $^{181}$Ta, $^{182}$W, $^{195}$Pt, $^{197}$Au, $^{202}$Hg, $^{205}$Tl, $^{208}$Pb, $^{209}$Bi, $^{232}$Th and $^{238}$U). Memory effects and instrumental drift sensitivities were monitored by taking regular measurements of the background and calibration standards before and after analysis of each image. The detection limits for individual elements were estimated from noise-on-gas background for each map and are provided in Appendix H2.

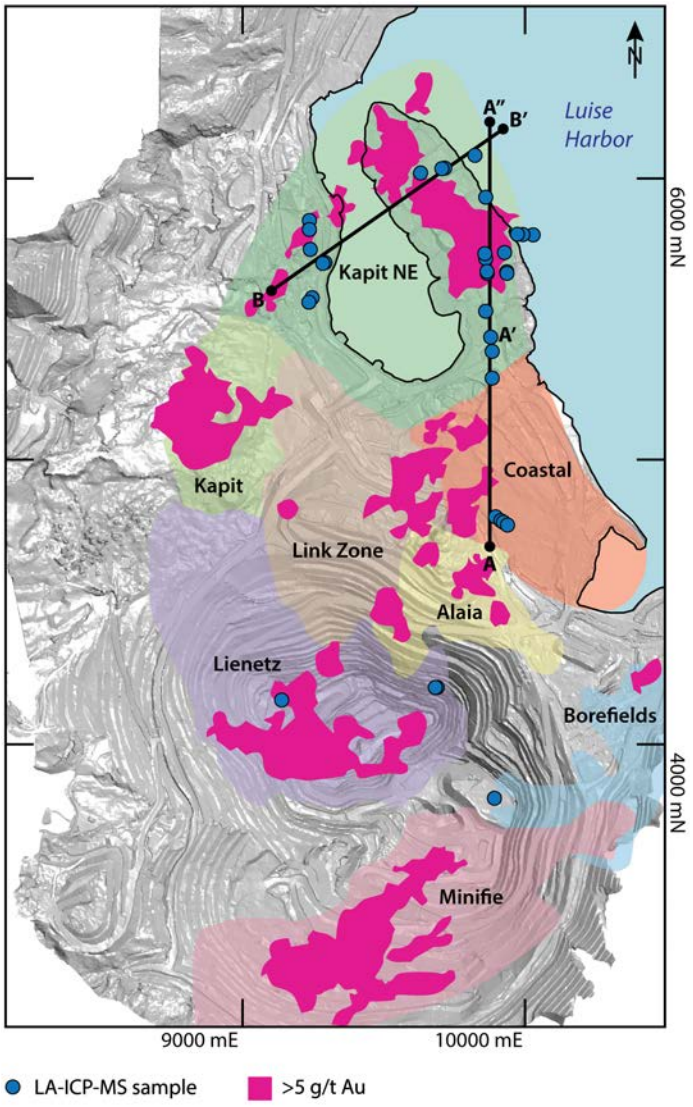


**Fig. 5.1.** Map view of the digital elevation model for the Lihir gold mine (December 2012), showing the locations of the LA-ICP-MS samples, cross sections A–A'–A" and B–B' and the >5 g/t Au grade shells. White areas are outside of the limits of the DEM. The location of LA-ICP-MS samples from Kapit NE and Coastal are also shown in Figure 5.2. Coordinates, descriptions and other sample metadata are provided in Table 5.1 and Appendices A2 and H1.

Measurements below the detection limit threshold values were replaced by half of the detection limit.

For each polished mount, one to three raster images and approximately 10 additional lines were analyzed, totaling 60 images and 413 lines (Table 5.1). Areas corresponding to each map and line are shown on reflected light mosaics for each polished mount in Appendix H1. LA-ICP-MS imaging proceeded by ablating the surface of each pyrite grain following the methods outlined in Large et al. (2009), Danyushevsky et al. (2011), and Gregory et al. (2013). Imaging was conducted using a set of parallel lines with spacing equal to the laser beam size to cover the area of interest. Each line was pre-ablated to remove surface deposition from previous ablations and other surface contaminants. Square laser beams with side lengths ranging from 11 and 25 μm were used, depending on the size and resolution of the image required (Table 5.1). Lines were ablated using a constant scanning speed set at two times the beam size. By mistake, sample DDHL1856 162.8 m was ablated at a speed of 54.8 μm/s instead of 34 μm/s (2× the spot size of 17 μm). The pixels resulting from the increased speed are rectangular (long axis directed along the line; Appendix H1). This has implications for the position at which different elements were detected by the mass spectrometer (e.g., sulfur would be analyzed at a different position within the pixel than potassium). Sample DDHL1856 162.8 has therefore been excluded from further analysis. However, the LA-ICP-MS element maps for this sample are provided in Appendix H1.

Raster images and lines were processed using an unpublished Python script that was developed at the University of Tasmania. The software uses known compositions for reference standards to convert signals collected for each measured element (cps) into concentrations (ppm) and displays this data in X–Y space. Concentrations of lithophile elements were calculated using an in-house glass standard (GSD; Guillong et al., 2005) and chalcophile elements were calculated using a lithium-borate glass standard (STDGL-2b2; Danyushevsky et al., 2011). Due to the high volatility of Hg, it is not included within the reference standards. Therefore, its concentration was not calculated.

### *5.2.4 Statistical analysis*

The statistical analysis of pyrite LA-ICP-MS raster map data used in this study was modified from the workflow described in Ahmed (2019) for the analysis of epidote LA-ICP-MS raster map data, which was based on the methods

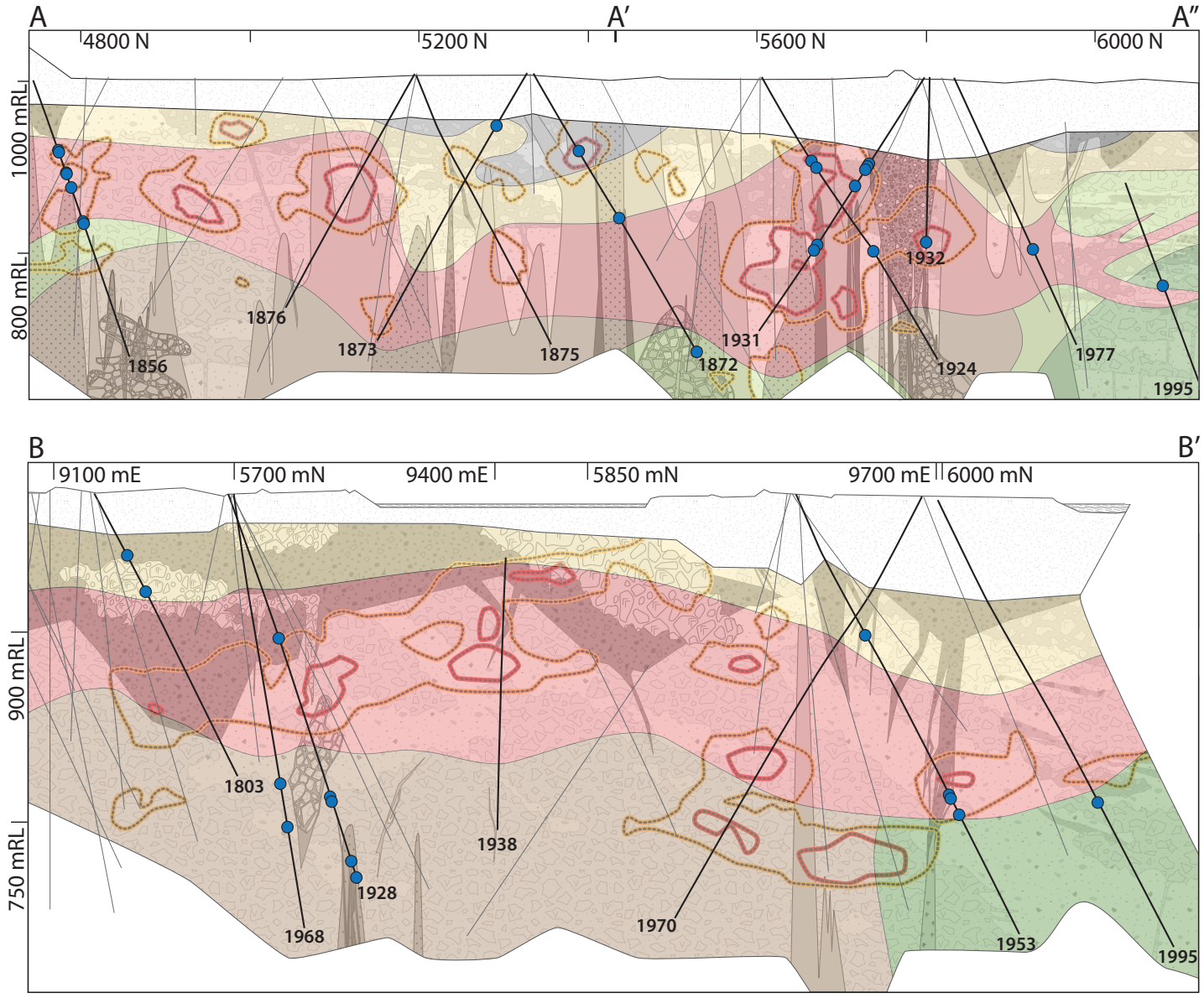


**Fig. 5.2.** Location of LA-ICP-MS samples along cross sections A–A'–A" (*top*) and B–B' (*bottom*). The geology (Chapter 3), pervasive alteration zones (Chapter 4), drill traces and Au grade shells are shown for reference. Coordinates, descriptions and other sample metadata are provided in Table 5.1 (LA-ICP-MS samples) and Appendices A2 and H1.

**Table 5.1.** Locations and descriptions of samples selected for LA-ICP-MS raster imaging. Vein and alteration stages are described in Chapter 4. UTM coordinates are reported in AGD84 (Zone 56S). Mineral abbreviations: ab = albite, ad = adularia, anh = anhydrite, cal = calcite, ccp = chalcopyrite, chl = chlorite, goe = goethite, hem = hematite, ill = illite, ill-sme = illite-smectite, mnt = montmorillonite, mo = molybdenite, mrc = marcasite, or = orthoclase, phl = phlogopite, py = pyrite, qtz = quartz, rt = rutile, tenn-ttr = tennantite-tetrahedrite.

| Sample ID | Location | Easting | Northing | Elevation (m rsl) | Vein stage | Form | Alteration halo | Pervasive alteration | Maps | Lines | Spot size (µm) |
|---|---|---|---|---|---|---|---|---|---|---|---|
| **DDHL1856 111.0** | Coastal | 459960 | 9654802 | – 78 | 3C | Breccia | Ad – py – qtz | A4 | 1 | 13 | 11 |
| **DDHL1856 114.2A** | | 459959 | 9654803 | – 80 | 3C | Breccia | Ad – py – qtz | A4 | 1 | 13 | 11 |
| **DDHL1856 114.2B** | | 459959 | 9654803 | – 80 | 3C | Vein | Ad – py – qtz | A4 | 1 | 13 | 11 |
| **DDHL1856 142.4** | | 459947 | 9654812 | – 104 | 3A | Vein | – | A3 | 1 | 13 | 11 |
| **DDHL1856 143.9** | | 459946 | 9654812 | – 106 | 2D | Gouge | – | A3 | 1 | 13 | 11 |
| **DDHL1856 162.8** | | 459938 | 9654818 | – 122 | 2A, 2D, 3C | Vein | – | A3 | 1 | 10 | 17 |
| **DDHL1856 207.6** | | 459919 | 9654831 | – 161 | 2A, 3A | Vein | – | A3 | 1 | 10 | 17 |
| **DDHL1856 209.8** | | 459919 | 9654832 | – 162 | 2D | Breccia | Py – ad – qtz | A4 | 1 | 13 | 11 |
| **DDHL1873 65.6** | | 459906 | 9655321 | – 51 | 5B, 1E | Vein | Py – goe – ill + rt | A6 | 3 | 0 | 11 |
| **DDHL1803 51.8** | Kapit NE | 459260 | 9655592 | – 40 | 5A | Vein | Py | A6 | 1 | 13 | 11 |
| **DDHL1803 84.5** | | 459268 | 9655605 | – 68 | – | Alteration | – | A6, A3 | 1 | 13 | 11 |
| **DDHL1872 99.0** | | 459907 | 9655417 | – 79 | 5B, 2A | Vein | Py – ccp – tenn-ttr – ad – qtz | A7 | 2 | 10 | 17 |
| **DDHL1872 192.3** | | 459901 | 9655466 | – 158 | 5B, 3C | Breccia | Ad – qtz – ill – py + mnt – mrc – py | A6 | 1 | 10 | 17 |
| **DDHL1872 372.9** | | 459882 | 9655558 | – 313 | 1F | Vein | Chl – or – hem | A1 | 1 | 10 | 17 |
| **DDHL1924 110.8** | | 459958 | 9655693 | – 92 | 2D | Breccia | Anh – py + mnt | A4 | 1 | 10 | 17 |
| **DDHL1924 119.0** | | 459958 | 9655697 | – 99 | 2A | Vein | Py – mrc – ad | A4 | 1 | 10 | 17 |
| **DDHL1924 237.4** | | 459950 | 9655765 | – 195 | 3B | Vein | Qtz – py – ad | A4 | 2 | 10 | 17 |
| **DDHL1928 128.8** | | 459262 | 9655778 | – 106 | 5C | Vein | Py – qtz – cal – ad | A3 | 1 | 10 | 17 |
| **DDHL1928 274.1** | | 459261 | 9655846 | – 234 | 1I, 1G | Vein | – | – | 1 | 10 | 17 |
| **DDHL1928 280.5** | | 459261 | 9655849 | – 239 | 3A, 1E | Vein | Ill-sme + mnt + or – anh – phl – py – mo – ccp | A1 | 1 | 10 | 17 |
| **DDHL1928 344.3** | | 459260 | 9655878 | – 296 | 1E, 1B | Vein | Anh – phl – py – ccp | A1 | 1 | 10 | 17 |
| **DDHL1928 347.1** | | 459260 | 9655880 | – 298 | 1B | Vein | Anh – ab + or + hem + py | A1 | 1 | 10 | 17 |
| **DDHL1931 118.0** | | 459880 | 9655762 | – 97 | 2A | Vein | Py – mrc – ad | A3 | 3 | 9 | 11 |
| **DDHL1931 121.0** | | 459881 | 9655760 | – 100 | 2A | Vein | Py – mrc – ad | A3 | 1 | 0 | 22 |
| **DDHL1931 124.2** | | 459881 | 9655758 | – 102 | 2A | Breccia | Py – mrc – ad | A3 | 1 | 0 | 22 |
| **DDHL1931 149.0** | | 459883 | 9655745 | – 123 | 2A | Vein | Py – mrc – ad | A3 | 2 | 0 | 22 |
| **DDHL1931 230.2** | | 459888 | 9655700 | – 190 | 2A, 3A | Vein | Py – mrc – ad | A3 | 1 | 0 | 15 |
| **DDHL1931 237.1A** | | 459888 | 9655696 | – 196 | 3B | Vein | Qtz – py – ad | A3 | 3 | 14 | 11 |
| **DDHL1931 237.1B** | | 459888 | 9655696 | – 196 | 3B | Vein | Qtz – py – ad | A3 | 2 | 0 | 22 |
| **DDHL1932 225.5** | | 459996 | 9655830 | – 185 | 1I | Vein | – | A3 | 1 | 13 | 11 |
| **DDHL1932 255.0** | | 460013 | 9655829 | – 209 | 3C | Vein | Qtz – py | A3 | 1 | 13 | 11 |
| **DDHL1932 322.8** | | 460050 | 9655829 | – 266 | 3A | Vein | Py – ccp – cal | A3 | 1 | 10 | 25 |
| **DDHL1953 126.7** | | 459652 | 9656047 | – 103 | 3B | Vein | Qtz – mrc – py – ad | A6 | 1 | 10 | 25 |
| **DDHL1953 275.2** | | 459728 | 9656062 | – 230 | 4C, 3C | Breccia | – | A5 | 2 | 10 | 17 |
| **DDHL1953 278.5** | | 459729 | 9656062 | – 233 | 3C | Breccia | – | A5 | 2 | 10 | 17 |
| **DDHL1953 293.7** | | 459737 | 9656064 | – 246 | 3B | Vein | – | A3 | 1 | 10 | 25 |
| **DDHL1968 232.6** | | 459306 | 9655728 | – 221 | 2D | Gouge | – | A1 | 3 | 7 | 11 |
| **DDHL1968 267.7** | | 459313 | 9655729 | – 255 | 3A, 1G | Vein | – | – | 1 | 10 | 17 |
| **DDHL1977 216.2** | | 459883 | 9655961 | – 192 | 3A | Vein | Py – ccp | A3 | 1 | 13 | 11 |
| **DDHL1995 273.2** | | 459845 | 9656109 | – 236 | 2D | Fault | Py – chl– ad – ill – mo | A3 | 1 | 10 | 17 |
| **DDHL0791 226.8** | Lienetz | 459162 | 9654188 | – 179 | $V4_{quartz}$ [1] | Vein | – | – | 3 | 10 | 11 |
| **LI12EL002A** | | 459707 | 9654229 | – 202 | $Bx3_{py-adu}$ [2] | Breccia | Ad ± qtz ± ill | – | 1 | 10 | 13 |
| **LI12EL002B** | | 459712 | 9654229 | – 202 | $Bx3_{py-adu}$ [2] | Breccia | Ad ± qtz ± ill | – | 1 | 10 | 13 |
| **LI12EL005** | Minifie | 459914 | 9653835 | – 133 | – | Alteration | – | A3 | 1 | 10 | 13 |

[1]Quartz – anhydrite veins, breccia veins, and vug fill ($V4_{quartz}$; Sykora, 2017); [2]Pyrite – adularia-cemented breccias ($Bx3_{py-adu}$; Sykora, 2017; Sykora et al, 2018a and b).

for the principal component analysis of pyrite LA-ICP-MS spot data from Román et al. (2018) and cluster analysis of principal components by Gazley et al. (2015). Data compilation was conducted in Microsoft Excel. Data transformations and statistical analysis were performed using ioGAS.

LA-ICP-MS raster map data were compiled into three CSV files due to the large size of the dataset and imported into ioGAS. Compiled data were filtered for pixels composed of pyrite (and compositionally equivalent marcasite) using probability plots (Fe >35 wt%, S >43 wt%). Analyses of mineral inclusions smaller than the pixel width used (Table 5.1) were not filtered out of the dataset. Filtered pixels were visualized in map space and compared to reflected light images to ensure that all other mineral phases were excluded. Values for 21 elements (i.e., those known to substitute into pyrite: Ag, As, Au, Bi, Cd, Co, Cr, Cu, In, Mn, Mo, Ni, Pb, Sb, Se, Sn, Te, Tl, V, W, and Zn) for each pixel of pyrite were exported and combined into a spreadsheet. Values for mercury were not included, since the data were not able to be converted from cps and are therefore not comparable with the rest of the dataset. The values were compared against the maximum detection limit determined for each element. Eleven elements had more than 50% of the data above the maximum detection limit and were selected for statistical analysis (i.e., Ag, As, Au, Co, Cu, Mn, Pb, Tl, V and Zn; Appendix H2). The pyrite-only data was subjected to a centered log-ratio (CLR) transformation to eliminate closure effects and resultant spurious correlations. These data were then normalized using a Z-score transformation, which sets the mean of the dataset to zero and the standard deviation to one.

Principal component analysis (PCA) was undertaken on the transformed data to reduce the dimensionality of the dataset for cluster analysis. The results of the PCA were visualized in X–Y space. K-means clustering was then applied to the principal components. The number of principal components used in the cluster analysis was chosen as the minimum number required to account for at least 90% of the total variance in the dataset. The number of random starting positions was set at 50 and the maximum number of clusters was set at 12. The number of clusters (K) selected for K-means cluster analysis was determined using the elbow method. The clusters were then interrogated in X–Y space to assess spatial continuity and to relate the clusters with pyrite types and textures within the context of the hydrothermal paragenesis described in Chapter 4. Tukey box plots for the transformed data used in the cluster analysis, grouped by cluster, were used to determine the relative abundances of elements in different clusters. Tukey box plots for mercury (in cps) and elements with less than half of the values below the maximum detection limit (in ppm), colored by cluster, were used to evaluate potential correlations between cluster types and element concentrations. Due to the positive skew of the untransformed data, the y-axis was logged to allow improved visualization of the data distribution.

## 5.3 Results

Univariate LA-ICP-MS element maps and lines for all samples are included in Appendix H1. In this appendix, LA-ICP-MS images for Au have been placed in position on reflected light mosaics to provide spatial and textural context for the element maps. Concentration data (ppm) for each pixel associated with the LA-ICP-MS element maps are tabulated in Appendix H3.

### *5.3.1 Principal component analysis*

Eleven elements were considered in the PCA (Ag, As, Au, Co, Cu, Mn, Pb, Sb, Tl, V, Zn), as these elements display the highest variance and have a high proportion of values above the detection limit. Nine of the elements have at least 70% of values above the detection limit (Ag, As, Au, Cu, Mn, Pb, Sb, Tl, V), and the remaining two elements (Co and Zn) have >50% of values above detection limit (Appendix H2).

A full report for the results of the PCA is provided in Appendix H4. Principal component (PC) values for each pixel are provided in Appendix H5 and ranked variable principal component maps are included for all samples in Appendix H6. Scaled coordinates that define the principal components are presented in Table 5.2, Figure 5.3A–D and Appendix H4. The scree plot for the PCA (Fig. 5.3A) and table of eigenvalues for the eleven principal components (Table 5.3) show that PC1, PC2 and PC3 account for the majority of variance in the dataset (73%). Principal component 1 has an eigenvalue of 4.79 and accounts for 44% of variance of the eleven elements considered (Table 5.3). High PC1 values are associated with elevated concentrations of Pb, Co, Cu and Ag, moderate concentrations of V and Au, and low concentrations of Tl, As, Sb, Zn and Mn (Table 5.2; Fig. 5.3B and C). Principal component 2 has an eigenvalue of 2.31 and accounts for 21% of variance (Table 5.3). High PC2 values indicate elevated concentrations of Au, Ag, Sb, Tl and As, moderate concentrations of Pb and Cu, and low concentrations of Zn, Co, Mn and V (Table 5.2; Fig. 5.3B and D). Principal component 3 accounts for 9% of variance (Table 5.3). High PC3 values are associated with elevated concentrations of Cu, As, Co, Ag and Zn, moderate concentrations of Mn, Pb and Tl, and low concentrations of V, Au, and Sb (Table 5.2; Fig. 5.3C and D).

### *5.3.2 Cluster analysis*

Principal component 1 through PC7 were used in the K-means cluster analysis, because they account for almost all (>90%) of the variance in the dataset (Table 5.2). The number of clusters (k) selected for K-means clustering was determined from Figure 5.4 using the elbow method. The most significant change in slope of the sum of squares and Delta lines occurs where k = 6, suggesting that six is the number of discrete groups that will extract the maximum number of features from the dataset. Therefore, six clusters were selected for K-means clustering.

A principal component biplot (RQ1 vs. RQ2) for transformed pyrite concentration data, colored by cluster, is presented in Figure 5.5. Tukey box plots for each PC grouped by cluster are presented in Appendix H8. Clusters 1 and 6 are strongly controlled by PC1 (Fig. 5.5). Cluster 1 is associated with high PC1 values and Cluster 6 is associated with low PC1 values. Clusters 2 and 3 are strongly controlled by PC2 (Fig. 5.5). Cluster 2 is associated with high PC2 values and Cluster 3 is associated with low PC2 values. Cluster 4 is most influenced by its positive correlation with PC1 and PC2, and Cluster 5 is most influenced by its negative correlation with PC1 (Fig. 5.5, Appendix H8).

Tukey box plots of CLR-transformed and Z-score nor-

**Table 5.2.** Scaled coordinates for the principal component analysis. The elements have been subjected to a centered log ratio transformation and have been Z-score normalized. For each principal component, elements are listed in order from highest to lowest values.

| PC1 | | PC2 | | PC3 | | PC4 | | PC5 | | PC6 | | PC7 | | PC8 | | PC9 | | PC10 | | PC11 | |
|---|---|---|---|---|---|---|---|---|---|---|---|---|---|---|---|---|---|---|---|---|---|
| Pb | 0.85 | Au | 0.77 | Cu | 0.31 | Mn | 0.50 | Ag | 0.39 | As | 0.34 | Ag | 0.28 | Cu | 0.20 | Mn | 0.22 | Sb | 0.29 | Co | $3.89 \times 10^{-8}$ |
| Cu | 0.81 | Ag | 0.54 | As | 0.19 | Ag | 0.31 | As | 0.31 | Co | 0.31 | Tl | 0.16 | Zn | 0.14 | Cu | 0.13 | Ag | 0.08 | Tl | $3.03 \times 10^{-8}$ |
| Co | 0.62 | Sb | 0.46 | Co | 0.16 | Au | 0.29 | V | 0.25 | Au | 0.14 | Co | 0.16 | Tl | 0.12 | Tl | 0.13 | Mn | 0.06 | Pb | $2.89 \times 10^{-8}$ |
| Ag | 0.58 | Tl | 0.34 | Ag | 0.15 | Zn | 0.16 | Cu | 0.08 | Ag | 0.09 | Pb | 0.06 | Co | 0.12 | Sb | 0.10 | Zn | 0.05 | Zn | $2.71 \times 10^{-8}$ |
| V | 0.21 | As | 0.18 | Zn | 0.15 | Cu | 0.00 | Zn | 0.05 | Mn | 0.08 | Zn | 0.04 | Ag | 0.08 | V | 0.05 | Co | 0.03 | Mn | $2.65 \times 10^{-8}$ |
| Au | 0.19 | Pb | 0.02 | Mn | 0.10 | V | -0.01 | Pb | -0.02 | V | 0.03 | Sb | 0.01 | V | 0.07 | Ag | 0.03 | Au | 0.00 | Ag | $2.64 \times 10^{-8}$ |
| Mn | -0.62 | Cu | 0.02 | Pb | -0.02 | Tl | -0.09 | Sb | -0.06 | Tl | -0.14 | Mn | -0.05 | Au | 0.04 | Co | 0.01 | V | -0.01 | Cu | $2.59 \times 10^{-8}$ |
| Zn | -0.66 | V | -0.46 | Tl | -0.03 | Pb | -0.13 | Tl | -0.08 | Sb | -0.19 | V | -0.07 | Sb | -0.01 | Pb | -0.08 | Cu | -0.02 | Au | $2.40 \times 10^{-8}$ |
| Sb | -0.72 | Mn | -0.49 | Sb | -0.11 | As | -0.22 | Mn | -0.13 | Cu | -0.21 | Au | -0.15 | As | -0.16 | As | -0.10 | As | -0.06 | As | $2.32 \times 10^{-8}$ |
| As | -0.76 | Co | -0.53 | Au | -0.28 | Co | -0.32 | Co | -0.27 | Zn | -0.25 | As | -0.23 | Mn | -0.20 | Au | -0.18 | Pb | -0.07 | Sb | $2.31 \times 10^{-8}$ |
| Tl | -0.84 | Zn | -0.57 | V | -0.82 | Sb | -0.34 | Au | -0.36 | Pb | -0.26 | Cu | -0.38 | Pb | -0.43 | Zn | -0.32 | Tl | -0.29 | V | $2.24 \times 10^{-8}$ |

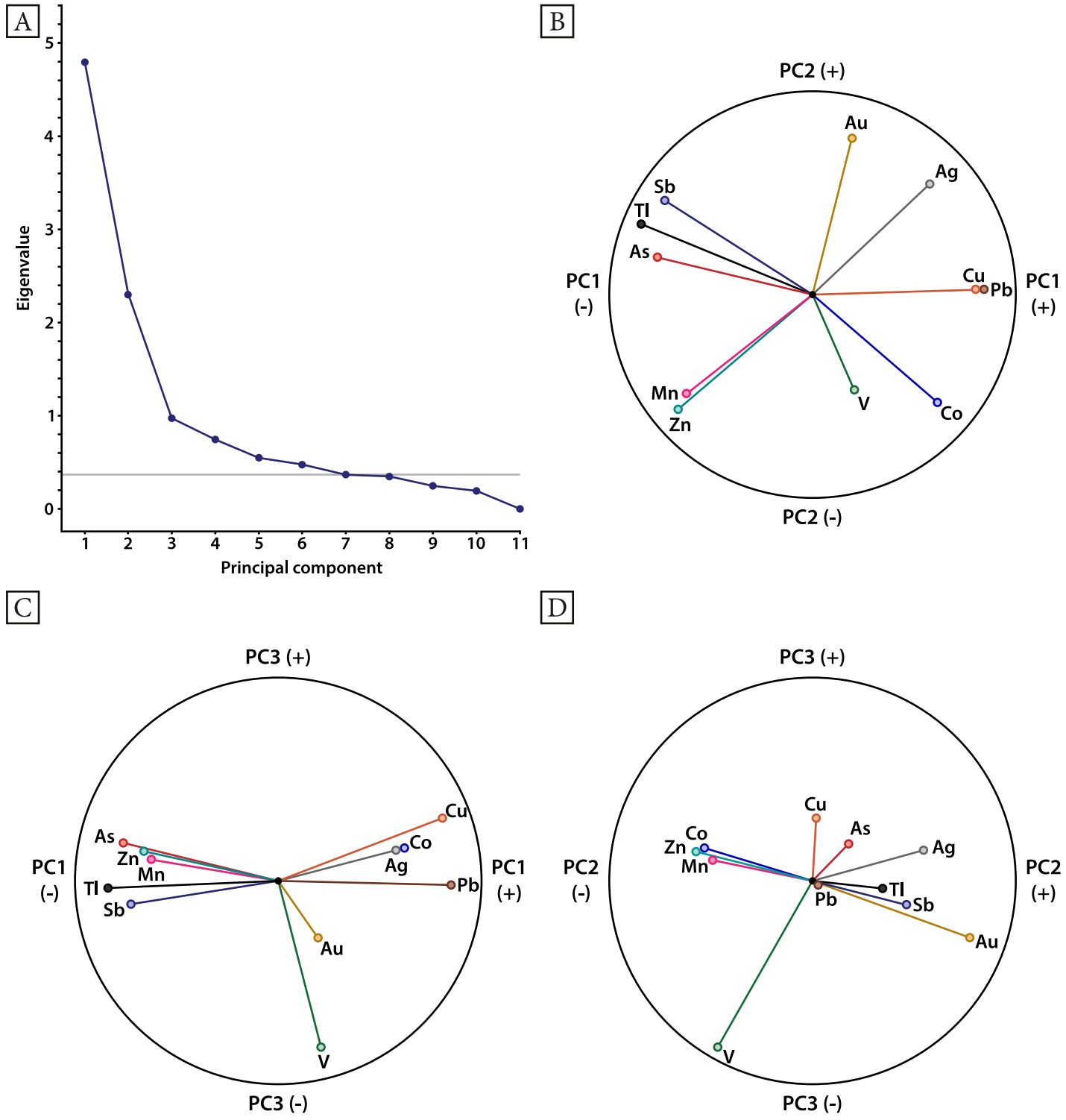


**Fig. 5.3.** Results from the principal component analysis. A full report is provided in Appendix H4 and principal component values for each pixel are provided in Appendix H5. **A.** Scree plot for the principal component analysis, showing eigenvalues determined for each principal component. The gray line is aligned with the first principal component with a cumulative percentage contribution >90%. **B., C.** and **D.** Scaled coordinate values for PC1 vs. PC2, PC1 vs. PC3 and PC2 vs. PC3, respectively. Scaled coordinates for all of the principal components are reported in Table 5.3 and Appendix H4.

**Table 5.3.** Eigenvalues for the eleven principal components defined in the PCA. Also reported are the percentage of variance accounted for by each principal component and the cumulative percentage with each successive principal component.

| Principal Component | Eigenvalue | Percent | Cumulative Percentage |
|---|---|---|---|
| 1 | 4.79 | 44 | 44 |
| 2 | 2.31 | 21 | 65 |
| 3 | 0.97 | 9 | 73 |
| 4 | 0.74 | 7 | 80 |
| 5 | 0.55 | 5 | 85 |
| 6 | 0.48 | 4 | 89 |
| 7 | 0.37 | 3 | 93 |
| 8 | 0.35 | 3 | 96 |
| 9 | 0.25 | 2 | 98 |
| 10 | 0.19 | 2 | 100 |
| 11 | $8.22 \times 10^{-15}$ | 0 | 100 |

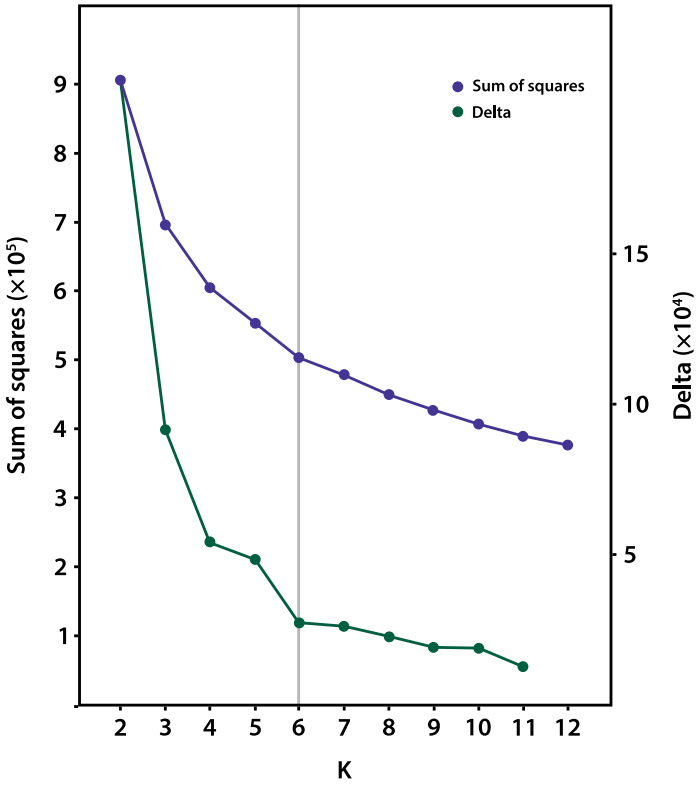


**Fig. 5.4.** Line graph used to select the number of clusters for K-means cluster analysis. The line graph shows the sum of squares of the distances of the data points to the mean of their respective cluster, and delta, the difference between the total sum of squares, as the number of clusters (K) increases. According to the elbow method, the flattening of the slope of both the sum of squares and delta lines at K = 6, suggests that six is the optimal number of clusters to select for K-means cluster analysis.

malized concentration data for elements used in the statistical analysis, grouped by cluster, are presented in Appendix H9. Tukey box plots of concentration data for Au and for trace elements not included in the statistical analysis, grouped by cluster, are also presented in Appendix H9. The Tukey boxplot for Hg uses concentration data in cps, however, this type of data is sufficient to provide information about the relative enrichment or depletion of Hg between clusters. Summary statistics for the concentrations of all 21 elements of interest in pyrite are tabulated in Appendix H9. The geochemical characteristics of each pyrite cluster as determined via interrogation of the Tukey box plots is summarized in Table 5.4. A mean concentration parallel coordinates plot for elements determined to display significant variation between clusters is provided in Figure 5.6 and also describes the geochemical characteristics of the pyrite clusters. Overall, concentrations of elements in the pyrites analyzed range from below detection limit values up to several percent (Appendix H9). Orders of magnitude differences in elemental concentrations exist both between and within pyrite grains (Appendix H1). Spurious high concentrations of base metals are interpreted to reflect micro-inclusions of sulfide minerals. For example, the maximum concentration of Cu (3.9%) in a pixel of Cluster 1 pyrite is interpreted to reflect analysis of an inclusion of chalcopyrite. The highest mean concentrations of elements range from near detection limit values (e.g., 0.08 ppm In) to greater than one percent (e.g., 1.5% As). Orders of magnitude differences in mean elemental concentrations exist between pyrite clusters (Fig. 5.6).

Clusters 1 and 3 are low in total trace elements, with mean values of ~0.4 wt% and ~0.7 wt%, respectively. Clusters 2, 4, 5 and 6 contain an order of magnitude greater concentration of total trace elements than Clusters 1 and 3, with Cluster 2 containing the highest mean value (~3.1 wt%; Table 5.4; Appendix H10). Clusters 4 and 5 are the most abundant pyrite clusters and have been assigned to over half of all pixels (54% of pixels). Cluster 6 is the least abundant cluster (8% of pixels; Table 5.4). Three clusters are associated with high concentrations of Au: Cluster 2 ($\bar{x}$ = 46.21 ppm Au), Cluster 4 ($\bar{x}$ = 60.50 ppm Au) and Cluster 5 ($\bar{x}$ = 40.73 ppm Au; Table 5.4; Appendix H9). Cluster 2 has a composition dominated by high Ag and Au and has low

**Table 5.4.** Characteristics of pyrite clusters. Note that Cd, In, Sn, and W had very low overall concentrations in pyrite and did not show significant variation between pyrite clusters (Appendix H9). Therefore, these elements are not considered characteristic of any particular pyrite cluster.

| Cluster | Color | Association | Pixel count | % | Total trace elements (ppm)[1] | % of pixels above Au solubility curve[2] | Au (ppm) | | Elements in PCA | | Elements excluded from PCA | |
|---|---|---|---|---|---|---|---|---|---|---|---|---|
| | | | | | | | Mean | Median | High[3] | Low[4] | High[3] | Low[4] |
| 1 | Red | Porphyry | 13,846 | 11 | 6,675 | 0.6 | 1.52 | 0.30 | ***Cu, Co, Pb,*** Ag | ***Sb, Tl,*** As, Au, Mn, V, Zn | ***Bi, Se,*** Te, Ni | ***Hg,*** Mo |
| 2 | Yellow | Epithermal | 31,960 | 25 | 31,784 | 0.2 | 46.21 | 19.61 | ***Ag, Au,*** Tl, As, Sb | ***Co, V,*** Pb, Zn | Mo, Te | Ni, Bi |
| 3 | Green | Porphyry | 20,154 | 16 | 4,183 | 0.4 | 3.50 | 0.61 | V, Co, Pb, Mn | ***As,*** Sb, Tl, Au, Ag | ***Ni, Cr,*** Mo | Se, Hg |
| 4 | Light blue | Epithermal | 37,116 | 29 | 18,160 | 2.9 | 60.50 | 25.64 | Pb, Ag, Au, Co, Cu | ***Mn, Zn,*** As | ***Mo, Te,*** Cr, Bi, Ni | |
| 5 | Dark blue | Epithermal | 16,280 | 13 | 18,314 | 1.6 | 40.73 | 1.90 | Tl, Sb, Mn, As, Zn, Au | ***Ag,*** Pb, Cu, Co | ***Hg,*** Se | Mo, Ni, Cr, Bi |
| 6 | Purple | Epithermal | 10,547 | 8 | 20,776 | 0.0 | 0.08 | 0.00 | ***Zn, As, Mn, Tl, Sb*** | ***Au, Cu, Pb,*** Ag, Co | Hg | ***Te, Se, Ni, Mo, Cr, Bi*** |

[1]Mean total content for 21 elements in pyrite (ppm). Calculations provided in Appendix H10.
[2]As defined in Reich et al. (2005; Fig. 5.7).
[3]Elements listed in order of decreasing contribution to each cluster, then in order of decreasing abundance. Elements in bold italic font have the strongest positive correlation with that cluster or highest mean concentration (ppm).
[4]Elements listed in order of decreasing contribution to each cluster, then in order of increasing abundance. Elements in bold italic font have the strongest negative correlation with that cluster or lowest mean concentration (ppm).

values of Co and V. Cluster 4 is defined by high Pb, Ag, Au, Mo and Te, with low Mn and Zn. Cluster 5 is Tl-, Sb- and Hg-rich, with low Ag. Clusters 1 and 3 contain elevated Co and Ni, are rich in base metals (Cu, Co, Pb) and contain low As, Sb, Tl, Hg and Au. Cluster 1 is associated with high Ag. Cluster 6 does not contain Au (values below or just above detection limit). It is associated with high concentrations of Zn, As, Mn, Tl, Sb and Hg, and has low Ag, Te, Se, Ni, Mo, Cr and Bi concentrations.

## 5.4 Discussion

### *5.4.1 Gold deportment*

LA-ICP-MS pyrite data for each cluster was plotted on a Au–As scattergram showing the Au solubility curve as defined in Reich et al. (2005; Fig. 5.7). The curve represents the solubility limit of Au as a function of As concentrations. Data points above the curve indicate micro- to nano-scale inclusions of $Au^0$ in pyrite, whereas data points below the line indicate either pyrite that: (1) contains $Au^+$ in the crystal lattice, (2) contains $Au^0$ in inclusions that are undetectable at the spot sizes used in this study, or (3) does not contain Au. The majority of data for all clusters plots below the Au solubility curve, inferring Au most commonly occurs as a structurally bound element ($Au^+$) in pyrite. Clusters 1–5 contain a small proportion of data that plot above the Au solubility curve (e.g., up to a maximum of 2.9% in Cluster 4; Fig. 5.7; Table 5.4).

Kapit NE and Coastal samples containing pyrite concentration data that plots above the Au solubility curve are from Stages 2D, 3A–C and 5B. A sample from a stage $V4_{qtz}$ quartz vein from Lienetz (DDHL0791 226.8 m; equivalent to Stage 3B) also plots above the curve. This is consistent with petrographic and SEM observations that native gold, electrum and/or precious metal tellurides occur in Stage 3A and 3B (Figs. 4.24–4.26) and $V4_{qtz}$ veins (Sykora et al., 2018b). A ternary plot of Ag–Au–Te for all data points that plot above the curve, colored by cluster (Fig 5.8), confirms that there are at least three types of inclusions: (1) Te-rich inclusions with variable proportions of Ag and Au (precious metal tellurides and/or native tellurium); (2) Te-poor inclusions with variable proportions of Ag and Au (electrum and/or native silver); and (3) Au-rich inclusions with low proportions of Ag and Te (native gold). The Te-rich inclu-

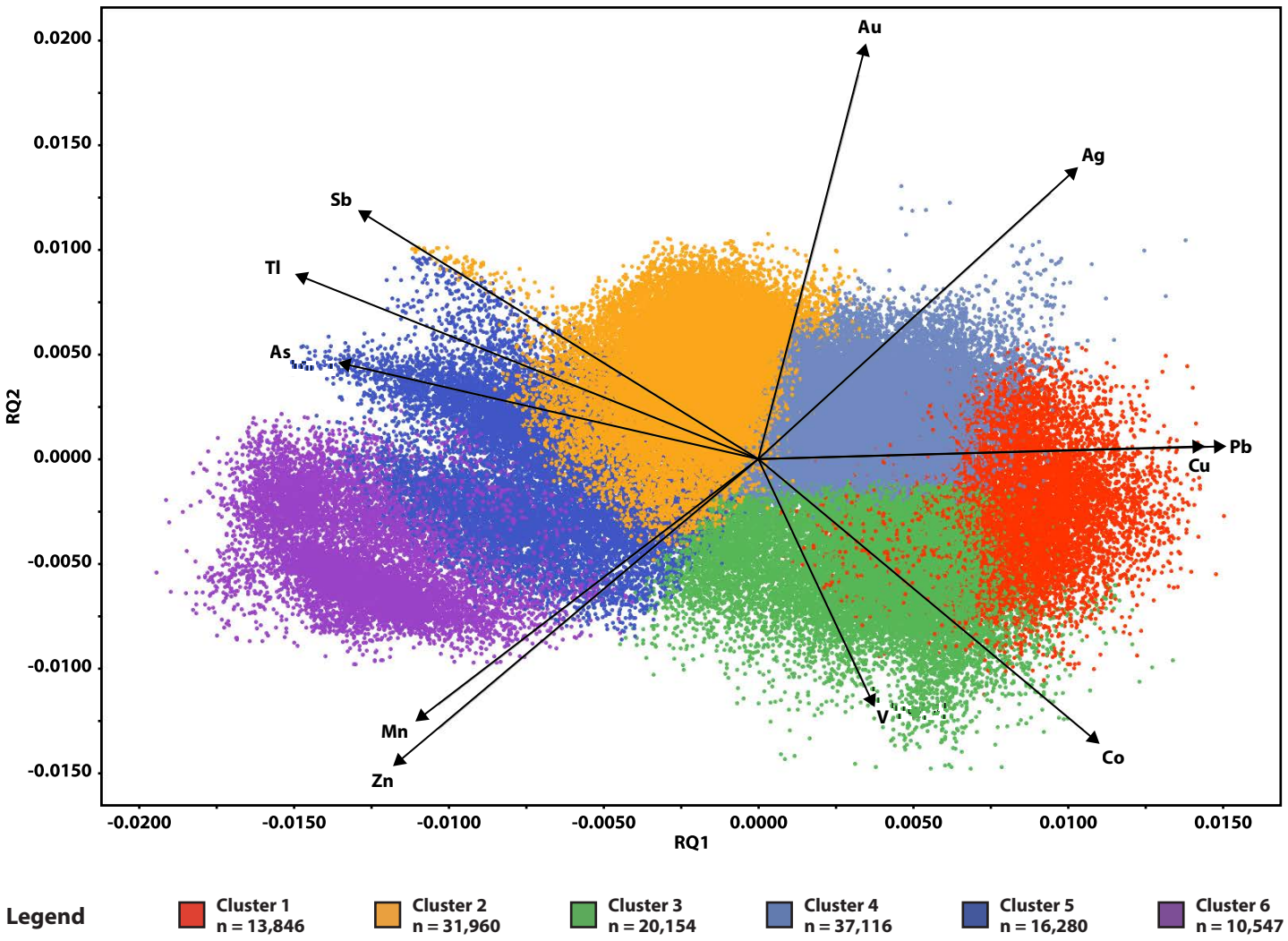


**Fig. 5.5.** Principal component biplot for CLR-transformed and Z-score normalized pyrite concentration data, colored by K-means cluster. The arrows show the geochemical relationship between different elements with respect to RQ1 and RQ2, the loadings of PC1 and PC2, respectively.

sions typically have a higher proportion of Ag compared to Au (Fig. 5.8). Cluster 5 contains only native gold inclusions with >95% Au (Fig. 5.8). In Clusters 1–4, precious metal telluride inclusions are most abundant. Clusters 1 and 3 also contain minor native silver, native tellurium and electrum inclusions. Clusters 2 and 4 also contain native gold and electrum, typically with >60% Au (Fig. 5.8).

### *5.4.2 Geological significance of K-means pyrite clusters*

LA-ICP-MS raster maps colored by K-means cluster are presented in Figures 5.9–5.13 (representative samples) and Appendix H11 (all samples). The number and percentage of pixels assigned to different K-means pyrite clusters for each sample and for each stage of the paragenesis (Chapter 4) is tabulated in Appendix H12 and summarized in Table 5.5. The overprinting relationships between pyrite clusters were documented for each sample through observation of the textural characteristics of K-means cluster maps in comparison with hand sample photographs and reflected light images (Appendix H1, H11–H12). The resultant paragenesis of pyrite clusters is presented in Figure 5.14.

Cluster 1 and Cluster 3 pyrite commonly occur together and display similar textural characteristics. They form relatively coarse-grained cubic crystals or massive anhedral

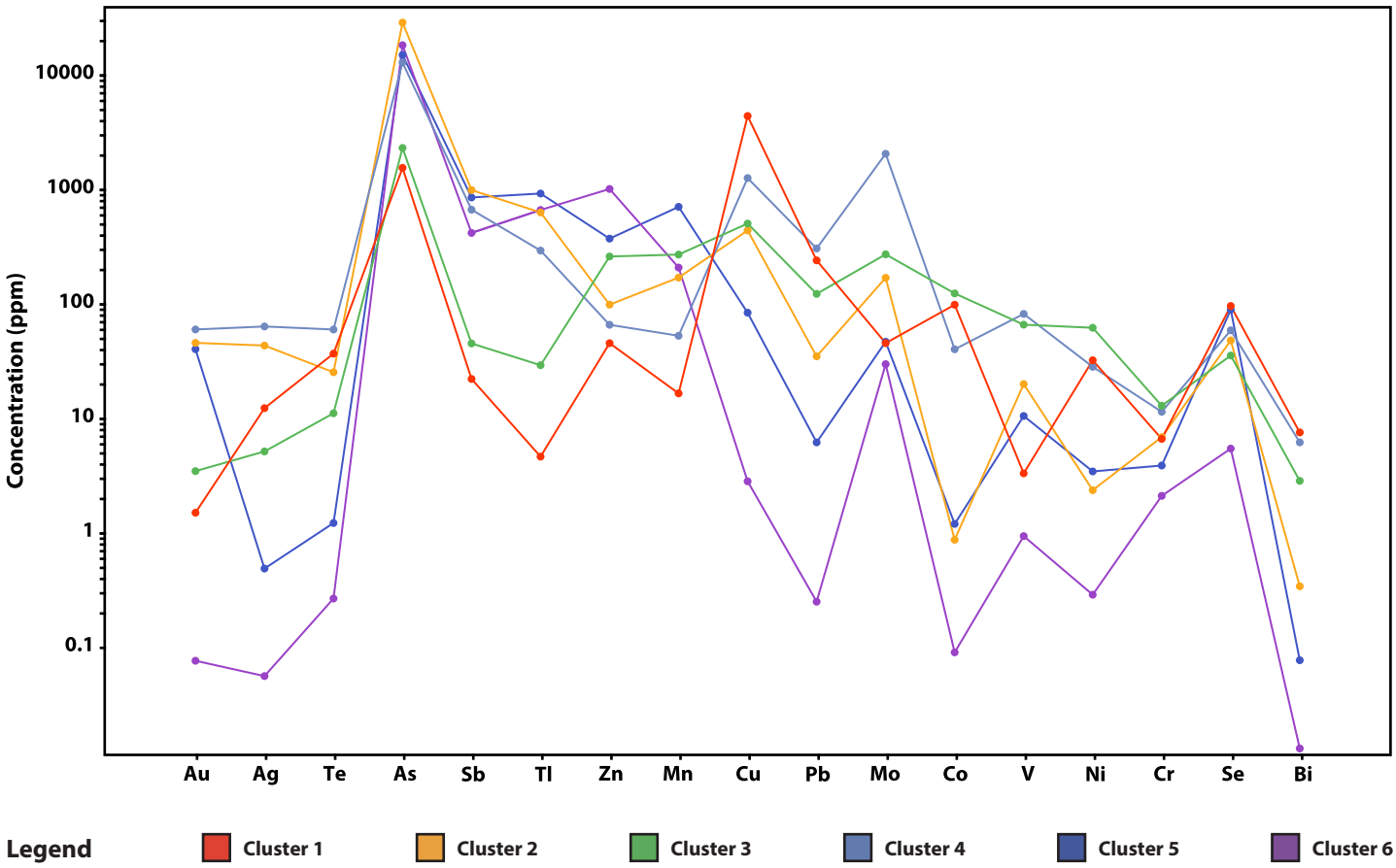


**Fig. 5.6.** Concentration parallel coordinate plot for selected minor and trace elements in K-means pyrite clusters identified in this study. Nodes along the line correspond to the mean concentration (ppm) of a particular element in that cluster.

aggregates (Appendix H11). Some crystals are zoned, from a core of Cluster 1 pyrite to an outer margin of Cluster 3 pyrite (e.g., Fig. 5.12C). Corrosion textures, such as rounded margins, small pits and/or larger vugs, are common (e.g., Fig. 5.13B and F). Mineral inclusions observed include chalcopyrite, sphalerite, galena, magnetite, telluride minerals and electrum. Cluster 1 and Cluster 3 pyrites typically form the cores of composite grains and are rimmed by later generations (e.g., Cluster 4, Fig. 5.9F; Cluster 2 and 5, Fig. 5.12C).

Stage 1 samples (n = 4) contain dominantly Cluster 1 (69%) and/or Cluster 3 pyrite (25%; Table 5.5; Appendix H11 and H12). Some pyrites in Stage 1 veins have rims of Cluster 4 (Appendix H11 and H12), which likely crystallized during an overprinting alteration event. It is interpreted that Cluster 1 and Cluster 3 pyrite formed under porphyry-style conditions, due to their association with Stage 1 anhydrite veins and high-temperature minerals (e.g., biotite, magnetite, orthoclase, etc.; Chapter 4). Stage 2–5 vein and breccia samples and stage A4 and A6 alteration samples contain substantial proportions of Cluster 1 and Cluster 3 pyrite (Table 5.5), which is interpreted to have been deposited during the porphyry stage associated with Stage 1 veins or stage A1–A2 alteration. This interpretation is made based on the observation that Cluster 1 and Cluster 3 pyrite are typically partly replaced by Cluster 2, 4, 5 or 6 pyrite or occupies the core of composite pyrite grains (e.g., Fig. 5.12C). Cluster 1 and Cluster 3 pyrite have also been incorporated as clasts into Stage 2D fault zones, Stage 3 quartz – chalcedony-cemented breccias and Stage 4 volcanic-hydrothermal breccias (Appendix H1 and H12). For example, in a sample from a Stage 2D fault zone (Fig. 5.9A and C), Cluster 1 and Cluster 3 are associated with pyrite

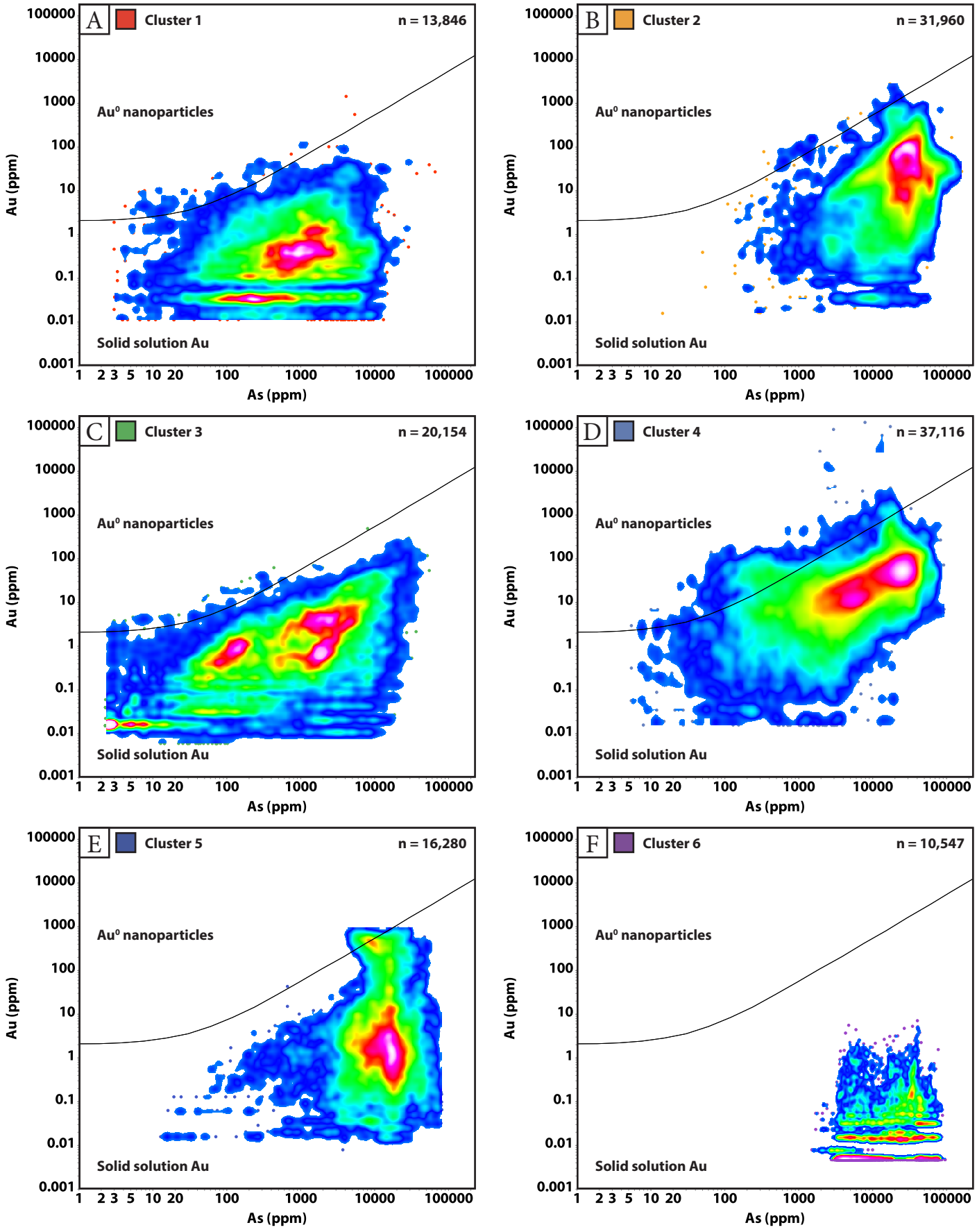
A
Cluster 1
n = 13,846
B
Cluster 2
n = 31,960
C
Cluster 3
n = 20,154
D
Cluster 4
n = 37,116
E
Cluster 5
n = 16,280
F
Cluster 6
n = 10,547
Au⁰ nanoparticles
Solid solution Au
Au (ppm)
As (ppm)
100000
10000
1000
100
10
1
0.1
0.01
0.001
1 2 3 5 10 20 100 1000 10000 100000

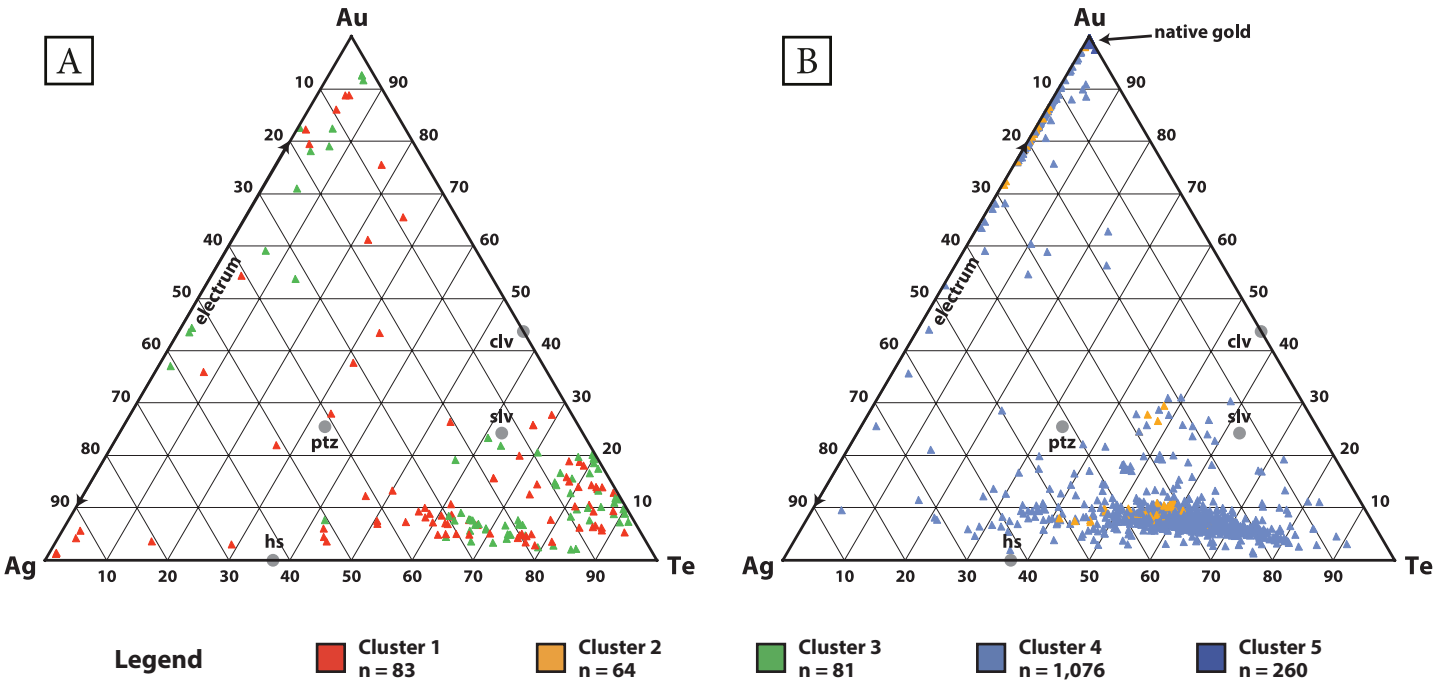


**Fig. 5.8.** Ag–Au–Te ternary plots for pyrite LA-ICP-MS data that plot above the Au solubility curve (Fig. 5.7). The data points have been colored by K-means pyrite cluster. Electrum plots along the Ag–Au axis and has >20% Ag, whereas native gold has <20% Ag. Mineral nodes for common precious metal tellurides have also been plotted (*gray circles*). **A.** Porphyry-stage pyrite clusters (Clusters 1 and 3). **B.** Epithermal-stage pyrite clusters (Clusters 2, 4 and 5). All of the Cluster 5 data plots in the field for native gold. Abbreviations: clv = calaverite, hs = hessite, ptz = petzite, slv = sylvanite.

from Stage 1G vein clasts, whereas Cluster 4 is associated with Stage 2D marcasite.

Cluster 2, 4, 5 and 6 pyrites are visually distinct from Cluster 1 and 3 pyrite; however, they display a wide range of crystal habits and textures. They may form individual or aggregated, fine-grained crystals with octahedral, pyritohedral, tabular, acicular or dendritic habit (Appendix H1 and H11). The crystals commonly have a porous, spongy texture and contain abundant inclusions of wallrock, pyrite (Cluster 1 or Cluster 3), chalcopyrite, galena, sphalerite, telluride minerals, rutile, gold and/or electrum. Single acicular crystals can appear randomly oriented (e.g., Fig. 5.11A and C) or aligned (Fig. 5.9A and E). Acicular and elongate crystal aggregates form banded rims (e.g., Fig. 5.12A and C), colloform banded vein infill or cockade textured cement with oscillatory zonation (e.g., Figs. 5.10A and C, and 5.13A and E). There does not appear to be a difference between epithermal-stage pyrite grains compared to the epithermal-stage banded rims of composite pyrite grains; both styles of epithermal pyrite may consist of Cluster 2, 4, 5 and/or 6 pyrite in variable proportions.

Cluster 2, 4, 5 and 6 pyrites are associated with Stage 2 (n = 8), Stage 3 (n = 17), Stage 4 (n = 1) and Stage 5 (n = 8) samples (Table 5.5) and are therefore interpreted to have been deposited under epithermal conditions. Each of the epithermal stages (Stage 2–5) display a characteristic progression from Cluster 4 to Cluster 2 to Cluster 5 pyrite (e.g., Fig. 5.11C; Appendix H12), demonstrating that there was a repeated compositional evolution of the mineralizing fluids throughout the epithermal life cycle. This may indicate that

**Fig. 5.7.** (*Previous page*) Arsenic vs. Au diagrams for pyrite clusters identified in this study. The diagrams show the Au solubility curve as defined by Reich et al. (2005), which represents the solubility limit of Au as a function of As concentrations. The curve is defined by the equation $C_{Au} = 0.02 \times C_{Au} + 4 \times 10^{-5}$. Data that plot above the Au solubility curve indicate $Au^0$ occurring as nanoparticles in pyrite, whereas data that plot below the curve indicate $Au^+$ occurring in the crystal lattice of pyrite (Reich et al., 2005; Román et al., 2018). **A.** Cluster 1. **B.** Cluster 2. **C.** Cluster 3. **D.** Cluster 4. **E.** Cluster 5. **F.** Cluster 6.

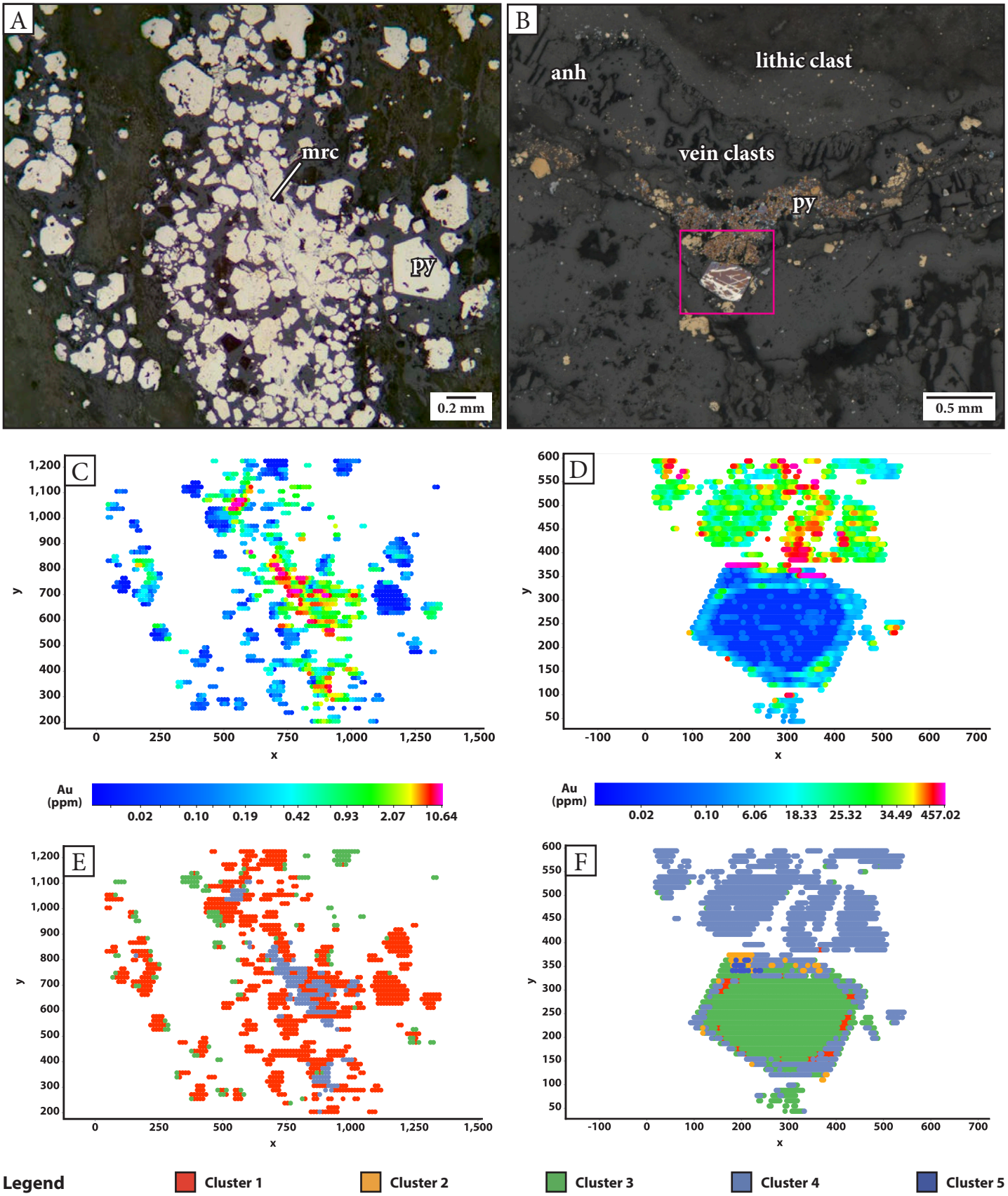
A
mrc
py
0.2 mm
B
anh
lithic clast
vein clasts
py
0.5 mm
C
y
x
Au (ppm)
0.02 0.10 0.19 0.42 0.93 2.07 10.64
D
y
x
Au (ppm)
0.02 0.10 6.06 18.33 25.32 34.49 457.02
E
y
x
F
y
x
Legend
Cluster 1
Cluster 2
Cluster 3
Cluster 4
Cluster 5

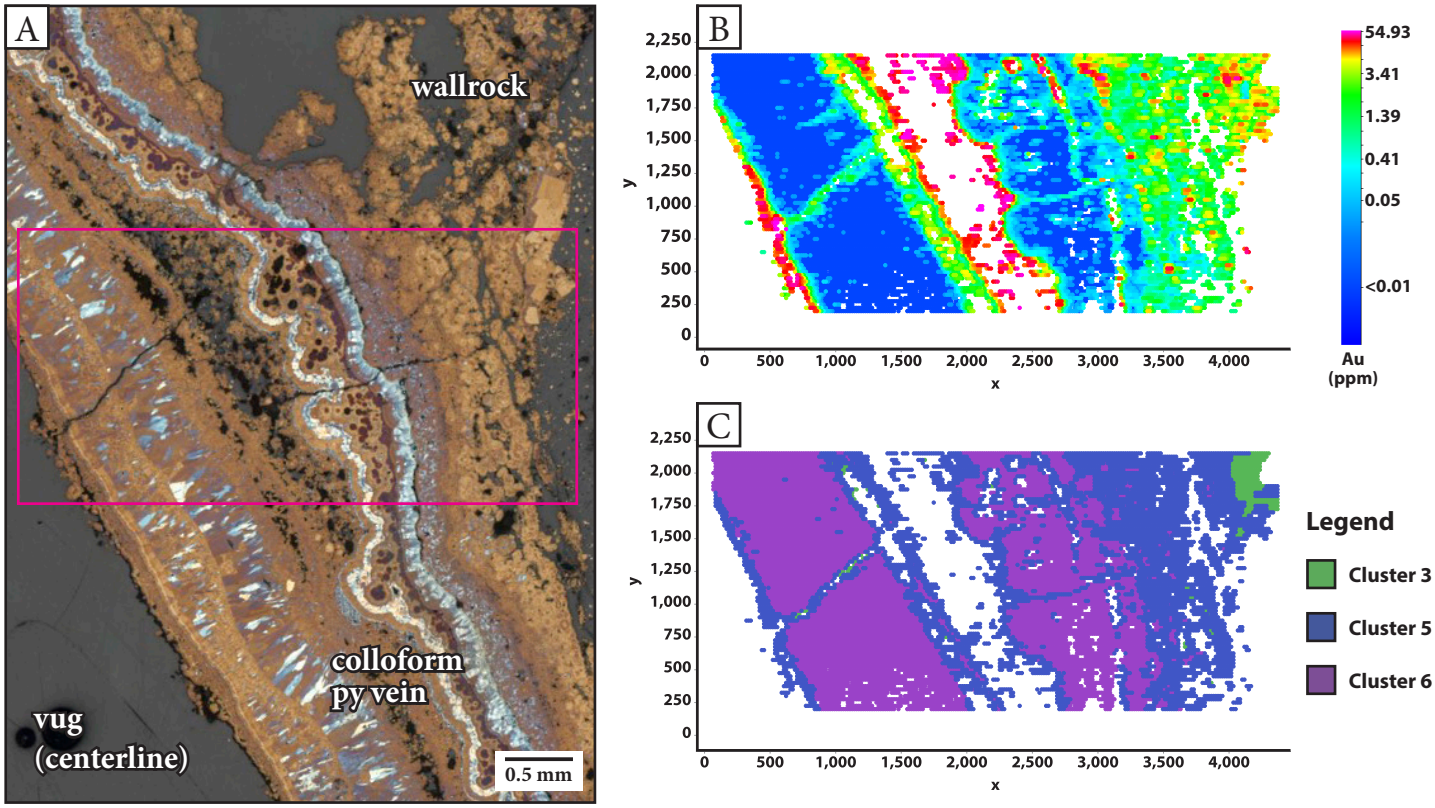


**Fig. 5.10.** Distribution of gold and K-means clusters in pyrite from a Stage 2A pyrite vein. Sample: DDHL1931 118.0 m. **A.** Reflected light photomicrograph of a Stage 2A colloform and botryoidal pyrite vein, showing textures revealed by NaOCl etching. Textures include oscillatory zonation of overgrowths on fine-grained euhedral pyrite aggregates and colloform bands of pyrite that have stained different colors due to etching (*bright blue, white, mauve, brown and orange*). The pink box outlines the area of the LA-ICP-MS raster maps in Figures 5.10B and C. **B.** LA-ICP-MS raster map of Au (ppm). **C.** LA-ICP-MS raster map colored by K-means cluster. Abbreviations: py = pyrite.

there were pulses of mineralizing fluids exsolving from a magmatic source, instead of just one evolving fluid that was depleted over time. Cluster 6 pyrite is the least abundant cluster and always occurs in alternating colloform layers with Cluster 5 pyrite (e.g., Fig. 5.10).

### *5.4.3 Composition of porphyry- and epithermal-stage pyrite*

Porphyry-stage pyrite grains (Clusters 1 and 3) have low mean total trace element values (<7,000 ppm) and low mean gold concentrations ($\bar{x}$ < 4 ppm Au). They are relatively enriched in Co, Pb and Ni and depleted in As, Sb, Tl, Au and Hg.

Epithermal-stage pyrite grains (Clusters 2, 4, 5 and 6) have high mean total trace element values (>18,000 ppm). High concentrations of trace elements are permitted during rapid disequilibrium precipitation of pyrite under supersaturation conditions. This increases the number of crystallographic defects (e.g., point defects) that lead to charged crystal growth surfaces and adsorption of metal ions onto successive layers of pyrite. Other than the high mean total trace element values, there are no shared chemical characteristics between all epithermal pyrite clusters. The majori-

**Fig. 5.9.** (*Previous page*) Distribution of gold and K-means clusters in pyrite from Stage 2D pyritic fault zones. Figures 5.9A, C and E correspond to sample DDHL1995 273.2 m, whereas Figures 5.9B, D and F correspond to sample DDHL1968 232.6 m. **A.** Reflected light image of the area of the LA-ICP-MS raster maps in Figures 5.9C and E. The image shows a band of blocky and fragmented pyrite grains (Stage 1G) and an aggregate of marcasite needles that are aligned with the shear fabric (Stage 2D). **B.** Reflected light photomicrograph of NaOCl etched pyrite from a Stage 2D fault zone with lithic clasts and Stage 1G anhydrite – pyrite vein clasts . The image shows a band of pyrite includes several types of pyrite that have stained different colors due to etching (1: early, patchy textured, brown, mauve and blue stained pyrite; 2: late, oscillatory zoned, yellow and brown stained pyrite, which also partly replaces and mantles the earlier formed pyrite). The pink box outlines the area of the LA-ICP-MS raster maps in Figures 5.9D and F. The white crosshatch marks on the large pyrite grain are scratches on the etched surface. **C.** and **D.** LA-ICP-MS raster maps for Au (ppm). **E.** and **F.** LA-ICP-MS raster maps colored by K-means cluster. Abbreviations: anh = anhydrite, mrc = marcasite, py = pyrite.

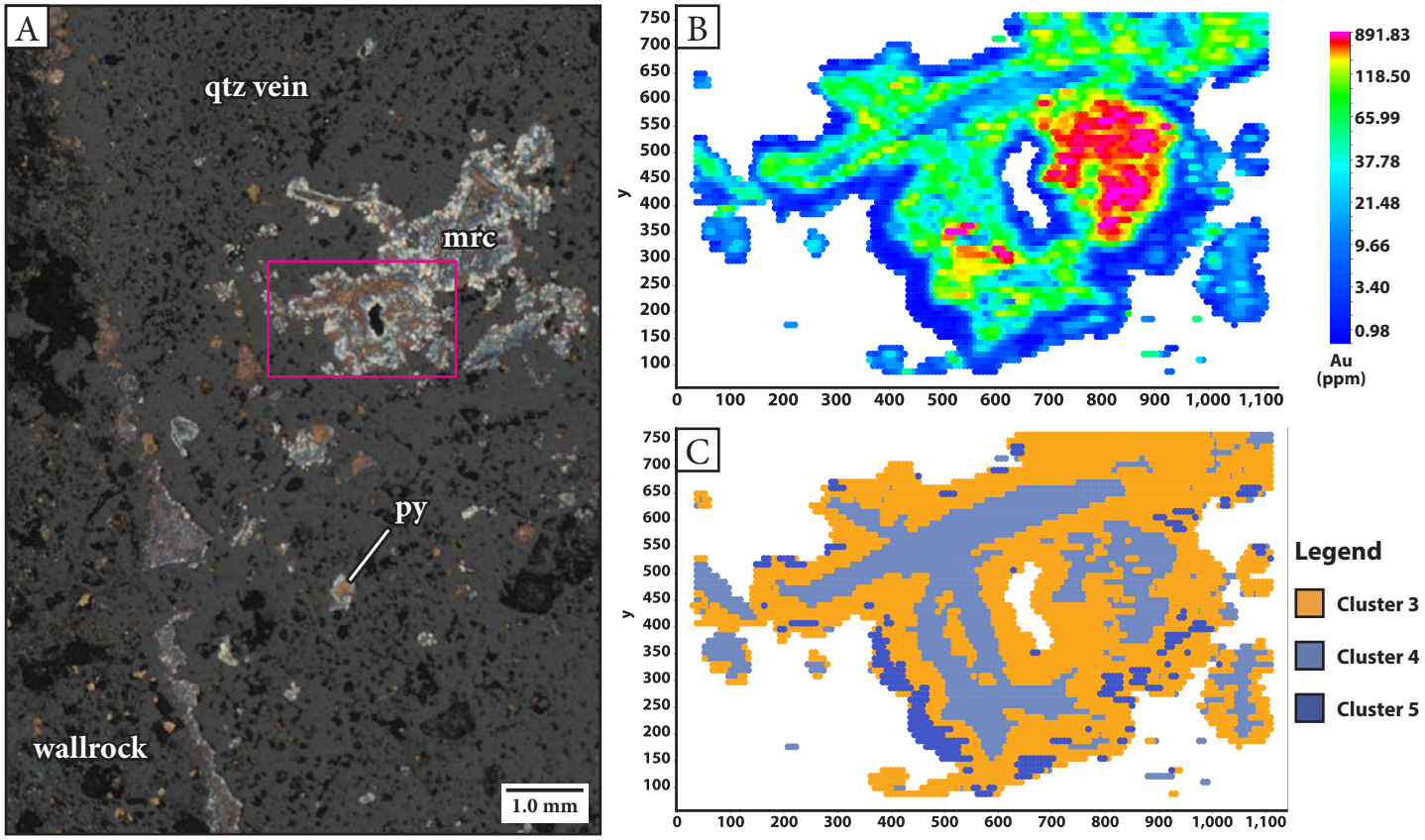


**Fig. 5.11.** Distribution of gold and K-means clusters in pyrite and marcasite from a Stage 3B quartz – marcasite – pyrite vein. Sample: DDHL1931 237.1A m. **A.** Reflected light image of NaOCl etched marcasite needles and pyrite crystals (*brown*) in a quartz vein. The vein wall and several of the pyrite and marcasite grains in the vein are locally mantled by a later generation of pyrite (*bright blue*). The pink box outlines the area of the LA-ICP-MS raster maps in Figures 5.11B and C. **B.** LA-ICP-MS raster map for Au (ppm). **C.** LA-ICP-MS raster map colored by K-means cluster. Abbreviations: mrc = marcasite, py = pyrite, qtz = quartz.

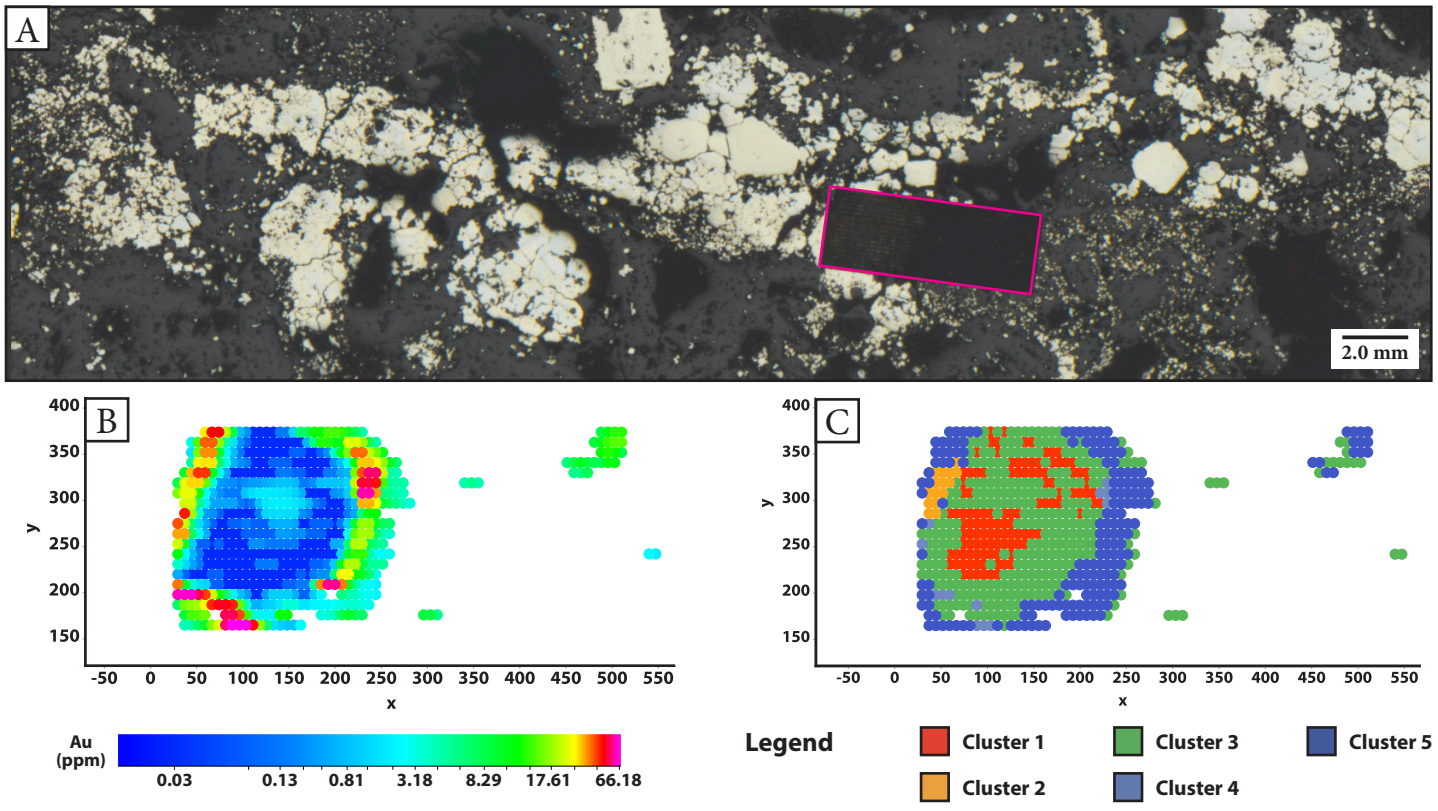

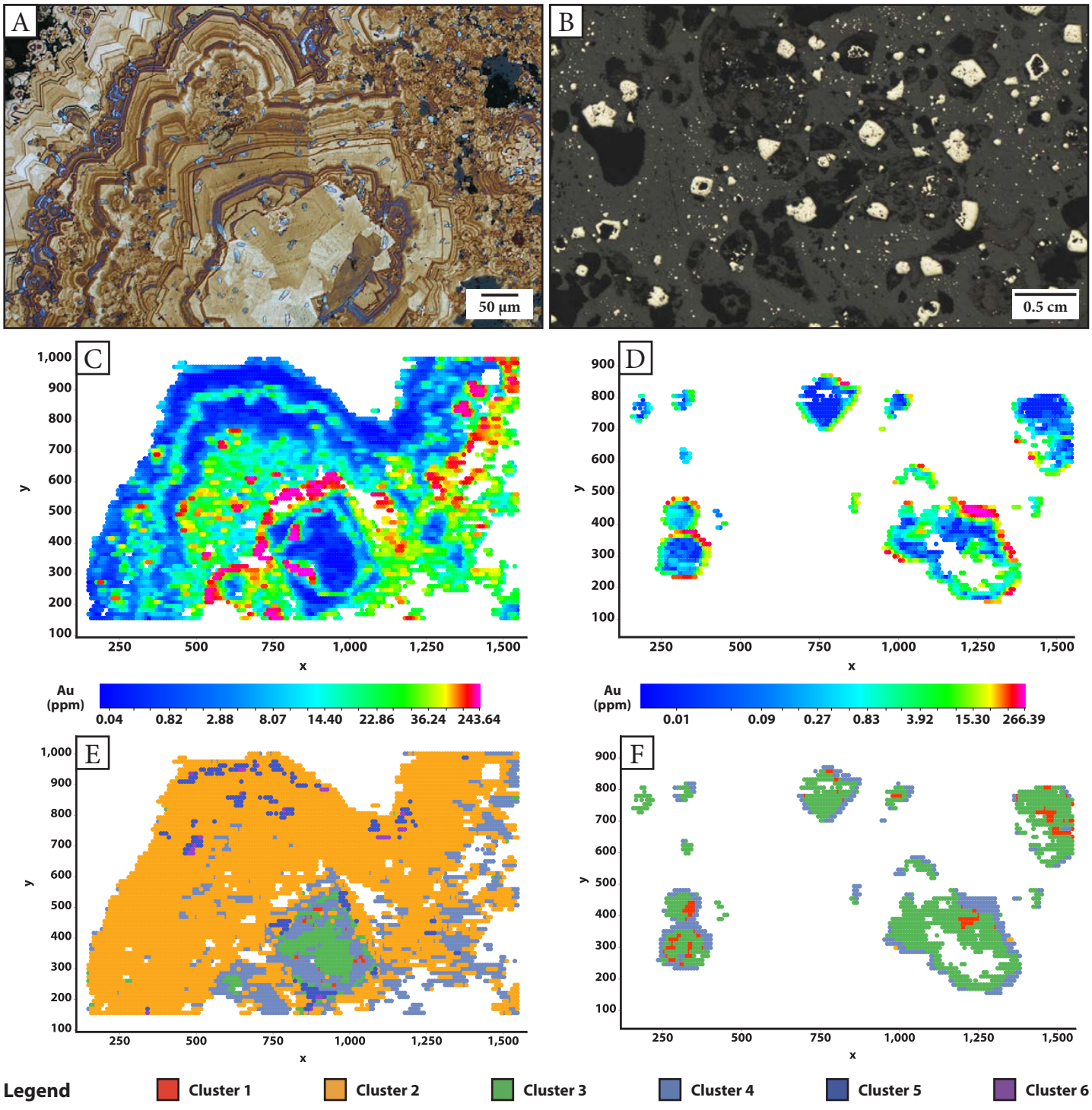


**Fig. 5.13.** Distribution of gold and K-means clusters in pyrite from Lienetz (Figs. 5.13A,C and E; Sample: LI12EL002A) and Minifie (Figs. 5.13B, D and F; Sample: LI12EL005). **A.** Reflected light photomicrograph of NaOCl etched pyrite from a $V3_{adu}$ vein from Lienetz, exhibiting oscillatory zoning. Image from Sykora et al. (2018b). **B.** Reflected light photomicrograph of disseminated pyrite from a vuggy adularia alteration zone in Minifie. The disseminated pyrite grains are porous and have rounded, corroded margins. The majority of the pyrite grains have been mantled by a later generation of pyrite. **C.** and **D.** LA-ICP-MS raster maps for Au (ppm). **E.** and **F.** LA-ICP-MS raster maps colored by K-means cluster.

**Fig. 5.12.** (*Previous page*) Distribution of gold and K-means clusters in pyrite from a Stage 5A pyrite vein. Sample: DDHL1803 51.8 m. **A.** Reflected light photomicrograph showing a dendritic pyrite veinlet with vein-halo disseminated pyrite. There are two generations of pyrite in the image: (1) early, sparse, coarse-grained pyrite and (2) late, fine-grained, euhedral to anhedral pyrite disseminations and overgrowths. The pink box outlines the area of the LA-ICP-MS raster maps in Figures 5.12B and C. **B.** LA-ICP-MS raster map for Au (ppm). **C.** LA-ICP-MS raster map colored by K-means cluster.

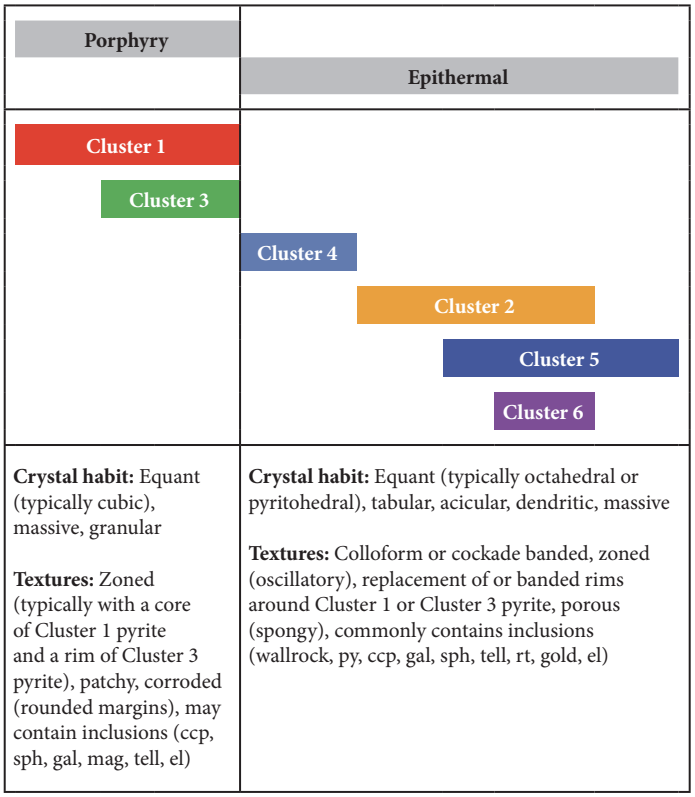


**Fig. 5.14.** Generalized paragenesis and textural characteristics of K-means pyrite clusters based on textural relationships observed in LA-ICP-MS raster maps (Appendices H11 and H12) and reflected light photomicrographs. Abbreviations: ccp = chalcopyrite, el = electrum, gal = galena, mag = magnetite, py = pyrite, rt = rutile, sph = sphalerite, tell = telluride minerals.

**Table 5.5.** Percentage of pixels assigned to different K-means pyrite clusters for each stage of the paragenesis as defined in Chapter 4. The clusters are listed in order of their interpreted paragenetic order as shown in Figure 5.14. Note that entire samples (maps and lines) were designated as belonging to a single stage of the paragenesis (Table 5.1). Therefore, overprinting relationships are reflected in the table below. The quartz vein from Lienetz ($V4_{qtz}$; DDHL0791_226.8) has been assigned its equivalent stage name in Kapit NE and Coastal (Stage 3) and the pyrite cemented breccias from Lienetz ($Bx3_{py-adu}$; LI12EL002A and LI12EL002B) have been assigned their equivalent stage name in Kapit NE and Coastal (Stage 2).

| | Vein or breccia stage | | | | | Alteration stage | |
|---|---|---|---|---|---|---|---|
| Cluster | Stage 1 | Stage 2 | Stage 3 | Stage 4 | Stage 5 | A4 | A6 |
| 1 | 69% | 9% | 10% | 7% | 11% | 7% | <1% |
| 3 | 25% | 18% | 25% | 52% | 26% | 71% | 20% |
| 4 | 6% | 28% | 44% | 41% | 36% | 21% | 50% |
| 2 | 0% | 20% | 20% | 1% | 6% | <1% | 21% |
| 5 | 0% | 7% | 1% | 0% | 20% | 0% | 9% |
| 6 | 0% | 17% | <1% | 0% | <1% | 0% | 0% |

ty (Clusters 2, 4 and 5) have high mean gold concentrations ($\bar{x}$ > 40 ppm Au); however, Cluster 6 does not contain detectable Au.

Cluster 4 is the most abundant epithermal-stage pyrite (Table 5.4) and is therefore a key contributor to the epithermal resource. It is enriched in Pb, Ag, Au, Mo and Te and has relatively low Mn, Zn and As compared to other clusters. Cluster 4 has the highest mean concentration of Au ($\bar{x}$ = 61 ppm), Ag ($\bar{x}$ = 64 ppm) and Te ($\bar{x}$ = 60 ppm), and has an order of magnitude higher concentration of Mo ($\bar{x}$ = 2,073 ppm) compared to other clusters ($\bar{x}$ = 113 ppm; Fig. 5.6). It is interesting that Cluster 4 has the highest mean concentration of Au, yet has relatively low As compared to other clusters. Nevertheless, the pyrite data for Cluster 4 do show a strong positive correlation between Au and As concentrations (Fig. 5.7).

Like the porphyry-stage pyrites, Cluster 4 is enriched in Co, Pb and Ni. For Cluster 1, 3 and 4 pyrite data, a well-defined positive correlation exists between Co and Ni (approximately 1:1; Fig. 5.15). It is likely that Co and Ni were incorporated via stoichiometric substitution of Fe in these pyrites, implying higher temperatures and slower rates of crystallization (e.g., Klemm, 1965). It may be that pulses of magmatic-hydrothermal fluids were discharged cyclically during each epithermal stage, and cooled through deposition of Cluster 4, then Cluster 2, then Cluster 5 pyrite. The large spot size and close proximity of Cluster 4 with Clusters 1 and 3 pyrites provide an alternative explanation for the elevated Co and Ni in Cluster 4 pyrite.

The other epithermal-stage clusters (Clusters 2, 5 and 6) display a typical enrichment in As, Tl and Sb and depletion in Co, Pb, Ni and Bi. Clusters 5 and 6 share additional compositional similarities: enrichment in Mn, Zn and Hg; depletion in Ag, Cu, Mo and Cr; and low median Au contents (<2 ppm Au). They differ in that Cluster 5 contains relatively elevated Au and Se, and high mean Au content ($\bar{x}$ = 40.73 ppm Au), whereas Cluster 6 does not contain gold.

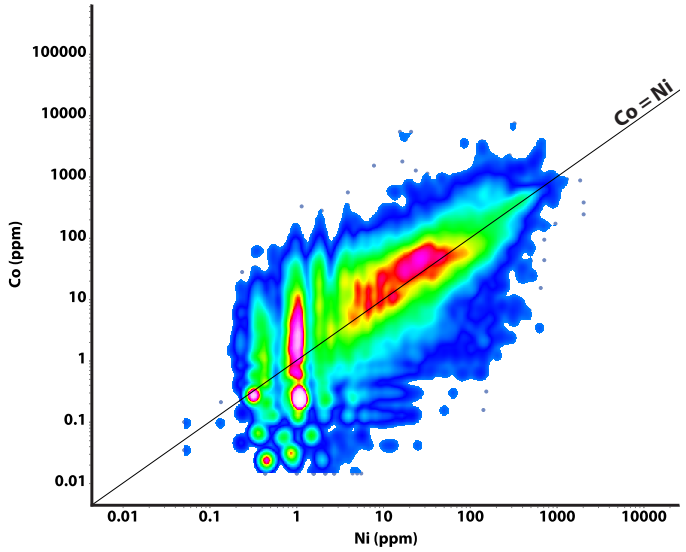


**Fig. 5.15.** Co–Ni scatterplot for Cluster 1, Cluster 3 and Cluster 4 pyrite data (n = 71,116).

The pyrite grains analyzed in this study typically have high As concentrations ($\bar{x}$ = 1.48 wt% As; maximum 15.98 wt% As; Appendix H9), consistent with observations from previous studies (Moyle et al., 1990; Ageneau, 2012; Sykora et al., 2018b). In general, the pyrite data show a strong positive correlation between Au and As (Fig. 5.7). Cluster 6 pyrite does not exhibit this relationship, alternatively having low Au concentrations at variable and high As concentrations (Fig. 5.7F). Cluster 3 pyrite has a low Au (<0.1 ppm) and low As (<30 ppm) population, similar to the porphyry-stage pyrites and composite pyrite cores grouping defined by Sykora et al. (2018b) for samples from Lienetz. The other porphyry-stage pyrite cluster identified in this study (Cluster 1) does not have a population of data that plots in this low Au/low As field. Instead, Cluster 1 has a population with low Au concentrations at variable As concentrations (Fig. 5.7A). Cluster 2, 5 and 6 pyrite data display a near-vertical slope on Au–As scatterplots, whereas Cluster 1, 3 and 4 pyrite data define a flatter slope (Fig. 5.7).

## 5.5 Summary and conclusions

Pyrite is ubiquitous at Lihir. It is a common mineral in every ore zone and each paragenetic stage including porphyry, epithermal and modern-day geothermal. This study has shown that LA-ICP-MS raster maps can be used to identify compositional and micro-textural features of pyrite that are not discernible using conventional petrographic techniques. Six varieties of pyrite have been distinguished using a two-part statistical analysis of the LA-ICP-MS pyrite data. Two of the pyrite types are associated with porphyry-style conditions and four are associated with the ore-forming epithermal system.

Porphyry-stage pyrites are typically coarse-grained and exhibit well-formed cubic crystal habit. They contain elevated Co, Ni and Pb, consistent with crystallization in a high temperature environment. Epithermal-stage pyrites are texturally and compositionally variable. They are typically fine-grained and may display octahedral, pyritohedral, tabular, acicular or dendritic habit. The minerals commonly form colloform or anhedral aggregates with oscillatory zoning. It is common for porphyry-stage pyrites to be partly replaced or mantled by epithermal-stage pyrites, forming composite grains. Many of the porphyry-stage pyrites have pits, vugs and irregular, rounded margins, which suggest that they have experienced corrosion during later hydrothermal fluid interaction.

Pyrite that was deposited during each of the epithermal stages underwent a characteristic chemical progression, demonstrating that there was a repeated compositional evolution of the mineralizing fluids throughout the epithermal life cycle. This may indicate that mineralizing fluids were generated episodically by exsolution from a magmatic source. This is consistent with the dominantly oxidized, magmatic source of sulfur determined for Lihir pyrite and anhydrite (e.g., Gemmell et al, 2004; Sykora, 2017; Cooke et al., in press). Each pulse of epithermal mineralization was accompanied by a transition from high to low temperature conditions, and the associated pyrite types evolved from: (1) Ag- and Au-rich with Pb, Mo and Te; to (2) Ag-and Au-rich with Tl, As, Sb, Mo and Te; to (3) Au-rich with Tl, Sb, Mn, As, Zn, Hg and Se; to (4) Au barren and strongly enriched in Zn, As, Mn, Tl and Sb, with very low concentra-

tions of other trace elements. Gold occurs primarily in the crystal structure of pyrite and as micro- and nano-inclusions of native gold, electrum and precious metal tellurides (Ag>Au).

# CHAPTER 6

# Conclusions

## 6.1 Introduction

This thesis has documented the geology of the Kapit NE and Coastal ore zones of the Lihir alkalic epithermal gold deposit, part of the TLTF island chain of northeastern Papua New Guinea. This chapter presents a genetic model for the evolution of Kapit NE and Coastal in the greater context of the Lihir gold deposit and Luise volcano, based on the results from previous chapters. This chapter concludes with a discussion of the potential significance of this study and provides recommendations for future research.

## 6.2 Genesis of the Kapit NE and Coastal ore zones

The following sections highlight key aspects of the major geologic events in the formation and evolution of the Kapit NE and Coastal ore zones, some of which are schematically illustrated in Figure 6.1.

### *6.2.1 Geological setting*

Lihir gold deposit is located on the eastern shore of Lihir Island, in the TLTF island chain of New Ireland Province, Papua New Guinea. Its formation has been coincident with shoshonitic, volatile-rich, silica-undersaturated, and highly oxidized magmatism along arc-oblique extensional structures and sinistral rotation in the back-arc of the New Britain subduction zone. The deposit is located beneath the floor of an elliptical, north-northeast-trending sector collapse amphitheater at the core of Luise Volcano, part of a Pliocene to Recent alkalic stratovolcano complex that comprises Lihir Island.

The Kapit NE and Coastal ore zones are located at the northwestern periphery of Lihir, in an area that presently spans a subaerial to submarine environment (Fig. 3.1). Examination of least-altered drill core (e.g., from DDHL1995; Fig. 3.5) allowed for documentation and interpretation of the host rocks in these areas. The stratigraphy is dominated by northeast-dipping (20–30˚), mafic volcano-sedimentary rocks consisting primarily of polymict matrix-supported breccia (Tables 3.1–3.2), which is interpreted to have formed by the successive accumulation of subaerially-derived volcanic material from high-energy, gravity-driven debris flows in a submarine environment. On the same stratigraphic level at Minifie (~1.5 km to the southeast), the volcano-sedimentary sequence is dominated by south-dipping, intercalated volcanic debris flow deposits and minor pyroclastic facies that indicate subaerial deposition close to a vent. This suggests that at the time of sedimentation, the Luise volcano was locally emergent, with a subaerial depocenter at Minifie and submarine flanks in the areas of Kapit NE and Coastal (Fig. 3.27). Sometime later, suspension-settled mudstones were deposited over top of the coarse volcaniclastic deposits at Minifie, reflecting a change in basin geometry and a local transition from a subaerial to a subaqueous environment (Blackwell, 2010). Widespread, andesitic to basaltic sills and dikes with peperitic margins were then emplaced, consistent with continued volcanism in a submarine setting. Volcanic activity persisted, resulting in the accumulation of a further ~1 km of volcano-sedimentary material.

A change to a more compressive local stress regime promoted magmatism at depth and a hiatus in volcanic activity. Under the confining pressure of the Luise volcanic

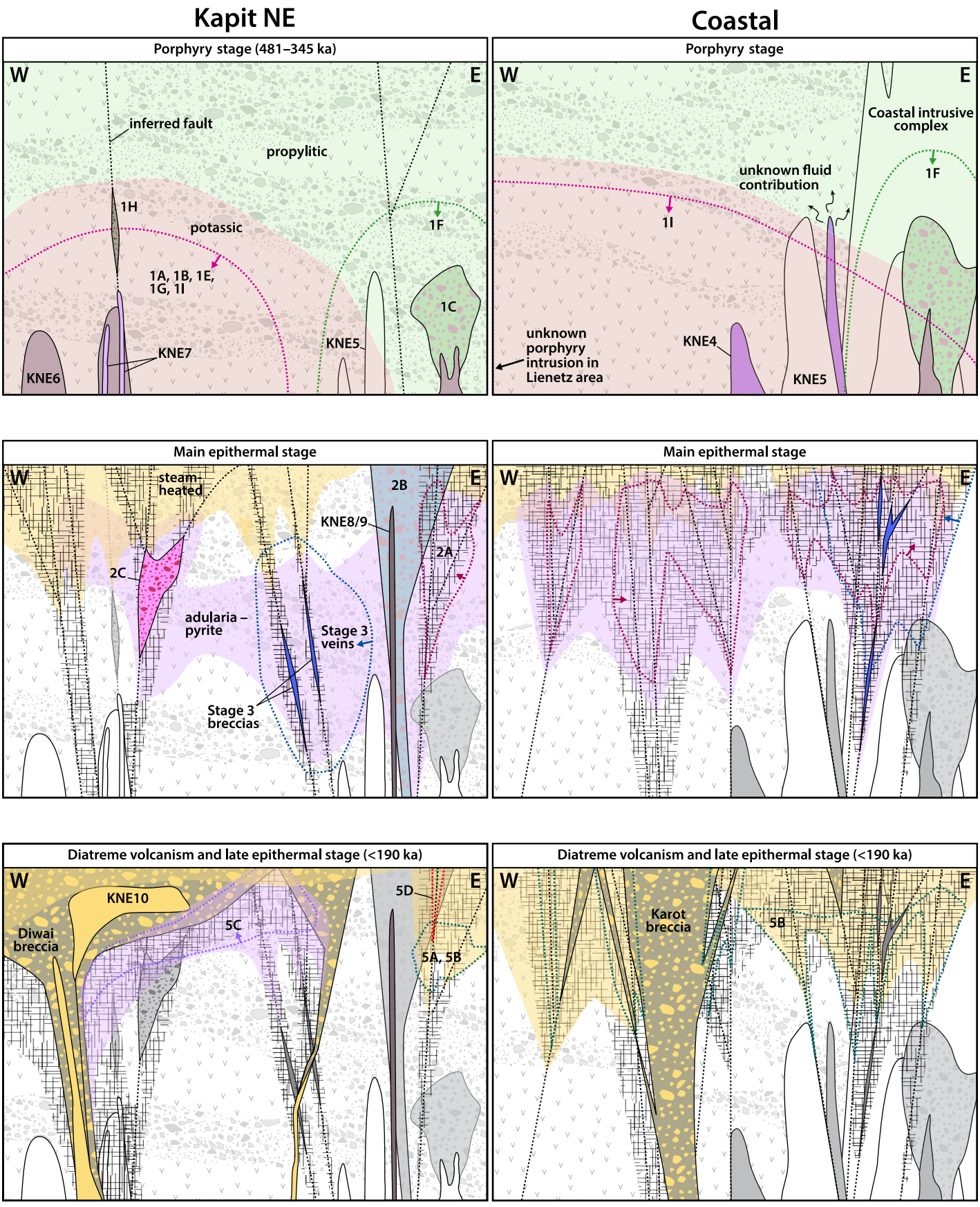
Kapit NE
Coastal
Porphyry stage (481–345 ka)
Porphyry stage
W
E
inferred fault
propylitic
1H
potassic
1A, 1B, 1E, 1G, 1I
1F
1C
KNE7
KNE6
KNE5
Coastal intrusive complex
unknown fluid contribution
1I
unknown porphyry intrusion in Lienetz area
KNE4
Main epithermal stage
steam-heated
2B
KNE8/9
2A
2C
adularia – pyrite
Stage 3 veins
Stage 3 breccias
Diatreme volcanism and late epithermal stage (<190 ka)
KNE10
Diwai breccia
5C
5D
5A, 5B
Karot breccia
5B

edifice, the volcano-sedimentary sequence was intruded by a voluminous, north-trending intrusive complex that spans from Coastal to Kapit NE (Coastal intrusive complex; Tables 3.2–3.3). It consists of irregular, multiphase dikes such as porphyritic nepheline-bearing monzonite, hornblende-biotite-bearing monzonite and hornblende-bearing gabbro. Some of the porphyritic nepheline-bearing monzonite intrusions contain miarolitic cavities, which provide evidence for exsolution of a volatile phase. However, no evidence has been found for a genetic link between these intrusive phases and porphyry or epithermal mineralization. At Kapit NE, further magmatic activity generated sparse, narrow dikes composed of hornblende-bearing gabbro and crystal-poor plagioclase-phyric trachyte of unknown orientation, and a swarm of northeast-trending, zoned feldspar-phyric latite dikes with coarse-grained cores and trachytic margins. Crosscutting relationships imply that the hornblende-bearing gabbro and crystal-poor plagioclase-phyric trachyte intrusions were emplaced synchronously with porphyry-style hydrothermal activity and that all of the intrusions were emplaced prior to epithermal mineralization. Whole-rock geochemical analysis suggests that these intrusions are ubiquitously shoshonitic and have geochemical signatures consistent with emplacement in a suprasubduction zone environment (Figs. 3.21–3.23).

### *6.2.2 Porphyry stage*

Porphyry-style hydrothermal activity at Kapit NE and Coastal occurred prior to sector collapse, under the confining pressure of the Luise Volcano (Fig. 6.1). Porphyry- stage features include pervasive alteration domains (at >150 m bsl) composed of phlogopite – K-feldspar ± magnetite (potassic) and chlorite – calcite (propylitic) assemblages, and widespread, low grade (<1 ppm Au and <0.3 wt% Cu) anhydrite-rich breccias and veins. Pyrites associated with the porphyry stage form coarser-grained, euhedral, cubic and zoned crystals with corrosion vugs and rounded margins. LA-ICP-MS analysis shows that these pyrites have elevated Co, Ni and Pb (Table 5.4), consistent with formation under high-temperature conditions. They have relatively low concentrations of gold ($\bar{x}$ = 2.7 ppm Au; maximum 1,445 ppm Au) and total trace elements ($\bar{x}$ = 5,429 ppm). New geochronological age constraints suggest that porphyry-style hydrothermal activity occurred episodically in Kapit NE area between ~481 ka and 345 ka (Table 4.7). The age of a pyroxene-hornblende-phyric monzodiorite (497.4 ka ± 9.0 ka) provides a maximum age for minor porphyry-stage mineralization intersected at the northern margin of the Lihir amphitheater. This suggests that there were multiple pulses of magmatism that were associated with porphyry-style activity.

In western Kapit NE, there is an apparent zonation of pervasive alteration from proximal potassic to distal propylitic assemblages surrounding crystal-poor feldspar-phyric trachyte dikes (Fig. 4.1). A variety of veins and breccias are also concentrated around the trachyte dikes, including chalcopyrite-bearing anhydrite – magnetite veins and a minor biotite-altered pebble dike, suggesting a possible link between these intrusions and porphyry-style mineralization in Kapit NE. These dikes have not been documented elsewhere at Lihir and cannot account for the distribution of porphyry-style hydrothermal features across the entire deposit.

In general, the major center for porphyry-style activity appears to have been northern Lienetz, which hosts anhy-

**Fig. 6.1.** Summary of the genetic model for the Kapit NE (*left hand panels*) and Coastal (*right hand panels*) ore zones, from porphyry to main-stage epithermal to diatreme volcanism and late-stage epithermal. Lithotype and paragenetic stage descriptions can be found in chapters 3 and 4, respectively. Abbreviations: 1A = albite ± actinolite veinlets, 1B = anhydrite – magnetite ± chalcopyrite ± chlorite veins and amygdules,1C = polymict anhydrite – chlorite – calcite-cemented breccias, 1E = anhydrite – pyrite veins, 1F = anhydrite – calcite – chlorite veins, 1G = tabular anhydrite and carbonate veins, 1H = biotite-altered pebble dike, 1I = massive and banded anhydrite ± pyrite breccias and veins, 2A = pyrite – marcasite-cemented breccias and stockwork veins, 2B = quartz – pyrite-cemented breccias, 2C = zoned quartz – pyrite – anhydrite – calcite-cemented to matrix-rich breccia, Stage 3 = quartz veins and breccias, 5A = dendritic pyrite veins and disseminated pyrite, 5B = clay – pyrite-cemented breccias and veins, 5C = calcite – quartz – adularia – pyrite – limonite-cemented veins and breccias, 5D = orpiment – realgar veinlets and breccias, KNE4 = biotite-feldspar-phyric nepheline-bearing monzonite, KNE5 = hornblende-biotite-bearing monzonite, KNE6 = hornblende-bearing gabbro, KNE7 = crystal-poor feldspar-phyric trachyte, KNE8/9 = feldspar-phyric latite, KNE10 = feldspar-phyric andesite and associated monomict breccia.

drite – biotite veins and a major magmatic-hydrothermal breccia complex that was associated with alkalic porphyritic dikes (Sykora et al., 2018a). Fluid inclusion assemblages from porphyry-stage anhydrite veins at Lienetz and Minifie contain polyphase hypersaline, vapor-rich, and/or liquid-rich fluid inclusion types (Carman, 1994, 2003). These inclusions have salinities ranging from 7 to 56 wt% NaCl and homogenization temperatures from 408°C to 110°C. Sulfur isotope values of pyrite (–3.2‰ to +2.2‰) and oxygen isotope values of hydrothermal phlogopite (+6.2‰) are consistent with deposition from a magmatic-hydrothermal fluid (Carman, 1994; Müller et al., 2002b; Carman, 2003). Sulfur isotopic analyses of anhydrite from porphyry-stage veins and altered rocks yielded values of 7.2‰ to 10.5‰, consistent with deposition from oxidized, magmatic-hydrothermal fluids (Cooke et al., in press).

The transition from porphyry to epithermal conditions most likely occurred as a result of volcanic sector collapse. This catastrophic mass wasting event would have depressurized rocks that had previously been at depth, resulting in extensional fracturing and increasing the hydraulic conductivity of the rock mass. It is interpreted that sector collapse occurred during a period of magmatic-hydrothermal quiescence. Observations that support this interpretation include: (1) the lack of evidence for pre- to syn- mineralization volcanic-hydrothermal breccias (Chapter 4), and (2) that the porphyry and epithermal stages were separated by a period of anhydrite dissolution (possibly associated with infiltration of cool groundwater; Sykora et al., 2018a). There is abundant evidence of anhydrite dissolution in Kapit NE and Coastal, including pervasive domains of vuggy adularia alteration (Figs. 4.1 and 4.4; Table 4.4). This style of alteration provided much of the porosity and permeability required for later hydrothermal fluid flow and ore deposition.

### *6.2.3 Main epithermal stage*

Low sulfidation epithermal-style mineralization and alteration were superimposed onto porphyry-stage features at Lihir after sector collapse (Fig. 6.1). Geochronological data constrain main-stage epithermal activity to between 345 and 55 ka (Fig. 4.54). The epithermal stage produced several discrete mineralized bodies at shallow levels including those at Kapit NE and Coastal, both of which are dominated by refractory gold in pyrite (and marcasite; Fig. 5.7). Auriferous and arsenian pyrite is abundant, occurring as infill in hydrothermal breccias and veins with variably abundant gangue minerals (adularia, quartz, chalcedony, carbonate, anhydrite and/or illite) and in altered wallrocks (Figs. 4.20–4.27). In contrast to the porphyry-stage veins, epithermal anhydrite veins are characterized by euhedral, commonly bladed, anhydrite crystals that do not display dissolution or deformation textures (Fig. 4.23). Epithermal gold mineralization was associated with intense, pervasive adularia – pyrite and/or quartz – illite – pyrite alteration, which overprinted early porphyry-style alteration (Figs. 4.1, 4.5–4.6, and 4.19; Table 4.4). A subset of quartz ± anhydrite veins locally contain small amounts of free gold and/or precious metal tellurides (Figs. 4.23–4.24, 4.26, and 5.7–5.8), and locally have bonanza gold grades that exceed 100 g/t.

Pyrites associated with the epithermal stage are texturally variable. They commonly form rims around earlier-formed porphyry-stage grains, or occur as fine-grained, anhedral to euhedral (equant, acicular, dendritic), porous and inclusion-rich aggregates with colloform, botryoidal or granular habit. LA-ICP-MS analysis shows that there are four chemically distinct types of pyrite associated with the epithermal stage, three of which contain high concentrations of gold ($\bar{x}$ = 51.3 ppm Au; maximum 131,619 ppm Au), and one that has gold in concentrations that are below detection limit. Each epithermal stage displays a characteristic progression of pyrite chemistry, demonstrating that there was a repeated compositional evolution of the mineralizing fluids throughout the epithermal life cycle.

In Lienetz, epithermal breccias and veins were localized

along northeast to east-northeast-striking faults that reactivated porphyry-stage veins with low-angle dips to the north. This resulted in the formation of composite porphyry – epithermal anhydrite veins that exhibit complex overgrowths of epithermal-stage, gold-rich pyrite rims around gold-poor, porphyry-stage pyrite cores (Sykora et al., 2018b). This hybrid style of mineralization is not common in Kapit NE or Coastal. It is best developed in the areas closest to Lienetz. Instead, the majority of gold mineralization in Kapit NE and Coastal was associated with intensely developed pyritic stockwork veins, tabular monomict breccias, polymict breccia pipes and fault zones that are apparently steeply dipping (Figs. 4.19–4.22). Their formation is interpreted to have involved long quiescent periods when banded vein infill and small-scale hydraulic breccias formed, and brief chaotic periods of tectonism and phreatic brecciation.

Homogenization temperatures and salinities from epithermal-stage quartz- and calcite-hosted fluid inclusions from Lienetz and Minifie range from 394°C to 98°C and from 0.2 to 7.8 wt% NaCl eq. (Carman, 1994, 2003). The range of temperatures and salinities are interpreted to indicate mixing between low-salinity meteoric water and moderate- to high-salinity magmatic-hydrothermal brine and vapor. The coexistence of liquid and vapor-rich fluid inclusions provides evidence of boiling, which is inferred as a key ore-forming process for the epithermal mineralization at Lihir (Carman, 2003). Sulfur isotopic analyses of pyrite (−13.0 to 3.6‰) and anhydrite (mostly between 7.2 and 13.6‰), and strontium isotopic analyses of anhydrite (0.7040 to 0.7042) from Lihir preclude any significant involvement of seawater (Cooke et al., in press).

### *6.2.4 Diatreme volcanism*

Episodic volcanic-hydrothermal eruptions occurred at Lihir after main-stage epithermal mineralization (Fig. 6.1). Andesite dikes intruded the paleowater table and reacted explosively, feeding phreatomagmatic and phreatic eruptions that formed subsurface diatreme breccia bodies and related maar deposits. Contact breccias formed by quenching and disaggregation of feeder dikes where they came into contact with abundant hydrothermal fluids and by implosion or collapse of wall rocks in the root zone. Several episodes of phreatomagmatic activity occurred, as evidenced by crosscutting relationships between diatreme breccia facies, and in some cases, incorporation of earlier-formed breccias as clasts. Phreatomagmatic eruptions led to draw-down and carbonization of organic material (e.g., tree trunks) and slumping of tephra from the sides of the vents. Slumped blocks of tephra ranged in scale from meters to tens of meters in diameter. Some of the slumping occurred via normal faulting along tabular phreatic breccias. In total, seven large phreatomagmatic breccia bodies were formed, focused along north- to northeast-trending structures at the margins of the major ore zones.

As magmatic input subsided, phreatic activity became increasingly abundant, forming irregular breccia bodies and small breccia pipes and dikes that crosscut phreatomagmatic breccias within and surrounding the diatremes. Late-stage intrusion of andesitic magma into the unconsolidated diatreme fill produced brecciated andesite sills and dikes with quench fragmentation textures and/or peperitic margins. Eventually volcanism ceased entirely, and the surficial maar deposits were predominantly eroded away, exposing the diatreme pipes and dikes at the present-day surface.

Diatreme volcanism most likely took place in a subaerial environment under epithermal conditions, as indicated by the incorporation of terrestrial plant material and the moderate-temperature (~310°C–220°C) syn-brecciation alteration assemblage of quartz, illite and pyrite. It is estimated that diatreme volcanism occurred between 190 and 55 ka, based on attempted radiocarbon dating of charcoal fragments and Blackwell's (2010) estimate of the maximum age of the sector collapse event. The causative andesitic dikes and associated juvenile magmatic clasts have not been dated effectively. A detailed geochronology study of

these features is required to resolve whether the diatremes formed at one time from multiple eruption points or if this phase of volcanic activity was polygenetic with repeated diatreme-forming phreatomagmatic events.

After diatreme volcanism ceased, a new, steady-state hydrological regime was established, associated with renewed epithermal gold mineralization that was focused along the margins of the NE-trending Diwai breccia in Kapit and Kapit NE and around phreatic breccia pipes and dikes in Coastal area. This suggests that the diatremes acted as aquitards to hydrothermal fluid flow and that fluids were focused along marginal fractures that were generated during breccia emplacement (Fig. 4.52).

### *6.2.5 Geothermal activity*

Geothermal activity has produced an extensive near-surface clay alteration zone via steam-heated processes (Browne, 1978; Moyle et al., 1990; Carman, 1994; Jansen et al., 2017; Fig. 4.1). In Kapit NE and Coastal, steam-heated alteration consists of smectite – kaolinite (argillic) and kaolinite – alunite (advanced argillic) assemblages (Fig. 4.1; Table 4.4). The steam-heated zone has locally overprinted the volcanic-hydrothermal breccia complex (Blackwell, 2010; Ageneau, 2012; Lawlis et al., 2015; Fig. 4.1). The steam-heated alteration zone locally contains dendritic pyrite veinlets (Fig. 4.42), fine-grained disseminated pyrite (Fig. 4.42), and variable, multi-stage clay – pyrite ± sulfate-cemented breccias and veins (Fig. 4.43) with disseminated vein-halo pyrite ± marcasite. The pyrite in these veins commonly forms banded overgrowths around earlier-formed disseminated sulfides (Fig. 4.44F). These structures locally host moderate grade gold mineralization (1–5 g/t Au). It is possible that due to a drop in the paleowater table (e.g., caused by a landslide), acidic steam-heated fluids were able to percolate downward through large volumes of previously formed epithermal mineralization. The gold in solution could then be mobilized and precipitated as fine-grained disseminations and overgrowths of pyrite and marcasite in a process similar to supergene enrichment (e.g., Ebert and Rye, 1997).

The modern high-temperature geothermal system was most likely already established in the Luise amphitheater by the time of diatreme formation, and definitely by 0.15 Ma, based on a K–Ar whole-rock age determination of 0.151 ± 0.015 Ma obtained from an alunite-rich rock (Davies and Ballantyne, 1987; Moyle et al., 1990; Table 4.11). Boiling geothermal waters and steam still discharge throughout the Lihir gold mine today, altering rocks, causing episodic phreatic brecciation and depositing gold (Pichler et al., 1999; Simmons and Brown, 2006). Oxygen and hydrogen isotopic analyses of modern geothermal waters provide evidence for mixing of meteoric water with a deep geothermal brine that has an isotopic composition between end-member magmatic water and seawater (Carman, 1994). The geothermal system is interpreted to represent the waning ancient auriferous hydrothermal system (Williamson, 1983; Simmons and Brown, 2006).

## 6.3 Significance and exploration implications

Lihir is a rare and valuable alkalic-type epithermal gold deposit and is an attractive target for companies exploring in the southwest Pacific region. Alkalic-type epithermal deposits are commonly not considered in models of low sulfidation epithermal deposits (e.g., John et al., 2018) and are comparatively less well understood. This study has provided a comprehensive description of the host rocks and hydrothermal features of a giant alkalic-type epithermal deposit and summarizes these findings in a new genetic model. It contributes to our understanding of the geological setting, lifetime and evolution of an alkalic-type epithermal deposit. It adds new ideas to the porphyry-epithermal model that may have implications for exploration in the TLTF island chain and worldwide. Some contributions and exploration implications from this study include:

- *Recognition of a shoaling seamount geological setting.*

Kapit NE and Coastal ore zones, as well as nearby Conical Seamount (polymetallic Zn-Pb-Ag-Au-As-Sb veins; ~10 km south of Lihir), have evolved and continue to exist in a submarine environment. This suggests that alkalic submarine volcanics present a permissive geological environment for epithermal gold mineralization. Rocks from similar geological settings may previously have been overlooked during exploration. Lihir's young age and position in a tectonically active oceanic crustal setting with high regional uplift rates suggest that this type of ore deposit would not easily be preserved in the rock record and may help explain why so few similar giant alkalic epithermal deposits have been discovered.

- *Association of gold ore with a variety of mutli-stage breccia bodies and large volumes of stockwork veins.* While breccias and stockwork veins are typical in other epithermal deposits, they are commonly subordinate to high-grade or bonanza ore shoots with strong structural controls. Breccia- and stockwork-hosted mineralization allow for high-grade and tonnage orebodies that have relatively small footprints and that are amenable to open pit mining. These styles of orebodies should not be overlooked when exploring for epithermal deposits.

- *Sulfide mineralogy of the porphyry-related alteration and veins may imply a hidden porphyry target at depth.* The widespread occurrence of pyrite and paucity of chalcopyrite in the potassic alteration zone at Kapit NE suggest a medial position relative to an intrusive center, implying that there is potential for discovery of a porphyry-style mineralized intrusive complex at depth.

- *Rapid formation of a giant epithermal gold deposit.* Lihir evolved from an incipient porphyry system to one of the world's largest epithermal gold resources over a very short geological time span (<345 k.y.) that included intermittent periods of hydrothermal quiescence. This was accompanied by multiple pulses of intrusive activity and volcanism as well as significant modification of the volcanic landscape. The majority of epithermal gold mineralization was deposited prior to the emplacement of the Lihir diatreme complex, further constraining the time required by >60 k.y..

- *Detailed investigation of the Lihir diatreme breccia complex has changed the proposed genetic model of ore formation at Lihir.* This study highlights a lack of evidence for early-formed diatreme breccias, and also for a genetic relationship with epithermal gold mineralization, instead concluding that diatreme volcanism had a late-mineralization timing.

- *The late-mineralization timing of diatreme volcanism has implications for brownfields exploration in the Luise amphitheater.* It is important to define the extents and timing of volcanic-hydrothermal brecciation, since diatremes are known to occur at all stages in the porphyry-epithermal lifecycle (Table 4.10). In the case of late-stage phreatomagmatic activity, as at Lihir, it is important to note that the main orebody may be truncated, disrupted and/or redistributed. This is pertinent to exploration as it implies that additional mineralization may be on the far side of a barren and potentially large body of matrix-rich breccias. At Lihir, it implies there is the possibility for high-grade gold mineralization on the far side of the volcanic-hydrothermal breccias to the north and west, beneath the amphitheater walls. There is also the possibility for gold mineralization to be discovered further along the trend of the diatreme contact to the northeast, within the floor of the Pacific Ocean.

- *The 3D diatreme breccia model (Fig. 4.28) is a valuable resource for mine engineers designing the Kapit open pit extension.* Kapit and Kapit NE areas feature large volumes of poorly consolidated volcanic-hydrothermal breccias at shallow depths, which pose risks to exploitation of the resource in these areas. The 3D model of the Lihir diatreme breccia complex can help engineers decide where lower angle bench walls may be appropriate

to mitigate risks in the open pit.

- *Diatreme breccias may pinpoint areas to explore for further epithermal gold mineralization in the TLTF island chain.* Recognition of porphyry and epithermal clasts would provide excellent indication for gold mineralization peripheral to the breccia body. Diatreme margins at Lihir and at several other porphyry-epithermal deposits worldwide have been shown to have provided a favorable conduit for fluid flow and mineralization and these areas warrant investigation. Diatreme breccias and porphyry-style copper-gold mineralization associated with the Matangkaka intrusive complex have been identified at Ambitle Volcano in the Feni Island Group of the TLTF island chain (Lindley, 2016). Similarly, diatremes and weak gold anomalies are known to occur within the Kinami volcanic amphitheater on Lihir Island. These sites would be prime areas to follow up with detailed mapping and scoping of diatremes.

- *Statistical and machine learning techniques can be applied to pyrite LA-ICP-MS raster map data to objectively define pyrite groups, with a broad range of implications for processing of refractory ore and research into the conditions and mechanisms of formation of Au-rich pyrite.* For example:

    - Pyrite groups may correlate with different textures or paragenetic stages and can be used to visualize textural features in composite grains (e.g., cores and rims, oscillatory bands, etc.). This can provide insight into the chemistry of pyrite crystallized under various physicochemical conditions. For instance, the chemistry of pyrite groups related to boiling textures (e.g., pyrite associated with bladed calcite and adularia alteration) from a range of low- and intermediate-sulfidation epithermal deposits could be investigated. These data could potentially then be used to help vector towards Au-Ag mineralization formed via boiling hydrothermal fluids in prospective areas with widespread pyrite.

    - Porphyry and epithermal pyrites can be distinguished. The distribution of porphyry and epithermal pyrite groups could then be used to visualize overprinting relationships in telescoped ore deposits.

    - These techniques allow for greater control in selecting chemical data from different paragenetic stages of pyrite, which may be useful for vectoring and fertility studies.

    - Geometallurgical characteristics of the pyrite groups can be defined, and the presence or absence of these pyrite groups can be visualized in the context of individual ore blocks or the entire ore deposit. This may help with the classification and domaining of ore types and the optimization of mineral processing. For example:

        - The variability of the pyrite (e.g., number of pyrite groups present in a sample) across the deposit can be evaluated.

        - The reactivity of pyrite groups can be assessed based on associated characteristics such as grain size and texture. For example, a pyrite group associated with finely colloform banded texture would be more reactive than a pyrite group associated with coarse-grained euhedral pyrite. Ores with higher proportions of reactive pyrite are likely to oxidize more rapidly and may therefore require a lower autoclave residence time.

        - Pyrite containing gold in inclusions can be differentiated from pyrite containing gold in the crystal lattice. Ore with a substantial proportion of gold as inclusions in pyrite may recover additional free gold through the use of gravity concentration methods.

- The association of benign, beneficial and/or deleterious elements with each pyrite group can be determined, which can inform on best practices for waste management.

- Gold deportment in composite grains can be established. This type of data may be used to inform mineral processing decisions. For example, if gold is enriched in the rims and not present in the core of a composite pyrite grain, then a shorter period of oxidation and leaching may be required to liberate the majority of gold from the grain.

- *LA-ICP-MS raster maps of pyrite show that there was episodic, most likely intrusion-related, fluid input during each stage of epithermal mineralization at Lihir.* Re–Os geochronology of molybdenite from Kapit NE porphyry veins also show that there were multiple stages of porphyry mineralization. Previous studies indicated that sulfur in pyrite and anhydrite have a predominantly magmatic source. This supports a strong link between alkalic magmatism and mineralization throughout the porphyry-epithermal lifecycle.

### 6.4 Recommendations for further research

Some recommendations for future research at Lihir include:

- *Refining the tectonic history of the New Guinea islands region over the last four million years.* This should involve a combination of seismic tomography, igneous geochronology and incorporation of existing datasets to produce improved plate-tectonic reconstructions and sea level models. This would provide further insight into the geodynamic processes and paleodepth conditions that resulted in the formation of such a unique, high grade and tonnage gold deposit.

- *Mapping the geology and structures of the TLTF islands (especially Lihir Island).* This will enhance the geological context with respect to the island history and further exploration efforts.

- *Deep drilling and exploration for igneous intrusions related to mineralization in the area of the Lihir gold deposit.* Since the Lihir porphyry and epithermal ores have a strong magmatic signature, these rocks would provide valuable information about the geochemical characteristics of a highly fertile magma. Melt inclusion studies on permissive igneous minerals (e.g., apatite) could be performed to estimate the volatile contents, P–T conditions and chemistry of the melts at the time of entrapment (e.g., Thomas and Klemm, 1997).

- *Determining the absolute timing of further key magmatic and hydrothermal events at Lihir.* Some suggested targets for geochronology include: (1) juvenile magmatic clasts from the various diatreme breccias, (2) ash from sector collapse or phreatomagmatic eruption deposits that may exist on neighboring islands (e.g., Mali and Masahet), (3) intrusions genetically related to porphyry mineralization, (4) molybdenite (and potentially other sulfide minerals) from epithermal-stage veins, and (5) volcanic and intrusive rocks from across Lihir Island (e.g., Ilkot prospect basalts). Note that high resolution U–Pb dating of minerals such as monazite or apatite may be required due to the paucity of zircons in some intrusions and lavas.

- *Studying the role of recent geothermal activity in the redistribution of gold ore at the base of the steam-heated zone.* This would involve the establishment of a comprehensive geological and hydrological model for the modern hydrothermal system, and analysis of the physicochemical conditions of the deep and shallow geothermal waters (including acid mine drainage), to see how surface fluids are altered as a result of interaction with the orebodies. An LA-ICP-MS pyrite raster map statistical appraisal could be applied to pyrite samples taken from

around the base of the steam-heated zone across the Lihir deposit, to better evaluate whether the pyrite rims that have been identified in this zone are syngenetic.

- *Applying the statistical and machine learning algorithm for LA-ICP-MS pyrite data used on this study to further samples from Lienetz and Kapit ore zones.* This method could be used to objectively identify pyrite types and textures for the optimization of future ore processing of Lienetz and Kapit ores. This may include the reprocessing of data from previous studies (e.g., Sykora et al., 2018b, Ageneau, 2012, and in-house studies by Newcrest Mining Limited).

# REFERENCES

Ageneau, M., 2012, Geology of the Kapit ore zone and comparative geochemistry with Minifie and Lienetz ore zones, Ladolam Gold Deposit, Lihir Island, Papua New Guinea: Unpublished Ph.D. thesis, Hobart, Australia, University of Tasmania, 269 p.

Ageneau, M., Cooke, D.R., Gemmell, J.B., Danyushevsky, L.V., and Rutter, J., 2011, The Kapit ore zone of the Ladolam low-sulfidation epithermal gold deposit: Geology, alteration, and comparison with the Lienetz and Minifie ore zones: Society for Geology Applied to Mineral Deposits (SGA), 11th Biennial SGA Meeting, Antofagasta, Chile, 2011, Proceedings, p. 718–720.

Ahmad, M., Solomon, M., and Walshe, J.L., 1987, Mineralogical and geochemical studies of the Emperor gold telluride deposit, Fiji: Economic Geology, v. 82, p. 345–370.

Ahmed, A.D., 2019, Epidote and chlorite mineral chemistry from the Yerington porphyry copper district, USA: Genetic and exploration implications: Unpublished Ph.D. thesis, Hobart, Australia, University of Tasmania, 468 p.

Allen, R.L., 1988, False pyroclastic textures in altered silicic lavas, with implications for volcanic-associated mineralization: Economic Geology, v. 83, p. 1424–1446.

Allen, R.L., 1992, Reconstruction of the tectonic, volcanic and sedimentary setting of strongly deformed Zn–Cu massive sulfide deposits at Benambra, Victoria, Australia: Economic Geology, v. 87, p. 825–854.

Ambler, E.P., 1979, The geology and geochemistry of the Yeoval porphyry copper prospect, NSW: Unpublished Ph.D. thesis, Sydney, Australia, Macquarie University, 235 p.

Appleby, K., Circosta, G., Fanning, M., and Logan, K., 1996, New model for controls on gold-silver mineralization on Misima Island: Mining Engineering, v. 48, p. 33–36.

Arribas, A., Hedenquist, J.W., Itaya, T., Okada, T., Concepcion, R.A., and Garcia, J.S., 1995, Contemporaneous formation of adjacent porphyry and epithermal Cu-Au deposits over 3000 ka in northern Luzon, Philippines: Geology, v. 23, p. 337–340.

Auer, A., Martin, U., and Németh, K., 2007, The Fekete-hegy (Balaton Highland Hungary) "soft-substrate" and "hard-substrate" maar volcanoes in an aligned volcanic complex – Implications for vent geometry, subsurface stratigraphy and the palaeoenvironmental setting: Journal of Volcanology and Geothermal Research, v. 159, p. 225–245.

Bainbridge, A.L., Hitchman, S.P., and DeRoss, G.J., 1998, Nena copper-gold deposit, *in* Berkman, D.A., and Mackenzie, D.H., eds., Geology of Australian and Papua New Guinean mineral deposits: Melbourne, The Australasian Institute of Mining and Metallurgy, p. 855–861.

Baldwin, S.L., Fitzgerald, P.G., and Webb, L.E., 2012, Tectonics of the New Guinea region: Annual Review of Earth and Planetary Sciences, v. 40, p. 495–520.

Baumgartner, R., Fontbonté, L., Spikings, R., Ovtcharova, M., Schaltegger, U., Schneider, J., Page, L., and Gutjahr, M., 2009, Bracketing the age of magmatic-hydrothermal activity at the Cerro de Pasco epithermal polymetallic deposit, Central Peru: A U-Pb and $^{40}Ar/^{39}Ar$ study: Economic Geology, v. 104, p. 479–504.

Bendezú, R., and Fontboté, L., 2009, Cordilleran epithermal Cu-Zn-Pb-(Au-Ag) mineralization in the Colquijirca district, Central Peru: Deposit-scale mineralogical patterns: Economic Geology, v. 104, p. 905–944.

Benning, L.G., Wilkin, R.T., and Barnes, H.L., 2000, Reaction pathways in the Fe–S system below 100°C: Chemical Geology, v. 167, p. 25–51.

Beverly, R.K., Beaumont, W., Tauz, D., Patel, S., Ormsby, K.M., von Reden, K., Santos, G.M., and Southon, J.R., 2010, The Keck Carbon Cycle AMS Laboratory, University of California, Irvine: Status report: Radiocarbon, v. 52, p. 301–309.

Blackwell, J.L., 2010, Characteristics and origins of breccias in a volcanic-hosted alkalic epithermal gold deposit, Ladolam, Lihir Island, Papua New Guinea: Unpublished Ph.D. thesis, Hobart, Australia, University of Tasmania, 203 p.

Blackwell, J.L., Cooke, D.R., McPhie, J., and Simpson, K.A., 2014, Lithofacies associations and evolution of the volcanic host succession to the Minifie ore zone, Ladolam gold deposit, Lihir Island, Papua New Guinea: Economic Geology, v. 109, p. 1137–1160.

Blount, C.W., and Dickson, F.W., 1969, The solubility of anhydrite ($CaSO_4$) in NaCl-$H_2O$ from 100 to 450°C and 1 to 1000 bars: Geochimica et Cosmochimica Acta, v. 33, p. 227–245.

Bortnikov, N., 1995, Sphalerite–galena geothermometers; distribution of cadmium, manganese and the fraction of sulfur isotopes: Economic Geology, v. 90, p. 155–180.

Boulter, C.A., 1993, High-level sills at Rio Tinto, Spain: Implications for stratigraphy and mineralization: Transactions of the Institute of Mining and Metallurgy (Section B: Applied Earth Science), 102, p. B30–B38.

Branney, M., and Suthren, R., 1988, High-level peperitic sills in the English Lake district: Distinction from block lavas, and implications for Borrowdale Volcanic Group stratigraphy: Geological Journal, v. 23, p. 171–187.

Braxton, D.P., 2007, Boyongan and Bayugo porphyry copper gold deposits NE Mindanao, Philippines: Geology, geochemistry and tectonic evolution: Unpublished Ph.D. thesis, Hobart, Australia, University of Tasmania, 277 p.

Braxton, D.P., Cooke, D.R., Ignacio, A.M., Rye, R.O., and Waters, P.J., 2009, Ultra-deep oxidation and exotic copper formation at the late Pliocene Boyongan and Bayugo porphyry copper-gold deposits, Surigao, Philippines: Geology, mineralogy, paleoaltimetry, and their implications for geologic, physiographic, and tectonic controls: Economic Geology, v. 104, p. 333–349.

Brooks, E.R., 1995, Paleozoic fluidization, folding, and peperite formation, northern Sierra Nevada, California: Canadian Journal of Earth Sciences, v. 32, p. 314–324.

Brown, K.L., and Bixley, P.F., 2005, Geochemistry of the Lihir geothermal field, Papua New Guinea: World Geothermal Congress, Antayla, Turkey, 2005, Proceedings, p. 1–6.

Brown, R.J., Branney, M.J., Maher, C., and Dávila-Harris, P., 2010, Origin of accretionary lapilli within ground-hugging density currents: Evidence from pyroclastic couplets on Tenerife: Geological Society of America Bulle-

tin, v. 122, p. 305–320.

Browne, P., 1978, Hydrothermal alteration in active geothermal fields: Annual Review of Earth and Planetary Sciences, v. 6, p. 229–250.

Bruns, T.R., Vedder, J.G., and Culotta, R.C., 1989, Structure and tectonics along the Kilinailau Trench, Bougainville–Buka Island region, Papua New Guinea, *in* Vedder, J.G., and Bruns, T.R., eds., Geology and offshore resources of Pacific Islands arcs – Solomon Islands and Bougainville, Papua New Guinea region: Circum Pacific Council for Energy and Mineral Resources Earth Science Series, v. 12, p. 93–123.

Buchanan, L.J., 1981, Precious metal deposits associated with volcanic environments in the southwest: Arizona Geological Society Digest, v. 14, p. 237–262.

Burkett, B., 2017, The geological evolution of the Kulumadau epithermal gold deposit, Woodlark Island, Papua New Guiea: Unpublished Ph.D. thesis, Kensington, Australia, University of New South Wales, 260 p.

Busby-Spera, C.J., and White, J.D.L., 1987, Variation in peperite textures associated with differing host-sediment properties: Bulletin of Volcanology, v. 49, p. 765–777.

Candela, P.A., 1997, A review of shallow, ore-related granites: Textures, volatiles, and ore metals: Journal of Petrology, v. 38, p. 1619–1633.

Cannell, J.B., 2004, El Teniente porphyry copper-molybdenum deposit, central Chile: Unpublished Ph.D. thesis, Hobart, Australia, University of Tasmania, 317 p.

Cannell, J., Cooke, D.R., Walshe, J.L., and Stein, H., 2005, Geology, mineralization, alteration, and structural evolution of the El Teniente porphyry Cu–Mo deposit: Economic Geology, v. 100, p. 979–1003.

Carman, G.D., 1994, Genesis of the Ladolam gold deposit, Lihir Island, Papua New Guinea: Unpublished Ph.D. thesis, Melbourne, Australia, Monash University, 381 p.

Carman, G.D., 2003, Geology, mineralization, and hydrothermal evolution of the Ladolam gold deposit, Lihir Island, Papua New Guinea: Society of Economic Geologists, Special Publication 10, p. 247–284.

Cas, R.A.F., and Wright, J.V., 1987, Volcanic successions: Modern and ancient: A geological approach to processes, products and successions: London, Allen & Unwin, 528 p.

Cater, G., 2002, Deep hydrothermal alteration at the Ladolam epithermal gold deposit, Lihir Island, Papua New Guinea: Unpublished M.Sc. thesis, Auckland, New Zealand, The University of Auckland, 94 p.

Chappell, J., 1974, The geomorphology and evolution of small valleys in dated coral reef terraces, New Guinea: The Journal of Geology, v. 82, p. 795–812.

Chapple, K.G., and Ibil, S., 1998, Gameta gold deposit, *in* Berkman, D.A., and MacKenzie, D.H., eds., Geology of Australian and Papua New Guinean mineral deposits: Melbourne, Australasian Institute of Mineralogy and Metallurgy, p. 849–854.

Chang, Z., Hedenquist, J.W., White, N.C., Cooke, D.R., Roach, M., Deyell, C.L., Garcia, J., Gemmell, J.B., McKnight, S., and Cuison, A.L., 2011, Exploration tools for linked porphyry and epithermal deposits: Example from the Mankayan intrusion-centered Cu-Au district, Luzon, Philippines: Economic Geology, v. 106, p. 1365–1398.

Chiaradia, M., Schaltegger, U., Spikings, R., Wotzlaw, J.F.,

and Ovtcharova, M., 2013, How accurately can we date the duration of magmatic-hydrothermal events in porphyry systems?—an invited paper: Economic Geology, v. 108, p. 565–584.

Chase, C.G., 1971, Tectonic history of the Fiji Plateau: Geological Society of America Bulletin, v. 82, p. 3087–3110.

Chivas, A.R., and McDougall, I., 1978. Geochronology of the Koloula porphyry copper prospect, Guadalcanal, Solomon Islands: Economic Geology, v. 73, p. 678–689.

Cioni, R., Sbrana, A., and Vecci, R., 1992, Morphologic features of juvenile pyroclasts from magmatic and phreatomagmatic deposits of Vesuvius: Journal of Volcanology and Geothermal Research, v. 51, p. 61–78.

Clode, C., Proffett, J., Mitchell, P., and Munajat, I., 1999, Relationships of intrusion, wall-rock alteration and mineralization in the Batu Hijau copper-gold porphyry deposit: Pacrim '99 Congress, Bali, Indonesia, 1999, Proceedings, p. 485–498.

Cloos, M., Sapiie, B., van Ufford, A.Q., Weiland, R.J., Warren, P.Q., and McMahon, T.P., 2005, Collisional delamination in New Guinea: The geotectonics of subducting slab breakoff: Geological Society of America Special Paper 400, 51 p.

Cooke, D.R., McPhail, D.C., and Bloom, M.S., 1996, Epithermal gold mineralization, Baguio district, Philippines: Geology, mineralization, alteration, and the thermochemical environment of ore deposition: Economic Geology, v. 91, p. 243–272.

Cooke, D.R., Hollings, P., and Walshe, J.L., 2005, Giant porphyry deposits: Characteristics, distribution, and tectonic controls: Economic Geology, v. 100, p. 801–818.

Cooke, D.R., Sykora, S., Lawlis, E., Blackwell, J.L., Ageneau, M., Jansen, N.H., Harris, A.C., and Selly, D., in press, Lihir alkalic epithermal gold deposit, Papua New Guinea: Society of Economic Geologists, Special Publication XXX, p. XXX–XXX.

Cooper, P., and Taylor, B., 1987, Seismotectonics of New Guinea: A model for arc reversal following arc-continent collision: Tectonics, v. 6, p. 53–67.

Cooper, P., and Taylor, B., 1989, Seismicity and focal mechanisms at the new Britain Trench related to deformation of the lithosphere: Tectonophysics, v. 164, p. 25–40.

Corbett, G., 2018, Epithermal gold-silver and porphyry copper-gold exploration: Chapter 4 breccias (https://corbettgeology.com/wp-content/uploads/2018/02/Chapter-4-Breccias-single-page18-2-18_-interactive.pdf).

Corbett, G., and Leach, T., 1998, Southwest Pacific Rim gold-copper systems: Structure, alteration, and mineralization: Society of Economic Geologists, Special Publication 6, 238 p.

Corbett, G., Hunt, S., Cook, A., Tamaduk, P., and Leach, T., 2001, Geology of the Ladolam gold deposit, Lihir Island, from exposures in the Minifie open pit: PNG Geology, Exploration and Mining Conference, Port Moresby, Papua New Guinea, 2001, Proceedings, p. 69–77.

Crawford, A.J., Meffre, S., Squire, R.J., Barron, L.M., and Falloon, T.J., 2007, Middle and Late Ordovician magmatic evolution of the Macquarie Arc, New South Wales: Australian Journal of Earth Sciences, v. 54, p. 181–214.

Crowe, B.M., and Fisher, R.V., 1973, Sedimentary structures in base-surge deposits with special reference to cross-bedding, Ubehebe craters, Death Valley, California: Geological Society of America Bulletin, v. 84, p.

663–682.

Dahl, P.S., 1996, The crystal-chemical basis for Ar retention in micas: Inferences from interlayer portioning and implications for geochronology: Contributions to Mineralogy and Petrology, v. 123, p. 22–39.

Danyushevsky, L., Robinson, P., Gilbert, S., Norman, M., Large, R., McGoldrick, P., and Shelley, M., 2011, Routine quantitative multi-element analysis of sulphide minerals by laser ablation ICP-MS: Standard development and consideration of matrix effects: Geochemistry: Exploration, Environment, Analysis, v. 11, p. 51–60.

Davies, H.L., 1973, Gazelle Peninsula, New Britain, 1:250 000 Geological Series—Explanatory Notes: Canberra, Bureau of Mineral Resources, Geology & Geophysics, 24 p.

Davies, A.G.S., 2002, Geology of the Kelian gold deposit: Unpublished Ph.D. thesis, Hobart, Australia, University of Tasmania, 404 p.

Davies, H.L., 2012, The geology of New Guinea: The cordilleran margin of the Australian continent: Episodes, v. 35, p. 87–102.

Davies, R.H., and Ballantyne, G.H., 1987, Geology of the Ladolam gold deposit Lihir Island, Papua New Guinea: The Australasian Institute of Mining and Metallurgy, Pacific Rim Congress 87, Gold Coast, Australia, 1987, Proceedings, p. 943–949.

Davies, A.G.S., Cooke, D.R., Gemmell, J.B., van Leeuwen, T., Cesare, P., and Hartshorn, G., 2008a, Hydrothermal breccias and veins at the Kelian gold mine, Kalimantan, Indonesia: Genesis of a large epithermal gold deposit: Economic Geology, v. 103, p. 717–757.

Davies, A.G.S., Cooke, D.R., Gemmell, J.B., and Simpson, K.A., 2008b, Diatreme breccias at the Kelian gold mine, Kalimantan, Indonesia: Precursors to epithermal gold mineralization: Economic Geology, v. 103, p. 689–716.

Douglass, D.L., Shing, C., and Wang, G., 1992, The light-induced alteration of realgar to pararealgar: American Mineralogist, v. 77, p. 1266–1274.

Dugmore, M.A., and Leaman, P.W., 1998, Mount Bini copper-gold deposit, *in* Berkman, D.A., and Mackenzie, D.H., eds., Geology of Australian and Papua New Guinean mineral deposits: Melbourne, The Australasian Institute of Mining and Metallurgy, p. 843–848.

Ebert, S.W., and Rye, R.O., 1997, Secondary precious metal enrichment by steam-heated fluids in the Crofoot-Lewis hot spring gold-silver deposit and relation to paleoclimate: Economic Geology, v. 92, p. 578–600.

Einaudi, M.T., 1997, Mapping altered and mineralized rocks: An introduction to the "Anaconda method": Stanford, Stanford University, 16 p.

Einaudi, M.T., Hedenquist, J.W., and Esra Inan, E., 2003, Sulfidation state of fluids in active and extinct hydrothermal systems: Transitions from porphyry to epithermal environments: Society of Economic Geologists, Special Publication 10, p. 285–313.

Exon, N.F., and Tiffin, D.L., 1984, Geology and petroleum prospects of offshore New Ireland Basin in northern Papua New Guinea, *in* Watson, S.T., ed., Transactions of the Third Circum-Pacific Energy and Mineral Resources Conference: Tulsa, American Association of Petroleum Geologists, p. 623–630.

Exon, N.F., Stewart, W.D., Sandy, M.J., and Tiffin, D.L., 1986, Geology and offshore petroleum prospects of the eastern New Ireland Basin, northeastern Papua New Guinea: BMR Journal of Australian Geology and Geo-

physics, v. 10, p. 39–51.

Exon, N.F., Stewart, W.D., Sandy, M.J., and Tiffin, D.L., 1987, Geology and offshore petroleum prospects of the eastern New Ireland Basin, northeastern Papua New Guinea: Journal of Australian Geology and Geophysics, v. 10, p. 39–53.

Faulkner, D.R., Jackson, C.A.L., Lunn, R.J., Schlische, R.W., Shipton, Z.K., Wibberley, C.A.J., and Withjack, M.O., 2010, A review of recent developments concerning the structure, mechanics and fluid flow properties of fault zones: Journal of Structural Geology, v. 32, p. 1557–1575.

Ferrini, V., Martarelli, L., De Vito, C., Çina, A., and Deda, T., 2003, The Koman dawsonite and realgar-orpiment deposit, northern Albania: Inferences on processes of formation: The Canadian Mineralogist, v. 41, p. 413–427.

Fleet, M.E., Chryssoulis, S.L., MacLean, P.J., Davidson, R., and Weisener, C.G., 1993, Arsenian pyrite from gold deposits; Au and As distribution investigated by SIMS and EMP, and color staining and surface oxidation by XPS and LIMS: The Canadian Mineralogist, v. 31, p. 1–17.

Foland, K.A.,1994, Argon diffusion in feldspars, *in* Parsons, I., ed., Feldspars and their reactions: Dordrecht, Kluwer Academic Publishers, NATO ASI Series C421, p. 415–447.

French, D.J., 1966, The geology of southern New Ireland: Bureau of Mineral Resources, Geology and Geophysics, Record 1966/179, 21 p.

Gallasch, H., 1976, A solution cave in volcanolithic arenite – Lihir Island: Niugini Caver, v. 4, p. 31–33.

Garcia, Jr., J.S., 1991, Geology and mineralization characteristics of the Mankayan mineral district, Benguet, Philippines: Geological Survey of Japan, Report 277, p. 21–30.

Garwin, S.L., 2000, The setting, geometry and timing of intrusion-related hydrothermal systems in the vicinity of the Batu Hijau porphyry copper-gold deposit, Sumbawa, Indonesia: Unpublished Ph.D. thesis, Perth, Australia, University of Western Australia, 320 p.

Gazley, M., Collins, K., Robertson, J., Hines, B., Fisher, L., and McFarlane, A., 2015, Application of multivariate statistics and cluster analysis to mineral exploration and mine geology, *in* AusIMM New Zealand Branch Annual Conference 2015: Dunedin, The Australasian Institute of Mining and Metallurgy, New Zealand Branch, p. 131–139.

Gemmell, J.B., Sharpe, R., Jonasson, I.R., and Herzig, P.M., 2004, Sulfur isotope evidence for magmatic contributions to submarine and subaerial gold mineralization: Conical seamount and the Ladolam gold deposit, Papua New Guinea: Economic Geology, v. 99, p. 1711–1725.

Gena, K., 2013, Deep sea mining of submarine hydrothermal deposits and its possible environmental impact in Manus Basin, Papua New Guinea: Procedia Earth and Planetary Science, v. 6, 226–233.

Gifkins, C., Herrmann, W., and Large, R., 2005, Altered volcanic rocks: A guide to description and interpretation: Hobart, Centre for Ore Deposit Research, University of Tasmania, 275 p.

Giggenbach, W.F., 1997, The origin and evolution of fluids in magmatic-hydrothermal systems, *in* Barnes, H.L., ed., Geochemistry of hydrothermal ore deposits, 3rd ed.: New York, John Wiley & Sons, p. 737–796.

Global Volcanism Program, 2013a, Volcanoes of the world, v. 4.8.5. Venzke, E., ed.: Smithsonian Institution, (https://doi.org/10.5479/si.GVP.VOTW4-2013).

Global Volcanism Program, 2013b, Smithsonian Institution, National Museum of Natural History, Global volcanism program: (https://volcano.si.edu/).

Grant, J.N., and Nielsen, R.L., 1975, Geology and geochronology of the Yandera porphyry copper deposit, Papua New Guinea: Economic Geology, v. 70, p. 1157–1174.

Grégoire, M., McInnes, B.I.A, and O'Reilly, 2001, Hydrous metasomatism of oceanic sub-arc mantle Lihir, Papua New Guinea Part 2, Trace element characteristics of slab-derived fluids: Lithos, v. 59, p. 91–108.

Gregory, M.J., Lang, J.R., Gilbert, S., and Hoal, K.O., 2013, Geometallurgy of the Pebble porphyry Cu-Au-Mo deposit, Alaska: Implications for gold distribution and paragenesis: Economic Geology, v. 108, p. 463–482.

Griffen, D.T., 1992, Silicate crystal chemistry: New York, Oxford University Press, 442 p.

Grove, M., and Harrison, T.M., 1996, $^{40}Ar^{*}$ diffusion in Fe-rich biotite: American Mineralogist, v. 81, p. 940–951.

Guillong, M., Hametner, K., Reusser, E., Wilson, S.A., and Günther, D., 2005, Preliminary characterisation of new glass reference materials (GSA1G, GSC1G, GSD1G, and GSE1G) by laser ablation-inductively coupled plasma-mass spectrometry using 193 nm, 213 nm, and 266 nm wavelengths: Geostandards and Geoanalytical Research, v. 29, p. 315–331.

Gutscher, M- A., Maury, R., Eissen, J.P., and Bourdon, E., 2000, Can slab melting be caused by flat subduction?: Geology, v. 28, p. 535–538.

Halevy, I., and Bachan, A., 2017, The geologic history of seawater pH: Science, v. 355, p. 1069–1071.

Hall, R., 2002, Cenozoic geological and plate tectonic evolution of SE Asia and the SW Pacific: Computer-based reconstructions, model and animations: Journal of Asian Earth Sciences, v. 20, p.353–431.

Hames, W.E., and Bowring, S.A., 1994, An empirical evaluation of the argon diffusion geometry in muscovite: Earth and Planetary Science Letter, v. 124, p. 161–169.

Hannington, M.D., and Scott, S.D., 1985, A caldera-hosted silica-sulfate-sulfide deposit, Axial Seamount, central Juan de Fuca Ridge, N.E. Pacific Ocean: G.A.C.-M.A.C. Joint Annual Meeting, Fredericton, Canada, 1985, Program with Abstracts, v. 10, p. A24.

Hanor, J.S., 2000, Barite–celestine geochemistry and environments of formation, *in* Alpers, C.N., Jambor, J.L., and Nordstrom, D.K., eds., Sulfate minerals: Crystallography, geochemistry and environmental significance, 40: Blacksburg, Virginia, p. 193–275.

Hanson, R.E., 1991, Quenching and hydroclastic disruption of andesitic to rhyolitic intrusions in a submarine island-arc sequence, northern Sierra-Nevada, California: Geological Society of America Bulletin, v. 103, p. 804–816.

Hanson, R.E., and Hargrove, U.S., 1999, Processes of magma/wet sediment interaction in a large-scale Jurassic andesitic peperite complex, northern Sierra Nevada, California: Bulletin of Volcanology, v. 60, p. 610–626.

Harrison, R.L., 2018, The Tumpangpitu porphyry gold-copper-modlybdenum and high-sulfidation epithermal gold-silver deposit, Tujuh Bukit, Southeast Java, Indonesia: Unpublished Ph.D. thesis, Hobart, Australia, University of Tasmania, 311 p.

Harrison, T.M., 1981, Diffusion of $^{40}$Ar in hornblende: Contributions to Mineralogy and Petrology, v. 78, p. 324–331.

Harrison, T.M., and McDougall, I., 1980, Investigations of an intrusive contact, northwest Nelson, New Zealand - I. Thermal, chronological and isotopic constraints: Geochimica et Cosmochimica Acta, v. 44, p. 1985–2004.

Harrison, T.M., Duncan, I., and Dougall, I., 1985, Diffusion of $^{40}$Ar in biotite: Temperature, pressure and compositional effects: Geochimica et Cosmochimica Acta, v. 49, p. 2461–2468.

Heaney, P.J., 1993, A proposed mechanism for the growth of chalcedony: Contributions to Mineralogy and Petrology, v. 115, p. 66–74.

Hedenquist, J.W., and Henley, R.W., 1985, Hydrothermal eruptions in the Waiotapu geothermal system, New Zealand: Their origin, associated breccias, and relation to precious metal mineralization: Economic Geology, v. 80, p. 1640–1668.

Hedenquist, J.W., Arribas, A., and Reynolds, T.J., 1998, Evolution of an intrusion-centred hydrothermal system: Far Southeast-Lepanto porphyry and epithermal Cu-Au deposits, Philippines: Economic Geology, v. 93, p. 373–404.

Hedenquist, J.W., Arribas, A., and Gonzalez-Urien, E., 2000, Exploration for epithermal gold deposits: Society of Economic Geologists Reviews, v. 13, p. 245–277.

Henley, R.W., and Ellis, A.J., 1983, Geothermal systems ancient and modern: A geochemical review: Earth Science Reviews, v. 19, p. 1–50.

Herzig, P.M., 1996, Tectonics, petrology and hydrothermal processes in areas of alkaline island-arc volcanoes in the Southwest Pacific: The Tabar-Lihir-Tanga-Feni island chain, Papua New Guinea; Final Report Sonne-94, BMFT FK 03G0094A0, *in* Herzig, P.M., and Becker, K.-P., eds.: Freiberg, Freiberg University of Mining and Technology, p. 289.

Herzig, P.M, Hannington, M., Stoffers, P., and Shipboard Scientific Party, 1994, Tectonics, petrology, and hydrothermal processes in areas of alkaline island-arc volcanoes in the southwest Pacific: The Tabar–Lihir–Tanga–Feni island chain, Papua New Guinea: Cruise report Sonne-94: Freiberg, Freiberg University of Mining and Technology, 273 p.

Herzig, P.M, Hannington, M., Stoffers, P., and Shipboard Scientific Party, 1998, Petrology, gold mineralization, and biological communities at shallow submarine volcanoes of the New Ireland fore-arc (Papua New Guinea): Preliminary results of R/V Sonne cruise SO-133: InterRidge News , v. 7, p. 34–38.

Herzig, P.M., Petersen, S. and Hannington, M.D., 1999, Epithermal-type gold mineralization at Conical seamount: A shallow submarine volcano south of Lihir Island, Papua New Guinea, *in* Stanley, C.J., et al., eds., Mineral deposits: Processes to processing, v. 1: 5$^{th}$ biennial SGA meeting and the 10$^{th}$ Quadrennial IAGOD symposium, London, England, 1999, Proceedings, p. 527–530.

Herzig, P.M., Petersen, S., Kuhn, T., Hannington, M.D., Gemmell, J.B., and Skinner, A.C., 2003. Shallow drilling of seafloor hydrothermal systems: The missing link, *in* Eliopoulos, D.G., et al., eds., Mineral exploration and sustainable development: Rotterdam, Millpress, p. 103–105.

Hilde, T.W.C., Uyeda, S., and Kroenke, L., 1977, Evolution of the western Pacific and its margin: present state of plate tectonics: Tectonophysics, v. 38, p. 145–165.

Hill, K.C., and Hall, R., 2003, Mesozoic-Cenozoic evolution of Australia's New Guinea margin in a west Pacific context: Geological Society of America Special Paper 372, p. 265–290.

Hill, K.C., and Raza, A., 1999, Arc-continent collision in Papua Guinea: Constraints from fission track thermochronology: Tectonics, v. 18, p. 950–966.

Hine, R., Bye, S.M., Cook, F.W., Leckie, J.F., and Torr, G.L., 1978, The Esis porphyry copper deposit, East New Britain, Papua New Guinea: Economic Geology, v. 73, p. 761–767.

Hohnen, P.D., 1978, Geology of New Ireland, Papua New Guinea, Bureau of Mineral Resources, Geology and Geophysics, Bulletin 194, p. 1–39.

Hollings, P., Wolfe, R., Cooke, D.R., and Waters, P., 2011, Geochemistry of Tertiary igneous rocks of northern Luzon, Philippines: Evidence for a back-arc setting for alkalic porphyry copper-gold deposits and a case for slab rollback?: Economic Geology, v. 106, p. 1257–1277.

Holm, R.J., and Richards, S.W., 2013, A re-evaluation of arc-continent collision and along-arc variation in the Bismarck Sea region, Papua New Guinea: Australian Journal of Earth Sciences, v. 60, p. 605–619.

Holm, R.J., Spandler, C., and Richards, S.W., 2013, Melanesian arc far-field response to collision of the Ontong Java Plateau: Geochronology and petrogenesis of the Simuku Igneous Complex, New Britain, Papua New Guinea: Tectonophysics, v. 603, p. 189–212.

Holm, R.J., Spandler, C., Richards, S.W., 2015, Continental collision, orogenesis and arc magmatism of the Miocene Maramuni arc, Papua New Guinea: Gondwana Research, v. 28, p. 1117–1136.

Holm, R.J., Rosenbaum G., and Richards, S.W., 2016, Post 8 Ma reconstruction of Papua New Guinea and Solomon Islands: Microplate tectonics in a convergent plate boundary setting: Earth-Science Reviews, v, 156, p. 66–81.

Hope, A.R., 2011, The Hope Factor: Mineral discoveries Australasia, Papua New Guinea and the Philippines: Battery Point, Anthony R. Hope, 536 p.

Horz, K.H., Worthington, T.J., Winn, K., and Stoffers, P., 2004, Late Quaternary tephra in the New Ireland Basin, Papua New Guinea: Journal of Volcanology and Geothermal Research, v. 132, p. 73–95.

Houghton, B.F., and Smith, R.T., 1993, Recycling of magmatic clasts during explosive eruptions: Estimating the true juvenile content of phreatomagmatic volcanic deposits: Bulletin of Volcanology, v. 55, p. 414–420.

Howell, F.H., and Molloy, J.S., 1960, Geology of the Braden orebody, Chile, South America: Economic Geology, v. 55, p. 863–905.

Ishikawa, Y., Sawaguchi, T., Iwaya, S., and Horiuchi, M., 1976, Delineation of prospecting targets for Kuroko deposits based on modes of volcanism of underlying dacite and alteration halos: Mining Geology, v. 26, p. 105–117 (in Japanese with English abstract).

Jakeš, P., and Gill, J., 1970, Rare earth elements and the island arc tholeiitic series: Earth and Planetary Science Letters, v. 9, p. 17–28.

James, A.N., and Lupton, A.R., 1978, Gypsum and anhydrite in foundation of hydraulic structures: Geotechnique, v. 28, p. 249–272.

Jansen, N.H., and Cooke, D.R., 2013, Geology and geochemistry of the Lihir steam-heated blanket: Final re-

port 1 of 2: Unpublished report to Newcrest Mining Limited, 18 p.

Jansen, N.H., Cooke, D.R., Harris, A.C., and McKnight, S.W. 2017, Near-infrared effectiveness on degraded core in tropical climates: Economic Geology, v. 112, p. 1011–1019.

Jaques, A.L., and Webb, A.W., 1975, Geochronology of 'porphyry copper' intrusives from Manus Island, Papua New Guinea: Geological Survey of Papua New Guinea, Report 75/5, 7 p.

Jébrak, M., 1997, Hydrothermal breccias in vein-type ore deposits: A review of mechanisms, morphology and size distribution: Ore Geology Reviews, v. 12, p. 111–134.

Jensen, E.P., 2003, Magmatic and hydrothermal evolution of the Cripple Creek gold deposit, Colorado, and comparisons with regional and global magmatic-hydrothermal systems associated with alkaline magmatism: Unpublished Ph.D. thesis, Tuscon, USA, University of Arizona, 846 p.

Jensen, E.P., and Barton, M.D., 2000, Gold deposits related to alkaline magmatism: Reviews in Economic Geology, v. 13, p. 279–314.

JICA (Japan International Cooperation Agency), 1983, Report on Acupan-Itogon geothermal development, First phase survey, 94 p.

Jimenez Torres, C.A., 2018, Geology, hydrothermal alteration, geochemistry, mineral geochemistry, and alteration textures of the lithocap at Bantug, Negros-Philippines: Unpublished Ph.D. thesis, Hobart, Australia, University of Tasmania, 381 p.

John, D.A., Vikre, P.G.; du Bray, E.A., Blakely, R.J., Fey, D.L., Rockwell, B.W., Mauk, J.L., Anderson, E.D., and Graybeal, F.T., 2018, Descriptive models for epithermal gold-silver deposits: USGS scientific investigation report 2010-5070-Q: Washington, United States Government Publishing Office, 247 p.

Johnson, R.W., 1979, Geotectonics and volcanism in Papua New Guinea: A review of the late Cainozoic: Bureau of Mineral Resources Journal of Australian Geology and Geophysics, v. 4, p. 181–207.

Johnson, H.D., and Baldwin, C.T., 1996, Shallow clastic seas, *in* Reading, H.G., ed., Sedimentary environments: Processes, facies and stratigraphy, 3rd ed.: Oxford, Wiley-Blackwell, 704 p.

Johnson, D.M., and Christiansen, E.H., 2016, The nature and origin of pebble dikes and associated alteration: Tintic mining district (Ag-Pb-Zn-Au), Utah, *in* Comer, J.B., Inkenbrandt, P.C., Krahulec, K.A., and Pinnell, M.L., eds., Resources and geology of Utah's West Desert: Salt Lake City, Utah Geological Association, v. 45, p. 13–42.

Johnson, R.W., Wallace, D.A., and Ellis, D.J., 1976, Feldspathoid-bearing potassic rocks and associated types from volcanic islands off the coast of New Ireland, Papua New Guinea: A preliminary account of geology and petrology, *in* Johnson, R.W., ed., Volcanism in Australasia, Elsevier Amsterdam, p. 297–316.

Johnson, R.W., Mackenzie, D.E., and Smith, I.E.M., 1978, Delayed partial melting of subduction-modified mantle in Papua New Guinea: Tectonophysics, v. 46, p. 197–216.

Johnson, R.W., Mutter, J.C. and Arculus, R.J., 1979, Origin of the Willaumez-Manus rise, Papua New Guinea: Earth and Planetary Science Letters, v. 44, p. 247–260.

Johnson, R.W., Itikarai, I., Patia, H., and McKee, C.O., 2010, Volcanic systems of the northeastern Gazelle Peninsula, Papua New Guinea: Synopsis, evaluation, and a model for Rabaul Volcano: Kokopo, Papua New Guinea Department of Mineral Policy and Geohazards Management and the Australian Agency for International Development, Port Moresby, Rabaul Volcano Workshop Report, 84 p.

Jordan, S.C., Cas, R.A.F., and Hayman, P.C., 2013, The origin of a large (>3 km) maar volcano by coalescence of multiple shallow craters: Lake Purrumbete maar, southeastern Australia: Journal of Volcanology and Geothermal Research, v. 254, p. 5–22.

Kamenov, G.D., Perfit, M.R., Jonasson, I.R., Mueller, P.A., 2005, High-precision Pb isotope measurements reveal magma recharge as a mechanism for ore deposit formation: Examples from Lihir Island and Conical seamount, Papua New Guinea: Chemical Geology, v. 219, p. 131–148.

Kamenov, G.D., Perfit, M.R., Mueller, P.A., and Jonasson, I.R., 2008, Controls on magmatism in an island arc environment: Study of lavas and sub-arc xenoliths from the Tabar-Lihir-Tanga-Feni island chain, Papua New Guinea: Contributions to Mineralogy and Petrology, v. 155, p. 635–656.

Kennedy, A.K., Groves, D.I., and Johnson, R.W., 1990a, Experimental and major element constraints on the evolution of lavas from Lihir Island, Papua New Guinea: Contributions to Mineralogy and Petrology, v. 104, p. 722–734.

Kidd, R.P., and Robinson, J.R., 2004, A review of the Kapit orebody Lihir Island Group, Papua New Guinea: The Australasian Institute of Mining and Metallurgy, Pacific Rim Congress 04, Adelaide, Australia, 2004, Proceedings, p. 323–331.

Klemm, L.M., 1965, Synthesen und analysen in den dreiecksdiagrammen FeAsS–CoAsS–NiAsS und $FeS_2$–$CoS_2$–$NiS_2$: Neues Jahrbuch für Mineralogie, v. 103, p. 205–255.

Klemm, L.M., Pettke, T., Heinrich, C.A., and Campos, E., 2007, Hydrothermal evolution of the El Teniente deposit, Chile: Porphyry Cu-Mo ore deposition from low-salinity magmatic fluids: Economic Geology, v. 102, p. 1021–1045.

Klimchouk, A., 1996, The dissolution and conversion and gypsum and anhydrite: International Journal of Speleology, v. 25, p. 21–36.

Kokelaar, B.P., 1982, Fluidization of wet sediments during the emplacement and cooling of various igneous bodies: Journal of the Geological Society, London, v. 139, p. 21–33.

Komyshan, P., 1999, Geological interpretations of Lihir Island: Unpublished report (R8.99) prepared for Lihir Gold Limited (LGL), August 1999, Consulting Scientists of Australia (CSA Australia Pty. Ltd.), 40 p.

Koppers, A.A.P., 2002, ArArCALC—software for $^{40}Ar/^{39}Ar$ age calculations: Computers & Geosciences, v. 28, p. 605–619.

Kroenke, L.W., 1984, Cenozoic tectonic development of the southwest Pacific: U.N. ESCAP, CCOP/SOPAC Technical Bulletin 6, p. 111–122.

Kuiper, K.F., Deino, A., Hilgen, F.J., Krijgsman, W., Renne, P.R., and Wijbrans, J.B., 2008, Synchronizing rock clocks of Earth history: Science, v. 320, p. 500–504.

Landtwing, M.R., Dillenbeck, E.D., Leake, M.H., and Heinrich, C.A., 2002, Evolution of the breccia-hosted porphyry Cu-Mo-Au deposit at Agua Rica, Argentina: Pro-

gressive unroofing of a magmatic hydrothermal system: Economic Geology, v. 97, p. 1273–1292.

Langmead, R.P., and McLeod, R.L., 1990, Tolukuma gold deposit, *in* Hughes, F.E., ed., Geology of the Mineral Deposits of Australia and Papua New Guinea: Melbourne, The Australasian Institute of Mining and Metallurgy, p. 1777–1781.

Large, R.J., Gemmell, B., Paulick, H. and Houston, D.L., 2001, The alteration box plot: A simple approach to understanding the relationship between alteration mineralogy and lithogeochemistry associated with volcanic-hosted massive sulfide deposits: Economic Geology, v. 96, p. 957–971.

Large, R.R., Danyushevsky, L., Hollit, C., Maslennikov, V., Meffre, S., Gilbert, S., Bull, S., Scott, R., Emsbo, P., Thomas, H., Singh, B., and Foster, J., 2009, Gold and trace element zonation in pyrite using a laser imaging technique: Implications for the timing of gold in orogenic and Carlin-style sediment-hosted deposits: Economic Geology, v. 104, p. 635–668.

Large, S.J.E., von Quadt, A., Wotzlaw, J.-F., Guillong, M., and Heinrich, C.A., 2018, Magma evolution leading to porphyry Au-Cu mineralization at the Ok Tedi deposit, Papua New Guinea: Trace element geochemistry and high-precision geochronology of igneous zircon: Economic Geology, v. 113, p. 39–61.

Lawley, C.J.M., and Selby, D., 2012, Re-Os geochronology of quartz-enclosed ultrafine molybdenite: Implications for ore geochronology: Economic Geology, v. 107, p. 1499–1505.

Lawlis, E., Cooke, D.R., and Harris, A.C., 2015, Volcanic-hydrothermal breccias at the Lihir alkalic gold deposits, Papua New Guinea: 13th Biennial SGA Meeting, Nancy, France, 2015, Extended Abstract, p. 317–320.

Le Bas, M.J., Le Maitre, R.W., Steckeisen, A., and Zanettin, B., 1986, A chemical classification of volcanic rocks based on the total alkali–silica diagram: Journal of Petrology, v. 27, p. 745–750.

Le Bas, M.J., Le Maitre, R.W., and Woolley, A.R., 1992, The construction of the total alkali–silica chemical classification of volcanic rocks: Mineralogy and Petrology, v. 46, p. 1–22.

Le Maitre, R. W., 1989, A classification of igneous rocks and glossary of terms: Recommendations of the International Union of Geological Sciences subcommission on the systematics of igneous rocks, 1st ed.: Oxford: Blackwell, 193 p.

Lechler, P.J., and Desilets, M.O., 1987, A review of the use of loss on ignition as a measurement of total volatiles in whole-rock analysis: Chemical Geology, v. 63, p. 341–344.

Leys, C., Cloos, M., New, B.T.E., and MacDonald, D.G., 2012, Gold, copper ± molybdenum deposits of the Ertsberg-Grasberg district, Papua, Indonesia: Economic Geology, v. 16, p. 215–235.

Licence, P., Terrill, J., and Fergusson, L., 1987, Epithermal gold mineralisation, Ambitle Island, Papua New Guinea: Pacific Rim Congress, 1987, p. 273–278.

Lindley, I.D., 1988, Early Cainozoic stratigraphy and structure of the Gazelle Peninsula, East New Britain: An example of extensional tectonics in the New Britain arc-trench complex: Australian Journal of Earth Sciences, v. 35, p. 231–244.

Lindley, I.D., 1990, Wild Dog gold deposit, *in* Hughes, F.E., ed., Geology of the Mineral Deposits of Australia and Papua New Guinea: Melbourne, The Australasian Institute of Mining and Metallurgy, p. 1789–1792.

Lindley, I.D., 1998, Mount Sinivit gold deposits, *in* Berkman, D.A., and Mackenzie, D.H., eds., Geology of Australian and Papua New Guinean mineral deposits: Melbourne, The Australasian Institute of Mining and Metallurgy, p. 821–826.

Lindley, I.D., 2006a, Extensional and vertical tectonics in the New Guinea islands: Implications for island arc evolution: Annals of Geophysics, v. 49, p. 403–426.

Lindley, I.D., 2006b, New Britain trench, Papua New Guinea: An extensional element in a regional sinistral strike-slip system: New Concepts in Global Tectonics Newsletter, v. 41, p. 16–28.

Lindley, I.D., 2016, Plate flexure and volcanism: Late Cenozoic tectonics of the Tabar–Lihir–Tanga–Feni alkalic province, New Ireland Basin, Papua New Guinea: Tectonophysics, p. 312–323.

Longo, A.A., Dilles, J.H., Grunder, A.L., and Duncan, R., 2010, Evolution of calc-alkaline volcanism and associated hydrothermal gold deposits at Yanacocha, Peru: Economic Geology, v. 105, p. 1191–1240.

Lorenz, V., 1974, Vesiculated tuffs and associated features: Sedimentology, v. 21, p. 273–291.

Lorenz, V., 1985, Maars and diatremes of phreatomagmatic origin, a review: Transactions of the Geological Society of South Africa, v. 88, p. 459–470.

Lorenz, V., 2003, Maar-diatreme volcanoes, their formation, and their setting in hard-rock or soft-rock environments: Geolines, v. 15, p. 72–83.

Lorenz, V., and Kurszlaukis, K., 2007, Root zone processes in the phreatomagmatic pipe emplacement model and consequences for the evolution of maar-diatreme volcanoes: Journal of Volcanology and Geothermal Research, v. 159, p. 4–32.

Lottermoser, B.G., 1990, Rare-earth element and heavy-metal behavior associated with the epithermal gold deposit on Lihir Island, Papua New Guinea: Journal of Volcanology and Geothermal Research, v. 40, p. 269–289.

Love, D.A., Clark, A.H., Hodgson, C.J., Mortensen, J.K., Archibald, D.A., and Farrar, E., 1998, The timing of adularia-sericite-type mineralisation and alunite-kaolinite-type alteration, Mount Skukum epithermal gold deposit, Yukon Territory, Canada: $^{40}$Ar-$^{39}$Ar and U-Pb geochronology: Economic Geology, v. 93, p. 437–462.

Lovera, O.M., Richter, F.N., and Harrison, T.M., 1989, The $^{40}$Ar/$^{39}$Ar thermochronometry for slowly cooled samples having a distribution of diffusion domain sizes: Journal of Geophysical Research, v. 94, p. 17917–17935.

Lovera, O.M., Richter, F.N., and Harrison, T.M., 1991, Diffusion domains determined by $^{39}$Ar released during step heating: Journal of Geophysical Research, v. 96, p. 2057–2069.

Lovera, O.M., Grove, M., Harrison, T.M., and Mahoni, K.I., 1997, Systematic analysis of K-feldspar $^{40}$Ar/$^{39}$Ar step heating results: I. Significance of activation energy determinations: Geochimica et Cosmochimica Acta, v. 61, p. 3171–3192.

Macdonald, G.A., 1939, An intrusive peperite at San Pedro Hill, California: University of California, Department of Geological Sciences Bulletin, v. 24, p. 329–338.

MacDonald, G.D., and Arnold, L.C., 1994, Geological and geochemical zoning of the Grasberg igneous complex, Irian Jaya, Indonesia: Journal of Geochemical Exploration, v. 50, p. 143–178.

Maicher, D., White, J.D.L., and Batiza, R., 2000, Sheet hyaloclastite: Density-current deposits of quench and bubble-burst fragments from thin, glassy sheet lava flows, Seamount Six, Eastern Pacific Ocean: Marine Geology, v. 171, p. 75–94.

Markey, R.J., Stein, H.J., and Morgan, J.W., 1998, Highly precise Re-Os dating for molybdenite using alkaline fusion and NTIMS: Talanta, v. 45, p. 935–946.

Marlow, M.S., Exon, N.F., Ryan, H.F., and Dadisman, S.V., 1988, Offshore structure and stratigraphy of New Ireland Basin in northern Papua New Guinea, *in* Marlow, M.S., Dadisman, S.V., and Exon, N.F., eds., Geology and offshore resources of Pacific island arcs—New Ireland and Manus region, Papua New Guinea: Houston, Circum-Pacific Council for Energy and Mineral Resources, Earth Science Series, v. 9, p. 137–155.

Martin, U., and Németh, K., 2007, Blocky versus fluidal peperite textures developed in volcanic conduits, vents and crater lakes of phreatomagmatic volcanoes in Mio/Pliocene volcanic fields of Western Hungary: Journal of Volcanology and Geothermal Research, v. 159, p. 164–178.

Martinez, F., and Taylor, B., 1996, Back arc spreading, rifting and microplate rotation, between transform faults in the Manus basin: Marine Geophysical Researches, v. 18, p. 203–224.

Maryono, A., Priowasono, E., 2000, Final report on the Gold-Ridge-Santong program: Unpublished internal technical report for PT, Newmont Nusa Tenggara, 6 p.

Maryono, A., and Setyandhaka, D., 2001, Rinti project report 2001, Sumbawa, Indonesia: Newmont internal company report, 45 p.

Maryono, A., Lubis, H., Perdankusumah, A. and Hermawan, W., 2005, The Elang porphyry copper and gold mineralization style Sumbawa, Indonesia: Indonesian Minerals and Coal Discoveries: IAGI conference, p. 34–51.

Maryono, A., Rompo, I., and Maula S., 2013, Brambang project report 2010 to 2012, SW Lombok: Buena Persada internal company report, 89 p.

Masterman, G., 2003, Geology of the Rosario Cu-Mo-Ag Mine, Collahuasi, Chile: Unpublished Ph.D. thesis, Hobart, Australia, University of Tasmania, 253 p.

Maynard, S.R., 1995, Gold mineralization associated with mid-Tertiary magmatism and tectonism, Ortiz Mountains, Santa Fe County, New Mexico: Geology of the Santa Fe Region: New Mexico Geological Society 46th Annual Fall Field Conference Guidebook, p. 161–166.

McCue, K.F., 1988, Earthquakes and crustal stress in the north Bismarck Sea, *in* Marlow, M.S., Dadisman, S.V., and Exon, N.F., eds., Geology and offshore resources of Pacific island arcs—New Ireland and Manus region, Papua New Guinea: Houston, Circum-Pacific Council for Energy and Mineral Resources, Earth Science Series, v. 9, p. 41-46.

McInnes, B.I.A, 1992, A glimpse of ephemeral subduction zone processes from Simberi Island, Papua New Guinea: Unpublished Ph.D. thesis, Ottawa, Canada, University of Ottawa, 224 p.

McInnes, B.I.A., and Cameron, E.M., 1994, Carbonated, alkaline hybridizing melts from a sub-arc environment: Mantle wedge samples from the Tabar–Lihir–Tanga–Feni arc, Papua New Guinea: Earth and Planetary Science Letters, v. 122, p. 125–141.

McInnes, B.I.A., and Amiribesheli, S., 2018, An active petroleum system in the New Ireland Basin: Papua New

Guinea's new frontier carbonate play: PESGB Asia Pacific E & P Conference, London, England, 2018, Abstract, 1 p.

McInnes, B.I.A., Gregoire, M., Binns, R.A., Herzig, P.M., and Hannington, M.D., 2001, Hydrous metasomatism of oceanic sub-arc mantle, Lihir, Papua New Guinea: Petrology and geochemistry of fluid-metasomatised mantle wedge xenoliths: Earth and Planetary Science Letters, v. 188, p. 169–183.

McKenzie, D., 1978, Some remarks on the development of sedimentary basins: Earth and Planetary Science Letters, v. 40, p. 25–32.

McNeil, P.A., 1990, Wapolu gold deposit, Fegusson Island: Australasian Institute of Mineralogy and Metallalurgy, Monograph Series 14, p. 1783–1788.

McPhie, J., Doyle, M., and Allen, R., 1993, Volcanic textures: A guide to the interpretation of textures in volcanic rocks: Hobart, CODES Key Centre, University of Tasmania, 196 p.

Migdisov, A.A., and Bychkov, A.Y., 1998, The behaviour of metals and sulphur during the formation of hydrothermal mercury–antimony–arsenic mineralization, Uzon caldera, Kamchatka, Russia: Journal of Volcanology and Geothermal Research, v. 84, p. 153–171.

Moon, H-S., Song, Y., and Lee, S.Y., 1994, Supergene vermiculitization of phlogopite and biotite in ultramafic and mafic rocks, central Korea: Clays and clay minerals, v. 42, p. 259–268.

Moore, J.G., and Peck, D.L., 1962, Accretionary lapilli in volcanic rocks of the western continental United States: The Journal of Geology, v. 70, p. 182–194.

Moore, J.G., and Lockwood, J.P., 1978, Spreading cracks on pillow lava: Journal of Geology, v. 86, p. 661–671.

Mort, K., and Woodcock, N.H., 2008, Quantifying fault breccia geometry: Dent Fault, NW England: Journal of Structural Geology, v. 30, p. 701–709.

Moyle, A.J., Doyle, B.J., Hoogvliet, H., and Ware, A.R., 1990, Ladolam gold deposit, Lihir Island, *in* Hughes, F.E., ed., Geology of the mineral deposits of Australia and Papua New Guinea: Melbourne, The Australasian Institute of Mining and Metallurgy, p. 1793–1805.

Müller, D., Rock, N.M.S., and Groves, D.I., 1992, Geochemical discrimination between shoshonitic and potassic volcanic rocks in different tectonic settings: A pilot study: Mineralogy and Petrology, v. 46, p. 259–289.

Müller, D., Franz, L., Herzig, P.M., and Hunt, S., 2001, Potassic igneous rocks from the vicinity of epithermal gold mineralization, Lihir Island, Papua New Guinea: Lithos, v. 57, p. 163–186.

Müller, D., Herzig, P., Scholten, J., and Hunt, S., 2002a, Ladolam gold deposit, Lihir Island, Papua New Guinea: Gold mineralization hosted by alkaline rocks: Society of Economic Geologists, Special Publication 9, p. 367–382.

Müller, D., Kaminski, K., Uhlig, S., Graupner, T., Herzig, P.M., and Hunt, S., 2002b, The transition from porphyry- to epithermal-style gold mineralization at Ladolam, Lihir Island, Papua New Guinea: A reconnaissance study: Mineralium Deposita, v. 37, p. 61–74.

Müller, D., Franz, L., Petersen, S., Herzig, P.M., and Hannington, M.D., 2003, Comparison between magmatic activity and gold mineralization at Conical Seamount and Lihir Island, Papua New Guinea: Mineralogy and Petrology, v. 79, p. 259–283.

Murrowchick, J.B., and Barnes, H.L., 1986, Marcasite precipitation from hydrothermal solutions: Geochimica et Cosmochimica Acta, v. 50, p. 2615–2629.

Nelson, R.W., Bartram, J.A., and Christie, M.H., 1990, Hidden Valley gold-silver deposit, *in* Hughes, F.E., ed., Geology of the mineral deposits of Australia and Papua New Guinea: Melbourne, The Australasian Institute of Mining and Metallurgy, p. 1763–1767.

Németh, K., Martin, U., and Harangi, S., 2001, Miocene phreatomagmatic volcanism at Tihany (Pannonian Basin, Hungary): Journal of Volcanology and Geothermal Research, v. 111, p. 111–135.

Newcrest Mining Ltd., 2019, Annual mineral resources and ore reserves statement - 31 December 2018, (https://www.newcrest.com/sites/default/files/2019-10/181231_Newcrest%20December%202018%20Resources%20and%20Reserves%20-%20Statement.pdf).

Noble, D., Vidal, C., Miranda, M., Amaya, W., and McCormack, J., 2011, Ovoidal-and mottled-textured rock and associated silica veinlets and their formation by high-temperature outgassing of subjacent magma, *in* Steininger, R., and Pennell, B., eds., Geological Society of Nevada 2010: Symposium Great Basin Evolution and Metallogeny: Lancaster, DEStech Publications, Inc., p. 795–811.

Noku, S.K., Masahide, A., and Hiroharu, M., 2010, The Crater Mountain deposit, Papua New Guinea: Porphyry-related Au–Te system: Resource Geology, v. 61, p. 63–75.

O'Kane, T., 2008, 3-D structure and tectonic evolution of the Papua New Guinea and Solomon Islands region and its relationship to Cu–Au mineralization: Unpublished B.Sc. Honours thesis, Australian National University, 74 p.

Oreskes, N., and Einaudi, M.T., 1990, Origin of rare earth element-enriched hematite breccias at the Olympic Dam Cu-U-Au-Ag deposit, Roxby Downs, South Australia: Economic Geology, v. 85, p. 1–28.

Orovan, E.A., 2016, Geology, geochemistry, and genesis of the Namosi porphyry Cu-Au deposits, Fiji: Unpublished Ph.D. thesis, Hobart, Australia, University of Tasmania, 292 p.

Page, R.W., and McDougall, I., 1972a, Ages of mineralization of gold and porphyry copper deposits in the New Guinea highlands: Economic Geology, v. 67, p. 1034–1048.

Page, R.W., and McDougall, I., 1972b, Geochronology of the Panguna porphyry copper deposit, Bougainville Island, New Guinea: Economic Geology, v. 67, p. 1065–1074.

Peccerillo, A., and Taylor, S.R., 1976, Geochemistry of Eocene calc-alkaline volcanic rocks from the Kastamonu area, northern Turkey: Contributions to Mineralogy and Petrology, v. 58, p. 63–81.

Peterson, E.C., and Mavrogenes, J.A., 2014, Linking high-grade gold mineralization to earthquake-induced fault-valve processes in the Porgera gold deposit, Papua New Guinea: Geology, v. 42, p. 383–386.

Petersen, S., Herzig, P.M., Hannington, M.D., Jonasson, I.R., and Arribas, A., 2002, Submarine gold mineralization near Lihir Island, New Ireland fore-arc, Papua New Guinea: Economic Geology, v. 97, p. 1795–1813.

Petterson, M.G., Babbs, T., Neal, C.R., Mahoney, J.J., Saunders, A.D., Duncan, R.A., Tolia, D., Magu, R., Qopoto, C., Mahoa, H., Natogga, D., 1999, Geological-tectonic framework of Solomon Islands, SW Pacific: crustal ac-

cretion and growth with an intra-oceanic setting: Tectonophysics, v. 301, p. 35–60.

Pettijohn, F.J., 1975, Sedimentary rocks, 2nd edition: New York, Harper and Row Publishers, 628 p.

Pichler, T., Giggenbach, W.F., McInnes, B.I.A., Buhl, D., and Duck, B., 1999, Fe sulfide formation due to seawater-gas-sediment interaction in a shallow-water hydrothermal system at Lihir Island, Papua New Guinea: Economic Geology, v. 94, p. 281–288.

Pigram, C.J., and Davies, H.L., 1987, Terranes and the accretion history of the New Guinea orogen: BMR Journal of Australian Geology and Geophysics, v. 10, p. 193–211.

Piquer, J., Skarmeta, J., and Cooke, D.R., 2015, Structural evolution of the Rio Blanco-Los Bronces district, Andes of central Chile: Controls on stratigraphy, magmatism and mineralization: Economic Geology, v. 110, p. 995–2023.

Pollard, P.J., Taylor, R.G., and Peters, L., 2005, Ages of intrusion, alteration, and mineralization at the Grasberg Cu-Au deposit, Papua, Indonesia: Economic Geology, v. 100, p. 1005–1020.

Pridmore, D.F., 1991, Aeromagnetic interpretation at Lihir Island: Unpublished report prepared for Kennecott Explorations (Australia) Ltd., April 1991, World Geoscience Corporation Ltd., 9 p.

Rae, A.J., Ramirez, L.E., Villafuerte, G., Kilgour, G., Milicich, S.D., Fraser, H., and Bignall, G., 2010, Recent exploration drilling at Lihir geothermal field, PNG: Effects of catastrophic sector collapse on a magmatic-hydrothermal system: World Geothermal Congress, Bali, Indonesia, 2010, Proceedings, p. 1–5.

Reich, M., Kesler, S.E., Utsunomiya, S., Palenik, C.S., Chryssoulis, S.L., and Ewing, R.C., 2005, Solubility of gold in arsenian pyrite: Geochimica et Cosmochimica Acta, v. 69, p. 2781–2796.

Reyes, A.G., 1990, Petrology of Philippine geothermal systems and the application of alteration mineralogy to their assessment: Journal of Volcanology and Geothermal Research, v. 43, p. 279–309.

Richards, J.P., 1995, Alkalic type epithermal deposits—a review: Mineralogical Association of Canada Short Course Series, v. 23, p. 367–400.

Richards, J.P., 2003, Tectono-magmatic precursors for porphyry Cu-(Mo-Au) deposit formation: Economic Geology, v. 96, p. 1515–1533.

Richards, J.P., and Ledlie, I., 1993, Alkalic intrusive rocks associated with the Mount Kare gold deposit, Papua New Guinea; comparison with the Porgera intrusive complex: Economic Geology, v. 88, p. 755–781.

Richards, J.P., Wilkinson, D., and Ullrich, T., 2006, Geology of the Sari Gunay epithermal gold deposit, northwest Iran: Economic Geology, v. 101, p. 1455–1496.

Rickwood, P.C., 1989, Boundary lines within petrologic diagrams which use oxides of major and minor elements: Lithos, v. 22, p. 247–263.

Rinne, M., 2015, Geology, alteration, and mineralisation of the Golpu porphyry and Wafi epithermal deposit, Morobe Province, Papua New Guinea: Unpublished Ph.D. thesis, Hobart, Australia, University of Tasmania, 255 p.

Rinne, M.L., Cooke, D.R., Harris, A.C., Finn, D.J., Allen, M.A., Heizler, M.T., and Creaser, R.A., 2018, Geology and geochronology of the Golpu porphyry and Wafi epithermal deposit, Morobe Province, Papua New Guinea: Economic Geology, v. 113, p. 271–294.

Roache, M.W., Allen, S.R., and McPhie, J., 2000, Surface and subsurface facies architecture of a small hydroexplosive, rhyolitic centre in the Mesoproterozoic Gawler Range Volcanics, South Australia: Journal of Volcanology and Geothermal Research, v. 101, p. 237–259.

Robbins, G.A., 1972, Radiogenic Ar diffusion in muscovite under hydrothermal conditions: Unpublished M.Sc. thesis, Providence, USA, Brown University, 38 p.

Rogerson, R.J., Hilyard, D.B., Finlayson, E.J., Holland, D.J., Nion, S.T.S., Sumaiang, R.M., Duguman, J., and Loxton, C.D.C., 1987, The geology and mineral resources of the Sepik headwaters region, Papua New Guinea: Geological Survey of Papua New Guinea, Memoir 12, 130 p.

Román, N., Reich, M., Leisen, M., Morata, D., Barra, F., and Deditius, A.P., 2018, Geochemical and micro-textural fingerprints of boiling in pyrite: Geochimica et Cosmochimica Acta, v. 246, p. 60–85.

Rompo, I., Maryono, A., and Rowe, A., 2012, Porphyry Cu-Au and epithermal Au-Ag mineralization systems in southwest Lombok: Conference paper MGEI BESA (Indonesian Society of Economic Geologists, Eastern Sunda Banda Arc) Resources Seminar Malang, E. Java, Indonesia, 13 p.

Ronacher, E., Richards, J.P., Villeneuve, M.E., and Johnston, M.D., 2002, Short life-span of the ore- forming system at the Porgera gold deposit, Papua New Guinea: Laser $^{40}Ar/^{39}Ar$ dates for roscoelite, biotite, and hornblende: Mineralium Deposita, v. 37, p. 75–86.

Ross, M.E., 1986, Flow differentiation, phenocryst alignment, and compositional trends within a dolerite dike at Rockport, Massachusetts: Geologic Society of America Bulletin, v. 97, p. 232–240.

Russell, P.J., and Finlayson, E.J., 1987, Volcanic-hosted epithermal mineralization on Woodlark Island, Papua New Guinea: The Australasian Institute of Mining and Metallurgy, Pacific Rim Congress 87, Gold Coast, Australia, 1987, Proceedings, p. 381–385.

Rutter, J., Blackwell, J.L., Carmen, G.D., Cooke, D.R., Dala, K., Javati, N., Johnstone, R., Kikiha, D., Likia, B., McPhie, J., and O'Sullivan, T., 2008, The character and spatial distribution of epithermal gold mineralisation at the Ladolam gold deposit, Lihir Island, Papua New Guinea: The Australasian Institute of Mining and Metallurgy, Pacific Rim Congress 08, Gold Coast, Australia, 2008, Proceedings, p. 433–438.

Ruxton, B.P., 1966, Correlation and stratigraphy of dacitic ash-fall layers in northeastern Papua: Journal of the Geological Society of Australia, v. 13, p. 41–67.

Ryan, W.B.F., Carbotte, S.M., Coplan, J.O., O'Hara, S., Melkonian, A., Arko, R., Weissel, R.A., Ferrini, V., Goodwillie, A., Nitsche, F., Bonczkowski, J., and Zemsky, R., 2009, Global multi-resolution topography synthesis: Geochemistry, Geophysics, Geosystems, v. 10, Q03014, doi:10.1029/2008GC002332.

Rytuba, J.J., McKee, E.H., and Cox, D.P., 1993, Geochronology and geochemistry of the Ladolam gold deposit, Lihir Island, and gold deposits and volcanoes of Tabar and Tatau, Papua New Guinea: United States Geological Survey Bulletin, v. 2039, p. 119–126.

Santos, G.M., Southon, J.R., Druffel-Rodriguez, K., Griffin, S., and Mazon, M., 2004, Magnesium perchlorate as an alternative water trap in AMS graphite sample preparation: A report on sample preparation at the KCCAMS Facility at the University of California, Irvine: Radiocarbon, v. 46, p. 165–173.

Santos, G.M., Moore, R.B., Southon, J.R., Griffin, S., Hinger, E., and Zhang, D., 2007, AMS $^{14}C$ sample preparation

at the KCCAMS/UCI facility: Status report and performance of small samples: Radiocarbon, v. 49, p. 255–269.

Schardt, C., Cooke, D.R., Gemmell, J.B., and Large, R.R., 2001, Geochemical modeling of the zoned footwall alteration pipe, Hellyer volcanic-hosted massive sulfide deposit, Western Tasmania, Australia: Economic Geology, v. 96, p. 1037–1054.

Schoonen, M.A.A., and Barnes, H.L., 1991a, Reactions forming pyrite and marcasite from solution: II. Via FeS precursors below 100°C: Geochimica et Cosmochimica Acta, v. 55, p. 1505–1514.

Schoonen, M.A.A., and Barnes, H.L., 1991b, Mechanisms of pyrite and marcasite formation from solution: III. Hydrothermal processes: Geochimica et Cosmochimica Acta, v. 55, p. 3491–3504.

Schumacher, R., and Schminke, H.-U., 1991, Internal structure and occurrence of accretionary lapilli - A case study at Laacher See Volcano: Bulletin of Volcanology, v. 53, p. 612–634.

Schumacher, R., and Schminke, H.-U., 1995, Models for the origin of accretionary lapilli: Bulletin of Volcanology, v. 56, p. 626–639.

Seedorff, E., Dilles, J.H., Proffett, Jr., J.M., Einaudi, M.T., Zurcher, L., Stavast, W.J.A., Johnson, D.A., and Barton, M.D., 2005, Porphyry deposits: Characteristics and origin of hypogene features: Economic Geology 100th Anniversary Volume, p. 251–298.

Selby, D., and Creaser, R.A., 2004, Macroscale NTIMS and microscale LA-MC-ICP-MS Re-Os isotopic analysis of molybdenite; testing spatial restrictions for reliable Re-Os age determinations, and implications for the decoupling of Re and Os within molybdenite: Geochimica et Cosmochimica Acta, v. 68, p. 3897–3908.

Self, S., and Sparks, R.J.S., 1978, Characteristics of widespread pyroclastic deposits formed by the interaction of silicic magma and water: Bulletin of Volcanology v. 41, p. 196–212.

Sharp, W.D., and Clague, D.A., 2006, 50 Ma initiation of Hawaiian-Emperor bend records major change in Pacific plate motion: Science, v. 313, p. 1281–1284.

Sherlock, R., 2000, The association of gold–mercury mineralization and hydrocarbons in the coast ranges of northern California, *in* Glikson, M., and Mastalerz, M., eds., Organic matter and mineralization: Thermal alteration, hydrocarbon generation and the role of metallogenesis: Dordrecht, Springer, p. 378–399.

Sillitoe, R.H., 1985, Ore-related breccias in volcanoplutonic arcs: Economic Geology, v. 80, p. 1467–1514.

Sillitoe, R.H., 1989, Gold deposits in western Pacific island arcs: The magmatic connection: Economic Geology Monograph 6, p. 274–291.

Sillitoe, R.H., 1994, Erosion and collapse of volcanos: Causes of telescoping in intrusion-centered ore deposits: Geology, v. 22, p. 945–948.

Sillitoe, R.H., 2010, Porphyry copper systems: Economic Geology, v. 105, p. 3–41.

Sillitoe, R.H., and Bonham, H.F., 1984, Volcanic landforms and ore deposits: Economic Geology, v. 79, p. 1286–1298.

Sillitoe, R.H., Baker, E.M., and Brook, W.A., 1984, Gold deposits and hydrothermal eruption breccias associated with a maar volcano at Wau, PNG: Economic Geology, v. 79, p. 638–655.

Sillitoe, R.H., Grauberger, G.L., and Elliott, J.E., 1985, A di-

atreme-hosted gold deposit at Montana Tunnels, Montana: Economic Geology, v. 80, p. 1707–1721.

Sillitoe, R.H., Tolman, J., and Van Kerkvoort, G., 2013, Geology of the Caspiche porphyry gold-copper deposit, Maricunga Belt, northern Chile: Economic Geology, v. 108, p. 585–604.

Simmons, S.F., and Christenson, B.W., 1994, Origins of calcite in a boiling geothermal system: American Journal of Science, v. 294, p. 361–400.

Simmons, S.F., and Brown, K.L., 2006, Gold in magmatic hydrothermal solutions and the rapid formation of a giant ore deposit: Science, v. 314, p. 288–291.

Simmons, S.F., and Browne, P.R.L., 2000, Hydrothermal minerals and precious metals in the Broadlands-Ohaaki geothermal system: Implications for understanding low-sulfidation epithermal environments: Economic Geology, v. 95, p. 971–999.

Simmons, S.F., Mauk, J.L., and Simpson, M.P., 2000, The mineral products of boiling in the Golden Cross epithermal deposit: New Zealand Minerals & Mining Conference, Wellington, New Zealand, 2000, Conference Proceedings, p. 209–216.

Simmons, S.F., White, N.C., and John, D.A., 2005, Geological characteristics of epithermal precious and base metal deposits: Economic Geology 100th Anniversary Volume, v. 29, p. 485–522.

Simon, G., Kesler, S.E., Essene, E.J., and Chryssoulis, S.L., 2000, Gold in porphyry copper deposits: Experimental determination of the distribution of gold in the Cu-Fe-S system at 400° to 700°C: Economic Geology, v. 95, p. 259–270.

Singer, D.A., Berger, V.I., and Moring, B.C., 2008, Porphyry copper deposits of the world—Database and grade and tonnage models, 2008: U.S. Geological Survey Open File Report 2008–1155, 45 p.

Sinton, J.M., Ford, L.L., Chappell, B., and McCulloch, M.T., 2003, Magma genesis and mantle heterogeneity in the Manus back-arc basin, Papua New Guinea: Journal of Petrology, v. 44, p. 159–195.

Skilling, I.P., White, J.D.L., and McPhie, J., 2002, Peperite: A review of magma-sediment mingling: Journal of Volcanology and Geothermal Research, v. 114, p. 1–17.

Smith, T.L, and Batiza, R., 1989, New field and laboratory evidence for the origin of hyaloclastite flows on seamount summits: Bulletin of Volcanology, v. 51, p. 96–114.

Smith, G.A., and Lowe, D.R., 1991, Lahars: Volcano-hydrologic events and deposition in the debris flow—hyperconcentrated flow continuum, *in* Fisher, R.V., and Smith, G.A., eds., Sedimentation in volcanic settings, SEPM Special Publication: Tulsa, Society for Sedimentary Geology, v. 45, p. 60–70.

Spry, P.G., and Scherbarth, N.L., 2006, The gold–vanadium–tellurium association at the Tuvatu gold–silver prospect, Fiji: Conditions of ore deposition: Mineralogy and Petrology, v. 87, p. 171–186.

Sohn, Y.K., Park, K.H., 2004. Composite tuff ring/cone complexes in Jeju Island, Korea: Possible consequences of substrate collapse and vent migration: Journal of Volcanology and Geothermal Research, v. 141, p. 157–175.

Stoffregen, R.E., and Alpers, C.N., 1987, Woodhouseite and svanbergite in hydrothermal ore deposits: products of apatite destruction during advanced argillic alteration: The Canadian Mineralogist, v. 25, p. 201–211.

Stow, D.A.V., 2005, Sedimentary rocks in the field: A colour guide: London, Manson Publishing, 320 p.

Stuiver, M., and Polach, H., 1977, Discussion reporting of $^{14}C$ data: Radiocarbon, v. 19, p. 355–363.

Sun, S.-S., and McDonough, W.F., 1989, Chemical and isotopic systematics of oceanic basalts: Implications for mantle composition and processes, *in* Saunders, A. D., and Norry, M. J., eds., Magmatism in the ocean basins: Geological Society of America Special Publication 42, p. 313–345.

Sutopo, B., 2013, The Martabe Au-Ag high-sulfidation epithermal deposits, Sumatra, Indonesia: Implications for ore genesis and exploration: Unpublished Ph.D. thesis, Hobart, Australia, University of Tasmania, 352 p.

Sykora, S., 2017, Origin, evolution and significance of anhydrite-bearing vein arrays and breccias, Lienetz orebody, Lihir gold deposit, Papua New Guinea: Ph.D. thesis, Hobart, Australia, University of Tasmania, 149 p.

Sykora, S., Selley, D., Cooke, D.R., and Harris, A.C., 2018a, The structure and significance of anhydrite-bearing vein arrays, Lihir gold deposit, Papua New Guinea: Economic Geology, v. 113, p. 237–270.

Sykora, S., Cooke, D.R., Meffre, S., Stephanov, A.S., Gardner, K., Scott, R., Selley, D., and Harris, A.C., 2018b, Evolution of pyrite trace element compositions from porphyry-style and epithermal conditions at the Lihir gold deposit: Implications for ore genesis and mineral processing: Economic Geology, v. 113, p. 193–208.

Tămaş, C.G., and Milési, J.-P., 2002, Hydrovolcanic breccia pipe structures - General features and genetic criteria - I. Phreatomagmatic breccias: Studia Universitatis Babeş-Bolyai Geologia, v. 47, p. 127–147.

Tămaş, C.G., and Milési, J.-P., 2003, Hydrothermal breccia pipe structures - General features and genetic criteria - II. Phreatic breccias: Studia Universitatis Babeş-Bolyai Geologia, v. 48, p. 55–66.

Taylor, B., 1979, Bismarck Sea: Evolution of a back-arc basin: Geology, v. 7, p. 171–174.

Taylor, F.W., Bevis, M.G., Schutz, B.E., Kuang, D., Recy, J., Calmant, S., Charley, D., Regnier, M., Perin, B., Jackson, M., and Reichenfeld, C., 1995, Geodetic measurements of convergence at the New Hebrides island arc indicate arc fragmentation caused by an impinging aseismic ridge: Geology, v. 23, p. 1011–1014.

Taylor, B., Goodliffe, A.M., and Martinez, F., 1999, How continents break up: Insights from Papua New Guinea: Journal of Geophysical Research, v. 104, p. 7497–7512.

Teal, L., and Benevides, A., 2010, History and geologic overview of the Yanacocha mining district, Cajamarca, Peru: Economic Geology, v. 105, p. 1173–1190.

Thomas, R., and Klemm, W., Microthermometric study of silicate melt inclusions in Variscan granites from SE Germany: Volatile contents and entrapment conditions: Journal of Petrology, v. 38, p. 1753–1765.

Thompson, T.B., 1992, Mineral deposits of the Cripple Creek district, Colorado: Mining Engineering, v. 44, p. 135–138.

Thompson, T.B., Trippel, A.D., and Dwelley, P.C., 1985, Mineralized veins and breccias of the Cripple Creek district, Colorado: Economic Geology, v. 80, p. 1669–1688.

Titley, S.R., 1978, Geologic history, hypogene features, and processes of secondary sulfide enrichment at the Plesyumi copper prospect, New Britain, Papua New

Guinea: Economic Geology, v. 73, p. 768–784.

Titley, S.R., 1982, The style and progress of mineralization and alteration in porphyry copper systems, *in* Titley, S.R., ed., Advances in geology of the porphyry copper deposits: Southwestern North America: Tuscon, University of Arizona Press, p. 93–116.

Torckler, L.K., McKay, D., and Hobbins, J., 2006, Geology and exploration of the Favona Au-Ag deposit, Waihi, Hauraki goldfield: The Australasian Institute of Mining and Metallurgy, Monograph 25, p. 179–184.

Tregoning, P., 2002, Plate kinematics in the western Pacific derived from geodetic observations: Journal of Geophysical Research: Solid Earth, v. 107, p. 1–7.

Tregoning, P., and Gorbatov, A., 2004, Evidence for active subduction at the New Guinea Trench: Geophysical Research Letters, v. 31, L13608, doi: 10.1029/2004GL020190.

Tregoning, P., Lambeck, K., Stolz, A., Morgan, P., McClusky, S.C., van der Beek, P., McQueen, H., Jackson, R.J., Little, R.P., Laing, A., and Murphy, B., 1998, Estimation of current plate motions in Papua New Guinea from Global Positioning System observations: Journal of Geophysical Research: Solid Earth, v. 103, p. 12181–12203.

Tregoning, P., McQueen, H., Lambeck, K., Jackson, R., Little, R., Saunders, S., and Rosa, R., 2000, Present-day crustal motion in Papua New Guinea: Earth, Planets and Space, v. 52, p. 727–730.

Turner, S.J., 1997, The Yanacocha epithermal gold deposits, northern Peru: High-sulfidation mineralization in a flow dome setting: Unpublished Ph.D. thesis, Golden, USA, Colorado School of Mines, 341 p.

Üner, S., 2014, Seismogenic structures in Quaternary lacustrine deposits of Lake Van (eastern Turkey): Geologos, v. 20, p. 79–87.

van Ufford, A.Q., and Cloos, M., 2005, Cenozoic tectonics of New Guinea: The American Association of Petroleum Geologists Bulletin, v. 89, p. 119–140.

van Hinsberg, V.J., Henry, D.J., and Marschall, H.R., 2011, Tourmaline: An ideal indicator of its host environment: The Canadian Mineralogist, v. 49, p. 1–16.

Valentine, G.A., White, J.D.L., Ross, P.-S., Graettinger, A.H., and Sonder, I., 2017, Updates to concepts on phreatomagmatic maar-diatremes and their pyroclastic deposits: Frontiers in Earth Science, v. 5, p. 1–7.

Verave, R.T., and Kawagle, S.A., 2010, The geological framework of Papua New Guinea—An overiew, *in* Miura, S., Noguchi, N., Coffin, M.F., Kawagle, S.A., and Verave, R.T., eds., Cruise report R/V Kairei KR10-05 high resolution deep seismic study of the Ontong Java Plateau: Yokosuka, Japan Agency for Marine-Earth Science and Technology, 88 p.

Vidal, C., and Ligarda, R., 2004, Enargite-gold deposits at Marcapunta, Colquijirca mining district, central Perú: Mineralogic and geochemical zoning in subvolcanic, limestone-replacement deposits of high-sulfidation epithermal type: Society of Economic Geologists, Special Publication 11, p. 231–242.

Walker, G.P.L., 1992, Morphometric study of pillow-size spectrum among pillow lavas: Bulletin of Volcanology, v. 54, p. 459–474.

Wallace, D.A., Johnson, R.W., Chappell, B.W., Arculus, R.J., Perfit, M.R., and Crick, I.H., 1983, Cainozoic volcanism of the Tabar, Lihir, Tanga, and Feni Islands, Papua New Guinea; geology, whole-rock analyses, and rock-form-

ing mineral compositions: Bureau of Mineral Resources, Geology and Geophysics Report, v. 243, 62 p.

Wallace, L.M., Stevens, C., Silver, E., McCaffrey, R., Loratung, W., Hasiata, S., Stanaway, R., Curley, R., Rosa, R., and Taugaloidi, J., 2004, GPS and seismological constraints on active tectonics and arc-continent collision in Papua New Guinea: Implications for mechanics of microplate rotations in a plate boundary zone: Journal of Geophysical Research: Solid Earth, v. 109, p. 1–16.

Wallace, L.M., McCaffrey, R., Beavan, J., and Ellis, S., 2005, Rapid microplate rotations and backarc rifting at the transition between collision and subduction: Geology, v. 33, p. 857–860.

Wallier, S., Rey, R., Kouzmanov, K., Pettke, T., Heinrich, C.H., Leary, S., O'Connor, G., Tămaş¸ C.G., Vennemann, T., and Ullrich, T., 2006, Magmatic fluids in the breccia-hosted epithermal Au-Ag deposit of Roşia Montană, Romania: Economic Geology, v. 101, p. 923–954.

Warnaars, F.W., Holmgren, C., and Barassi, S., 1985, Porphyry copper and tourmaline breccias at Los Bronces-Rio Blanco, Chile: Economic Geology, v. 80, p. 1544–1565.

Webb, L.E., Baldwin, S.L., and Fitzgerald, P.G., 2014, The Early-Middle Miocene subduction complex of the Louisiade Archipelago, southern margin of the Woodlark Rift: Geochemistry, Geophysics, Geosystems, v. 15, p. 4024–4046.

Weissel, J.K., and Hayes, D.E., 1977, Evolution of the Tasman Sea reappraised: Earth and Planetary Science Letters, v. 36, p. 77–84.

Wessel, P., and Kroenke, L.W., 2000, Ontong Java Plateau and late Neogene changes in Pacific plate motion: Journal of Geophysical Research: Solid Earth, v. 105, p. 28255–28277.

Whalen, J.B., Britten, R.M., and McDougall, I., 1982, Geochronology and geochemistry of the Frieda River prospect area, Papua New Guinea: Economic Geology, v. 77, p. 592–616.

White, J.D.L., 1996, Impure coolants and interaction dynamics of phreatomagmatic eruptions: Journal of Volcanology and Geothermal Research, v. 74, p. 155–170.

White, N.C., and Hedenquist, J.W., 1995, Epithermal gold deposits: styles, characteristics, and exploration: Economic Geology, v. 23, p. 9–13.

White, P., Ussher, G., and Hermoso, D., 2010, Evolution of the Ladolam geothermal system on Lihir Island, Papua New Guinea: World Geothermal Congress, Bali, Indonesia, 2010, p. 25–29.

Wilkinson, J.J., Chang, Z., Cooke, D.R., Baker, M.J., Wilkinson, C.C., Inglis, S., Chen, H., and Gemmell, J.B., 2015, The chlorite proximitor: A new tool for detecting porphyry ore deposits: Journal of Geochemical Exploration, v. 152, p. 10–26.

Williams, N.C., and Davidson, G.J., 2004, Possible submarine advanced argillic alteration at the Basin Lake prospect, Western Tasmania, Australia: Economic Geology, v. 99, p. 987–1002.

Williamson, A., 1983, Thermal activity on Lihir Island, New Ireland Province: Port Moresby, Geological Survey of Papua New Guinea, Report 83/15, p. 1–21.

Williamson, A., and Hancock, G., 2005, The geology and mineral potential of Papua New Guinea: Port Moresby, Papua New Guinea Department of Mining, 154 p.

Wilson, J.C., 1975, Ore-magma relation in a late-stage dike, *in* Bray, R.E., and Wilson, J.C., eds., Guidebook to the Bingham mining district, Society of Economic Geologists, October 23, 1975: Bingham Canyon, Kennecott Copper Corporation, p. 99–103.

Wilson, J.C., 1978, Ore fluid-magma relationships in a vesicular quartz latite porphyry dike at Bingham, Utah: Economic Geology, v. 73, p. 1287–1307.

Wilson, M.J., 1989, Igneous petrogenesis: London, Unwin Hyman, 466 p.

Wohletz, K.H., 1998, Pyroclastic surges and compressible two-phase flow, *in* Freundt, A., and Rosi, M., eds., From magma to tephra: Amsterdam, Elsevier, p. 247–312.

Woodcock, N.H., and Mort, K., 2008, Classification of fault breccias and related fault rocks: Geological Magazine, v. 145, p. 435–440.

Woodhead, J., Hergt, J., Sandiford, M., and Johnson, W., 2010, The big crunch: Physical and chemical expressions of arc/continent collision in the Western Bismarck arc: Journal of Volcanology and Geothermal Research, v. 190, p. 11–24.

Wright, A., 1983, The Ortiz gold deposit (Cunningham Hill)—Geology and exploration, *in* Krawl, V.E. et al., eds., Papers given at the precious-metals symposium: Sparks, Nevada Bureau of Mines and Geology, Report 36, p. 42–51.

Xu, Q., and Scott, S.D., 2005, Spherulitic pyrite in seafloor hydrothermal deposits: Products of rapid crystallization from mixing fluids, *in* Mao, J., and Bierlein, F.P., eds., Mineral deposit research: Meeting the global challenge, v. 1: Berlin, Springer, p. 711–713.

Yamagishi, H., 1987, Studies on the Neogene subaqueous lavas and hyaloclastites in southwest Hokkaido: Geological Survey of Hokkaido, Report 59, p. 55–117.

Yamagishi, H., 1991, Morphological features of Miocene submarine coherent lavas from the "Green Tuff" basins: Examples from basaltic and andesitic rocks from the Shimokita Peninsula, northern Japan: Bulletin of Volcanology, v. 53, p. 173–181.

Yamamoto, H., and Kennedy, G.C., 1969, Stability relations in the system $CaSO_4$–$H_2O$ at high temperatures and pressures: American Journal of Science, v. 267A, p. 550–557.

Zhu, Y., An, F., and Tan, J., 2011, Geochemistry of hydrothermal gold deposits: A review: Geoscience Frontiers, v. 2, p. 367–374.